PHASE TRANSITIONS, ANISOTROPY AND DOMAIN ENGINEERING: THE PIEZOELECTRIC PROPERTIES OF RELAXOR-FERROELECTRIC SINGLE CRYSTALS

THÈSE N^{O} 3513 (2006)

PRÉSENTÉE LE 19 MAI 2006

À LA FACULTÉ SCIENCES ET TECHNIQUES DE L'INGÉNIEUR

Laboratoire de céramique

SECTION DE SCIENCES ET GÉNIE DES MATÉRIAUX

ÉCOLE POLYTECHNIQUE FÉDÉRALE DE LAUSANNE

POUR L'OBTENTION DU GRADE DE DOCTEUR ÈS SCIENCES

PAR

Matthew DAVIS

Master of natural sciences, University of Cambridge, Royaume-Uni
et de nationalité britannique

acceptée sur proposition du jury:

Prof. H. J. Mathieu, président du jury
Prof. N. Setter, Dr D. Damjanovic, directeurs de thèse
Prof. I. Botsis, rapporteur
Prof. E. Cross, rapporteur
Prof. J. Trodahl, rapporteur

ÉCOLE POLYTECHNIQUE
FÉDÉRALE DE LAUSANNE

Suisse
2006

Abstract

Relaxor-ferroelectric single crystals PZN-*x*PT [(1-x)Pb($Zn_{1/3}Nb_{2/3}$)O_3-x$PbTiO_3$] and PMN-*x*PT [(1-x)Pb($Mg_{1/3}Nb_{2/3}$)O_3-x$PbTiO_3$] continue to attract much interest due to their anomalously large piezoelectric properties (d_{33} > 2000 pm/V; k_{33} > 90%) when poled ("domain-engineered") along a non-polar $[001]_C$ direction. In this thesis, the bulk dielectric, pyroelectric, ferroelectric and piezoelectric properties of single crystal PMN-xPT and PZN-xPT with morphotropic phase boundary (MPB) compositions are investigated.

The concept of "pseudo-rhombohedral" ("R") and "pseudo-orthorhombic" ("O") phases is introduced to encompass the rhombohedral, orthorhombic, and monoclinic (M_A, M_B and M_C) ferroelectric phases occurring in *poled* crystals; all bulk measurements are rationalized in this way. Poling in different orientations affects the thermal stabilities of the "R", "O" and tetragonal (T) phases, likely due to the presence of *residual bias fields*.

Phase diagrams are constructed for $[001]_C$-poled crystals based on bulk electrical measurements, which agree well with those derived elsewhere from diffraction experiments. Large pyroelectric coefficients ($< 1000\ \mu Cm^{-2}K^{-1}$) are evidenced in $[111]_C$-poled PMN-28PT; these might be exploitable in heat sensing and thermal imaging applications.

A "R" phase is induced *metastably* in otherwise pseudo-orthorhombic PZN-8PT by poling along the $[111]_C$ direction at sub-zero temperatures. The related *electric field induced* ("O" - "R") *phase transition* is evidenced in strain-field measurements and, *in situ*, by polarized light microscopy. Hysteresis, and discontinuities in polarization and strain, are due to nucleation and growth of the induced phase; this *first-order* phase transition corresponds to a discontinuous "jump" of the polar vector within the M_B plane.

Further electric-field induced phase transitions are evidenced in unipolar strain-field loops for $[001]_C$-poled PZN-xPT and PMN-xPT, with various MPB compositions, at temperatures between 25°C and 100°C. In PZN-6.5PT, PMN-30PT and PMN-30.5PT, the polarization rotation path "R" - "O" - T is evidenced by *two* first-order "jumps" in strains, one *between* the M_A and M_C monoclinic planes, and one *within* the M_C plane to the tetragonal phase. Electric field-temperature (*E*-*T*) phase diagrams are constructed from the experimental data; trends for the electrical stabilities of the "R", "O" and T phases are shown.

The (direct) piezoelectric response of $[001]_C$-poled PZN-4.5PT, PZN-6.5PT, PZN-8PT and PMN-31PT is investigated under compressive stresses both *along* and *perpendicular to* the poling direction (*longitudinal* d_{33} and *transverse* d_{31} modes, respectively). Dynamic measurements are made in a Berlincourt-type press, over a range of stresses (< 20 MPa) and temperatures (25 to 200°C). In the longitudinal mode, Rayleigh-law hysteresis and non-linearity indicates a significant *extrinsic* contribution from the irreversible (pinned) motion of *interfaces*, and likely ferroelastic domain walls; however, domain switching is not generally expected in domain engineered, pseudo-rhombohedral crystals. It is postulated that domain wall motion is driven by a local stress-induced phase transition, clearly evidenced in quasi-static,

charge-stress loops and *in situ* X-ray diffraction at larger stresses (< 100 MPa).

The reversible contribution to the response is always found to be larger than the irreversible (extrinsic) contribution in the "R" and "O" phases, the latter accounting for around 20% of d_{33} in PZN-8PT, at room temperature, and 5% in PZN-4.5PT. Both contributions are shown to increase upon heating towards the tetragonal phase; the increase in extrinsic contribution is likely due to increased domain wall mobility as the ferroelectric-ferroelectric phase transition temperature is approached.

In contrast, the transverse response of PMN-31PT and PZN-4.5PT is anhysteretic ("non-lossy") and linear at low stresses (< 10 MPa). This might be exploitable in sensing applications. The difference between the behaviors is likely related to differing directions of polarization rotation. In the transverse mode, rotation is *towards* the $[001]_C$ poling direction and the domain engineered structure is retained during the stress-induced phase transition.

Lastly, published monodomain properties are used to calculate the piezoelectric (d_{33}* and d_{31}*) coefficients of domain-engineered *3m* PMN-33PT and *mm2* PZN-9PT; both positive and negative transverse coefficients can be application tailored by domain-engineering. According to such calculations, *intrinsic crystal anisotropy* accounts for at least 50% of the "giant" piezoelectric response of polydomain, $[001]_C$-poled, PMN-33PT and PZN-9PT. Both compositions show inherently strong piezoelectric anisotropy ($d_{15}/d_{33} \gg 1$) in accordance with an "easy" *polarization rotation*. This is related to a high *dielectric anisotropy* ($\varepsilon_{11}/\varepsilon_{33}$) and the degeneracy of the "R", "O" and T phases near the MPB. Similar effects are observed in all ferroelectric perovskites, although the effect is *uncommonly* large in PMN-xPT and PZN-xPT: it is noted that *all* monodomain compliances, piezoelectric coefficients and permittivities are around an order of magnitude larger in PMN-xPT and PZN-xPT compared to their simpler perovskite relatives. This is likely a result of their background "relaxor" nature.

Finally, it is suggested that the presence of zero-field monoclinic phases in PMN-xPT and PZN-xPT is related to their inherently large piezoelectric response in the presence of residual stresses and bias fields, not the other way round as is commonly accepted.

Key words: ferroelectric, piezoelectric, dielectric, anisotropy, phase transitions.

Résumé

Les monocristaux de type relaxeur-ferroéléctrique PZN-*x*PT [(1-x)$Pb(Zn_{1/3}Nb_{2/3})O_3$-x$PbTiO_3$] et PMN-*x*PT [(1-x)$Pb(Mg_{1/3}Nb_{2/3})O_3$-x$PbTiO_3$] sont attirants à cause de leurs propriétés piézoélectriques élevées (d_{33} > 2000 pm/V; k_{33} > 90%) lorsqu'ils sont polarisés (« domain-engineered ») selon une direction $[001]_C$ non-polaire. Dans ce travail de thèse, les propriétés diélectriques, pyroélectriques, ferroélectriques et piézoélectriques des monocristaux de PMN-xPT et PZN-xPT avec des compositions proche de la *morphotropic phase boundary* (frontière de phase morphotropique, « MPB ») sont étudiées.

Le concept de phases « pseudo-rhomboédriques » ("R") et « pseudo-orthorhombiques » ("O") est introduit pour englober les phases ferroélectriques rhomboédriques, orthorhombiques et monocliniques (M_A, M_B et M_C) qui se trouvent dans les cristaux *polarisés*; toutes les données mesurées sont rationalisées dans cette manière. La polarisation en fonction de différentes orientations a l'effet de modifier les stabilités des phases "R", "O" et tétragonale (T), probablement à cause de la présence de *champs électriques résiduels*.

Des diagrammes de phases sont construits pour les cristaux polarisés selon $[001]_C$ après des mesures électriques, qui s'accordent avec ceux dérivés d'études de diffraction trouvées dans la littérature. Des coefficients pyroélectriques jusqu'à 1070 $\mu Cm^{-2}K^{-1}$ d'échantillons de PMN-28PT polarisés selon $[111]_C$ sont mesurés; il est possible que de telles propriétés soient exploitables dans des applications d'imagerie thermique et de détecteurs de chaleur.

Une phase "R" métastable est induite dans le PZN-8PT, qui est autrement pseudo-orthorhombique, en le polarisant selon $[111]_C$ à une température inférieure à 0°C. La transition de phase ("O" - "R") induite par le champ électrique se manifeste dans les mesures de déformation en fonction du champ et a été suivie, *in situ*, par microscopie à lumière polarisée. De l'hystérèse et des discontinuités dans la polarisation et la déformation découlent de la nucléation et croissance de la phase induite; cette transition de phase de premier ordre est liée à un « saut » discontinu du vecteur de polarisation dans le plan M_B.

D'autres transitions de phases sont observées dans des mesures de déformation en fonction du champ pour différentes compositions morphotropiques de PZN-xPT et PMN-xPT polarisés selon $[001]_C$, aux températures entre 25°C et 100°C. Pour PZN-6.5PT, PMN-30PT et PMN-30.5PT, la « chemin » de la rotation de la polarisation est "R" - "O" - T, évidente par la présence de *deux* « sauts » de déformation, indicatifs de transitions de premier ordre, la première *entre* les plans monocliniques M_A et M_C et la deuxième *dans* le plan M_C à la phase tétragonale. Les diagrammes de phases du champ électrique en fonction de la température (*E*-*T*) sont construits à partir des données expérimentales; les tendances des stabilités électriques des phases "R", "O" et T sont montrées.

La réponse piézoélectrique directe des PZN-4.5PT, PZN-6.5PT, PZN-8PT et PMN-31PT polarisés selon $[001]_C$ est étudiée sous contrainte compressive *le long de* la direction de polarisation ainsi que

perpendiculairement à celle-ci, respectivement les modes *longitudinal* (d_{33}) et *transverse* (d_{31}). Les mesures dynamiques sont accomplies dans une presse de type « Berlincourt », pour une gamme de contraintes (< 20 MPa) et températures (25 à 200°C). Dans le mode longitudinal, une hystérèse et la non-linéarité selon la loi de Rayleigh sont indicatifs d'une contribution *extrinsèque* du déplacement irréversible des *interfaces* et probablement des parois de domaines ferroélastiques; cependant, ce dernier n'est pas prévu à cause du stabilité de la structure « domain-engineered », au moins dans les cristaux pseudo-rhomboédriques. On postule que la force motrice pour le mouvement des parois de domaines est une transition de phase locale qui est nettement évidente dans des mesures quasi-statiques de charge en fonction de contrainte et dans une étude *in situ* de diffraction des rayons X aux contraintes plus élevées (< 100 MPa).

La contribution réversible de la réponse directe est toujours plus grande que la contribution irréversible (extrinsèque) dans les phases "R" et "O" ; cette dernière représente 20% du d_{33} pour le PZN-8PT, à température ambiante, et 5% pour le PZN-4.5PT. Les deux contributions croissent en augmentant la température vers la phase tétragonale; l'augmentation de la contribution extrinsèque provient probablement d'une augmentation de mobilité des parois de domaines.

Par contre, la réponse transverse des PMN-31PT et PZN-4.5PT non-hystérétique est linéaire aux basses contraintes (< 10 MPa), ce qui pourrait être exploitable dans des applications de détecteur. La différence entre ces comportements est probablement due aux différentes directions de rotation de la polarisation. Dans le mode transverse, la rotation est *vers* la direction $[001]_C$ et la structure « domain-engineered » est retenue pendant la transition de phase induite par la contrainte.

Les propriétés monodomaines publiées sont utilisées pour calculer les coefficients piézoélectriques (d_{33}* et d_{31}*) des PMN-33PT (*3m*) et PZN-9PT (*mm2*) « domain-engineered »; des coefficients transverses positifs et négatifs peuvent être façonnés par la méthode dite de « domain-engineering ». Selon de tels calculs, plus de 50% de la réponse piézoélectrique « géante » des PMN-33PT et PZN-9PT, polydomaines et polarisés selon $[001]_C$ est à cause de *l'anisotropie intrinsèque*. Les deux compositions montrent une anisotropie piézoélectrique très importante ($d_{15}/d_{33} \gg 1$) en accordance avec une rotation de polarisation très « facile ». Ceci est lié à une forte anisotropie *diélectrique* ($\varepsilon_{11}/\varepsilon_{33}$) et des énergies des phases "R", "O" et T très proches près de la MPB. Des effets similaires sont observés dans toutes les pérovskites ferroélectriques, sauf que pour les PMN-xPT et PZN-xPT l'effet est *extraordinairement* grand: il est à noter que *tous* les coefficients élastiques, piézoélectriques et diélectriques sont environ dix fois plus élevés dans PMN-xPT et PZN-xPT en comparaison avec les pérovskites plus simples. Ceci est probablement dû à leur caractère « relaxeur» caché.

Finalement, il est suggéré que la présence des phases monocliniques à champ électrique nul dans le PMN-xPT et le PZN-xPT est à cause de leur forte réponse piézoélectrique inhérente en présence de contraintes et champs résiduels, et non pas au phénomène inverse comme on le pense souvent.

Acknowledgements

Firstly, I would like to thank my thesis director, Professor Nava Setter, for kindly offering me a studentship at the Laboratory of Ceramics (LC), and for her many useful questions, suggestions and ideas during our regular meetings.

Above all, I would like to thank my thesis supervisor, Dr. Dragan Damjanovic, for all his guidance, wisdom and encouragement during my thesis work. I am indebted to him for originally suggesting such a fruitful and exciting research area, giving me all the tools I needed to carry out my work, and for giving me the freedom to look in many different directions while knowingly guiding me to what was important. I am thankful for all his kindness, patience and inspiration, and for teaching me so much.

I would like to thank everyone at LC for all their help over the last three and a half years both professionally and personally, especially in my early days in a foreign land. I would like to acknowledge: Dr. Abdolghaffar Barzegar for his finite element modeling, for building such a fine Berlincourt-type press and showing me how to use it, and for teaching me the skill of good design; Dr. Simon Bühlmann for his help with the deposition of transparent electrodes; Mr. Lino Olivetta for all his help with all things electronic and his constant good humor; Dr. Sandrine Gentil and Ms. Evelyn Hollenstein for their general help around the lab, especially in the beginning; Mr. Guido Gerra for his help with Mathematica and many questions physical; Dr. Vladimir Cherman for his help with all computer-related problems; Dr. Enrico Colla for his LabView automation of the press; and Dr. Marco Cantoni for his help with EDS analysis. I would also like to thank Prof. Alexandre Tagantsev and Prof. Paul Muralt for their useful comments at Lab. seminars. Not least, I would like to thank my partner-in-crime, Dr. Marko Budimir, for the many useful discussions about ferroelectrics and otherwise. Finally, thanks to the rest of the LC All-Stars: you know who you are!

I am grateful to all the members of the Materials Department workshop for building my designs to such perfection and for helpfully suggesting ways to improve them. I also gratefully acknowledge funding from the Swiss National Science Foundation. *Merci* to Mr. Didier Hayem for working so hard and doing such a good semester project with me.

I am also grateful to Mr. Pierre-Eymeric Janolin and Dr. Brahim Dkhil at l'Ecole Centrale de Paris for a very useful and enjoyable collaboration.

I would like to thank the members of my thesis jury: Prof. Hans Jörg Mathieu and Prof. Iaonnis Botsis from EPFL, and especially Prof. Eric Cross and Prof. Joe Trodahl for coming such a long way. Thanks again to Evelyn Hollenstein for correcting (rewriting!) the French version of my abstract.

I would also like to thank Prof. Andreas Mortensen at the Laboratory of Mechanical Metallurgy (LMM), EPFL for inviting me for an undergraduate summer placement in the summer of 2000; indeed, thanks to all the members of LMM for making my stay then so enjoyable. It not for you, I would never have come back to Lausanne.

Finally, thanks to my family and friends, wherever in the world you are, for all your love and support.

And especially to mum and dad. *You* wrote this.

Contents

List of common abbreviations and symbols

Abbreviation	Definition
T_d	Depoling temperature (see chapter four)
T_C	Curie temperature (or, better, “Curie point”)
T_m	Temperature of peak permittivity (see chapter four)
T_{FE-FE}	Temperature of a phase transition between two ferroelectric phases; see chapter six.
T_f	Freezing temperature (see chapter four)
T_B	Burns temperature (see chapter four)
σ	Stress /[MPa]
S	Strain /[%]
E	Electric field /[V/mm]
D	Electrical displacement field /[C/m^2]
P	Polarization /[C/m^2]
d_{ijk} (or d_{ij})	Piezoelectric coefficient /[pC/N] or [pm/V]
ε_{ij}	Relative permittivity (sometimes “dielectric constant”)
s_{ijkl}	Elastic compliance /[m^2N^{-1}]
FE	Ferroelectric
HRD	High resolution (neutron or X-ray) diffraction
XRD	X-ray diffraction
PLM	Polarized light microscopy (as explained in appendix III)
TEM	Transmission electron microscopy
SEM	Scanning electron microscopy
SFM	Scanning force microscopy (also known as atomic force microscopy, or “AFM”)
$[UVW]_C$	Lattice direction defined with respect to the pseudocubic unit cell (see appendix I)
$(hkl)_C$	Lattice plane defined with respect to the pseudocubic unit cell (see appendix I)
PMN-xPT	The lead manganese niobate - lead titanate solid solution $[(1-x)Pb(Mg_{1/3}Nb_{2/3})O_3\text{-}xPbTiO_3]$. “x” is the PT-content usually in mol. %; where it is given as an absolute fraction, the inferred value should be clear.
PZN-xPT	The lead zinc niobate lead titanate - solid solution $[(1-x)Pb(Zn_{1/3}Nb_{2/3})O_3\text{-}xPbTiO_3]$. “x” is the PT-content usually in mol. %; where it is given as an absolute fraction, the inferred value should be clear.
PZT	The lead zirconate titanate solid solution $[(1-x)PbZrO_3\text{-}xPbTiO_3]$

BT	Barium titanate, $BaTiO_3$
PT	Lead titanate, $PbTiO_3$
KN	Potassium niobate, $KNbO_3$
DW	Domain wall
4R, 4O etc.	Theoretical domain-engineered structures (defined in chapter five)
“4R”, “4O” etc.	Domain-engineered structures allowing for small monoclinic distortions of the high symmetry rhombohedral and orthorhombic phases: that is, domain-engineered “pseudo-rhombohedral” and “pseudo-orthorhombic” crystals (as defined in chapter six).
1T, 1O, 1R	Theoretical monodomain crystals (see chapter five)
“1T”, “1O”, “1R”	Quasi-monodomain structures which occur due to instability of the truly monodomain state
R, O, T, M_A, M_B, M_C	Rhombohedral, orthorhombic, tetragonal and monoclinic phases observed in the mixed-oxide ferroelectric perovskites (see appendix I)
EFIPT	Electric-field induced phase transition (see chapter seven)
CIPT	Chemically induced phase transition (as occur with changing PT contents in PMN-xPT and PZN-xPT)
SIPT	Stress induced phase transition (see chapter nine)
TIPT	Temperature induced phase transition (see chapter six)

Chapter one

Introduction

crystal n. and adj. n. **1 a** a clear transparent mineral, esp. rock crystal ... **5** *Chem.* **a** an aggregation of atoms or molecules with a regular internal structure and the external form of a solid enclosed by symmetrically arranged plane faces. **b** a solid whose constituent particles are symmetrically arranged... [from Greek *krustallos* 'ice, crystal'].

crystal clear 1 unclouded, transparent. **2** readily understood.

The Oxford English Dictionary

I. COMPLEX RELAXOR-FERROELECTRIC SINGLE CRYSTALS

We start with a brief history of piezoelectricity and technologically-applicable piezoelectric materials up to, and including, the recent resurgence of relaxor-ferroelectric single crystals.

Early piezoelectric single crystals

The *direct piezoelectric effect*, or the generation of electrical charge by an applied stress, was first discovered by the brothers Pierre and Jacques Curie in 1880, in a selection of crystals including cane sugar, topaz, and most notably, quartz. The *converse piezoelectric effect*, where a crystal is deformed by application of an electric field, was theoretically predicted the following year and confirmed experimentally by the Curie brothers soon afterwards.

After the first use of quartz crystals in underwater sensing applications during the First World War ("sonar" from "sound navigation and ranging"), interest in piezoelectrics centered solely on single crystals with special interest in finding new applications for quartz. However, although quartz is cheaply abundant, it also shows a comparatively weak piezoelectric effect and new higher performance materials were sought. These were to come from an important sub-class[1] of piezoelectric crystals, the *ferroelectrics*.

Barium titanate

One of the biggest turning points in the history of piezoelectricity was the discovery of ferroelectricity in mixed-oxide *perovskites*, abundant minerals with the chemical formula ABO_3. Ferroelectricity had previously been a scientific curiosity observed only in two chemically-unstable, water-soluble crystals, Rochelle salt and KDP (potassium dihydrogen phosphate). Then, during the Second World War, Arthur Von Hippel and coworkers identified ferroelectricity in barium titanate ($BaTiO_3$) ceramics[2]. Ferroelectricity would later be discovered in more perovskites, including potassium niobate ($KNbO_3$) and lead titanate ($PbTiO_3$)[3] and the era of piezoelectric ceramics was born.

Since that time mixed oxide ceramics have been used extensively in capacitors for their usefully-high dielectric properties; barium titanate still dominates the ceramic capacitor market. Moreover, ferroelectrics are inherently piezoelectric and the piezoelectric properties of "poled[3]" (i.e. remanently polarized) barium titanate were soon found to yield piezoelectric coefficients two orders of magnitude better than quartz. Barium titanate, therefore, offered vastly improved sensitivity over quartz in marine sensing applications; it has led in no small part to the dominance of the US Navy during and since World War Two[2].

Quartz did remain the material of choice for certain applications, including resonators and filters for radio transmitters and receivers, and for time-keeping. In the 1960s, there was a brief resurgence in interest in single crystal piezoelectrics with the advent of mixed oxide, lithium niobate ($LiNbO_3$) and lithium tantalate ($LiNbO_3$)[4-6]. Both were found to exhibit strong electro-

optic properties[4] useful for the modulation and second-harmonic generation of light[5]. They also showed good piezoelectric properties, with electromechanical coupling factors five times better than quartz, high mechanical quality factors, dielectric constants and hardness[4]. They were developed as replacements for quartz in many of the above applications and are still used today in specific applications that include surface acoustic wave (SAW) devices and oscillators, and in optics, where a large piezoelectric response is not critical[7].

Lead zirconate titanate (PZT)

In spite of this, poled mixed-oxide ceramics remained the norm, especially for transducer applications and in a growing number of other spin-off applications, both commercial and medical[2]. The next biggest development in piezoelectric ceramics came in the early 1950s with the discovery of ferroelectricity in "PZT" [$Pb(Ti_xZr_{1-x})O_3$], the solid solution formed between lead zirconate ($PbZrO_3$) and lead titanate; lead zirconate titanate, doped with various additives, has remained the dominant piezoelectric ceramic in transducer and actuator technologies ever since[8]. Critically, large piezoelectric coefficients were achieved in PZT in certain compositions close to the "morphotropic phase boundary". The phase diagram for PZT was refined over many years and the generally accepted version is that found in Jaffe, Cook and Jaffe (1971)[3]; it is reproduced here in figure 1.

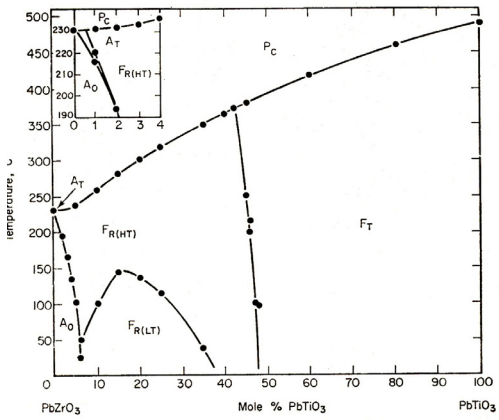

Fig. 1. The low temperature phase diagram for lead zirconate titanate (PZT) showing the cubic paraelectric phase and tetragonal and rhombohedral ferroelectric phases. Taken from Jaffe et al. (1971)[3].

The nearly vertical, or temperature-independent, phase boundary between the low lead-titanate content *3m* rhombohedral phase and the high lead-titanate content *4mm* tetragonal phase was termed the *morphotropic phase boundary* (MPB)[3], meaning literally "the boundary between two forms[9]". It is the most technologically significant part of the phase diagram with the strongest dielectric and piezoelectric coefficients being found at nearby compositions: piezoelectric coefficients (d_{33}) ranging from around 200 to 750 pm/V can be achieved with different dopants[10] compared to around 2 pm/V in quartz.

However, despite significant scientific interest, the exact nature of the MPB and the reason for its enhanced properties remained poorly understood. Various models were proposed including those of a finite region of two phase coexistence, where perhaps one phase is metastable, and a true boundary where the observed coexistence can be explained by unwanted compositional fluctuations[8]. It was believed that such a two-phase coexistence gave rise to stronger piezoelectric response in the poled ceramic due to "an increased ease of reorientation during poling[3]". That is, the coexistence of rhombohedral and tetragonal phases presented a greater number of possible domain variants and hence a better "polarizability".

Importantly, PZT proved nearly impossible to grow in single crystal form[11]. Because of this, and due to the technological prominence of PZT polycrystalline ceramics, research into single crystal piezoelectrics took a back seat.

Relaxor-ferroelectrics

In 1958 Smolenskii and Agranovskaya[12] reported unusual dielectric behavior in complex perovskites with the general formula $Pb(B',B'')O_3$, where B' is a low valence cation (e.g. Mg^{2+}, Ni^{2+}, Fe^{3+}) and B'' is a high valence cation (e.g. Nb^{5+}, Ta^{5+}, W^{6+}). Later named *relaxor-ferroelectrics*[13], these materials exhibited broad, diffuse peaks in permittivity at what was thought to be the phase transition between high- and low- symmetry phases, quite different to the sharp peak observed in the simpler perovskite ferroelectric, barium titanate[3]. Of such materials, lead magnesium niobate "PMN" [$Pb(Mg_{1/3}Nb_{2/3})O_3$] proved to be of most interest, having an anomalously high dielectric constant at room temperature just above a broad dielectric maximum at around 0°C[13,14].

In contrast to barium titanate, PMN retained an averagely cubic (*m3m*) symmetry down to around 5 K[15] and hence was not piezoelectric. However, it was found to exhibit a strong and usefully anhysteretic *electrostrictive* effect [Uchino et al. (1979)[16]] mainly due to the high polarizability of the relaxor state[17]. It was suggested that this could be exploited in specialized actuator and transducer applications such as micropositioners and adaptive optic systems where its relatively small thermal expansion coefficient would also be an advantage[17].

It was found that the dielectric constant of PMN could be increased by doping with another perovskite, lead titanate; addition of lead titanate, which transforms from its paraelectric phase at around 490°C[3], actually increased the phase transition temperature of PMN to above room temperature. Moreover, the electrostrictive coefficients of the resultant $(1-x)Pb(Mg_{1/3}Nb_{2/3})O_3$-$xPbTiO_3$ [PMN-xPT] solid solution were found to increase with increased PT content, with the strain remaining predominantly electrostrictive to around 13 mol.% PT[17].

In 1982, a new method for synthesis of ceramic PMN and other complex mixed oxide ceramics was devised by Swartz and Shrout, which greatly reduced the presence of unwanted pyrochlore phase[18]. Usefully large *pyroelectric* coefficients were also identified in poled PMN-xPT ceramics, which thus appeared a promising material for pyroelectric point detectors[19].

It was also discovered that, upon further addition of lead titanate to PMN-xPT, more "classical" ferroelectric behavior was observed. Upon poling samples of a large enough PT content, PMN-xPT assumed a rhombohedral (*3m*) ferroelectric phase, and therefore became piezoelectric. The entire phase diagram for PMN-xPT was subsequently mapped out for ceramic PMN-xPT[14,20] in 1989 revealing a morphotropic phase boundary between *3m* rhombohedral and *4mm* tetragonal phases very similar to that in PZT; it is shown in figure 2. Again, the piezoelectric coefficient and the relative permittivity peaked at the MPB, at around 700 pm/V and 5000, respectively[20].

Relaxor-ferroelectric single crystals

The useful properties of relaxor-ferroelectric *single crystals* were first reported by Nomura and coworkers around the early 1970s. This time, the solid solution involved was based on another (albeit related) relaxor, lead zinc niobate "PZN" [$Pb(Zn_{1/3}Nb_{2/3})O_3$]; PZN exhibits a diffuse phase transition closer to 100°C and is rhombohedral when poled at room temperature[21]. Although polycrystalline samples were difficult to synthesize[22], single crystals of the lead zinc niobate lead titanate solid solution [$(1-x)Pb(Zn_{1/3}Nb_{2/3}O_3$-$xPbTiO_3$ or "PZN-xPT"] could be readily grown by a flux method. The solution exhibited a morphotropic phase boundary, very similar to that in PZT and PMN-xPT, between rhombohedral and tetragonal phases at around 9 wt.% $PbTiO_3$; it is also shown in figure 2. Again, as in PZT and PMN-xPT ceramics, dielectric and piezoelectric properties were found to peak close to this phase boundary.

In the early 1980s, Nomura revisited PZN-xPT[23,24]. Single crystals were grown and oriented along both $[111]_C$ and $[001]_C$ directions[25]. Although modest piezoelectric coefficients were found in $[111]_C$-poled crystals, "giant" d_{33} coefficients > 1500 pm/V were measured in rhombohedral compositions near the MPB, *cut and poled along the non-polar* $[001]_C$ *direction*.

Critically, such behavior might have been unexpected by users of poled ceramic piezoelectrics[3] where properties are always measured, necessarily, along the polar (poling) axis and values of around 700 pm/V are achieved[20]. Notably, the authors [Kuwata et al. (1982)[24]] explained the discrepancy between polar and non-polar orientations by a strong *crystal anisotropy*, as might be expected from basic property-symmetry relationships in crystalline materials[1] and, especially, the large piezoelectric shear coefficient d_{15} of the monodomain $[111]_C$-oriented crystal.

Likewise, studies of the PMN-xPT solution had hitherto only been carried out on polycrystalline samples when, in 1990, Shrout et al. published a series of measurements on flux-grown crystals with a range of compositions close to the MPB ($0.3 \le x \le 0.4$)[26]. Similar to the findings of Kuwata et al., the largest piezoelectric coefficients and dielectric constants were observed in rhombohedral crystals with MPB compositions oriented along the *non-polar* $[001]_C$ direction. A piezoelectric coefficient d_{33} of 1000-1500 pm/V was reported for $[001]_C$-poled PMN-30PT, around five times higher than that measured along the $[111]_C$ polar axis (300 pm/V), and twice as high as that

measured in poled ceramics. A new dawn for piezoelectric crystals was nearing.

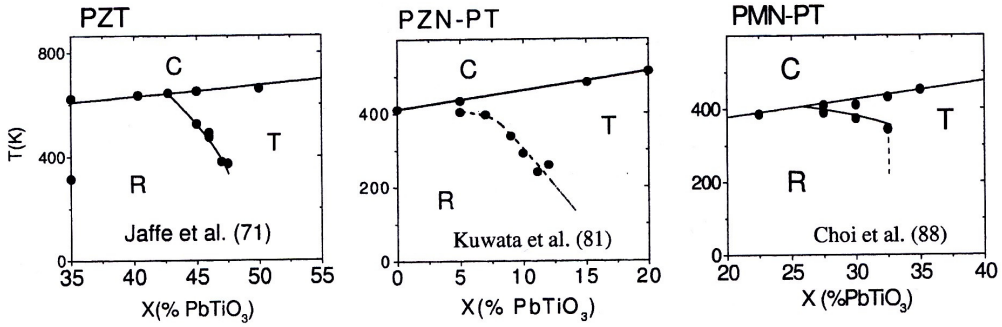

Fig. 2. Partial phase diagrams for the PZT, PZN-xPT and PMN-xPT solid solutions as commonly accepted in 1990. Taken from Jaffe et al. (1971)[3], Kuwata et al. (1981)[23] and Choi et al. (1989)[14].

A new era of relaxor-ferroelectric single crystals

In 1997, Park and Shrout[7] reported a series of systematic measurements of the piezoelectric properties of PMN-xPT and PZN-xPT single crystals cut and poled along a variety of different crystallographic directions. Not only were piezoelectric coefficients (d_{33} > 2500 pm/V) and electromechanical coupling factors (k_{33} < 0.94) highest in <001>$_C$-oriented rhombohedral crystals, *anhysteretic* strain-field responses were also observed.

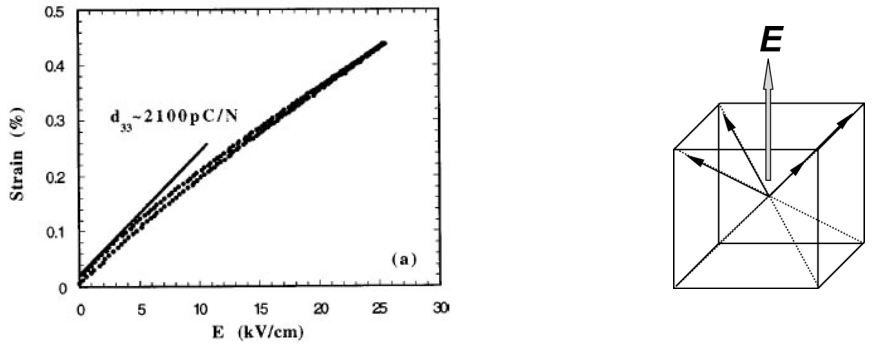

Fig. 3. Characteristic converse piezoelectric response to an unipolar electric field in a $[001]_C$-oriented sample of PZN-4.5PT [taken from Liu et al. (1999)[27]].

One of the main drawbacks of PZT is that to achieve the highest piezoelectric coefficients, doping with additives is needed[3]; the strain-field loops in such "soft" PZT ceramics are characteristically *hysteretic* due to a large *extrinsic* contribution, typically from domain wall motion[28], resulting in poor positioning accuracy, high dielectric loss and hence significant heat generation during use[7]. Although the piezoelectric response to a unipolar electric field applied along the polar $[111]_C$ direction was found to be weak and hysteretic, anhysteretic strains < 0.6% were observed in $[001]_C$-poled samples of rhombohedral "PZN-8PT". Similarly attractive behavior was

observed in rhombohedral PZN-4.5PT, as shown in figure 3, indicative of little extrinsic, domain wall contribution to the piezoelectric response.

The absence of domain wall motion was explained by the stable domain structure formed by poling a rhombohedral crystal, containing eight possible ferroelectric *domain variants*[29,30] (*or orientation states*) with spontaneous polarization vectors $\boldsymbol{P_s}$ along the <111>$_C$ directions, along a non-polar <001>$_C$ direction. For example, when a sufficiently strong electric field is applied along the [001]$_C$ direction, four degenerate domain variants will be stabilized, with polar vectors along the [111]$_C$, [1$\bar{1}$1]$_C$, [$\bar{1}$11]$_C$ and [$\bar{1}\bar{1}$1]$_C$ directions. This is also shown in figure 3. Subsequent application of an applied field to this *engineered-domain*[7] structure will not favor any further domain wall motion: the polar vectors in each domain variant will simply rotate continuously towards the direction of applied field (*polarization rotation* or "inclination[7]") as shown in figure 4.

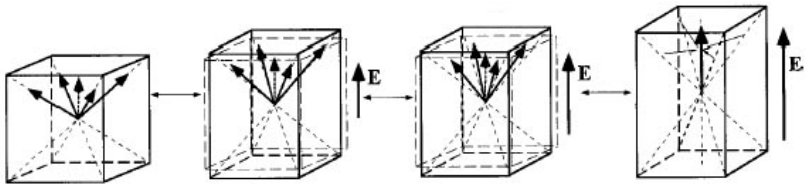

Fig. 4. Piezoelectric response of the domain engineered structure in [001]$_C$-poled rhombohedral crystals of PMN-xPT and PZN-xPT to subsequent application of an electric field along [001]$_C$. Taken from Liu et al. (1999)[27].

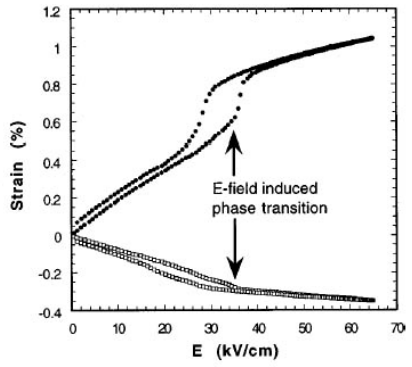

Fig. 5. Longitudinal and transverse electric field induced strains in a [001]$_C$-oriented sample of PZN-4.5PT evidencing an electric field induced phase transition to a tetragonal phase. Taken from Liu et al. (1999)[27].

Then, at a sufficiently high electric-field, an *electric-field induced phase transition* to a tetragonal phase will occur where all polarizations "collapse into the [001]$_C$ direction[7]". This too was evident in hysteretic strain-field loops at high fields, indicative of a first order, rhombohedral-to-tetragonal phase transition, as shown in figure 5. A subsequent *in situ* X-ray diffraction study by Durbin et al. (1999)[31] showed that the hysteretic strain observed in such high-field strain loops for [001]$_C$-oriented PZN-8PT was well reflected in the deformation of the crystal lattice and, therefore, almost entirely *intrinsic* in nature. This was further evidence of the inherent stability of the domain engineered structure.

New monoclinic phases and polarization rotation

At around the same time, something quite unexpected happened: a monoclinic phase was observed by high resolution X-ray diffraction in morphotropic phase boundary PZT (with a PT content of 48 mol.%) just below room temperature [Noheda et al. (1999)[32]]. After further investigation of other compositions, the monoclinic phase was subsequently found to occupy a narrow "triangle[8]" in between the rhombohedral and tetragonal phase fields of figure 1. At 20 K, the monoclinic phase was found for compositions $0.46 \leq x \leq 0.51$ [Noheda et al. (2000)[9]]. Critically, in this ferroelectric monoclinic phase of space group *Cm* (later named "M_A")[33], the only remaining symmetry element is a single $\{1\bar{1}0\}_C$ mirror plane. Therefore, instead of being fixed to lie along a single direction, the polar vector $\boldsymbol{P_S}$ is free to rotate within this plane between $[111]_C$ and $[001]_C$ limiting directions[34]; this can be seen in figure 6.

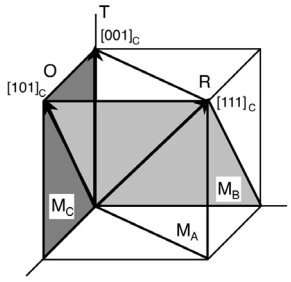

Fig. 6. Mirror planes of the monoclinic phases recently discovered at the morphotropic phase boundaries of PZT, PMN-xPT and PZN-xPT. The polar axes of the monoclinic phases are not fixed but are free to rotate within their mirror plane between the limiting directions of the rhombohedral (R), orthorhombic (O) and tetragonal (T) phases. The notation is that according to Vanderbilt and Cohen (2001)[33].

Du et al. had already shown using phenomenological Landau-Ginzburg-Devonshire theory[35] that in PZT, as in PZN-xPT and PMN-xPT, the highest piezoelectric properties were expected for $<001>_C$-oriented rhombohedral crystals with compositions close to the morphotropic phase boundary. Again, as observed for PZN-xPT and PMN-xPT single crystals, much smaller piezoelectric coefficients were predicted for crystals oriented along the $<111>_C$ polar axis. Although this result could not be confirmed experimentally (due to the lack of adequately-sized PZT single crystals[11]), as suggested experimentally by Park and Shrout[7], a large piezoelectric response did seem to be generated by a "*polarization rotation*" mechanism where the polarization vector rotates continuously towards an electric field applied off-axis. Suddenly, the newly found M_A monoclinic phase in PZT seemed to lend a mechanism for this rotation: i.e. the monoclinic plane acts as a "*structural bridge*[8]", facilitating the polarization rotation, therefore leading to enhanced piezoelectric properties in PZT around the morphotropic phase boundary.

Further support for the importance of polarization rotation came from *in situ* X-ray diffraction study of PZT ceramics under an applied electric field

[Guo et al. (2000)[36]]. The results showed that even in averagely-oriented polycrystalline PZT, in both tetragonal and rhombohedral MPB phases, the piezoelectric distortion of the unit cell is most strongly due to rotation of the polarization vector, not its elongation. Then, in 2000, first principles calculations by Fu and Cohen[37] showed explicitly that in rhombohedral barium titanate (at 0 K), under an electric field applied along the $[001]_C$ direction, "a large piezoelectric response could be driven by polarization rotation". Similar was later shown by the *ab initio* calculations of Bellaiche et al. (2001)[38] for the tetragonal and rhombohedral phases of PZT. According to these calculations, the polarization vector can also rotate continuously within the monoclinic plane as a function of composition[8], as well as upon application of a field. A breakthrough seemed to have been made: the monoclinic phase forms a convenient structural bridge across the first order, morphotropic phase boundary in PZT and also explains the elevated piezoelectric response found there[8].

Even more support for this model came from the theoretical work of Vanderbilt and Cohen[33] (2001). Previous phenomenological theories disallowed the presence of a monoclinic phase[8] although a fuller expansion of the Landau-Ginzburg-Devonshire free energy function[39] to eighth-order (as opposed to a standard sixth[35]) was found to predict not only one monoclinic phase but two, alongside the rhombohedral (R), orthorhombic (O) and tetragonal (T) phases found in barium titanate[3]. The second monoclinic phase had space group *Cm*, this time with the $\{010\}_C$ mirror plane its only remaining symmetry element. This phase, named "M_C", is also shown in figure 6. Its polar vector is constrained to lie within the $\{010\}_C$ plane between tetragonal and orthorhombic limiting directions: therefore, the orthorhombic phase is, in fact, the limiting case of M_C phase and might be termed "pseudomonoclinic[8]". A "universal phase diagram[40]" was proposed showing phase-fields for all five symmetries, R, O, T, M_A and M_C, linked by various polarization rotation "paths[8]"; the simplest of such paths, R - M_A - T, path can be seen quite easily in figure 6.

It was only a matter of time before monoclinic phases were also discovered at the MPBs in PMN-xPT and PZN-xPT. Intriguingly, it was not the M_A phase that was found but M_C. Many high resolution (X-ray and neutron) diffraction studies[8] were carried out in single crystals, ceramics and ground powders and strong evidence was found for an intermediate M_C phase in both poled[41,42] and unpoled[43,44] samples. The monoclinic phase was also clearly identified by optical microscopy in PMN-xPT [Bokov and Ze (2002)[45]] and new phase diagrams were soon published for PZN-xPT [La-Orauttapong et al. (2002)[42]] and PMN-xPT [Noheda et al. (2002)[43]] based on the new measurements. Later X-ray diffraction work by Singh and Pandey[44,46] gave evidence for the presence of an M_A phase alongside the M_C phase in the PMN-xPT solid solution, suggesting a R - M_A - M_C - T progression with increasing PT content. This too has very recently been confirmed by careful optical microscopy [Zekria et al. (2005)[47]]. More *in situ* diffraction studies evidenced the same R - M_A - M_C - T polarization rotation path upon application of an electric field along the $[001]_C$ direction of MPB rhombohedral crystals[8,48-50], the M_C phase often being induced irreversibly.

Present paradigm

The phase diagrams of PMN-xPT and PZN-xPT remain the matter of some debate, especially since the phase present in the material can often be altered irreversibly be poling, and sometimes differently depending on the direction of the applied field[51,52]. In many cases, poling of the crystals is in fact necessary before structural investigation to induce long range ferroelectric order in the materials, a consequence of their background "relaxor" nature which will be discussed further in chapter four. However, at the beginning of this thesis it is worth summarizing the generally accepted paradigm for the origin of the "giant" piezoelectric response of relaxor-ferroelectric single crystals. The commonly accepted belief is that:

> *Polarization rotation, in the presence of one or more monoclinic phases, is responsible for the "giant" piezoelectric properties in PMN-xPT and PZN-xPT single crystals with morphotropic phase boundary compositions, when oriented and poled along a non-polar <001>$_C$ direction.*

There has up until now been few or perhaps only one[53] audible critic of this explanation. In this thesis work, a slightly different perspective will be presented.

II. THESIS SUMMARY

A summary of this thesis is as follows. In chapter two, the main experimental methods used in this thesis work are explained. A novel "Berlincourt-type" press, built in-house for measurement of the direct (charge-stress) piezoelectric effect in bulk piezoelectrics, is described. Descriptions are also given of two apparatuses, built especially as part of this work, for converse (strain-field) piezoelectric measurements.

The commercially-supplied single crystals used in this work are listed in chapter three. The quality of these samples are assessed in terms of orientation and compositional homogeneity and notes are given about sample preparation, i.e., crystal handling, polishing, electroding, and annealing. Included is a brief review of the methods used to grow single crystals of PMN-xPT and PZN-xPT.

In chapter four, the phase diagrams of the relaxor-ferroelectric solid solutions PMN-xPT and PZN-xPT are reviewed, paying special attention to the position and nature of the high- to low- symmetry transition temperature from the paraelectric phase. Using a wide variety of data, the transition temperature is determined as accurately as possible as a function of composition. The use of this data to back-calculate the composition of as-grown crystals is discussed. Finally, an overview is given of the complex physical behavior of relaxor-ferroelectric crystals, and the various models used to describe them.

In chapter five, the room temperature, microstructural features of PMN-xPT and PZN-xPT single crystals are investigated by polarized light

microscopy (PLM). Domain wall structures in both poled and unpoled conditions are discussed. The concept of domain engineering is explained.

In chapter six, measurements of the dielectric, pyroelectric and ferroelectric properties of PMN-xPT and PZN-xPT are presented, in both poled and unpoled conditions. Based on the measurements, updated phase diagrams are drawn up showing the phase stabilities of the ferroelectric phases in *[001]$_C$-poled* crystals close to the MPB. Potentially useful pyroelectric properties are evidenced in rhombohedral crystals oriented and poled along polar <111>$_C$ directions.

In chapter seven, various electric-field induced phase transitions are evidenced in PMN-xPT and PZN-xPT macroscopically, by strain-field measurements, and *in situ* using polarized light microscopy. From the measurements, electric field-temperature phase diagrams are constructed showing the various stabilities of the differing MPB phases. Conclusions are made about the *order* of the phase transitions and how this is important to the concept of the monoclinic phase as a *zero-field phase*.

In the next two chapters, novel measurements of the direct (charge-stress) effect in PMN-xPT and PZN-xPT are presented. In chapter eight, measurements of the longitudinal (d_{33}) and transverse (d_{31}) piezoelectric coefficients, respectively, are made under dynamic stresses (< 20 MPa). The non-linearity of the two coefficients as a function of frequency and amplitude is investigated. The variation of the dynamic, direct piezoelectric response with temperature and sample orientation is investigated in chapter nine. Finally, stress-induced phase transitions are evidenced under larger (< 100 MPa), quasi-static stresses. Their relevance to the small-stress, dynamic response is discussed.

Finally, the importance of intrinsic *crystal anisotropy* to the large piezoelectric response in [001]$_C$-poled PMN-xPT and PZN-xPT is addressed in chapter ten. The extent of any *extrinsic* contribution to the dielectric, piezoelectric and elastic properties of various domain engineered perovskites, including PMN-33PT and PZN-9PT, is also quantified. The origins of large piezoelectric anisotropy in perovskite ferroelectrics is discussed. Lastly, the importance of crystal anisotropy to the transverse piezoelectric coefficient in domain engineered crystals and ceramics is investigated in chapter eleven.

The thesis is concluded in chapter twelve.

III. REVIEW AND SYNTHESIS

Along with presenting new results, this work also aims to review, as far as is relevant, the vast body of work already published in the field. Literally hundreds of articles have appeared on the properties and structure of PMN-xPT and PZN-xPT since their “rediscovery” in 1997 and it is now becoming more and more difficult to keep abreast of all the collected knowledge in the field. One of the major problems is that the articles have come from many differing perspectives: crystallographers have presented important high resolution X-ray and neutron diffraction data on the crystalline structure of PMN-xPT and PZN-xPT at the Angstrom scale; microscopists have published transmission electron microscopy (TEM), atomic force microscopy (SFM) and polarized light microscopy (PLM) images of their microstructure at the

nanometer and micron scale; and specialists in ferroelectric and piezoelectrics have reported bulk, macroscopic measurements of their dielectric, pyroelectric, ferroelectric and piezoelectric properties. Furthermore, these studies have been made: for a variety of crystal compositions in both poled and virgin states; for various crystallographic orientations; at zero field and under electrical bias; under various mechanical stresses for varying loading geometries; at various temperatures from high above the Curie point to cryogenic temperatures; and, finally, on crystals with various thermal, electrical and mechanical histories. Few authors have made systematic studies over a range of compositions; fewer still have combined bulk characterization, microstructural and high-resolution diffraction studies together. In many ways, therefore, researchers in the field are like the protagonists in the parable of the four blind men and the elephant:

> *Four blind men encounter an elephant. One grabs the leg and concludes it is a tree trunk. One holds the tail thinking it is a whip. Another touches the elephant's trunk and decides it's a hose and the fourth man pats the side concluding it's a wall.*

All are right, of course, though none completely. We have yet to picture the whole beast.

REFERENCES

1 J. F. Nye, *Physical properties of crystals*, 2nd ed. (Clarendon Press, Oxford, 1985).

2 R. E. Newnham and L. E. Cross, MRS Bulletin **30,** 845-848 (2005).

3 B. Jaffe, W. R. Cook, and H. Jaffe, *Piezoelectric Ceramics* (Academic Press, 1971).

4 R. T. Smith, Appl. Phys. Lett. **11,** 146-148 (1967).

5 T. Yamada, H. Iwasaki, and N. Niizeki, Jpn. J. Appl. Phys. **8,** 1127-1132 (1969).

6 A. W. Warner, M. Onoe, and G. A. Coquin, J. Acoust. Soc. Am. **42,** 1223-1231 (1966).

7 S.-E. E. Park and T. R. Shrout, J. Appl. Phys. **82,** 1804-1811 (1997).

8 B. Noheda, Current Opinion in Solid State and Materials Science **6,** 27-34 (2002).

9 B. Noheda, D. E. Cox, G. Shirane, R. Guo, B. Jones, and L. E. Cross, Phys. Rev. B **63,** 014103 (2000).

10 S.-E. Park and T. R. Shrout, Mat. Res. Innovat. **1,** 20-25 (1997).

11 X. Liu, E. F. McCandlish, L. E. McCandlish, K. Mikulka-Bolen, R. Ramesh, F. Cosandey, J. George A. Rossetti, and R. E. Riman, Langmuir **21,** 3207-3212 (2005).

12 G. A. Smolenskii and A. I. Agranovskaya, Sov. Phys. Solid State**,** 1429-(1959).

13 L. E. Cross, Ferroelectrics **76,** 241-267 (1987).

14 S. W. Choi, T. R. Shrout, S. J. Jang, and A. S. Bhalla, Materials Letters **8,** 253-255 (1989).

[15] A. Lebon, H. Dammak, G. Calvarin, and I. O. Ahmedou, J. Phys.: Condens. Matter **14,** 7035-7043 (2002).
[16] K. Uchino, S. Nomura, L. E. Cross, S. J. Jang, and R. E. Newnham, J. Appl. Phys. **51,** 1142-1145 (1980).
[17] S. J. Jang, K. Uchino, S. Nomura, and L. E. Cross, Ferroelectrics **27,** 31-34 (1980).
[18] S. L. Swartz and T. R. Shrout, Materials Research Bulletin **17,** 1245-1250 (1982).
[19] D. J. Taylor, D. Damjanovic, and A. S. Bhalla, Ferroelectrics **118,** 143-155 (1991).
[20] S. W. Choi, T. R. Shrout, S. J. Jang, and A. S. Bhalla, Ferroelectrics **100,** 29-38 (1989).
[21] M. L. Mulvihill, L. E. Cross, W. Cao, and K. Uchino, J. Am. Ceram. Soc **80,** 1462-1468 (1997).
[22] D.-H. Lee and N.-K. Kim, Materials Letters **34,** 299-304 (1998).
[23] J. Kuwata, K. Uchino, and S. Nomura, Ferroelectrics **37,** 579-582 (1981).
[24] J. Kuwata, K. Uchino, and S. Nomura, Jpn. J. Appl. Phys. **21,** 1298-1302 (1982).
[25] Throughout this thesis all crystalline lattice vectors will be expressed with respect to pseudocubic unit cell.
[26] T. R. Shrout, Z. P. Chang, N. Kim, and S. Markgraf, Ferroelectrics Letters **12,** 63-69 (1990).
[27] S.-F. Liu, S.-E. Park, T. R. Shrout, and L. E. Cross, J. Appl. Phys. **85,** 2810-2814 (1999).
[28] D. Damjanovic, J. Am. Ceram. Soc **88,** 2663-2676 (2005).
[29] J. Erhart, Phase Transitions **77,** 989-1074 (2004).
[30] J. Fousek and V. Janovec, J. Appl. Phys. **40,** 135-142 (1969).
[31] M. K. Durbin, E. W. Jacobs, and J. C. Hicks, Appl. Phys. Lett. **74,** 2848-2850 (1999).
[32] B. Noheda, D. E. Cox, G. Shirane, J. A. Gonzalo, L. E. Cross, and S.-E. Park, Appl. Phys. Lett. **74,** 2059-2061 (1999).
[33] D. Vanderbilt and M. H. Cohen, Phys. Rev. B **63,** 094108 (2001).
[34] R. E. Newnham, *Properties of materials* (Oxford University Press, Oxford, 2005).
[35] M. J. Haun, E. Furman, S. J. Jang, and L. E. Cross, Ferroelectrics **99,** 13-25 (1989).
[36] R. Guo, L. E. Cross, S.-E. Park, B. Noheda, D. E. Cox, and G. Shirane, Phys. Rev. Lett. **84,** 5423-5426 (2000).
[37] H. Fu and R. E. Cohen, Nature **403,** 281-283 (2000).
[38] L. Bellaiche, A. Garcia, and D. Vanderbilt, Phys. Rev. B **64,** 060103(R) (2001).
[39] M. E. Lines and A. M. Glass, *Principles and applications of ferroelectrics and related materials* (Clarendon Press, Oxford, 1977).
[40] D. E. Cox, B. Noheda, G. Shirane, Y. Uesu, K. Fujishiro, and Y. Yamada, Appl. Phys. Lett. **79,** 400-402 (2001).
[41] Z.-G. Ye, B. Noheda, M. Dong, D. Cox, and G. Shirane, Phys. Rev. B **64,** 184114 (2001).
[42] D. La-Orauttapong, B. Noheda, Z.-G. Ye, P. M. Gehring, J. Toulouse, D. E. Cox, and G. Shirane, Phys. Rev. B **65,** 144101 (2002).

[43] B. Noheda, D. E. Cox, G. Shirane, J. Gao, and Z.-G. Ye, Phys. Rev. B **66,** 054104 (2002).
[44] A. K. Singh and D. Pandey, Phys. Rev. B **67,** 064102 (2003).
[45] A. A. Bokov and Y.-G. Ye, Phys. Rev. B **66,** 094112 (2002).
[46] A. K. Singh and D. Pandey, Phys. Rev. B **68,** 172103 (2003).
[47] D. Zekria, V. A. Shuvaeva, and A. M. Glazer, J. Phys.: Condens. Matter **17,** 1593-1600 (2005).
[48] B. Noheda, D. E. Cox, G. Shirane, S.-E. Park, L. E. Cross, and Z. Zhong, Phys. Rev. Lett. **86,** 3891 (2001).
[49] B. Noheda, Z. Zhong, D. E. Cox, G. Shirane, S.-E. Park, and P. Rehrig, Phys. Rev. B **65,** 224101 (2002).
[50] K. Ohwada, K. Hirota, P. W. Rehrig, P. M. Gehring, B. Noheda, Y. Fujii, S.-E. Park, and G. Shirane, J. Phys. Soc. Jpn. **70,** 2778-2783 (2001).
[51] F. Bai, N. Wang, J. Li, D. Viehland, P. M. Gehring, G. Xu, and G. Shirane, J. Appl. Phys. **96,** 1620-1627 (2004).
[52] H. Cao, F. Bai, N. Wang, J. Li, D. Viehland, G. Xu, and G. Shirane, Phys. Rev. B **72,** 064104 (2005).
[53] E. H. Kisi, R. O. Piltz, J. S. Forrester, and C. J. Howard, J. Phys.: Condens. Matter **15,** 3631-3640 (2003).

Chapter two

Experimental techniques

In this chapter, the techniques used to measure the dielectric, piezoelectric, pyroelectric and ferroelectric properties of PMN-xPT and PZN-xPT are described. Three experimental methods specific to this thesis work are discussed in detail. Firstly, two techniques for measuring electric-field induced strains are discussed, the first based on a magnetic induction technique and the second based on reflected light. Secondly, an in-house built, Berlincourt-type press used for sophisticated measurement of the direct piezoelectric effect is presented.

I. STANDARD EXPERIMENTAL TECHNIQUES

For all electrical techniques, samples were prepared in *parallel-plate capacitor* geometry. Electrodes were sputtered onto the two largest parallel surfaces of a cuboid sample, with geometry defined by the surface area of the electrodes A and the distance between them (or thickness) t. For such geometry, the capacitance of the sample C is related to the dielectric permittivity by:

$$C = \frac{\varepsilon_0 \varepsilon A}{t} \qquad [1]$$

where ε is the *relative permittivity* in the direction perpendicular to the electrodes, or the *dielectric constant*, and ε_0 is the permittivity of free space ($8.8514 \times 10^{-12} F/m$).

Pyroelectric measurements

To determine the usefulness of a polar material for pyroelectric applications such as heat sensors and thermal imagers, any figure of merit must contain the pyroelectric coefficient[1] p. Measurement of the pyroelectric coefficient can also be used to check if a ferroelectric material has been well poled (in unpoled materials p is generally small or zero). Furthermore, pyroelectric measurement can be used to check for polarity in unpoled crystals or ceramics or its direction, in poled samples, wherever it is unknown. The pyroelectric properties of PMN-xPT and PZN-xPT single crystals are discussed in chapter six.

The free pyroelectric effect (at constant stress[2]) can be written as:

$$dD_i = p_i^{\sigma} dT \qquad [2]$$

where D_i is the electric displacement field[3,4], T is the temperature and p_i^{σ} are the components of the rank-one[2] pyroelectric tensor or vector $\boldsymbol{p}$. At constant electric field (short-circuited conditions[2]), we can write:

$$dP_i = p_i^{\sigma} dT \quad \text{or} \quad p_i^{\sigma} = \left(\frac{\partial P_i}{\partial T} \right)_{\sigma} \qquad [3]$$

where P_i is the *polarization* of the crystal. The change in polarization can be related to a surface charge Q distributed over the sample surface (area A); that is, $dP = \pm(dQ/A)$, where dP is the component of $d\boldsymbol{P}$ perpendicular to the electrodes. The pyroelectric coefficient is thus:

$$p = \frac{1}{A} \left(\frac{\partial Q}{\partial T} \right)_{\sigma} \qquad [4]$$

The flow of this charge into an external circuit is known as the pyroelectric current i_p. In terms of the rate of change of temperature and the pyroelectric current, we can write the pyroelectric coefficient as:

$$p = \frac{i_p}{A\left(\frac{dT}{dt}\right)} \qquad [5]$$

The conventional units for *p* are $\mu C m^{-2} K^{-1}$.

The traditional method for measuring *p* is the *Byer-Roundy* technique[5,6]. Here, the sample temperature is ramped at a constant rate (*dT/dt*) whilst measuring the thermally-stimulated current, *i*, flowing between the electrodes. The pyroelectric coefficient is then calculated via equation [5] assuming that *i* is solely due to the pyroelectric effect. The spontaneous polarization can be calculated via subsequent integration.

The main problem with this method is that it is impossible to distinguish between the reversible pyroelectric current and the irreversible thermally stimulated current, which is not necessarily pyroelectric in origin[5]. This can lead to large errors in *p*.

For this thesis work a different technique, a temperature-oscillation (or *dynamic*) method, was used to measure the pyroelectric coefficient. The setup used is similar to that described by Dalglish (1998)[5]. During the measurement, the temperature of the sample is modulated by a Peltier element in a regular periodic fashion (a triangular wave), whilst the current waveform is recorded. The temperature is regulated by a thermocouple positioned close to that sample and a feed-back mechanism; a thermometer is used to measure the sample temperature. The temperature is cycled at a low frequency (around 10 mHz) with a peak-to-peak amplitude of 1 K. The sample sits on the Peltier element while the top connection is made with a brass spring and the current signal is first converted, electronically, to a voltage and then amplified.

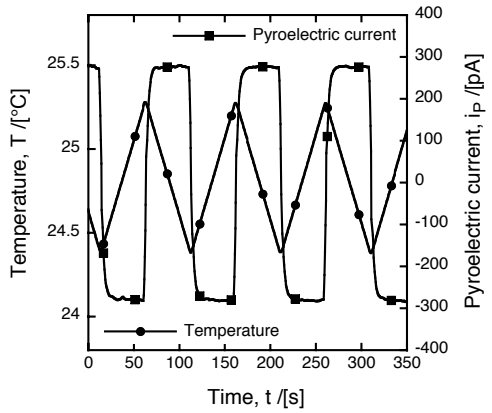

Fig. 1. Typical pyroelectric current response to an applied triangular temperature waveform for a sample of single crystal PMN-xPT.

The pyroelectric current response is a distorted square wave signal, as shown in figure 1; the phase of the response signal shown would change by

180˚ if the sample were placed upside down (with reverse polarity). The entire setup is controlled automatically by a computer running a LabView[7] program, which also records all data. The program performs a Fourier-transform to find the amplitude of the fundamental square wave current response, i_p. p is then calculated via equation [5]. For improved accuracy, pyroelectric coefficients from multiple cycles can be taken and averaged.

During any measurement of the pyroelectric effect it is important that temperature be uniform: thin plates samples of maximum thickness 0.5 mm were therefore used. If temperature gradients result in a sample from non-uniform heating, a "tertiary" pyroelectric effect can arise, which will render even non-polar crystals pyroelectric and lead to erroneous measurements of p[5].

Ferroelectric properties: hysteresis loops

Ferroelectric materials can be characterized by measuring their *polarization* P as a function of applied AC electric field: that is, by measurement of the charge-field, or *P(E), hysteresis loop*[8,9]. Evidence of a hysteresis is sometimes taken as evidence of ferroelectricity itself[9].

Such measurement are, in reality, measurement of the *displacement field D(E)* or *charge density*[4]. For linear dielectrics, we can write:

$$D_i = \varepsilon_0 E_i + P_i = \varepsilon_0 \varepsilon_{ij} E_j \qquad [6]$$

where ε_{ij} generalizes the relative permittivity of equation [1]. For most ferroelectrics, P is much larger than $\varepsilon_0 E$ such that $D \cong P$. Most importantly, ferroelectrics are strongly non-linear in their dielectric behavior[4,10]: the variation of polarization with field $P(E)$ is generally hysteretic as a consequence of domain wall motion[9,10].

Polarization- or charge-field loops are usually made using the simple *Sawyer-Tower* method[9]. An alternating voltage is applied to the electroded sample and the instantaneous charge stored on the sample is related to the instantaneous voltage. Here, charge measurement involves placing a large "sensing" capacitance C_{sense} in series with the sample (C_{sample}) to form a capacitive voltage-divider: the voltage across C_{sense} is proportional to the charge produced by the sample. The simplified circuit is shown in figure 2. The set-up works well for insulating samples, although any conduction in the sample leads to ellipse shaped loops due to a constant phase shift[9]. The method also suffers from unwanted parasitic capacitances, and is limited by the accuracy to which C_{sense} is known[9]. The sensing capacitance should be well chosen so that it is suitably larger than the capacitance of the sample (such that $C_{total} \approx C_{sample}$), but not so large that the voltage measured is too small such that accuracy is reduced: for plate samples of PMN-xPT and PZN-xPT a sensing capacitance of 2 μF was found to be work well.

A set-up based on this circuit was used for this thesis work. Samples were placed in a bath of silicon oil during measurements, to reduce the risk of sparking due to the breakdown of air at high fields. A high voltage amplifier

(TREK) is used to amplify a low voltage signal; AC electric fields (with triangular waveform) are applied to the samples at a defined amplitude, usually around 1500 V/mm. The setup is controlled, again, by a computer running a LabView program, which also records the instantaneous (high) voltage and the sensing voltage across the series capacitor. The frequency could also be controlled, although since the data acquisition rate of the computer interface (DAQ card) is predefined, fewer data points can be taken at higher frequencies. The maximum sampling rate was around 1×10^6 measurements/second. Typically 200 points were recorded at a sampling rate of 10 000 Hz such that the measurement frequency was 50 Hz; more points can be taken at lower frequencies. Higher frequencies are limited by the maximum current from the high voltage amplifier.

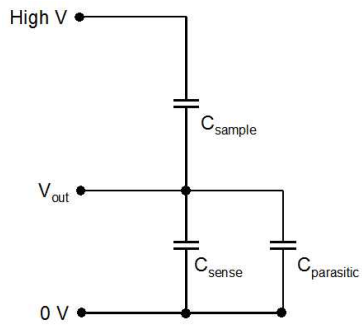

Fig. 2. Schematic representation of a Sawyer-Tower circuit for measurement of ferroelectric hysteresis loops.

Impedance analysis and dielectric properties

The impedance of a sample generalizes resistance, capacitance and inductance. In the Sawyer-Tower circuit a series capacitor can used to measure the capacitance, and thus the *dielectric permittivity* ε (via equation [1]), of a ferroelectric sample. Similarly, the resistance of a sample might be measured by recording the voltage dropped across it and the current passing through it. However, more accurate measurements can be made using a *bridge* method, based on certain reference impedances, the concept used in most commercially-available *impedance analyzers*.

The *impedance Z* of a sample generalizes Ohm's law for the opposition of an electrical circuit to a sinusoidal electric current under application of an alternating voltage $V = V_0 \exp(i\omega t)$. It is a complex quantity (measured in ohms Ω) and given by:

$$Z = R + iX \qquad [7]$$

where *R* is the *resistance* and *X* is the *reactance*. The real resistive part of the electrical circuit (i.e. the resistors) leads to no phase difference between the alternating current and voltage but is dissipative in energy. The reactive part (from the capacitors and inductors) does lead to a phase difference between voltage and current, but is not dissipative: i.e. any energy absorbed

by reactive components is returned to the circuit at some point later in the cycle. The difference in phase, or "phase angle", θ is given by the ratio of the resistance and reactance ($\tan\theta = X/R$). The impedance of a resistor is simply *R*. The impedance of a capacitor is $1/i\omega C$ where *C* is the capacitance and ω is the angular frequency. The impedance of an inductance *L* is $i\omega L$. We can also define the *admittance* of a circuit *Y* (measured in siemens S) as the inverse of the impedance:

$$Y \equiv \frac{1}{Z} = G + iB \qquad [8]$$

It can again be split in to real and imaginary components where *G* is the *conductance* and *B* is the *susceptance*.

Impedance analyzers are usually based on a bridge method, where the circuit (shown simplified in figure 3) is automatically balanced by the presence of an operational amplifier. An AC signal is applied to the high voltage terminal of the sample (H). The low voltage terminal (L) is fixed at zero volts (a "virtual earth") by the action of the amplifier such that the currents through the series resistor *R* and sample Z_S are equal. The voltage dropped across the resistor V_R is then compared to that across the sample V_S: for this simplified circuit, $Z_S = -R\left(V_S/V_R\right)$.

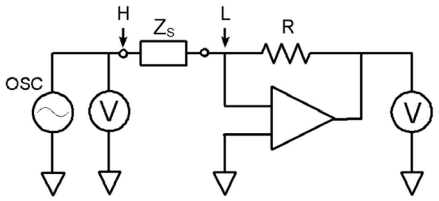

Fig. 3. Simplified electrical circuit of an automatically balancing bridge used in common impedance analyzers[11].

Importantly, the impedance analyzer measures the real and imaginary components of impedance (or admittance) but does not directly measure the capacitance. It can extract the capacitance of the sample, however, by fitting the measured impedance to that expected from an equivalent circuit consisting of resistive and reactive elements. The resistances, capacitances and inductances of the equivalent circuit can be arranged in parallel or series. Thus the impedance analyzer gives two possible measures of capacitance: C_P from the parallel equivalent circuit model and C_S from the series. Only for purely inductive and capacitive (non-dissipative) samples are the values the same. Otherwise, the difference is given by:

$$C_P = \frac{1}{1 + 1/\tan^2\theta} C_S \qquad [9]$$

However, for the samples of PMN-xPT and PMN-xPT studied, the loss tangent was very small (often less than 0.01 at 1 kHz) such that $\theta \approx -90°$ and both values differed very little ($C_P \approx C_S$). All values of permittivity ε quoted in this thesis were calculated, via equation [1], from the parallel capacitance C_P. Dielectric *loss tangents* $\tan\delta$, defined as the ratio between the imaginary and real parts of the permittivity ($\varepsilon = \varepsilon' + i\varepsilon''$) were also recorded.

Four-terminal HP 4194A and HP 4284A impedance analyzers (now from Agilent[12]) were used during this thesis work. The former contains a color CRT display and can measured impedance spectra for frequencies in the range 100 Hz to 40 MHz. The latter has a digital readout and can measure between 20 Hz and 1 MHz. All connections to the sample were made via four BNC cables attached to the high current ("Hc"), low current ("Lc"), high voltage ("Hp") and low voltage ("Lp") terminals of the bridge. "Four-terminal" connections were used to reduce stray capacitances. An excitation signal of 1 V (amplitude) was used.

For all measurements, samples were mounted on a flat, brass plate acting as the bottom connection and held in place by a light, spring-loaded, brass top connection. Temperature dependent measurements were made by placing samples inside a furnace (Delta Chamber 9023[13]), which could be heated to around 300°C or cooled, using liquid nitrogen, to around -170°C. Nitrogen could also be pumped into the chamber during cooling experiments to avoid condensation of moisture on the sample surfaces. An in-house built furnace was also available for higher temperature dielectric measurements up to 550°C. In all cases, the sample temperature was recorded using a thermocouple placed as closely as possible to the samples.

Measurements were usually made at five frequencies between 100 Hz and 1 MHz, more than sufficient to evidence frequency dispersion over the Curie range in relaxor-ferroelectric compositions. Where the room temperature "dielectric constant" of the sample is quoted, a conventional[9] measurement frequency of 1 kHz is inferred. Such low frequency measurements will be a very close approximation[9] to the free (unclamped[2]) dielectric constant ε^{σ} defined in appendix II.

II. STRAIN MEASUREMENTS

One way of determining piezoelectric coefficients is by measurement of the strain induced by an applied electric field. That is, the *converse* piezoelectric effect which, for the longitudinal piezoelectric coefficient (d_{33})[2], is defined by:

$$S_3 = d_{33}E_3 \qquad [10]$$

where S_3 is the strain resulting from electric field E_3. All piezoelectric coefficients of a given crystal or poled ceramic can, in fact, be measured by the *resonance method*, based on the measurements of impedance as a function of frequency[14-16], and by *ultrasound* techniques[17]. However, although both are good ways of characterizing a piezoelectric crystal, they only sample

their small-field, linear response: generally, the AC fields applied in the resonance method should be less than around 1 V/mm[9].

However, in certain applications such as in actuators[18-20], large drive fields will lead to non-linearity where the proportionality in equation [10] breaks down. Generally, the converse piezoelectric response will saturate at high fields. Hysteresis might also be observed due to *extrinsic* contributions to the response at high fields[21,22], e.g. from domain wall motion in ferroelectrics or conduction in imperfect insulators. Hysteresis is generally unwanted in actuation as it leads to a loss of precision. In ferroelectric materials, a sufficiently high field may even induce phase transitions; this is shown to be an important effect in PMN-xPT and PZN-xPT single crystals in chapter nine. Thus, it is important to characterize the high-field response of piezoelectric, i.e.:

$$S_3 = d_{33}(E_3)E_3 \qquad [11]$$

During this thesis work, piezoelectric coefficients in the order of 100-2000 pm/V were to be measured in samples of PMN-xPT and PZN-xPT. Electric fields of around 2000 V/mm can be safely applied to a sample without risk of sparking and thus breaking of the samples (higher fields are possible by coating the outside of the sample in vacuum grease or submerging in silicon oil). Hence, for a sample 0.5 mm thick, maximum displacements of 0.1 - 2 microns were to be measured. Hence, very sensitive experimental techniques were needed to measure them. Two methods were used, one based on magnetic induction and one based on the reflection of light. They are described below.

Magnetic induction method

A *linear variable differential transformer* (LVDT) is an electromechanical transducer that produces an electrical output proportional to the displacement of a separate, moveable, high-permeability core. Briefly, the transformer consists of three coils or windings, one primary and two secondary as shown in figure 4.

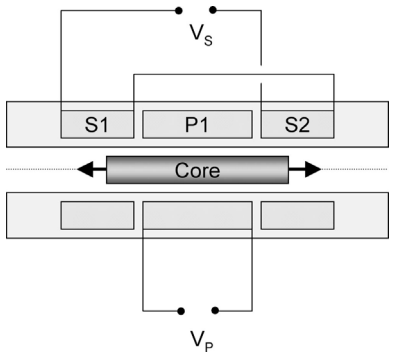

Fig. 4. Schematic of a linear variable differential transformer (LVDT). S1, S2 are the secondary coils connected in series and P1 is the primary coil.

The two secondary coils are connected in series as shown in the diagram. Application of an AC signal to the primary coil V_P induces a magnetic field inside the transformer. The magnetic flux couples to the secondary coils via the moveable core, which leads to an output signal V_S. Importantly, the two secondary coils are connected in such a way that the output voltage is the difference between the induced signal in each coil. In this differential arrangement, with the core at the centre of the LVDT, the secondary output is zero. However, when the core is moved laterally, as indicated in figure 4, more magnetic flux will couple to one secondary coil at the expense of the other and a non-zero output voltage V_S will be produced. Usefully, for small displacements, the output voltage is linearly proportional to the displacement of the core from its centre point.

LVDTs with very high spatial resolution are available. For this thesis work a highly sensitive LVDT (model "050 HR") was purchased from Schaevitz[23] which shows only a small deviation from linearity ($\pm 0.1\%$) for a linear range of 0.6 mm and has a sensitivity of around 300 mV/mm. The displacement of the core could be coupled to the displacement of a sample under applied field via a stiff, non-magnetic, metal rod (also from Schaevitz). The apparatus[24] built specially to house the LVDT and the sample is shown in figure 5.

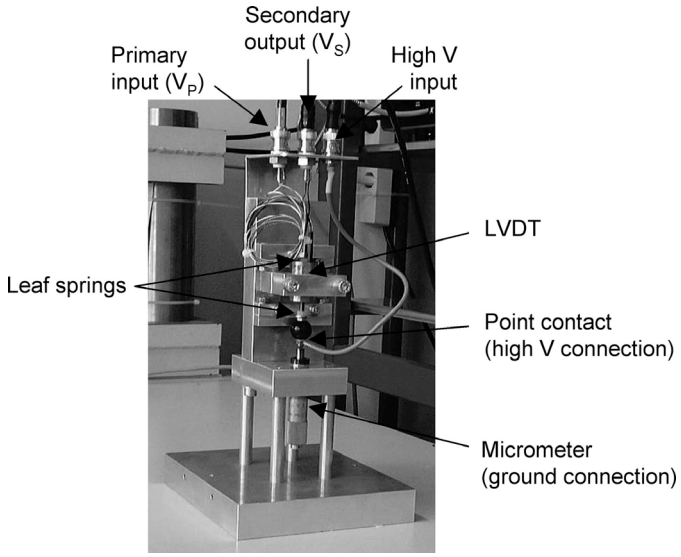

Fig. 5. Experimental apparatus based on an LVDT transducer built for strain-field measurements.

The non-magnetic rod carrying the core is held in place at the centre of two leaf springs. A ball bearing is connected to the bottom of the rod, insulated by stiff bakelite which forms the high voltage connection when in contact with the sample. The sample sits on the flat end of an upturned micrometer, which acts as the ground (0 V) electrical connection and is used to screw the sample upwards into contact with the high voltage connection before each experiment. The leaf springs provide a small restoring force, sufficient to keep the sample in electrical contact during the strain-field loop.

The position of the rod and core is adjusted so that, at the zero position, the restoring force is as small as possible. The high voltage is applied by a function generator via a high-voltage, x1000 amplifier (from Trek[25]). Low frequency, sinusoidal driving signals were applied, typically of 0.1 - 10 Hz to reduce the risk of breaking the samples. Only unipolar fields were applied during this thesis work, unless stated otherwise, in the direction of the polarity of the poled sample.

Since the output voltage of the secondary coils is small, typically around 0.1 mV, a lock-in technique is required. Thus, the reference signal of a lock-in amplifier (SR530, Stanford Research Systems[26]) was used to drive the primary coil (3 Vrms, 2500 Hz). Critically, this frequency is much higher than that of the high voltage signal. The output of the secondary coils V_S is then fed into the input of lock-in amplifier, which "locks in" at the reference frequency. The output from the lock-in is thus the amplitude of the high voltage signal, which is proportional to the displacement of the core and thus the distortion of the sample, changing at the driving frequency (0.1 - 10 Hz). The driving signal applied to the sample and the displacement are fed into a two-channel digital oscilloscope (TDS 410, Tektronix[27]), which is interfaced to a computer running a suitable LabView program to record the data. The electronics used in the measurements are shown in figure 6.

Notably, the method is not "single shot". The sample is left under high voltage cycling and the digital oscilloscope records the two signals over a certain time interval (usually one cycle). Multiple measurements were taken to see any temporal variation in the behavior.

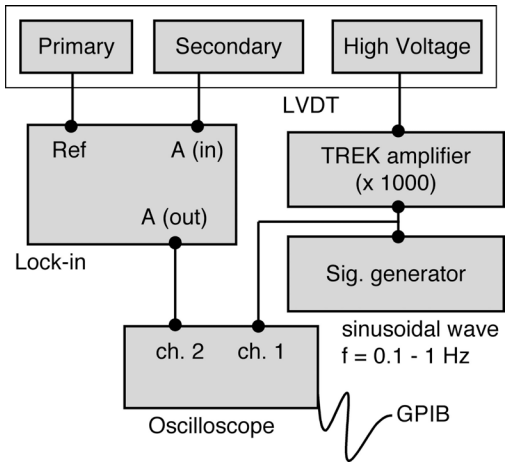

Fig. 6. Schematic of the electronic equipment used for strain-field measurements using the LVDT set-up shown in figure 10.

Optical method

The other method used as part of this thesis work was based on the reflection of white light. To this end, a *Fotonic sensor* (MTI-2000) by MTI instruments[28] was used. The Fotonic sensor is a fiber-optic measurement system designed for both vibration and displacement measurement. In theory, it can measure displacements in the range 10 nm to 5 mm statically or

at frequencies up to 150 kHz. The probe consists of a bundle of optical fibers, half of which emit white light, and the other half of which receive the light reflected back from an optically-reflective surface. The two sets of fibers are randomly arranged and the intensity of reflected light I detected by the sensor is a function of the distance x between the probe and the sample surface. When the probe is in contact with the reflective surface ($x = 0$), no light is reflected back to the sensor ($I = 0$). When the probe is placed a long way from the reflective surface ($x = \infty$) again no light is reflected back and again the intensity is zero. Between these two points, there a position of maximum intensity (I_{max}).

Importantly, between the maximum in intensity ($I = I_{max}$) and the zero point ($I = 0$) there is a region of linearity. By calibrating the position of maximum intensity (x_{max}, I_{max}) for surfaces of varying reflectivities, and therefore different reflected intensities of light, the sensor can give an accurate measure of the distance between the surface and the probe and thus the distortion of the sample.

A special housing was built to hold the sample and probe in place. It was designed to be heavy and robust in order to limit spurious vibrations. In the apparatus, the probe is fixed to a micrometer such that it can first lowered to find the position of maximum reflection from the sample and then lowered again into the linear region of the $I(x)$. The sample is placed on a flat metal plate which acts as the high voltage connection. The top (ground) connection is made by the fine point of a light copper spring which also holds the sample in place. The Fotonic sensor itself is also grounded to minimize the risk of sparking between the sensor and the top electrode.

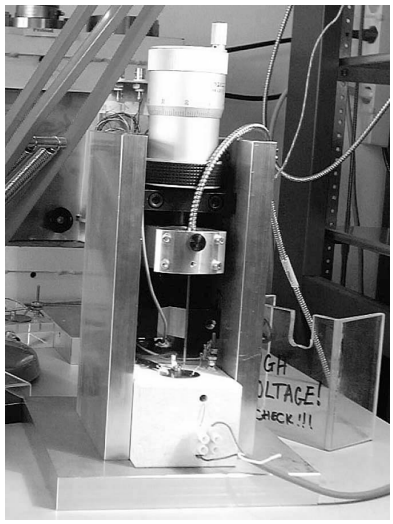

Fig. 7. Experimental setup based on a Fotonic optical probe for strain-field measurements.

A small, resistively-heated furnace was later added to the setup. The furnace, of dimensions roughly $6 \times 5 \times 10$ cm^3, was used to heat the high voltage bottom plate. A thermocouple was positioned as close as possible to the sample, insulated by hard, air-drying cement, and the temperature was

controlled by the necessary feed-back electronics (Eurotherm). Maximum temperatures of around 150°C could be achieved, limited by the working temperature of the Fotonic probe.

The enclosed setup is shown in figure 7. It was generally mounted on an anti-vibration table, primarily used for interferometric measurements.

The same electrical setup used for the LVDT measurements (small field function generator plus high voltage amplifier) was used to apply the high voltage to the sample, as shown in figure 8. Again, only unipolar electric fields (0 - 2000 V/mm) were applied, generally in the direction of the polarization of the sample to avoid depoling. An LCD readout on the Fotonic sensor gives the displacement, directly, in microns. The displacement can be fed into a digital oscilloscope and compared to the high voltage signal. Data for a single loop is then captured by a computer running a suitable LabView program.

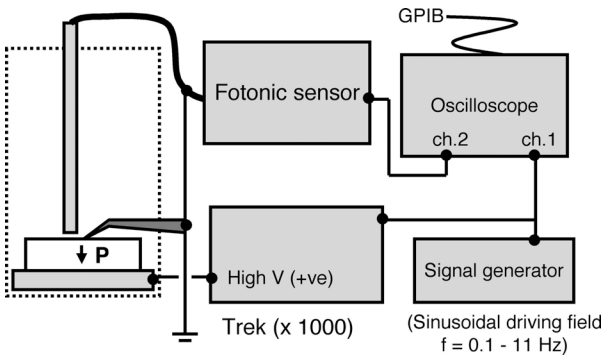

Fig. 8. Schematic of the electronic equipment used for strain-field measurements based on the Fotonic set-up shown in figure 7.

Comparison of Fotonic and LVDT methods

The strain-field responses for the same sample of poled, $[001]_C$-oriented PMN-32PT measured using the two measurement methods is shown in figure 9. At low fields, the responses match very well. Even at high fields the strains typically agree to within 5%. However, a slight difference in the linearity of the two measured responses is evident, which is probably related to the inherent linearity of the LVDT and the $I(x)$ response of the Fotonic sensor. The LVDT also seemed to give a slightly more hysteretic response. This was a general observation and is probably a consequence of the electronic filtering (lock-in amplification) of the signal.

One advantage of the LVDT method is that it does not require reflective surfaces and can hence be used for samples electroded with transparent indium tin oxide. It is also faster since it does not require calibration, more sensitive to small displacements than the Fotonic sensor, and less sensitive to electronic noise. Whereas flat plate samples (of thickness 0.5 mm) were more suited for Fotonic measurements, the LVDT setup could easily accommodate more cuboid samples including those designed primarily for measurement in the Berlincourt-type press described in section III.

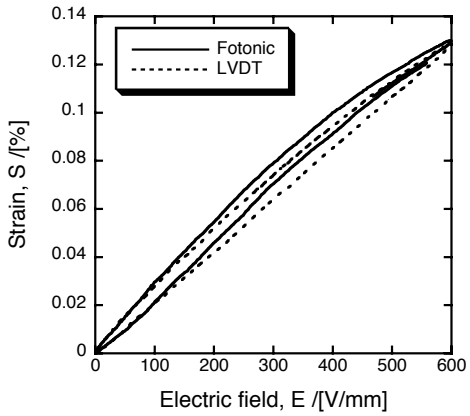

Fig. 9. Comparison of the Fotonic and LVDT based methods for measurement of strain as a function of field. The converse piezoelectric response of a $[001]_C$-oriented sample of PMN-32PT is shown for a measurement frequency of 0.1 Hz.

The main advantage of the Fotonic sensor is that no electronics or special sample holders, which could introduce unwanted phase angles to the measurement, are needed to treat the signal and hold the sample. However, it was difficult to avoid a low level of 50 Hz noise in the fiber-optic measurements, corresponding to displacements of around 10 nm. As electronic filtering can lead to unwanted phase lags, and therefore spurious hysteresis, a numerical curve "smoothing" procedure was preferred to remove the 50 Hz noise; this is shown in figure 10 for a sample of "hard[9]" PZT. Due to the large response of domain-engineered PMN-xPT and PZN-xPT, however, such curve smoothing was not generally necessary.

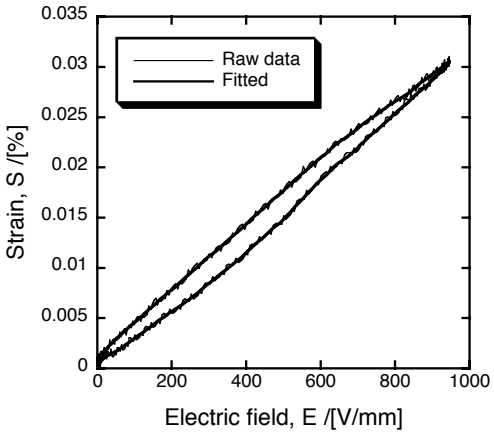

Fig. 10. Strain-field response of a sample of poled, hard PZT ceramic ("Pz26" from Ferroperm, Denmark[29]) measured using the Fotonic sensor. A numerical fitting process can be used to remove the 50 Hz noise with little effect on the true response.

It is finally worth noting that both LVDT and Fotonic strain-measurements are *localized* (not global) since the Fotonic probe and top contact in the LVDT setup will measure the displacement of a finite area of the sample (around $1mm^3$). Hence, the observed response will depend, wherever the strain-field response is inhomogeneous, on the position of the sample. This can be the case during first order electric-field induced phase transitions, as will shown in chapter seven, in complex relaxor-ferroelectric single crystals. Spatial variations in the measured threshold field for the transition do occur,

as shown in figure 11. Moreover, any bending of the crystal, due to frictional clamping of the transverse piezoelectric effect, will also lead to a lateral variation in the measured displacement. Hence, good practice involves measuring the strain at the center after probing varying other positions of the sample first.

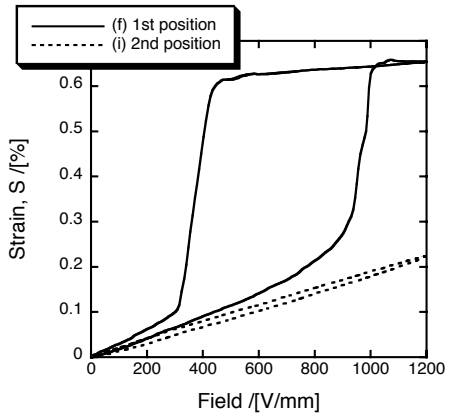

Fig. 11. Lateral spatial variation of the strain-field response of a 5 x 5 x 0.5 mm^3 plate sample of PZN-8PT oriented along the $[001]_C$ direction (at f = 0.1 Hz). In one part of the sample a field-induced phase transition is evidenced. In another, no transition is observed. The threshold field for the crystal is spatially heterogeneous.

III. DIRECT PIEZOELECTRIC EFFECT

Another way to measure the piezoelectric response of a crystal or ceramic is via the *direct piezoelectric effect*, that is the production of charge upon application of an applied stress. In Voigt notation[2], the longitudinal piezoelectric coefficient d_{33} is given by:

$$D_3 = d_{33}\sigma_3 \qquad [12]$$

where σ_3 is the applied stress and D_3 is the resultant charge density.

As such, d_{33} can be measured in a "Berlincourt-type press". In this method, named after Berlincourt, the electroded sample (of area A and piezoelectric coefficient d_S) is squeezed between two metal surfaces, which also act as electrical connections to conduct the charge. The charge released by the sample Q_S ($D_3 = Q_S/A$) is measured via a parallel sensing (or "shunt") capacitance C_S which should be large enough such that it draws all piezoelectrically-induced charge from the sample, though not so large that the measured voltage is too small. The sinusoidal force is applied by a piezoelectric actuator driven by a signal generator; it is measured by a reference piezoelectric element with a known piezoelectric coefficient d_R placed in series, mechanically, with the sample such that it feels the same force F. The set-up is shown schematically in figure 12. The charges produced by the reference piezoelectric and the sample, Q_R and Q_S, are measured as voltages across the parallel capacitances C_R and C_S, respectively.

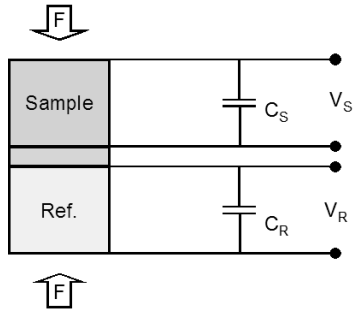

Fig. 12. Schematic set-up of a Berlincourt-type meter used for measuring the piezoelectric coefficient of a piezoceramic.

Since both elements feel the same force, and since $Q_S = d_S F$ and $Q_R = d_R F$:

$$d_S = d_R \left(\frac{Q_S}{Q_R} \right) \qquad [13]$$

We can equate this to the measured voltages since $Q_S \approx C_S V_S$ and $Q_R \approx C_R V_R$. We arrive at:

$$d_S = d_R \times \left(\frac{C_S}{C_R} \right) \times \left(\frac{V_S}{V_R} \right) \qquad [14]$$

d_R is a known quantity and the ratio C_S/C_R can be set to unity. Hence by measuring the two voltages V_S and V_R we can calculate the piezoelectric coefficient of the sample. The force applied is, in fact, dynamic so that the ratio of the *amplitudes* of the measured voltages gives the value of d_S.

Berlincourt "d_{33}-" or "piezo-" meters working on this principle are available commercially[30], or can be built quite simply. However, although they are generally low cost, easy to use and accurate, they usually only allow measurements at sinusoidal driving forces of fixed amplitude and frequency. This is in spite of the fact that for all real piezoelectrics at finite fields there will always be a finite dependence of both the piezoelectric and dielectric response on the amplitude and frequency of the driving (electrical or mechanical) field[31-33]. This can be especially strong in materials, such as "soft[9]" PZT ceramics which show a significant *extrinsic*[33] contribution to both responses from the motion of ferroelastic-ferroelectric domain walls[34-38]. Simple Berlincourt-type meters cannot be used to measure non-linear or hysteretic effects, important for any piezoelectric element for use in actuators and transducer elements especially where large stresses will be involved.

As well as being unsophisticated, they are also prone to error. Importantly, the shape of mechanical contacts used in the ensemble will, in general, have significant effect[39] on the measured piezoelectric coefficient,

d_{33}^{eff}. Point contacts give rise to inhomogeneous stresses in the sample[39], which will affect the measured value. Flat contacts give more homogenous stresses but, due to the effect of clamping due to friction between the sample and plates, unwanted lateral stresses which tend to reduce the measured coefficient[40].

Berlincourt-type press

As part of this thesis a more sophisticated, in-house built[41], Berlincourt-type press was used to measure the direct piezoelectric properties of PMN-xPT and PZN-xPT single crystals. A picture of the setup is shown in figure 13; it is also shown schematically in figure 14.

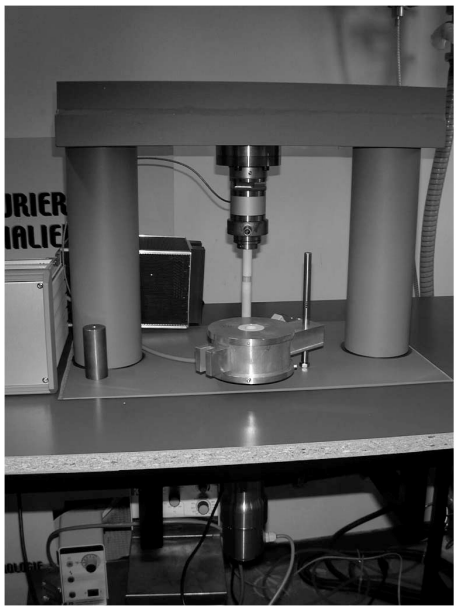

Fig. 13. In-house built, Berlincourt-type press used for measurement of the direct piezoelectric properties of PMN-xPT and PZN-xPT single crystals.

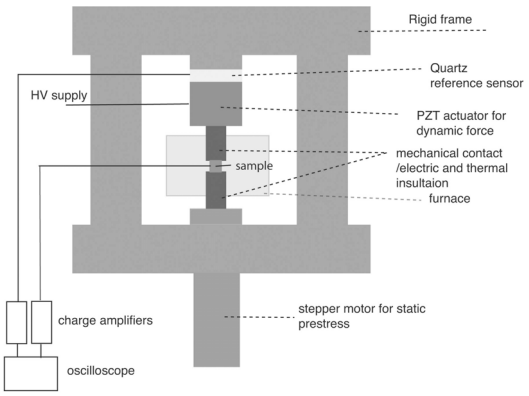

Fig. 14. Schematic of the Berlincourt-type press shown in figure 13.

In the press, a series assembly of a quartz reference sensor, PZT actuator and sample, mounted between two zirconia columns, is held within a rigid cast iron frame. The quartz sensor (Kistler 9061A[42]) is used to measure the force in the setup, and thus on the sample. A charge amplifier (Kistler, type 5011) is used to measure the charge, by conversion to an electrical signal, which is fed in to channel one of a digital oscilloscope (Tektronix 430A). The PZT actuator (from PI systems[43]) , driven by a signal generator via a high voltage amplifier, applies both static and dynamic components of force, defined by the offset bias and amplitude of the sinusoidal voltage, respectively. Flat, parallel, stainless steel plates are fixed to the ends of two stiff, zirconia columns which act as both mechanical contacts to the sample and electrical contacts for collection of charge. A second charge amplifier is used to measure the piezoelectrically-induced charge from the sample, which is connected to channel two of the oscilloscope. A sophisticated LabView program is used to automatically adjust the time-base and scale and record the data from the oscilloscope; it also controls the frequency, offset and amplitude of the sinusoidal signal fed to the PZT actuator, and the stepper motor.

The maximum frequency for measurement is around 70 Hz, limited by the resonant frequency of the ensemble. At low frequencies, in low response materials, “charge drift” can become a problem leading to unclosed charge-stress loops. A maximum static force of around 4000 N can be applied corresponding to a stress of 160 MPa for a sample of area 25 mm^2. The maximum dynamic force is around 1000 N. Most measurements were taken at room temperature although the zirconia columns and sample can be placed inside a furnace for temperature dependent measurements (up to 450 °C).

For all measurements, a prestress (P) is first applied by raising the bottom contact with the stepper motor to put the entire system in compression. For static measurements, force is applied to the sample by upwards motion of the stepper motor alone. For dynamic measurements, after loading a fixed amount of prestress, the PZT actuator applies further dynamic [$\sigma_{DY} = \sigma_0 sin(\omega t)$] and static pressures ($\sigma_{ST}$). The total prestress ($P + \sigma_{ST}$) is adjusted automatically, via a feed-back loop, to the specified amount. Importantly, the dynamic stress amplitude is never greater than the total prestress such that the system is always in compression.

One important difference between the setup described here and many commercial setups is that the pressure is applied across the entire electroded surface of the sample. As noted above, flat contacts lead to more homogeneous forces but, due to the friction-impeded lateral expansion of the sample under pressure, lateral forces in the sample as well. This will typically lead to a reduction in d_{33}^{eff} dependent on the aspect ratio of the sample. Fortunately, this effect can be modeled numerically and analytically[40,44], and is nearly absent in samples of sensibly-chosen dimensions; this is discussed further in chapter eight.

Lastly, we note that the metal contacts are designed to be flat and parallel. However, any small deviation from this will lead to shear stresses in the sample and thus error in the measured piezoelectric coefficient[40]. Unfortunately, methods generally used in mechanical presses to homogenize the stress applied to a sample will often introduce losses into the system and

thus unwanted phase angles which will be manifest in measurements of non-linearity and hysteresis. Hence, they were not used. However, the uniformity of the pressure was checked by pressing a sheet of carbon paper and a sheet of clean, white paper to 1000 N between one of the metal contacts and a disc sample, 8 mm in diameter. Good uniformity across the imprinted pattern was indicative of homogeneous pressure.

Finally, lubricants are often used in mechanical testing to reduce laterals stresses from clamping. However, for this thesis work, no suitable conductive lubricant could be found.

REFERENCES

1 R. W. Whatmore, Rep. Prog. Phys. **49,** 1335-1386 (1986).

2 J. F. Nye, *Physical properties of crystals*, 2nd ed. (Clarendon Press, Oxford, 1985).

3 A. Isaacs, *A Dictionary of Physics*, 3rd ed. (Oxford University Press, Oxford, 1996).

4 C. Kittel, *Introduction to solid state physics*, 7th ed. (Wiley, New York, 1996).

5 M. Daglish, Integrated Ferroelectrics **22,** 473-488 (1998).

6 D. J. Taylor, D. Damjanovic, and A. S. Bhalla, Ferroelectrics **118,** 143-155 (1991).

7 www.ni.com

8 M. E. Lines and A. M. Glass, *Principles and applications of ferroelectrics and related materials* (Clarendon Press, Oxford, 1977).

9 B. Jaffe, W. R. Cook, and H. Jaffe, *Piezoelectric Ceramics* (Academic Press, 1971).

10 F. Jona and G. Shirane, *Ferroelectric crystals* (Pergamon Press, New York, 1962).

11 www.home.agilent.com

12 www.home.agilent.com

13 www.deltad.com

14 D. Berlincourt, D. R. Curran, and H. Jaffe, *Physical Acoustics*, Vol. 1A (Academic Press, New York, 1964).

15 Proc. IRE **49,** 1161 (1961).

16 American National Standards Institute (1987).

17 W. Jiang, R. Zhang, B. Jiang, and W. Cao, Ultrasonics **41,** 55-63 (2003).

18 K. Bhattacharya and G. Ravichandran, Acta Mater. **51,** 5941-5960 (2003).

19 K.-W. Tang, H. L.-W. Chan, C.-L. Choy, Y.-M. Cheung, and P. C.-K. Liu, Ferroelectrics **263,** 223-228 (2001).

20 S.-E. E. Park and T. R. Shrout, J. Appl. Phys. **82,** 1804-1811 (1997).

21 D. Berlincourt and H. H. A. Kreuger, J. Appl. Phys. **30,** 1804-1810 (1959).

22 Q. M. Zhang, H. Wang, N. Kim, and L. E. Cross, J. Appl. Phys. **75,** 454-459 (1994).

23 www.schaevitz.com

[24] The setup was built based on a design by Paul Moses at Penn State University.
[25] www.trekinc.com
[26] www.thinksrs.com
[27] www.tek.com
[28] www.mtiinstruments.com
[29] www.ferroperm-piezo.com
[30] There are various commercial suppliers of "Berlincourt" or "piezo" meters including, for example, Piezotest (www.piezotest.com) and KCF Technologies (www.kcftech.com).
[31] D. Damjanovic, M. Demartin, H. S. Shulman, M. Testorf, and N. Setter, Sensors and Actuators A **53,** 353-360 (1996).
[32] D. Damjanovic, J. Appl. Phys. **82,** 1788-1797 (1997).
[33] D. Damjanovic and M. Demartin, J. Phys.: Condens. Matter **9,** 4943-4953 (1997).
[34] A. B. Schäufele and K. H. Härdtl, J. Am. Ceram. Soc **79,** 2637-2640 (1996).
[35] D. Zhou and M. Kamlah, J. Appl. Phys. **96,** 6634-6641 (2004).
[36] Q. M. Zhang and J. Zhao, IEEE Transactions on Ultrasonics, Ferroelectrics and Frequency Control **46,** 1518-1526 (1999).
[37] D. Zhou, Z. Wang, and M. Kamlah, J. Appl. Phys. **97,** 084105 (2005).
[38] E. Burcsu, G. Ravichandran, and K. Bhattacharya, Proc. SPIE, Smart Structures and Materials 2001: Active Materials: Behavior and Mechanics, C. S. Lynch, Ed. **4333** (2001).
[39] J. Erhart and L. Burianova, Journal of the European Ceramic Society **21,** 1413-1415 (2001).
[40] A. Barzegar, D. Damjanovic, and N. Setter, IEEE Transactions on Ultrasonics, Ferroelectrics and Frequency Control **51,** 262-270 (2003).
[41] The press was designed and built by Abdolghaffar Barzegar and Dragan Damjanovic at the Laboratory of Ceramics, EPFL.
[42] www.kistler.com
[43] www.physikinstrumente.com
[44] A. Barzegar, D. Damjanovic, and N. Setter, Proc. IEEE Ultrasonics Symposium **2,** 1185-1188 (2002).

Chapter three

Single crystal samples

In this chapter, details of the single crystal samples used in this thesis work are given. Methods for verifying their orientation and composition are discussed along with details of how the samples were prepared (cut, polished and annealed) for the measurements described in the previous chapter. In addition, the methods used to grow PMN-xPT and PZN-xPT single crystals are reviewed; the origins of compositional heterogeneity in as-grown single crystals are discussed.

I. SINGLE CRYSTAL SAMPLES

All single crystal samples used for this thesis work were either supplied by various European partners or obtained commercially.

Commercial crystal growers

There are now at least a handful of commercial growers of PMN-xPT and PZN-xPT single crystals; the suppliers found by an internet search in early 2003 are listed in table I. At that time prices ranged from around $100-200 for a $[001]_C$-oriented plates (10 x 10 x 0.5 mm^3) to up to more than $1000 for $[111]_C$-cut crystals, the latter being a more wasteful cut. No doubt, with the growth of the interest in such crystals from large piezoelectric end-users (including Philips, Siemens and Toshiba[1]) and improved expertise in the growth process, the number of compositions and orientations available will since have increased; prices too are likely to have fallen.

Table I
Growers and suppliers of single crystal PMN-xPT and PZN-xPT.

Company	Location	Compositions, x /[mol. %]	Orientations	Maximum dimension
MTI Corporation	Hefei, P.R. China and Richmond, CA, USA	PMN-33PT	$[001]_C$	25 mm
Piezo Partners	USA	PMN-xPT		80 mm
Sinoceramics[a]	State College, PA, USA	PMN-xPT (x = 30 - 39 PT)	$[001]_C$, $[101]_C$, $[111]_C$	
Kawatetsu Mining Co. Ltd.[b]	Japan	PZN-9PT	$[001]_C$, $[101]_C$, $[111]_C$	
Ibule Photonics[c]	Kyunggido, Korea	PMN-xPT	$[001]_C$	25 mm
TRS Ceramics	State College, PA, USA	PMN-xPT, PZN-xPT	$[001]_C$, $[101]_C$, $[111]_C$	
Microfine Materials Technologies Pte Ltd.[d]	Singapore	PMN-xPT, PZN-xPT	$[001]_C$, $[101]_C$, $[111]_C$	> 25 mm
HC Materials[e]	Urbana, IL, USA	PMN-xPT (x = 28, 30, 32)	$[001]_C$, $[101]_C$, $[111]_C$	50 mm
APC International Ltd.	Mackeyville, PA, USA	PMN-xPT		

a. Minli Fu <minli@sinocera.net>; b. Yosuke Iwasaki <yo-iwasaki@kawako.kawatetsu.ne.jp>; c. Suhan Yu <suhanyu@ibule.com>; d. L. C. Lim <mpelimic@nus.edu.sg>; e. Pendgi Han <han@hcmat.com>.

Crystal inventory

At the beginning of this thesis work a few $[001]_C$-oriented samples of (target compositions) PMN-33PT and PZN-9PT were supplied by partners of

a joint European project[2]. Additionally, samples were purchased from TRS Ceramics[3], HC Materials[4] and Microfine Technologies[5]; these are listed in table II. Cuboid samples were procured with direct piezoelectric measurements in mind (chapters eight and nine), as well as more standard 0.5 mm thick plates.

Table II
Inventory of commercial samples of PMN-xPT and PZN-xPT obtained for use in this work.

Nominal composition	Orientation	Sample Type	Dimensions	Quantity	Supplier
PMN-33PT	$[001]_C$	Plate	10 x 10 x 0.5 mm^3	5	HC Materials
PMN-33PT	$[011]_C$	Plate	10 x 10 x 0.5 mm^3	5	HC Materials
PMN-33PT	$[111]_C$	Plate	10 x 10 x 0.5 mm^3	5	HC Materials
PMN-28PT	$[001]_C$	Plate	10 x 10 x 0.5 mm^3	5	HC Materials
PMN-28PT	$[011]_C$	Plate	10 x 10 x 0.5 mm^3	5	HC Materials
PMN-28PT	$[111]_C$	Plate	10 x 10 x 0.5 mm^3	5	HC Materials
PZN-8PT	$[001]_C$	Plate	10 x 10 x 0.5 mm^3	5	Microfine Tech.
PZN-8PT	$[011]_C$	Plate	10 x 10 x 0.5 mm^3	5	Microfine Tech.
PZN-8PT	$[111]_C$	Plate	10 x 10 x 0.5 mm^3	5	Microfine Tech.
PZN-4.5PT	$[001]_C$	Plate	10 x 10 x 0.5 mm^3	5	TRS Ceramics
PZN-32PT	$[001]_C$	Plate	10 x 10 x 0.5 mm^3	5	TRS Ceramics
PZN-4.5PT	$[001]_C$	Cuboid	4 x 4 x 2 mm^3	5	TRS Ceramics
PMN-32PT	$[001]_C$	Cuboid	4 x 4 x 2 mm^3	5	TRS Ceramics
PZN-4.5PT	$[111]_C$	Cuboid	4 x 4 x 2 mm^3	5	TRS Ceramics
PZN-4.5PT	$[001]_C$	Cube	3 x 3 x 3 mm^3	2	TRS Ceramics
PZN-8PT	$[001]_C$	Cube	3 x 3 x 3 mm^3	2	TRS Ceramics
PMN-32PT	$[001]_C$	Cube	3 x 3 x 3 mm^3	2	TRS Ceramics
PZN-7PT	$[001]_C$	Plate	10 x 10 x 0.5 mm^3	2	Microfine Tech.
PZN-7PT	$[011]_C$	Plate	10 x 10 x 0.5 mm^3	2	Microfine Tech.
PZN-7PT	$[111]_C$	Plate	10 x 10 x 0.5 mm^3	2	Microfine Tech.
PZN-7PT	$[001]_C$	Cuboid	5 x 5 x 3 mm^3	2	Microfine Tech.
PZN-7PT	$[011]_C$	Cuboid	5 x 5 x 3 mm^3	2	Microfine Tech.
PZN-7PT	$[111]_C$	Cuboid	5 x 5 x 3 mm^3	2	Microfine Tech.

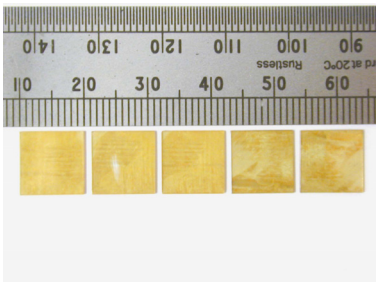

Fig. 1. $[001]_C$-oriented plate samples of nominal composition PZN-8PT as supplied by Microfine Technologies (mirror-lapped). A complex domain structure is visible.

Most plate samples, as supplied, had a yellow or beige tinge. Thicker cuboid samples supplied by TRS had either a strong orange (PZN-xPT) or a strong green (PMN-xPT) color. All were free from cracks and other visible defects. Most crystals were supplied in an as-cut condition with a certain surface roughness and were therefore opaque. Only the samples from Microfine Technologies were supplied polished (or "mirror-lapped"). These crystals were clearly transparent, as shown in figure 1, where a complex domain structure is visible to the naked eye.

II. GROWTH OF SINGLE CRYSTAL PMN-xPT AND PZN-xPT

A brief review of the techniques used to grow PMN-xPT and PZN-xPT single crystals is given below. This is relevant since any problems in the growth process will result in imperfect and defected crystals, which will have an important effect on properties. As will be explained, compositional heterogeneity is perhaps the biggest challenge facing crystal growers of PMN-xPT and PZN-xPT.

For completeness, we start with the synthesis of ceramic samples.

Ceramic PMN-xPT and PZN-xPT

Ceramic PMN-xPT can be difficult to prepare in polycrystalline ceramic form because of the formation of a stable, low permittivity, pyrochlore phase[6]. Hence, the "columbite precursor method" is generally adopted[7-11] as developed in 1982 by Swartz and Shrout[6]. Here oxides of PbO, MgO, Nb_2O_5 and TiO_2 are used as starting reagents. Importantly, the magnesium and niobium oxides are pre-reacted to form the columbite phase $MgNb_2O_6$ prior to reaction with PbO and TiO_2. An excess of MgO also helps to eliminate the pyrochlore phase[6]. Other minor additions are sometimes made: $PbZrO_3$ powder for example is sometimes added to control the Pb stoichiometry[8] and small amounts of manganese oxide can be added to decrease breakdown effects under high electric field[9].

Attempts to synthesize PZN ceramics with a perovskite structure by such a mixed-oxide process (replacing MgO with ZnO) under atmospheric pressure have been less successful[12]. However, addition of PT in excess of around 20 mol% helps stabilizes the perovskite phase over the pyrochlore

and PZN-xPT ceramics with lead titanate contents of 0.2, 0.4, 0.6 and 0.8 mol% have been successfully synthesized by Lee et al. (1998)[12]. In contrast, *single crystals* of PZN-xPT with lower PT contents can be synthesized[13,14].

Single crystal growth

The mostly widely applicable method of single crystal synthesis is *high temperature solution growth* (HTSG)[15] and is the main technique used to grow single crystal PMN-xPT and PZN-xPT. In the process, material begins dissolved in a suitable solvent (or "flux"). Crystallization occurs at the point of *supersaturation*, which is generally promoted by evaporation of the solvent or by cooling of the solution below the saturation temperature T_S. The main advantage of this method is that growth can occur at much lower temperatures than those required for growth from the melt. This is particularly advantageous in: (i) incongruously melting crystals, i.e. those which thermally decompose before melting (this includes both PMN-xPT and PZN-xPT); (ii) materials which undergo a phase transition which results in severe strain and possible fracture (this is true in high PT content crystals); (iii) materials with a very high vapor pressure at the melting point; and (iv) materials which have a very volatile constituent (including lead). Another advantage of the method is that the growing crystal is not exposed to steep temperature gradients. Moreover, it allows crystals to grow in an unconstrained fashion and hence develop natural growth facets. As a result, HTSG often results in better quality crystals, with less point defects, dislocations etc., compared to melt-grown crystals if various parameters like the thermal profile, soaking temperature, and cooling rate can be optimized[16].

HTSG is sometimes referred to as *flux growth*[15] wherever the solvent is a molten salt or oxide. The word "flux" is derived from the more general term for a substance used to reduce the melting temperature, or to dissolve oxides for example in soldering.

Nucleation control

One of the main difficulties with any growth technique is that where nucleation is spontaneous, and left to occur at the free surface of the container for example, grown crystals are often quite small. Because of this, modifications to the above techniques are required.

The most popular means of nucleation control is by "top-seeding", or the use of a previously grown "seed" crystal of required material. The seed crystal, often at the end of an alumina rod, is introduced into the solution or melt; it can be rotated and/or slowly withdrawn from the liquid phase as the crystallization takes place. By precisely controlling the temperature gradient, pulling speed and the rate of rotation it is possible to extract large singe crystals. Critically, where the technique is applied to solution growth, knowledge of the saturated solubility of the solid (or the saturation temperature for a given composition T_S) is required. If the seed crystal is introduced into the solution above T_S it will dissolve; if the temperature is too low, spontaneous nucleation will result in many smaller crystals[16].

Top seeding is used to produce the majority of commercially-available single crystals, especially oxides and semiconductors like silicon and gallium arsenide. Perhaps its most important application is in the growth of large cylindrical "boules" of high quality silicon from the liquid phase; here the process is commonly known as the *Czochralski method*.

Another popular method of nucleation control is the *Bridgman growth technique* [Bridgman (1925)[17]] where controlled freezing is allowed to take place under conditions of solid-liquid equilibrium in a temperature gradient. The solid-liquid interface is moved slowly (at just 5-50 mm per day) until solidification is complete. In the *vertical Bridgman method* the melt is lowered through a temperature gradient[16]. Where the liquid phase is a supersaturated solution instead of a pure melt, the technique is referred to as the "solution Bridgman technique[16]".

Growth of single crystal PZN-xPT and PMN-xPT

Much work has been carried out over the last decade on growth of PZN-xPT and PMN-xPT single crystals. PMN-xPT and PZN-xPT solid solutions crystallize from quarternary phase systems of PbO - MgO or ZnO - TiO_2 - Nb_2O_5, often via complex crystallization pathways. They both decompose into a pyrochlore phase when heated at atmospheric pressure suggesting incongruent melting and, therefore, all techniques are based on high temperature solution (or flux) growth. Early growth of PZN-xPT [Nomura et al. (1973)[18]] involved flux growth with PbO as a solvent. More recently, a mixture of PbO and B_2O_3 has been found to be an effective solvent for PMN-xPT crystals[16,19-22] although the amount of flux used must be carefully controlled to avoid the inclusion of PbO and pyrochlore phases in the as-grown crystals[16]. For growth of PZN-xPT, too low a PbO content results in growth of pyrochlore crystals ($Pb_{1.88}Zn_{0.3}Nb_{1.25}O_{5.305}$)[23]. High purity powders are used and in some cases $PbTiO_3$ and $ZnNb_2O_6$ (or $MgNb_2O_6$) precursors are first formed using the same columbite technique[6] used for ceramics[24,25].

Small, cubic crystals (1-4 mm) of PMN-xPT can be grown by spontaneous nucleation[19,21]. However, to achieve larger crystals nucleation-control can be achieved by three main techniques. Firstly, *top-* or *bottom-cooled solution growth* (TCSG or BCSG) has been successfully applied. In top-cooling a self-cooled or air-cooled sharpened Pt wire/rod is merged into the top of the melt and, in the latter, the airflow is adjusted to achieve single nucleation around the wire[23]. PMN-7PT boules of 15 x 12 x 10 mm^3 in dimension have been grown by this technique. In bottom-cooling (or "spot-cooling") a similar technique is used from the bottom of the container[26] or cold oxygen gas is blown at the Pt crucible to trigger nucleation. The latter approach has been used to grow large crystals of PZN-4.5PT[16]. Top seeded solution growth, using spontaneously grown crystals as seeds[21], is another popular approach and has been used to grow large crystals of PZN-xPT ($\phi > 30$ mm) with a cubic morphology enclosed by natural $\{001\}_C$ growth facets[16,27]. Smaller crystals of PMN-xPT have also been grown by top-seeding[21]. Problems can be encountered if the seed crystal corrodes at an early stage by reacting with the vapor[23]. Finally, the *(solution) Bridgman* technique[26,28-30] offers perhaps the best hope for scaling up crystal growth of

PMN-xPT and PZN-xPT for mass production, being the simplest and most economic[16]. It has been combined with bottom cooling, for example with a Pt cooling rod[26], to control nucleation; 75 mm diameter boules of PZN-9PT have been grown using this method [Matsushita et al. (2002)[26]]. Seed crystals can also be used. Good quality boules (ϕ > 40 mm) of PMN-xPT[31] and PZN-xPT[20] have been grown by this method.

By adding other mixed oxides to the solution, PZN-xPT and PMN-xPT crystals can be doped to modify their properties. Doping with Fe has a hardening effect, leading to a lower dielectric loss[24,25], just as it does in PZT[32]. Fe-doped PMN-38PT may prove useful for their pyroelectric properties in high-performance infrared detectors[25].

The crystal growth mechanism for PZN-9PT has been investigated[20]. Crystals grown by a seeded Bridgman method tended to have growth facets close to the $\{001\}_C$ crystallographic planes[26]. Growth proceeds by a layer-growth mechanism with $[BO_6]$ octahedral units being incorporated fastest along the $<111>_C$ directions such that the $\{111\}_C$ faces disappear. The bonding force is lowest for the $\{001\}_C$ crystallographic planes and hence the growth rate here is lowest.

As grown crystals are usually separated from the unwanted flux by washing in hot nitric acid (20-50%) for several hours[19,21]. They are commonly oriented long one of the $<001>_C$, $<101>_C$ or $<111>_C$ crystallographic direction using Laue X-ray back diffraction, sliced into wafers of varying thicknesses and sometimes mirror-lapped. Grown crystals of PMN-xPT and PZN-xPT tend to be yellow in color or light brown with increasing size[21,22,26,31]. This was true of all as-received plate samples. As noted above, larger cuboid samples from TRS ceramics were distinctly orange or green.

Compositional heterogeneity and property fluctuation

The main problem facing growers of PMN-xPT and PZN-xPT is the variation of materials properties resulting in as-synthesized crystals ("property fluctuation"). In solution-grown PZN-xPT crystals, flux inclusions are the most common defect and result in inferior piezoelectric properties[33]. However, the main reason for property variation remains *compositional heterogeneity*, that is *spatial variation in PT content* (x); it can be particularly important in large crystals grown using nucleation control. Compositional heterogeneity is particularly problematic for the characterization of PMN-xPT and PZN-xPT single crystals and will be discussed further in later chapters.

In one study, quantitative X-ray fluorescence was used to measure the composition variation in a 75 mm diameter boule of PZN-9PT grown by the Bridgman method. The PT content in successive slices varied by 0.6 mol% over a distance of around 20 mm along the length of the crystal[26]. This corresponds to a change in Curie temperature of around 10 °C and is not too much smaller than the room-temperature width of the morphotropic phase boundary region (< 2 mol%) in PZN-xPT[34]. Hence changes in phase can be expected due to such heterogeneity and, therefore, large property fluctuations. The coexistence of phases (rhombohedral, monoclinic and tetragonal) is commonly observed in crystals of PMN-xPT and PZN-xPT around the morphotropic phase boundary[35-37].

Severe property fluctuation was observed in certain as-received samples. Figure 2 shows a large variation in permittivity for two halves of a 15 x 15 mm^2, PMN-33PT plate.

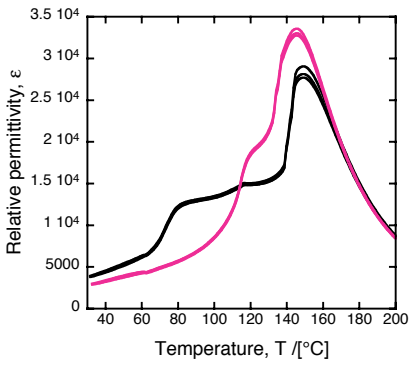

Fig. 2. Dielectric constant measured as a function of temperature upon heating in two unpoled, $[001]_C$-oriented crystals of PMN-33PT cut from the same 15 x 15 mm^2 plate (measured at frequencies 1, 10 and 100 kHz).

Such heterogeneity is due to differences in the equilibrium segregation coefficient of the component cations[23,26]. The segregation coefficient is thought to be greater for Ti than for the other B-site cations such that the concentration of Ti in solution decreases faster than that of the other cations during growth. Hence the first-grown crystal is Ti rich and the last-grown Ti poor and the spatial variation is worst along the growth direction (close to $<111>_C$)[23]. Where wafers are cut at any angle other than 90° to the growth direction, as is the case for $<001>_C$ slices, spatial variation of PT content will also be observed within the wafer. Differences of up to 0.3mol% have been observed within three inch wafers of PZN-9PT[26]. Elsewhere, a 0.4 mol% variation was found across 3 inch $(001)_C$ wafers of PZN-8PT grown by the flux technique; the authors of the study suggest that a variation in T_C of less than $\pm 3°C$ is necessary to keep variations in coupling factor to within $\pm 10\%$. While it seems that homogeneity can be improved by optimizing growth parameters[16] it will be very difficult to eliminate[31]. It remains one of the largest problems facing growers of PMN-xPT and PZN-xPT single crystals for large-scale use in commercial applications.

Determination of composition

Because of this problem the compositions of all supplied crystals in table II were treated as “nominal” and a convenient method for verification of their composition was sought. EDS (energy dispersive spectroscopy[38]) analysis, using a spectrometer built into a scanning electron microscope, was attempted for various single crystal $[001]_C$ plates of PZN-xPT and PMN-xPT. In this technique, X-ray emission from the excited sample due to various electronic transitions from various (K, L, M, O etc.) electronic shells is analyzed in energy (wavelength) and intensity to give a quantitative measure of the concentration of each element in the structure. The results of one such EDS measurement, for a 12 x 12 mm^2 sample of “PZN-9PT”, are shown in table III and figure 3.

Table III
EDS compositional analysis of a crystal with nominal composition PZN-9PT. The various elemental concentrations for the three spatial positions shown schematically in figure 3 are given; the electronic transitions for each measurement are also listed in parentheses. Also given are the expected concentrations based on the nominal stoichiometry.

Element	Stoichiometry /[at.%]	Element (transition)	Position 1 /[at.%]	Position 2 /[at.%]	Position 3 /[at.%]
Pb	20	Pb (M)	15.7	19.2	20.3
Zn	6.1	Zn (L)	7.2	7.0	7.38
Nb	12.1	Nb (L)	10.7	12.9	13.8
Ti	1.8	Ti (K)	1.6	2.4	2.2
O	60	O (K)	64.7	58.6	56.4

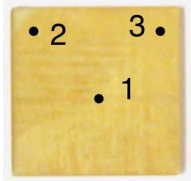

Fig. 3. Beam positions (schematic) across a 12 x 12 mm^2 "PZN-9PT" crystal for the EDS analysis shown in table III.

Although the values in table III do not match perfectly the nominal stoichiometry the agreement is close. There is evidence of some lead deficiency, especially in position 1, and a spatial variation in Ti content. It is confusing, however, that the Zn content also seems to be higher where the Ti content is highest, since mutually-exclusive B-site occupancy should preclude this. Moreover, repeated measurements at the same position led to variations of around 0.8 at.% in the measured concentrations; this was probably an effect of sample charging.

In conclusion, EDS did not prove to be a good quantitative method for compositional analysis of PMN-xPT and PZN-xPT single crystals. Better results might be achieved by calibrating the measurement with standards[38] but there will always be problems in measurements of non-conductive samples due to charging. As well as X-ray fluorescence analysis (XFA)[26,31], other methods have been used by researchers to determine true composition including inductively coupled plasma optical emission spectrometry (ICP-OES)[23] and electron probe microanalysis[35,39]. However, none of these methods were readily available and it would be extremely time consuming to measure the compositions all of the samples in table II with these techniques.

Therefore, for this thesis work, compositions were determined by comparison of phase transition temperatures to those reported in the literature. For all samples received (or for at least one sample cut from each crystal) the peak permittivity temperature, or otherwise, was measured and used to determine the composition. This method is discussed further in the next chapter. Suffice to say, however, it is not 100% accurate and thus there will be some slight error in all compositions reported in this thesis. Importantly, any error will not affect any of the conclusions drawn.

Finally, compositional homogeneity of the commercial samples was generally very good; this is shown in figure 4 by dielectric measurement for samples of PZN-8PT (Microfine) and PMN-28PT (HC Materials).

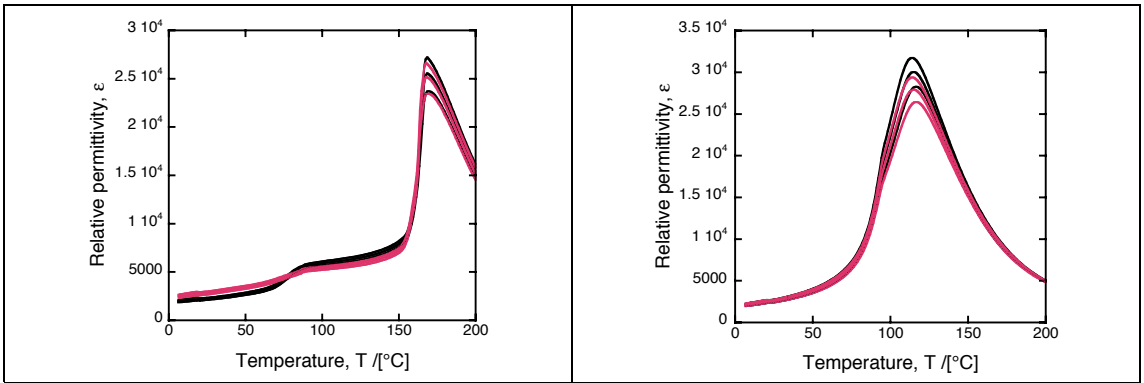

Fig. 4. Dielectric constant (heating; f = 1, 10, 100 kHz) measured as a function of temperature in two quarters cut from two commercially supplied 10 x 10 mm^2 plates of PZN-8PT (left) and PMN-28PT (right).

III. SINGLE CRYSTAL ORIENTATION

As noted above, single crystals usually grow faster along certain directions than others and, hence, develop natural growth facets. However, to determine the orientations of these facets with respect to the internal crystal lattice and, likewise, to orient and cut a crystal parallel to a $\{001\}_C$, $\{101\}_C$ or $\{111\}_C$ crystallographic plane, the Laue X-ray diffraction method is used. The same technique was useful as part of this thesis work to verify the nominal orientations given to us by the crystal growers as listed in table II. Crystal misalignment would be particularly important in domain engineering, as introduced in chapter one, where degeneracy of domain variants in the presence of an applied electric field (or stress) depends on the polarization vector of all domain variants being equally inclined to the field.

Laue diffraction

The technique of Laue diffraction is well explained elsewhere[38,40]. Briefly, a continuous spectrum of X-ray radiation is incident on a flat sample surface and the Bragg "reflections[38]" are recorded on photographic film placed perpendicularly to the beam direction and parallel to the sample. The solution to Bragg's law in three dimensions is an assortments of "spots" in an arrangement which must reflect the elements of the point group symmetry of the crystal.

Back reflection geometry[38] was used for this work with a film-sample separation of 3-5 cm. The sample was mounted, using double-sided scotch tape, to a three-axial cradle. The sample holder was first aligned using a well-oriented (001) silicon wafer. A typical accelerating voltage for the continuous Cu X-ray radiation was 20 kV; a 35 mA beam current was used. A 10-30 minute exposure time for the quick developing Polaroid film (type 57) was sufficient.

The Laue photos clearly showed the rotation axes and mirror planes of the crystals' point groups. Since the as-received, virgin crystals are macroscopically cubic (point group *m3m*)[41], $<001>_C$, $<101>_C$ and $<111>_C$ oriented crystals should reveal four-fold, two-fold, and three-fold rotation axes respectively[42]. This was the case, as shown in figure 5. The Laue photos produced were generally quite blurred, possibly due to a high domain density and a degree of disorder characteristic of relaxor-ferroelectric crystals. Reflections were also quite weak, likely due to the high lead contents of the crystals[40].

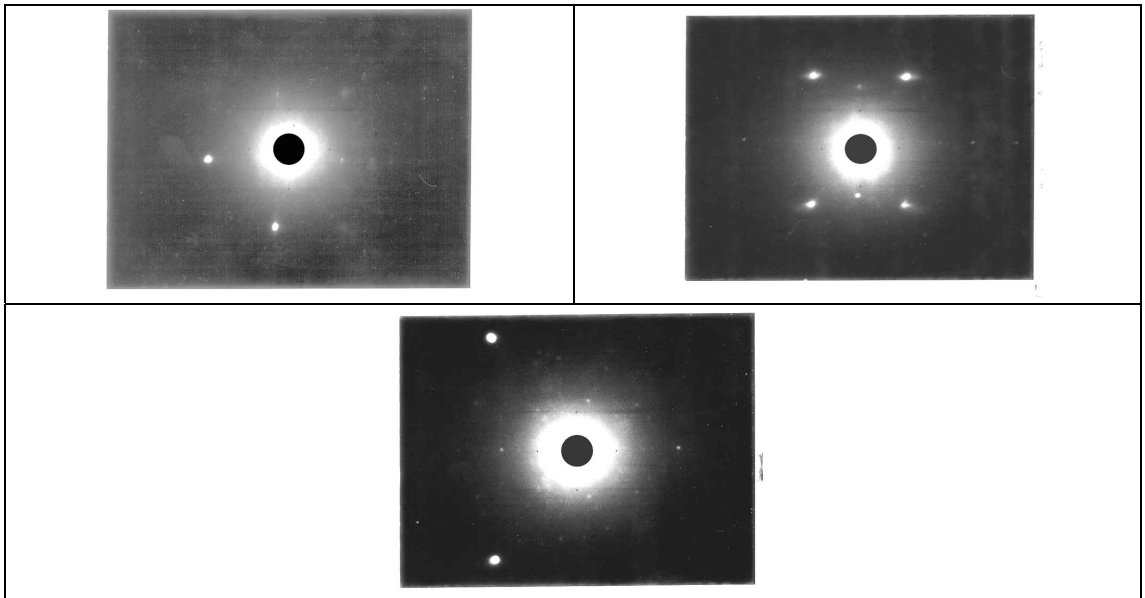

Fig. 5. Laue X-ray back reflection photos taken from samples of $(001)_C$, $(101)_C$ and $(111)_C$ oriented PZN-8PT (top left, top right and bottom, respectively).

Using these Laue patterns, and if the crystal symmetry is known, any misalignment can be calculated. To do this, a software package "Orientexpress", available as freeware, was used[43]. By inputting the point group of the crystal lattice (assumed to be *m3m*), the film size and distance from the sample, and the nominal orientation of the crystal, a Laue pattern could be generated and overlaid on the scanned photo. A process of trial and error was then used to fit the two patterns together and yield the three angles of misorientation. The commercially supplied samples were all found to be correctly oriented to within at least $\pm 1°$.

IV. SAMPLE PREPARATION

Single crystals are generally much more fragile than polycrystalline ceramics and therefore their manipulation, and the preparation of samples for structural and electrical characterization, is more involved. The various stages are briefly described below.

Cutting

The 10 x 10 mm^2 plate samples were generally cut into four equally-sized pieces. Where necessary, cuboid samples were also cut to yield better aspect ratios for direct measurements as discussed in chapter eight. Either a circular diamond saw or a wire saw was used. The wire saw was found to dice much more cleanly, leading to less chipping of the material, better edges and less waste material (a smaller "kerf"). Where the diamond saw was used, the lowest possible angular velocity was used to minimize chipping. Quick-drying liquid cyanoacrylate glue was preferred and used to adhere the crystals to a graphite cutting block. Use of glue avoids heating the crystals, as is necessary with wax as an adhesive, and thus the risk of cracking due to constricted thermal expansion; the glue could easily be removed by soaking in acetone.

Polishing

For electrical measurements, the surfaces were either left untouched (where as-cut) or roughened with abrasive silicon carbide paper, where mirror-lapped, for better electrode adherence. However, for optical investigation (polarized light microscopy) the samples were polished with progressively fine silicon carbide paper (Struers 1000, 2400 and 4000 grades) and then diamond paste (6 micron and 1 micron). Ethanol was found to be a good enough lubricant for polishing on a polishing wheel. The samples were stuck into adjustable-height aluminum sample holders and an automated machine (DAP-7, Struers) was preferred to avoid beveling. Between polishing steps the samples were soaked in soapy water in an ultrasonic bath to remove embedded diamond particles, the crystals being relatively soft mechanically. Samples were removed from the glue by soaking in acetone.

Annealing

After cutting, and especially after polishing, PMN-xPT and PZN-xPT single crystals tend to contain residual stresses which affect their general ferroelastic domain structure. For example, initial structural investigation by polarized light microscopy of as-polished PMN-28PT and PMN-33PT plates revealed many spindle- or "tweed-" like domains with widths around 1 μm, albeit in organized crystallographic directions; this is shown in figure 6. It was speculated that the uniformity of the domain size was due to the size of the diamond paste used (1 micron). Therefore, after polishing, all samples were annealed before structural characterization.

Most researchers working with PMN-xPT and PZN-xPT who do anneal their crystals do so at around 250-500°C for 0.5 to 20 hours[44-48]. A sufficiently slow heating and cooling rate should be chosen to avoid breaking the crystals. For this work annealing was carried out at 400 °C for 10 hours, conservatively, via heating and cooling at 2°C/min. The importance of this annealing step is shown in figures 7 and 8. In as-polished samples of PZN-9PT (fig. 7) and PMN-33PT (fig. 8), annealing leads to bulk "relaxation" of the microstructure, and coarsening and removal of the fine domain structure.

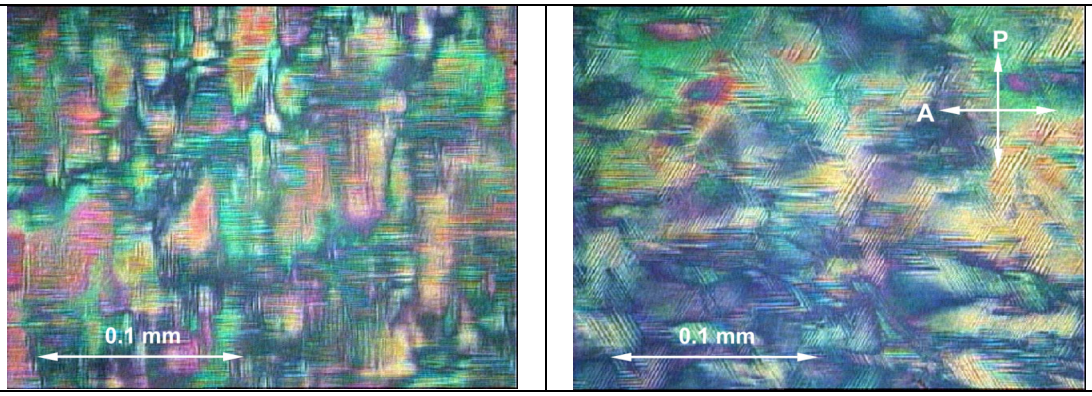

Fig. 6. Polarized light micrographs showing the $(101)_C$ [left] and $(111)_C$ [right] surfaces of two PMN-28PT samples, taken between crossed polarizers. The samples were first polished using 1 micron diamond paste which is manifest in the observed domain size.

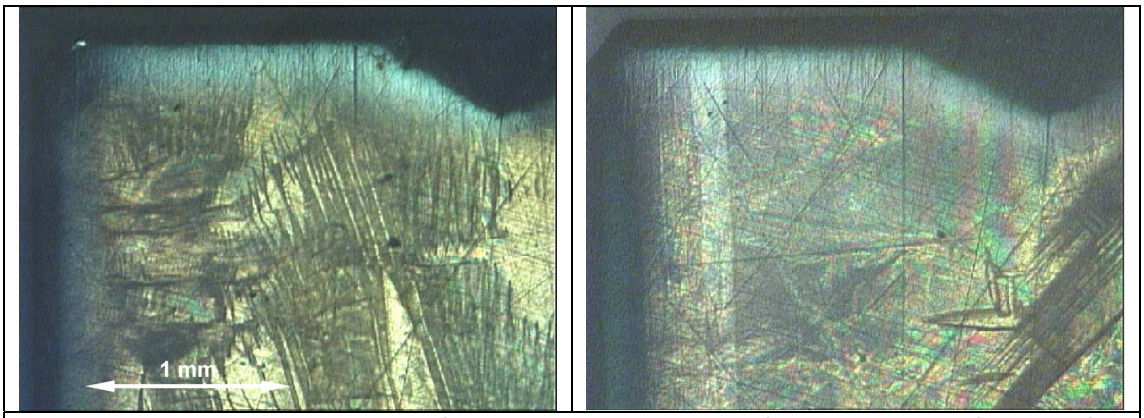

Fig. 7. $[001]_C$-oriented sample of virgin PZN-9PT (IKZ) after polishing (left) and after annealing at 450 °C for 24 hours (right) to remove residual stresses. The micrograph was taken between crossed polarizers. A coarser domain structure results from heat treatment and subsequent cooling through the Curie temperature.

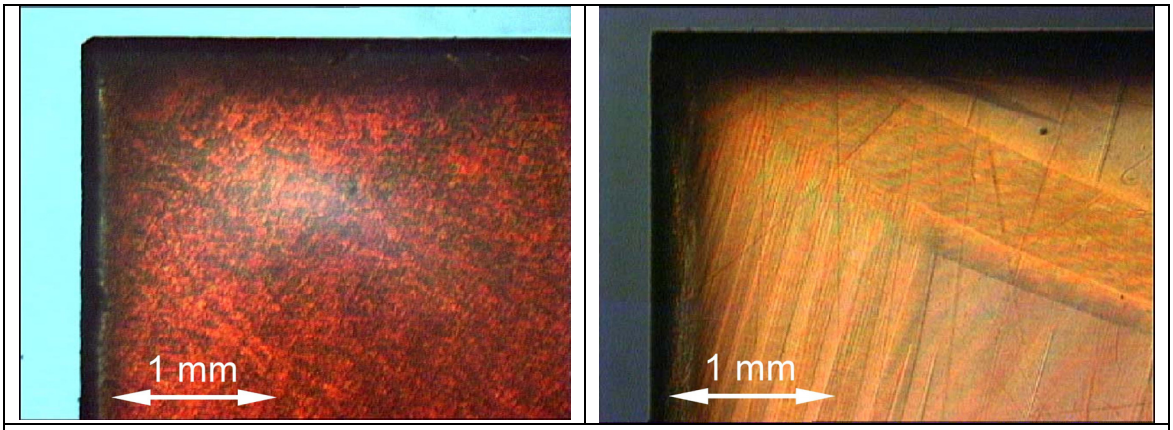

Fig. 8. Two $[111]_C$-oriented, unpoled, plate samples of PMN-33PT after polishing (left), and after polishing and subsequent annealing (right). The micrographs were taken between crossed polarizers. Annealing seems necessary to regain an equilibrium domain structure.

Electroding

Gold was used as the main electrode material for dielectric and piezoelectric measurements, deposited by sputtering in a commercial machine (Balzers) in argon at 40 kV. Gold electrodes are usefully reflective for strain measurements with the Fotonic sensor described in chapter two. For better adherence the surfaces were left unpolished before sputtering.

Where transparent electrodes were required for polarized light microscopy (chapter seven), indium tin oxide $0.9(In_2O_3)$-$0.1(SnO_2)$ was used as the electrode material. Indium tin oxide (ITO) is used in a range of optoelectronic devices[49] including liquid crystal flat panel displays[50]. Its conductivity and transparency is strongly affected by the number of oxygen vacancies. Annealing can also change its properties considerably. Hence, control of oxygen during sputtering is key during sputtering from a stoichiometric ceramic target. A brief literature search[49-52] and a few trial runs yielded the following optimal sputtering conditions: 4" x 0.125" 99.99% purity ITO ceramic target (Kurt J. Lesker, PA, USA); DC sputtering; 5 mT pressure; room temperature; 4.0 sccm Argon; 0.5 sccm O_2; 150 W. By adjusting the deposition conditions good conducting electrodes with high transparency could be deposited. However, although such electrodes give good conductivity and transparency, they are much less convenient to deposit than gold ones.

REFERENCES

1 All presented research on single crystal transducers for medical imaging applications at the IEEE Ultrasonics Symposium, Rotterdam, the Netherlands in 2005.

2 DORIS Project ("Development of relaxor-based improved piezoelectric single crystals")

3 TRS Ceramics, Penn State, PA, USA (www.trsceramics.com)

4 H.C. Materials Corporation, Urbana, Illinois, USA (www.hcmat.com)

5 Microfine Materials Technologies Ltd., Singapore (www.microfine-piezo.com)

6 S. L. Swartz and T. R. Shrout, Materials Research Bulletin **17,** 1245-1250 (1982).

7 S. J. Jang, K. Uchino, S. Nomura, and L. E. Cross, Ferroelectrics **27,** 31-34 (1980).

8 S. W. Choi, J. M. Jung, and A. S. Bhalla, Ferroelectrics **189,** 27-38 (1996).

9 O. Noblanc, P. Gaucher, and G. Calvarin, J. Appl. Phys. **79,** 4291-4297 (1996).

10 J. Carreaud, P. Gemeiner, J. M. Kiat, B. Dkhil, C. Bogicevic, T. Rojac, and B. Malic, Phys. Rev. B **72,** 174115 (2005).

11 A. D. Hilton, C. A. Randall, D. J. Barber, and T. R. Shrout, Ferroelectrics **93,** 379-386 (1989).

12 D.-H. Lee and N.-K. Kim, Materials Letters **34,** 299-304 (1998).

[13] J. Kuwata, K. Uchino, and S. Nomura, Ferroelectrics **37,** 579-582 (1981).
[14] J. Kuwata, K. Uchino, and S. Nomura, Jpn. J. Appl. Phys. **21,** 1298-1302 (1982).
[15] D. Elwell and H. J. Schell, *Crystal growth from high-temperature solutions* (Academic Press, London, 1975).
[16] Z.-G. Ye, in *Piezoelectric Single Crystals and Their Application*, edited by S. Trolier-McKinstry, L. E. Cross, and Y. Yamashita (2004), p. 297-322.
[17] P. Bridgman, Proc. Am. Acad. **60,** 305-315 (1925).
[18] S. Nomura, H. Arima, and F. Kojima, Jpn. J. Appl. Phys. **12,** 531-535 (1973).
[19] X. Jiang, F. Tang, J. T. Wang, and T.-P. Chen, Physica C **364-365,** 678-683 (2001).
[20] B.-J. Fang, H.-Q. Xu, T.-H. He, H.-S. Luo, and Z.-W. Yin, J. Crystal Growth **244,** 318-326 (2002).
[21] M. Dong and Z.-G. Ye, Journal of Crystal Growth **209,** 81-90 (2000).
[22] T. R. Shrout, Z. P. Chang, N. Kim, and S. Markgraf, Ferroelectrics Letters **12,** 63-69 (1990).
[23] R. Bertram, G. Reck, and R. Uecker, J. Crystal Growth **253,** 212-220 (2003).
[24] S. Zhang, L. Lebrun, D.-Y. Jeong, C. A. Randall, Q. Zhang, and T. R. Shrout, J. Appl. Phys. **93,** 9257-9262 (2003).
[25] X. Wan, X. Tang, J. Wang, H. L. W. Chan, C. L. Choy, and H. Luo, Appl. Phys. Lett. **84,** 4711-4713 (2004).
[26] M. Matsushita, Y. Tachi, and K. Echizenya, J. Crystal Growth **237,** 853-857 (2002).
[27] W. Chen and Z.-G. Ye, Journal of Crystal Growth **233,** 503-511 (2001).
[28] K. Harada, S. Shimanuki, T. Kobayashi, S. Saitoh, and Y. Yamashita, Key Engineering Materials **157-158,** 95-102 (1999).
[29] K. Harada, Y. Hosono, T. Kobayashi, Y. Yamashita, S. Wada, and T. Tsurumi, J. Crystal Growth **237,** 848-852 (2002).
[30] Z.-G. Ye, M. Dong, and Y. Yamashita, J. Crystal Growth **211,** 247-251 (2000).
[31] H. Luo, G. Xu, H. Xu, P. Wang, and Z. Yin, Jpn. J. Appl. Phys. Pt. 1 **39,** 5581-5585 (2000).
[32] B. Jaffe, W. R. Cook, and H. Jaffe, *Piezoelectric Ceramics* (Academic Press, 1971).
[33] S.-E. E. Park and W. Hackenberger, Current Opinion in Solid State and Materials Science **6,** 11-18 (2002).
[34] D. La-Orauttapong, B. Noheda, Z.-G. Ye, P. M. Gehring, J. Toulouse, D. E. Cox, and G. Shirane, Phys. Rev. B **65,** 144101 (2002).
[35] V. A. Shuvaeva, A. M. Glazer, and D. Zekria, J. Phys.: Condens. Matter **17,** 5709-5723 (2005).
[36] Z.-G. Ye, Current Opinion in Solid State and Materials Science **6,** 35-44 (2002).
[37] G. Xu, H. Luo, H. Xu, and Y. Yin, Phys. Rev. B **64,** 020102(R) (2001).
[38] T. Mulvey and R. K. W. (ed.), *Modern physical techniques in materials technology* (Oxford University Press, London, 1974).

[39] D. Zekria, V. A. Shuvaeva, and A. M. Glazer, J. Phys.: Condens. Matter **17,** 1593-1600 (2005).
[40] B. D. Cullity, *Elements of X-ray diffraction*, 2nd ed. (Addison-Wesley, Masschusetts, 1978).
[41] J. F. Nye, *Physical properties of crystals*, 2nd ed. (Clarendon Press, Oxford, 1985).
[42] R. E. Newnham, *Properties of materials* (Oxford University Press, Oxford, 2005).
[43] http://www.ccp14.ac.uk/ccp/web-mirrors/lmgp-laugier-bochu/
[44] D. Li, P. Wang, X. Pan, H. Luo, and Z. Yin, J. Mater. Res **16,** 1252-1255 (2001).
[45] J.-K. Lee, J. Y. Yi, K.-S. Hong, S.-E. Park, and J. Millan, J. Appl. Phys. **91,** 4474 (2002).
[46] D.-L. Li, G.-S. Xu, P.-C. Wang, X.-M. Pan, H.-S. Luo, and Z.-W. Yin, Ferroelectrics **253,** 31-38 (2001).
[47] S. Wada, S.-E. Park, L. E. Cross, and T. R. Shrout, Ferroelectrics **221,** 147-155 (1999).
[48] F. Bai, J. Li, and D. Viehland, Appl. Phys. Lett. **85,** 2313-2315 (2004).
[49] J. Dutta and S. Ray, Thin Solid Films **162,** 119-127 (1988).
[50] D.-H. Yoo and M.-W. Shin, Materials Science Forum **449-452,** 1001-1004 (2004).
[51] B. L. Gehman, S. Jonsson, T. Rudolph, M. Scherer, M. Weigert, and R. Werner, Thin Solid Films **220,** 333-336 (1992).
[52] MRS Bulletin **25** (2000).

Chapter four

Relaxor-ferroelectric phase transition in PMN-xPT and PZN-xPT solid solutions

In this chapter, an in-depth review is given of the physical behavior and structure of PMN-xPT and PZN-xPT relaxor-ferroelectrics in terms of the various models postulated to describe their behavior. Various key temperatures are defined which characterize their ("relaxor to ferroelectric") transition from a short-range ordered, non-polar (relaxor) phase at high temperatures and low PT contents to long-range ordered, polar (ferroelectric) phases at low temperatures and high PT contents. It is noted that in low PT-content samples, long-range ordered, ferroelectric phases can only be induced by application of an electric field (poling).

Furthermore, published measurements of these phase transition temperatures for PMN-xPT and PZN-xPT single crystals and ceramics are thoroughly reviewed; the collected data is used to construct phase diagrams which accurately show the phase transition from short- to long-range ordered phases in PMN-xPT and PZN-xPT solid solutions. Lines of best fit are derived which should prove more accurate in back-determining the composition of as-grown samples than those quoted elsewhere. Finally, important similarities between the two phase diagrams are discussed, especially with respect to the position of the morphotropic phase boundary.

I. INTRODUCTION

Although the origins of the large piezoelectric response in PMN-xPT and PZN-xPT are the subject of debate, the answer must lie to some extent in their complex chemistry and related "relaxor" behavior. As yet, no definitive phase diagram exists for PMN-xPT or PZN-xPT which reflects the transition from relaxor behavior at low lead titanate (PT) contents to more classical, long-range ordered, ferroelectric behavior at high PT contents; nor does one exist which faithfully describes the nature of the transition from the high-temperature, paraelectric phase to the low-temperature, polar phases.

As will become apparent, there is a transition in dielectric behavior across the PMN-xPT phase diagram from one exhibiting a diffuse dielectric maximum, with a peak permittivity temperature T_m dependent on frequency, in PMN (x = 0) to a dielectric behavior showing a true, sharp Curie-Weiss transition at a frequency-independent temperature T_C in PT (x = 1)[1-4]. The same is true for PZN-xPT[5]. Moreover, low PT-content, unpoled PMN-xPT and PZN-xPT remain macroscopically pseudocubic and therefore non-polar to low temperatures; they are *not* ferroelectric in the traditional sense. Only after poling do certain compositions become long-range ordered. Importantly, PMN-xPT and PZN-xPT will look very different in their poled and unpoled conditions.

In spite of all this, the temperature of maximum permittivity T_m is often confused with the Curie temperature even for low PT contents; this is far from the truth in low PT compositions where no structural phase transition occurs at T_m. The two temperatures T_m and T_C converge only at around x = 0.40-0.50 in PMN-xPT[6,7], for example. The two most recent phase diagrams published for PMN-xPT [Noheda et al. (2002)][8] and PZN-xPT [La-Orauttapong et al. (2002)][9] are based on synchrotron X-ray diffraction experiments and concentrate on the crystal structure around the morphotropic phase boundary. In both cases, data is borrowed from elsewhere to define the temperature of transformation from the cubic phase. For example, in the PZN-xPT diagram[9], the cubic to -low symmetry transition temperature plotted corresponds to the permittivity maximum T_m as measured on a series of PZN-xPT single crystals, at 1 kHz, in the original paper by Kuwata[10] et al. The plotted phase boundary will not therefore correspond to a true structural phase transition (T_C) as might be observed by X-ray diffraction, at least for low PT-content crystals.

Thus, commonly-used phase diagrams for PMN-xPT and PZN-xPT often confuse the real, diffuse phase transition with a classically sharp ferroelectric phase transition. One of the aims of this chapter is to clarify this issue. To this end, phase diagrams will be constructed based on data from unpoled and poled crystals which accurately describe the "relaxor-to-ferroelectric" transition that occurs with decreasing temperature and increasing PT content. The phase stabilities of the *macroscopically polar* (ferroelectric) phases of *poled* PMN-xPT and PZN-xPT, and the position of the morphotropic phase boundary, will be discussed in chapter six.

Back determination of composition

Out of literally hundreds of papers on PMN-xPT and PZN-xPT published over the last decade, only a handful have included direct measurements of composition. The overwhelming majority of authors assume the stoichiometry fixed by the quantities of starting reagents used in the ceramic processing or crystal growth and, therefore, "nominal" compositions. As discussed in the previous chapter, due to Pb segregation, different samples cut from the same boule can have PT contents significantly different to the target composition.

Some authors, however, have taken to comparison of the "Curie temperature", measured as the temperature of maximum dielectric constant $\varepsilon(T)$ and therefore really T_m, to published phase diagrams to determine crystal composition. For instance, the $x = \left(T_C + 10\right)/5$ "rule" has been used by a variety of authors[11-13] to calculate the PT content (in mol. %) of PMN-xPT. However, as will be shown in this chapter, this formula is very far from numerically accurate. Secondly, it is also not clear to which temperature "T_C" corresponds. Thirdly, it neglects the fact that the Curie temperature for ferroelectric crystals shows significant *thermal hysteresis*, or a difference in transition temperature upon heating and cooling [$T_C^{heat} = T_C^{cool} + \Delta T$], resulting from a range of *metastability* wherever the transition is first order; the size of the hysteresis ΔT_C is around 5°C in barium titanate[14] (see fig. 2). Thus, for a phase diagram to be useful as a means of determining composition one should be clear as to whether T_C corresponds to heating or cooling. Accordingly, another objective of this chapter is to set up a phase diagram which can be used to determine the composition of as-received crystals to good degree of accuracy. This involved sifting through a vast quantity of published data.

Literature review

A summary of all the data collected for this review is plotted in figure 1. The data is shown unsorted, that is: from dielectric, PLM and XRD studies; taken upon either heating or cooling; at various measurement frequencies from 1 to 100 kHz; in either poled or unpoled conditions; and, finally, either with or without electrical bias. All the temperatures, "T_m", "T_C", "T_d" and "T_f" will be clearly defined in section III.

Various important points can be made. Firstly, the amount of data readily available for PMN-xPT far outstrips that available for PZN-xPT. This is probably due to the difficulty in producing ceramic PZN-xPT, as mentioned in chapter one. Secondly, we should be very careful in defining and plotting the differing transition temperatures. Thirdly, greatest care is needed in defining the phase transition at low PT contents ($x < 0.4$). Finally, assumption of linearity in the phase transition temperature across the entire solid solution ($0 \le x \le 1$) cannot be made.

Refinements of the phase diagrams for unpoled PMN-xPT and PZN-xPT are presented in sections IV and V, respectively. First relaxor-

ferroelectric behavior will be reviewed in terms of various theoretical models in order to define the various transitions that occur in ferroelectrics which lack complete long range order.

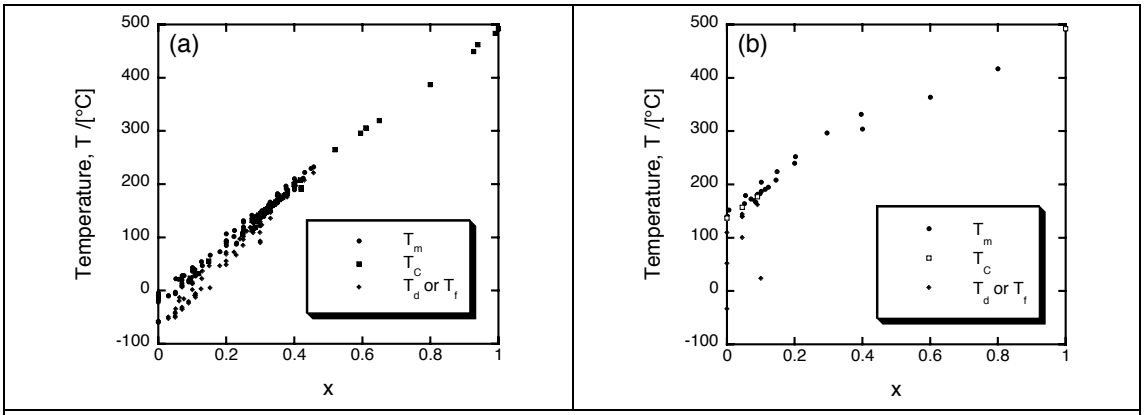

Fig. 1. Summary of all published data collected defining the phase transition from the cubic paraelectric phase in PMN-xPT (a) and PZN-xPT (b). The transition temperatures are defined in table I.

II. RELAXOR FERROELECTRICS

The prototypic "relaxor-ferroelectric[15]", or ferroelectric exhibiting a diffuse phase transition[16,17], is lead magnesium niobate or $Pb(Mg_{1/3}Nb_{2/3})O_3$ [PMN]; it is closely related to lead zinc niobate or $Pb(Zn_{1/3}Nb_{2/3})O_3$ [PZN]. PMN and PZN both assume a ABO_3 prototypic perovskite structure (see appendix I) like that of more classical barium titanate[14] (BT) and lead titanate (PT), except with mixing of two cations (Mg^{2+} and Nb^{5+} in PMN) on the B-site and hence a degree of *substitutional disorder*[17,18].

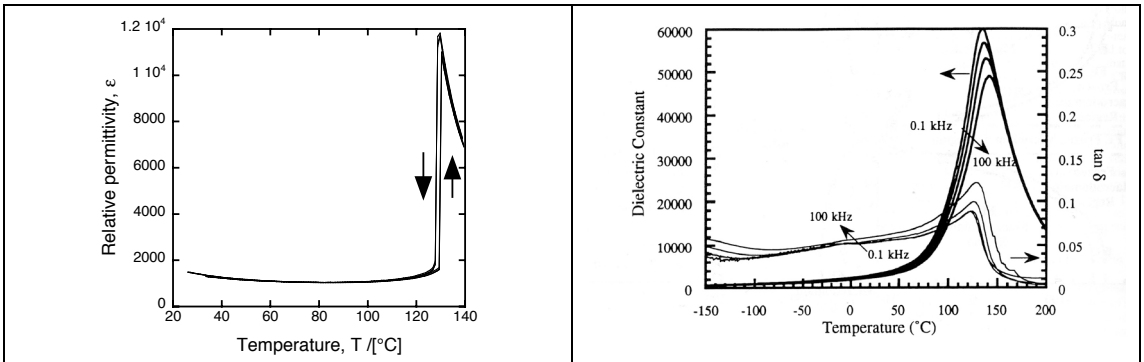

Fig. 2. (Left) Curie-Weiss behavior at the paraelectric-ferroelectric phase transition in barium titanate. Barium titanate lowers its symmetry from cubic *m3m* to tetragonal *4mm* upon cooling through T_C. (Right) Permittivity versus temperature for an unpoled PZN single crystal at 0.1, 1, 10 and 100 kHz upon cooling taken from Mulvihill et al. (1997)[19]. There is no displasive phase transition at T_m.

Non Curie-Weiss behavior: the Curie "range"

Instead of showing a sharp, frequency independent Curie transition from a high temperature, high symmetry (cubic *m3m*), paraelectric phase to a

distorted lower symmetry phase, as observed in the more classically ferroelectric barium titanate[20], PMN instead exhibits what has been described as a Curie temperature "range[19]". Most characteristically, the small-field permittivity shows a diffuse maximum with a peak (T_m, ε_m) which is dependent on measurement frequency[15]. For ceramic PMN at 1 kHz the maximum permittivity is approximately 20000 and occurs at around 0°C[21]. Very similar behavior is observed for PZN with a maximum permittivity of 56000 measured in a $[111]_C$-oriented single crystal at T_m = 140°C (again at 1 kHz)[19]. The typical dielectric behavior of PZN is shown in the right of figure 2.

As mentioned, this behavior is distinct from Curie-Weiss behavior shown by "classical" perovskite ferroelectrics[14,22] [fig. 2 (left)]. Upon cooling through the Curie temperature T_C, BT and PT undergo a symmetry lowering from the cubic phase; this transition is characterized by localized, ergodic displacements of the B-site cation which are correlated across each domain, typically on the scale of microns. The volume average (over each domain) of all the local dipoles created during the transition corresponds to a net spontaneous polarization $\boldsymbol{P_S}$. The transition occurs at the well defined temperature (T_C) which, for first order phase transitions, corresponds to the maximum in permittivity T_m ($T_C = T_m$). Above T_C the permittivity ε is described by the Curie-Weiss law:

$$\varepsilon = 1 + \frac{C}{T - T_0} \approx \frac{C}{T - T_0} \qquad [1]$$

where C is the Curie-Weiss constant and $T_C > T_0$ for first order phase transitions. Such behavior is well predicted by phenomenological Landau-Ginzburg-Devonshire theory[23,24]. Within the framework of this theory there is no frequency dependence of T_C.

In contrast, no structural phase transition occurs at T_C in PMN[25] and PZN[19]. Although the matter of some debate[26,27], it seems like no long-range ordered, lower-symmetry phase (with a correlation length above 70 nm[28]) is observed without application of an electric field and that they both remain globally cubic to very low temperature[19,25]. The peak in permittivity at T_m does not result from a phase transition, at least in a traditional sense. Whereas the main contribution to the dielectric anomaly at T_C in normal perovskite ferroelectrics comes from the peak in susceptibility of the ionic lattice caused by phonon softening ("soft mode" theory[22,23]), it amounts to less than 1% of the total permittivity in PMN at 1kHz[29].

Smolenskii description of relaxors

The original explanation for the relaxor-ferroelectric behavior of PMN postulated by Smolenskii cites *disordering* of the Mg^{2+} and Nb^{5+} ions on the B site[15]. That is, the *Curie range* observed is due to fluctuations in the local Mg:Nb concentration leading to different volumes of material with different average compositions and, therefore, differing Curie temperatures. Assuming a local Gaussian distribution of Curie temperatures[30] we can write:

$$\varepsilon = \varepsilon_m \exp\left[-\frac{(T-T_m)^2}{2\delta^2}\right] \qquad [2]$$

The standard deviation of the Gaussian function δ thus gives a measure of the spread of Curie temperatures and hence the "diffuseness[30,31]" of the transition. Rearranging and taking a limited series expansion we arrive at the common Smolenskii[29,31] description of frequency dispersion in relaxors:

$$\frac{1}{\varepsilon} = \frac{1}{\varepsilon_m} + \frac{(T-T_m)^2}{2\delta^2\varepsilon_m} \qquad [3]$$

The dielectric behavior of many relaxor-ferroelectrics has been found to fit this law well[7,29] for a range of temperatures above T_m. In fact, the two have been combined into a single empirical formula:

$$\frac{1}{\varepsilon} = \frac{1}{\varepsilon_m} + \frac{(T-T_m)^\gamma}{2\delta^2\varepsilon_m} \qquad [4]$$

In this expression, as γ tends to 1 there is a tendency towards Curie-Weiss behavior with $T_C = T_m$; for $\gamma = 2$ we have relaxor behavior (equation [3])[31,32].

If the Smolenskii Curie-range model is valid then the diffuseness of a mixed $A(B'_x,B''_{1-x})O_3$ perovskite relaxor should be sensitive to the degree of ordering of the B-site cation. That is, by creating a 1:1 ordered "super structure" of repeating B' and B'' cations in adjacent unit cells, the Curie range should collapse to a single Curie temperature[15]. This has been shown to be the case in the "$x = 1/2$[33]" relaxor perovskite $Pb(Sc_{1/2}Ta_{1/2})O_3$ (PST) where 1:1 ordering is allowed by stoichiometry to go to completion across the entire crystal[33]. Where quenching of PST leads to disordered B site occupancy and relaxor behavior, annealing leads to a 1:1 ordered superstructure with a sharper, frequency-independent peak permittivity T_m characteristic of a "normal" ferroelectric[15].

However, where the mixed B-site cations have differing valences, for instance in "$x = 1/3$" perovskites $Pb(Mg_{1/3}Nb_{2/3})O_3$ and $Pb(Zn_{1/3}Nb_{2/3})O_3$, 1:1 ordering cannot occur across the sample. In PMN, 1:1 ordered regions on the scale of 6 nm have been evidenced by TEM studies embedded in a disordered matrix[33]. Such 1:1 ordered regions are necessarily rich in Mg whereas the disorder matrix will be rich in Nb. Due to the differing valences of the Mg^{2+} and Nb^{5+} cations, the order/disordering will necessarily lead to net *space charge formation*[33] and, unless these charges can be fully compensated in some way, internal electric fields within the sample. The size of the ordered regions will depend on the energy penalty presented by these fields. It is also noteworthy that, after substantial doping of the PMN with PT to form PMN-0.40PT, ordering regions were no longer observed; PT doping seems to reduce the tendency of the Mg^{2+} and Nb^{5+} cations to order[33].

Random field model

In the "random field" model[34,35], the electric fields creating by such spatial charge separation might account for the lack of *ergodicity* or *long-range order* in the low temperature phase of PMN. In this theory, a statistical approach is taken to model the quenched random fields[34] that could be generated for example by substitutional ordering (as in PMN), ionic shifts from equilibrium positions in an ideal lattice, or by lead and oxygen vacancies (from excess charge compensation). All of these will lead to imperfections, whether point charges, dilatational centers or electric dipoles, which can destroy long-range order[34]. In the model, the random field distribution is defined by some most probable field $\boldsymbol{E_0}$ and the half-width of the distribution $\boldsymbol{\Delta E}$. With increasing $\boldsymbol{\Delta E}$ there is a lesser tendency for long range ordering and a propensity for relaxor behavior[34].

Martensite analogy and "tweed"

In the context of this theory, random fields can be seen to frustrate the Curie-Weiss transition and stabilize the high temperature, non-polar, cubic phase down to temperatures below the thermodynamic equilibrium temperature it would otherwise have. Noting this persistence of the parent cubic phase down to low temperatures, Schmidt[36] and others[19,37] have pointed out the similarity between relaxor-ferroelectric phase transitions and martensitic phase transitions. Importantly, the martensite model for relaxor-ferroelectric transformations is backed up by strong microstructural similarities.

Martensitic[36,38,39] or "diffuse[17,36,38]" phase transitions characteristically occur far from thermal equilibrium, over a range of temperatures usually defined as the "*martensite start*" and "*martensite finish*" temperatures, M_S and M_F, respectively[39]. Nucleation of the low temperature phase within the parent phase matrix begins at M_S and becomes self-terminating at M_F where some parent phase is typically left untransformed resembling domain boundaries between regions (domains) of the low temperature phase[36]. Growth of the martensitic phase is usually strongly anisotropic with one or more preferred growth direction[39]. Importantly, the nucleation and growth are non-equilibrium processes and the transformation never goes to completion.

Due to coexistence of the lower symmetry phase with the parent, the associated lattice mismatch becomes very important to the kinetics, thermodynamics and microstructural characteristics of the phase transition[40]. The effect of lattice mismatch can become important to a phase transition whenever:

$$\mu S_{LM}^{\ 2} > \Delta G_V \qquad [5]$$

where S_{LM} is a typical crystal-lattice rearrangement strain characterizing the mismatch between the low temperature and parent phases, μ is a typical shear modulus, and ΔG_V is the driving force for the transformation equal to the difference between free energies of the stress-free product and parent

phases[40]. When the mismatch energy becomes comparable to the driving force for the transition, as is the case for martensitic phase transitions[39], the high temperature phase will be stabilized down to low temperatures. The phase transition can then only proceed if complete accommodation of the lattice mismatch is provided and a twinned, mesoscopic plate (or lamella) structure of the lower temperature phase results. The macroscopically average structure of such a structure should form an invariant plane strain[39] (IPS) with the parent phase for energy minimization. In such a case the average lamella spacing or twin size is given by:

$$\lambda \sim \left[\frac{\gamma D}{\mu S_{LM}^{\ 2}} \right]^{1/2} \qquad [6]$$

where D is the plate width and γ is the twin surface/interface energy. Characteristically fine ("mesoscale[41,42]") scale domain structures result due to the low energy of the (preferred) domain walls (with typical domain sizes varying with $\sqrt{\gamma}$ where γ is the domain wall energy[43]).

Cross-hatched, "tweed" microstructures are often observed, composed of finely-twinned, "needle"-shaped domains. Such tweed structures are observed, for example, in ferroelastic, martensitic alloys Fe-Pd and Ni-Al[44]. They are also observed in the high temperature superconductor yttrium barium copper oxide, $YBa_2Cu_3O_{7-\delta}$ (YBCO)[42,45,46]. YBCO transforms from a high temperature tetragonal phase to an orthorhombic one at around 700 K[45]. Twinning of the orthorhombic phase is observed on $\{110\}_C$ planes and domain sizes in the range 10 nm to 100 microns have been observed[42].

The domain structures induced in the surfaces of PMN-28PT single crystals by polishing (chapter three, figure 6) can also be described as tweed. There, the microstructure was of fine needle-shaped domains, of around 1 μm thickness, twinned on well-defined crystallographic planes. Such a microstructure implies a low domain wall energy in relaxor-ferroelectric PMN-28PT. Importantly, this tweed is a consequence of residual stresses from the polishing process. Since the points of intersection between such tweed domains are high energy points[47], and since annealing will tend to remove such residual stresses, the structure is thus unstable and coarsening of the "tweed" is indeed observed upon annealing. This is a strain-related, ferroelastic effect, albeit implying a low domain wall energy in relaxor-ferroelectric PMN-xPT as discussed elsewhere[48].

Tweed microstructures in PMN-xPT

Tweed microstructures have also been observed in relaxor-ferroelectric PMN-xPT by Viehland and coworkers, using both transmission electron microscopy[49] (TEM) and atomic force microscopy[50,51] (AFM) to achieve sub-micron resolutions unavailable in optical microscopy.

Using bright-field TEM, the authors have evidenced the evolution of the microstructure in unpoled PMN-xPT ceramics with increasing PT content from 10 to 60 mol.% [Viehland et al. (1995)[44]]. In PMN-10PT at room temperature

very fine, irregular “polar nano domains” were evidenced with an average size of around 5 nm. Such features were found to increase in size, upon increasing PT content, to around 10-15 nm in PMN-20PT. However, for PMN-35PT a clear cross-hatched tweed-like structure was evident with tweeds around 200 nm long and 20 nm wide. In contrast, normal micron-sized domains were observed in tetragonal PMN-40PT, similar to those observed in tetragonal barium titanate[52,53].

Seemingly, the room temperature microstructure coarsens with increased PT content from nano-sized domains in PMN, through a tweed structure in PMN-35PT to a micron-sized domain state, characteristic of classical ferroelectrics in PMN-40PT[44]. The microstructural coarsening mirrors the effect of lowering the temperature and it seems that there is a “common sequence of domain-like states[37]” starting with the formation and coarsening of nano-sized domains, the formation of a textured nanodomain structure (tweed) and finally the formation of micron-sized domains; this is shown in figure 3.

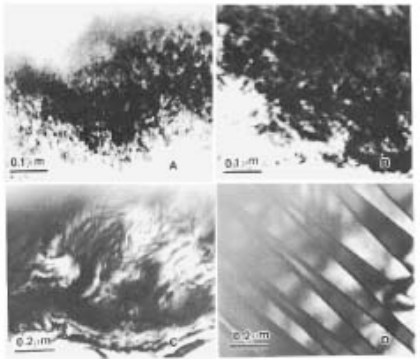

Fig. 3. Bright field TEM images for various PMN-xPT compositions: (a) 10, (b) 20, (c) 35, and (d) 40 mol% PT taken from Viehland et al. (1995)[44]. A “tweed”-like microstructure is observed in (c).

Observations of microstructure with TEM does, however, have certain disadvantages. First of all, due to a certain amount of beam heating, it is difficult to know the exact temperature of the sample during measurement, even if the sample is attached to a heating/cooling stage. Moreover, non-conducting ceramic samples often require coating with carbon[37,44] to avoid charging effects. Charging can have a profound effect on the observed domain structure observed in ferroelectrics where the crystal structure will couple to electric perturbations due to its intrinsic polarization. In the study by Viehland and coworkers, the texture of the tweed-like mesostructure in PMN-35PT was found to change with varying electron beam intensity[44].

Another problem with TEM is in the specimen preparation. Very thin wedge-shaped samples must be prepared, by grinding and polishing, followed by iron milling by argon bombardment. The effect of this process on the presence of defects and artefacts[54] is unclear and few, if any, authors anneal their prepared samples before examination, possibly due to the risk of breaking them; this will have strong consequences to the observed domain

structure especially in PMN-xPT where the domain wall energy is low and residual stresses have a profound effect on microstructure.

Atomic force microscopy and its derivative, piezoforce microscopy (PFM)[55], is perhaps a more reliable solution, although the effect of the field applied at the tip in PFM might locally destroy the domain structure especially at higher temperatures [Okino et al. (2004)[56]].

Viehland and coworkers have made a similar systematic study, using PFM, of $(001)_C$-oriented PMN-xPT single crystals with a range of compositions (x = 10, 20, 30, 35 and 40 mol.%). In their article [Bai et al. (2004)[57]], the authors combine their results with those from optical microscopy (PLM). Importantly, this time, the samples were *annealed* after polishing such that the effect of residual stresses can be ignored.

In low PT-content PMN-10PT and PMN-20PT, no domain contrast was observed by PLM. However, a broken "fingerprint" pattern was observed with SFM with an irregular structure and feature size of around 40 nm (close to the resolution limit). In PMN-30PT, spindle-like ferroelastic domains were observed by PLM, with domain walls breaking at the $(001)_C$ surface close to $<110>_C$ directions: this is indicative of $\{110\}_C$ domain walls characteristic of rhombohedral symmetry[58]. The "macrodomains" were around 1 micron wide and 20 microns in length, similar to those observed in PZN under applied field by Mulvihill et al. (1997)[19]. Inside the ferroelastic domain structure a fingerprint pattern, was observed via PFM with a larger and more regular pattern of domains and a feature size of around 300 nm.

In (pseudo)orthorhombic PMN-35PT, large, macroscopic, ferroelastic domains were observed by PLM, partitioned by $\{100\}_C$ domain walls. Embedded in these domains is again a textured fingerprint pattern with domain striations of width < 500 nm extending in $<110>_C$ directions.

Finally, in tetragonal PMN-40PT, gross tetragonal domains separated by 90° domain walls were observed. Based on their observations, the authors discuss a domain "hierarchy" based on the "assembly" of nanodomains with increasing PT content.

Ferroelectric tweed

Ferroelastic, residual-strain effects cannot fully explain the fact that the fine tweed microstructures observed in low PT content PMN-xPT by Viehland et al. do *not* tend to coarsen upon annealing[44] (although a low domain wall energy might explain the propensity for finer domain structures). The lack of a coarse, long-range ordered microstructure might have a different origin in low PT-content PMN-xPT and PZN-xPT. Importantly, in relaxor-ferroelectrics, electric fields will couple to the order parameter via the spontaneous polarization. At high PT contents the propensity for the formation of 1:1 ordered regions is reduced; no chemically-ordered regions are observed by TEM in PMN-0.40PT[33]. However, at low PT contents, such charged, compositionally-ordered regions in *x = 1/3* perovskites do tend to exist. According to the random-field model, the resultant electric fields would break up the long-range order of the low-temperature polar phase[59] and favor the high temperature, non-polar phase; if this occurred we would have increased

structural disorder (due to increased *compositional order*) with decreasing PT content.

Burns temperature and root mean square polarization

To continue with the martensite analogy we can look back at the martensite analogy and attempt to identify analogous temperatures for those that define the phase transition range, M_S and M_F.

In 1982, Burns and Dacol demonstrated that there is a deviation from a linear temperature dependence of the refractive index *n(T)* in barium titanate at a temperature of around 180°C above its Curie temperature[60]. Although the remnant polarization $\langle P_i \rangle$ in barium titanate goes to zero at the Curie temperature, the deviation of *n(T)* suggested that some root mean square (RMS) polarization $\sqrt{\langle P_i^2 \rangle}$ persists to temperatures high above T_C. Although this result undermines the classical soft mode theory[22] of the ferroelectric phase transition in T_C[60], and suggests fundamental differences between the ferroelectric behavior of barium titanate and lead titanate where no such behavior is observed[61], it has more immediate consequences for relaxor theory.

Subsequent measurements found similar deviations in PZN and PMN at so-called *Burns temperatures* T_B of around 480°C and 345 °C, respectively[18]. Further experiments have shown that at around the same temperature there is a deviation from linear thermal expansion, also accounted for by a root mean square polarization coupling via electrostriction[15], and a deviation from the Curie-Weiss law[21,35] at around 330°C in PMN[21]. Inelastic neutron scattering has also revealed that the transverse acoustic phonon mode becomes strongly damped upon cooling at around 380°C[62]. The Burns temperature, therefore, is a strong candidate for M_S in the martensitic analogy, as it indicates the temperature where the low temperature, polar, rhombohedral phase first begins to nucleate.

Superparaelectric model

The existence of root mean square (RMS) polarization was accounted for by the nucleation and growth of small polar regions ("*polar nanoregions*" or *PNR*s) within the non-polar, cubic matrix. Rhombohedral PNRs would have local short-range order over their volume, locally correlated $\langle 111 \rangle_C$ atomic shifts, and hence a net RMS polarization, but would show no long range correlation between them[15,18]. Assuming a volume of around $(10\ nm)^3$, Cross showed that such PNRs would be dynamical at high temperatures with a switching energy approaching kT[15]. Following an analogy with superparamagnetism, he thus accounted for the behavior of relaxor-ferroelectrics above T_m (and below T_B) by a "superparaelectric model". He suggested a gradual agglomeration of PNRs into superparaelectric clusters with decreasing temperature. In this model, the clusters can react to an applied electric field either by switching, by changing the magnitude of their dipole moment $\boldsymbol{p}$ or by a change in their volume[15]. Critically, at high

temperatures, such clusters should be non-interacting and the dielectric response should follow a Debye-type relaxation[63,64] with a relaxation time spectrum as given by:

$$\tau = \tau_0 \exp\left(\frac{E_a}{kT}\right) \qquad [7]$$

τ is the relaxation time, E_a is the activation energy, k is the Boltzmann constant, and T is the temperature.

However, as the number of polar regions or clusters increases due to further nucleation, as their volume increases due to clustering or growth, or as the interactions become stronger[64], the interaction between clusters cannot be ignored and the superparaelectric model breaks down. Here we can define some order parameter Q to measure the correlation of the dipoles in the structure and, hence, the degree of ergodicity or long range order. We can write $Q = \left\langle P_i . P_j \right\rangle^{1/2}$ where P_i and P_j denote neighboring cluster-sized dipole moments[21]. As T_m is approached, and Q increases, Debye relaxation is no longer observed and the relaxation law becomes more complicated[63].

Glassy freezing

In the "dipolar-glass[21,64,65]" model proposed by Viehland et al., the increased interaction between polar regions in relaxor-ferroelectrics at lower temperatures, whether elastic or dielectric in nature, is analogous to glassy "freezing[64]" with a broad spectrum of relaxation times[66]. Dynamical fluctuations of the polar clusters are increasingly frustrated as the temperature is lowered until they are frozen at out at some temperature, T_f. Fittingly, the dielectric relaxation of relaxor-ferroelectrics around T_m can be well described by a Vogel-Fulcher law[63,64], as observed in structural glasses (see equation [8]). Such a law can be interpreted as an activation energy that increases with decreasing temperature, i.e. due to increasing interaction between neighboring clusters[64].

$$\tau = \tau_0 \exp\left[\frac{E_a}{k(T - T_f)}\right] \qquad [8]$$

T_f is the static "freezing temperature". For the dielectric response we can write this in another form to describe explicitly the frequency dependence of T_m[64]:

$$f = f_0 \exp\left[\frac{-E_a}{k(T_m - T_f)}\right] \qquad [9]$$

The Vogel-Fulcher law has been shown to fit well the dielectric response of PZN-xPT and PMN-xPT[29,63,64,67,68] for a range of low PT content

compositions strongly supporting the glassy-polar model of increasingly interacting polar regions below the Burns temperature. Therefore, the freezing temperature might seem fittingly analogous to the martensite finish temperature, M_F, if it is indeed the temperature at which the phase transition from the parent phase becomes self-stopping.

Structural evidence for PNRs: X-ray and neutron scattering

Over the last decade much work has been done to find direct structural proof for the existence of interacting polar nanoregions and to follow their development upon cooling from the Burns temperature down to the freezing temperature. Inelastic neutron scattering has evidenced strong damping of a transverse acoustic[22] (TA) phonon mode below 377 °C in PMN[62]. This is very close to the T_B = 345°C reported by Burns and Dacol[18] and was explained by the authors as "some kind of phase transition into a superparaelectric phase[62]".

Importantly, no direct *structural* evidence for the emergence of PNRs at such high temperatures has yet been observed in PZN or PMN. However, evidence for the presence of localized structural distortions, with only short-range order, at temperatures much below the reported Burns temperatures has come from measurements of diffuse X-ray or neutron scattering[69,70]. In complex perovskites like PMN and PZN, diffuse scattering can originate from the differing scattering factors of the two B-site cations (compositional heterogeneity), or local static displacements away a particular site, or both[71]. Diffuse scattering should be more extended in a direction where the correlation length is shorter[71].

In one scattering study, La-Orauttapong and coworkers evidenced a diffuse phase transition in single crystal PZN upon cooling from 550 K to room temperature[71]. The Bragg peak width plotted as a function of temperature deviated from a straight line at a temperature (later named "T*")[72] of around 177°C, around 40°C above T_m. At around the same temperature there was a simultaneous increase in Bragg intensity[26]. Notably, this is far below the Burns temperature reported from the deviation of the refractive index (T_B = 480 °C)[18] which might suggest that this temperature is the point at which the polar regions cluster or grow to a detectable size[35], or that the change in birefringence at the Burns temperature is only due to "local asymmetric structural distortions that do not yet have a polar character[72]".

Dkhil et al. have observed a very similar phase transition in single crystal PMN by X-ray and neutron diffraction[25]. Evolution of the pseudocubic lattice parameter was found to be linear upon cooling to a temperature (T*) of 77 °C, around 80°C above T_m and much below the Burns temperature T_B = 345°C[18].

Non-polar unpoled PMN-xPT and PZN-xPT

Most importantly, many authors have found *no* structural evidence for a long range-ordered rhombohedral phase in unpoled PMN-xPT and PZN-xPT with low PT contents. Rietveld analysis of the diffuse scattering observed in

diffraction patterns of PMN taken at 5 K fits well a model of short-range ordered (polar) regions embedded in a long-range disordered structure with average cubic symmetry[69]. The analysis suggested an average correlation length of 20 nm, with the polar regions occupying only 20% of the volume at 5 K.

In contrast, Xu and coworkers have concluded that the bulk crystal structure of PZN remains cubic, with no evidence of any localized rhombohedral symmetry, to very low temperature[26]; the low temperature crystal structure was subsequently named the "X-phase". The authors speculated that the X-phase is the true ground state phase of PZN and, although it does not exclude the existence of polar regions, it does suggest that the local polarizations must be decoupled from the lattice distortion. Later neutron diffraction studies by the same authors on PZN-8PT[73] and PMN-10PT[74] found no evidence for rhombohedral distortion in unpoled crystals and hence evidence for the existence of a similar X-phase. However, this picture is not without critics[26,74] and a rhombohedral phase has also been claimed in PZN at room temperature[27].

To summarize, there is good structural evidence for the emergence of PNRs at temperatures above T_m in PMN-xPT and PZN-xPT; thus, in the martensite model, we can safely identify T_B (or perhaps more conservatively T*) as the martensite start temperature, M_S. However, in unpoled PMN-xPT and PZN-xPT, for very low PT contents, there is no evidence for a martensite finish temperature M_F. In fact, the only way we can promote the transition to the erstwhile equilibrium, low temperature, long-range ordered phase is by further doping with ferroelectric lead titanate, or by application of a perturbing stress or electric field[25].

Long range ordering by perturbing field

It is fitting from the martensitic analogy that a perturbing stress or field can induce a long-range ordered rhombohedral phase in PZN and PMN, and equally in PLZT[44]. In martensitic zirconia[36], for example, addition of CaO suppresses the tetragonal to monoclinic phase transition, stabilizing the higher symmetry phase down to room temperature. Application of a non-centrosymmetric stress to this metastable state can however induce the transformation resulting in a net energy dissipation and therefore toughening of the zirconia. Similarly, in ferroelectrics, an electric field can also perturb the short-range ordered relaxor into a long-range ordered state.

In the optical study of $[111]_C$-oriented single crystal PZN by Mulvihill[19] et al., no birefringence contrast was observable at zero field. However, at fields above a threshold value E_T of around 70 V/mm a "micro-to-macrodomain" phase transition was observed for temperatures below a critical temperature T_d. Above this field level lenticular macrodomains oriented along the $<10\bar{1}>_C$ direction of around 5 microns in length could be observed, with extinction characteristic of macroscopic rhombohedral symmetry. With increasing field, the domain wall density was seen to increase, with the macrodomains becoming longer and narrower, although a monodomain state could not be achieved even at fields as high as 1500

V/mm. This is in contrast to the behavior of more classical perovskites like barium titanate where a monodomain state can be stabilized by poling.

Poling experiments were also performed on the crystals. Importantly, although in the zero-field cooled (ZFC) condition no macrodomains were observed, cooling below the critical temperature T_d^{cool} under fields above E_T (during "field cooling" or FC) did result in a macrodomain state. The transition temperature was marked by a kink, or "shoulder[19]", in the dielectric permittivity measured as a function of temperature (as shown in figure 4) whereas only a broad relaxor peak was observed in the ZFC condition (figure 2). Critically, this kink corresponded to the point below which no frequency dispersion in the permittivity is observed.

Upon heating, the macrodomains disappeared at a temperature T_d^{heat} which was dependent on field magnitude. In contrast, they appear at a temperature T_d^{cool}, essentially independent of the level of bias field above E_T. T_d^{cool} has been referred to as a first order "spontaneous relaxor-ferroelectric phase transition[29]". T_d^{heat} is known as the "depoling temperature" in that it is the temperature at which net polarization $\langle P_i \rangle$ is lost, even if mean square polarization remains; this is shown in figure 5. Some thermal hysteresis was observed by Mulvihill et al. for the micro-to-macrodomain transition ($\Delta T = T_d^{heat} - T_d^{cool}$) which increased with increasing electric bias field. In contrast, the temperature of the dielectric peak, T_m, was found to be independent of bias field.

Similar behavior has been shown by Colla[68] et al. for PMN-xPT single crystals. In PMN, the threshold field needed for formation of a macrodomain, polar state during field cooling was 170 V/mm. This is around twice that needed in PZN.

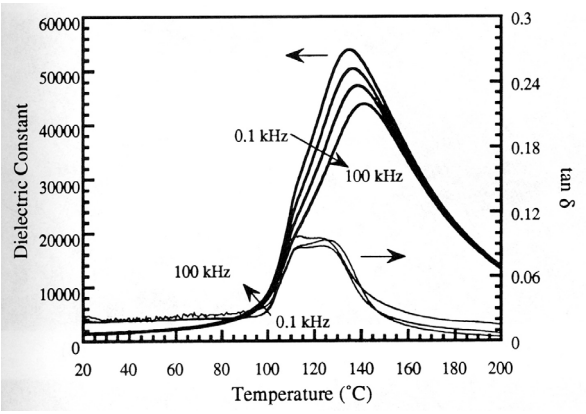

Fig. 4. Relative permittivity versus temperature for $[111]_C$-oriented single crystal PZN taken upon cooling under a bias field of 1500 V/mm at 0.1, 1, 10 and 100 kHz. The figure is taken from Mulvihill et al. (1997)[19]. The frequency dispersion disappears in the "shoulder" at around 110°C.

As pointed out by the Mulvihill et al.[19], the temperature at which the macrodomains are first observed during field cooling T_d^{cool} is a candidate for the martensite finish temperature M_F in the martensitic analogy. Furthermore, there is significant evidence that T_d lies very close to the freezing temperature T_f, as determined by a Vogel-Fulcher fit of dielectric data[7,29,64,68].

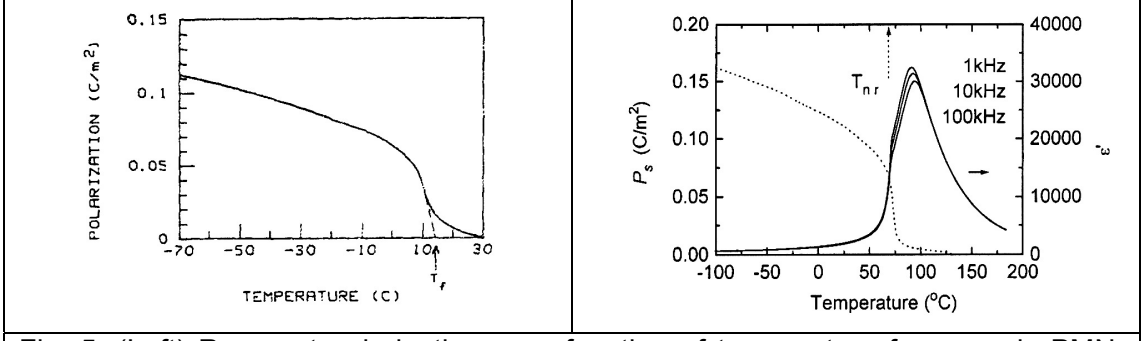

Fig. 5. (Left) Remnant polarization as a function of temperature for ceramic PMN-10PT taken from Viehland et al. (1990). (Right) Spontaneous polarization and dielectric permittivity as a function of temperature for ceramic PMN-20PT upon heating from an unpoled state taken from Fan et al. (1999)[6]. The shoulder in permittivity T_d is clearly seen to coincide with the point of maximum gradient in polarization (maximum pyroelectric coefficient).

Long range ordering by addition of lead titanate

The other way[25] to induce long-range polar ferroelectric order in PMN and PZN is to substitute the B site cations with Ti^{4+} by addition of true ferroelectric $PbTiO_3$. As noted above, TEM and PFM studies strongly indicate an increase in long-range structural order, from nanoregions, through a tweed-like microstructure, to micron size ferroelectric domains, on increasing PT content in PMN-xPT[37,44,57]. Moreover, although La-Orauttapong et al. evidence a *diffuse* transition in neutron scattering studies of PZN, *sharp* transitions, are observed in PZN-4.5PT and PZN-9PT at well-defined temperatures[72].

Dielectric data also evidences an increase in long range order upon increasing PT content, with the phase transition becoming less and less diffuse and more and more like that typical of Curie-Weiss behavior[3,6,7,68]. This will be shown explicitly in chapter six. The threshold field needed for long-range ordering in PMN-xPT has been shown to decrease from 170 V/mm in PMN to zero at a PT content of around 15 mol%[68]. As will be shown in the phase diagrams of PMN-xPT and PZN-xPT, and experimentally in chapter six, there is a convergence of all three temperatures, T_m, T_d and T_C with increasing PT content; at the same time, the frequency dispersion in T_m decreases with addition of PT.

Summary

PMN and PZN show a broad, frequency-dependent peak in permittivity at $T_m(f)$ which is not the result of an abrupt, structural phase transition. Instead, there is significant experimental evidence for the nucleation of local, non-correlated, rhombohedral polar regions at temperatures far above T_m. Upon cooling, there is increased interaction, and therefore correlation, between these PNRs and a gradual "freezing" takes place. Close to the freezing temperature T_f, there is a spontaneous transition from the high-temperature, short-range ordered, non-polar, micro-domain "relaxor" state to a long-range ordered, macrodomain, "ferroelectric" state at a temperature T_d. This only occurs in PMN-xPT and PZN-xPT of a high-enough PT content and/or under a sufficiently-strong perturbing field.

There are many similarities between martensitic phase transformations and the diffuse phase transitions that occur in PMN-xPT and PZN-xPT; this includes similarities in microstructure. However, whereas strain is the most important parameter to ferroelastic martensites, electric fields can also couple to the order parameter in relaxor-ferroelectrics via the spontaneous polarization. Thus, the effect of random electric fields resulting from B-site ordering in low PT-content PMN-xPT and PZN-xPT also have an effect; these cannot be annealed out as residual stresses can.

In brief, the behavior of relaxor-ferroelectrics PMN and PZN, and likewise PMN-xPT and PZN-xPT with low PT contents, is very different to that observed in simpler perovskites barium titanate and lead titanate, which transform to a long-range ordered ferroelectric phase at a well defined temperature T_C. In contrast, the phase transition in PMN-xPT and PZN-xPT is diffuse and characterized by more than one temperature: these are summarized in table I. Phase diagrams for relaxor-ferroelectric PMN-xPT and PZN-xPT will therefore look qualitatively different to those for simpler ferroelectric solid solutions, like that of PZT, which do not show a relaxor to ferroelectric phase transition.

III. PHASE DIAGRAMS OF RELAXOR-FERROELECTRICS

In order to construct phase diagrams for PMN-xPT and PZN-xPT we must first define the important temperatures which characterize each composition; this has been done in table I. Notably, from now on, the Curie temperature "T_C" will imply an abrupt, structural phase transition, evidenced by diffraction experiments or by optical microscopy. Furthermore, we must be very careful in specifying exactly how each temperature is defined, or in how it is measured.

For example, the measurement frequency can have a huge effect on T_m. In the dielectric study of Choi et al. a T_m variation of 16°C was found for frequencies between 0.1 and 100 kHz. This dropped to zero at around 0.3 mol% PT[75]. Where T_m is plotted on the phase diagram, 1 kHz seems like a good frequency to choose, although this should be specified.

Secondly, the diffuse phase transition at T_m is not a true first order phase transition and shows very little thermal hysetersis[6], especially for low PT contents. However where thermal hysteresis is observed, for example in

single crystal PMN-33PT[76] (where T_m approaches T_C) it is always smaller than that observed in T_d. Therefore we will not specify on the phase diagram whether it has been measured on heating or cooling. It seems that for many compositions T_d, T_C and T_f match each other very closely; T_C and T_d are most likely equivalent. The structural transition at T_C (T_d) is certainly first order[6] involving significant thermal hysteresis[6,76,77] (ΔT_d or ΔT_C).

Moreover, we note that the application of a bias field will alter the phase stabilities of the polar phases[78,79] and will therefore shift T_C or T_d. In PZN[19] the bias field is shown to alter the depoling temperature T_d^{heat} but not T_d^{cool}. T_C has clearly been shown to increase with increasing bias field along $[001]_C$ in PZN-9PT[80]. Moreover, at a high enough bias field the phase transition becomes second order[80] as observed in other perovskites like barium titanate[14]. Therefore, we prefer data that has not been taken under bias, i.e. that taken in zero field heating (ZFH) or cooling (ZFC) runs, even though T_m does not seem to be shifted by bias field[81,82].

At this point, however, we will assume that poling (for instance by field cooling) should only ensure long range order. It is not expected to change the position of T_d in subsequent zero-field heating runs. This indeed seems to be the case, for example in PMN-20PT, where T_d upon heating is identical for poled and unpoled conditions[6]. The possibility that poling gives rise to *residual bias fields*, which might shift the depoling temperature, will be discussed in chapter six. Poling does seem to shift the position of T_m, however. In their study of PMN-xPT ceramics, Choi et al. evidence a significant discrepancy between T_m values measured upon heating (at 1 kHz and 4°C/min) in virgin and field-cooled (poled) conditions. This is shown in figure 6. A similar trend was observed by Noblanc[1] et al. Therefore, we specify whether T_m values have been measured on poled or unpoled samples.

Finally, the cooling rate through the phase transition seems to have very little effect on the position of T_m[76,83]. Therefore we ignore any kinetic effects. Most cooling and heating rates used to measure the dielectric and pyroelectric properties reported in the literature are in the range 1-4°C/min.

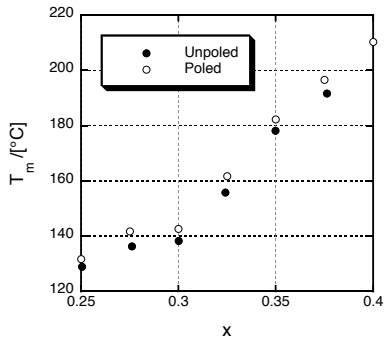

Fig. 6. T_m measured upon heating in ceramic samples of PMN-xPT in poled and unpoled conditions. Poling seems to increase T_m by a few degrees [data taken from Choi et al. (1989)[84]].

As a last note, in constructing the diagrams we give preference to data from ceramic samples over single crystals. As noted the PT content can vary

dramatically within a single crystal sample from the “nominal” composition[7]. We expect that in ceramic samples the PT content will be closer to that defined by the starting stoichiometry and that it will be more homogeneously distributed, although of course not perfect[77]. The exception will be in single crystals where the composition has been checked quantitatively, e.g. in the study by Zekria et al. (2005)[77]. Of course, we ignore data where the composition has been back-calculated from previous phase diagrams.

Table I.
Definition of various key temperatures relevant to the high- to low-symmetry phase transition in relaxor-ferroelectrics PMN-xPT and PZN-xPT

Temperature	Symbol	Definition
Permittivity maximum	T_m	Temperature of maximum permittivity, $T_m(f)$. Strongly dependent on frequency for relaxor compositions (small PT contents). For example, over the range 0.1 kHz-100 kHz the variation in T_m is around 16°C in PMN[75]. T_m does not correspond to a classical first order transition, nor an abrupt structural phase transition; it shows no significant thermal hysteresis except at higher PT contents where T_C and T_m converge.
Curie temperature	T_C	True structural phase transition as evidenced by a clear anomaly in the lattice parameter by X-ray/neutron diffraction, or by polarized light microscopy. Characteristically first order and therefore accompanied by significant thermal hysteresis ($\Delta T_C \equiv T_C^{heat} - T_C^{cool}$). Moved by bias fields which stabilize the polar phase.
Freezing temperature	T_f	As found by a Vogel-Fulcher fit of permittivity-temperature data for various frequencies. Generally found to lie close to T_d.
Depoling temperature	T_d	"Depoling" or "macro- to microdomain transition" temperature upon zero-field heating from spontaneously long-range ordered or poled condition (T_d^{heat}) or "relaxor-ferroelectric transition" temperature (T_d^{cool}) during zero-field heating where occurring. Evident as a peak in pyroelectric coefficient and as a "shoulder" in the permittivity below which no frequency dispersion occurs. Accompanied by significant thermal hysteresis ($\Delta T_d \equiv T_d^{heat} - T_d^{cool}$) and moved by bias fields.
Burns temperature	T_B	Temperature at which PNRs start to appear, as evidenced by the emergence of root mean square polarization (e.g. by deviation from linear thermal expansion).

IV. PHASE DIAGRAM FOR PMN-xPT

Various data was taken from published articles. Where the data was not given explicitly, relevant figures were digitized and data taken from them.

We start by precising the structure-temperature characteristics of the two end-members, PMN and PT (lead titanate). PT transforms from a *4mm* tetragonal phase into a cubic *m3m* phase at a Curie temperature of around 492 °C[20,85]. No other phase transition is observed below T_C in contrast to perovskite barium titanate and potassium niobate[14]. Again in contrast to barium titanate[60] and potassium niobate[61] there is no evidence for the emergence of short range polar order at temperatures above T_C and therefore no Burns temperature.

The Burns temperature for PMN has been found via measurements of refractive index[18] as 345°C, a deviation from the Curie-Weiss law[21] as 327°C and by a strong damping of the transverse acoustic soft mode[62] as around 377°C. We can therefore calculate a Burns temperature of T_B (PMN) = $(350 \pm 25)°C$. Values for T_m measured at 1 kHz upon either zero field heating or cooling (unpoled) from a variety of sources are: -13°C (permittivity[84]), -8°C (permittivity[1]), -19°C (Young's modulus[67]), -16°C (permittivity[67]), -4°C (permittivity[68]), and -10°C (permittivity[6]). All temperatures except one[68] are taken from measurements on ceramics. This yields T_m = $(-11.6 \pm 5.3)°C$. Two values for T_d (or, more precisely, the depoling temperature T_d^{heat}) can be taken from Yan et al. (2003)[67] based on measurements for ceramic samples upon heating: they are -61°C (from measurements of the Young's modulus in an unpoled condition) and -61°C (from permittivity, poled). The same authors calculate T_f from a Vogel-Fulcher fit as -57°C (permittivity, unpoled). Single crystal measurements upon heating[68] also give T_f = -57°C (permittivity, unpoled) and T_d = -57°C (permittivity, poled). Measurements on ceramic PMN upon heating[1] give T_d = -60 °C (permittivity, poled). We include these together (assuming $T_f \approx T_d^{heat}$) and calculate T_d = $(-58.8 \pm 1.8)°C$.

Various authors have published phase diagrams, or partial phase diagrams, for PMN-xPT. In 1989, Choi et al. published a phase diagram[2] covering the range $0 \le x \le 0.5$ based on dielectric measurement of ceramics, produced by the newly reported "columbite precursor" method of Swartz and Shrout (1982)[86]. However, in their article it is not clearly specified how the "T_C" points were determined. A later paper by Choi et al., again on ceramic samples, gives another phase diagram over the same composition range, this time with "T_C" determined as the dielectric maximum T_m upon heating at 1 kHz[84]. To our knowledge, the first phase diagram to include data from single crystals appeared in 1990[87]. However, here the authors (Shrout et al.) used a straight line fit of the "Curie temperatures" from the two previous publications of Choi et al. to back-calculate the compositions of the crystals; we therefore ignore this data. A later paper by Choi et al. (1996)[75] contains a much more complete phase diagram for PMN-xPT again for the composition range $0 \le x \le 0.5$. Importantly, this time the authors plot two "transition temperatures": T_m based on dielectric data (1 kHz, heating) and T_d based on pyroelectric measurements (heating) for poled ceramic samples. The convergence of the two temperatures at higher PT contents is made clear.

Another useful paper[1], again from 1996, is that by Noblanc et al. Similarly, for a range of compositions $0 \le x \le 0.4$ they plot T_m taken from dielectric data (cooling, unpoled), although the temperature at which the values were taken is unclear, and T_d taken from the shoulder in the permittivity data (heating, poled samples). Again a clear convergence of T_C and T_d is observed with increasing x. In 1998, Colla et al. published a partial phase diagram based on the T_m data by Choi et al. for ceramic samples but with added values for single crystals in the range $0 \le x \le 0.4$ based on dielectric data (heating, 1 kHz)[68]. There is significant spread in the data, however, and the crystal compositions were not checked. Importantly, they fit two straight lines through the data, instead of the usual one, with a change in gradient of T_m at around 0.26 (very close to the morphotropic phase boundary). In the article by Noheda et al. (2002) on the "phase diagram of (1-x)$Pb(Mg_{1/3}Nb_{2/3})O_3$-x$PbTiO_3$", the authors construct a phase diagram in the range $0.30 \le x \le 0.39$ based on synchrotron X-ray diffraction data concentrating on the structure at the morphotropic phase boundary (MPB) and the presence of a monoclinic phase[8]. However, the straight line they plot for the transition to the cubic phase is the "average of the two temperatures reported by Noblanc[1] et al.".

Another partial phase diagram has been offered by Han et al. (2003) based on single crystal dielectric data although it concentrates mainly on the phase transitions at the MPB. A paper by Yan et al. (2003)[67] includes a partial phase diagram in the range $0 \le x \le 0.23$. T_m as measured on ceramic samples is marked by peaks in the dielectric constant (unpoled, 1 kHz) and by an anomaly in the Young's modulus (unpoled, again at 1 kHz). The two values agree to within a few degrees. T_d is also marked, as measured by kinks in the dielectric constant (poled, heating) and the Young's modulus curves. T_f as derived from a Vogel-Fulcher fit of the dielectric data matches both T_d values closely. Clear convergence of the two temperatures is evidenced.

Finally, the recent paper by Zekria et al. (2005)[77] includes perhaps the best attempt so far at a complete phase diagram for PMN-xPT. Here, single crystals of PMN-xPT with composition gradients were used to cover the entire composition range. Polarized light microscopy was utilized to study localized structural phase transitions (including that at T_C) upon both heating and cooling and to precise the symmetry of the various phases. The local composition across each sample was measured by electron probe microanalysis with a lateral resolution of 10 microns. In their article T_C is plotted for compositions in the range $0.1 \le x \le 1.0$. Critically, a kink in the T_C-T data is observed at around 50 mol% PT. Instead of a single straight line fit, the authors suggest two straight lines with T_C (in °C) given by (-37 + 586x) for x < 0.5 and (20 + 465x) for x > 0.5. Neither is close to the "x = (T_C +10)/5 rule".

Refined phase diagram

To construct our phase diagram we use only certain selected data. T_d values plotted are those measured either from permittivity, or in special cases pyroelectric[75] or Young's modulus[67], data upon heating (T_d^{heat}) for poled or

unpoled samples, but not under bias. T_m values are for unpoled samples taken at 1 kHz upon heating or cooling, in general, from permittivity data, or in one case from Young's modulus measurement[67]. The T_C data from Zekria et al. measured from polarized light microscopy upon heating (T_C^{heat}) is also plotted. Values are taken for ceramic samples [Choi et al. (1989)[84], Noblanc et al. (1996)[1], Viehland et al. (1990)[64], Yan et al. (2003)[67], and Choi et al. (1996)[75]] and single crystal samples [Zekria et al. (2005)[77], Colla et al. (1998)[68], Han et al. (2003)[4], Tu et al. (2004)[88], Cao et al. (2003)[89], Viehland et al. (2001)[90], and Yan et al. (2002)[76]]. Only for the T_C data from Zekria et al. has the composition been determined experimentally. Otherwise, the compositions are assumed from stoichiometry. T_C for lead titanate is taken to be 492 °C[85]. The Burns temperature T_B for PMN-0.2PT is taken to be 350 °C from thermal expansion measurements by Fan[6] et al.; T_B for PMN-0.5PT is taken as 340 °C from Bokov et al. (deviation from the Curie-Weiss law)[7].

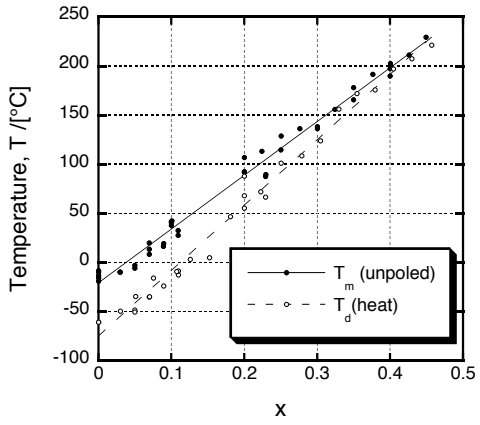

Fig. 7. Collected data for the transition to the cubic phase in ceramic samples of PMN-xPT.

The collected data for ceramic samples show good correlation (see figure 7) although with a large degree of experimental uncertainty. Lines of best fit give $T_m = (-20.6 + 547.1x)\,°C$ and $T_d = (-74.6 + 665.2x)\,°C$. They converge at exactly x = 0.457 close to the point at which Zekria et al. suggest a kink in the T_C-T data. Taking this intersection point and fixing the lower end at the values calculated previously [T_m = (-11.6 ± 5.3)°C and T_d = (-58.8 ± 1.8)°C] we derive:

$$T_m = (-12 + 527x)\,°C \qquad (x < 0.457)$$
$$T_d = (-59 + 631x)\,°C \qquad (x < 0.457) \qquad [10]$$

We conclude that the "$(T_C + 10)/5$" rule corresponds, in reality, to the frequency-dependent T_m. The latter equation for T_d^{heat} was used to determine the composition of all samples of PMN-xPT used in this thesis. Taking minimum and maximum slopes through the scatter in $T_d^{heat}(x)$ we calculate a maximum spread in x of 1 mol. % for a transition temperature of 100°C. This spread will be smaller at higher PT contents.

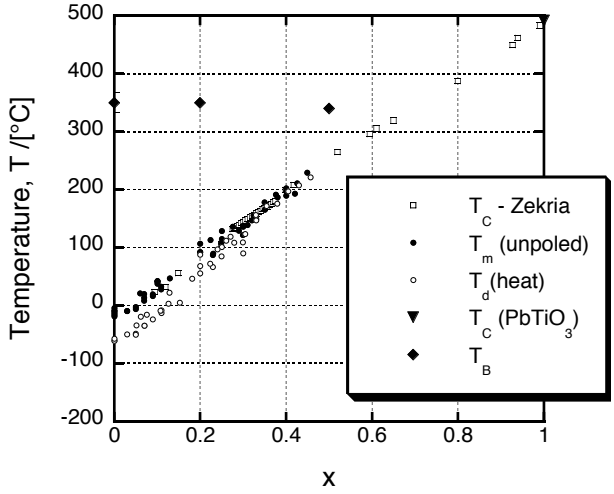

Fig. 8. Refined phase diagram for PMN-xPT based on collected data. T_m is taken at 1 kHz from unpoled samples. T_d is taken upon heating in unbiased samples (depoling temperature or "macro- to micro-domain transition temperature"). T_C corresponds to measurement of a clear structural transition by polarized light microscopy upon heating (Zekria et al.).

The complete set of data is plotted in figure 8. Addition of the single crystal data yields more uncertainty in the values of T_d and T_m at low x, especially around the MPB. This is probably due to the additional uncertainty in composition for single crystal samples. The addition of the data from Zekria et al. is most confusing as at low x their T_C values sit much closer to the T_m values than the T_d values. Above x = 0.5, however, the data fits nicely with the projection of the lower x data to the T_C point for lead titanate. The origin for this discrepancy is unclear.

V. PHASE DIAGRAM FOR PZN-xPT

There is *much* less data available for the PZN-xPT solid solution; it is therefore much more difficult to be ruthless in choosing points for the phase diagram. Moreover, the picture for low PT contents, and especially for PZN, is decidedly unclear[26,28,71]. The first plot of the "peak temperature" T_m in PMN-xPT appeared in the article by Nomura et al. (1973)[5] for the range $0 \le x \le 4.0$ as measured from dielectric data at 100 kHz (single crystals, unpoled). In a later article by Kuwata et al. (1981) a phase diagram is given showing both "transition temperature" T_m from dielectric data (1 kHz, poled) for the range $0 \le x \le 2.0$ and the position of the morphotropic phase boundary[10]. However the compositions of the single crystals used to measure T_m in this study were back-determined from their previous data[5], which is less than ideal. The same phase diagram was reprinted in a later article [Kuwata et al. (1982)[91]] in which, again, their previous data was used to determine the composition of a PZN-0.9PT crystal "within $\pm$ 0.5% on the basis of the lattice parameter as well as the Curie temperature[91]". In the recent "phase diagram" paper by La-Orauttapong et al. (2002)[9] the authors use the same data from Kuwata et al. (1981)[10] to mark the transition to the cubic phase for the range

$0 \le x \le 2.0$. Lu et al. (2002)[79] have published a limited phase diagram based on dielectric data for PZN-0.045PT, PZN-0.08PT and PZN-0.1PT single crystals for various poling and bias field directions. Finally, Shen et al. (2005)[92] have proposed an updated phase diagram for PZN-xPT where the orthorhombic MPB phase persists all the way to 0 mol% PT. To the best of our knowledge, no complete phase diagram exists for PZN-xPT based on ceramic samples, except for that in the article by Lee et al. (1998)[3] where "T_C" (T_m) is given for ceramic samples of PZN-xPT at x = 0.2, 0.4, 0.6, and 0.8 (dielectric, unpoled, cooling).

The Burns temperature T_B of PZN from refractive index measurement is 480°C[18]. For T_d we take the value of T_d^{heat} extrapolated to zero bias field as plotted by Mulvihill et al. in their E-T phase diagram for PZN (see figure 6), i.e. T_d = 100 °C. Note that this agrees poorly with a freezing temperature T_f of -33°C measured by a Vogel-Fulcher fit[63] and the assorted values of "T_C" measured by high resolution diffraction: e.g. the diffuse "T_C" of 137°C measured by La-Orauttapong[71,72]. However, since diffuse transitions do not correspond to a clearly defined transition from a long-range ordered to a short range ordered state, they will be omitted.

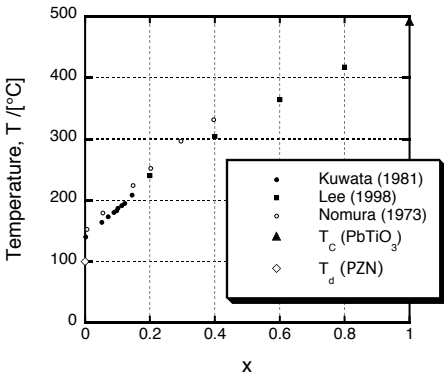

Fig. 9. Selected key data on the temperature of the transition to the cubic phase in PZN-xPT from Kuwata et al. (1981)[10], Lee et al. (1998)[3] and Nomura et al. (1973)[5].

It is difficult to choose a measurement frequency for which to plot T_m. Key data for PZN-xPT is plotted in figure 9. All data taken corresponds to the peak permittivity temperature T_m for the following differing conditions: heating of poled single crystals for a frequency of 1 kHz (Kuwata); cooling of unpoled ceramics at 10 kHz (Lee); and heating of unpoled single crystals at 100 kHz (Nomura). Since the data for Nomura is taken at a non-"standard" 100 kHz and seems to agree poorly with that of Lee et al. at high PT contents (even accepting a small thermal hysteresis and an even smaller frequency dispersion of less than 2°C[3]), we disregard their data. We therefore take the data from Lee, although noting that it is T_m taken upon cooling and will be subject to thermal hysteresis (the frequency dispersion is however witheringly small[3]). We also take the data from Kuwata et al. for T_m although we note that it was measured from poled samples (heating).

We take values of T_d measured on poled single crystals of PZN-4.5PT upon heating based on dielectric and pyroelectric data from Shen et al. (2005)[92]. We take T_d (zero field heating, poled) and T_m (zero field heating, poled, 1 kHz) for 4.5PT from the permittivity data of Shen et al. (2004)[82]. We

also take T_m from Tu et al. (2000)[93] from permittivity data (heating). We take data for PZN-4.5PT and 12PT from Lima-Silva et al. (2004)[94], again from permittivity data (1 kHz, heating, unpoled). Finally, we take data for T_d in PZN-8PT from the peak in the pyroelectric coefficient for poled crystals (heating) form Priya et al. (2002)[95].

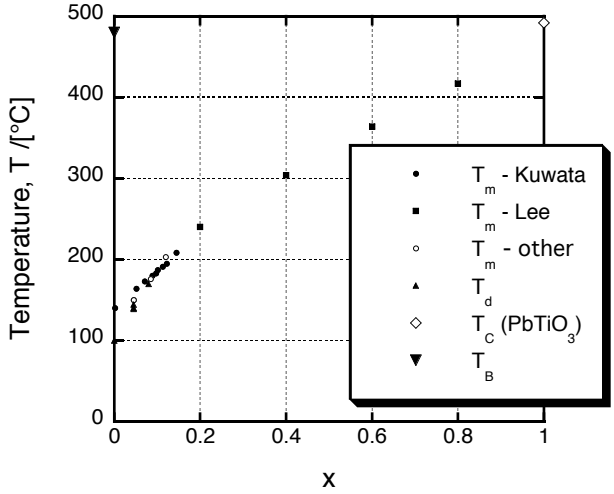

Fig. 10. Refined phase diagram for the PZN-xPT solid-solution based on selected data. T_m corresponds to the maximum in permittivity measured at 1 kHz, in general, for poled samples. T_d is the depoling temperature measured upon heating without bias. Key data is from Kuwata et al. (1981)[10] and Lee et al. (1998)[3].

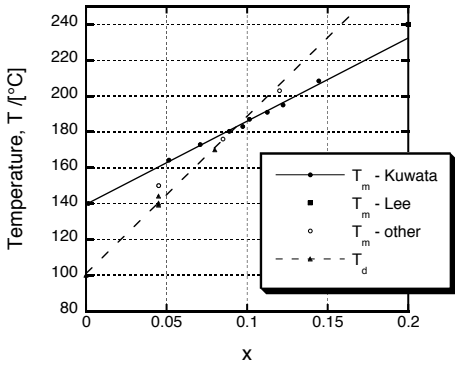

Fig. 11. Low PT content section of the phase diagram for PZN-xPT (figure 12). Lines of best fit for T_m and T_d are shown which intersect at around x = 0.09.

The complete phase diagram is shown in figure 10. A partial phase diagram is shown in figure 11. The diagram is qualitatively similar to that for PMN-xPT. Lines of best fit for T_d and T_m clearly converge, albeit at a much lower PT content (x = 0.093) than in PMN-xPT. Lines of best fit give:

$$T_m = (140 + 464x)\,°C \qquad (x < 0.093)$$
$$T_d = (101 + 878x)\,°C \qquad (x < 0.093) \qquad [11]$$

The lines intersect at a much lower PT content than in PMN-xPT and, as will be shown in chapter six, very close to the position of the morphotropic phase boundary in this system[9]. The latter equation for T_d^{heat} was again used in this

thesis, with care, to determine the composition of the as-received samples of PZN-xPT. Since equation [11] is fitted from much less data, its accuracy is perhaps worse than the equivalent for PMN-xPT.

VI. DISCUSSION

In summary, phase diagrams have been drawn up using data from poled and unpoled crystals which show the transition from short-range ordered relaxor behavior at low PT contents to the long-range ordered behavior of lead titanate. The various temperatures plotted have been clearly defined and thus the diagram can be more safely used for back-calculation of composition.

Importantly, convergence of the three transition temperatures T_m, T_d and T_C is clearly shown at a critical PT content. This convergence is not seen in the phase diagram of PZT (chapter one, fig. 1) and is an important feature of relaxor-ferroelectrics. Furthermore, it seems that linearity of transition temperature vs. composition cannot be assumed across the entire diagram; notably, the gradient seems to change close to the point of convergence.

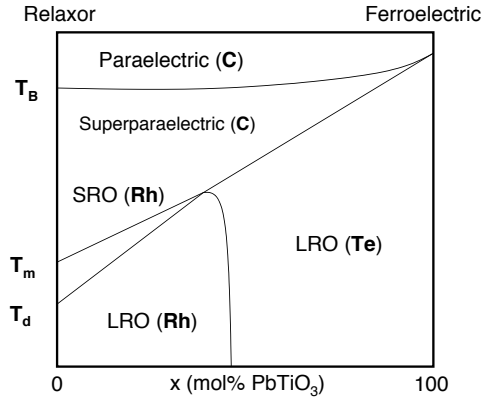

Fig. 12. Proposed "universal phase diagram for "*x = 1/3*" perovskite, relaxor-ferroelectric solid solutions like PMN-xPT and PZN-xPT. A truly paraelectric, cubic phase exists above T_B. Below T_B, polar nanoregions with a locally rhombohedral (Rh) symmetry begin to nucleate and grow to form a short-range ordered (SRO), locally-rhombohedral, pseudocubic phase. At low enough temperatures, or upon poling below T_d, a long-range ordered (LRO), ferroelectric, rhombohedral phase is formed. This is unstable above T_d. At higher PT contents, upon crossing the morphotropic phase boundary, there is a transition to a LRO tetragonal (Te) phase.

Universal phase diagram

What is more, the phase diagrams of PMN-xPT (figure 8) and PZN-xPT (figure 10), have certain similarities. For both, addition of the relaxor to lead titanate can be seen to stabilize the cubic phase to lower and lower temperatures, fitting well with the martensite analogy. Likewise, for both solid-

solutions, the Burns temperature is lower than the Curie temperature of lead titanate; for PMN-xPT it is fairly independent of PT content.

Most interestingly, for both systems, the MPB (see chapter one, figure 2) lies close to composition where T_m and T_d converge (around 0.09 in PZN-xPT and around 0.46 in PMN-xPT). This last observation might imply that there is some relationship between the point at which relaxor-ferroelectric behavior is replaced by more classically ferroelectric behavior, and the point at which structural transitions from a rhombohedral, through an orthorhombic (monoclinic), to a tetragonal phase occur in poled crystals. This is in fact observed in other "$x = 1/3$" relaxor-ferroelectric solid solutions. In $Pb(Ni_{1/3}Nb_{2/3})O_3$-$xPbTiO_3$ [PNN-xPT], a morphotropic phase boundary between rhombohedral and tetragonal phases lies at around x = 34 - 38 mol.%; notably, frequency dispersion disappears and T_m and T_C converge at around 40 mol. %[96]. Likewise, in $Pb(W_{1/3}Fe_{2/3})O_3$-$xPbTiO_3$ [PFW-xPT] T_m and T_d converge very close to a similar MPB at around 25 mol. % PT[97]. The interesting possibility that the presence of a rhombohedral phase is correlated with increased structural disorder at low PT contents is worthy of future investigation.

Ferroelectric-ferroelectric phase transitions

Finally, proper discussion of the phase diagram of PMN-xPT and PZN-xPT cannot ignore the ferroelectric-ferroelectric phase transitions that occur in the vicinity of the morphotropic phase boundary (MPB) separating the low PT content rhombohedral phase (point group *3m*) and the high PT content tetragonal phase (*4mm*). As discussed in chapter one, monoclinic phases have been held responsible for the enhanced piezoelectric properties of PMN-xPT and PZN-xPT near the MPB, and have been evidenced by X-ray and neutron diffraction[98]. These, however, are polar phases and only become relevant when a crystal becomes macroscopically polar.

As noted in section II, the short range ordered "X-phase" has been evidenced in unpoled PZN-xPT right up to the MPB (8 mol.% PT)[73]. Without a long range ordered ground state it is very difficult to discuss the make up of the ferroelectric phases around the morphotropic phase boundary. In most cases structural characterization of PMN-xPT and especially PZN-xPT at the MPB can only be done in the poled condition[98], especially for lower PT content compositions.

In *poled* samples, however, we can start to discuss the phases around the MPB as true, long-range ordered, ferroelectric phases. This has been the approach taken by the vast majority of authors working with PMN-xPT and PZN-xPT and will be the approach taken for the rest of this thesis. From now, therefore, we will leave the *relaxor-ferroelectric* nature of PMN-xPT and PZN-xPT as a background effect, albeit a very important one.

REFERENCES

1 O. Noblanc, P. Gaucher, and G. Calvarin, J. Appl. Phys. **79,** 4291-4297 (1996).

[2] S. W. Choi, T. R. Shrout, S. J. Jang, and A. S. Bhalla, Ferroelectrics **100,** 29-38 (1989).
[3] D.-H. Lee and N.-K. Kim, Materials Letters **34,** 299-304 (1998).
[4] J. Han and W. Cao, Phys. Rev. B **68,** 134102 (2003).
[5] S. Nomura, H. Arima, and F. Kojima, Jpn. J. Appl. Phys. **12,** 531-535 (1973).
[6] H. Fan, L. Kong, L. Zhang, and X. Yao, J. Mat. Sci. **34,** 6143-6149 (1999).
[7] A. A. Bokov, H. Luo, and Z.-G. Ye, Materials Science and Engineering B **120,** 206-209 (2005).
[8] B. Noheda, D. E. Cox, G. Shirane, J. Gao, and Z.-G. Ye, Phys. Rev. B **66,** 054104 (2002).
[9] D. La-Orauttapong, B. Noheda, Z.-G. Ye, P. M. Gehring, J. Toulouse, D. E. Cox, and G. Shirane, Phys. Rev. B **65,** 144101 (2002).
[10] J. Kuwata, K. Uchino, and S. Nomura, Ferroelectrics **37,** 579-582 (1981).
[11] R. R. Chien, V. H. Schmidt, L.-W. Hung, and C.-S. Tu, J. Appl. Phys. **97,** 114112 (2005).
[12] Y. Tang, X. Wan, X. Zhao, X. Pan, D. Lin, H. Luo, J. Sun, X. Meng, and J. Zhu, J. Appl. Phys. **98,** 084104 (2005).
[13] Z. Feng, H. Luo, Y. Guo, T. He, and H. Xu, Solid State Communications **126,** 347-351 (2003).
[14] B. Jaffe, W. R. Cook, and H. Jaffe, *Piezoelectric Ceramics* (Academic Press, 1971).
[15] L. E. Cross, Ferroelectrics **76,** 241-267 (1987).
[16] G. A. Smolenskii and A. I. Agranovskaya, Sov. Phys. Solid State**,** 1429- (1959).
[17] A. A. Bokov, Ferroelectrics **131,** 49-55 (1992).
[18] G. Burns and F. H. Dacol, Solid State Communications **48,** 853-856 (1983).
[19] M. L. Mulvihill, L. E. Cross, W. Cao, and K. Uchino, J. Am. Ceram. Soc **80,** 1462-1468 (1997).
[20] Z. Li, M. Grimsditch, X. Xu, and S.-K. Chan, Ferroelectrics **141,** 313-325 (1993).
[21] D. Viehland, S. J. Jang, L. E. Cross, and M. Wuttig, Phys. Rev. B **46,** 8003-8006 (1992).
[22] C. Kittel, *Introduction to solid state physics*, 7th ed. (Wiley, New York, 1996).
[23] M. E. Lines and A. M. Glass, *Principles and applications of ferroelectrics and related materials* (Clarendon Press, Oxford, 1977).
[24] M. J. Haun, E. Furman, S. J. Jang, and L. E. Cross, Ferroelectrics **99,** 13-25 (1989).
[25] B. Dkhil, J. M. Kiat, G. Calvarin, G. Baldinozzi, S. B. Vakhrushev, and E. Suard, Phys. Rev. B **65,** 024104 (2001).
[26] G. Xu, Z. Zhong, Y. Bing, Z.-G. Ye, C. Stock, and G. Shirane, Phys. Rev. B **70,** 064107 (2004).
[27] E. H. Kisi and J. S. Forrester, J. Phys.: Condens. Matter **17,** L381-L384 (2005).
[28] A. Lebon, H. Dammak, G. Calvarin, and I. O. Ahmedou, J. Phys.: Condens. Matter **14,** 7035-7043 (2002).

[29] H. Wang, H. Xu, H. Luo, and Z. Yin, Appl. Phys. Lett. **87,** 012904 (2005).
[30] K. Uchino, S. Nomura, L. E. Cross, S. J. Jang, and R. E. Newnham, J. Appl. Phys. **51,** 1142-1145 (1980).
[31] C.-S. Tu, C.-L. Tsai, V. H. Schmidt, H. Luo, and Z. Yin, J. Appl. Phys. **89,** 7908-7916 (2001).
[32] Z. Li, Z. Xi, Z. Xu, and X. Yao, J. Mat. Sci Lett. **21,** 1325-1327 (2002).
[33] A. D. Hilton, C. A. Randall, D. J. Barber, and T. R. Shrout, Ferroelectrics **93,** 379-386 (1989).
[34] M. D. Glinchuk, British Ceramics Transactions **103,** 76-82 (2004).
[35] Z.-G. Ye, Y. Bing, J. Gao, A. A. Bokov, P. Stephens, B. Noheda, and G. Shirane, Phys. Rev. B **67,** 104104 (2003).
[36] G. Schmidt, Ferroelectrics **78,** 199-206 (1988).
[37] Z. Xu, M.-C. Kim, J.-F. Li, and D. Viehland, Philosophical Magazine A **74,** 395-406 (1996).
[38] G. Schmidt, G. Borchhardt, J. V. Cieminksi, D. Grützmann, E. Purinsch, and V. A. Isupov, Ferroelectrics **42,** 3-9 (1982).
[39] D. A. Porter and K. E. Easterling, *Phase transformations in metals and alloys*, 2nd ed. (Chapman and Hall, London, 1992).
[40] A. G. Khachaturyan, S. M. Shapiro, and S. Semenovskaya, Phys. Rev. B **43,** 832-843 (1991).
[41] E. K. H. Salje, *Phase transitions in ferroelastic and co-elastic crystals* (Cambridge University Press, Cambridge, 1993).
[42] E. K. H. Salje, Acta Cryst. A **47,** 453-469 (1991).
[43] Y. M. Jin, Y. U. Wang, and A. G. Khachaturyan, J. Appl. Phys. **94,** 3629-3640 (2003).
[44] D. Viehland, M.-C. Kim, Z. Xu, and J.-F. Li, Appl. Phys. Lett. **67,** 2471-2473 (1995).
[45] E. Salje and K. Parlinski, Supercond. Sci. Tech. **4,** 93-97 (1991).
[46] K. Parlinski, V. Heine, and E. K. H. Salje, J. Phys.: Condens. Matter **5,** 497-518 (1993).
[47] E. K. H. Salje and Y. Ishibashi, J. Phys.: Condens. Matter **8,** 8477-8495 (1996).
[48] D. Viehland, J. Appl. Phys. **88,** 4794 (2000).
[49] T. Mulvey and R. K. W. (ed.), *Modern physical techniques in materials technology* (Oxford University Press, London, 1974).
[50] B. Bhushan, H. Fuchs, and S. H. (ed.), *Applied Scanning Probe Methods* (Springer, 2002).
[51] A. Gruverman, O. Auciello, and H. Tokumoto, Annu. Rev. Mater. Sci. **28,** 101-123 (1998).
[52] F. Jona and G. Shirane, *Ferroelectric crystals* (Pergamon Press, New York, 1962).
[53] W. J. Merz, Phys. Rev. B **95,** 690-698 (1954).
[54] X. Meng, K. Baba-Kishi, H. Chan, C.-l. Choy, and H. Luo, Jpn. J. Appl. Phys. Part 1 **41,** 2999-3005 (2002).
[55] V. V. Shvartsman and A. L. Kholkin, Phys. Rev. B **69,** 014102 (2004).
[56] H. Okino, J. Sakamoto, and T. Yamamoto, Jpn. J. Appl. Phys. **43,** 6808-6811 (2004).
[57] F. Bai, J. Li, and D. Viehland, Appl. Phys. Lett. **85,** 2313-2315 (2004).
[58] J. Erhart, Phase Transitions **77,** 989-1074 (2004).

[59] A. R. James, S. Priya, K. Uchino, K. Srinivas, and V. V. Kiran, Jpn. J. Appl. Phys. Pt. 1 **8,** 5272-5276 (2002).
[60] G. Burns and F. H. Dacol, Solid State Communications **42,** 9-12 (1982).
[61] G. Burns, F. H. Dacol, J. P. Remeika, and W. Taylor, Phys. Rev. B **26,** 2707-2709 (1982).
[62] A. Naberezhnov, S. Vakhrushev, B. Dorner, D. Strauch, and H. Moudden, Eur. Phys. J. B **11,** 13-20 (1999).
[63] S.-A. Seo, K. H. Noh, and S.-I. Kwun, Journal of the Korean Physical Society **35,** 496-499 (1999).
[64] D. Viehland, S. J. Jang, and L. E. Cross, J. Appl. Phys. **68,** 2916-2921 (1990).
[65] D. Viehland, J. F. Li, S. J. Jang, and L. E. Cross, Phys. Rev. B **43,** 8316-8320 (1991).
[66] H.-K. Guo, G. Fu, X.-G. Tang, J.-X. Zhang, and Z.-X. Chen, J. Phys.: Condens. Matter **10,** L297-L302 (1998).
[67] F. Yan, P. Bao, and Y. Wang, Appl. Phys. Lett. **83,** 4384-4386 (2003).
[68] E. V. Colla, N. K. Yushin, and D. Viehland, J. Appl. Phys. **83,** 3298-3304 (1998).
[69] N. d. Mathan, E. Husson, G. Calvarin, J. R. Gavarri, A. W. Hewat, and A. Morell, J. Phys.: Condens. Matter **3,** 8159-8171 (1991).
[70] H. You and Q. M. Zhang, Phys. Rev. Lett. **79,** 3950-3953 (1997).
[71] D. La-Orauttapong, J. Toulouse, J. L. Robertson, and Z.-G. Ye, Phys. Rev. B **64,** 212101 (2001).
[72] D. La-Orauttapong, J. Toulouse, Z.-G. Ye, W. Chen, R. Erwin, and J. L. Robertson, Phys. Rev. B **67,** 134110 (2003).
[73] K. Ohwada, K. Hirota, P. W. Rehrig, Y. Fujii, and G. Shirane, Phys. Rev. B **67,** 094111 (2003).
[74] P. M. Gehring, W. Chen, Z.-G. Ye, and G. Shirane, J. Phys.: Condens. Matter **16,** 7113-7121 (2004).
[75] S. W. Choi, J. M. Jung, and A. S. Bhalla, Ferroelectrics **189,** 27-38 (1996).
[76] F. Yan, P. Bao, Y. Wang, H. L. W. Chan, and C. L. Choy, Appl. Phys. Lett. **81,** 4580-4582 (2002).
[77] D. Zekria, V. A. Shuvaeva, and A. M. Glazer, J. Phys.: Condens. Matter **17,** 1593-1600 (2005).
[78] A.-E. Renault, H. Dammak, G. Calvarin, P. Gaucher, and M. P. Thi, J. Appl. Phys. **97,** 044105 (2005).
[79] Y. Lu, D.-Y. Jeong, Z.-Y. Cheng, T. Shrout, and Q. M. Zhang, Appl. Phys. Lett. **80,** 1918-1920 (2002).
[80] D. H. Kim, J.-H. Ko, C. D. Feng, and S. Kojima, J. Appl. Phys. **98,** 044106 (2005).
[81] S. G. Lu, Z. Xu, and H. Chen, Phys. Rev. B **72,** 054120 (2005).
[82] M. Shen and W. Cao, J. Appl. Phys. **95,** 8124 (2004).
[83] H. Okino, J. Sakamoto, and T. Yamamoto, Jpn. J. Appl. Phys. **44** (2005).
[84] S. W. Choi, T. R. Shrout, S. J. Jang, and A. S. Bhalla, Materials Letters **8,** 253-255 (1989).
[85] M. J. Haun, E. Furman, S. J. Jang, H. A. McKinstry, and L. E. Cross, J. Appl. Phys. **62,** 3331-3338 (1987).

[86] S. L. Swartz and T. R. Shrout, Materials Research Bulletin **17,** 1245-1250 (1982).
[87] T. R. Shrout, Z. P. Chang, N. Kim, and S. Markgraf, Ferroelectrics Letters **12,** 63-69 (1990).
[88] C.-S. Tu, R. R. Chien, F.-T. Wang, V. H. Schmidt, and P. Han, Phys. Rev. B **70,** 220103(R) (2004).
[89] H. Cao, B. Fang, H. Luo, Y. Sun, and J. Guo, Ceramics International **29,** 145-150 (2003).
[90] D. Viehland, J. Powers, L. E. Cross, and J. F. Li, Appl. Phys. Lett. **78,** 3508-3510 (2001).
[91] J. Kuwata, K. Uchino, and S. Nomura, Jpn. J. Appl. Phys. **21,** 1298-1302 (1982).
[92] M. Shen, D. Yao, and W. Cao, Materials Letters **59,** 3276-3279 (2005).
[93] C.-S. Tu and C.-L. Tsai, J. Appl. Phys. **87,** 2327-3176 (2000).
[94] J. J. Lima-Silva, I. Guedes, J. M. Filho, A. P. Ayala, M. H. Lente, J. A. Eiras, and D. Garcia, Solid State Communications **131,** 111-114 (2004).
[95] S. Priya, J. Ryu, L. E. Cross, K. Uchino, and D. Viehland, Ferroelectrics **274,** 121-126 (2002).
[96] C. Lei, K. Chen, X. Zhang, and J. Wang, Solid State Communications **123,** 445-450 (2002).
[97] L. Feng and Z.-G. Ye, Journal of Solid State Chemistry **163,** 484-490 (2002).
[98] B. Noheda, Current Opinion in Solid State and Materials Science **6,** 27-34 (2002).

Chapter five

Structural characterization

In this chapter, the microstructural features of PMN-xPT and PZN-xPT in both poled and unpoled conditions are examined using polarized light microscopy (PLM). A brief review of the theory of permissible domain walls in ferroelectrics is given followed by a thorough discussion of the concept of *domain engineering*.

In annealed (unpoled) samples of PMN-33PT and PZN-8PT complex domain structures are observed, likely related to compositional inhomogeneity and their proximity to the morphotropic phase boundary. A monoclinic phase is evidenced by PLM in unpoled PMN-33PT. However, it is noted that monoclinic phases are generally difficult to resolve from their rhombohedral and orthorhombic parents in domain-engineered (poled) crystals. In agreement with work done elsewhere, the domain structures of $[001]_C$-poled, domain-engineered (nominally 4R) PMN-28PT and $[001]_C$-poled (nominally 4O) PZN-8PT are shown to be built up from alternating, "interwoven" twin pairs ("two-variant twinning"). The domain walls occurring in relaxor-ferroelectric PMN-xPT and PZN-xPT can be predicted based on permissible domain wall theory, just as they can for simpler ferroelectrics.

I. INTRODUCTION

A perfect crystal could be described as a perfectly periodic structure extending in three dimensions to each of its bounding surfaces[1]. Every structural feature of a crystal that does not have translational symmetry in three dimensions might be summarized in its *microstructure*[2]. Although more modern techniques like atomic force microscopy (AFM), scanning electron microscopy (SEM) and transmission electron microscopy (TEM) are necessary to probe the sub-micron *mesoscale* structure of unpoled relaxor-ferroelectrics (chapter four), many structural features of poled and unpoled PMN-xPT and PZN-xPT are visible on a scale of 1 μm or above; they can thus be imaged by optical microscopy, and especially using *polarized light*.

In ferroelectric single crystals like barium titanate and lead titanate, which (by definition) do not contain grain boundaries, the main structural feature dominating the microstructure are domains and *domain walls*. These generally take certain *permissible* crystallographic orientations which can be predicted based on the symmetry of the phase using the methods developed by Sapriel (1975)[3] and Fousek and Janovec (1969)[4]. Any other microstructural feature, including two-phase coexistence due to compositional heterogeneity, can generally be classified as a *defect* and will usually have a detrimental effect on properties.

We start with some brief theory regarding the domain structures in ferroelectric crystals.

180° and non-180° domain walls

Upon cooling through T_C, a general ferroelectric crystal will transform into a lower symmetry phase composed of various possible *orientation states*[4], or *variants*[5], with the same symmetry but differing orientations for their spontaneous polarization vector $\boldsymbol{P_s}$ or spontaneous strain tensor $\boldsymbol{S_s}$ (where the transition is also *ferroelastic*).

Tetragonal *4mm* lead titanate (see appendix I) will contain six variants each with a different direction for $\boldsymbol{P_S}$; these are the six $<001>_C$ cubic directions. The variants are, in fact, comprised of three pairs of two orientation states with identical spontaneous strain tensors. In the *mm2* orthorhombic phase barium titanate and potassium niobate there are 12 ferroelectric domain variants; these have their polar vector along one of the 12 $<101>_C$ face-diagonals of the pseudocubic unit cell (appendix I). In the *3m* rhombohedral phase of $BaTiO_3$ and $KNbO_3$ there are 8 ferroelectric domain variants, this time with polar vectors along one of the $<111>_C$ body diagonals of the pseudocubic cell. The spontaneous polarization vectors and strain tensors of all the ferroelectric point groups have been listed by Erhart[5].

The boundary regions between these domains are known as *domain walls*, and are commonly defined by the angle formed between the polarization directions of the neighboring domains. They can be split into two types:

Firstly, “180° domains” refer to domain walls (DWs) between two orientation states with antiparallel polarizations but with strain tensors that are

necessarily the same. Such domain walls will generally be moved by the application of an electric field $\boldsymbol{E}$ due to a driving force of $-\boldsymbol{E}.\boldsymbol{P_S}$; they can be referred to as *ferroelectric* domain walls. However, they will not be moved by the application of a mechanical stress since both neighboring variants have the same strain tensor.

Secondly, "non-180°" domain walls refers to walls between variants which differ in both polarization vector and strain tensor. For example, in tetragonal lead titanate 90° DWs are observed. They are therefore generally moved by both stress (due to a driving force $-\boldsymbol{\sigma}\cdot\boldsymbol{S_s}$) and electric field and are often referred to as *ferroelastic-ferroelectric* domain walls. Both 180° domain walls and 90° domain walls are observed in tetragonal lead titanate[6] and barium titanate[7-9] at room temperature. Both 180° and 90° DWs generally form to decrease the effects of depolarization fields, whereas only 90° domain walls may minimize the elastic energy[10].

Permissible domain walls

All permissible non-180° domain walls for all ferroelectrics and ferroelastic species have been calculated by Erhart (2004)[5] using the more general Sapriel[3], rather than Fousek and Janovec[4] method, based on conditions of *strain compatibility*. Both *charged*[11] ("head-to-head" or "tail-to-tail") and *neutral* ("head-to-tail") are listed. Two types of domain wall are differentiated[4]. "W_f" walls have fixed crystallographic orientations whereas "*S*" walls have orientations that depend on the components of the spontaneous strain tensor of the adjacent domains; the latter can thus be dependent on temperature.

Most usefully for this present thesis work, his article includes all the possible domain walls for the five *ferroelectric* phases[12] that occur in perovskite crystals below the Curie temperature, that is: rhombohedral *3m*, orthorhombic *mm2*, tetragonal *4mm*, and monoclinic *m* (M_A and M_C). In the M_A and M_C phases both charged and neutral, *S* and W_f walls are possible; W_f walls are $\{10\bar{1}\}_C$ and $\{010\}_C$. In the tetragonal phase charged and neutral W_f walls of type $\{10\bar{1}\}_C$ appear. These are "90°" domain walls since the angle between the polar vectors in adjacent domains is 90°, excepting some small misfit angle[13]. In the orthorhombic phase, both *S* and W_f walls are permissible; W_f walls are $\{10\bar{1}\}_C$ (60° or 120°) and $\{010\}_C$ (90°), both charged and neutral. Similarly, in the rhombohedral phase both $\{10\bar{1}\}_C$ (109.5°) and $\{010\}_C$ (70.5°) type W_f walls are permissible, both charged and uncharged.

Finally we note that there is no general condition of mechanical compatibility for 180° domain walls. They must be parallel to the polar vector for charge neutrality but otherwise can form any irregular shape. They result in "fingerprint[9]" patterns in unpoled crystals, and "watermark[8]" and "herringbone[9]" patterns when they appear superposed with 90° domain walls.

Poling

Virgin ferroelectric crystals tend to be macroscopically cubic (*m3m*) in their as-cooled state due to energetically degenerate, and therefore equally-likely, domain variants[14]. Therefore, they are macroscopically non-polar ($\sum \boldsymbol{P}^{(i)}$) and hence do not show any pyroelectricity or piezoelectricity. They must be *poled* (or "remanently polarized") to render them useful[15]. As stated above, 180° and non-180° domain walls in ferroelectrics will generally moved by application of a sufficiently strong electric field; this is known as ferroelectric "*switching*[10]" and occurs at a threshold field, known as the coercive[11,16] field, E_C. *Ferroelastic switching* is also possible, in any ferroelastic material, by application of a stress larger than the coercive value, σ_c. This has also been extensively studied in both ceramics[17-21] and single crystals[22-24] and will be returned to in chapters eight and nine.

Usually, a ferroelectric crystal might be poled *along* the polar axis of one of its domain variants thus favoring one domain over the rest and therefore a monodomain crystal. For example, poling a *3m* rhombohedral crystal along the $[111]_C$ direction will energetically favor one domain variant, with $\boldsymbol{P}_s$ parallel to the poling direction. However, as noted in the introduction, the most exciting piezoelectric properties of PMN-xPT and PZN-xPT result from poling along *non-polar* directions.

II. DOMAIN ENGINEERED STRUCTURES

By poling a *3 m* rhombohedral crystals along either a $<001>_C$ or $<101>_C$, non-polar direction, a special, polydomain state will be induced: this is the basis of *domain engineering* introduced in chapter one.

Domain engineering

Park and Shrout first noted that the anhysteretic field-induced strain response of $[001]_C$-oriented, nominally-rhombohedral PMN-xPT and PZN-xPT might be due to its special "engineered-domain" configuration[25]. In the virgin, unpoled state a *3m* rhombohedral crystal will be divided into eight possible, degenerate domain variants, with polar vectors $\boldsymbol{P}_S$ along one of the eight[5] $<111>_C$ body diagonals of the pseudocubic unit cell. For crystal dimensions much larger than the average domain size (and ignoring the need for permissible domain walls) we can assume that the crystal will contain equal volume fractions of each variant. We will denote this virgin state "8R"; its eight degenerate polar vectors are shown with respect to the pseudocubic unit cell in the left hand column of figure 1. Likewise virgin *mm2* orthorhombic, with polar vectors along $<101>_C$, and virgin *4mm* tetragonal crystals, with $<001>_C$ polar axes, are shown as "12O" and "6T", respectively.

In the simplest case, application of an electric field (above some coercive value) along one of the 8, 12 or 6 potential polar directions of the

virgin R, O or T crystal will lead to one of three *monodomain* states, i.e.: "1R", "1O" and "1T"; these are also shown in the body diagonal of figure 1.

Critically, however, if the crystal is poled along a *non-polar* $<001>_C$, $<101>_C$ or $<111>_C$ direction, the resultant structure will be polydomain since more than one domain variant will be energetically favored by the poling field. For example, if an 8R rhombohedral crystal is subject to a strong enough electric field $\boldsymbol{E}$ along the $[001]_C$ direction, four of the eight domain variants will be energetically favored by a bias energy $-\boldsymbol{E}.\boldsymbol{P_s} = EP_s\cos\theta$, where θ is the angle between the polar vector $\boldsymbol{P_s}$ and the poling direction. These degenerate variants will have polar vectors along $[111]_C$, $[\bar{1}\bar{1}1]_C$, $[1\bar{1}1]_C$ and $[\bar{1}11]_C$; importantly, the polar vectors of these four domain variants are *equally inclined* (by $\theta = 54.7°$) to the poling direction. The resultant domain engineered state, labeled "4R", is shown in figure 5. As apparent in figure 3 of chapter one, upon further application of an electric field parallel to the poling direction, there is no driving force for domain wall motion and the strain-field response is characteristically linear and anhysteretic.

In fact, for all the ferroelectric phases observed in the classical ferroelectric perovskites[16], *3m* rhombohedral (R), *mm2* orthorhombic (O) and *4mm* tetragonal (T), domain engineered structures can be formed by poling in a non-polar direction. A good definition, of a domain engineered structure is that given by Bell (2001)[26] where a domain engineered crystal is:

> *"A ferroelectric crystal that has been poled by the application of a sufficiently large field along one of the possible polar axes of the crystal other than the zero-field polar axis, creating a set of domains in which the polarizations are oriented so that their angles to the poling direction are minimized."*

Thus, for the three classical ferroelectric phases, poling along a non-polar $<001>_C$, $<101>_C$ or $<111>_C$ direction leads to *3 x 2 = 6* possible domain engineered structures and *3 x 1 = 3* theoretically monodomain structures. They are all shown in figure 1.

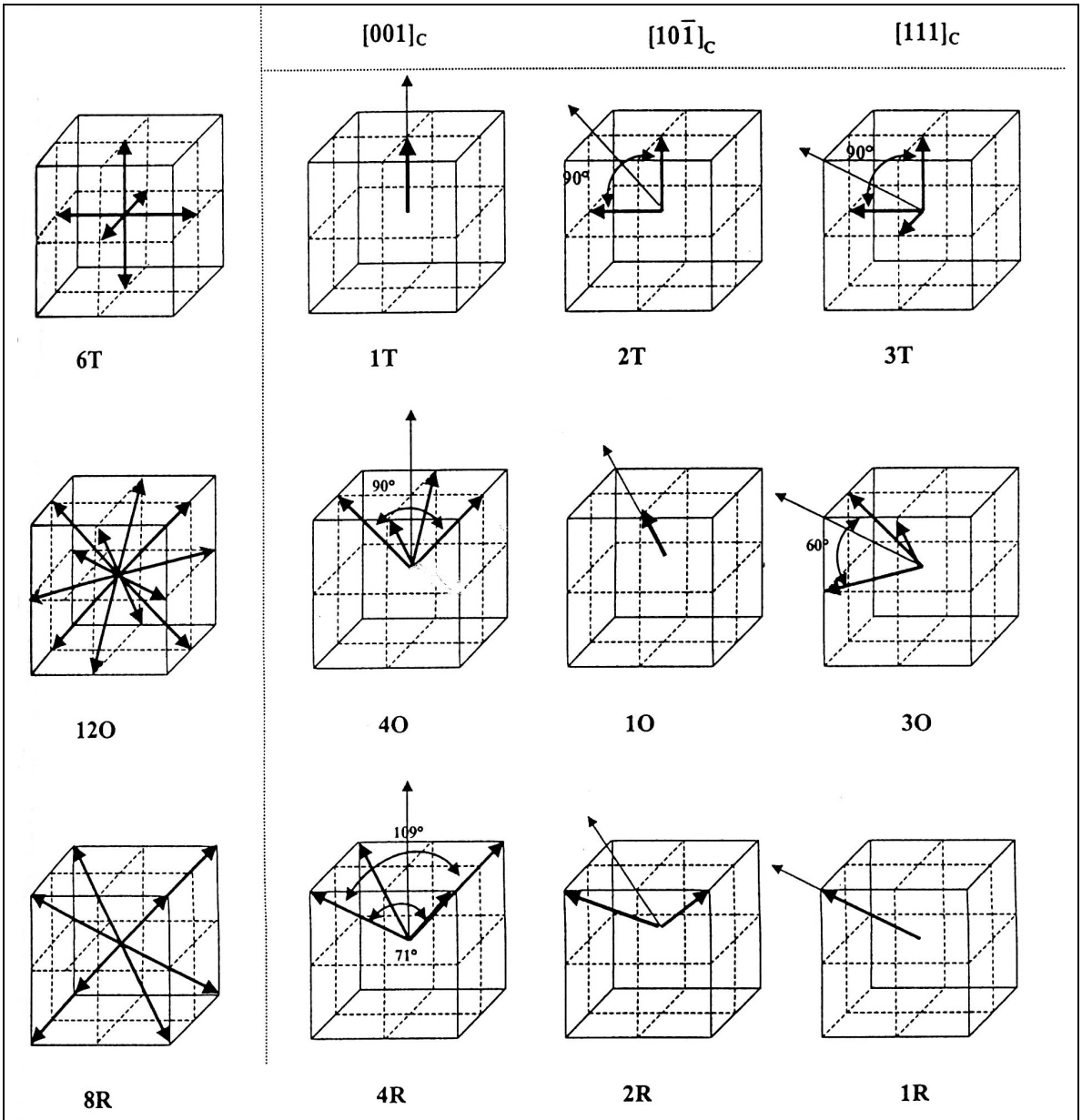

Fig. 1. Possible domain engineered and monodomain structures formed in *3m* rhombohedral (R), *mm2* orthorhombic (O) and *4mm* tetragonal (T) ferroelectric perovskites by poling at sufficiently high fields along <001>$_C$, <10$\bar{1}$>$_C$ and <111>$_C$ directions.

Macroscopic symmetry of domain engineered crystals

Just as the theoretical macroscopic symmetry of an unpoled ferroelectric R, O or T crystal is cubic *m3m*[27], the macroscopic symmetry of a domain engineered crystal will also be different to that of its constituent domain variants. The effective symmetry of a domain average engineered structure can easily be derived if an equal number of each domain variants is assumed[28,29]. For example, 4R and 4O domain engineered crystals will be macroscopically tetragonal (*4mm*) providing all the domain variants are present in equal quantity[25]; of course, this will probably only be possible in crystals where the domain size is small compared the dimensions of the sample.

If unequal numbers of domain variants exist in the domain engineered crystal, then lower symmetry macroscopic symmetries result. Various permutations of this have been calculated by Hatch et al. (2003)[27] using group theory for non-equal domain concentrations in domain average engineered R, O and T single crystals.

Domain average engineering

Notably, Fousek and coworkers specify two different types of domain engineering[28]. Firstly, "*domain geometry engineering*" is defined for a multidomain sample for which the spatial distribution of domains in the structure is important to its macroscopic response to an applied field. That is, the boundary conditions at the domain walls are important to the response. In contrast, "*domain average engineering*" is defined for a situation in which a ferroelectric is subdivided into a very large number of domains (with the domain size much smaller than the wavelength of externally applied fields) such that the spatial distribution of the domains in the structure is irrelevant to the macroscopic response. In this situation, the spatial arrangement of polar directions is most important to the piezoelectric and dielectric properties.

Other constraints on domain-engineered structures

As noted above, the simple domain-engineering theory laid out in figure 1 ignores interactions between domains. With this in mind, Erhart and Cao have investigated the *permissible* domain engineered structure in R, O and T perovskite crystals with the criterion that the structure must be able to form a two-dimensional superlattice: that is, the domain structure must have translational symmetry. In their analysis, only one domain is allowed to exist in a given volume and the orientation of permissible domain walls are taken into account. This is in contrast to the purely statistical analysis[27-29] outlined above where domains are allowed to overlap in space.

Importantly, the authors conclude that certain domain engineered structures cannot actually be realized. This includes the both $[111]_C$-poled structures, 3O and 3T, shown in figure 1.

Charged domain walls

Finally, we note that the six engineered structures shown in figure 1 will necessarily contain *charged domain walls*[5,11]; this is not generally expected in ferroelectric crystals.

II. POLARIZED LIGHT MICROSCOPY

Optical microscopy and, especially, polarized-light microscopy (PLM) provide a straightforward and powerful tool for examining the domain structure of ferroelectric crystals with features above 1 μm in size.

In opaque samples, etching can be used to pick out ferroelectric domain features in polished samples; a standard optical microscope working with reflected light can then be used to image the structure[9]. In transparent samples, however, the use of polarized, transmitted light provides a non-destructive way of imaging ferroelectric domain structures.

The principles of polarized light microscopy are laid out in appendix III. The method used for this thesis work, and the general method used by others, is as follows.

Imaging of ferroelectric domains

First all samples are cut to size, polished and annealed, as described in chapter three. Plate type samples of thickness 0.5 mm were used. The thickness after grinding and polishing was generally between 400 and 450 μm. Samples are then placed between crossed polarizers in an optical microscope. White light is shone through the polarizers and crystals perpendicular to the largest surface of the crystal. The setup is shown in the left of figure 2.

The crystal is then rotated about the beam axis and "positions of extinction" are sought for the various ferroelectric domains present; these are shown in the right of figure 2. Positions of extinction give information about the high-symmetry, or polar, axis of a domain (i.e. the direction of spontaneous polarization $\boldsymbol{P_S}$) since it will have a fixed geometrical relationship with the optical ellipse (appendix III). In certain conditions, where the principal axes of the optical ellipse coincide with the axes of the polarizer and analyzer no light will be transmitted through the crystal and crossed polarizers. This is called *extinction*. Moreover, if the beam direction is parallel to an optic axis (high symmetry axis) the crystal is isotropic along this direction and no light will pass through the crossed polarizers; again we have extinction.

The general method is also discussed elsewhere[30-34].

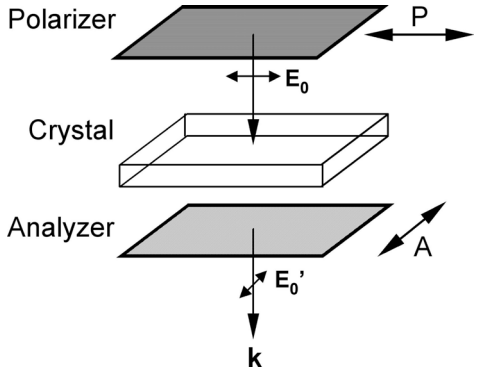

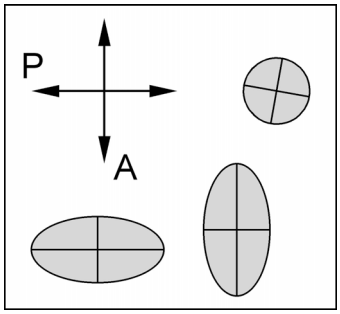

Fig. 2. (Left) Setup for polarized light microscopy (PLM) showing a thin, transparent specimen between crossed polarizers (A and P). (Right) Various positions of extinction for the optical ellipse of individual ferroelectric domains.

PLM has been used quite extensively to image the domain structure of PMN-xPT and PZN-xPT single crystals. In the next two sections, optical studies of the domain structure in poled and unpoled PMN-28PT, PMN-33PT and PZN-8PT single crystals are presented alongside results from the literature.

III. UNPOLED PMN-xPT AND PZN-xPT

Firstly, various authors have pointed out the tendency for *two-phase coexistence* in as-grown (unpoled) PMN-xPT and PZN-xPT with morphotropic phase boundary compositions. The coexistence of rhombohedral (R) and tetragonal (T) phases has been evidenced by differing positions of extinction in PZN-9PT and PMN-35PT [Ye (2002)[35]], PZN-9PT [Fujishiro et al. (1998)[36]], and PMN-xPT [Shuvaeva et al. (2005)[37]]. The coexistence is a consequence of compositional heterogeneity, which is difficult to avoid in flux-grown crystals (chapter three).

By heating a sample of PMN-35PT, containing both R and T phases at room temperature, Ye and Dong[38] have evidenced the transition to the cubic phase at T_C. During the transition the tetragonal-cubic (first order) phase boundary is shown to sweep across the sample over a temperature range of nearly 40°C, suggesting a huge composition gradient (chapter four): this corresponds to a compositional change in the order of 4 mol.% PT, close to the width of the morphotropic phase boundary[39].

Indeed, the domain structure in as-cooled, unpoled PMN-xPT and PZN-xPT with compositions close to the morphotropic phase boundary is generally complex. The microstructures of polished and annealed, $[111]_C$-oriented PZN-8PT and PMN-33PT plate samples are shown in figure 3. Some monodomain areas can be seen, along with large macrodomains and fine, overlapping features. The microstructure is characteristic of domains formed by a nucleation and growth mechanism during a first order phase transition, satisfying complex electrical and mechanical[10], and possibly chemical (compositional), boundary conditions.

Fig. 3. Domain structure of $[111]_C$-oriented PZN-8PT (left) and PMN-33PT (right) viewed between crossed polarizers. The polarizer and analyzer directions are parallel to the face edges and the plate dimensions are 10 x 10 x 0.5 mm^3. A complex domain structure is observed. Images from this thesis work.

Monoclinic phases

Monoclinic phases, where the positions of extinction do not correspond to the $<001>_C$, $<101>_C$ or $<111>_C$ polar vectors of the *4mm* tetragonal (T), *mm2* orthorhombic (O) and *3m* rhombohedral (R) phases (chapter one, fig. 6), have also been evidenced by PLM. For example, Guisheng et al. have evidenced a monoclinic phase in unpoled $(001)_C$ plates of PMN-33PT[40]. Fujishiro et al. have also evidenced a monoclinic phase in unpoled, $[111]_C$-oriented PZN-9PT as a finite rotation of the extinction angle away from that permitted by rhombohedral and tetragonal symmetries. The rotation was found to be strongly dependent on temperature. Similarly, Iwata et al. have evidenced a lower symmetry, monoclinic phase in unpoled plates of PZN-5PT and PZN-8PT, again with temperature dependent extinction angles[41].

Extinction positions indicative of a low symmetry phase were observed in certain, unpoled, samples of PZN-xPT and PMN-xPT. In a $[111]_C$-oriented sample, with sides parallel to $[1\bar{1}0]_C$ and $[11\bar{2}]_C$, extinction is expected at angles of 0°, 30°, 60° or 90° from the sample edges for rhombohedral, orthorhombic and tetragonal symmetries. Extinction at angles other than this is evidence of a lower symmetry, monoclinic phase. This was found, for example, in the sample of PMN-33PT shown in figure 3. Extinction positions of 35° degrees from the $[1\bar{1}0]_C$ direction were observed, as shown in figure 4, characteristic of a monoclinic *m* phase.

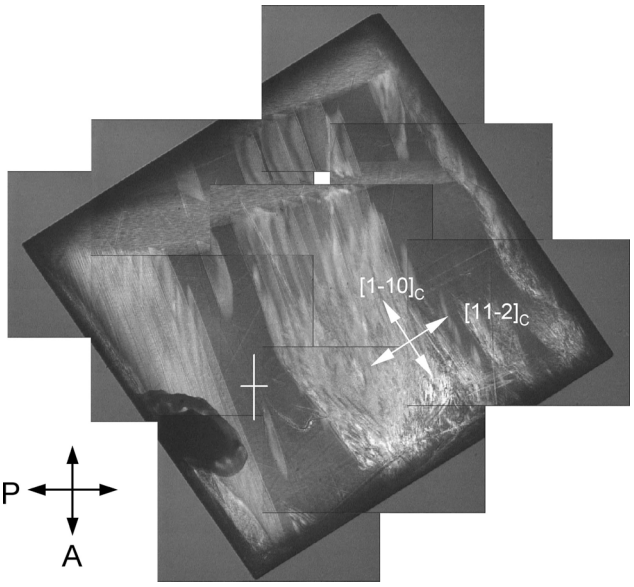

Fig. 4. Extinction under crossed polarizers for the sample of $[111]_C$-oriented PMN-33PT shown in figure 3. The angle of extinction (35°), which is not equal to 30°, is evidence of monoclinic symmetry.

Bokov and Ye have studied the domain structure in monoclinic (M_C) PMN-33PT, in both poled and unpoled conditions[30]. Perhaps artificially, they only looked at samples of nominal composition "PMN-33PT" which contained no rhombohedral, orthorhombic or tetragonal phase in their as-grown state; samples not meeting this criterion were not studied. Elsewhere, by careful measurement of extinction positions, Zekria and coworkers have used PLM to evidence a transition from rhombohedral to tetragonal phases via both monoclinic M_A and M_C symmetries upon increasing the PT content in unpoled PMN-xPT.

Finally, it should be noted that monoclinic phases will not always be distinguishable from higher symmetry phases in PLM. Critically, monoclinic M_A and M_C phases will only be distinguishable from higher symmetry phases by PLM when the symmetry-lowering rotation of their polar axis $\boldsymbol{P_S}$ from one of the rhombohedral $<111>_C$, orthorhombic $<110>_C$ or tetragonal $<001>_C$ limiting directions *lies in the plane of the sample being viewed*. That is, they will not be detectable by PLM when their $\{010\}_C$ or $\{1\bar{1}0\}_C$ monoclinic plane is perpendicular to the plane of the sample. This is shown explicitly for $[001]_C$-oriented samples in figure 5. Importantly, in domain engineered PMN-xPT and PZN-xPT samples oriented and poled along the $[001]_C$-direction, the 4R and 4O domain engineered structures of figure 1 will not be discernible from monoclinic $4M_A$ and $4M_C$ structures, respectively; these are shown in figure 6. Where Bokov and Ye investigated the $4M_C$ structure of poled PMN-33PT[30], they started with a structure containing only M_C domains, with polar vectors necessarily in the $(001)_C$ plane of the sample, and *then* poled along $[001]_C$.

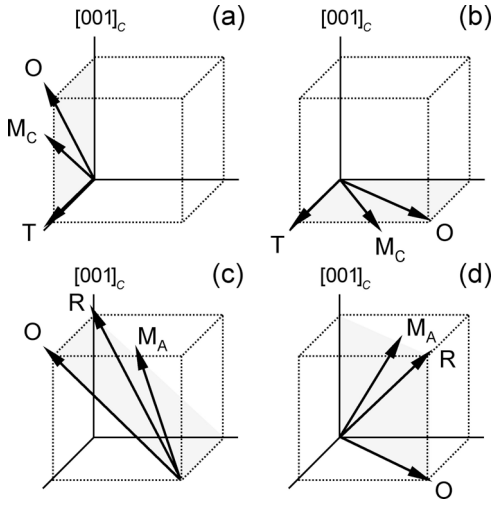

Fig. 5. In crystals viewed down the $[001]_C$ direction, for example, monoclinic phases will only be distinguishable from the higher symmetry R, O and T phases when their monoclinic plane is not perpendicular to the $(001)_C$ sample surface. In (a) PLM cannot resolve the O, M_C and T phases. In (d), M_A, R and T phases will have the same extinction position. Only in (b) and (c) are the phases resolvable.

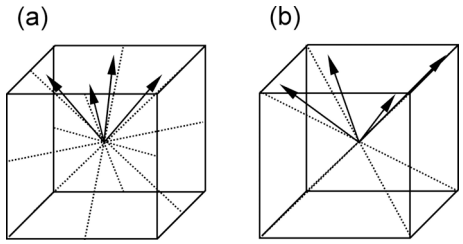

Fig. 6. (a) $4M_C$ and (b) $4M_A$ domain engineered structures; they can be seen as distorted versions of the 4O and 4R structures shown in figure 1.

Tweed microstructures

As discussed in chapter three, fine, diffuse, tweed-like structures were observed in samples of PMN-33PT and PMN-28PT before annealing. A close-up of the as-polished domain structure of a sample of PMN-33PT is shown in figure 7. All samples displaying such a microstructure generally had an opaque, milky appearance to the naked eye. Such “milkiness”, and the fine scale domain structure, was generally removed by either annealing, as discussed in chapter three, or by poling. The fact that the short-range ordered, tweed microstructure can be removed by an electric field fits well with the martensite analogy laid out in chapter four.

Diffuse, tweed-like microstructures were not, however, seen in PZN-8PT samples in the as-polished state. This is perhaps indicative of a higher domain wall energy and would follow from a higher PT content and a more long-range ordered, “ferroelectric” character.

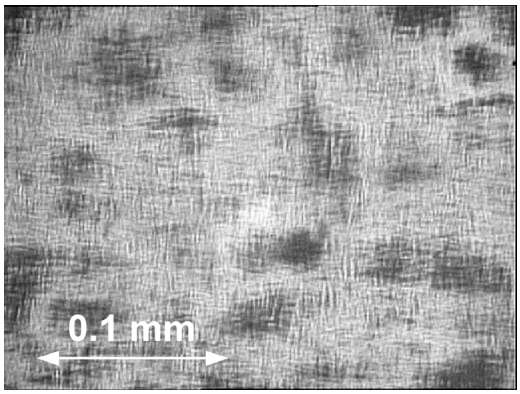

Fig. 7. Close-up of the fine domain-structure observed in an unpoled $[001]_C$-oriented plate of PMN-33PT in the as-polished condition. Image from this thesis work.

IV. POLED PMN-xPT AND PZN-xPT

The ferroelastic domain structures of PMN-xPT and PZN-xPT single crystals poled along non-polar directions are an important subject of investigation, especially since the resultant "domain-engineered" structures seem to be the origin of their usefully anhysteretic strain-field response.

Of most interest is the domain-engineered structure formed in rhombohedral PMN-xPT and PZN-xPT poled along a non-polar $<001>_C$ direction. This (nominally) 4R structure has been investigated by Han and Cao by PLM in $[001]_C$-oriented PMN-32PT[42].

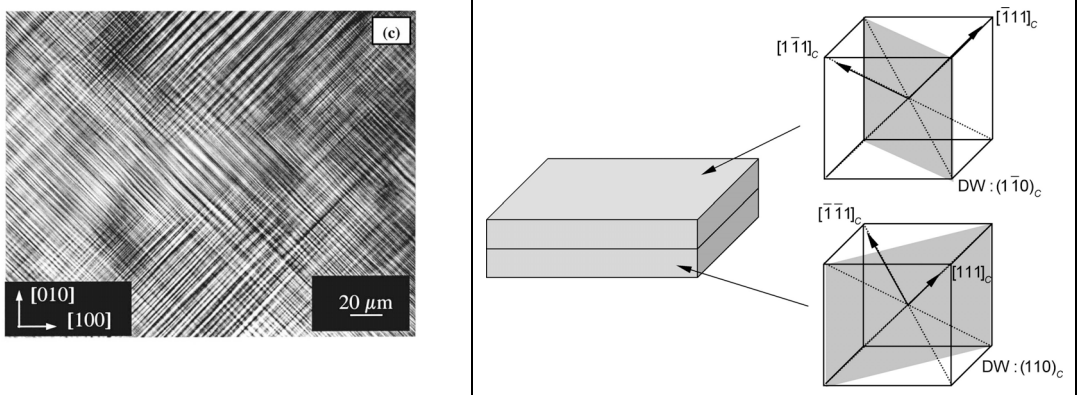

Fig. 8. (Left) Domain-engineered, nominally-4R structure in $[001]_C$-oriented PMN-32PT after poling by field cooling [from Han and Cao (2003)[42]]. (Right) The structure consists of stacked pairs of 109.5° twins.

After poling, the domain structure was comprised of superimposed (or rather stacked) sets of ferroelastic twins about 1-2 μm in width (see figure 8). Importantly, each set contained a pair of domain variants separated by $\{10\bar{1}\}_C$ (109.5°) domain walls. The domain walls of each set of twins are perpendicular to each other when viewed along $[001]_C$. The variant pairs were found to be stacked on top of one another, in a layers around 50 μm

thick[42]. This stacked structure is shown schematically in the right of figure 8. Notably, as with all domain engineered structures, all domain walls are necessarily charged with the spontaneous polarization vectors of neighboring domains being "head-to-head" ("tail-to-tail").

$[001]_C$-oriented samples of PZN-8PT, PMN-28PT and PMN-33PT were poled by field cooling, as described in the next chapter, after polishing, annealing, and electroding with gold. The electrodes were finally removed by gently rubbing with tissue and acetone.

The resultant $[001]_C$-poled crystals exhibited similar "interwoven" domain structures. This is shown in figure 9 for samples PZN-8PT and PMN-28PT. In $[001]_C$-poled PZN-8PT the extinction directions evidence an orthorhombic, nominally 4O (or $4M_C$) structure. In $[001]_C$-poled PMN-28PT, the extinction was evidence of a 4R rhombohedral (or $4M_A$) structure. The interwoven structures suggesting stacked layers of alternating pairs of domain variants, as seen in PMN-32PT (fig. 8). In figure 9, however, there is less domain wall contrast; this is probably since the samples used were thicker (0.5 mm instead of 0.36 mm). In PZN-8PT domains had widths around 20-40 μm; in PMN-28PT they were finer, being around 1-5 μm wide. Assuming that the domain walls breaking at the $(001)_C$ surface run vertically down into the sample we can see that the domain structure is formed by $\{10\bar{1}\}_C$ domain walls in PZN-8PT; in PMN-28PT, the domain walls are $\{010\}_C$. All are permissible, according to Erhart[5].

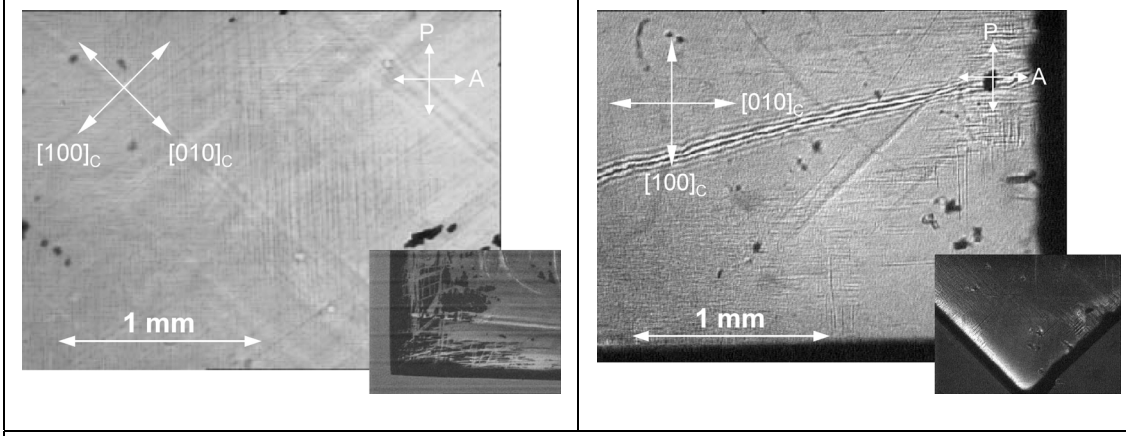

Fig. 9. $[001]_C$-oriented, domain-engineered PZN-8PT (left) and PMN-28PT (right) plates after field-cooling (poling). The images were taken between crossed-polars. Positions of extinction, corresponding to a rotation of the crystal by 45°, are shown in-set. This thesis work.

Macroscopic symmetry

Statistically, the macroscopic symmetry of these 4R ($4M_A$) and 4O ($4M_C$) domain-engineered structures should be *4mm* tetragonal. However, as discussed in section II, this will only be true when the scale of the domain structure is much smaller than the dimensions (including the thickness) of the crystal. As shown, the real domain structures of domain engineered PMN-xPT and PZN-xPT tend to be formed by layers of alternating pairs of twins. Thus, if only one twin layer were present, for example in a very thin crystal,

the macroscopic symmetry of the crystal would actually be lower than that predicted (*4mm*). For example, *mm2* symmetry results in $[001]_C$-poled rhombohedral crystals if only two of the four domain variants are present[43,44].

This is in fact a general result. The domain-engineered structures of figure 1, predicted by simple energetic degeneracy in the presence of an applied electric field, might not always exist in real crystals with real electrical and mechanical boundary conditions. That is, *domain averaging engineering* might not generally hold. Permissible domain walls[5] have to be formed, the charging of domain walls[45] needs to be considered and the filling of 3D space is also a requirement[46].

Importantly, the formation of domain engineered structures from sets of twins containing only two domain variants, in some kind of "hierarchy[43]", seems to be quite general. In fact, this "two-variant twinning" seems to be the basis of all multidomain structures, as discussed by Erhart and Cao (1999)[44]. Apart from in poled PMN-xPT[42] and PZN-xPT[45], it has also been observed in poled potassium niobate[47,48] ($KNbO_3$) and barium titanate[49] ($BaTiO_3$) as well. A PLM image of the $(001)_C$ surface of unpoled barium titanate[50] is shown in figure 10; perpendicular, stacked layers of 90° twins are clearly visible[51].

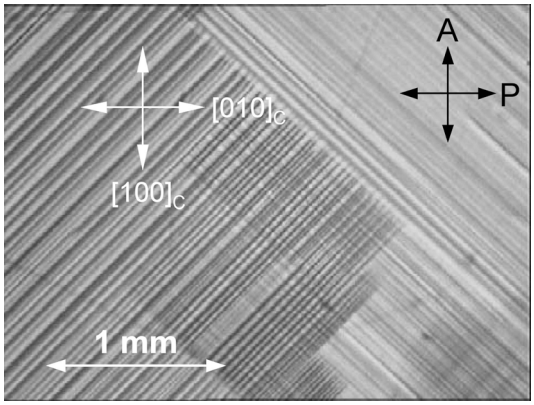

Fig. 10. Domain structure consisting of alternating sets of 90° domains in $[001]_C$-oriented, unpoled barium titanate. Image from this thesis work.

Charged walls

As mentioned in section II, the 4R domain-engineered structure necessarily contains "head-to-head", charged domain walls. Charged domain walls are unexpected in ferroelectrics since they will be associated with a electrostatic energy penalty unless charged dopants or defects can redistribute themselves to neutralize their effect[45]. The presence of charged domain walls on the piezoelectric properties of PMN-xPT and PZN-xPT will by discussed briefly in chapter ten.

Application of an electric field

Finally, the domain-engineered structures of PMN-xPT and PZN-xPT have been observed, *in situ*, under application of an electric field. Importantly, the 4R domain-engineered structure has been shown to be stable to electric fields applied along the $[001]_C$ poling direction[52]. No domain wall motion occurs, as originally suggested by Park and coworkers[53].

V. SUMMARY AND CONCLUSIONS

The domain structures of PMN-28PT, PMN-33PT and PZN-8PT samples, in both poled and unpoled conditions, have been observed by polarized light microscopy.

In unpoled PMN-33PT and PMN-28PT, fine, diffuse, "tweed-like" domain structures are observed in the as-polished state. As discussed in chapter four, these are related to residual strains in the sample surface; they can be removed by annealing, to relax the residual strain energy, or by poling.

Importantly, fine domain structures are only seen in PMN-33PT and PMN-28PT. There are not observed in PZN-8PT, even after polishing. Since fine domain structures indicate a low domain wall energy, as discussed in chapter four, this suggests the domain wall energy is higher PZN-8PT. As shown by the phase diagrams in chapter four, PZN-8PT is very close to the point at which T_m and T_d converge (x = 9 mol. %). On the other hand, PMN-33PT and PMN-28PT are further from this point (> 40 mol. % in PMN-xPT). This reiterates the fact that low domain wall energies, and fine domain structures, are a property of low PT-content crystals with more "relaxor" character. In contrast, higher PT-content "ferroelectric" compositions show coarser, more long-range ordered domain structures more typical of those seen in the simpler perovskites.

Complex domain structures are observed in annealed, unpoled PMN-33PT and PZN-8PT crystals. As will be shown in the next chapter, these two compositions are very close to the morphotropic phase boundary in PMN-xPT and PZN-xPT. Such complex domain structures will be partly due to finite compositional heterogeneity and, quite possibly, two-phase coexistence in the unpoled crystals.

A monoclinic phase has been evidenced in the complex microstructure of unpoled PMN-33PT by an extinction position different to that expected by rhombohedral, orthorhombic or tetragonal symmetry. It is noted that monoclinic phases can only be resolved in PLM when the monoclinic plane is *not* perpendicular to the plane of the sample.

Importantly, no evidence for two-phase coexistence or a diffuse microstructure is observed in $[001]_C$-poled PMN-28PT, PMN-33PT and PZN-8PT. Extinction directions are those expected of either 4R or 4O domain-engineered structures. Notably, these can not be distinguished from $4M_A$ or $4M_C$.

The nominally 4R and 4O domain engineered structures of PMN-28PT and PZN-8PT, respectively, show "interwoven" patterns similar to that seen by Han and Cao in PMN-32PT[42]. This suggests a layered structure formed by alternating *pairs* of domain variants. It has been pointed out that only when

both sets of domain variants appear in equal number will 4R and 4O domain-engineered crystals be macroscopically $4mm$. The construction of multidomain structures from "two-variant twinning[44]" seems to be general; for example, similar interwoven domain structures are observed in barium titanate.

Finally, *poled* PMN-xPT and PZN-xPT form domain structures in accordance with the general theory laid out for ferroelectric crystals[5]. Although the domain sizes are small (1.5 μm in PMN-28PT and 20-40 μm in PZN-8PT) there is no conceptual difference between these domain engineered relaxor-ferroelectrics and other ferroelectric perovskites. This gives some validity to the treatment of poled PMN-xPT and PZN-xPT, with the compositions studied in this thesis, as true *ferroelectrics*.

REFERENCES

1 A. Putnis, *Introduction to mineral sciences* (Cambridge University Press, Cambridge, 1992).

2 R. Phillips, *Crystals, defects and microstructures* (Cambridge University Press, Cambridge, 2001).

3 J. Sapriel, Phys. Rev. B **12,** 5128-5140 (1975).

4 J. Fousek and V. Janovec, J. Appl. Phys. **40,** 135-142 (1969).

5 J. Erhart, Phase Transitions **77,** 989-1074 (2004).

6 P. Lehnen, J. Dec, and W. Kleemann, J. Phys. D: Appl. Phys. **33,** 1932-1936 (2000).

7 M. Abplanalp, L. M. Eng, and P. Günter, Appl. Phys. A **66,** S231-S234 (1998).

8 G. Arlt and P. Sasko, J. Appl. Phys. **51,** 4956-4960 (1980).

9 J. A. Hooton and W. J. Merz, Phys. Rev. **98,** 409-413 (1955).

10 D. Damjanovic, Rep. Prog. Phys. **61,** 1267-1324 (1998).

11 F. Jona and G. Shirane, *Ferroelectric crystals* (Pergamon Press, New York, 1962).

12 D. Vanderbilt and M. H. Cohen, Phys. Rev. B **63,** 094108 (2001).

13 L. Inovecky, Acta. Phys. Pol. A **93,** S-11 (1998).

14 Of course this assumes the dimension of the sample is much bigger than the dimension of the domains present.

15 The same is true of ceramics.

16 B. Jaffe, W. R. Cook, and H. Jaffe, *Piezoelectric Ceramics* (Academic Press, 1971).

17 A. Schnell, Ferroelectrics **28,** 351-353 (1980).

18 J. Shieh, J. E. Huber, and N. A. Fleck, Acta Mater. **51,** 6123-6137 (2003).

19 C. S. Lynch, Acta Mater. **44,** 4137-4148 (1996).

20 H. Cao and A. G. Evans, J. Am. Ceram. Soc **76,** 890-896 (1993).

21 A. B. Schäufele and K. H. Härdtl, J. Am. Ceram. Soc **79,** 2637-2640 (1996).

22 V. C. S. Prasad and E. C. Subbarao, Appl. Phys. Lett. **22,** 424-425 (1973).

[23] E. Burcsu, G. Ravichandran, and K. Bhattacharya, Proc. SPIE, Smart Structures and Materials 2001: Active Materials: Behavior and Mechanics, C. S. Lynch, Ed. **4333** (2001).
[24] K. Nakamura, N. Chiba, and S. Ito, in *Conversion of 45° rotated X-cut $KNbO_3$ plates to Y-cut plates by compression*, Montréal, Canada, 2004.
[25] S.-E. E. Park and T. R. Shrout, J. Appl. Phys. **82,** 1804-1811 (1997).
[26] A. J. Bell, J. Appl. Phys. **89,** 3907-3914 (2001).
[27] D. M. Hatch, H. T. Stokes, and W. Cao, J. Appl. Phys. **94,** 5220-5227 (2003).
[28] J. Fousek, D. B. Litvin, and L. E. Cross, J. Phys.: Condens. Matter **13,** L33-L38 (2001).
[29] J. Fuksa and V. Janovec, J. Phys.: Condens. Matter **14,** 3795-3812 (2002).
[30] A. A. Bokov and Z.-G. Ye, J. Appl. Phys. **95,** 6347-6359 (2004).
[31] C.-S. Tu, H. Schmidt, I.-C. Shih, and R. Chien, Phys. Rev. B **67,** 020102(R) (2003).
[32] C.-S. Tu, I.-C. Shih, V. H. Schmidt, and R. Chien, Appl. Phys. Lett. **83,** 1833-1835 (2003).
[33] R. R. Chien, V. H. Schmidt, C.-S. Tu, L.-W. Hung, and H. Luo, Phys. Rev. B **69,** 172101 (2004).
[34] C.-S. Tu, L.-W. Hung, R. R. Chien, and V. H. Schmidt, J. Appl. Phys. **96,** 4411-4415 (2004).
[35] Z.-G. Ye, Current Opinion in Solid State and Materials Science **6,** 35-44 (2002).
[36] K. Fujishiro, R. Vlokh, Y. Uesu, Y. Yamada, J.-M. Kiat, B. Dkhil, and Y. Yamashita, Jpn. J. Appl. Phys. Pt. 1 **37,** 5246-5248 (1998).
[37] V. A. Shuvaeva, A. M. Glazer, and D. Zekria, J. Phys.: Condens. Matter **17,** 5709-5723 (2005).
[38] Z.-G. Ye and M. Dong, J. Appl. Phys. **87,** 2312-2319 (2000).
[39] B. Noheda, Current Opinion in Solid State and Materials Science **6,** 27-34 (2002).
[40] G. Xu, H. Luo, H. Xu, and Y. Yin, Phys. Rev. B **64,** 020102(R) (2001).
[41] M. Iwata, T. Araki, M. Maeda, I. Suzuki, H. Ohwa, N. Yasuda, H. Orihara, and Y. Ishibashi, Jpn. J. Appl. Phys. Pt. 1 **11B,** 7003-7006 (2002).
[42] J. Han and W. Cao, Appl. Phys. Lett. **83,** 2040-2042 (2003).
[43] J. Yin and W. Cao, J. Appl. Phys. **92,** 444-448 (2002).
[44] J. Erhart and W. Cao, J. Appl. Phys. **86,** 1073-1081 (1999).
[45] J. Yin and W. Cao, J. Appl. Phys. **87,** 7438-7441 (2000).
[46] J. Erhart and W. Cao, J. Appl. Phys. **94,** 3436-3445 (2003).
[47] K. Nakamura, T. Tokiwa, and Y. Kawamura, J. Appl. Phys. **91,** 9272-9276 (2002).
[48] S. Wada, K. Muraoka, H. Kakemoto, T. Tsurumi, and H. Kumagai, Jpn. J. Appl. Phys. Part 1 **43,** 6692-6700 (2004).
[49] S. Wada, K. Yako, H. Kakemoto, T. Tsurumi, and T. Kiguchi, J. Appl. Phys. **98,** 014109 (2005).
[50] Samples of barium titanate were kindly supplied by Dr. Daniel Ritz of FEE, Idar Oberstein, Germany.

[51] Interestingly, this fine domain structure tended to coarsen with time at room temperature. After a few weeks the same sample became nearly monodomain.

[52] S. Wada, S.-E. Park, L. E. Cross, and T. R. Shrout, Ferroelectrics **221,** 147-155 (1999).

[53] D.-S. Paik, S.-E. Park, S. Wada, S.-F. Liu, and T. R. Shrout, J. Appl. Phys. **85,** 1080-1083 (1999).

Chapter six

Dielectric, ferroelectric and pyroelectric characterization

In this chapter, the dielectric, pyroelectric and ferroelectric properties of PMN-xPT and PZN-xPT with MPB compositions are presented. Firstly, the smooth transition between short-range ordered, *relaxor* behavior and long-range ordered, *ferroelectric* behavior upon increasing PT content, as discussed in chapter four, is clearly evidenced in unpoled samples in measurements of permittivity. Secondly, poling of crystals to produce truly long-range ordered, ferroelectric (polar), and thus piezoelectric, phases is discussed. It is noted that poling in different orientations induces differing monoclinic phases. Thus, the concept of "pseudo-rhombohedral" *"R"* and "pseudo-orthorhombic" *"O"* phases is introduced to encompass both the higher symmetry rhombohedral and orthorhombic phases and their "slightly-distorted" monoclinic relatives. Notably, poling in different orientations can affect the phase stabilities of the "R", "O" and tetragonal (T) phases close the MPB; this might be due to the presence of *residual bias fields* in as-poled crystals. Since, $[001]_C$-poled crystals are most technologically useful, it makes sense to draw up phase diagrams for this orientation.

The position of the ("R"/T or "O"/T) phase transition to the tetragonal phase can be determined by measurements of permittivity as a function of temperature. However, the "R"/"O" phase boundary is nearly *vertical* in the temperature vs. composition phase diagram for $[001]_C$-poled PMN-xPT and PZN-xPT such that it is not observed upon heating. Instead, the room temperature phase can be determined, indirectly, by dielectric, pyroelectric and polarization measurements in $[001]_C$-, $[101]_C$ and $[111]_C$-poled samples of a given composition. Notably, ratios between the pyroelectric coefficients and spontaneous polarizations of samples measured in the three orientations can be predicted with some accuracy based on simple *domain average engineering*; this gives validity to the notion of "slightly-distorted" pseudo-rhombohedral and pseudo-orthorhombic" phases.

Usefully large pyroelectric coefficients (< 1070 $\mu Cm^{-2}K^{-1}$) are reported for $[111]_C$-poled PMN-28PT. Finally, it is shown that a "R" phase can be induced *metastably* in otherwise pseudo-orthorhombic PZN-8PT by poling along the $[111]_C$ direction at sub-zero temperatures.

I. INTRODUCTION

As discussed in chapter one, the morphotropic phase boundaries in PMN-xPT and PZN-xPT were original assumed to be similar to that in PZT[1], i.e. steep first-order boundaries separating low PT-content *3m* rhombohedral and high PT-content *4mm* tetragonal phases. Phase diagrams showing them as such can be seen in the early publications of Nomura and coworkers (PZN-xPT)[2,3] and Shrout and coworkers (PMN-xPT)[4,5]; original phase diagrams derived from dielectric measurements on $[001]_C$-oriented single crystals are reproduced in figure 1.

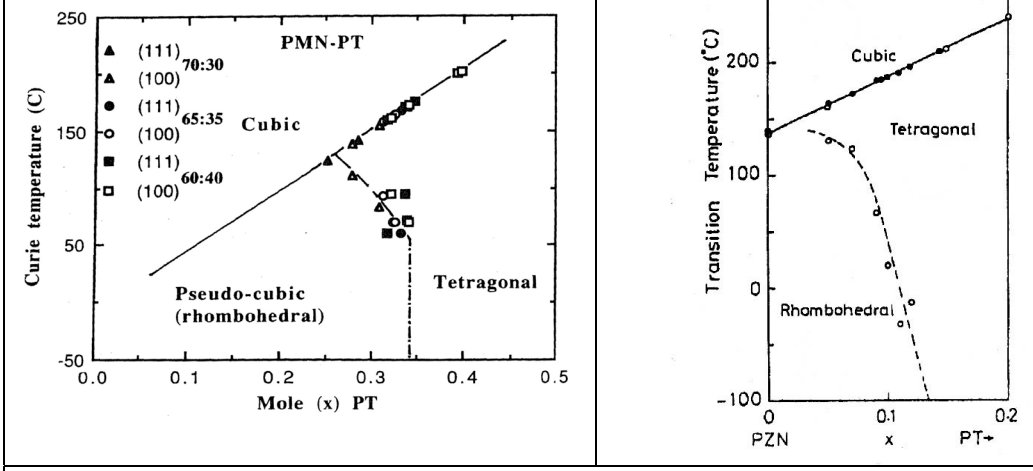

Fig. 1. Original phased diagrams showing the position of the MPB in PMN-xPT (left) and PZN-xPT (right) single crystals taken from Kuwata et al. (1981)[2] and Shrout et al. (1990)[5], respectively. The transition temperatures plotted are taken from dielectric measurement on $[001]_C$-oriented crystals.

Notably, when these phase diagrams were published, monoclinic or orthorhombic phases had not yet been discovered at the MPB. This is for two main reasons. Firstly, it is very difficult to resolve lower symmetry monoclinic phases from higher symmetry rhombohedral and orthorhombic phases with conventional X-ray techniques. Secondly, for $[001]_C$-oriented crystals, the transitions from the rhombohedral, orthorhombic or monoclinic phases to the higher-temperature, tetragonal phase look identical in measurements of permittivity as a function of temperature. This will be shown in section II.

Thus, it was only after the M_A monoclinic phase had been discovered at the MPB in PZT, and higher resolution (synchrotron X-ray and neutron) diffraction methods were applied to the PZN-xPT and PMN-xPT systems, that new MPB phases were found.

New phases at the MPB in PMN-xPT and PZN-xPT

Whereas the ferroelectric phase found between rhombohedral and tetragonal phases in PZT was monoclinic M_A, the first "MPB phases" to be found in PMN-xPT and PZN-xPT were monoclinic M_C and orthorhombic, respectively[6-10]. As noted in chapter one, M_A (and M_B) phases were later found at lower PT contents[11-13] between rhombohedral and M_C phase fields.

In the three "classical" ferroelectric phases of barium titanate[1,14], *3m* rhombohedral (R), *mm2* orthorhombic (O) and *4mm* tetragonal (T), the spontaneous polarization vector $\boldsymbol{P_S}$ is fixed along the high symmetry, polar axis of the unit cell, i.e., along $<111>_C$, $<101>_C$ and $<001>_C$, respectively (see figure 2). As discussed in chapter one, however, the polar vectors of the two monoclinic planes (point group *m*) are not fixed. Instead, they are constrained to lie in the remaining mirror plane but are otherwise free to *rotate*[15] within it.

In the M_C phase[16] (space group *Cm*) the remaining symmetry element is a $\{010\}_C$ mirror plane and hence the polarization vector can rotate anywhere between the O and T limiting directions; this can be seen in figure 2. In the M_A phase[16] (space group *Pm*), the remaining element is a dodecahedral $\{1\bar{1}0\}_C$ plane and the polar vector is instead constrained to lie between R and T limiting directions. A third monoclinic phase "M_B" is also defined[16]. It is identical to the M_A phase (*Pm*) in space group but is used to describe the case where the polarization vector lies between R and O limiting directions (rather than R and T), as shown in figure 2.

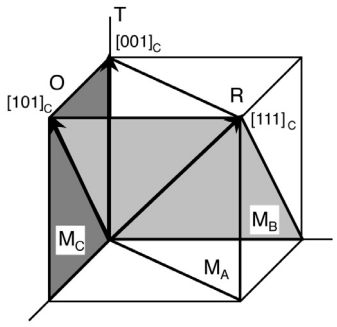

Fig. 2. The spontaneous polarization vectors of the rhombohedral (R), orthorhombic (O), and tetragonal (T) phases occurring in perovskite ferroelectrics with respect to the pseudocubic unit cell. Also shown are the monoclinic $(1\bar{1}0)_C$, $(10\bar{1})_C$ and $(010)_C$ mirror planes of the M_A, M_B and M_C phases, observed in PMN-xPT and PZN-xPT, in which their polarization vectors are constrained to lie. The labels M_A and M_B shown here are only valid for rotations between the three limiting directions shown.

"Pseudo-rhombohedral" and "pseudo-orthorhombic" phases

In the room temperature, ferroelectric M_C phases evidenced by high-resolution X-ray powder diffraction in unpoled ceramic samples of PMN-31PT, PMN-33PT and PMN-35PT[6], the polar vector $\boldsymbol{P_S}$ is only *slightly* rotated away from the $[101]_C$ orthorhombic limiting direction. The a_M and c_M lattice parameters of the *Pm* monoclinic phases differ by between only 0.2 and 0.4%, respectively, for the three compositions listed above (although this difference was found to be larger at lower temperatures[6]). Therefore, the room temperature M_C phase might be considered only a *slightly distorted orthorhombic phase*; indeed, the observed O phase is the limiting case of M_C (where $a_M = c_M$)[8]. Importantly, the lattice parameters suggest that the polar vector is rotated, within the $(010)_C$ monoclinic plane, by less than 1° from the $[101]_C$ direction.

In the M_C monoclinic phase discovered at very low temperature (35 K) in unpoled PZN-9PT by powder neutron diffraction[17], derived atomic shifts suggest the polar vector is close to $[304]_C$. This corresponds to a rotation of around 8° from the $[101]_C$ direction. Moreover, as discussed in chapter five, the rotation of the polar vector in the M_C phase will result in rotated angles of extinction in PLM. In the M_C monoclinic phase evidenced in $[001]_C$-oriented, unpoled PMN-33PT single crystals by Bokov and Ye (2004)[18], the angle of extinction was only around 3° away from the position expected for an orthorhombic phase. In chapter five, a deviation in extinction angle of around 5° was observed in room temperature PMN-33PT.

In all of these cases we might refer to the M_C phase, where the polar vector is rotated by only a small angle away from the orthorhombic limiting direction, as "pseudo-orthorhombic". Of course, as can be seen in figure 2, this will not be valid where it becomes "pseudo-tetragonal" in its other limit.

Following the discovery of pseudo-orthorhombic phases, high resolution X-ray diffraction[11,12] and polarized light microscopy[19] studies also evidenced a *Cm* monoclinic phase at the MPB in PZN-xPT and PMN-xPT. Importantly, the observed M_A (or M_B) monoclinic phases were only slightly distorted versions of the rhombohedral phase; PLM evidenced polar vector rotations of around 3° in room temperature PMN-xPT[19]. Thus, the observed phases, where the polar vector is only slightly rotated away from the rhombohedral limiting direction, might be described as "pseudo-rhombohedral".

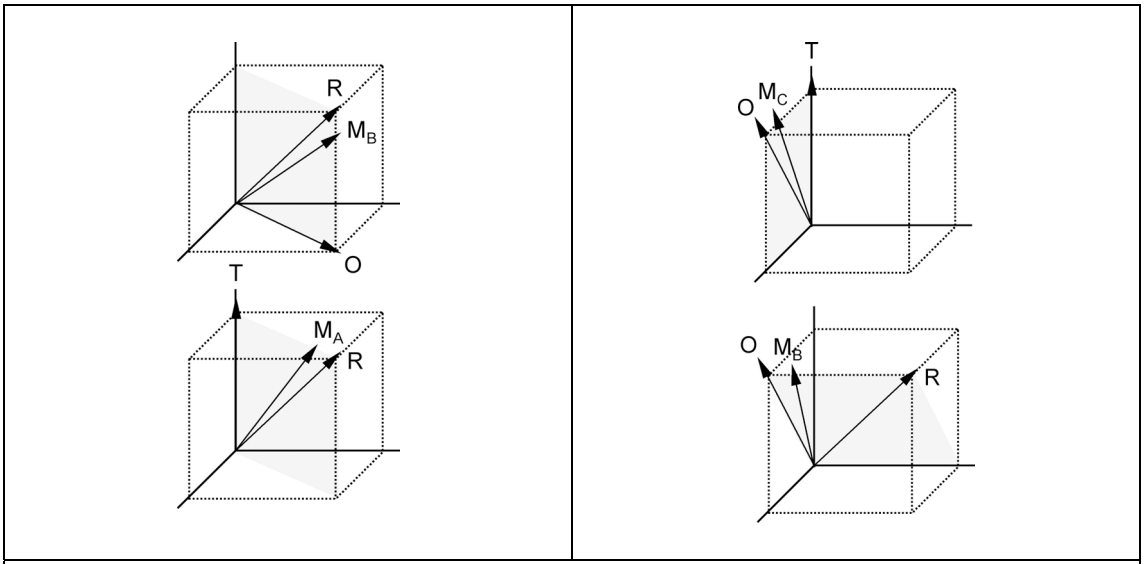

Fig. 3. (Left) Direction of the polar vector in the R, M_A and M_B "pseudo-rhombohedral" phases with respect to the pseudocubic unit cell. The rotations of the polar vector away from the $[111]_C$ direction are exaggerated. (Right) Polar vectors of the O, M_C and M_B "pseudo-orthorhombic" phases.

From now on, "pseudo-orthorhombic" (or "O") will be used to mean either orthorhombic or monoclinic, wherever the polar vector is rotated by a small amount away from a $<101>_C$ limiting direction. As shown in figure 3, pseudo-orthorhombic can thus refer to both M_B and M_C monoclinic phases. Likewise, "pseudo-rhombohedral" (or "R") will be used to mean rhombohedral or monoclinic, where the polar vector is rotated by a small amount from a

<111>$_C$ limiting direction. Both M_A and M_B phases can be pseudo-rhombohedral (see figure 3).

Using this terminology we could summarize all the recent high-resolution diffraction and optical studies as the discovery of a new *ferroelectric, pseudo-orthorhombic phase between pseudo-rhombohedral and tetragonal ferroelectric phases at the MPB in PZN-xPT and PMN-xPT*. Notably, this transition series mirrors the R - O - T transition sequence observed in the classical perovskites, barium titanate and potassium niobate, upon heating[1].

New phase diagrams

The pseudo-orthorhombic phase can be seen in the updated phase diagrams published in 2002 by Noheda, La-Orauttapong and coworkers; these are shown in figure 4. Notably, the phase boundaries partitioning the tetragonal phase field have not moved from figure 1. In contrast to the original diagrams, however, the original rhombohedral phases field are now split into pseudo-rhombohedral ("R") and pseudo-orthorhombic ("O") phases by a new, *nearly-vertical* phase boundary. The new phase diagrams not only show phase transitions between (pseudo-) rhombohedral and tetragonal, ferroelectric phases, but between these phases and a pseudo-orthorhombic phase as well.

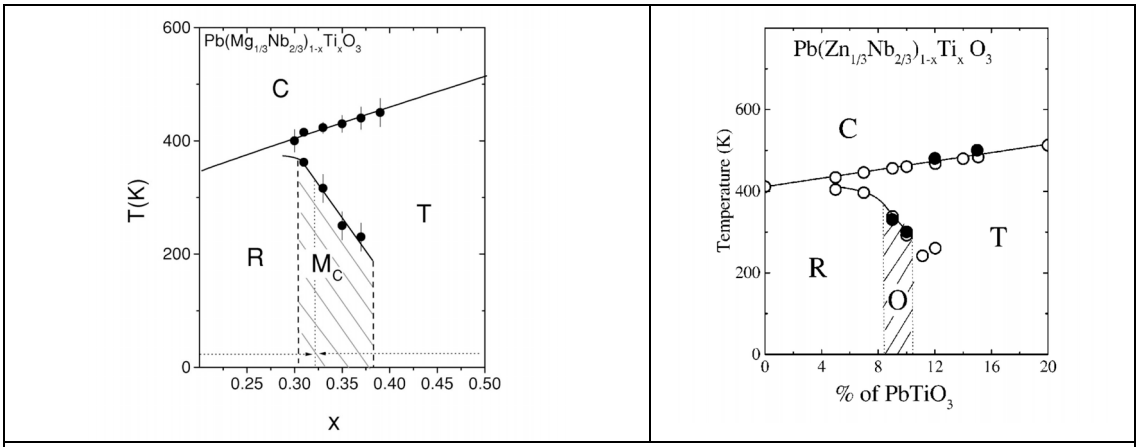

Fig. 4. Recently updated phase diagrams for relaxor-ferroelectric PMN-xPT (left) and PZN-xPT (right), taken from Noheda et al. (2002)[6] and La-Orauttapong et al. (2002)[7], respectively. For PMN-xPT the phase transition temperatures plotted are derived from high-resolution X-ray diffraction studies of unpoled ceramic samples. For PZN-xPT, the data is taken from synchrotron X-ray studies of $[001]_C$-poled crystals.

The steepness of the "R"/"O" boundary is perhaps the reason why the pseudo-orthorhombic phase was left undiscovered for so long. Importantly, it might be too steep to be measured accurately, rising as it does within a very small width (Δx < 1 mol.%), due to the problems of compositional uncertainty outlined in chapter four. Further complications in producing more definitive phase diagrams for PZN-xPT and PMN-xPT include the following.

Firstly, all boundaries between the "O", "R" and T phases are *first order*, as will be discussed further in chapter seven. As such, the three phases can coexist (metastably) with one another over a finite range of

compositions. Such heterophase coexistence is commonly observed by PLM in unpoled crystals (chapter five). It has also been evidenced by X-ray diffraction[6,11] where coexistence is found to extend over large ranges of composition (1-2 mol.%). Thus, especially in unpoled crystals, precise determination of the phase boundary will be difficult. The problem is exacerbated by compositional heterogeneity.

Secondly, and perhaps most importantly, unpoled, low PT-content samples (perhaps up to and including PZN-8PT[10]) of PMN-xPT and PZN-xPT are pseudocubic; as discussed in chapter four, they have only short-range order characteristic of the relaxor state. They require poling to induce a long-range ordered ferroelectric phase. This will have consequences when drawing up phase diagrams for PMN-xPT and PZN-xPT.

Phase diagrams for poled PMN-xPT and PZN-xPT

Ideally, one would plot a temperature vs. composition (*T*-*x*) phase diagram showing the *lowest energy, stable phase at a given temperature or composition for a perfect, unpoled single crystal under zero mechanical or electrical bias*. However, such a diagram would not be technologically useful for PMN-xPT and PZN-xPT: first of all, the unpoled phase can be short-range ordered and therefore not ferroelectric; secondly, piezoelectricity is only shown by the poled (polar), ferroelectric state. In chapter four, we drew up phase diagrams that described the relaxor to ferroelectric phase transition in *unpoled* PMN-xPT and PZN-xPT. For application of these materials, a more useful phase diagram will contain information about the ferroelectric phases in *poled* samples.

Unfortunately, drawing phase diagrams for poled PMN-xPT and PZN-xPT crystals is non-trivial. Notably, it has been shown that *different monoclinic phases can be induced by poling PMN-xPT and PZN-xPT in different directions*[20,21]. For example, in $[001]_C$-oriented PMN-30PT poling by field cooling results in a room temperature M_A phase[21]. In contrast, field cooling of $[101]_C$-oriented PMN-30PT results in M_B symmetry[20]. However, in both cases the phase is pseudo-rhombohedral. Thus, we can simplify the problem by drawing up phase diagrams considering three *poled, zero-field phases* of PMN-xPT and PZN-xPT: that is, pseudo-rhombohedral ("R"), pseudo-orthorhombic ("O") and tetragonal (T). We define "poled, zero-field phase" as the phase present at a given temperature, for a given composition, under zero electrical field or mechanical stress in the as-poled condition.

However, as will be shown in this chapter, which of the "R", "O" or T phases is present at a given temperature can depend on the thermal and electrical parameters of the poling protocol used and, importantly, the direction of poling. Poling in different directions does have a remnant effect on the relative stabilities of each phase with changing temperature. Thus, we should in fact specify both the poling direction and the poling protocol used when drawing up a phase diagram for PMN-xPT and PZN-xPT single crystals. Since $[001]_C$-orientated crystals show the highest piezoelectric properties, it perhaps makes sense to construct phase diagrams showing the zero-field phase for *$[001]_C$-poled crystals*.

Determining the zero-field phase

High resolution, X-ray or neutron, diffraction provides an accurate way of determining the zero-field phases of PMN-xPT and PZN-xPT and the phase transitions between them; it was used to derive the phase diagrams shown in figure 4. However, the method is time consuming and hence only applicable for a small number of samples; moreover, it can only yield a volume-averaged lattice structure due to a finite beam size[22,23]. In contrast, polarized light microscopy can be used to spatially resolve coexisting phases, including monoclinic phases, especially in unpoled samples. Unfortunately, as discussed in chapter five, rhombohedral, tetragonal, orthorhombic and monoclinic phases cannot always be resolved in certain crystal orientations.

However, the poled, zero-field phase present in PZN-xPT and PMN-xPT at a given temperature can often be determined by bulk, electrical characterization of electroded samples: that is, by measurement of their dielectric, pyroelectric and ferroelectric properties. Although, monoclinic phases cannot be resolved in this way, pseudo-rhombohedral, pseudo-orthorhombic and tetragonal phases can generally be distinguished. This will be shown in the rest of the chapter.

II. DIELECTRIC CHARACTERIZATION

The measurement of the low frequency (unclamped[1]) dielectric constant ε and loss tangent ($D = \tan\delta$) over a range of temperatures is an important way of characterizing the phase transitions that occur in ferroelectric materials[1]. For example, as discussed in chapter four, a sharp discontinuity in permittivity is observed at the Curie temperature in the simple perovskite ferroelectric, barium titanate; moreover, anomalies in dielectric constant are also observed at ferroelectric-ferroelectric (FE-FE) phase transitions between the R, O and T phases. Indeed, the phase diagrams shown in figure 1 were derived from dielectric measurements.

Experimental

Dielectric constants and loss tangents were measured using an impedance analyzer, as described in chapter two. First, $[111]_C$-, $[101]_C$- and $[001]_C$-oriented crystals were prepared as described in chapter three. Samples of nominal size 5 x 5 x 0.5 mm^2 were cut from as-supplied plate samples and electroded with gold. Then, measurements of permittivity were made between 5°C and 200°C, at a heating or cooling rate of 2°C/min and at frequencies between 0.1 and 100 kHz, in both virgin and poled conditions.

Nominal sample compositions (see table II, chapter three) were checked by comparison of the dielectric data with the lines of best fit derived in chapter four (equations [10] and [11]); the depolarization temperature T_d was used where possible. For many samples, the back-calculated composition was found to be around 0.5 mol.% lower than the nominal value. However, for certain crystals much larger discrepancies were found.

Fortunately, however, this did mean that a greater range of compositions (from as low as 24 mol.% PT in PMN-xPT) could be characterized.

Virgin samples

The relative permittivities and loss tangents of unpoled, virgin samples of PMN-xPT and PZN-xPT, as a function of temperature, are shown in figures 5 to 8. The unpoled crystals are macroscopically cubic (*m3m*)[24]; that is, they are either short-range ordered (chapter four) or with a relative domain size (< 100 μm) much smaller than the dimensions of the sample. They will thus be dielectrically isotropic[25]; therefore, the crystallographic orientations of the samples are irrelevant and are not specified.

The "relaxor to ferroelectric" phase transition discussed in chapter four is evident. It is marked by a transition from a broad "Curie range", characteristic of *relaxor-ferroelectric* PMN and PZN, to a sharper dielectric anomaly at higher PT contents, as observed in *ferroelectric* lead titanate. The same trend has been shown elsewhere[4,26-28].

In all compositions, upon both heating and cooling, the peak permittivity (T_m, ε_m) is frequency dependent (figures 5 and 7). Upon heating, a "shoulder" in the permittivity corresponding to the depoling temperature (T_d^{heat}) is clearly seen in all compositions; it is the temperature above which frequency-dispersion is observed. The convergence of T_m and T_d at higher PT contents is also evident.

Interestingly, upon cooling, the dielectric shoulder expected at T_d^{cool}, corresponding to the "relaxor to ferroelectric" transition, is not generally observed except in higher PT-content samples (PZN-6.7PT and PZN-7.9PT in figure 7). Instead, for low PT-content samples, the frequency dispersion converges smoothly at temperatures much lower than T_m; this suggests a large thermal hysteresis ΔT_d. Similar features can be observed in the dielectric loss (figures 6 and 8).

For higher PT-content crystals a third anomaly is also observed in the permittivity and loss: see PMN-28PT and PMN-30PT (figures 5 and 6), and PZN-6.7PT and PZN-7.9PT (figures 7 and 8). These can be identified as (FE-FE) phase transitions between long-range ordered ferroelectric phases. According to the phase diagrams in figure 1, the high temperature phase is surely tetragonal.

In each case the transition is characterized by another "shoulder" in permittivity at a temperature T_{FE-FE}. For PZN-6.7PT and PZN-7.9PT (fig. 7), the transition is accompanied by significant thermal hysteresis ($\Delta T_{FE-FE} = T_{FE-FE}^{heat} - T_{FE-FE}^{cool}$) as expected for a first order phase transition. For PZN-7.9PT the thermal hysteresis $\Delta T_{FE-FE} \approx 25°C$.

Noticeably, however, the transition only occurs upon cooling where the transition to a long-range ordered FE phase (at T_d^{cool}) has already occurred; notably, T_d^{cool} shoulders are evident in PZN-6.7PT and PZN-7.9PT at

temperatures above T_{FE-FE}^{cool} (see fig. 7). If not, the short-range ordered phase persists down to low temperatures where the low-temperature ferroelectric phase eventually forms at T_d^{cool}. This is the case for PMN-28PT and PMN-30PT (fig. 5), and PZN-4.5PT (fig. 7). Seemingly, there is a complex superposition of both *relaxor-ferroelectric* and *ferroelectric-ferroelectric* transitions in unpoled PMN-xPT and PZN-xPT. The latter, necessarily, presupposes the former.

Finally, the variation of the permittivity above T_m in PMN-xPT and PZN-xPT has been shown to follow the empirical formula[29,30]:

$$\frac{1}{\varepsilon} = \frac{1}{\varepsilon_m} + \frac{(T - T_m)^{\gamma}}{C'} \qquad [1]$$

where C' is a constant and γ is the "diffusiveness exponent[29]". As noted in chapter four, for $\gamma = 2$ the equation becomes the Smolenskii description of relaxor-ferroelectrics; in contrast, Curie-Weiss behavior[14,31] is approached as γ approaches unity.

Both coefficients can be obtained using a suitable double logarithmic plot. This is shown in figure 9 for samples of PZN-4.5PT and PZN-7.9PT. In both cases, the dielectric data taken from figure 7 was found to fit the equation well for temperatures at least 10°C higher than T_m. Notably, this empirical formula breaks down very close to the dielectric maximum.

For PZN-4.5PT, a value of $\delta = 1.7$ was obtained whereas the fit gave $\delta = 1.5$ for PZN-7.9PT. There is indeed a trend for decreasing "diffusiveness" with increasing PT content, as might be expected for the gradual transition from relaxor-ferroelectric to ferroelectric behavior.

Lastly, we note that the variation of permittivity with temperature in PZN-7.9PT (fig. 7) looks very similar to that observed in unpoled, ceramic barium titanate[1]; this follows from the dielectric *isotropy* of their *m3m* cubic macroscopic symmetry. In contrast, poled crystals will show much different dielectric anomalies as a general result of their resultant *crystal anisotropy*. This is discussed below.

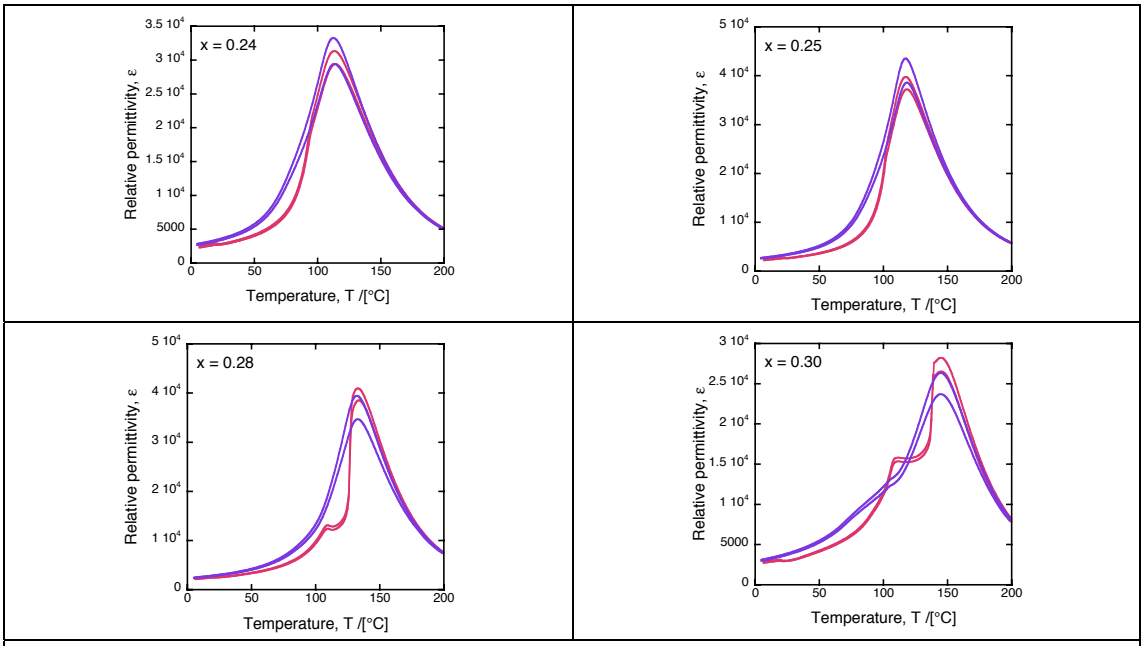

Fig. 5. Dielectric constant as a function of temperature for samples of unpoled PMN-xPT (24, 25, 28 and 30 mol. %) upon heating and cooling at 2°C/min. The darker curves correspond to cooling runs. Measurements were taken at both 0.1 and 1 kHz. A higher frequency gives a lower dielectric response.

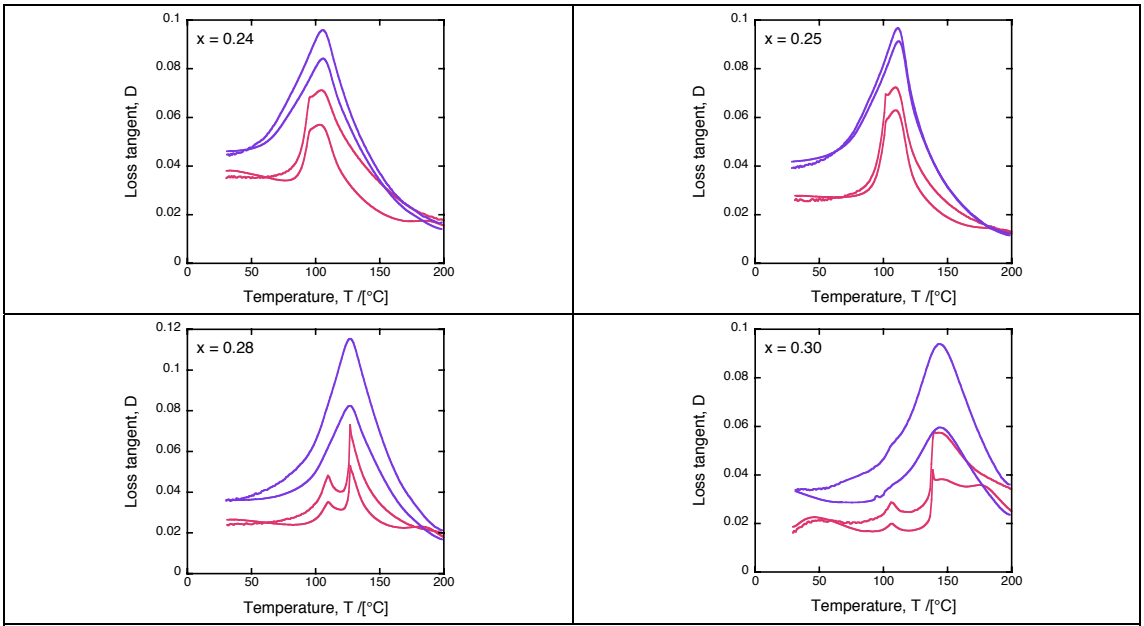

Fig. 6. Dielectric loss tangent as a function of temperature for samples of unpoled PMN-xPT (24, 25, 28 and 30 mol. %) upon heating and cooling at 2°C/min. The darker curves correspond to cooling runs. Measurements were taken at both 0.1 and 1 kHz. A higher frequency generally gives a lower dielectric loss.

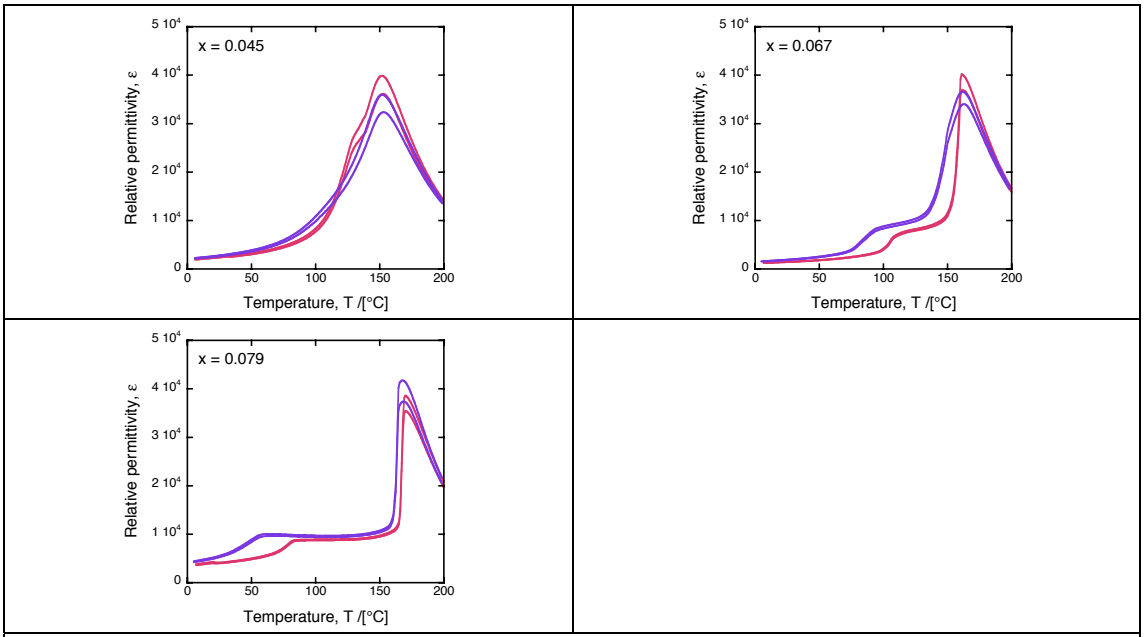

Fig. 7. Dielectric constant as a function of temperature for samples of unpoled PZN-xPT (4.5, 6.7 and 7.9 mol.%) upon heating and cooling at 2°C/min. The darker curves correspond to cooling runs. Measurements were taken at both 0.1 and 1 kHz. A higher frequency gives a lower dielectric response.

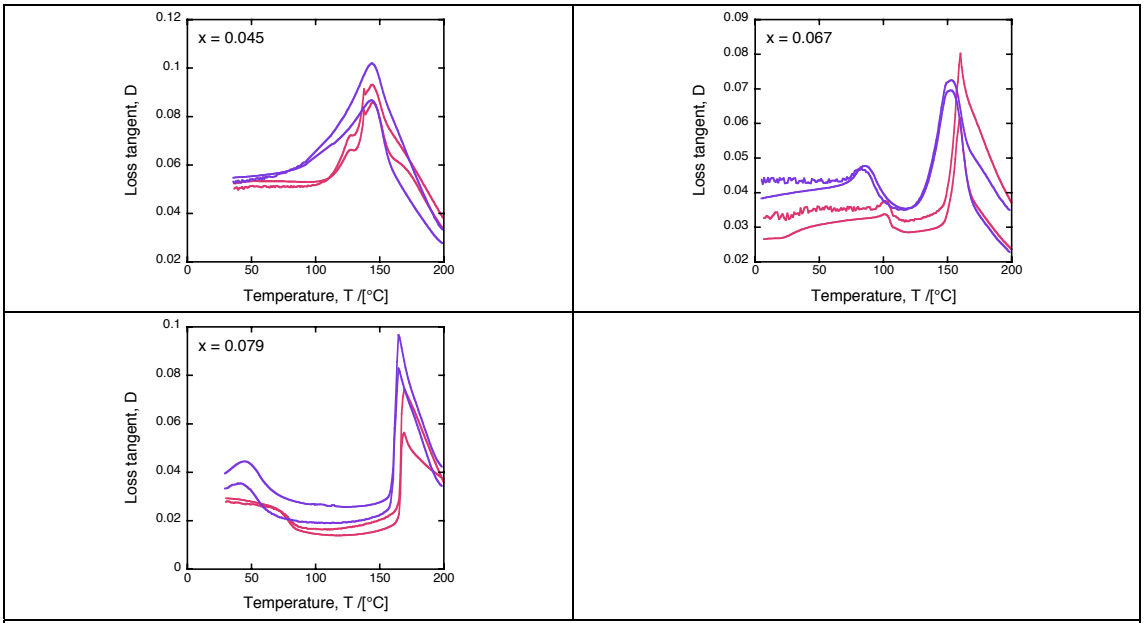

Fig. 8. Dielectric loss tangent as a function of temperature for samples of unpoled PZN-xPT (4.5, 6.7 and 7.9 mol.%) upon heating and cooling at 2°C/min. The darker curves correspond to cooling runs. Measurements were taken at both 0.1 and 1 kHz. A higher frequency generally gives a lower dielectric loss.

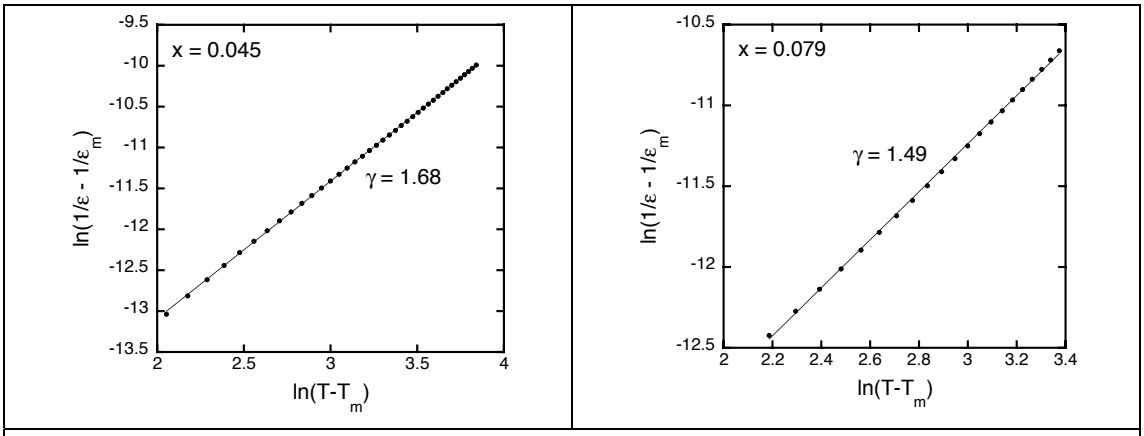

Fig. 9. Derivation of the ("diffusiveness") exponent δ of equation [1] using high temperature dielectric data taken from figure 7 for unpoled PZN-xPT (at 1 kHz): (left) PZN-4.5PT and (right) PZN-7.9PT.

Dielectric anisotropy in poled crystals

Whereas the dielectric constant of an unpoled ceramic will be isotropic, the permittivity ε_{33}* (defined by $D_3 = \varepsilon_0 \varepsilon_{33}{}^* E_3$)[25] for a monodomain single crystal will generally be a strong function of orientation; the asterisk "*" is used to imply measurement in an arbitrary, *non-polar* direction. For ferroelectric perovskites, like $BaTiO_3$ and $KNbO_3$, the relative permittivity measured along the polar axis is generally smaller than that measured away from to it (i.e. $\varepsilon_{33} < \varepsilon_{33}{}^*$) and is generally largest perpendicular to the polar axis[1]. This is a consequence of their inherent *crystal anisotropy*, the origins of which will be discussed in chapter ten. Importantly, the same will be true of the "R", "O" and T phases of PMN-xPT and PZN-xPT; thus, we can use such dielectric anisotropy to distinguish "R", "O" and T phases in *poled* PMN-xPT and PZN-xPT single crystals.

As shown in chapter five (figure 1), when "R", "O" or T phases are poled along $<001>_C$, $<101>_C$ or $<111>_C$ directions, three *monodomain* and six *domain-engineered* states result. From now on, we will refer to the three monodomain states as "1R", "1O" and "1T". This is because truly monodomain 1R, 1O and 1T states are often unstable, especially in PMN-xPT and PZN-xPT[32,33] where a degree of back-switching can generally be expected upon removal of the poling field. Importantly, the permittivity of $[001]_C$-poled "1T", $[101]_C$-poled "1O" and $[111]_C$-poled "1R" samples (measured necessarily along the poling direction) will be characteristically small.

However, the permittivity of *domain-engineered* "R", "O" or T crystals, measured along the poling direction, is expected to be much larger than that of *monodomain* "1R", "1O" and "1T" samples, respectively. Ignoring for now any extrinsic contribution from the domain structure itself[34], and therefore assuming "domain average engineering" (see chapter five), the relative

permittivity ε_{33}* of domain-engineered crystals will be determined solely by the anisotropy of the individual domain variants it contains. This is shown schematically for the case of a 4R structure in figure 10. As stated in chapter five, the polar vectors in a domain engineered crystal will be inclined to the poling direction by the same angle, θ. The closer this angle is to 90°, the larger the permittivity is expected to be.

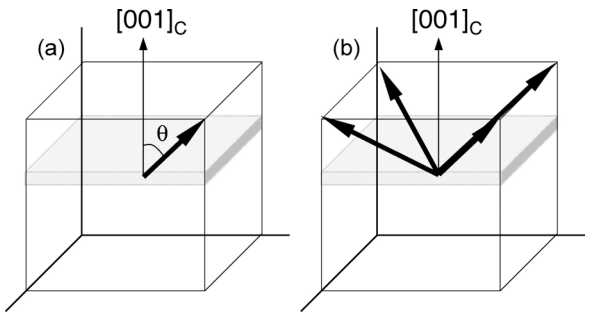

Fig. 10. (a) The relative permittivity of a rhombohedral crystal measured along the $[001]_C$ direction is expected to be higher than that along its $[111]_C$ polar axis as a consequence of crystalline anisotropy. The permittivity measured along the $[001]_C$ poling direction of a 4R domain-engineered crystal (b) will also be high, as a consequence of the anisotropy of its four domain variants. Where "domain average engineering" applies, the same permittivity will be measured along the $[001]_C$ direction in both (a) and (b).

From now on, "4R" will be used to mean either the true 4R structure *or* a slightly-distorted structure derived from pseudo-rhombohedral domain variants; this will include the $4M_A$ structure shown in figure 6 of chapter 5. Likewise, "4O" will include the $4M_C$ domain-engineered structure. Similar notation is used to generalize all six domain-engineered structures listed in chapter five.

Poling protocols

Ferroelectrics can be poled in a variety of ways. Two main poling regimes are generally used for PMN-*x*PT and PZN-*x*PT single crystals. The most widely used choice, "static field" (SF) poling[35-37], involves the application of a high field (usually 1000-2000 V/mm) at room temperature for a period of 10 minutes to one hour. Another popular poling protocol is "high temperature field cooling" (HTFC) whereby the sample is cooled from the paraelectric phase to room temperature, usually under a smaller field (200-1000 V/mm)[35,38,39]. Although the use of lower fields is advantageous, cooling down from the Curie temperature might lead to unwanted high temperature phases in the poled crystal, especially for compositions close to the morphotropic phase boundary. To help promote only the lowest temperature, rhombohedral phase another method can be used, the here-named "low temperature field heating" (LTFH), in which the sample is heated from sub-zero temperatures to room temperature under field. For this thesis work, all three poling protocols

were used at different times; in most, but not all cases, they induce the same zero-field phase at room temperature.

After poling, samples were left to "age[1]" for at least 24 hours before measurement.

$[001]_C$-poled samples

Permittivity as a function of temperature upon heating for two $[001]_C$-poled samples of PMN-xPT (x = 0.29, 0.33) and two $[001]_C$-poled samples of PZN-xPT (x = 0.048, 0.081) is shown in figure 11. The dielectric losses are shown in figure 12. Anomalies are clearly evident at T_m and T_d^{heat} for the low PT-content samples (PMN-29PT and PZN-4.8PT); sharper peaks characteristic of a Curie-Weiss transition can be observed in higher PT-content samples (PMN-33PT and PZN-8.1PT) at "T_C". Lower temperature anomalies are indicative of phase transitions between ferroelectric phases (at T_{FE-FE}^{heat}). The samples were poled by HTFC poling under a field of 200 V/mm.

Although not shown in figures 11 and 12, a smooth transition between the behaviors of PMN-29PT and PZN-4.8PT, and PMN-33PT and PZN-8.1PT was observed for intermediate compositions. With increasing PT content, the "shoulder" (PMN-29PT) or peak (PZN-4.8PT) at T_d^{heat} and the dielectric peak at T_m converged to sharp phase transitions at a true T_C in PMN-33PT and PZN-8.1PT. Similar trends have been shown elsewhere[4,26,28,30,40].

As shown in figure 12, the losses were found to be low being generally less than 0.01 at room temperature. The kink observed close to the Curie temperature T_C in PMN-33PT [fig. 11(left)], also apparent as a double peak in the loss tangent (fig. 12), is probably a consequence of a sharp compositional heterogeneity, as discussed elsewhere[41].

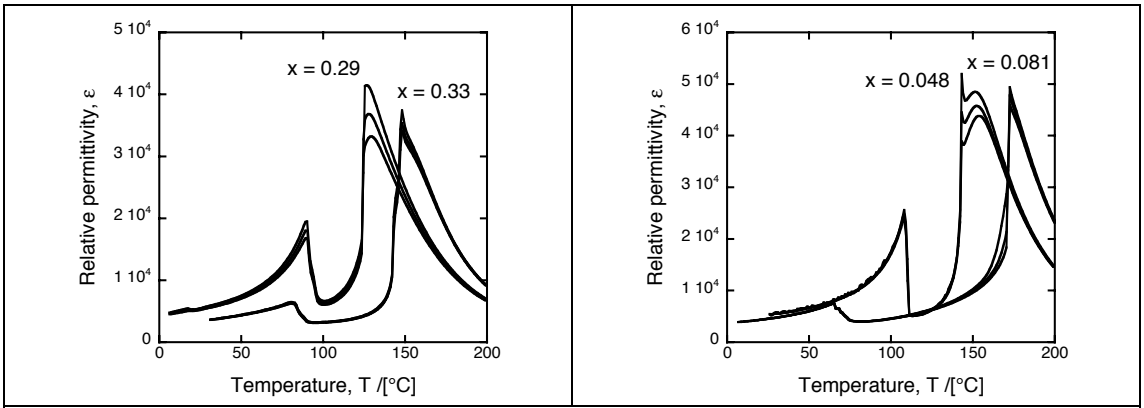

Fig. 11. (Left) Dielectric constant measured upon heating in HTFC-poled, $[001]_C$-oriented samples of PMN-xPT (x = 0.29 and 0.33). (Right) Dielectric constant measured upon heating in HTFC-poled, $[001]_C$-oriented samples of PZN-xPT (x = 0.048 and 0.081). The measurements were made at frequencies of 0.1, 1 and 10 kHz; the lowest dielectric response is seen at 10 kHz.

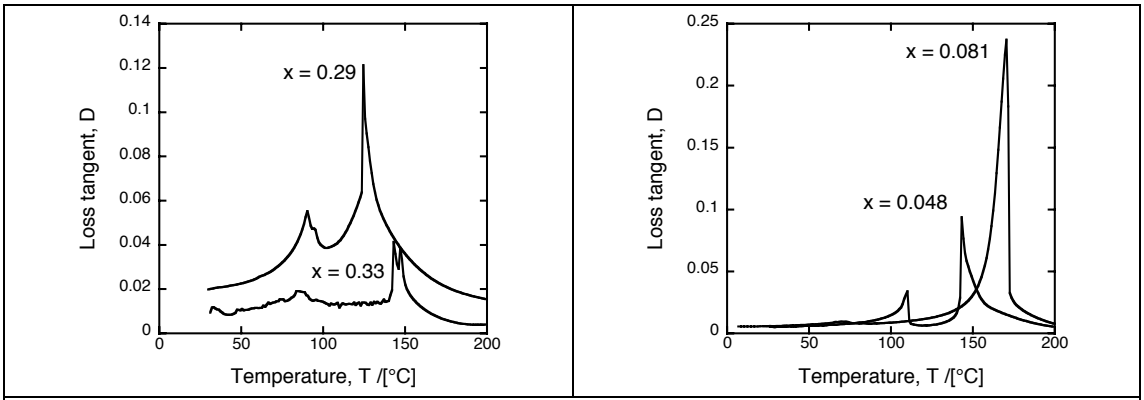

Fig. 12. Dielectric loss tangents measured upon heating in HTFC-poled, $[001]_C$-oriented samples of PMN-xPT (left) and PZN-xPT (right). The measurements were taken at a frequency of 1 kHz.

More interesting is the position of the second dielectric anomaly. According to the phase diagrams shown in figures 1 and 4, we can identify these features as FE-FE phase transitions to the T phase[42]. This transition, at T_{FE-FE}, is characterized by a sharp peak in permittivity followed by a subsequent drop. Assuming, that the crystal does not depole through the transition, which is reasonably to assume since during measurement the crystal is essentially open-circuited, the permittivity above T_{FE-FE} corresponds to that of the "1T" quasi-monodomain state.

According to the updated phase diagrams (figure 4), the permittivity below T_{FE-FE} corresponds to that of a "4R" of "4O" domain-engineered state. It is relatively high at room temperature, varying between 5800 and 3600 for PMN-29PT and PMN-33PT, respectively, and between 5900 and 4700 for PZN-4.8PT and PZN-8.1PT.

Most notably, between the compositions shown in figure 11, there was a smooth variation in the position of the FE-FE phase transition. For both PZN-xPT and PMN-xPT, there was no qualitative change in behavior upon crossing the nearly vertical, "R"/"O" phase boundary shown in figure 4 and no evidence for a "R" to "O" transition in any composition upon heating above room temperature. That is, in $[001]_C$-poled PMN-xPT and PZN-xPT, the "R"/"O" phase boundary does indeed appear to be vertical. The smooth transition in dielectric behavior upon crossing the "R"/"O" boundary in $[001]_C$-poled PMN-xPT and PZN-xPT single crystals (also observed in poled ceramics[4,26]) is one of the reasons why the pseudo-orthorhombic phase went undiscovered for so long.

Finally, in contrast, phase transitions between "R" and "O" phases *are* observed in $[101]_C$- and $[111]_C$-poled crystals; this will be shown next.

Experimentally derived phase diagram

The temperature of the phase transition to the tetragonal phase (T_{FE-FE}) derived from permittivity data for $[001]_C$-poled PMN-xPT and PZN-xPT with a range of compositions (including that shown in figure 11) were overlaid on the phase diagrams of Noheda, La-Orauttapong et al. (fig. 4).

The resultant phase diagrams for PMN-xPT and PZN-xPT are shown in figures 13 and 14, respectively.

There is reasonable correlation between the published transition temperatures, derived from diffraction experiments, and the dielectric data from this thesis work. The experimental scatter is probably a result of compositional uncertainty. As noted, dielectric measurements in $[001]_C$-poled crystals can not be used to confirm the position of the "R"/"O" phase boundary.

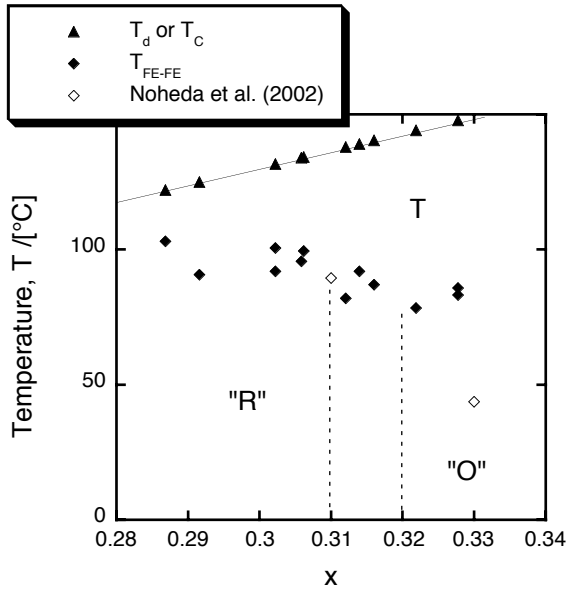

Fig. 13. Updated phase diagram showing the morphotropic phase boundary region in $[001]_C$-poled PMN-xPT. The temperature of the phase transition to a tetragonal phase T_{FE-FE} is plotted based on measurements of dielectric constant in $[001]_C$-poled samples. There is some uncertainty in the position of the "R"/"O" phase boundary.

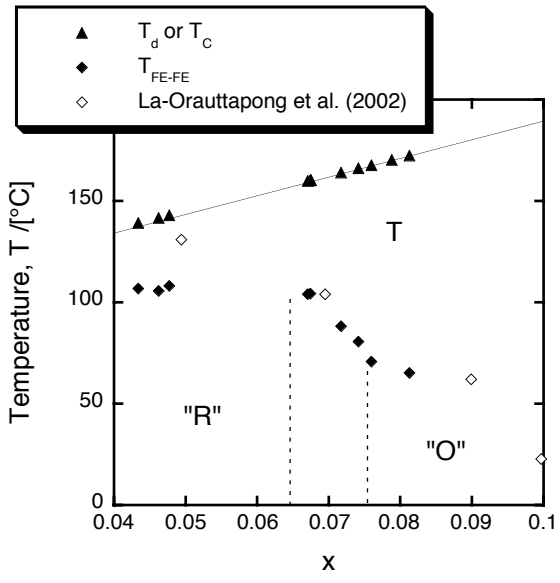

Fig. 14. Updated phase diagram showing the morphotropic phase boundary region in $[001]_C$-poled PZN-xPT. The temperature of the phase transition to a tetragonal phase T_{FE-FE} is plotted based on measurements of dielectric constant in $[001]_C$-poled samples. There is some uncertainty in the position of the "R"/"O" phase boundary.

$[111]_C$- and $[101]_C$-poled samples

As shown in figure 15(left), only one FE-FE transition is evident in $[111]_C$-poled PZN-7.5PT. If we assume a pseudo-orthorhombic phase at room temperature, and that the crystal does not depole at T_{FE-FE}, there is a transition between "3O" and "3T" domain-engineered structures; the large room temperature permittivity ($\varepsilon_{33}^* > 5000$) is indicative of a domain-engineered crystal.

In contrast, $[111]_C$-poled PZN-6.7PT shows two dielectric anomalies below T_d, evidence for *two* FE-FE phase transitions upon heating [fig. 15(right)]. Most importantly, a very small permittivity at low temperatures ($\varepsilon_{33} = 700$ at 30°C) suggests a pseudo-rhombohedral phase poled along its $[111]_C$ polar axis ("1R"). This implies that, in contrast to PZN-7.5PT, $[111]_C$-poled PZN-6.7PT is pseudo-rhombohedral at room temperature. Two sharp discontinuities are then evident upon increasing temperature before the crystal finally depoles at T_d; they can be assigned to successive transitions to two domain-engineered structures, "3O" and "3T".

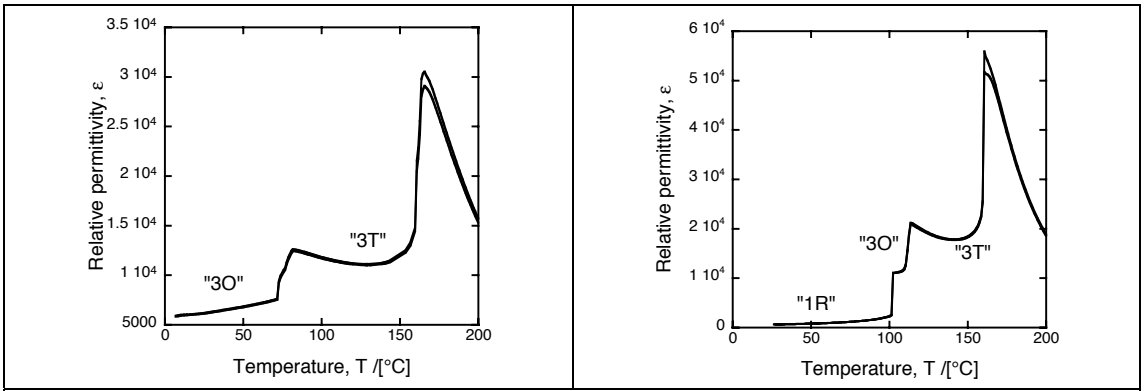

Fig. 15. Dielectric constant measured as a function of temperature in $[111]_C$-poled PZN-7.5PT (left) and PZN-6.7PT (right). Measurements were made at frequencies of 1 and 10 kHz upon heating. Crystals were poled by HTFC at 200 V/mm.

Permittivities of $[101]_C$-poled PZN-7.8PT and PZN-6.8PT as a function of temperature are shown in figure 16. In the case of PZN-7.8PT [fig. 16(left)], there is only evidence for a single FE-FE phase transition. The relatively low permittivity of the lower-temperature phase (1400 at 30°C) suggests a quasi-monodomain, pseudo-orthorhombic phase poled along its polar axis ("1O"). That is, $[101]_C$-poled PZN-7.8PT is "O" at room temperature. Notably, the permittivity of the higher-temperature, domain-engineered ("2T") phase is much higher ($\varepsilon_{33}^* > 10600$). Similar behavior has been reported in dielectric measurements of $[101]_C$-poled PZN-8PT[43], PMN-34PT[44] and PMN-35PT[44] suggesting that these compositions too are "O", at room temperature, in the $[101]_C$-poled condition.

In contrast, in $[101]_C$-poled PZN-6.7PT [fig. 16(right)], *two* FE-FE phase transitions are evident below T_d. A relatively low permittivity at intermediate temperatures ($\varepsilon_{33}^* = 1600$ at 80°C) is evidence of a $[101]_C$-oriented, "1O" state bounded by a low temperature, domain-engineered, pseudo-

rhombohedral state ("2R") and a domain-engineered, tetragonal phase ("2T"). Similar dielectric behavior has been observed in $[101]_C$-poled PMN-31PT[45], PMN-29.5PT[44] and PMN-30PT[44], suggesting that for all these compositions the zero-field, room temperature phase is "R", at least in the $[101]_C$-poled condition.

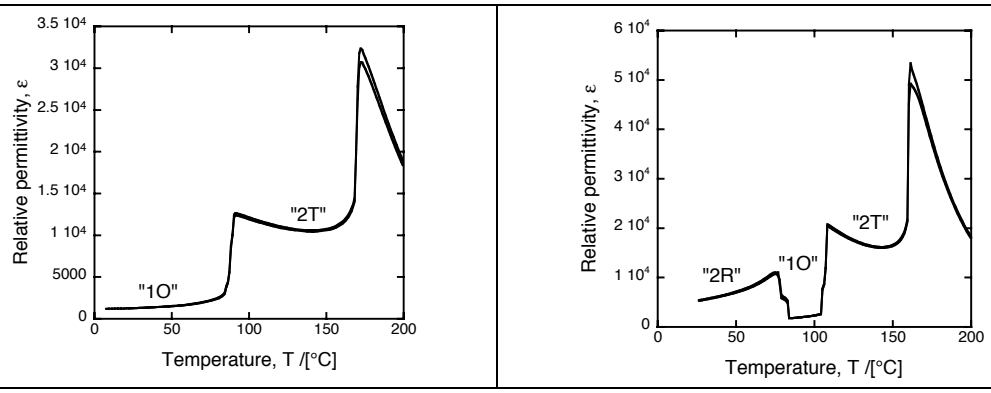

Fig. 16. Dielectric constant measured as a function of temperature in $[101]_C$-poled PZN-7.8PT (left) and PZN-6.7PT (right). Measurements were made at frequencies of 1 and 10 kHz upon heating. Crystals were poled by HTFC at 200 V/mm.

Finally, $[111]_C$-poled PMN-30PT (fig. 17) shows very similar dielectric behavior to PZN-6.7PT [fig. 15(right)]. We might conclude that the zero-field, room temperature phase of $[111]_C$-poled PMN-30PT is also "R".

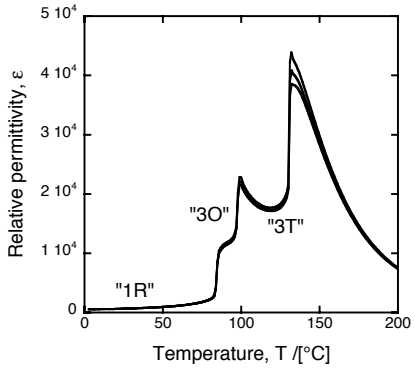

Fig. 17. Dielectric constant measured as a function of temperature in $[111]_C$-poled PMN-30PT. Measurements were made at frequencies of 0.1, 1 and 10 kHz upon heating. The crystal was poled by HTFC at 200 V/mm.

"R"/"O" phase transitions in $[101]_C$- and $[111]_C$-poled crystals

Thus, "R"/"O" phase transitions *are* evident upon increasing temperature in $[101]_C$- and $[111]_C$-poled samples of certain compositions. This is in stark contrast to $[001]_C$-poled crystals where only the "R"/T and "O"/T transitions are seen in dielectric measurements. Importantly, poling seems to affect the range of *thermal stability* of each phase, for a given composition. It follows that temperature-composition phase diagrams will look different for $[001]_C$-poled, $[101]_C$-poled and $[111]_C$-poled crystals. Whereas the "R"/"O" phase boundary is almost vertical for $[001]_C$-poled PMN-xPT and PZN-xPT, this is not the case in $[101]_C$- and $[111]_C$-poled crystals.

The reason for this is unclear. However, we might postulate that it is due to *residual bias fields* resulting from poling (field-cooling) in different directions.

Effect of residual bias fields

An electric field $\boldsymbol{E}$ will energetically bias a ferroelectric phase with spontaneous polarization $\boldsymbol{P_s}$ by an amount $-\boldsymbol{E}\cdot\boldsymbol{P_s} = -EP\cos\theta$, where θ is the angle between the electric field and the polar vector[46]. For example, in PMN-xPT and PZN-xPT, a bias field applied along $[001]_C$ is known to bias the tetragonal phase over the non-polar, cubic phase, increasing the depoling temperature (T_d^{heat})[47-49].

Likewise, electric fields will generally bias one ferroelectric phase over another; the favored phase will be that for which the angle θ is smallest. Hence, the presence of an electric field can alter the free energies of each phase $G(T,E,..)$, their ranges of thermal stability and, thus, the temperatures of the transitions between them[50].

This effect is known to be strong in PMN-xPT and PZN-xPT, near the morphotropic phase boundary, where "O", "R" and T phases are nearly degenerate[8]. For example, under zero field, PZN-4.5PT is rhombohedral at room temperature and transforms upon heating to a tetragonal phase[49]; however, when a bias field is applied along the $[101]_C$ direction, an orthorhombic phase is stabilized over a wide temperature range between rhombohedral and tetragonal phase fields[51]. Likewise, during cooling of *$[111]_C$-oriented* PZN-4.5PT, application of a strong bias field leads to a $\varepsilon(T)$ curve very similar to that shown by $[111]_C$-poled PMN-30PT (fig. 17) and $[111]_C$-poled PZN-6.7PT [fig. 15 (right)][49]. Therefore, a transition sequence via an otherwise-absent, pseudo-orthorhombic phase, T - "O" - "R", is observed in PZN-4.5PT under a $[111]_C$ bias.

This has important consequences. It means that, although a $[111]_C$ electric field biases the "R" phase (for which $\theta = 0°$) over the "O" phase (for which $\theta \approx 35.3°$), it also biases the "O" phase over the tetragonal one (for which $\theta \approx 54.7°$). As a result of a $[111]_C$ bias, a range of thermal stability appears for the "O" phase, to the detriment of the T phase, that otherwise would not exist.

Considering the results presented here it seems that, even under *zero external field*, $[111]_C$-poled PMN-30PT (fig. 17) and PZN-6.7PT [fig. 15 (right)] behave as if subject to a $[111]_C$-oriented *residual electric field*. Although it biases the "R" phase over the "O", this internal bias favors the "O" phase over the tetragonal phase such that a finite range of thermal stability is created for the "O" phase and a "R"/"O" phase transition is evident upon heating.

In $[101]_C$-poled PZN-6.7PT [fig. 16(right)], the residual bias field favors the "O" phase (for which $\theta = 0°$) over both the "R" phase ($\theta \approx 35.3°$) and the T phase ($\theta = 45°$). The "R"/"O" phase transition is again observed and the "O" is stable over a wide temperature interval ($\Delta T \sim 20°C$).

However, in $[001]_C$-poled samples, the residual bias field favors the tetragonal phase (for which $\theta = 0°$) over both the "O" ($\theta = 45°$) and "R"

($\theta \approx 54.7°$) phases, perhaps, by similar (though not identical) amounts. As a result no "R"/"O" phase transition is observed in $[001]_C$-poled PMN-xPT and PZN-xPT upon heating and the "R"/"O" phase boundary is essentially vertical. Notably, PMN-xPT (x = 29 - 33 mol.%) exhibits no third FE phase when cooled under a $[001]_C$ bias field of 100 V/mm[48]. However, it will be shown in chapter seven that large electric bias fields (< 1500 V/mm) applied along the $[001]_C$ direction do indeed bias the "O" phase over the "R".

The presence of just such an "internal bias" in HTFC-poled crystals has already been postulated by Shen and Cao (2005)[52]. In their study, the range of thermal stability in HTFC-poled, $[001]_C$-oriented PZN-8PT was found to be more than 20°C larger than that in samples poled at room temperature (SF poling). Although this does not preclude the presence of a residual bias field in SF-poled crystals, it does suggest it is stronger in HTFC-poled crystals. The authors postulate that poling leaves a "memory", probably of "dipolar defect alignment[52]". The associated residual field will then favor one ferroelectric phase over the others.

The presence of such residual bias fields would be worthy of future investigation.

Determination of the zero-field phase in $[001]_C$-poled crystals

These results can be used, indirectly, to determine whether given compositions are "R" or "O", at zero field and room temperature, in the $[001]_C$-poled condition. For example, since *$[111]_C$-poled* PZN-7.5PT is "O" at room temperature [fig. 15(left)], we can safely assume that $[001]_C$-poled PZN-7.5PT is likewise "O", at room temperature, below the phase transition to the T phase. In contrast, we *cannot* assume that $[001]_C$-poled PZN-6.7PT will be "R" at zero field and room temperature from the fact that $[111]_C$-poled PZN-6.7PT is "R" [fig. 15(right)].

However, we can conclude that $[001]_C$-poled PZN-6.7PT will be "R" at room temperature and zero-field from the fact that *$[101]_C$-poled* PZN-6.7PT is "R" at room temperature [fig. 16(right)]. Likewise, since PMN-29.5PT, PMN-30PT and PMN-31PT are "R" at room temperature in the $[101]_C$-poled condition[44,45], we can assume they will also be "R" at room temperature and zero field when poled along $[001]_C$.

Such information can be used to precise the position of the "R"/"O" phase boundary in the phase diagrams plotted in figures 13 and 14.

III. FERROELECTRIC HYSTERESIS LOOPS

The spontaneous polarization (P_S) of a ferroelectric crystal can be derived from measurement of charge ($D \cong P$) as a function of electric field E: that is, by measurement of *ferroelectric hysteresis loops*[1]. Properties derived from polarization loops (such as coercive field E_C and remanent polarization P_R)[1] are useful figures of merit for the application of ferroelectric materials in memory applications (FE-RAM)[53,54]. As will be shown, they can also be used to distinguish "R" and "O" phases in PZN-xPT and PMN-xPT single crystals.

Experimental

$[001]_C$-, $[101]_C$-and $[111]_C$-oriented plate samples (5 x 5 x 0.5 mm^3) of PMN-28PT and PZN-8PT were cut and electroded, as described in chapter three. $P(E)$ loops were then measured, at room temperature (and starting form the virgin, unpoled state), using the method described in chapter two. The spontaneous polarization was derived each time in the standard way[1] by extrapolating the high-field, linear segment of the loop back to the vertical ($E = 0$) axis.

Crystal anisotropy and domain engineering

At fields above the coercive level ($E > E_C$)[1], quasi-monodomain or domain-engineered states will be induced in "R", "O" or T crystals oriented along the $[111]_C$, $[101]_C$ or $[001]_C$ directions. For example, $[111]_C$-oriented "R" crystals and $[101]_C$-oriented "O" crystals will form "1R" and "1O" monodomain states at high field. The spontaneous polarization derived from $P(E)$ loops will correspond, in theory, to the intrinsic value along the polar axis of the monodomain crystal P_S. In contrast, at high fields, $[001]_C$-oriented "R" and "O" crystals will form domain-engineered states: respectively, "4R" and "4O". The derived spontaneous polarization P_S* will, in fact, be lower than the true spontaneous polarizations P_S of the component domain variants.

Again assuming "domain averaging engineering", based on crystal anisotropy[25], the experimentally derived polarization will be given simply by:

$$P_S^* = P_S \cos\theta \qquad [2]$$

where θ is the angle between the applied field and the polar vectors in the component domain variants. Since the spontaneous polarization is a vector $\boldsymbol{P_S}$ oriented along the polar axis, we assume that the measured value will be the component of that vector along the direction of applied field; this will necessarily be the same for all domain variants in a domain-engineered structure.

In this way, we can predict the ratios between values of P_S* we might derive from polarization loops for $[001]_C$-, $[101]_C$- and $[111]_C$-oriented crystals, assuming a given symmetry. This has been done for orthorhombic and rhombohedral crystals in table I; slight variations from this can be expected for distorted, pseudo-rhombohedral ("R") and pseudo-orthorhombic ("O") phases.

PMN-28PT

Polarization loops for samples of PMN-28PT [$x = (28.0 \pm 0.3)$ mol.%] with $[111]_C$, $[101]_C$ and $[001]_C$ orientations are shown in figure 18. Notably,

the coercive field E_C varied slightly between samples (from 280 to 380 V/mm); this might be partly explained by the small spread in composition[55].

Derived spontaneous polarizations were 0.38, 0.30 and 0.23 C/m^2 for the $[111]_C$-, $[101]_C$- and $[001]_C$-oriented crystals, respectively. This is exactly the order expected for pseudo-rhombohedral phases. Indeed, the ratios between these values are very close to those predicted in table I assuming rhombohedral symmetry; the ratios agree to within 5%.

The discrepancy between the theoretical and experimental ratio might result from the finite variation in composition between the samples. Furthermore, any zero-field, monoclinic distortions in the multidomain crystals will also lead to deviations from the "ideal" ratios.

Thus polarization loops can also be used to give information about the phase present in a given composition at a given temperature. The loops plotted in figure 18 are good evidence that the zero-field, room temperature phase in PMN-28PT is "R", irrespective of poling direction.

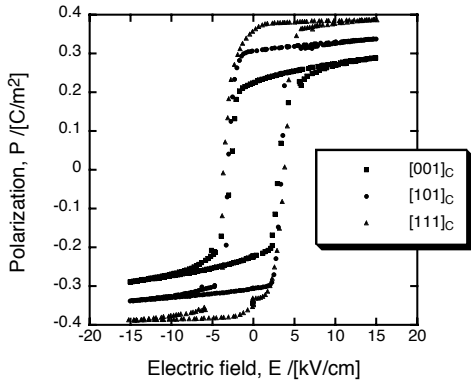

Fig. 18. Hysteresis loops from samples of initially-unpoled PMN-28PT cut and oriented along $[001]_C$, $[101]_C$ and $[111]_C$ directions. The loops were taken at room temperature, at 5kHz, and with a maximum field of 1500 V/mm.

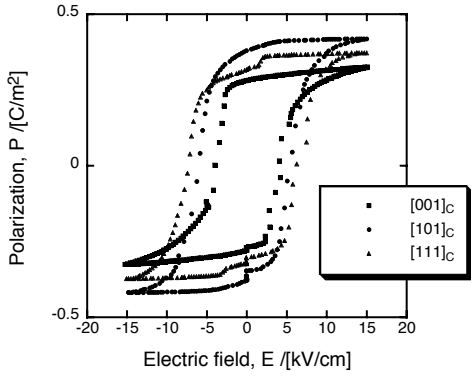

Fig. 19. Hysteresis loops from samples of initially-unpoled PZN-8PT cut and oriented along $[001]_C$, $[101]_C$ and $[111]_C$ directions. The loops were taken at room temperature, at 5kHz, and with a maximum field of 1500 V/mm.

PZN-8PT

More complex behavior was observed for $[111]_C$-, $[101]_C$- and $[001]_C$-orientated samples of PZN-8PT [$x = (7.9 \pm 0.2)$mol.%], as shown in figure 19.

Firstly, the measured spontaneous polarization was highest in the $[101]_C$-oriented sample (0.42 C/m^2), indicative of a pseudo-orthorhombic phase. The derived polarization for the $[001]_C$-cut crystal was 0.28 C/m^2. The ratio between the two is 0.67, very close to the ratio expected for orthorhombic symmetry (table I). Such good agreement (again to around 5%) is good evidence that the zero field phase is "O" in $[001]_C$-poled PZN-8PT.

Secondly, a large spread in coercive fields is evident for the three samples, ranging between 410 and 610 V/mm. This is unlikely to be due purely to compositional variation[56].

Finally, and perhaps most interestingly, a discontinuous "jump" in polarization can be seen upon increasing field for the $[111]_C$-oriented sample (fig. 19). The origin of this is an *electric-field induced phase transition*, as will become clear in the next chapter.

Determination of the zero-field phase in $[001]_C$-poled crystals

In summary, measurements of spontaneous polarization from ferroelectric charge-field loops can be used to indirectly determine the zero-field phase of a given composition. $[001]_C$-poled PMN-28PT is shown to be pseudo-rhombohedral at room temperature; $[001]_C$-poled PZN-8PT is evidently pseudo-orthorhombic. However, at least two orientations of each composition will be needed each time and the method will be sensitive to small compositional differences between the samples.

Table I
Expected ratios of measured polarization P_S* to the maximum value P_S measured in the monodomain crystal as expected from "domain average engineering" for both rhombohedral and orthorhombic symmetries. Also listed are the corresponding, experimental ratios derived from *P(E)* loops for PMN-28PT and PZN-8PT samples. The expected domain structure for each symmetry and orientation, and the angle between the polar axis and measurement direction are given.

Crystal orientation	$[001]_C$	$[101]_C$	$[111]_C$
		Rhombohedral ***P*****$_S$** along $<111>_C$	
Expected domain structure	4R	2R	**1R**
Angle θ	54.7°	35.3°	**0°**
Theoretical P_S^*/P_S	0.58	0.82	**1**
Measured P_S^*/P_S (PMN-28PT)	0.61	0.79	1
		Orthorhombic ***P*****$_S$** along $<101>_C$	
Expected domain structure	4O	**1O**	3O
Angle θ	45°	**0°**	35.3°
Theoretical P_S^*/P_S	0.71	**1**	0.82
Measured P_S^*/P_S (PZN-8PT)	0.67	**1**	-

IV. PYROELECTRIC PROPERTIES

All ferroelectric phases are necessarily polar[25], and therefore *pyroelectric*. Pyroelectric materials are used in a range of thermal imaging and detection applications[57]. As discussed in chapter two, the pyroelectric vector[25,57] $\boldsymbol{p}$ is defined as the rate of change of spontaneous polarization $\boldsymbol{P_S}$ in a material with temperature T:

$$\boldsymbol{p} = \Delta \boldsymbol{P_s} / \Delta T \qquad [3]$$

As will be shown below, pyroelectric measurements can also be used to determine the zero-field phase in poled PMN-xPT and PZN-xPT single crystals. At the same time, the results of a systematic comparison of two poling protocols will be presented.

Experimental

The room temperature, pyroelectric coefficients of $[111]_C$-, $[101]_C$- and $[001]_C$-poled samples of PMN-28PT [$x = (28.0 \pm 0.3)$ mol.%] and PZN-8PT [$x = (7.9 \pm 0.2)$ mol.%] were measured using the method described in chapter two. For each composition and orientation, measurements were made on two 5 x 5 x 0.5 mm^3 plates cut from the same as-supplied crystal (see table II, chapter three). Room temperature dielectric constants and loss tangents were also measured.

Two poling protocols, HTFC and LTFH, were used. First, the samples were HTFC-poled by cooling from 200°C to room temperature under a small field (200 V/m). They were then depoled, by heating over the Curie temperature with shorted electrodes, and repoled (LTFH) by heating them from –70°C to room temperature under application of a field close to the coercive value (400 V/mm). The dielectric and pyroelectric data were then re-measured.

The values from each pair of samples were average and are listed in tables II and III. The error shown is one standard deviation. The measurement temperature was (24 ± 0.5)°C.

Crystal anisotropy and domain engineering

The ratios between the pyroelectric coefficients of samples poled in $[001]_C$, $[101]_C$ and $[111]_C$ directions can be predicted in much the same way as the polarization was in section III. For example, an “R” crystal poled along the $[111]_C$ direction will be quasi-monodomain “1R”. Here, the measurement of pyroelectric coefficient is along the polar axis and the derived value is p. In a $[001]_C$-poled “4R” crystal, however, the measured pyroelectric coefficient p^* will be smaller. Assuming “domain averaging engineering”, as before, the measured coefficient will be given by:

$$p^* = p \cos\theta \qquad [4]$$

where θ is the angle between the measurement direction (also the poling direction) and the polar vectors in the component domain variants; this is the same for all variants in a domain engineered structure. The relevant ratios are necessarily the same as those for the polarization, since both are parallel vector properties (equation [3]); they are repeated again in table IV.

Room temperature dielectric constants

For both the $[001]_C$ and $[101]_C$ samples of PMN-28PT, the relative permittivities (ε_{33} or ε) were comparable for the two poling schemes. However, for the $[111]_C$-oriented samples the permittivity after low LTFH poling ($\varepsilon = 660$) was around half that measured after HTFC poling (1260). This indicates that with the low temperature poling scheme, the $[111]_C$-oriented PMN-28PT samples approach more closely the (albeit unstable[32]) monodomain 1R rhombohedral state.

For PZN-8PT, the results were more complicated. After HTFC poling, the permittivity was large in the $[111]_C$-oriented samples ($\varepsilon^* = 6170$) indicating a domain-engineered structure. The lowest permittivity was observed in the $[101]_C$-cut samples ($\varepsilon = 1530$). After LTFH poling, however, the permittivity in the $[111]_C$-cut sample became much lower ($\varepsilon = 950$) although the permittivities for the $[001]_C$ and $[101]_C$ cuts changed very little.

Therefore, the room temperature dielectric measurements strongly suggest that: (i) with either poling protocol, we do form in $[001]_C$ and $[101]_C$ PZN-8PT samples the "4O" and "1O" pseudo-orthorhombic domain structures, as listed in table I; and (ii) on HTFC poling of the $[111]_C$ PZN-8PT sample we form a multidomain, pseudo-orthorhombic, "3O" structure ($\varepsilon^* = 6170$) whereas on LTFH poling we stabilize a quasi-monodomain "1R" state ($\varepsilon = 950$). Seemingly, different zero-field, room temperature phases are apparent in $[111]_C$-oriented PZN-8PT, poled by two different protocols.

"Frozen-in" pseudo-rhombohedral phase

To help confirm this last result the permittivity of the $[111]_C$-poled crystals were measured as a function of temperature in a series of heating and cooling runs. The results are shown in figures 20 and 21.

Upon heating from 5°C, a transition sequence from "3O" to "1T" to cubic was evident in $[111]_C$-oriented, HTFC-poled PZN-8PT (fig. 20). In contrast, the $[111]_C$-oriented, LTFH-poled sample showed evidence of a third, low temperature phase; its low permittivity is indeed indicative of a "1R" zero-field phase.

The question arises: what is the *lowest energy* (or *stable*) zero-field phase at room temperature, of $[111]_C$-poled PZN-8PT? Our first assumption might be that $[111]_C$-poled PZN-8PT is "O" at room temperature and zero-field, and that the "R" phase is induced *metastably* (or "frozen-in") by poling at sub-zero temperatures. To help confirm this an LTFH-poled, "R" sample was heated from 5°C over the first FE-FE phase transition temperature

($T_{FE-FE} \approx 32°C$) to 60°C and then cooled back down to room temperature; the corresponding variation in permittivity is shown in figure 21.

Upon heating through T_{FE-FE} there was a transition from the "1R" state to a domain-engineered "O" phase, clearly evident as an abrupt increase in permittivity (fig. 21). More importantly, upon subsequent cooling back to 5°C, the pseudo-rhombohedral phase was not recovered suggesting, as postulated, that the "R" phase was indeed *metastable* at room temperature. Seemingly, a metastable "R" phase can be "frozen-in" in otherwise pseudo-orthorhombic PZN-8PT by poling in the $[111]_C$ direction at sub-zero temperatures.

This results shows that, by altering the poling protocol employed not only the domain structure but the actual phase present in the material can be changed. Similar conclusions, also based on dielectric measurements, have been drawn by Lu *et al.* for PMN-33PT[58].

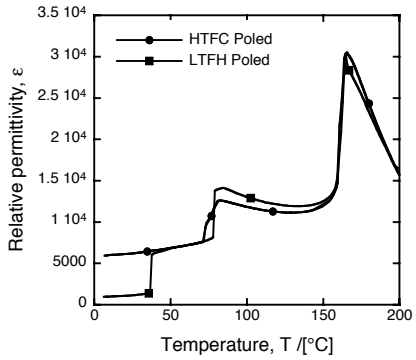

Fig. 20. Dielectric constant as a function of temperature measured upon heating from 5°C (at 2°C/min) for a sample of $[111]_C$-oriented PZN-8PT; the ramp rate was 2°C/min and the measurement frequency was 1 kHz). The sample was poled before measurement in one case by field cooling from high temperatures (HTFC) and in the other by poling at sub-zero temperatures (LTFH).

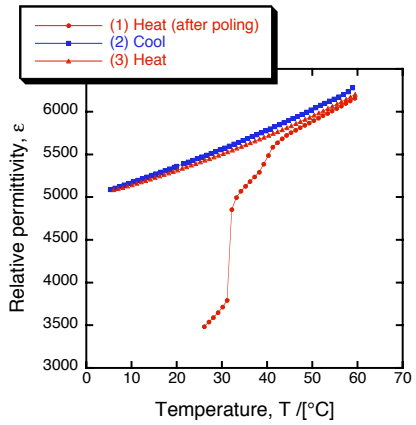

Fig. 21. Dielectric constant as a function of temperature for a sample of $[111]_C$-poled PZN-8PT: (1) upon heating after LTFH poling; (2) subsequent cooling; (3) repeat heating.

Pyroelectric coefficients

Firstly, since higher pyroelectric coefficients (and lower loss tangents) are indicative of better alignment of constituent polar vectors, the data in tables II and III suggests that the LTFH protocol better poles the samples.

Secondly, high values of p^* varying between 377 and 1071 $\mu Cm^{-2}K^{-1}$ are immediately apparent, comparing favorably to the room temperature values of 300 $\mu Cm^{-2}K^{-1}$ and 190 $\mu Cm^{-2}K^{-1}$ for commonly used pyroelectrics, triglycine sulfate (TGS) and $LiTaO_3$, respectively[59].

In the LTFH-poled state (table III), pyroelectric coefficients of the PMN-28PT samples increased in the order predicted by a pseudo-rhombohedral symmetry (table IV). The highest value of p^* observed, 1071 $\mu Cm^{-2}K^{-1}$, was measured in $[111]_C$-oriented PMN-28PT, corresponding to the quasi-monodomain state. After HTFC poling, the PMN-28PT samples generally showed smaller pyroelectric coefficients (table II).

Large pyroelectric coefficients were also measured in the PZN-8PT samples. For the $[101]_C$-oriented samples, the monodomain "1O" structure was more closely approached by LTFH poling evident in a higher pyroelectric coefficient (744 $\mu Cm^{-2}K^{-1}$). For the $[111]_C$-oriented samples, LTFH poling gave rise to a high pyroelectric coefficient (800 $\mu Cm^{-2}K^{-1}$), indicative of the metastable "1R" state; note that it is higher than that for the $[101]_C$-poled "1O" sample (table III). In contrast, after HTFC poling, $[111]_C$-oriented PZN-8PT sample was multidomain and pseudo-orthorhombic ("3O"), with a lower pyroelectric coefficient (650 $\mu Cm^{-2}K^{-1}$).

Alongside the theoretical ratios in table IV are the experimental values calculated from the values for LTFH-poled PMN-28PT and PZN-8PT (table III). The quantitative agreement is reasonable (to within 15%) except in the case of otherwise pseudo-orthorhombic $[111]_C$-oriented PZN-8PT where a "R" phase is frozen-in.

Figures of merit

Since a low permittivity is desirable in most pyroelectric applications, a useful comparative figure of merit (FOM) for a pyroelectric material is p^*/ε where ε is the dielectric constant[60]. For TGS and $LiTaO_3$, p^*/ε is 10 and 5, respectively[57].

FOMs calculated from the above pyroelectric and dielectric data are shown in tables II and III. In the present work, the highest FOMs[61] were observed in LTFH-poled crystals (see table III), although the maximum observed value (1.6 for $[111]_C$-oriented PMN-28PT) still compares poorly with those for TGS and $LiTaO_3$.

For pseudo-rhombohedral PMN-28PT, the highest FOMs were measured in the $[111]_C$-poled samples. For HTFC-poled PZN-8PT (table II), the highest FOM was seen in the "O" $[101]_C$-oriented crystal. For LTFH-poled PZN-8PT, the highest value was observed in the pseudo-rhombohedral $[111]_C$-cut sample.

Exploitation of the pyroelectric properties of PMN-xPT and PZN-xPT

The pyroelectric coefficient (1071 $\mu Cm^{-2}K^{-1}$) measured in $[111]_C$-poled PMN-28PT is exceedingly high for an unbiased[62] material. However, at first glance, these relaxor based ferroelectric single crystals do not make good candidates for pyroelectric detector applications[57,59] due to their high permittivities. However since publication[63] of these properties in 2004, more work has been published on the pyroelectric properties of single crystal PMN-xPT and PZN-xPT[64-66]. This work, involving more sophisticated, application-tailored figures or merit suggest that this might not always be the case.

TABLE II
Pyroelectric, loss and dielectric data measured for samples of PMN-28PT and PZN-8PT cut in three different crystallographic orientations. The samples were poled by applying a small field (200 V/mm) while cooling from the paraelectric phase to room temperature ("HTFC" poling).

Sample composition	Sample orientation	Pyroelectric coefficient (10 mHz), $\langle p^* \rangle$ /[$\mu Cm^{-2}K^{-1}$]	Relative permittivity (1 kHz), ε	Loss tangent, tan δ	p^*/ε^* /[$\mu Cm^{-2}K^{-1}$]
PMN-28PT	$[001]_C$	377 ± 37	3160 ± 120	0.014 ± 0.000	0.1
	$[011]_C$	888 ± 1	2510 ± 30	0.007 ± 0.002	0.4
	$[111]_C$	803 ± 30	1260 ± 140	0.017 ± 0.000	0.6
PZN-8PT	$[001]_C$	490 ± 1	3920 ± 80	0.015 ± 0.002	0.1
	$[011]_C$	650 ± 81	1530 ± 390	0.020 ± 0.009	0.4
	$[111]_C$	650 ± 4	6170 ± 270	0.013 ± 0.002	0.1

TABLE III
Pyroelectric, loss and dielectric data measured for samples of PMN-28PT and PZN-8PT cut in three different crystallographic orientations. The samples were poled by applying a field close to the coercive field while heating from –70°C to room temperature ("LTFH" poling).

Sample composition	Sample orientation	Pyroelectric coefficient (10 mHz), $\langle p^* \rangle$ /[$\mu Cm^{-2}K^{-1}$]	Relative permittivity (1 kHz), ε	Loss tangent, tan δ	p^*/ε^* /[$\mu Cm^{-2}K^{-1}$]
PMN-28PT	$[001]_C$	550 ± 25	5750 ± 1500	0.008 ± 0.004	0.1
	$[011]_C$	926 ± 10	2680 ± 80	0.004 ± 0.000	0.3
	$[111]_C$	1071 ± 8	660 ± 10	0.003 ± 0.001	1.6
PZN-8PT	$[001]_C$	520 ± 8	3820 ± 3	0.012 ± 0.001	0.1
	$[011]_C$	744 ± 11	1280 ± 40	0.005 ± 0.000	0.6
	$[111]_C$	800 ± 14	950 ± 190	0.003 ± 0.000	0.8

Table IV
Expected ratios of measured pyroelectric coefficient p^* to the maximum value p measured in the monodomain crystal as expected from "domain average engineering" for both rhombohedral and orthorhombic symmetries. Also listed are the corresponding, experimental ratios calculated from the data given in table III for LTFH samples. The expected domain structure for each symmetry and orientation, and the angle between the polar axis and measurement direction are given.

Crystal orientation	$[001]_C$	$[101]_C$	$[111]_C$
		Rhombohedral $\boldsymbol{P_S}$ along $<111>_C$	
Expected domain structure	4R	2R	**1R**
Angle θ	54.7°	35.3°	**0°**
Theoretical p^*/p	0.58	0.82	**1**
Measured p^*/p (PMN-28PT)	0.51	0.86	1
		Orthorhombic $\boldsymbol{P_S}$ along $<101>_C$	
Expected domain structure	4O	**1O**	3O
Angle θ	45°	**0°**	35.3°
Theoretical p^*/p	0.71	**1**	0.82
Measured p^*/p (PZN-8PT)	0.70	**1**	(1.08)

V. SUMMARY AND CONCLUSIONS

In this chapter, measurements of permittivity, pyroelectric coefficient and spontaneous polarization have been used to characterize the various phase transitions that occur between the short-range ordered (*relaxor*) state and the long-range ordered (*ferroelectric*) phases of PMN-xPT and PZN-xPT, especially close to the morphotropic phase boundary.

Phase diagrams for PMN-xPT and PZN-xPT

Ideally, (*T*-*x*) phase diagrams would be drawn up for PMN-xPT and PZN-xPT showing the lowest-energy, stable phase in the virgin (unpoled) condition, for a given composition at a given temperature, under zero external stress or field. However, for low PT-content samples, the unpoled state is often short-range ordered; only at higher PT contents, are long-range ordered,

ferroelectric phases apparent. Upon increasing PT content, and upon decreasing temperature, there is a complex, diffuse transition between them; this is evident in measurements of permittivity as a function of temperature (section II) and as a convergence of T_m and T_d in the phase diagrams plotted in chapter four. Most importantly, the various ferroelectric-ferroelectric (FE-FE) phase transitions that occur at the MPB in PMN-xPT and PZN-xPT are superimposed upon, and presuppose, the relaxor-ferroelectric phase transition (section II). It would be very difficult to plot a phase diagram for unpoled PMN-xPT and PZN-xPT that included phase fields for the ferroelectric phases.

Furthermore, such a diagram would not be technologically-useful since only the polar (*ferroelectric*) phases are piezoelectric and pyroelectric. A more useful phase diagram would therefore show the phase stabilities of poled, ferroelectric phases.

Unfortunately, poling along different directions[20,21] has been shown to result in different monoclinic phases, leading to a generally very complex picture. It is suggested, however, that the M_A, M_C and M_B monoclinic phases evidenced in PMN-xPT and PZN-xPT can be treated as slightly-distorted derivatives of their higher-symmetry, rhombohedral and orthorhombic phases (section I). A phase diagram might therefore consist of phase fields for just three ferroelectric phases: "pseudo-rhombohedral" ("R"), "pseudo-orthorhombic" ("O") and tetragonal (T).

A further complication is that poling along different orientations tends to alter the phase stabilities of the "R", "O" and T phases to different extents (section II). It is postulated that poling results in a residual, internal bias field which biases the phase whose polar vector lies closest to the poling direction; the presence of such an internal "memory", possibly due to defect dipoles, has also been suggested by Shen and Cao[52].

As a result, the zero-field phase at a given temperature can be different in $[001]_C$-, $[101]_C$ and $[111]_C$-poled crystals (section II). Therefore, the poling direction should be specified when drawing up a phase diagram for *poled* PMN-xPT and PZN-xPT. Since the most useful properties result from $[001]_C$-poled crystals on the low PT content side of the MPB[8,39], it makes sense to choose this poling direction for the phase diagram. The temperature of the FE-FE transition to the tetragonal phase can be determined by dielectric measurement; this has been shown in section II where the data is used to update the phase diagrams of Noheda and La-Orauttapong (figures 13 and 14). The difficulty in precising this boundary due to compositional uncertainty is shown.

Position of the "R"/"O" phase boundary

However, the "R"/"O" phase boundary is nearly vertical such that the phase transition between "R" and "O" phases is not apparent in dielectric measurements as a function of temperature (section II). The room temperature, zero-field state of $[001]_C$-poled crystals can be determined by X-ray diffraction[6,8]. However, it can also be determined, indirectly, by comparing measurements of permittivity (section II), polarization (section III) and

pyroelectric coefficient (section IV) for crystals cut and poled along $[001]_C$, $[101]_C$ and $[111]_C$ directions.

Permittivity measurements have shown that $[001]_C$-poled PZN-7.5PT is "O" at room temperature whereas $[001]_C$-poled PZN-6.7PT is "R". Analysis of dielectric data presented elsewhere[44,45] has shown that PMN-29.5PT, PMN-30PT and PMN-31PT are all "R", at room temperature, in the $[001]_C$-poled condition. Finally, measurements of pyroelectric coefficient (section IV) and spontaneous polarization (section III) have shown that $[001]_C$-poled PZN-8PT is "O" at room temperature whereas $[001]_C$-poled PMN-28PT is "R".

Unfortunately, this is too little information to accurately precise the "R"/"O" phase boundaries of figures 13 and 14. However, the boundary can be seen to lie between $x = 0.067$ and $x = 0.075$ in PZN-xPT, slightly lower than that marked (rather arbitrarily) on the phase diagram of La-Orauttapong et al. (fig. 4). Hence, we can now mark on the updated phase diagram of PZN-xPT (fig. 14) a vertical "R"/"O" phase boundary centered at $x = 0.07$, with an uncertainty of ± 0.5 mol.%; this is shown in figure 14.

We can say less about the phase boundary in PMN-xPT except that it should lie at a composition above $x = 0.31$; thus, it will be left at the position shown in the phase diagram of Noheda et al. (fig. 4), i.e., somewhere between $x = 31$ and $x = 32$ *mol. %*. It is marked as such in figure 15. More work is needed to precise the phase diagrams of PMN-xPT and PZN-xPT.

Pyroelectric coefficients

Usefully large pyroelectric coefficients (< 1071 $\mu Cm^{-2}K^{-1}$) have been evidenced in "R" and "O" PMN-xPT and PMN-xPT, poled along their polar directions (section IV). At a first glance, however, their permittivity seems too high for them to be useful in real pyroelectric devices; more recent work done elsewhere suggests otherwise[64-66].

Domain averaging engineering

It has been shown that simple *domain averaging engineering* can predict (to within 15%) the measured polarization and pyroelectric coefficients of domain-engineered PMN-28PT and PZN-8PT (tables I and IV). That is, the value measured parallel to the poling direction is very close to the monodomain value of each domain variant (along the polar axis) resolved onto the poling direction. This is good evidence that domain average engineering is valid, at least for rank-one tensor (or vector) properties, and that crystal anisotropy can explain the (vector) properties of domain-engineered PMN-xPT and PZN-xPT. Higher rank properties of domain-engineered PMN-xPT and PZN-xPT are discussed in chapter ten.

Lastly, the effect of any monoclinic distortion on these zero-field, physical properties is slight. For the rest of this thesis, all monoclinic phases will be considered as *pseudo-rhombohedral* or *pseudo-orthorhombic*.

Metastable phases

Finally, it has been shown that a metastable "R" phase can be induced in otherwise "O" $[111]_C$-poled PZN-8PT by application of the poling field at sub-zero temperatures. The $[111]_C$ poling field and the lower temperature both help "freeze-in" a metastable "R" phase at room temperature. In the next chapter it will be shown that this "O"/"R" phase transition can be induced in PZN-8PT by application of an electric field alone.

REFERENCES

1 B. Jaffe, W. R. Cook, and H. Jaffe, *Piezoelectric Ceramics* (Academic Press, 1971).

2 J. Kuwata, K. Uchino, and S. Nomura, Ferroelectrics **37,** 579-582 (1981).

3 J. Kuwata, K. Uchino, and S. Nomura, Jpn. J. Appl. Phys. **21,** 1298-1302 (1982).

4 S. W. Choi, T. R. Shrout, S. J. Jang, and A. S. Bhalla, Ferroelectrics **100,** 29-38 (1989).

5 T. R. Shrout, Z. P. Chang, N. Kim, and S. Markgraf, Ferroelectrics Letters **12,** 63-69 (1990).

6 B. Noheda, D. E. Cox, G. Shirane, J. Gao, and Z.-G. Ye, Phys. Rev. B **66,** 054104 (2002).

7 D. La-Orauttapong, B. Noheda, Z.-G. Ye, P. M. Gehring, J. Toulouse, D. E. Cox, and G. Shirane, Phys. Rev. B **65,** 144101 (2002).

8 B. Noheda, Current Opinion in Solid State and Materials Science **6,** 27-34 (2002).

9 K. Ohwada, K. Hirota, P. W. Rehrig, P. M. Gehring, B. Noheda, Y. Fujii, S.-E. Park, and G. Shirane, J. Phys. Soc. Jpn. **70,** 2778-2783 (2001).

10 K. Ohwada, K. Hirota, P. W. Rehrig, Y. Fujii, and G. Shirane, Phys. Rev. B **67,** 094111 (2003).

11 A. K. Singh and D. Pandey, Phys. Rev. B **67,** 064102 (2003).

12 A. K. Singh and D. Pandey, Phys. Rev. B **68,** 172103 (2003).

13 D. Zekria, V. A. Shuvaeva, and A. M. Glazer, J. Phys.: Condens. Matter **17,** 1593-1600 (2005).

14 F. Jona and G. Shirane, *Ferroelectric crystals* (Pergamon Press, New York, 1962).

15 This fits well with the concept of polarization rotation, as discussed in chapter one.

16 D. Vanderbilt and M. H. Cohen, Phys. Rev. B **63,** 094108 (2001).

17 J.-M. Kiat, Y. Uesu, B. Dkhil, M. Matsuda, C. Malibert, and G. Calvarin, Phys. Rev. B **65,** 064106 (2002).

18 A. A. Bokov and Z.-G. Ye, J. Appl. Phys. **95,** 6347-6359 (2004).

19 V. A. Shuvaeva, A. M. Glazer, and D. Zekria, J. Phys.: Condens. Matter **17,** 5709-5723 (2005).

20 H. Cao, F. Bai, N. Wang, J. Li, D. Viehland, G. Xu, and G. Shirane, Phys. Rev. B **72,** 064104 (2005).

[21] F. Bai, N. Wang, J. Li, D. Viehland, P. M. Gehring, G. Xu, and G. Shirane, J. Appl. Phys. **96,** 1620-1627 (2004).
[22] D. La-Orauttapong, J. Toulouse, Z.-G. Ye, W. Chen, R. Erwin, and J. L. Robertson, Phys. Rev. B **67,** 134110 (2003).
[23] D. La-Orauttapong, J. Toulouse, J. L. Robertson, and Z.-G. Ye, Phys. Rev. B **64,** 212101 (2001).
[24] D. M. Hatch, H. T. Stokes, and W. Cao, J. Appl. Phys. **94,** 5220-5227 (2003).
[25] J. F. Nye, *Physical properties of crystals*, 2nd ed. (Clarendon Press, Oxford, 1985).
[26] O. Noblanc, P. Gaucher, and G. Calvarin, J. Appl. Phys. **79,** 4291-4297 (1996).
[27] F. Yan, P. Bao, and Y. Wang, Appl. Phys. Lett. **83,** 4384-4386 (2003).
[28] H. Fan, L. Kong, L. Zhang, and X. Yao, J. Mat. Sci. **34,** 6143-6149 (1999).
[29] Z. Li, Z. Xi, Z. Xu, and X. Yao, J. Mat. Sci Lett. **21,** 1325-1327 (2002).
[30] A. A. Bokov, H. Luo, and Z.-G. Ye, Materials Science and Engineering B **120,** 206-209 (2005).
[31] C. Kittel, *Introduction to solid state physics*, 7th ed. (Wiley, New York, 1996).
[32] R. Zhang, B. Jiang, and W. Cao, Appl. Phys. Lett. **82,** 787-789 (2003).
[33] S.-F. Liu, W. Ren, B. K. Mukherjee, S. J. Zhang, T. R. Shrout, P. W. Rehrig, and W. S. Hackenberger, Appl. Phys. Lett. **83,** 2886-2888 (2003).
[34] Evidence for intrinsic contributions to the dielectric and piezoelectric properties of domain engineered PMN-xPT and PZN-xPT will be discussed in chapter ten.
[35] S.-E. E. Park and T. R. Shrout, J. Appl. Phys. **82,** 1804-1811 (1997).
[36] R. Zhang, B. Jiang, and W. Cao, J. Appl. Phys. **90,** 3471-3475 (2001).
[37] W. Ren, S.-F. Liu, and B. K. Mukherjee, Appl. Phys. Lett. **80,** 3174-3176 (2002).
[38] H. Dammak, A.-E. Renault, P. Gaucher, M. P. Thi, and G. Calvarin, Jpn. J. Appl. Phys. Pt. 1 **10,** 6477-6482 (2003).
[39] S.-E. E. Park and W. Hackenberger, Current Opinion in Solid State and Materials Science **6,** 11-18 (2002).
[40] C.-S. Tu, C.-L. Tsai, V. H. Schmidt, H. Luo, and Z. Yin, J. Appl. Phys. **89,** 7908-7916 (2001).
[41] R. R. Chien, V. H. Schmidt, L.-W. Hung, and C.-S. Tu, J. Appl. Phys. **97,** 114112 (2005).
[42] It should be noted that dielectric data alone cannot be taken as proof of a phase transition; changes in domain structure, without change in crystal phase, will also affect the relative permittivity. FE-FE phase transitions should be verified by high-resolution diffraction or microscopy.
[43] S. Priya, J. Ryu, L. E. Cross, K. Uchino, and D. Viehland, Ferroelectrics **274,** 121-126 (2002).
[44] Y. Guo, H. Luo, D. Ling, H. Xu, T. He, and Z. Yin, J. Phys.: Condens. Matter **15,** L77-82 (2003).
[45] Y. Guo, H. Luo, K. Chen, H. Xu, X. Zhang, and Z. Yin, J. Appl. Phys. **92,** 6134-6138 (2002).

[46] A. J. Bell, J. Appl. Phys. **89,** 3907-3914 (2001).
[47] E. V. Colla, N. K. Yushin, and D. Viehland, J. Appl. Phys. **83,** 3298-3304 (1998).
[48] J. Han and W. Cao, Phys. Rev. B **68,** 134102 (2003).
[49] M. Shen and W. Cao, J. Appl. Phys. **95,** 8124 (2004).
[50] Likewise, transitions between phases can occur at fixed temperatures due to the application of an electric field alone. Such "electric-field induced phase transitions" will be the subject of the next chapter.
[51] A.-E. Renault, H. Dammak, G. Calvarin, P. Gaucher, and M. P. Thi, J. Appl. Phys. **97,** 044105 (2005).
[52] M. Shen and W. Cao, Appl. Phys. Lett. **86,** 192909 (2005).
[53] M. Ozgul, K. Takemura, S. Trolier-McKinstry, and C. A. Randall, J. Appl. Phys. **89,** 5100-5106 (2001).
[54] I. Stolichnov, L. Malin, E. Colla, A. K. Tagantsev, and N. Setter, Appl. Phys. Lett. **86,** 012902 (2005).
[55] It might also be explained by different surface boundary conditions between the three samples. If nucleation of reversed domains was easier in one sample it would be evident in a lower coercive field.
[56] Again, the variation could also be due to surface effects.
[57] R. W. Whatmore, Rep. Prog. Phys. **49,** 1335-1386 (1986).
[58] Y. Lu, D.-Y. Jeong, Z.-Y. Cheng, Q. M. Zhang, H.-S. Luo, Z.-W. Yin, and D. Viehland, Appl. Phys. Lett. **78,** 3109-3111 (2001).
[59] A. Hossain and M. H. Rashid, IEEE Transactions on Industry Applications **27,** 824-829 (1991).
[60] The highest figures of merit are expected for crystals oriented along their polar axis where the pyroelectric coefficient is highest and the permittivity lowest.
[61] Note that the permittivity was measured at 1 kHz whereas the pyroelectric response was measured at 10 mHz; since these properties should be measured at the same frequency, the figure of merit reported here has only a relative character.
[62] D. J. Taylor, D. Damjanovic, and A. S. Bhalla, Ferroelectrics **118,** 143-155 (1991).
[63] M. Davis, D. Damjanovic, and N. Setter, J. Appl. Phys. **96,** 2811-2815 (2004).
[64] X. Wan, K.-H. Chew, H. L. W. Chan, C. L. Choy, X. Zhao, and H. Luo, J. Appl. Phys. **97,** 064105 (2005).
[65] Y. Tang, X. Wan, X. Zhao, X. Pan, D. Lin, H. Luo, J. Sun, X. Meng, and J. Zhu, J. Appl. Phys. **98,** 084104 (2005).
[66] Y. Tang, X. Zhao, X. Feng, W. Jin, and H. Luo, Appl. Phys. Lett. **86,** 082901 (2005).

Chapter seven

Electric-field induced phase transitions

In this chapter, a series of *electric-field induced phase transitions* are evidenced in PZN-xPT and PMN-xPT with MPB compositions. Firstly, a pseudo-orthorhombic to rhombohedral ("O" - R) phase transition, via polarization rotation in the M_B monoclinic plane, is evidenced by macroscopic strain-field measurements and by *in situ* polarized light microscopy. The hysteretic discontinuity evident in strain-field loops is due to nucleation and growth of the high-field rhombohedral phase and is evidence of a *first-order* phase transition. It corresponds to a discontinuous "jump" of the polar vector within the M_B plane.

Secondly, a series of unipolar, strain-field measurements on $[001]_C$-poled PZN-xPT (x = 0.05, 0.065 and 0.085) and PMN-xPT (x = 0.25, 0.305, 0.31) are presented for temperatures between 25°C and 100°C, and electric fields between 0 and 1500 V/mm. Various electric-field induced phase transitions are evidenced as hysteretic (first-order), discontinuous "jumps" in strain. In certain compositions, at certain temperatures, the polarization rotation path "R" - "O" - T is evidenced by *two* first-order jumps in strains, one between the M_A and M_C monoclinic planes, and one within the M_C plane to the tetragonal phase. Electric field-temperature (*E-T*) phase diagrams are constructed from the experimental data for all six compositions; the trends for the complex, varying stabilities of the (non-zero field) M_A, M_C and tetragonal phases with changing composition around the MPB are shown. It is shown that the effect of electric field on the stability of the "R", "O" and T phases can be predicted by simple energetic arguments.

Lastly, the question of whether truly *zero-field* monoclinic phases occur in PMN-xPT and PZN-xPT at the morphotropic phase boundary is discussed: i.e., whether the monoclinic symmetry phases observed, both under field and in unpoled samples, are true *phases* or rather field-distorted versions of their higher-symmetry rhombohedral and orthorhombic parents. This involves discussion of the *order* of the phase transition. It is noted that distorted monoclinic phases might be observed under zero field due to residual stresses, or the presence of the residual bias fields postulated in chapter six. It is noted that all the observed behavior can be explained in terms of first-order phase transitions between field-distorted rhombohedral and orthorhombic, and tetragonal phases. The angular distortion (or *rotation*) of the polar vector at such a transition is estimated for the "O" - T transition in PZN-8PT.

I. INTRODUCTION

According to the thermodynamic theory of phase transitions[1-4] one phase will be more *stable* than another if it is lower in (Gibbs) free energy G. The *driving force*[1] for the phase transition between the two is the difference between the free energy of the two phases $\Delta G = G^{(1)} - G^{(2)}$. Importantly, the free energy of each phase will generally be a function of many thermodynamic variables[3,5] including temperature T, pressure p (or stress σ), electric field E, magnetic flux density B and chemical composition Ω. As a result, phase transitions between two distinct phases can be driven by changes in any one, or more, of these parameters.

Phase transitions via changes in temperature, electric field and stress

Temperature induced phase transitions (TIPT) are the most obvious examples, such as those evidenced in the previous chapter. These transitions appear along vertical sections of temperature vs. composition (*T-x*) phase diagrams. In ferroelectrics, and especially in PMN-xPT and PZN-xPT (chapter six), these transition temperatures are strongly affected by the application of an electrical bias field since the *order parameter*[3,6] of a ferroelectric phase corresponds to a spontaneous polarization. Likewise, transition temperatures will be strongly affected by stress wherever the order parameter is related to a *spontaneous strain*; this is true in ferroelastics[2].

Alternatively, we could fix the temperature (and other thermodynamic parameters) and vary only the electric field. Any resultant change in phase could be referred to as an *electric-field induced phase transition* (EFIPT). Likewise, we could imagine *stress induced phase transitions* (SIPT) and *magnetic-field induced phase transitions* (MFIPT), especially in ferroelastic and ferromagnetic materials.

Finally, phase transitions are also driven by changes in chemical composition. This is the case, for example, in PMN-xPT and PZN-xPT upon substitution of Mg (or Zn) and Nb B-site cations with Ti, as shown in horizontal sections of their (*T-x*) phase diagrams (chapter six). The “R” to “O” to T phase transitions that occur with increasing PT content in poled PZN-xPT and PMN-xPT can be referred to as “*chemically induced phase transitions*” (CIPT).

Displacive phase transitions

As noted in previous chapters, we can consider the ferroelectric phases that appear in PZN-xPT and PMN-xPT to be much like the *3m* rhombohedral (R), *mm2* orthorhombic (O) and *4mm* tetragonal (T) phases of the simpler perovskite ferroelectrics, lead titanate (PT), potassium niobate (KN) and barium titanate (BT)[7]. That is, we can treat them as truly long-range ordered and ignore any slight monoclinic distortion at zero field.

Excepting the possibility of some small order-disorder character[8-11], the phase transitions between the ferroelectric phases in the simple perovskites are *displacive*[3]; i.e., during the transitions various symmetry elements of the

point group of one phase are lost ("symmetry breaking[3]"), and other symmetry elements are created, purely by shifts in atomic position[12].

First and second order phase transitions

We can also broadly divide phase transitions (reconstructive[3], structural[3], displacive or otherwise) into two types. *First-order* (or *discontinuous*) phase transitions are those that involve latent heat; i.e., during such a transition a system either absorbs or releases a certain amount of energy. In a first order structural phase transition there is a discontinuity in order parameter, enthalpy, entropy, volume through the phase transition temperature and at the transition point the two phases can coexist in equilibrium. First order transitions are also often accompanied with a region where one phase is stable and the other metastable[13]. Accordingly, thermal hysteresis[7], where the Curie point is different upon heating and cooling, is commonly observed in ferroelectric perovskites. First order phase transitions usually occur by a mechanism of nucleation and growth of the new phase within the old.

Second order (or *continuous*) phase transitions, in contrast, do not involve the transfer of latent heat. Upon cooling through a second order structural transition temperature the order parameter increases continuously from zero at the phase transition temperature. There is no discontinuity in enthalpy, entropy or volume and continuous phase transitions are not accompanied by regions of metastability; even at the phase transition temperature only one phase can exist. In mixtures of vapor and liquid phases, for some special combination of temperature and pressure, the first order phase transition can become second order. This point is known as the critical point: at this point the fluid is sufficiently hot and compressed that the distinction between the liquid and gaseous phases becomes almost non-existent[4]. Analogously, in ferroelectrics, application of a sufficiently strong electric field along a $[001]_C$ direction will render the first order, tetragonal-cubic phase transition continuous[7].

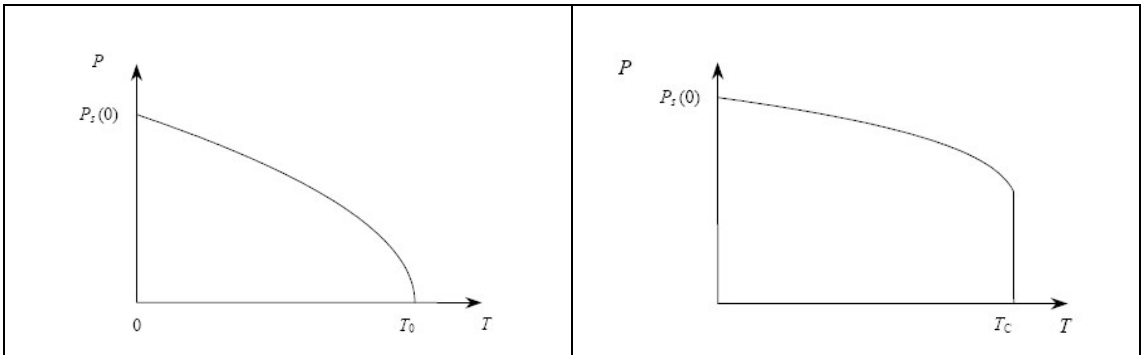

Fig. 1. Schematic representation of the evolution of the order parameter (or spontaneous polarization) *P* upon cooling through a ferroelectric phase transition: (left) second order transitions and (right) first order phase transitions.

Importantly, the *excess free energy* (or driving force) ΔG goes continuously to zero at the phase transition regardless of the order of the transition. The two types of phase transition are shown schematically in figure

1 for ferroelectric materials where the spontaneous polarization is proportional to the order parameter. A discontinuous "jump" in polarization is characteristic of a first order ferroelectric phase transition [fig. 1(right)].

Group theory and second order phase transitions

Landau was the first to apply the mathematics of group theory to phase transitions. His work showed that there are various conditions imposed by the (space) group symmetries of a given pair or crystalline phases on the permissibility of a second order phase transition between them; these are reviewed by Stokes and Hatch (1984)[14]. The main condition for a second order phase transition is that the two phases must be related by a *group-subgroup relationship*[14,15]. There is no general symmetry argument that forbids a first order phase transition[15,16]. Group-subgroup relationships for the R, O, T, M_C, M_B and M_A phases are shown in figure 4 of appendix I.

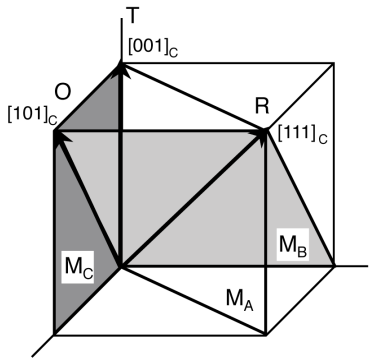

Fig. 2. Mirror planes of monoclinic "phases" appearing in PZN-xPT and PMN-xPT. Also shown are the polarization vectors of the *3m* rhombohedral (R), *mm2* orthorhombic (O) and *4mm* tetragonal (T) phases occurring in the simpler ferroelectric perovskites. Various electric-field induced rotations occur by polarization rotations within these monoclinic planes and "jumps" between them.

Polarization rotation mechanism

The concept of "*polarization rotation*" seems key to understanding the "giant" (d_{33} > 2000 pm/V)[17,18] piezoelectric properties of $[001]_C$-poled "4R" (and "4O") PMN-xPT and PZN-xPT. Since domain wall motion is restricted in these special, domain-engineered structures[18-20], an *intrinsic*[21] origin for this large piezoelectric response was sought.

According to the "polarization rotation theory[22]" outlined in chapter one, the high piezoelectric coefficients when an electric field is applied along the non-polar $[001]_C$ direction of a rhombohedral or orthorhombic crystal is due to the rotation[23] ("inclination[18]") of the polar vector and, importantly, its relative ease in the mirror plane of one or more monoclinic phases[24]; these are again shown, for convenience, in figure 2. First principles calculations[23,25] have indeed shown that the large piezoelectric response to an electric field applied

away from the polar axis is a consequence of the *rotation*, rather than *collinear extension*, of the polar vector. In this way, the M_A, M_B and M_C monoclinic planes can be thought of as "structural bridges[24]" between the R, O and T phases. Therefore, monoclinic phases are often assumed to be responsible for the enhanced piezoelectric properties of $[001]_C$-oriented PMN-xPT and PZN-xPT[22,24,26].

Polarization rotation path

Application of an electric field $\boldsymbol{E}$ along the $[001]_C$ poling direction of a "4R" (4R or $4M_A$) domain engineered crystal will lead to rotation of the polar vectors in the component domain variants $\boldsymbol{P_S}$ towards that direction. This rotation is driven by the competitive $-\boldsymbol{P_s} \cdot \boldsymbol{E} = -P_S E \cos\theta$ term in the free energy expansion for that phase (G)[27], where θ is the angle between the polar vector and the applied field; it is maximized at lower θ.

According to the model laid out by Park and Shrout (chapter one), at a sufficiently high field, the crystal will undergo a *electric-field induced phase transition* to a tetragonal phase. This will occur at (or perhaps after) the point at which the tetragonal phase becomes the lowest energy, *stable* phase due to the biasing affect of the electric field.

Of interest is the path taken by the polar vector, during this phase transition, starting from its zero-field position: i.e., the "polarization rotation path". In the original model[18], the rotation was predicted to proceed from the polar axis of the undistorted rhombohedral phase (e.g. $[111]_C$), via rotation in the $(1\bar{1}0)_C$ mirror plane of the M_A bridging monoclinic phase, to a final tetragonal phase ($[001]_C$). This is the same "R - M_A - T path" predicted by the *ab initio* calculations of Fu and Cohen (2000)[23] for the 0 K rhombohedral phase of barium titanate; it can be quite simply visualized with regard to figure 2.

Electric-field induced phase transitions in PMN-xPT and PZN-xPT

In this chapter, various electric-field induced phase transitions will be evidenced in PMN-xPT and PZN-xPT single crystals by macroscopic strain-field measurements and *in situ* optical microscopy (PLM). In each case, the polarization rotation path taken will be discussed.

II. ELECTRIC-FIELD INDUCED PHASE TRANSITION IN PZN-8PT

In the previous chapter, it was shown that in otherwise pseudo-orthorhombic, $[111]_C$-oriented PZN-8PT, a metastable, quasi-monodomain, pseudo-rhombohedral state could be irreversibly induced by poling the sample at sub-zero temperatures. The question remained, whether or not this rhombohedral phase could be induced, reversibly or otherwise, by the application of an electric field alone.

This was investigated by strain-field measurements.

Experimental

$[111]_C$-oriented (10 x 10 x 0.5 mm^3) plates of PZN-8PT and, for comparison PMN-28PT, were cut into four smaller pieces of area 5 x 5 mm^2. Two as-cut samples of each composition were then sputtered with gold electrodes. The two remaining samples were further ground and diamond polished to thicknesses above 200 microns and subsequently annealed to alleviate any residual stresses. The annealed samples were then sputtered with transparent indium tin oxide (ITO) electrodes, as described in chapter three.

All crystals were HTFC-poled under low field (200 V/mm). As discussed in the previous chapter, this induces a "O" phase in $[111]_C$-oriented PZN-8PT and a pseudo-rhombohedral phase in $[111]_C$-oriented PMN-28PT.

Room temperature permittivities were measured using an impedance analyzer (HP 4194), at 1 kHz, as described in chapter two.

Converse piezoelectric (strain-field) measurements were made using either using a linear variable differential transformer (LVDT), driven by a lock-in amplifier, or by a fiber-optic system (MTI-2000 Fotonic sensor); both methods are described fully in chapter two. Unipolar, sinusoidal fields were applied across the electrodes at low frequency (0.1 Hz).

In situ optical (PLM) micrographs were taken with the sample between crossed polarizers, as described in chapter five. The ITO-covered samples were mounted on a rotating stage and high voltage was applied via copper wires attached with silver paste.

Macroscopic strain-field loops

Figure 3 shows strain-field loops for a $[111]_C$-poled sample of PMN-28PT upon unipolar, electric-field cycling. Notably, the response is *hysteretic*, quite dissimilar to the anhysteretic strain-field response of domain-engineered, $[001]_C$-oriented "4R" PZN-4.5PT at low fields (see chapter one, fig. 3). Such hysteretic behavior is similar to that seen in soft PZT ceramics under unipolar fields[18]; there, hysteresis is the result of a significant *extrinsic* contribution from the motion of non-180° domain walls[28].

The origin of the hysteresis might be seen to be the same in "1R", $[111]_C$-poled PMN-28PT. As shown by others[29], only at high fields is the truly-monodomain 1R state stable; upon removal of this field, domain variants with polar vectors $<111>_C$ oriented away from the $[111]_C$ direction (70.5°, 109.5° and 180° domains) nucleate and grow in the crystal such that the crystal is no longer perfectly monodomain.

Upon application of the field, domain reorientation toward the monodomain 1R state occurs with a coercive field for switching of $E_C \approx 100$ V/mm [fig. 3(left)]. Motion of 70.5° and 109.5° domain walls is manifest as a hysteretic, extrinsic contribution to the strain-field response. Very similar has been observed in $[111]_C$-oriented rhombohedral PZN-4.5PT by Liu *et al.*[30]. At very high fields (around 3000 V/mm) the response becomes anhysteretic where the 1R monodomain state is approached [fig. 3(right)]. The gradient at

high field is $d_{33} \approx 70$ pm/V corresponding to the *collinear* piezoelectric response[31] of the rhombohedral phase; it is characteristically small. It is of the same order of magnitude as the corresponding value of 125 pm/V reported for rhombohedral PZN-4.5PT[30].

After repeated cycling, the dielectric constant and the loss tangent of the $[111]_C$ samples were reduced from 870 after HTFC poling to 560, indicating that the samples were better poled, approaching more closely the 1R monodomain state.

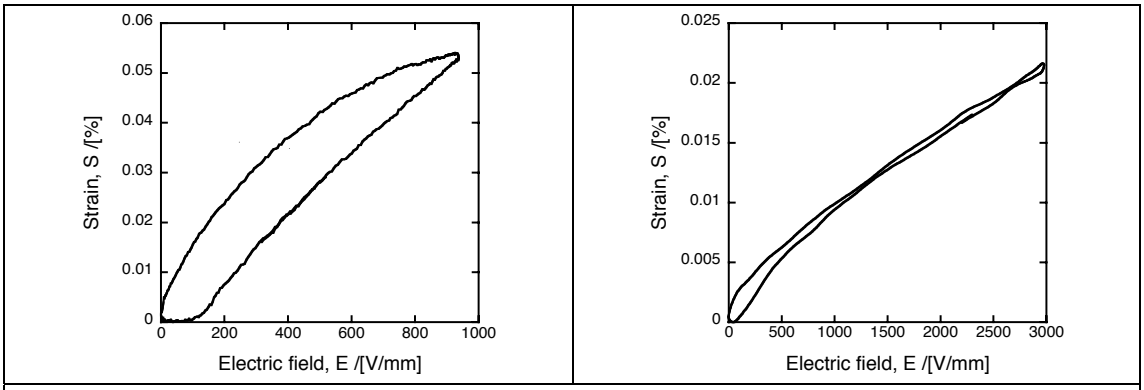

Fig. 3. Strain-field loops for a $[111]_C$-oriented sample of PMN-28PT, immediately after poling and upon unipolar cycling at electric fields E < 1000 V/mm (left) and E < 3000 V/mm (right). The loops were measured using an LVDT system at low frequency (0.1 Hz). Note that the hysteresis loops run anticlockwise.

In contrast, figure 4 shows the strain-field loop for an ITO-electroded, pseudo-orthorhombic, $[111]_C$-oriented sample of PZN-8PT for peak fields < 1400 V/mm. The difference between the behavior of "1R" PMN-28PT (fig. 3) and $[111]_C$-oriented, "O" PZN-8PT [fig. 4(left)] is clear: most significantly, the PZN-8PT sample shows a hysteretic "jump" in strain, characteristic of a *first order, electric-field induced phase transition*.

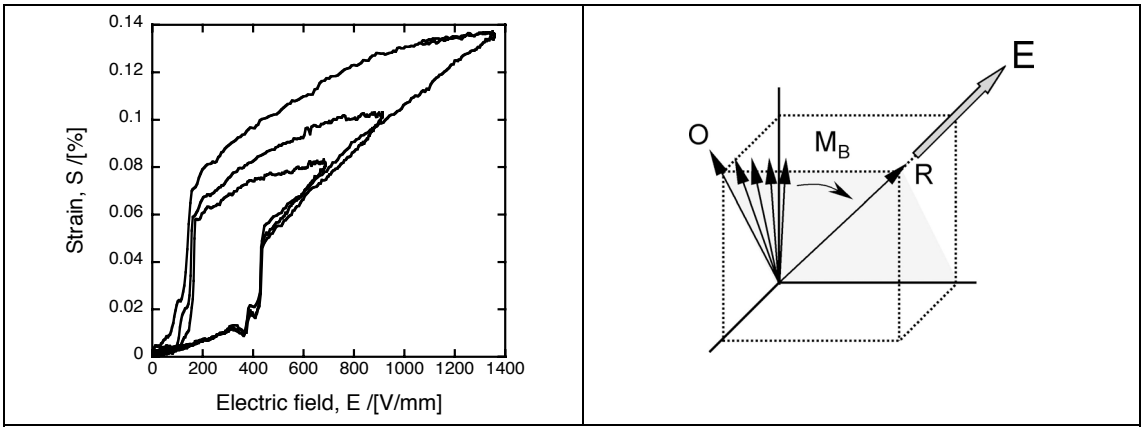

Fig. 4. (Left) Strain-field loop for a $[111]_C$-oriented pseudo-orthorhombic sample of PZN-8PT. The loop was taken using an LVDT system at room temperature upon application of a unipolar electric field at 0.1 Hz. A hysteretic, electric-field induced phase transition is evident. Note that the hysteresis loops run anticlockwise. (Right) The polarization rotation path is likely O - M_B - R.

As is the case for $[001]_C$-poled, "4R" PZN-4.5PT, the response at low fields is quasi-linear and anhysteretic; this will correspond to the piezoelectric

response of the "3O" domain engineered structure, $d_{33} \approx 430$ pm/V, calculated from the gradient of the initial, linear portion of the loop. Subsequently, at a threshold field $E_T \sim 400$ V/mm, there is large, vertical "jump" indicative of a (first-order) phase transition. Considering the results from the previous chapter, the induced phase is likely rhombohedral. Finally, the transition is followed by hysteretic behavior at higher fields resembling that of $[111]_C$-oriented PMN-28PT (fig. 3), where there is domain reorientation towards the monodomain 1R rhombohedral state.

In situ optical study

To be sure that the response was due to a phase transition (and not domain rearrangement, for example), polarized light microscopy (PLM) was used to confirm the presence of a high-field rhombohedral phase. Figure 5 shows a series of optical micrographs taken through crossed polarizers, upon *in situ* application of an electric field to the same, ITO-electroded sample of PZN-8PT. In this technique, most information about crystal structure can be attained by looking for directions of "extinction", as described in chapter five.

Under zero field, with the sample edges parallel to the polarizer (P) and analyzer (A) directions, the crystal was brightly birefringent as shown in figure 5(a). Moreover, the crystal showed complete extinction when the crystal was rotated in one direction $(30 \pm 90n)°$, where n is an integer. Such four-fold extinction is consistent with a zero-field, pseudo-orthorhombic phase.

As the field is increased, the same interference pattern was retained although the color observed was slightly shifted towards weaker birefringences [fig. 5(b)]. Then, just below the threshold field E_T, a new, characteristically extinct phase began to nucleate in one corner of the sample (c). As the field was increased over the threshold field E_T, there was nearly instantaneous growth of this new phase across the entire crystal (d). This high field phase (e) showed extinction at all angles, indeed consistent with a rhombohedral phase oriented along the $[111]_C$ direction (an *optic axis*). Upon removal of the field, the rhombohedral phase was stable until a field of around 100 V/mm; here the previous low-field phase began to nucleate and grow back out into the sample (f).

Finally, the initial nucleation of the rhombohedral phase in one corner of the sample is perhaps indicative of easier nucleation (due to surface effects) or of a lower local threshold field due to a composition gradient across the sample; this will be discussed below.

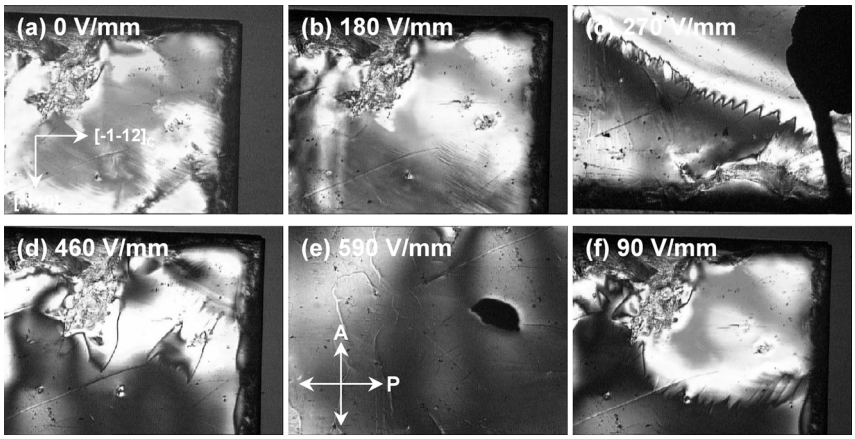

Fig. 5. Polarized light micrographs taken *in situ* of the electric-field induced phase transition from a pseudo-orthorhombic to a pseudo-rhombohedral phase on application of a field along the $[111]_C$ direction in PZN-8PT. Micrographs at zero field (a), increasing field (b-e) and decreasing field (f) are shown, where the field was ramped up and down manually in steps over a period of roughly 5 minutes. The corresponding strain-field loop for the same sample (at 0.1 Hz) is shown in figure 4. The sample orientation and the direction of polarizer and analyzer were the same for each image and are shown in (a) and (e), respectively.

Figure 6 shows the strain-field loop for another $[111]_C$-poled sample of PZN-8PT, this time electroded with gold, upon cycling to a much higher electric field > 3000 V/mm. The electric field induced transition is still evident, although this time at a smaller field $E_T \sim 250$ V/mm. Notably, there is a difference between the threshold fields measured for the two samples. This discrepancy in E_T could be, at least partially, due to a small variation in $PbTiO_3$ content.

After the phase transition, the loop is again somewhat hysteretic probably due to residual domain reorientation in the rhombohedral phase. However, anhysteretic behavior at higher fields suggests the sample approaches a monodomain (1R) state at fields > 3000 V/mm. The high-field gradient gives an estimate for d_{33} of 70 pm/V; this is very close to the values found for $[111]_C$-oriented PMN-28PT [fig. 3(right)].

Variation in threshold field

Apart from slight compositional variation, two other possible causes for the differing threshold fields noted above are the different electrode materials (gold and ITO) and the differing surface states, especially since the ITO-electroded sample had been previously diamond polished and annealed. Since nucleation of the new phase is most likely to occur heterogeneously at the crystal surface[32,33], the rough, as-cut, gold-electroded surface could facilitate the field-induced phase transition whereas the smooth, relaxed, ITO-electroded, less defective surface would not. The effect of the electrode material and the surface condition on the electric-field induced phase transition in these crystals, and indeed the nucleation and growth mechanism for the transition itself, would be worthy of further investigation.

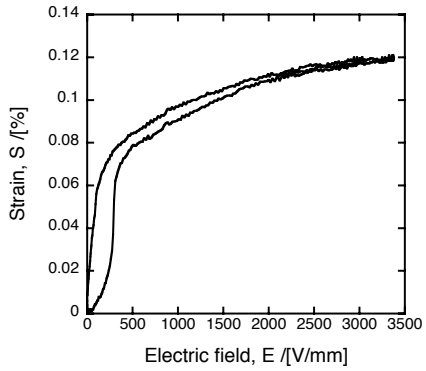

Fig. 6. Strain-field loop for a $[111]_C$-oriented sample of PZN-8PT after unipolar cycling to fields < 4000 V/mm. The strain was measured at a frequency of 0.1 Hz, using a fiber-optic system. Note that the hysteresis loop runs anticlockwise.

Reversible vs. irreversible phase transitions

Another point to note from figures 4 and 6 is that the field-induced phase transition is reversible overall: i.e. the "O" phase is retained upon removal of the field. In the previous chapter it was found that a pseudo-rhombohedral phase could be stabilized in a $[111]_C$-oriented sample of PZN-8PT by poling under 400 V/mm at sub-zero temperatures. The new results suggest that the low temperature is most important in "freezing-in" the *metastable* "R" phase.

We can also now explain the unusual $P(E)$ hysteresis loop measured for $[111]_C$-oriented PZN-8PT and shown in figure 19 of the last chapter. There, the same "O" - R electric-field induced phase transition is manifest as a discontinuity or "jump" in the polarization.

Polarization rotation path

Finally, it is interesting to speculate on the *polarization rotation path* taken under increasing field. Considering the limiting polarization directions of $[101]_C$ and $[111]_C$, and with regard to figure 2, it is likely that the simplest polarization rotation in the $(10\bar{1})_C$ plane will occur, i.e. via the M_B monoclinic phase. This O - M_B - R path is shown schematically in figure 4. Upon application of a field the polarization rotates *continuously* from the orthorhombic limiting direction, within the M_B plane, towards $[111]_C$. Then, at some critical field E_T there is a discontinuous "jump" of the polar vector, still within the same monoclinic plane, to its final $[111]_C$ position in the high-field, rhombohedral phase. This discontinuous, first order "jump" is shown by PLM to proceed by nucleation and growth of the new phase (fig. 5). Finally, in the notation defined in the last chapter, the phase transition can be described simply as one from a pseudo-orthorhombic phase to a rhombohedral phase: that is, "O" - R.

Although the M_B phase cannot be seen by PLM for the reason described in chapter five, the *in situ* observations are compatible with polarization rotation in the M_B plane. Furthermore, the O - M_B rotation and

discontinuous jump in strain to a rhombohedral phase have already been predicted for orthorhombic barium titanate by Bell, using phenomenological theory[27]. However, *in situ* diffraction studies are needed to confirm this path, which should be reconciled with the macroscopic strain-field loops and optical observations presented here.

Evidence of a first order phase transition

Importantly, the discontinuity or "jump" in strain, the accompanying hysteresis (fig. 4), and the nucleation and growth mechanism for the phase transition (fig. 5) are all characteristic of a *first order phase transition* between "O" (M_B) and R phases.

III. MORE ELECTRIC-FIELD INDUCED PHASE TRANSITIONS

Many other such electric-field induced phase transitions have been reported in PZN-xPT and PMN-xPT, evidenced both macroscopically, by measurement of polarization and strain, and microscopically by *in situ* high resolution (neutron or X-ray) diffraction (HRD) and polarized light microscopy (PLM). They are briefly reviewed here.

Fields applied along $[001]_C$

In unpoled PZN-4.5PT, upon application of an electric field along $[001]_C$, the transition R – M_A – T has indeed been observed both macroscopically[30,34] and by HRD[35]; as for the transition shown in figure 4, a "jump" in strain and hysteresis in the strain-electric field (S-E) loop suggests the rotation is not continuous, i.e. that is first order in character. The same path has been evidenced in PMN-24PT by PLM[36]. It might be more simply as "R" - T, although an undistorted R phase is retained upon removal of the field.

More complicated paths have been observed by HRD, for example in PZN-8PT[35,37,38], where the initially short-range ordered ("X-phase") crystal is transformed to the tetragonal phase via both M_A and M_C phases (and therefore rotations in *two* monoclinic planes and a "jump" between them). Upon removal of the field the pseudo-orthorhombic M_C phase[38] (or possibly orthorhombic phase[35]) is stable such that the overall rotation path is X – M_A – M_C – T – M_C, and therefore incompletely reversible. It could also be written X - "R" - "O" - T - "O".

The $[001]_C$-poled, or field cooled (FC), phase in PZN-8PT is also found[38] to be pseudo-orthorhombic M_C. Upon further field cycling, the polarization follows the path M_C – T in the $(010)_C$ monoclinic plane (fig. 2). This rotation is itself, in fact, hysteretic and first order like, as evidenced by hysteretic S-E loops[34,39].

Induced phase transition in $[001]_C$-oriented PZN-8PT

A strain-field (S-E) loop from a $[001]_C$-oriented sample of PZN-8PT is shown in figure 7. As observed elsewhere[20,38], the response is anhysteretic and linear before a large jump in strain at a critical threshold field, $E_T \sim 1200$ V/mm. There is a good qualitative agreement between this S-E loop and that from the *in situ* lattice constants measured by Ohwada *et al*.[38] Explicitly, at zero field the sample is pseudo-orthorhombic having either O or (slightly distorted) M_C symmetry. As the field is increased the polarization rotates continuously and reversibly in the $(010)_C$ mirror plane of the monoclinic phase before jumping, irreversibly, to a high-field, monodomain tetragonal state at E_T; this is shown schematically in fig. 7. On decreasing the field, the metastable tetragonal is retained until a second discontinuous jump, still within the $(010)_C$ plane, back to the M_C phase.

Notably, the gradient of the curve during the initial, continuous polarization rotation corresponds to a d_{33} of ~ 2000 pm/V. In contrast, the gradient corresponding to the collinear extension of the polarization vector in the high-field tetragonal phase is much smaller (670 pm/V).

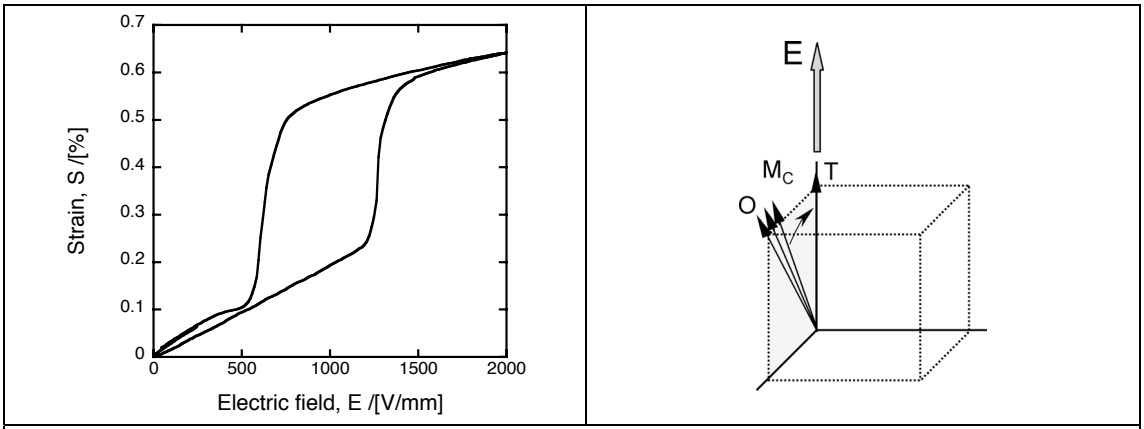

Fig. 7. (Left) Typical strain-field (S-E) loop for a $[001]_C$-oriented sample of PZN-8PT showing continuous rotation of the polarization within the $(010)_C$ plane of the monoclinic M_C phase before a hysteretic, discontinuous jump to the high-field tetragonal phase. The loop was measured using an LVDT system at a quasi-static frequency of 0.1 Hz. Note that the hysteresis loop runs anticlockwise. (Right) Schematic of the polarization rotation path.

Finally, in unpoled PMN-30PT the path R - M_A - M_C - T has been observed for an electric field applied along $[001]_C$; here, the pseudo-rhombohedral M_A phase is recovered upon removal of the field[22], and not the M_C phase as in PZN-8PT. The path might also be written as "R" - "O" - T for increasing field.

Fields applied along other directions

Fields applied in other directions lead to different polarization rotation paths. For PMN-30PT, with the field applied along $[101]_C$, the crystal undergoes a transition to an orthorhombic phase[26] R – M_B – O, which is characteristically anhysteretic[40]; it might more simply be written "R" - O. Upon

removal of the field the pseudo-rhombohedral M_B phase is retained[26]. Furthermore, as shown in section II, the reverse of this path ("O" - R) is observed in pseudo-orthorhombic PZN-8PT upon application of an electric field along the $[111]_C$ direction[39].

Electric-field induced phase transitions in simpler perovskites

Importantly, electric-field induced phase transitions are *not* unique to relaxor-ferroelectrics, even if the large resultant strains perhaps are. As noted in the introduction, they can generally be predicted for all ferroelectrics when sufficiently-high fields are applied in non-polar directions. In fact, in tetragonal $BaTiO_3$ at room temperature, application of an electric field along $[111]_C$ has been shown to induce a rhombohedral phase, via an intermediate (pseudo-) orthorhombic phase[41]. Here, the strain resulting from this T - "O" - R transition was of the order of 0.1%; this compares to around 0.6% for the "O" - T transition in $[001]_C$-oriented PZN-8PT (figure 7). The same transition sequence was later replicated in the phenomenological Landau-Ginzburg-Devonshire (LGD) calculations of Bell[27].

IV. EFFECT OF TEMPERATURE ON ELECTRIC FIELD-INDUCED PHASE TRANSITIONS

In the previous chapter, we drew up (*T*-*x*) phase diagrams for $[001]_C$-poled PMN-xPT and PZN-xPT at fixed (zero) electric field. Notably, FE-FE phase transition temperatures (T_{FE-FE}) were found to be strongly affected by non-zero fields. Alternatively, we could fix the temperature and investigate the various phase transitions that occur in samples of a given composition under an applied field (again, say, along the $[001]_C$ direction); we would expect some variation in threshold field with temperature. Finally, we could use this data to draw up another phase diagram showing, for a fixed composition, the phase stability under differing temperatures and electric fields.

Such electric-field vs. temperature (*E*-*T*) phase diagrams will be drawn up in this section for $[001]_C$-oriented samples of PMN-xPT and PZN-xPT. These diagrams will be derived from strain-field measurements, like that in figure 7, at a range of temperatures. As will be apparent, such measurements can give good insight into the behavior of poled PMN-xPT and PZN-xPT at the morphotropic phase boundary.

Experimental

The crystals used for converse (strain-field) measurements had compositions PZN-5PT, PZN-6.5PT, PZN-8.5PT, PMN-25PT, PMN-30.5PT and PMN-31PT. Samples of nominal dimensions 5 x 5 x 0.5 mm^3 were again cut from $[001]_C$-oriented plates and gold electrodes were sputtered onto the two largest $(001)_C$ faces. All strain-field measurements were made using the Fotonic sensor described in chapter two at temperatures between 25 and

150°C. Unipolar, sinusoidal fields up to 1500 V/mm were applied at low frequency (1 Hz). Samples were SF-poled (chapter five) prior to measurement by application of 1000 V/mm for 15 minutes at room temperature. The electric field was continuously cycled for at least 30 seconds after stabilization of the temperature before any data was recorded.

After strain-field measurements, the permittivities of the poled samples were measured as a function of temperature while heating at 2°C/min. The compositions of the crystals were determined by comparison of T_d to the phase diagrams drawn up in chapter four.

Strain-field measurements

Strain-field (S-E) loops at a variety of temperatures between 25°C and 100°C, for maximum fields up 1600 V/mm, are shown in figures 8 to 12 for $[001]_C$-oriented PZN-5PT, PZN-6.5PT, PZN-8.5PT, PMN-25PT, PMN-30.5PT, and PMN-31PT.

The S-E loop taken at 30°C for PZN-5PT (figure 8) is essentially anhysteretic and quasi-linear, characteristic of a "4R" domain-engineered state. The gradient of the loop ($d_{33} = dS_3 / dE_3$), taken as a tangent to the curve at zero field, is 1830 pm/V. The response was similar at all temperatures up to 50°C; d_{33} increased to 2220 pm/V over this range.

At 55 °C, however, the response became hysteretic with the loop opening up at a threshold field $E_{T(1)}$ of around 1100 V/mm. We define this threshold field as the point at which the gradient of the lower, *rising-field* portion of the loop changes sharply (taken at the point of intersection between two tangents, as shown explicitly for the curve at 90°C). At 65°C, the hysteretic section is completely terminated by two linear segments, at high and low fields. The two discontinuous "jumps" or kinks in strain, bounding the hysteresis upon increasing and decreasing field, are now clearly visible. Furthermore, $E_{T(1)}$ has decreased to 740 V/mm and the zero-field piezoelectric coefficient d_{33} has increased to 2490 pm/V. The gradient of the upper linear part of the loop is 2000 pm/V, lower than that of the lower field portion.

As an aside we note that we could define two threshold fields for this transition, one on increasing field ($E_T^{increase}$) and one on decreasing field ($E_T^{decrease}$), and therefore an "*electrical hysteresis*" ΔE_T ($= E_T^{increase} - E_T^{decrease}$). This is completely analogous to the "thermal hysteresis" ($\Delta T_{FE-FE} = T_{FE-FE}^{heat} - T_{FE-FE}^{cool}$) shown by temperature-induced phase transitions, as discussed in the last chapter. As discussed in section II, such hysteresis is evidence of *first-order* phase transitions.

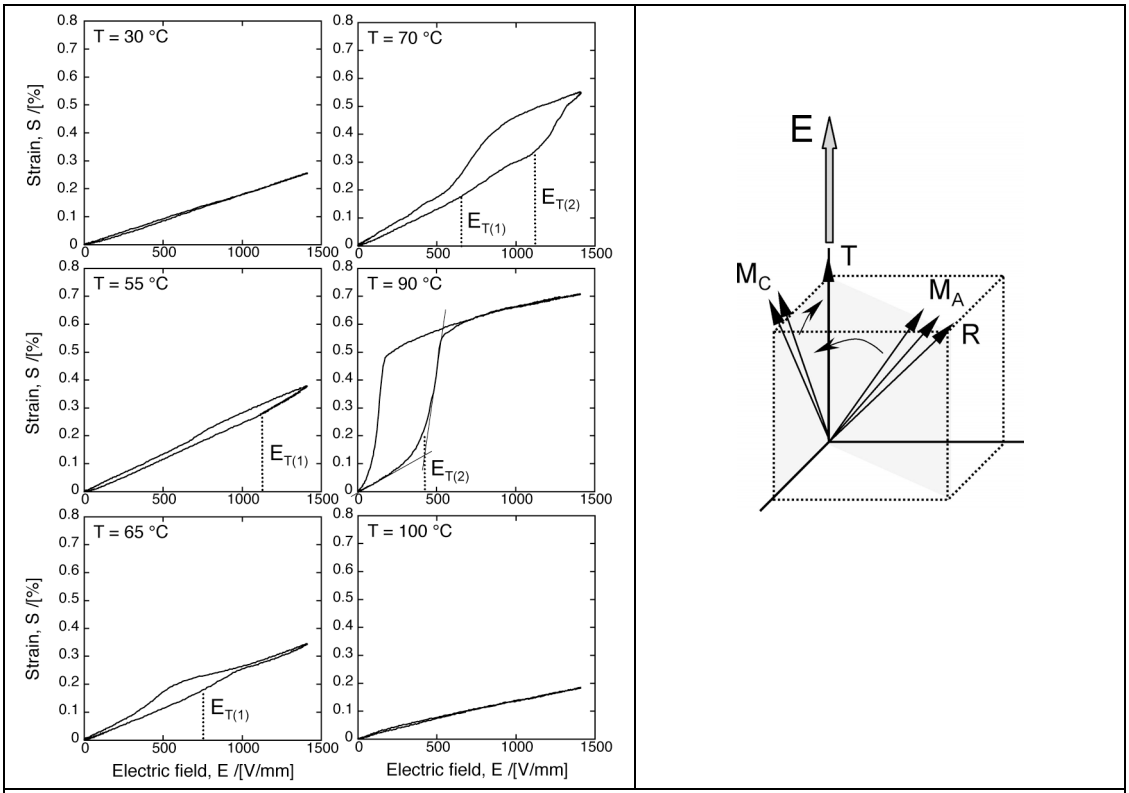

Fig. 8. (Left) Series of converse piezoelectric (strain-electric field) loops for $[001]_C$-oriented PZN-5PT, at varying temperatures between 30 °C and 100 °C. The threshold fields (upon increasing field) for the two electric field induced phase transitions, $E_{T(1)}$ and $E_{T(2)}$, are indicated by dotted lines. In each case they are derived from a tangent-intersection construction as shown explicitly for T = 90°C. (Right) Proposed polarization path taken at 70°C. Discontinuous "jumps" in strain correspond to "jumps" of the polar vector, first, between M_A and M_C monoclinic planes and, then, within the M_C monoclinic plane.

At 70 °C, the characteristic kink corresponding to $E_{T(1)}$ can still be weakly seen at a field of 630 V/mm. However, there is now a second discontinuity in strain, occurring after the first, at a threshold field $E_{T(2)}$ of around 1100 V/mm. An even bigger hysteresis is observed, and the accompanying strain is higher, reaching around 0.55%.

At 90 °C, the first discontinuity can no longer be seen, though the second hysteresis can be seen to terminate completely. The threshold field for the second transition $E_{T(2)}$ has dropped to around 400 V/mm. Again, the high field portion of the loop after the hysteresis is linear. The gradient is 1160 pm/V at maximum field compared to 3100 pm/V before the transition at zero field.

Finally, at 100 °C, no discontinuity can be seen. The response is again anhysteretic and linear with a gradient d_{33} (at high field) of 1190 pm/V.

Two sequential first-order phase transitions

Comparing to the results reviewed in section III, the behavior can be attributed to *two* sequential electric-field induced phase transitions, as follows.

At 30 °C, according to the phase diagram plotted in the last chapter, $[001]_C$-poled PZN-5PT is "R" at zero field. Initial application of an electric field along $[001]_C$ will lead to a rotation of the polar vector away from the $[111]_C$ direction within the $(1\bar{1}0)_C$ M_A plane; this is shown in figure 8. Even if the crystal was rhombohedral in its as-poled, zero-field state, application of an electric field along $[001]_C$ and the resultant piezoelectric[42] distortion will break the rhombohedral symmetry and result in M_A symmetry. Upon further field cycling, below a critical field $E_{T(1)}$, the polarization rotation *within the M_A plane* is continuous, reversible and anhysteretic.

Since no domain wall motion is expected due to the stable, domain engineered configuration[18], the two discontinuities in the strain-field loops at higher temperatures reflect discontinuities in the lattice strain[20] and, correspondingly, discontinuous rotations of the polar vector in its path towards $[001]_C$. As noted, discontinuous strain and accompanying hysteresis are evidence of a *first order*, electric field induced phase transition (EFIPT). In contrast, the anhysteretic, closed sections of the loops observed before such transitions suggest continuous polarization rotations *within a single monoclinic plane*. The gradient of each linear section represents the piezoelectric coefficient d_{33} associated with the corresponding rotation and is essentially constant over that field range.

The first EFIPT, observed above 55 °C, is gentle, involving a relatively small jump in strain and only a small decrease in gradient of the strain-field loop. According to HRD work presented elsewhere[22], the first transition will correspond to a jump from the $(1\bar{1}0)_C$ to the $(010)_C$ monoclinic plane, therefore representing a transition from pseudo-rhombohedral M_A to pseudo-orthorhombic M_C symmetry. The gradient of the low field section, d_{33} = 2490 pm/V, corresponds to rotation in the M_A plane; the smaller gradient of the second linear portion, d_{33} = 2000 pm/V, represents a slightly harder polarization rotation in the M_C plane.

The second EFIPT involves noticeably more severe jump in strains. By comparison to HRD results for PZN-8PT[38], we assign this transition to one between M_C and the final tetragonal phase. At fields just before the transition, and larger than $E_{T(1)}$, there is a continuous polarization rotation in the M_C plane. At $E_{T(2)}$, however, there is a second discontinuous jump in strain, within the M_C plane, to a T phase; the jumps in strain and hysteresis again suggest a first order transition.

Thus, the overall the polarization rotation path is "R" - "O" - T and involves two first order-like, discontinuous phase transitions, one *between* monoclinic planes (M_A - M_C), and one *within* the M_C plane to the tetragonal phase. It is shown schematically in figure 8. The strain-field loops for PZN-6.5PT (fig. 9), PMN-30.5PT and PMN-31PT (fig. 12) follow the same path. The two EFIPTs can be clearly seen within the same strain-field loop for PMN-30.5PT [fig. 12(left), 55°C] and PMN-31PT [fig. 12(right), 45°C].

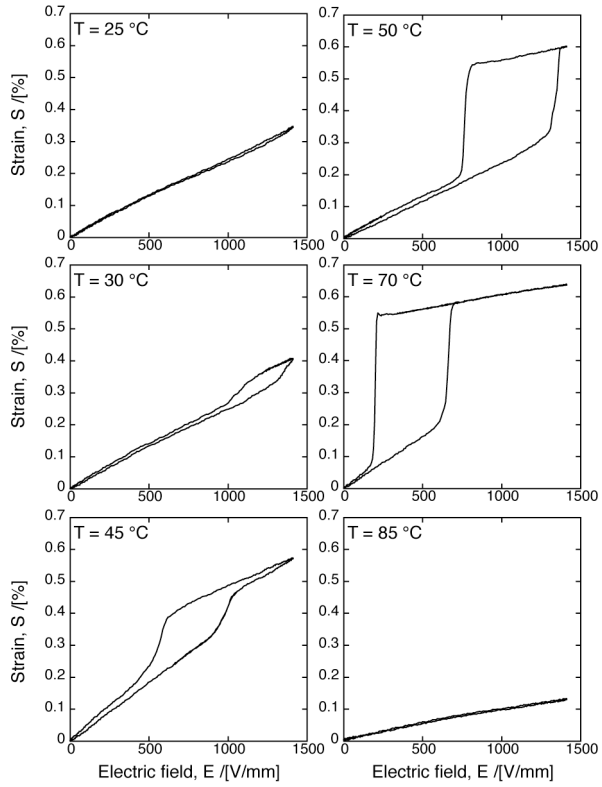

Fig. 9. Series of converse piezoelectric (strain-electric field) loops for $[001]_C$-oriented PZN-6.5PT, at varying temperatures between 25 °C and 85 °C.

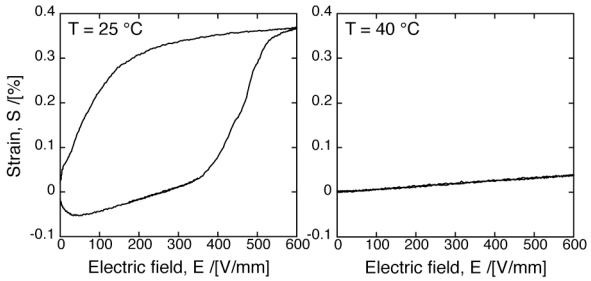

Fig. 10. Converse piezoelectric (strain-electric field) loops for $[001]_C$-oriented PZN-8.5PT, at 25 °C and 40 °C.

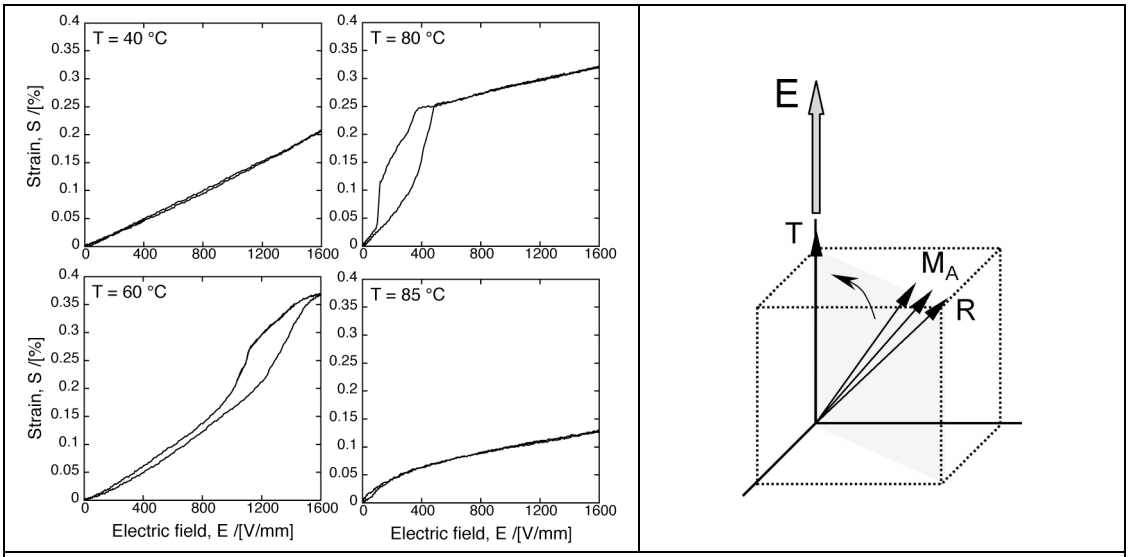

Fig. 11. (Left) Series of converse piezoelectric (strain-electric field) loops for $[001]_C$-oriented PMN-25PT, at varying temperatures between 40 °C and 85 °C. (Right) Proposed polarization rotation path.

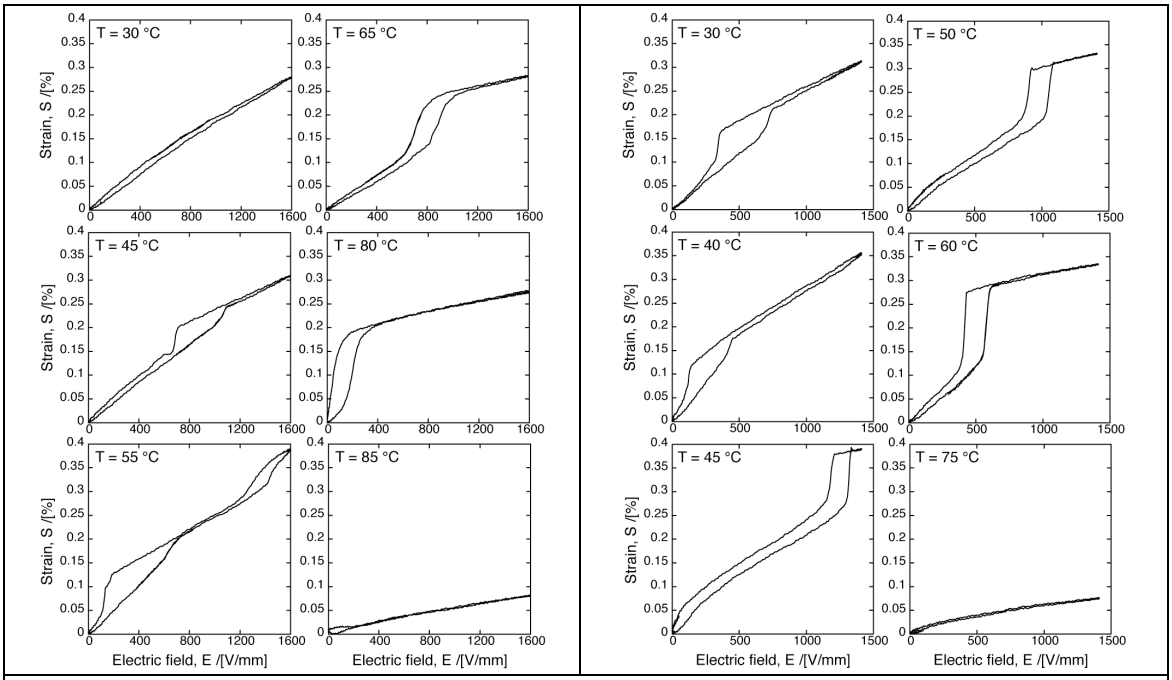

Fig. 12. Series of converse piezoelectric (strain-electric field) loops for $[001]_C$-oriented PMN-30.5PT (left) and PMN-31PT (right), at varying temperatures between 30 °C and 85 °C.

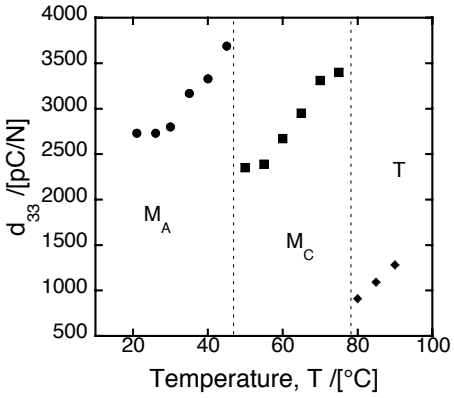

Fig. 13. d_{33} as a function of temperature for $[001]_C$-oriented PZN-6.5PT derived from the strain-field (S-E) measurements shown partially in figure 9. d_{33} is taken as the gradient of the S-E loop at zero field. At high temperatures in the tetragonal phase d_{33} corresponds to the *collinear extension* of the polar vector. At lower temperatures, d_{33} corresponds to *rotation* in either the M_A or M_C monoclinic plane, as marked.

The zero-field gradient d_{33} for PZN-6.5PT is shown as a function of temperature in figure 13. For different temperature ranges, the zero-field piezoelectric coefficients correspond to polarization rotations in the M_A or M_C monoclinic planes, as marked on the graph, or to collinear polarization extension (chapter ten) in the tetragonal phase T. In each case, d_{33} increases with increasing temperature especially close to temperature induced phase transitions where $E_{T(1)}$ and $E_{T(2)}$ decrease to zero. The largest d_{33} is found for the M_A rotation; d_{33} is slightly smaller for the M_C rotation though it is still above 2000 pm/V. In the tetragonal phase, where application of the field along the polar $[001]_C$ leads to a uniquely collinear[43] piezoelectric effect, d_{33} is characteristically much weaker. The reasons for this will be discussed in chapter ten.

Single first-order phase transitions

In PZN-8.5PT the behavior is different, as shown in figure 10. At 25°C the strain-field loop is already hysteretic; there is no linear portion of the curve and the initial negative strain observed on increasing field shows that the sample is at some metastable point within the hysteresis loop. According to the phase diagram in chapter six, $[001]_C$-poled PZN-8.5PT is pseudo-orthorhombic (M_C or O) at room temperature, and very close in energy to the neighboring tetragonal phase. Here, therefore, the hysteresis is due to the first-order (M_C - T) phase transition, between pseudo-orthorhombic and tetragonal phases. The threshold field at 25°C is small, $E_{T(2)}$ = 380 V/mm, reflecting the near degeneracy of the M_C and T phases in PZN-8.5PT at room temperature. At 40 °C, the sample is tetragonal at zero field.

The response of PMN-25PT, deep in the rhombohedral phase field (chapter six)[44,45], is again different (see figure 11). In this sample, only one transition was observed, and at much higher temperatures and fields. Since the induced phase is characteristically tetragonal (with a weak d_{33} = 710 pm/V at 80 °C), it seems that there is a direct EFIPT from a pseudo-rhombohedral to a tetragonal phase, via a discontinuous, first-order like rotation in the M_A monoclinic plane. This is shown schematically in figure 11. The same path has been observed in both rhombohedral PZN-4.5PT by macroscopic strain-field measurements[34] and HRD[35] and in rhombohedral PMN-24PT by PLM[36]. There is no evidence of a transition to the second, M_C monoclinic plane in this composition.

Diffuse phase transitions

As an aside, more can be said about the nature of the phase transition in the different compositions, especially in terms of the relative "diffuseness" of the transition. For example, comparing the transition to a tetragonal phase in PZN-5PT (fig. 8) and PZN-6.5PT (fig. 9) it is seemingly more abrupt in the latter case. Moreover, comparing the transition to a tetragonal phase in PMN-25PT (fig. 11) and PMN-31PT [fig. 12(right)], it is certainly better defined in the higher PT-content composition. This fits well with theoretical work by Bell (using PZT as a model system) which shows that the presence of random fields leads to more "diffuse" electric-field phase transitions[46]. That is, random fields can be seen to result in inhomogeneity of the threshold field for the transition E_T. As discussed in chapter four, random fields can be expected in PMN-xPT and PZN-xPT with lower PT-contents. In higher PT-content crystals, EFIPTs are generally sharper.

***E-T* phase diagrams**

Importantly, both fields $E_{T(1)}$ and $E_{T(2)}$ are functions of temperature. If the threshold field for one EFIPT is higher than the maximum field applied, it will not occur. If the threshold field for an EFIPT becomes zero at higher temperatures, i.e. if a temperature induced phase transition to a new ground state takes place, it will also not appear. Therefore, to summarize the results, electric field vs. temperature (*E*-*T*) phase diagrams were constructed based on plots of the threshold fields $E_{T(1)}$ and $E_{T(2)}$ as a function of temperature; they show the various phase stabilities of each composition, after poling, for electric fields applied along $[001]_C$.

The E-T phase diagrams are shown in figure 14 for PMN-xPT (x = 0.25, 0.305, 0.31; a-c respectively) and PZN-xPT (x = 0.05, 0.065, 0.085; d-f). Where the threshold field was difficult to judge from the strain-field curves, i.e. where the threshold field was close to zero or where the two phase transitions occurred very close together, they have been omitted. The phase fields are designated M_A, M_C and T and refer to the symmetry under non-zero fields applied along the $[001]_C$ direction.

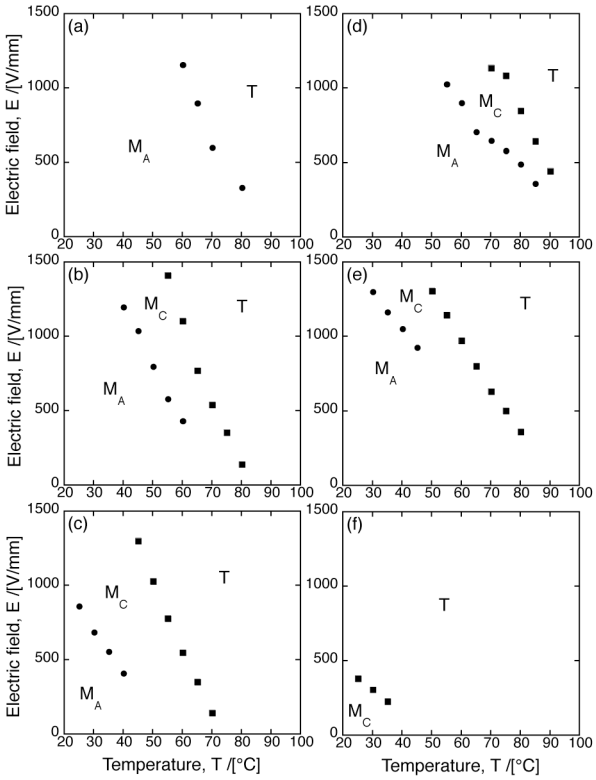

Fig. 14. Electric field-temperature phase diagrams, derived from the strain-field loops shown in figures 8 - 13, for (a) PMN-25PT, (b) PMN-30.5PT, (c) PMN-31PT, (d) PZN-5PT, (e) PZN-6.5PT, and (f) PZN-8.5PT. The phase fields are marked with the symmetry of the phase under finite field.

Various trends can be seen from the graphs. Firstly, with increasing temperature and/or electric field along $[001]_C$ the sequence of phases is generally M_A - M_C - T. The threshold temperatures and fields for the M_A - M_C and M_C - T transitions in PMN-30.5PT agree qualitatively well with those found by Bai *et al..* by *in situ* x-ray diffraction upon application of an electric field to PMN-30PT[22].

Secondly, the pseudo-orthorhombic M_C phase is favored by higher fields applied along $[001]_C$: notice the widening of the M_C "triangle" in figures 14(b) - (e). This might be expected from the simple energetic arguments laid out in chapter six since the angle between the polar vector and the applied field is lower in the pseudo-orthorhombic phase ($\theta < 45°$) compared to the pseudo-rhombohedral phase ($\theta < 54.7°$). Moreover, the tetragonal phase is favored over the other two by a field applied along $[001]_C$ ($\theta = 0°$).

Moreover, the pseudo-orthorhombic phase is also favored by higher PT contents. The M_C triangle noticeable decreases in width on lowering PT content [figures (c) - (b)] and is eventually "squeezed out" at very low PT contents. In PMN-25PT it no longer appears, and in PZN-5PT it is very narrow at low fields. As reported elsewhere, no M_C phase is observed at any field level in PZN-4.5PT[35]. Measurements by Ren *et al..* on PZN-4.5PT evidence only one first-order like EFIPT[34] upon application of an electric field along $[001]_C$ at temperatures between 25°C and 105 °C. This all suggests that the M_C triangle is also squeezed out in PZN-4.5PT, as observed here for PMN-25PT, and that the M_A - T path is followed. However, it has also been suggested that a small range of M_C phase stability persists to even lower PT

contents[47], although perhaps the phase field becomes so small as to be experimentally insignificant.

Finally, at a high enough PT content, the M_C triangle "sweeps out" to lower temperatures, replacing the (nominally zero-field) "R" phase as it does so. In PZN-8.5PT at room temperature, only the M_C - T EFIPT is observed.

Summary

Such E-T phase diagrams will be helpful in determining the electrical and thermal stability of PZN-xPT and PMN-xPT single crystals for use in high voltage applications. They also highlight the complex competition between pseudo-rhombohedral, pseudo-orthorhombic and tetragonal phases at ambient temperatures close to the morphotropic phase boundaries. Notably, phase transitions between "R", "O" and T phases can be induced by small changes in two thermodynamic parameters, temperature and electric field.

V. NATURE OF THE MONOCLINIC PHASE

Finally, it is worth discussing the nature of the pseudo-rhombohedral and pseudo-orthorhombic phases at finite, and zero, fields.

Extent of the monoclinic distortions

Firstly, we should perhaps confirm if the description of the M_A and M_C phases that appear under finite fields as "pseudo-rhombohedral" and "pseudo-orthorhombic" phases, respectively, is valid. That is, we should try to quantify how much the polar vectors are rotated away from the $<111>_C$ and $<101>_C$ limiting directions just before the first-order phase transitions that occur at the threshold field E_T.

This has been done for the room temperature "O" to "T" transition in $[001]_C$-oriented PZN-8PT shown in figure 7. First, we assume a very simple, geometrical model for the polar vector as having a fixed length; this is shown in figure 15. We also assume the polarization P_S is proportional to this length. Finally, we assume that the polar vector in the as-poled crystal lies very close to the $[101]_C$ limiting direction at zero-field. That is, the angular distortion is small, say, less than 1°. Indeed, any distortion is so small that both orthorhombic and M_C symmetries have been reported by HRD in $[001]_C$-poled PZN-8PT[24].

In chapter six, the polarization in $[001]_C$-oriented PZN-8PT was found to be 0.28 C/m^2; it was also shown to be (very close to) the component of P_S resolved along the non-polar $[001]_C$ direction: it is marked as such on figure 15. Measurements of polarization as a function of unipolar field[48], evidencing the same EFIPT, give the difference between the polarization at E_T (1200 V/mm) and zero-field to be around 0.05 C/m^2. This is also shown in figure 15.

Using these values, and by simple trigonometry, we calculate a polarization rotation $\alpha \approx 11°$.

We might conclude that, just before the first-order phase transition at E_T, the crystal is still pseudo-orthorhombic (rather than "pseudo-tetragonal", for example). We are justified in expressing this phase transition in terms of a first order phase transition between a pseudo-orthorhombic and a tetragonal phase.

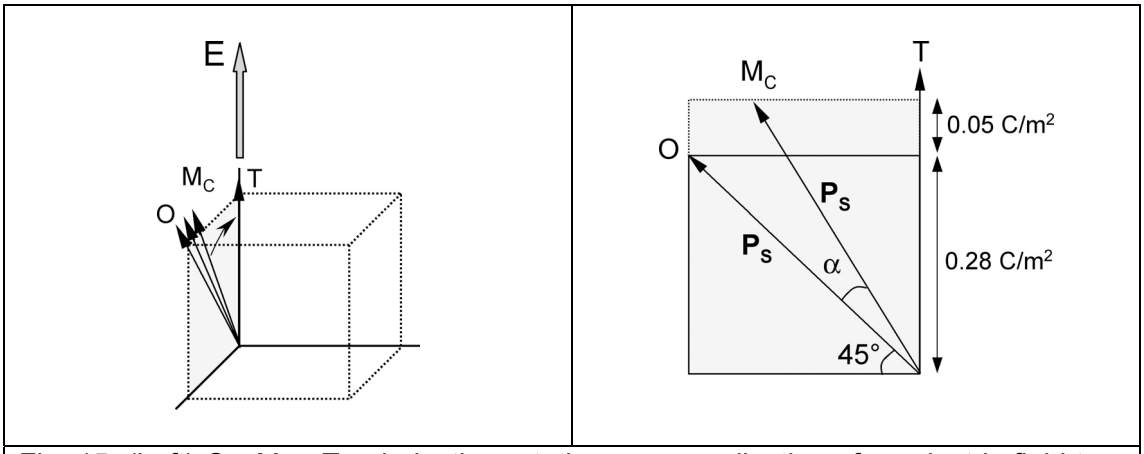

Fig. 15. (Left) O - M_C - T polarization rotation upon application of an electric field to a "O" crystal along $[001]_C$. (Right) Calculation of the (maximum) angular M_C distortion at the threshold field E_T just before the first-order "jump" of the polar vector to the tetragonal phase.

Notably, for the "R" - T transition that occurs in PZN-4.5PT upon application of a field along $[001]_C$, Cross and Hana[49] have derived (phenomenologically) a maximum angle of $\alpha \approx 25°$ at E_T for rotation of the polar vector in the M_A plane. Larger rotations might be expected at lower PT contents where the "R", "O" and T phases are further apart in energy. Although this is not a "slight" distortion, the crystal is still "pseudo-rhombohedral" rather than "pseudo-tetragonal" before the phase transition.

Zero-field monoclinic phases?

Next, we turn our attention to the question of the zero-field phase. That is, although M_A and M_C symmetries are clearly observed under electric field, do they correspond to true, zero-field phases?

In terms of a purely classical, 6th order LGD expansion of the free energy, monoclinic phases do not exist at zero stress or zero electric field. Only the rhombohedral, orthorhombic and tetragonal phases are generated, stably or metastably, in the phenomenological theories of barium titanate[27,50] and PZT[51] with polar vectors along the $<111>_C$, $<101>_C$ or $<001>_C$ directions, respectively. Application of an electric field along the polar direction of either phase itself can only lead to the elongation of the polar vector ***P*** (the collinear piezoelectric effect), which is characteristically weak[52].

However, upon application of an electric field along a $<111>_C$, $<101>_C$ or $<001>_C$ direction away from the polar direction of the respective R, O or T phase, the polarization vector will rotate towards that direction. This is the

physical meaning of the piezoelectric shear coefficients, as will be discussed in chapter ten. Most importantly, this polarization rotation will break the symmetry of the higher symmetry ferroelectric phase[42]. As described previously, if a field is applied along $[001]_C$ to a rhombohedral crystal the $[111]_C$ polar vector will rotate, within the M_A monoclinic phase, towards $[001]_C$. The rhombohedral symmetry is immediately broken and the sole remaining symmetry element will be the M_A monoclinic plane bridging the $[111]_C$ and $[001]_C$ directions. Critically, as pointed out by Kisi *et al.*, this can simply be regarded as a piezoelectric distortion, and not in fact a phase transition[42].

From this point of view, the induced M_A phase is not a *true* phase[53] and should be better labeled a monoclinic "distortion". All M_A, M_B and M_C monoclinic *distortions* become possible by permutating the three R, O and T ground states with the three $<111>_C$, $<101>_C$ and $<001>_C$ directions of applied field[27] within the framework of 6th order LGD theory.

The question therefore arises, whether or not the rotation that occurs at *infinitesimally* small electric fields (or stresses) corresponds to a true phase transition. This can be examined by considering the *order* of the phase transition. As discussed in section I, second-order transitions are characterized by a continuous change in the order parameter (polarization $\boldsymbol{P_s}$ in the case of ferroelectrics) whereas first-order phase transitions involve a discontinuity. First-order transitions are characteristically hysteretic due to the coexistence of metastable phases; in contrast, second-order transitions should be thermodynamically anhysteretic.

Forrester *et al.*[54] and Sergienko *et al.*[16] point out that, according to the group-theory based Landau condition[55], phase transitions between the rhombohedral phase and the M_A, M_B and M_C monoclinic phases cannot be second order (whereas O $\leftrightarrow$ M_B, O $\leftrightarrow$ M_C, T $\leftrightarrow$ M_C and T $\leftrightarrow$ M_A transitions can be first or second order[16]). There is no general argument that forbids a first order phase transition[16]. It follows that there can be no continuous rotation of the polar vector from the R to the M_A *phase*; where there is a continuous rotation, evidenced for example by the absence of hysteresis, the field-induced structure should perhaps be described as a monoclinic *distortion*.

Confusingly, in the first principles calculations of Bellaiche *et al.* for rhombohedral PZT near the MPB, application of an electric field along $[001]_C$ does lead to a discontinuous jump in strain between R and M_A phases indicating a true, first-order phase transition[25]. However, it was not reported in the first principles calculations of Fu and Cohen for low temperature, rhombohedral barium titanate for the same applied field direction, where the same R - M_A rotation is predicted[23]. In the *in situ* HRD work of Bai *et al.* on $[001]_C$-oriented PMN-30PT[22], a R - M_A transition is discussed, although the nature of the evolution of the lattice constant through the transition (whether continuous or discontinuous) is not presented. Similar work by the same authors on unpoled, $[101]_C$-oriented PMN-30PT[26] does not show clearly the nature of the corresponding R - M_B transition at low fields.

When higher (eighth) order terms are added to the LGD expansion, zero field monoclinic phases are predicted at zero field by phenomenological theory[56]. Experimentally, both M_A(M_B) and M_C monoclinic phases have been found to exist in as-grown, unpoled samples of PMN-xPT, at zero field, by both HRD[57] and PLM[45,58,59] (see also chapter five). In some studies the

undistorted rhombohedral phase is observed only at lower PT contents ($x \leq 0.26$)[57]. Furthermore, monoclinic phases have also been found to exist in samples after removal of an electrical field, in the as-poled condition. As discussed in chapter six, after removal of a field applied along $[001]_C$ to initially rhombohedral PMN-30PT, the M_A phase is stable[22]; when the field is applied along $[101]_C$ and removed the M_B phase remains[26].

Effect of residual fields and stresses

The question remains, whether or not these monoclinic phases are the true *zero-field* phases near the MPB in PMN-xPT and PZN-xPT and, if so, whether their presence is directly responsible for the usefully large piezoelectric response, as is often assumed.

Suggestions have been made that the presence of the monoclinic phase after high field poling is due to remnant tetragonal domains which strain the rhombohedral regions[48]. That is, residual stresses due to the coexistence of non-elastically matched phases are responsible for the monoclinic distortion. The monoclinic distortion as a "trapped metastable phase" has also been suggested[60]. Furthermore, a theoretical treatment[61] has shown that the presence of a monoclinic plane has an important role in relieving stress in samples where two phases coexist together in the same sample. As discussed in chapter five, such two phase coexistence is often observed in unpoled PMN-xPT and PZN-xPT near the MPB[45,62,63].

As well as internal stresses, internal electric fields might also be responsible for the presence of monoclinic phases in the poled state. The presence of residual, internal bias fields was postulated in chapter six. The presence of a "memory" has been evidenced in $[001]_C$-poled PZN-8PT, possibly due to the alignment of defect dipoles[64]. Such residual fields would also contribute to a remnant monoclinic distortion. Moreover, the presence of charged domain walls[65] in the domain engineered structure (chapter five), where uncompensated by mobile point charges, will also lead to internal fields.

Interestingly, Jin *et al.* have also proposed a model for the monoclinic and orthorhombic phases in PMN-xPT and PZN-xPT as *symmetry adaptive phases*, built up of tetragonal or rhombohedral microdomains[66]; here the domain-averaged symmetry can be orthorhombic or monoclinic depending on the nanoscale twinning of the domains.

Moreover, all the above discussion also ignores the background relaxor nature of PMN-xPT and PZN-xPT, and the presence of random fields. In the related solid solution PZT, the need for B-site disorder in stabilizing the M_A phase at the MPB has been discussed[67,68]. Moreover, in the solid solution $(1-x)PbSc_{1/2}Nb_{1/2}O_3$-$xPbTiO_3$ [PSN-xPT], which exhibits a MPB similar to PMN-xPT and PZN-xPT, first principles calculations suggest that the M_C monoclinic plane is promoted by the presence of nanoscale, chemically-ordered regions at higher PT contents, whereas the M_A phase is due to homogeneous B-site disorder[69].

Monoclinic distortions will also occur in classical perovskites, as shown phenomenologically for barium titanate[27]. That is, polarization rotation is not unique to relaxor-ferroelectrics. However, zero-field monoclinic phases are

not observed in barium titanate and potassium niobate, although they are in PZT near the morphotropic phase boundary[70]. As mentioned section III, application of a field along $[111]_C$ to the tetragonal phase of barium titanate results in the polarization path T - R via two intermediate monoclinic symmetry phases[27,41].

Importantly, as will be shown in chapter ten, polarization rotation will be much weaker in barium titanate than in PMN-xPT and PZN-xPT where the piezoelectric shear coefficient (d_{15}) is much smaller. Importantly, the size of *all* piezoelectric coefficients is much smaller in barium titanate and other classical perovskites[50] than in PZT, and especially PMN-xPT and PZN-xPT; for example PZN-xPT and PMN-xPT are around nine times softer elastically than other piezoelectric perovskites[42].

As a consequence, the monoclinic distortion itself will be much smaller in the simpler perovskites and therefore more difficult to detect. Therefore, the question remains, are the monoclinic phases really responsible for the large piezoelectric response in PMN-xPT and PZN-xPT? Or, alternatively, might the presence of the monoclinic phases in PZN-xPT and PMN-xPT under zero external field be due to their large piezoelectric response to small perturbing fields, including residual stresses, and internal electrical bias fields due to defects, charged domain walls and so forth? Critically, better *in situ* diffraction evidence of the R - M_A transition is needed to establish whether these transitions really corresponds to a true, first-order phase transition or rather a piezoelectric distortion. Unfortunately, this will be difficult experimentally due to the witheringly small lattice distortions involved.

Importance of polarization rotation

Irrespective of the zero-field phase and whether M_A and M_C observed are true phases or field-distorted versions of a higher symmetry phase, it is certainly the polarization rotations in the M_A and M_C monoclinic planes that are responsible for the giant piezoelectric response of PMN-xPT and PZN-xPT single crystals when a field is applied along the $[001]_C$ direction. As will be shown in chapter ten, these rotations are related to large shear coefficients, d_{15} and d_{24}, and the proximity of phase transitions between ferroelectric phases.

VI. SUMMARY AND CONCLUSIONS

Firstly, an electric-field induced phase transition has been observed in $[111]_C$-oriented, pseudo-orthorhombic PZN-8PT by strain-field measurements and *in situ* polarized light microscopy. The transition occurs most likely via continuous polarization rotation in the $(10\bar{1})_C$ mirror plane of a M_B monoclinic phase followed by a discontinuous "jump" in polarization to the $[111]_C$ direction; this "jump" occurs by nucleation and growth of the new phase, characteristic of a first order phase transition.

Many more electric-field induced phase transitions have been evidenced by macroscopic strain-field measurements in $[001]_C$-poled PZN-

xPT and PMN-xPT with various compositions around the morphotropic phase boundary. Unipolar electric fields up to 1500 V/mm have been applied at temperatures between 25 °C and 100 °C. For lower PT contents (PMN-25PT) the polarization rotation path is “R” - T where the polar vector rotates continuously in the M_A monoclinic plane before a first order, hysteretic jump within the same monoclinic plane to a tetragonal phase.

At higher PT contents (PZN-5PT, PZN-6.5PT, PMN-30.5PT, PMN-31PT), the polarization rotation path is “R” - “O” - T. This more complicated path involves continuous rotation within the M_A plane of the “R” phase before a first-order, hysteretic “jump” to the M_C monoclinic plane of an “O” phase, continuous rotation within this second plane, and finally a second, first-order, hysteretic jump to the tetragonal phase. Both first-order phase transitions can be observed within the same electric field cycle.

At even higher PT contents (PZN-8.5PT) the zero-field phase is already pseudo-orthorhombic and only the “O” - T phase transition occurs under field.

Trends in phase stability have been highlighted by constructing electric field vs. temperature (*E*-*T*) phase diagrams for each composition. The M_C phase field is noticeably “squeezed out” at lower PT contents. Both M_C and tetragonal fields are favored over the M_A phase by increases in temperature and electric field along $[001]_C$. The latter observation can be predicted from simple energetic arguments.

The question of whether the monoclinic phases are true zero-field phases has been considered; it is noted that the above behavior can be explained simply in terms of first order phase transitions between electric-field distorted rhombohedral and orthorhombic, and tetragonal phases. However, irrespective of whether it corresponds to a true monoclinic phase or simply the piezoelectric distortion of higher symmetry rhombohedral and orthorhombic parents, it is rotation of the polar vector in the M_A and M_C monoclinic planes that is responsible for the giant piezoelectric response. The reason for this will be discussed in chapter ten.

To conclude, such transitions between phases are a common feature of PZN-xPT and PMN-xPT around the morphotropic phase boundary, even for small changes in temperature or electric field. They highlight the complex competition between pseudo-rhombohedral, pseudo-orthorhombic and tetragonal phases at ambient temperatures close to the morphotropic phase boundaries; this must follow from their near degeneracy.

Finally, since the ferroelectric phases of PMN-xPT and PZN-xPT are also *ferroelastic*, their phase stabilities should also be affected by stresses. The response of PMN-xPT and PZN-xPT to applied stress will be discussed in the next two chapters.

REFERENCES

[1] D. A. Porter and K. E. Easterling, *Phase transformations in metals and alloys*, 2nd ed. (Chapman and Hall, London, 1992).

[2] E. K. H. Salje, *Phase transitions in ferroelastic and co-elastic crystals* (Cambridge University Press, Cambridge, 1993).

[3] E. K. H. Salje, Acta Cryst. A **47,** 453-469 (1991).

[4] D. Tabor, *Gases, liquids and solids and other states of matter*, 3rd ed. (Cambridge University Press, Cambridge, 1996).

[5] J. F. Nye, *Physical properties of crystals*, 2nd ed. (Clarendon Press, Oxford, 1985).

[6] A. Putnis, *Introduction to mineral sciences* (Cambridge University Press, Cambridge, 1992).

[7] B. Jaffe, W. R. Cook, and H. Jaffe, *Piezoelectric Ceramics* (Academic Press, 1971).

[8] G. Burns and F. H. Dacol, Solid State Communications **42,** 9-12 (1982).

[9] S. Wada, T. Suzuki, M. Osada, M. Kakihana, and T. Noma, Jpn. J. Appl. Phys. Part 1 **37,** 5385-5393 (1998).

[10] W. Zhong, D. Vanderbilt, and K. M. Rabe, Phys. Rev. Lett. **73,** 1861-1864 (1994).

[11] B. D. Chapman, E. A. Stern, S.-W. Han, J. O. Cross, G. T. Seidler, V. Gavrilyatchenko, R. V. Vedrinskii, and V. L. Kraizman, Phys. Rev. B **71,** 020102(R) (2005).

[12] Symmetry breaking can also occur by substitution of atoms on given atomic sites; in this case phase transitions are known as "order-disorder" phase transitions.

[13] M. E. Lines and A. M. Glass, *Principles and applications of ferroelectrics and related materials* (Clarendon Press, Oxford, 1977).

[14] H. T. Stokes and D. M. Hatch, Phys. Rev. B **30,** 4962-4967 (1984).

[15] C. Haas, Phys. Rev. **140,** 863-868 (1965).

[16] I. A. Sergienko, Y. M. Gufan, and S. Urazhdin, Phys. Rev. B **65,** 144104 (2002).

[17] S.-E. E. Park and W. Hackenberger, Current Opinion in Solid State and Materials Science **6,** 11-18 (2002).

[18] S.-E. E. Park and T. R. Shrout, J. Appl. Phys. **82,** 1804-1811 (1997).

[19] S. Wada, S.-E. Park, L. E. Cross, and T. R. Shrout, Ferroelectrics **221,** 147-155 (1999).

[20] M. K. Durbin, E. W. Jacobs, and J. C. Hicks, Appl. Phys. Lett. **74,** 2848-2850 (1999).

[21] D. Damjanovic, J. Am. Ceram. Soc **88,** 2663-2676 (2005).

[22] F. Bai, N. Wang, J. Li, D. Viehland, P. M. Gehring, G. Xu, and G. Shirane, J. Appl. Phys. **96,** 1620-1627 (2004).

[23] H. Fu and R. E. Cohen, Nature **403,** 281-283 (2000).

[24] B. Noheda, Current Opinion in Solid State and Materials Science **6,** 27-34 (2002).

[25] L. Bellaiche, A. Garcia, and D. Vanderbilt, Phys. Rev. B **64,** 060103(R) (2001).

[26] H. Cao, F. Bai, N. Wang, J. Li, D. Viehland, G. Xu, and G. Shirane, Phys. Rev. B **72,** 064104 (2005).

[27] A. J. Bell, J. Appl. Phys. **89,** 3907-3914 (2001).
[28] D. Damjanovic and M. Demartin, J. Phys.: Condens. Matter **9,** 4943-4953 (1997).
[29] R. Zhang, B. Jiang, and W. Cao, Appl. Phys. Lett. **82,** 787-789 (2003).
[30] S.-F. Liu, S.-E. Park, T. R. Shrout, and L. E. Cross, J. Appl. Phys. **85,** 2810-2814 (1999).
[31] The collinear piezoelectric effect will be clearly defined in chapter ten.
[32] W. Cao, S. Tavener, and S. Xie, J. Appl. Phys. **86,** 5739-5746 (1999).
[33] A. K. Tagantsev, I. Stolichnov, E. L. Colla, and N. Setter, J. Appl. Phys. **90,** 1387-1402 (2001).
[34] W. Ren, S.-F. Liu, and B. K. Mukherjee, Appl. Phys. Lett. **80,** 3174-3176 (2002).
[35] B. Noheda, Z. Zhong, D. E. Cox, G. Shirane, S.-E. Park, and P. Rehrig, Phys. Rev. B **65,** 224101 (2002).
[36] R. R. Chien, V. H. Schmidt, C.-S. Tu, L.-W. Hung, and H. Luo, Phys. Rev. B **69,** 172101 (2004).
[37] B. Noheda, D. E. Cox, G. Shirane, S.-E. Park, L. E. Cross, and Z. Zhong, Phys. Rev. Lett. **86,** 3891 (2001).
[38] K. Ohwada, K. Hirota, P. W. Rehrig, Y. Fujii, and G. Shirane, Phys. Rev. B **67,** 094111 (2003).
[39] M. Davis, D. Damjanovic, and N. Setter, J. Appl. Phys. **97,** 064101 (2005).
[40] D. Viehland and J. F. Li, J. Appl. Phys. **92,** 7690-7692 (2002).
[41] S. Wada, S. Suzuki, T. Noma, T. Suzuki, M. Osada, M. Kakihana, S.-E. Park, L. E. Cross, and T. R. Shrout, Jpn. J. Appl. Phys. Pt. 1 **38,** 5505-5511 (1999).
[42] E. H. Kisi, R. O. Piltz, J. S. Forrester, and C. J. Howard, J. Phys.: Condens. Matter **15,** 3631-3640 (2003).
[43] M. Davis, D. Damjanovic, and N. Setter, Appl. Phys. Lett. **87,** 102904 (2005).
[44] O. Noblanc, P. Gaucher, and G. Calvarin, J. Appl. Phys. **79,** 4291-4297 (1996).
[45] V. A. Shuvaeva, A. M. Glazer, and D. Zekria, J. Phys.: Condens. Matter **17,** 5709-5723 (2005).
[46] A. J. Bell, Appl. Phys. Lett. **76,** 109-111 (2000).
[47] M. Shen, D. Yao, and W. Cao, Materials Letters **59,** 3276-3279 (2005).
[48] M. K. Durbin, J. C. Hicks, S.-E. Park, and T. R. Shrout, J. Appl. Phys. **87,** 8159-8164 (2000).
[49] L. E. Cross and P. Hana, Proc. 9th US-Japan Seminar on Dielectric and Piezoelectric Ceramics (1999).
[50] M. Budimir, D. Damjanovic, and N. Setter, J. Appl. Phys. **94,** 6753-6761 (2003).
[51] A. Amin, M. J. Haun, B. Badger, H. McKinstry, and L. E. Cross, Ferroelectrics **65,** 107-130 (1985).
[52] M. Davis, D. Damjanovic, D. Hayem, and N. Setter, J. Appl. Phys. **98,** 014102 (2005).
[53] However, it could be argued that since an electric field is simply one of many thermodynamic parameters, like temperature, the description as a phase transition is as valid as the description as piezoelectric distortion.

[54] J. S. Forrester, R. O. Piltz, E. H. Kisi, and G. J. McIntyre, J. Phys.: Condens. Matter **13,** L825-L833 (2001).
[55] L. D. Landau and E. M. Lifshitz, *Statistical Physics Part 1*, 3rd ed. (Butterworth-Heinemann, Oxford, 1980).
[56] D. Vanderbilt and M. H. Cohen, Phys. Rev. B **63,** 094108 (2001).
[57] A. K. Singh and D. Pandey, Phys. Rev. B **67,** 064102 (2003).
[58] G. Xu, H. Luo, H. Xu, and Y. Yin, Phys. Rev. B **64,** 020102(R) (2001).
[59] A. A. Bokov and Z.-G. Ye, J. Appl. Phys. **95,** 6347-6359 (2004).
[60] K. K. Rajan and L. C. Lim, Appl. Phys. Lett. **83,** 5277-5279 (2003).
[61] V. Y. Topolov, Phys. Rev. B **65,** 094207 (2002).
[62] Z.-G. Ye and M. Dong, J. Appl. Phys. **87,** 2312-2319 (2000).
[63] K. Fujishiro, R. Vlokh, Y. Uesu, Y. Yamada, J.-M. Kiat, B. Dkhil, and Y. Yamashita, Jpn. J. Appl. Phys. Pt. 1 **37,** 5246-5248 (1998).
[64] M. Shen and W. Cao, Appl. Phys. Lett. **86,** 192909 (2005).
[65] J. Han and W. Cao, Appl. Phys. Lett. **83,** 2040-2042 (2003).
[66] Y. M. Jin, Y. U. Wang, and A. G. Khachaturyan, J. Appl. Phys. **94,** 3629-3640 (2003).
[67] L. Bellaiche, A. Garcia, and D. Vanderbilt, Phys. Rev. Lett. **84,** 5427-5430 (2000).
[68] J. Frantti, S. Eriksson, S. Hull, V. Lantto, H. Rundlöf, and M. Kakihana, J. Phys.: Condens. Matter **15,** 6031-6041 (2003).
[69] R. Haumont, A. Al-Barakaty, B. Dkhil, J. M. Kiat, and L. Bellaiche, Phys. Rev. B **71,** 104106 (2005).
[70] B. Noheda, D. E. Cox, G. Shirane, J. A. Gonzalo, L. E. Cross, and S.-E. Park, Appl. Phys. Lett. **74,** 2059-2061 (1999).

Chapter eight

Direct piezoelectric effect

In this chapter, the direct piezoelectric response of $[001]_C$-poled PZN-4.5PT, PZN-8PT and PMN-31PT is investigated. Measurements are made in a Berlincourt-type press, over a wide range of dynamic and static bias stresses (< 20 MPa), of both the longitudinal (d_{33}) and transverse (d_{31}) piezoelectric coefficients. In the longitudinal mode, where compressive stresses are applied *along* the $[001]_C$ poling direction, the charge-stress response is hysteretic and non-linear. For samples with suitable geometries, piezoelectric coefficients similar to those found by converse (strain-field) measurements are observed ($d_{33} > 2000$ pm/V). Coupling of the hysteresis and non-linearity via the Rayleigh law indicates a significant *extrinsic* contribution from irreversible, pinned *interface motion*. Comparison to similar behavior in ferroelectric ceramics suggests these interfaces can be identified as non-180° (ferroelastic) domain walls. However, domain wall motion is not expected in the "4R" domain engineered structure.

In the transverse mode, however, where the sample is loaded *perpendicular to* the poling direction, the charge-stress response of PMN-31PT and PZN-4.5PT is anhysteretic and linear at comparative stresses; large piezoelectric coefficients ($-d_{31} > 1000$ pm/V) are also observed. This might be exploitable in sensing applications where "lossy" materials, which lead to energy dissipation and a lack of precision, are avoided. Finally, it is postulated that the difference between the behaviors arises from differing directions of polarization rotation. It is noted that in the transverse mode, rotation is *towards* the $[001]_C$ poling direction; in the longitudinal mode it is *away*.

I. INTRODUCTION

As shown in the previous chapter, the *converse* piezoelectric (strain-field) response of "4R" and "4O" domain engineered crystals to fields applied along the $[001]_C$ poling direction is characteristically *anhysteretic*. The absence of a hysteretic, *extrinsic*[1] contribution to the converse piezoelectric response (see fig. 1) is one of the main reasons why PMN-xPT and PZN-xPT look so promising for actuator applications[2]. However, while the origin of the "giant" piezoelectric coefficients (d_{33} * > 2000 pm/V) remains the subject of debate, it seems certain that the large anhysteretic strain results from an absence of domain wall motion due to the inherent stability of the domain-engineered structure[3].

In contrast, as shown in the last chapter, the strain-field response of $[111]_C$-oriented pseudo-rhombohedral PMN-28PT (chapter seven, fig. 3) is characteristically *hysteretic* due to (non-180°) domain wall switching. Likewise, the strain-field response of "soft[4]" polycrystalline PZT *ceramics* is generally hysteretic[5]. Even when dopants[4] are added to PZT which pin domain walls, and thus restrict domain wall motion, a certain extrinsic contribution is often apparent. Compare the response of "hard[4]" PZT (chapter two, fig. 10) with that of domain-engineered PZN-8PT (fig. 1).

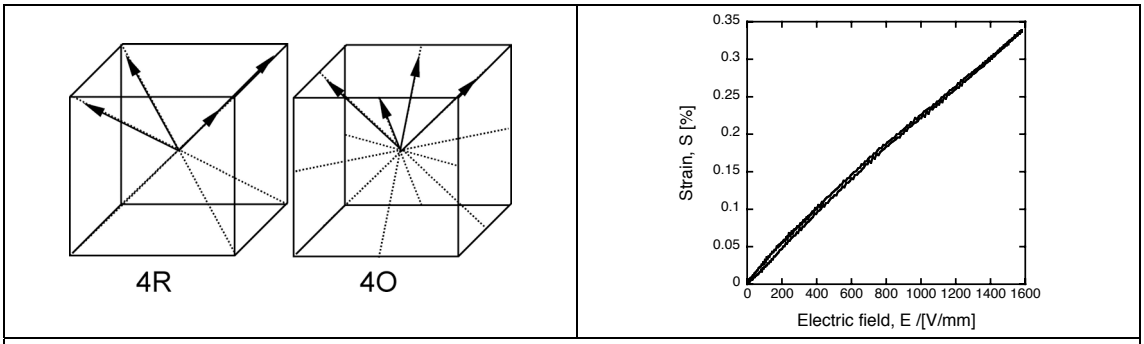

Fig. 1. (Left) Ideal 4R and 4O domain engineered structures formed in rhombohedral and orthorhombic crystals by poling along the $[001]_C$ direction. (Right) Converse piezoelectric response of "4O" domain engineered PZN-8PT. The response is anhysteretic indicating no ("extrinsic") contribution from domain wall motion.

The converse piezoelectric response can be written[6]:

$$S_{ij} = d_{kij} E_k \qquad [1]$$

where E_k is the applied electric field and S_{ij} is the resultant strain. Similarly, the *direct* piezoelectric effect is defined by the equation:

$$D_i = d_{ijk} \sigma_{jk} \qquad [2]$$

where D_i is the displacement field, equal to a change in polarization ΔP_i, due to an applied stress σ_{jk}. As shown in appendix II, the two piezoelectric coefficients are equivalent according to thermodynamic arguments. However,

this will only be true at small fields. At larger fields, the linearity of equations [1] and [2] will break down and the piezoelectric coefficients will become functions of the driving field or stress: $d = d(E)$ or $d = d(\sigma)$. As a consequence, their equivalence may no longer hold.

Direct piezoelectric effect

Until now, little work has been done on the direct piezoelectric response of PMN-xPT and PZN-xPT, that is, under dynamic or quasi-static compressive stress. This is the mode of response directly relevant to sensor applications, for example in accelerometers and *sonar* devices. A few authors have reported Berlincourt-type measurements of d_{33} which agree well with corresponding low-field resonance and converse (strain-field) measurements[5,7,8] although such measurements are not always reliable[9] and no dependence on the applied prestress was discussed. In deep-sea sensing applications, piezoelectric materials are subject to large hydrostatic pressures and acoustic transducers inherently need to be operated under uniaxial compressive stress[10]. Equally, no data are available for these crystals regarding the dependence of the direct piezoelectric response on dynamic pressure, nor on any hysteretic (lossy) effects. Hysteresis should be minimized[5] in all sensor applications since it leads to a loss in precision and means, inherently, that response (charge) is a multi-valued function of the perturbing stress.

The direct piezoelectric response of domain engineered PMN-xPT and PZN-xPT will be investigated in this chapter.

Response of ferroelectric materials to stress

As discussed in previous chapters, a given ferroelectric crystal with spontaneous polarization $\boldsymbol{P}_s$ will couple to an applied electric field $\boldsymbol{E}$ with an interaction energy $-\boldsymbol{E}\cdot\boldsymbol{P}_s$. Ferroelectric materials are generally split into more than one domain[1], i.e., finite volumes of material with different different *orientation states*[11] (*variants*) for the polarization vector. In all but special domain-engineered cases, application of an electric field will bias one domain variant over the others. Fields over a threshold value (the coercive field $\boldsymbol{E}_c$)[1] will lead to growth of the favored domain variant at the expense of the others, or ferroelectric domain "switching". In terms of the boundaries between these domains[12], or domain walls, we will have *domain wall motion*. Domain wall motion and domain switching are non-linear, *extrinsic* effects[13] and are characteristically hysteretic, as shown above.

As noted in chapter five, domain walls between variants with differing spontaneous strain tensors will have polarization vectors which are no longer antiparallel[14]. Such "non-180°" domain walls are also known as "ferroelectric-ferroelastic[13]" domain walls since they can be moved by applied stresses, over some coercive value ($\boldsymbol{\sigma}_c$), as well as by applied fields. Such *ferroelastic switching* will again occur to minimize the interaction energy, this time $-\boldsymbol{\sigma}\cdot\boldsymbol{S}_s$.

In *3m* rhombohedral crystals there are 8 variants (4 antiparallel pairs); ferroelastic domain walls are 109.5° and 70.5° (see chapter five). In *mm2* orthorhombic crystals, ferroelastic domain walls are 60°, 120° and 90°; there are 12 possible domain variants (6 pairs). In *4mm* tetragonal crystals there are 6 domain variants (3 pairs) and ferroelastic domain walls are 90°.

Ferroelastic domain switching has been studied extensively. Non-linear stress-strain curves have evidenced 90° domain wall motion in room temperature, single crystal barium titanate[15,16]. Successive application of a uniaxial, compressive stress ($\approx$20 MPa) along the $[100]_C$ and $[010]_C$ directions can be used to remove all 90° domain walls leading to antiparallel, 180° domains oriented along $\pm[001]_C$ ("mechanical poling")[17]. Such controlled ferroelastic switching has also been demonstrated in single crystal, orthorhombic potassium niobate ($KNbO_3$)[18]. The response of the 90° domain walls in single crystal barium titanate to mixed electrical and mechanical loading has been measured experimentally[19].

The electromechanical response of *polycrystalline ferroelectrics*, and especially PZT, has also been well documented. In polycrystalline ceramics, local polarizations will have random orientations with respect to an applied stress or field; gross ferroelastic and ferroelectric switching is therefore generally expected. Stress-strain curves for poled, PZT ceramics are characteristically non-linear and hysteretic. Upon removal of field, a remnant (compressive) strain is often observed due to irreversible non-180° domain switching. Ferroelastic switching is also evident in charge-stress curves since non-180° domain switching will also result in a macroscopic change in polarization. A remnant *depolarization* results from application of a compressive stress along the poling direction[20-22].

The combined effect of electrical and mechanical loading in poled PZT ceramics has also been studied[21,23-26]. The general response can be summarized as follows. Compressive stresses tend to depolarize PZT ceramics due to ferroelastic switching[21]. The strain or polarization response to subsequent application of an electric field along the poling direction is therefore characteristically hysteretic due to the resultant ferroelectric switching (repoling). That is, compressive prestresses initially tend to increase hysteresis in the unipolar, strain-field (and polarization-field) response[25]. In contrast, application of an electrical bias field tends to reduce hysteresis in the strain-stress response since it decreases the tendency for switching[21]. The overall behavior will be a complex function of stress and field and the coercive values, $\boldsymbol{\sigma_c}$ and $\boldsymbol{E_c}$, respectively.

Response of PMN-xPT and PZN-xPT to stress

Similar experiments have recently been made on domain-engineered PZN-xPT and PMN-xPT. Importantly, Viehland *et al.* have investigated the strain-electric field (*S*-*E*) response of $[001]_C$-oriented PMN-30PT crystals under varying mechanical prestresses[8,27-29]. They observed that the initial low-field response becomes more hysteretic with increasing prestress (see fig. 2). This is identical to the behavior in PZT ceramics suggesting that the uniaxial stress causes partial *depoling* of the sample (or ferroelastic switching) which is reversed by application of the electric field (*repoling*). The same

authors also investigated the strain-stress behavior of PMN-30PT[28], PMN-32PT and PZN-8PT[30] single crystals with and without DC electrical bias fields. Likewise, hysteresis was evident in the strain-stress response of both compositions under zero bias whereas under DC bias fields (> 200 V/mm) the response became anhysteretic; this again suggests competing ferroelectric and ferroelastic domain wall motion.

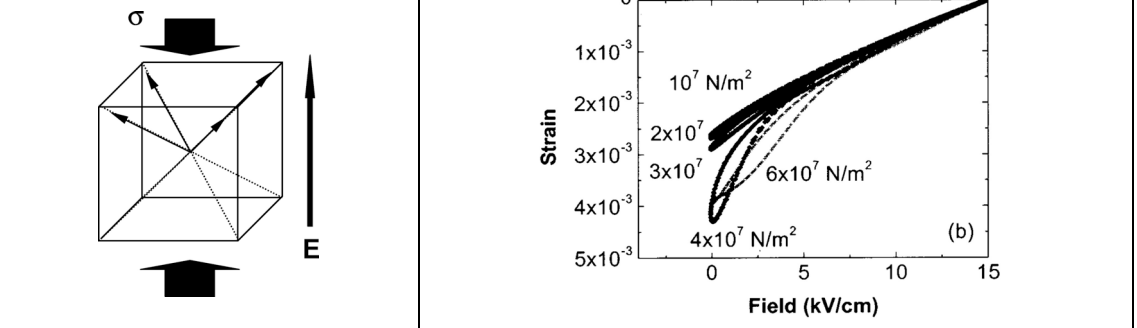

Fig. 2. Converse (strain-field) response of poled, $[001]_C$-oriented, "4R" PMN-30PT at varying levels of compressive prestress applied along the poling axis [taken from Viehland et al. (2001)[8]].

For a perfectly cut crystal in the ideal 4R multidomain state, assuming no phase transition occurs, this partial depoling under mechanical stress is unexpected. For example, switching of a $[111]_C$ rhombohedral domain to the $[11\bar{1}]_C$ state will yield no reduction in the thickness dimension of the sample; this is shown in fig. 3. It follows that switching should not be driven by mechanical pressure since it cannot lead to a reduction in strain energy.

The same will be true in distorted "4R" ($4M_A$) domain engineered crystals. Only in $[001]_C$-poled 4O crystals, can 60° switching (e.g. from $[101]_C$ to $[110]_C$) decrease the thickness dimension of the sample; this is shown in figure 4. This might explain the observed ferroelastic hysteresis[30] in pseudo-orthorhombic PZN-8PT and likewise PMN-32PT which has a composition very close to the "R"/"O" phase boundary (see chapter six). However, the hysteretic response of $[001]_C$-poled, "4R" PMN-30PT[8,27-29] is unexpected if it is indeed due to ferroelastic switching.

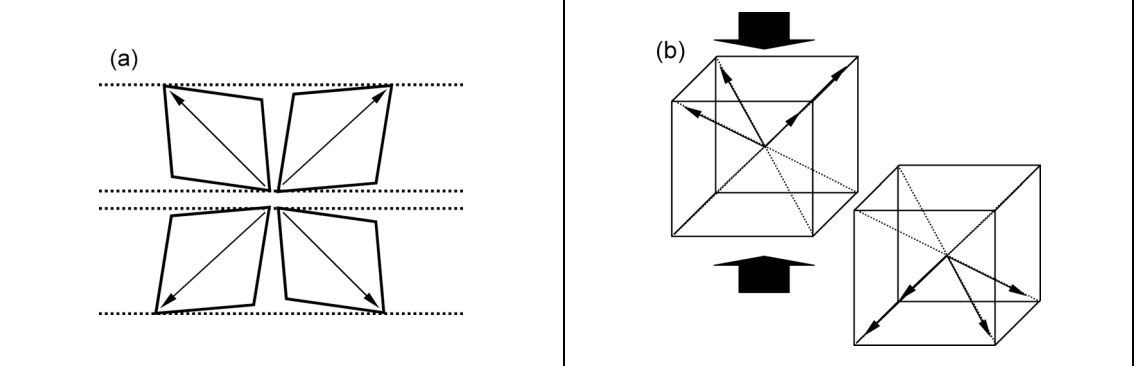

Fig. 3. In a 4R domain-engineered crystal no ferroelastic switching is expected upon application of a compressive stress along the $[001]_C$ direction since it will not reduce the resultant strain energy.

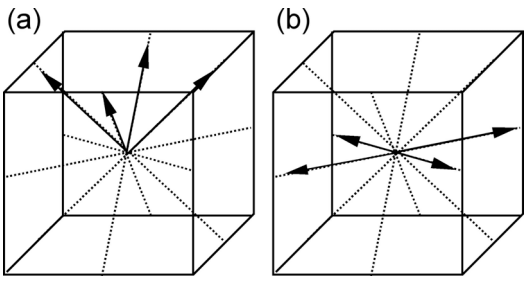

Fig. 4. 60° domain wall switching would be driven by application of a compressive stress along the $[001]_C$ direction in the 4O domain-engineered structure.

II. EXPERIMENTAL METHOD

All measurements were made using the Berlincourt-type press described in chapter two. For all measurements, pressure is applied to the sample between two flat, well-aligned steel plates (figure 5). Dynamic [$\sigma_{DY} = \sigma_0 \sin(\omega t)$] and static pressure ($\sigma_{ST}$) is applied to the sample by a PZT actuator and the resultant force on the sample is measured with a quartz sensor. A prestress P is first applied by a stepper motor to put the entire system in compression and the sample is left in place for about an hour to allow the system to relax. Importantly, the total static pressure ($P + \sigma_{ST}$) is always greater than the dynamic stress amplitude such that the system is always in compression. d_{33} is calculated as the ratio between the maximum dynamic force (F_{max}) applied to the sample and the maximum charge in the cycle (Q_{max}). A typical charge-stress response in shown in figure 6. Transverse piezoelectric coefficients (d_{31}) could also be measured by turning the samples and applying pressure to two non-electroded surfaces [see fig. 5(b)].

Unless otherwise stated, each series of measurements was begun at the highest static and dynamic stress combination, and at the highest frequency. For the measurements taken with varying bias stresses (σ_{ST}), the samples were first 'educated' at the largest value of static and dynamic stress for at least one hour, before subsequent measurements at lower static stresses, to ensure no depoling occurred *during* the experiment. All experiments were made without intermediate repoling of the samples; depoling and recovery of the crystals will be discussed later.

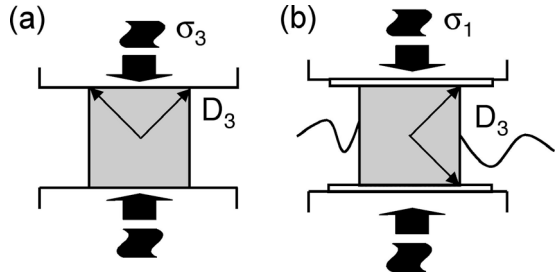

Fig. 5. Schematic of direct (charge-stress) measurements in the Berlincourt-type press. Longitudinal (a) and transverse (b) measurements were made.

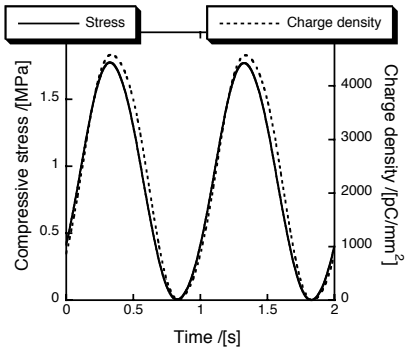

Fig. 6. Typical charge-stress response during measurements of the direct piezoelectric response (at 1 Hz).

Samples used

$[001]_C$- and $[111]_C$-oriented single crystals of PMN-31PT, PZN-4.5PT, PMN-6.5PT and PZN-8PT of various sizes and geometries were used for this study. In each case, gold electrodes were sputtered onto two parallel surfaces and the crystals were HTFC-poled at 200 V/mm. $[001]_C$-poled PZN-4.5PT and PZN-6.5PT are pseudo-rhombohedral "4R" (see chapter six); $[001]_C$-poled PZN-8PT, in contrast, is pseudo-orthorhombic "4O". $[001]_C$-poled PMN-31PT lies very close to the morphotropic phase boundary between the "R" and "O" phases; therefore, it could be either "4R" or "4O".

Aspect ratio effect

Sample aspect ratio is very important to all uniaxial compression testing. Ideally, we would like to test under conditions of perfectly uniaxial stress (σ_3 for longitudinal measurements). Assuming the steel plates are perfectly parallel to each other, and to the surfaces of the sample, we will have no shear stresses in the material [$\sigma_4 = \sigma_5 = \sigma_6 = 0$]. However, since the Poisson's ratio of the steel plates and our single crystal sample will generally be different (PMN-xPT and PZN-xPT are generally much softer), lateral forces will develop which are concentrated at the contacted surfaces of the sample[31-33]. That is, upon compression the sample will want to expand laterally more than the metal plates. Due to unavoidable friction between the sample

surfaces and the metal plates ("clamping"), the sample will feel transverse stresses, as shown in figure 7.

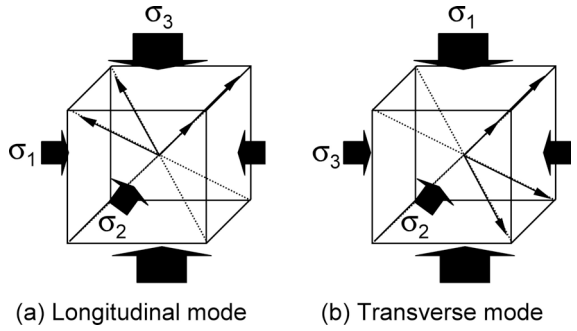

Fig. 7. Lateral stresses arising in longitudinal and transverse piezoelectric measurements due to clamping effects. The stresses are shown relative to the polarization vectors in the perfect 4R domain-engineered structure.

In the longitudinal mode [fig. 7(a)] this will mean that the transverse piezoelectric effect will contribute to the measured charge. In Voigt notation:

$$D_3^{total} = d_{33}\sigma_3 + d_{31}\sigma_1 + d_{32}\sigma_2 \qquad [3]$$

Since the lateral stresses will be inhomogeneous, σ_i are volume-averaged quantities. The measured (or *effective*) piezoelectric coefficient will be:

$$d_{33}^{eff} = \frac{D_3^{total}}{\sigma_3} = d_{33} + \left(\frac{\sigma_1}{\sigma_3}\right) d_{31} + \left(\frac{\sigma_2}{\sigma_3}\right) d_{32} \qquad [4]$$

d_{31} and d_{32} are commonly negative for many materials symmetries including those of poled ceramics and the 4O and 4R domain engineered structures[34]. Therefore, the measured longitudinal piezoelectric coefficient d_{33}^{eff} is expected to be less than the true value due to negative contributions from the transverse piezoelectric effect.

In the transverse mode [fig. 7(b)], the poling direction (x_3 by definition) is perpendicular to the applied stress, this time, σ_1. Thus, the measured charge is:

$$D_3^{total} = d_{31}\sigma_1 + d_{32}\sigma_2 + d_{33}\sigma_3 \qquad [5]$$

Therefore, the effective transverse piezoelectric coefficient is different to the true value d_{31} according to:

$$d_{31}^{eff} = \frac{D_3^{total}}{\sigma_1} = d_{31} + \left(\frac{\sigma_2}{\sigma_1}\right) d_{32} + \left(\frac{\sigma_3}{\sigma_1}\right) d_{33} \qquad [6]$$

There will be competing effects wherever d_{33} and d_{32} have differing signs. Thus, choosing a suitable aspect ratio will generally be more complicated for transverse measurements.

Lateral forces will be strongest close to the sample-contact interface and thus will be strongly dependent on the aspect ratio (AR) of the sample. The ratios of lateral to applied stress featuring in equations [4] and [6] can be calculated analytically for the case of complete clamping[33]. In fact, they can be shown to be inversely proportional to the sample aspect ratio or, more precisely*, the ratio of the height of the sample to its lateral dimension in the direction of the force*. For the longitudinal case, we can define the sample height c parallel to the x_3 direction and widths a and b in the x_1 and x_2 directions, respectively. The ratios between lateral and applied stresses are proportional to the ratio between the sample contact area and the area perpendicular to the stress. That is:

$$\left(\frac{\sigma_1}{\sigma_3}\right) \propto \frac{ab}{cb} = \frac{a}{c} = \frac{1}{AR} \qquad [7a]$$

$$\left(\frac{\sigma_2}{\sigma_3}\right) \propto \frac{ab}{ca} = \frac{b}{c} = \frac{1}{AR} \qquad [7b]$$

Quantitatively[33], the constants of proportionality depend on the Young's modulus and Poisson's ratio of the steel, Y and ν, and the transverse compliance of the crystal s_{13}^E:

$$\left(\frac{\sigma_1}{\sigma_3}\right) = -\frac{a}{c}\frac{Y}{4}\left(s_{13}^E + \frac{\nu}{Y}\right) \qquad [8]$$

Barzergar *et al.* have shown that d_{33} is diminished by as much as 30% in low aspect ratio (i.e. plate type) samples of PZT[31,32]. The experimental variation in longitudinal piezoelectric coefficient with increased aspect ratio for PZT ceramics (Pz27, Ferroperm, Denmark) is shown in figure 8. Also shown is a curve derived from numerical, finite element modeling (FEM) [Barzegar et al. (2004)[31]], which fits well to the data. As shown, lateral effects become negligible at aspect ratios of 1:2 (i.e. 0.5) or more.

Also shown in figure 8 is a FEM-derived curve for $[001]_C$-poled PZN-4.5PT using data from the literature[35] for which the aspect ratio effect is noticeably much stronger. This is a consequence of the higher compliance ("softness") of PZN-4.5PT[36]. The relevant compliance of Pz27[37] is $s_{13}^E = -8.6 \times 10^{-12}\,\mathrm{m^2/N}$. In contrast, $[001]_C$-poled PZN-4.5PT[34] is around five times more compliant with $s_{13}^E = -50.0 \times 10^{-12}\,\mathrm{m^2/N}$. Consequently, for PZN-4.5PT, lateral effects will not become negligible in longitudinal measurements until aspect ratios of > 2 or more (see fig. 8).

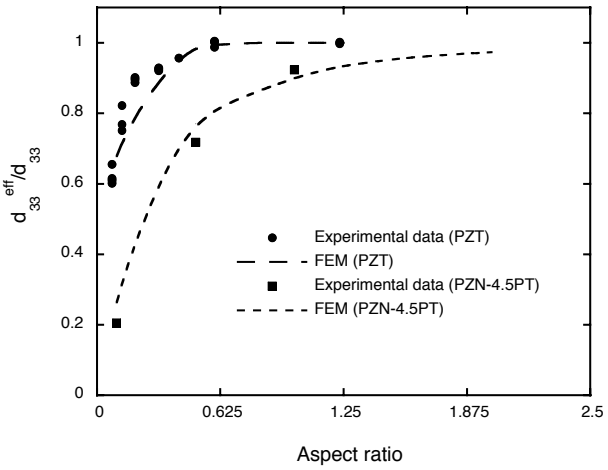

Fig. 8. The effect of aspect ratio on the measured piezoelectric coefficient normalized to the true value. Experimental data is also shown for poled PZT ceramic (Pz27, Ferroperm, Denmark) and $[001]_C$-poled PZN-4.5PT single crystals corresponding to the low stress response at 1 Hz. The data fits well to curves from finite element modeling (FEM)[38].

To summarize, as with any uniaxial compression testing, the measured longitudinal coefficient d_{33}^{eff} will more closely approach the true value d_{33} in taller, more columnar samples, although extreme aspect ratios will be less stable to bending and will be more difficult to pole. The same will be true for measurements of the transverse piezoelectric coefficient d_{31}. Ideally, however, to compare the two effects we would like to measure both d_{33} and d_{31} in the same sample. Unfortunately, we cannot cut crystals with large aspect ratios in more than one direction.

Regarding equation [6] the other way to approach a true measurement of the transverse piezoelectric coefficient ($d_{31}^{eff} = d_{31}$) is to fix:

$$\frac{\sigma_2}{\sigma_3} = -\frac{d_{33}}{d_{32}} \qquad [9]$$

The ratio $-d_{33}/d_{32}$ is around 2 for $[001]_C$-poled, "4R" and "4O" PMN-xPT[34,39,40] and PZN-xPT[34,35,41-43] (where $d_{32} = d_{31}$). Thus, according to relations like those in [7] (and ignoring the difference in the two compliances s_{12}^E and s_{13}^E) we require:

$$\frac{b}{c} = -\frac{d_{33}}{d_{32}} \approx 2 \qquad [10]$$

where *c* is the thickness of the sample parallel to the poling direction.

Sample dimensions

Accordingly, <001>$_C$-oriented, cuboid samples of nominal dimensions 4 x 4 x 2 mm^3 were used, electroded on the 4 x 4 mm^2 faces. The crystals had compositions PMN-31PT and PZN-4.5PT. For transverse measurements, the aspect ratio satisfied requirement [10]. For longitudinal measurements, the aspect ratio was 2:4 (0.5); therefore, for these samples, d_{33}^{eff} should be 60-80% of the true value d_{33} (see fig. 8).

Other aspect ratios were also used for measurements of the longitudinal effect. [001]$_C$-oriented 3 x 3 x 3 mm^3 cubes of PZN-8PT and PZN-4.5PT were acquired whose aspect ratio 3:3 (1) should lead to truer measurements of d_{33}; moreover, measurements were initially made on plate-like 5 x 5 x 0.5 mm^3 samples. Finally, the effect of aspect ratio on the measured hysteresis and non-linearity will be discussed below.

III. DYNAMIC MEASUREMENTS

Typical variations of the measured d_{33} coefficient with dynamic stress amplitude σ_0 for the [001]$_C$-poled samples of PZN-4.5PT and PMN-31PT are shown in figure 9. An unexpected non-linearity is clearly evident in the direct response with d_{33} increasing by as much as 40% over the dynamic stress range shown. d_{33} also decreased with increasing frequency for the entire range of stresses (see below). The relative hysteresis size [defined as the hysteresis width divided by the range of charge density, ΔD / (D_{max} - D_{min})] decreased monotonically with decreasing stress and increasing frequency such that at low dynamic stresses the response was essentially anhysteretic. Extrapolation of the low stress segment of the curve gives a static (or reversible) d_{33} figure (d_0) of ~1850 pC/N for PMN-31PT and ~1300 pC/N for PZN-4.5PT.

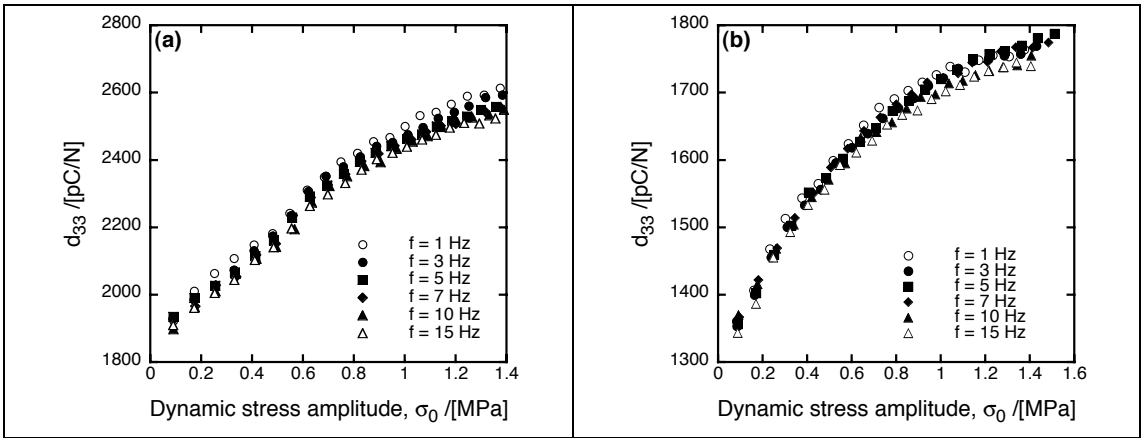

Fig. 9. Longitudinal piezoelectric coefficient as a function of dynamic stress amplitude (σ_0) for fixed values of prestress (P) and static bias stress (σ_{ST}) at frequencies between 1 and 15 Hz for [001]$_C$-poled samples of (a) PMN-31PT and (b) PZN-4.5PT [4 x 4 x 2 mm^3]. In both cases, (σ_{ST} + P) ~ 2.0 MPa.

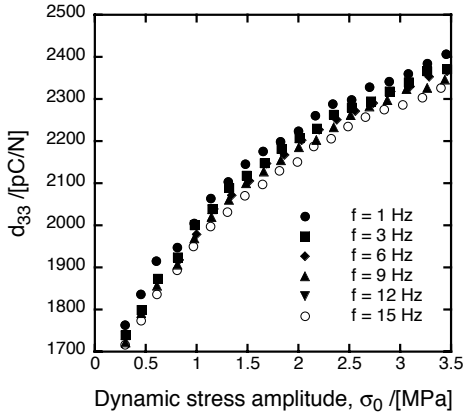

Fig. 10. Longitudinal piezoelectric coefficient as a function of dynamic stress amplitude at frequencies between 1 and 15 Hz for a $[001]_C$-poled sample of PZN-8PT [3 x 3 x 3 mm^3]. In both cases, (σ_{ST} + P) ~ 4.6 MPa.

Very similar behavior was observed for $[001]_C$-poled PZN-8PT (see fig. 10) where d_{33} again increased by around 40% over the range of stress amplitudes shown. Extrapolation of the low stress segment of the curve gives d_0 ~1650 pC/N.

Thus, both "4R" and "4O", $[001]_C$-poled crystals demonstrated significant non-linearity in their direct piezoelectric response [i.e. $d_{33} = d_{33}(\sigma_0)$]. This is in contrast to the converse effect where d_{33} is quasi-linear, decreasing only slightly at high fields (fig. 1). Such non-linearity is observed, however, in the converse response of ceramic PZT to unipolar electric fields [$d_{33} = d_{33}(E)$][44]. Moreover, it is seen in the direct response of PZT[13,45,46], barium titanate[13,46], $Bi_4Ti_3O_{12}$ (BIT)[46] and, to a lesser extent, Sm-modified lead titanate (Sm-PT)[46] ceramics. In all cases it is attributed to an extrinsic contribution to the piezoelectric response from the *irreversible* displacement of domain walls[13,46]. Motion of ferroelastic (90°) domain walls is retarded in modified lead titanate ceramics by its high tetragonality and the non-linearity is weak[46].

Frequency dependence

As evident in figures 9 and 10, the piezoelectric coefficient decreased with increasing frequency. The frequency dependence of d_{33} is further elucidated in figure 11 for PMN-31PT and PZN-8PT samples where, for fixed static and dynamic stresses, d_{33} decreases quasi-logarithmically with increasing frequency over two orders of magnitude. This quasi-logarithmic dependence is also observed in PZT, barium titanate and BIT ceramics[13,45,46] and is "characteristic of domain-wall vibration[46]". It is quite different to the broad Debye-type relaxation observed for Sm-PT ceramics which is more likely related to a different extrinsic contribution from ionic conductivity or point defects[46].

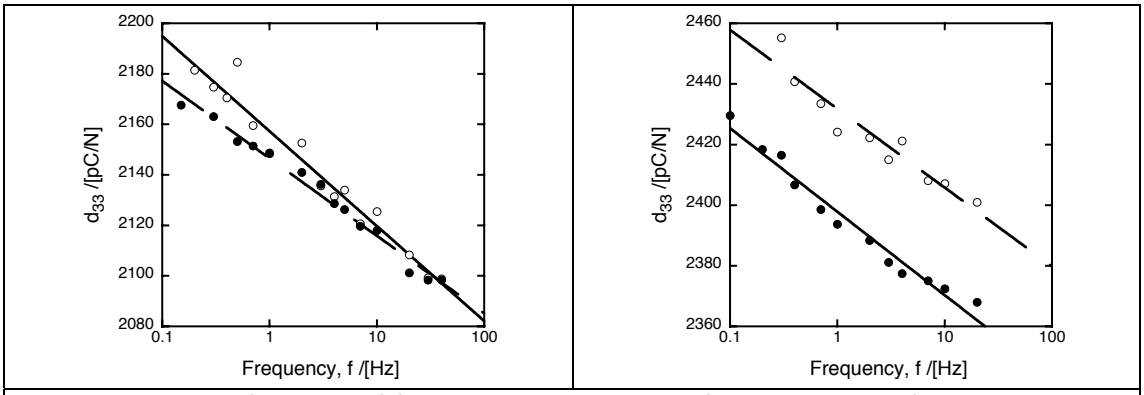

Fig. 11. d_{33} as a function of frequency in samples of PMN-31PT (left) and PZN-8PT (right) poled along the $[001]_C$ direction. The results for two subsequent measurements are shown. The prestress, static bias stress and dynamic stress amplitude were fixed at P ~ 0.6 MPa, σ_{ST} ~ 1 MPa and σ_0 = 1.0 MPa, respectively, for the PMN-31PT sample. For PZN-8PT, P ~ 1.1 MPa, σ_{ST} ~ 3.4 MPa and σ_0 = 3.4 MPa.

Rayleigh law

For piezoelectric materials obeying the Rayleigh law, the D-σ_{DY} (charge density-stress) loop can be directly calculated from a linear relationship between d_{33} and the dynamic stress amplitude σ_0, and vice versa[45]:

$$d_{33} = d_0 + \alpha\sigma_0 \qquad [11]$$

$$D = \left(d_0 + \alpha\sigma_0\right)\sigma_{DY} \pm \frac{\alpha}{2}\left(\sigma_{DY}^2 - \sigma_0^2\right) \qquad [12]$$

Equation [11] constitutes a linear description of the stress dependence (i.e. *non-linearity*) of d_{33}. d_0 is the static piezoelectric coefficient and describes the reversible component of d_{33}; this will include the *intrinsic* piezoelectric effect (equation [2]). On the other hand, $d_{33} - d_0 = \alpha\sigma_0$ is a purely *extrinsic* contribution[45].

Equation [12] describes a hysteretic, and therefore lossy, charge-stress loop with a finite width (at $\sigma_{DY} = 0$) of $\Delta D = \alpha\sigma_0^2$. The Rayleigh law describes a characteristically pointed and symmetric hysteresis loop, as shown in figure 12(a). It is quite different to the "rounded" hysteresis observed in slightly conducting ferroelectrics[4], or that resulting from a fixed phase angle between σ_{DY} and D [fig. 12(b)].

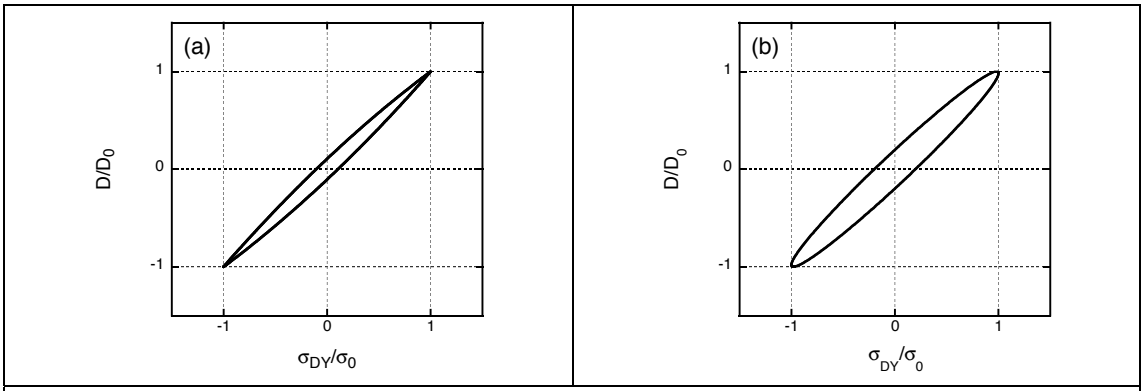

Fig. 12. (a) Rayleigh hysteresis loop. (b) Hysteresis loop for a fixed phase angle between driving stress and resultant charge.

The Rayleigh law was first formulated to describe the field-dependence of the dynamic, magnetic susceptibility in ferromagnetic materials. Here the behavior results from *pinning* of ferromagnetic domain walls by randomly distributed defects. A magnetic field greater than a *local*, coercive value is required to drive the domain wall past its pinning center, which constitutes a local energy minimum for the domain wall. The motion from one energy minimum to the next is *irreversible* and manifestly non-linear and hysteretic[45]. In fact, the Rayleigh law can seemingly be extended to any system where the pinning of interfaces occurs. This includes liquid-liquid interfaces in immiscible liquids and, more importantly, ferroelectric domain walls as well[45,47].

The coefficient α in equations [11] and [12] quantifies both the non-linearity and hysteresis in Rayleigh-law materials, and is found by experiment. At higher stresses, the relationship $d_{33} = d_{33}(\sigma_0)$ variation often deviates from the linear relationship (eq. [11]); if this occurs, it can instead be modeled by some polynomial function:

$$d_{33} = d_0 + \alpha\sigma_0 + \beta\sigma_0^2 + ... = d_0 + \alpha'\sigma_0 \qquad [13]$$

This new function $\alpha'(\sigma_0)$ is then substituted into equation [12] to give the relevant charge-stress loop at the chosen amplitude σ_0.

Importantly, such a Rayleigh, or quasi-Rayleigh, approach has been successfully applied to describe the piezoelectric response of many different piezoelectric ceramics including PZT[13,45] (see fig. 13) and barium titanate[13]. Observance of the Rayleigh law demonstrates unequivocal coupling of non-linearity to hysteresis and, most importantly, points to *pinned interface motion*. In poled ceramics, where ferroelastic switching can be expected, these interfaces can be identified as non-180° domain walls. Notably, it describes *local* rather than *global* switching and will occur at stresses *smaller* than the bulk coercive value σ_C; this point will be returned to in chapter nine.

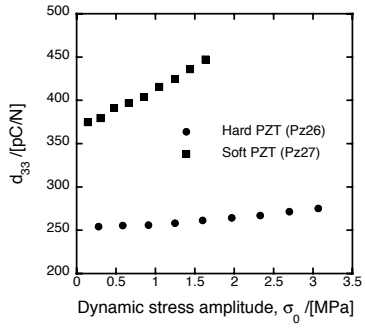

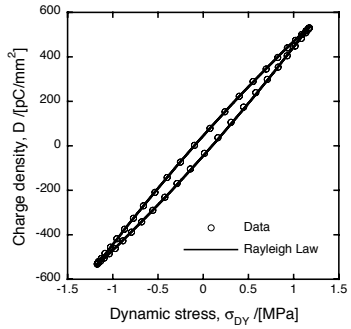

Fig. 13. Rayleigh law behavior in soft and hard PZT ceramics (Pz27 and Pz26 from Ferroperm, Denmark). An experimental charge-stress loop, and a fitted Rayleigh loop, are shown for the sample of soft PZT (Pz27).

Preisach model

As an aside, it has been shown that Rayleigh-type dependence can be derived mathematically based on a stochastic distribution of mobile interfaces in a random pinning field and their response to an applied mechanical or electrical perturbation or "field" F[47]. In this Preisach model[47], the local (piezoelectric) "response" R from such interface motion is modeled by a collection of bistable units which can take just two possible "states" $\pm R_0$. Furthermore, these units are "switched" by a field greater than the coercive value, F_C. Individual bistable units can be locally biased by a field F_B. The response of a given material to an applied field will then generally depend on a statistical distribution of local coercive and bias fields (F_C,F_B). Rayleigh behavior results when this distribution is uniform[47]; otherwise, more complex non-linearities and hystereses[47,48], including pinched loops[49], can result.

Experimental observation of the Rayleigh law

Rayleigh-type behavior was observed in the longitudinal piezoelectric response of all $[001]_C$-poled single crystals. The typical response is shown in figure 14 for a plate-type sample of PZN-8PT. An increasing hysteresis width ($\Delta D = \alpha\sigma_0^2$) is clearly obvious with increasing stress amplitude, accompanied by an increased overall piezoelectric response shown in the gradient of the loop [fig. 14(left)]. This is manifest in a linear increase in d_{33} as a function of σ_0 [fig. 14(right)].

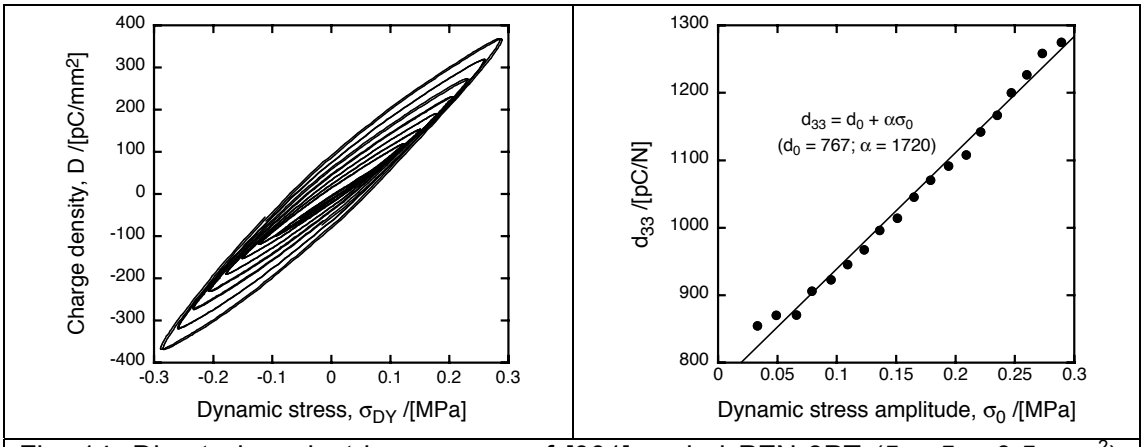

Fig. 14. Direct piezoelectric response of $[001]_C$-poled PZN-8PT (5 x 5 x 0.5 mm^2). The static pressure was ($P + \sigma_{ST}$) = 1.3 MPa; the frequency was 1 Hz.

Linear regression of the data in figure 14(right) gave the Rayleigh parameters $d_0 = 767$ pC/N and $\alpha = 1720$ pC/N/MPa. Note that d_0 is low due to an unfavorable aspect ratio. These parameters were then used to model the charge-stress loop, as shown in figure 15; the fit is good.

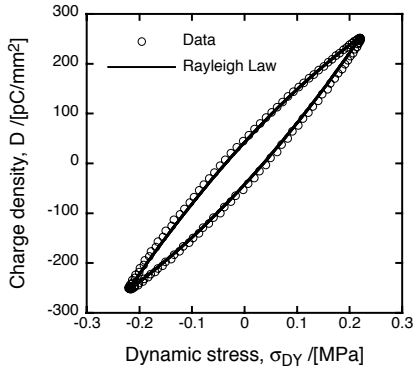

Fig. 15. Modeling of the charge-stress loop using the data for $[001]_C$-poled PZN-8PT shown in figure 14 (σ_0 = 0.2 MPa). The loop agrees well with the experimental data.

As a small aside, it is perhaps helpful to clarify the meaning of the horizontal axes chosen in figure 15. The time-dependent charge density (D) is plotted against the dynamic component of the stress (σ_{DY}) which is a zero-centered sinusoidal function. The charge density is center-shifted as a mathematical convenience.

Figure 16 shows two successful attempts to model the charge-stress loops measured in $[001]_C$-poled samples of PMN-31PT and PZN-4.5PT. In each case, α was derived by fitting a polynomial expression (equation [13]) to the $d_{33}(\sigma_0)$ data in figure 9. Figure 16(a) shows a characteristically hysteretic, *high-field* response for the two crystals; figure 16(b) shows a characteristic, anhysteretic *low-field* response. For both PMN-31PT and PZN-4.5PT samples there was a smooth transition from visibly anhysteretic to hysteretic behavior with increasing stress amplitude. The same trend is shown explicitly in figure 14 for PZN-8PT and is evidence for Rayleigh-law behavior.

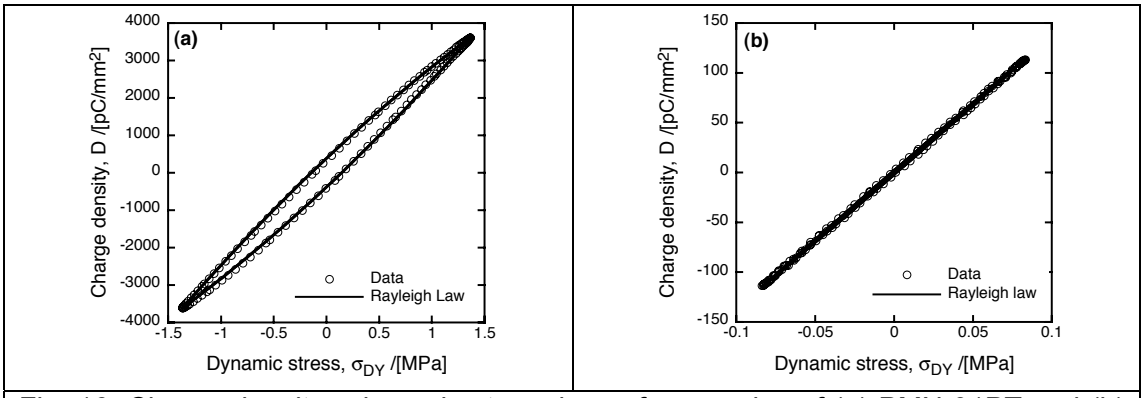

Fig. 16. Charge density - dynamic stress loops for samples of (a) PMN-31PT and (b) PZN-4.5PT. Appropriate Rayleigh law plots based on the data in figure 9 are also shown. In each case the frequency was 1 Hz; the values of static stress are the same as those in figure 9.

To summarize, figures 9, 10, 14, 15 and 16 demonstrate the hysteretic and non-linear behavior of $[001]_C$-poled PMN-xPT and PZN-xPT in the direct piezoelectric effect. Moreover, the clear coupling of non-linearity to hysteresis is demonstrated by the quasi-Rayleigh relationship. The hysteretic behavior itself, and the frequency dispersion of d_{33}, both indicate some irreversible interface motion in these materials. Comparing directly to the response of ferroelectric ceramics (fig 13), these might be identified as *ferroelastic domain walls*.

As discussed above, hysteresis in PMN-31PT and PZN-8PT might well be explained by a "4O", engineered, domain structure where all domain states are not equivalent with respect to the applied pressure (fig. 4). However in PZN-4.5PT, which certainly has a rhombohedral symmetry at room temperature[50] and therefore a "4R" poled domain state, ferroelastic switching is unexpected. Notably, both $[001]_C$-poled "4R" and "4O" compositions show qualitatively similar responses.

Effect of static pressure

The variation in $d_{33}(\sigma_0)$ with changing static bias stress σ_{ST} is shown in figure 17 for PMN-31PT. There is a clear decrease in d_{33} with increasing static stress which is more prominent at higher dynamic stresses. Measurement of the low dynamic stress portion of the curve is prone to error due to problems of charge drift; extrapolation of the curve to the vertical axis is also difficult due to its obvious non-linearity. It is therefore difficult to precise any effect of the static bias stress on the reversible piezoelectric coefficient (d_0) although the convergence of the data at low dynamic stresses indicates that d_0 is unaffected. This suggests that the sample is probably not depoling during the experiment.

However, the static bias stress clearly reduces the coefficient of non-linearity α and, therefore, the hysteretic component of the piezoelectric coefficient (i.e. $\alpha\sigma_0$ in equation [11]). This response is qualitatively the same as that seen in coarse-grained PZT and barium titanate ceramics where it is

assumed that static pressure effectively "clamps" non-180° domain wall motion[13]. The same behavior was likewise observed in $[001]_C$-poled PZN-8PT and PZN-4.5PT.

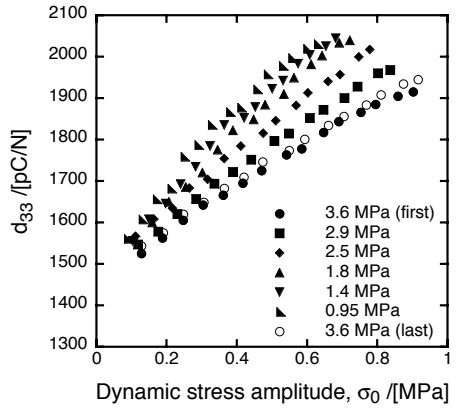

Fig. 17. d_{33} as a function of dynamic stress amplitude at varying static bias stresses (σ_{ST}) in $[001]_C$-poled PMN-31PT [4 x 4 x 2 mm^3]. The prestress and frequency were fixed at 0.6 MPa and 1 Hz, respectively. The measurements were taken for decreasing bias stresses. Finally, the first set of measurements (at ~ 3.6 MPa) was repeated.

By varying the prestress applied to the sample by the stepper motor (P) the effect of much larger uniaxial stresses was investigated. Figure 18 shows the response-diminishing effect of large compressive stresses and subsequent recovery with time for PMN-31PT. Firstly, a set of $d_{33} - \sigma_0$ measurements was taken at a prestress of 0.6 MPa and a bias stress of 1.8 MPa, i.e. with total static uniaxial stress ($P + \sigma_{ST}$) = 2.4 MPa. By increasing the prestress to 6 MPa and then 12 MPa, subsequent measurements were taken at total static stresses of 9.6 MPa and 17.0 MPa, respectively; a measurement was then again made at a total static stress of 2.4 MPa. Further measurements at total static stresses ~ 2.4 MPa were later made after 24 hours and after one week. Between each set of measurements the sample was completely unloaded. These results, plotted in figure 18, indicate that large uniaxial stresses *depole* the sample, as observed in ferroelectric ceramics[21] and as suggested by the results of Viehland *et al.* for $[001]_C$-poled PMN-30PT (section I). However, the effect is at least partially recoverable with time.

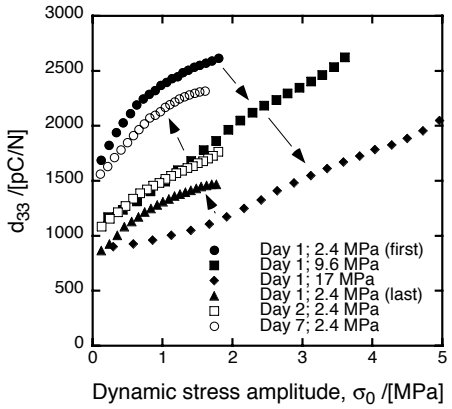

Fig. 18. A series of d_{33}-σ_0 measurements at various prestresses (P) and static bias stresses (σ_{ST}). The total static component of stress ($P + \sigma_{ST}$) for each data series is given in the legend.

Transverse piezoelectric effect

Measurements were also made of the *transverse* piezoelectric coefficient d_{31} and its non-linearity [in the geometry shown in fig. 5(b)]. Only samples of $[001]_C$-poled PZN-4.5PT and PMN-31PT having suitable aspect ratios (4 x 4 x 2 mm^3) were used. Importantly, relative to the longitudinal response, and for comparable static and dynamic stresses, the observed *transverse responses were found to be essentially linear and anhysteretic*.

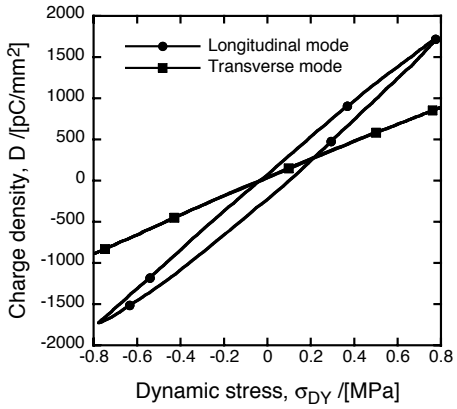

Fig. 19. Charge density-dynamic stress loops for transverse (d_{31}) and longitudinal (d_{33}) modes under comparable values of prestress (P), static bias stress (σ_{ST}) and dynamic stress amplitudes (σ_0). The measurements were taken on the same sample of $[001]_C$-poled PMN-31PT. For the transverse measurement: P = 0.6 MPa, σ_{ST} = 2.8 MPa and σ_0 = 0.8 MPa; the frequency was 1 Hz. For the longitudinal measurement: P = 0.6 MPa, σ_{ST} = 2.7 MPa and σ_0 = 0.8 MPa; the frequency was 10 Hz. The negative sign of d_{31} has been neglected here to facilitate comparison of the two loops.

Figure 19 gives the longitudinal and transverse, charge-stress loops for PMN-31PT where, in both cases, the prestress, static bias stress and dynamic stress were the same. Although the responses at two different frequencies are shown, the lower frequency for the less hysteretic transverse

response could only increase its relative hysteresis width (see figure 11). The charge-stress loop for the transverse measurement is anhysteretic with $d_{31} = -1100$ pC/N whereas the charge-stress loop for the longitudinal measurement is hysteretic with $d_{33} = -2200$ pC/N. The approximate ratio of 1:2 between the transverse and longitudinal coefficients relates favorably to results from resonance measurements elsewhere[40,42].

The difference between the non-linearity in $d_{33}(\sigma_0)$ and $d_{31}(\sigma_0)$ for the same sample of PMN-31PT is shown in figure 20. As shown, d_{33} had a marked non-linearity whereas d_{31} changed little (by 5%) over the same range of stresses. According to equation [11] the gradient of the normalized plot of d_{ij}/d_0 [fig. 20(right)] is α/d_0. Since d_0 is much smaller in the transverse mode, the much larger non-linearity α of the longitudinal mode becomes apparent. The transverse piezoelectric effect is effectively *linear*.

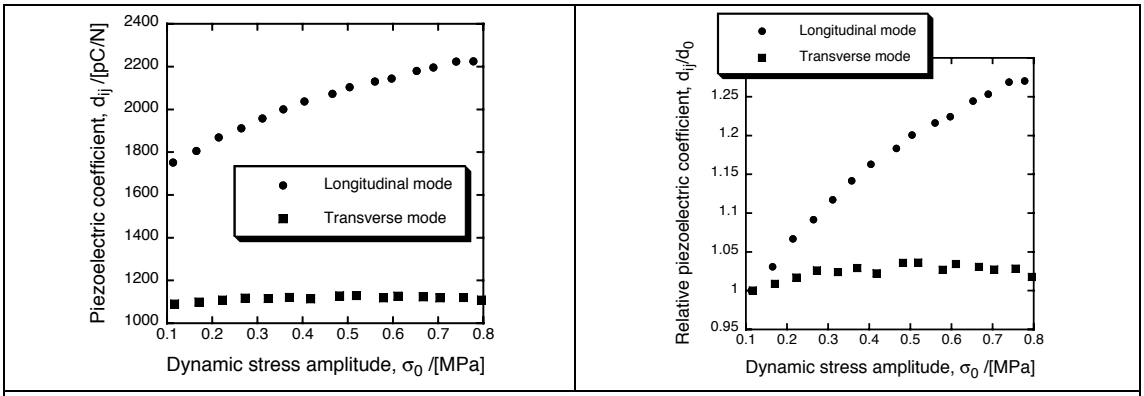

Fig. 20. Dependence of d_{33} and d_{31} on dynamic stress amplitude for a sample of PMN-31PT. The negative sign of d_{31} has been neglected. The values are shown normalized to their static value d_0 on the right.

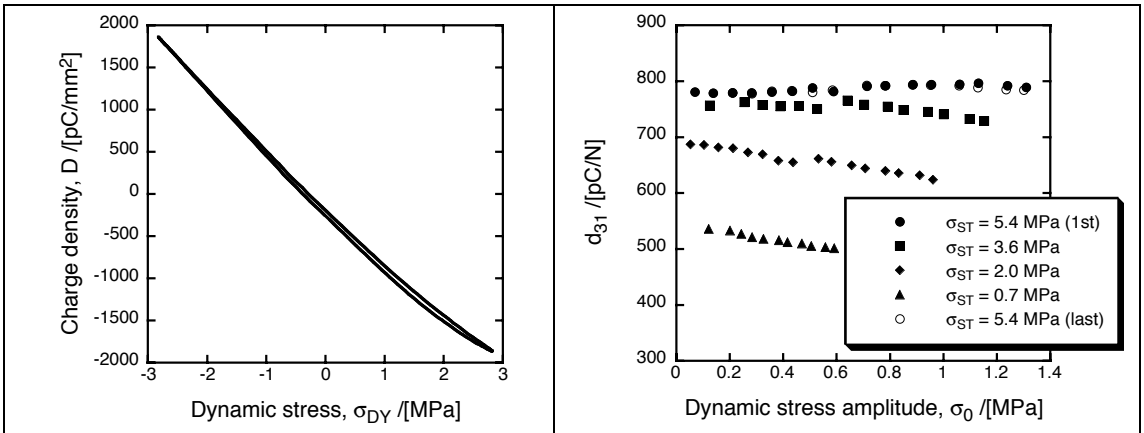

Fig. 21. (Left) Transverse piezoelectric response of $[001]_C$-poled PZN.4.5PT [f = 1 Hz, P = 1 MPa, σ_{ST} = 2.8 MPa]. (Right) Variation of $d_{31}(\sigma_0)$ with increasing static pressure for the same sample at the same prestress and frequency. The sign of d_{31} is negative.

The transverse response of $[001]_C$-poled PZN-4.5PT is shown in the left of figure 21 for higher dynamic stresses. Again, clearly anhysteretic

behavior was observed. For the same sample, d_{31} was found to increase with increasing static pressure σ_{ST} [fig. 21(right)], while remaining linear. In marked contrast to the longitudinal effect, it seems that higher transverse stresses effectively *pole* the sample.

Finally, however, at higher static pressures (> 8MPa), linearity was found to break down leading to hysteretic and non-linear behavior. This is shown in figure 22, again, for a sample of $[001]_C$-poled PZN-4.5PT. Initially, at a total static pressure ($P + \sigma_{ST}$) of 4.3 MPa, d_{31} was essentially linear. The observed decrease in d_{31} with increasing dynamic stress amplitude σ_0 is due to a bending of the charge-stress loops (as evident in fig. 21) and the method of calculating d_{31} based on maximum and minimum points. At 5.8 MPa pressure, the response was still anhysteretic and linear, and higher in magnitude. For higher static pressures (8.8, 12 and 17 MPa), however, the response became markedly non-linear, obeying a Rayleigh-type law. Importantly, upon re-measurement at a lower prestress (3.9 MPa), the behavior was again linear and hysteretic with evidence of a remnant poling effect; d_{31} increased from around 740 to 800 pC/N due to loading at high stresses.

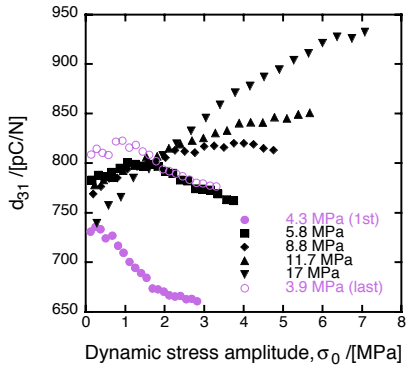

Fig. 22. Transverse piezoelectric response of PZN-4.5PT at various static pressures (P + σ_{ST}); the sign of d_{31} is negative.

Summary

In summary, dynamic measurements of the direct piezoelectric coefficient in $[001]_C$-poled PMN-xPT and PZN-xPT evidence important differences between the transverse and longitudinal effects, where the samples are loaded perpendicular to and along the poling direction, respectively. The origin of this difference will be discussed in section IV.

Aspect ratio effect on non-linearity

Finally, the effect of unwanted lateral stresses during measurements on the observed non-linearity and hysteresis should be discussed. As shown in section II, we can predict the variation in the low field or static piezoelectric

coefficient (d_0); however, prediction of the effect of lateral forces on the measured non-linearity is more involved.

From section II, we have the following expressions for the measured longitudinal and transverse piezoelectric coefficients:

$$d_{33}^{eff} = d_{33} + \left(\frac{\sigma_1}{\sigma_3}\right) d_{31} + \left(\frac{\sigma_2}{\sigma_3}\right) d_{32} = d_{33} + Ad_{31} + Bd_{32} \qquad [14]$$

$$d_{31}^{eff} = d_{31} + \left(\frac{\sigma_2}{\sigma_1}\right) d_{32} + \left(\frac{\sigma_3}{\sigma_1}\right) d_{33} = d_{31} + Xd_{32} + Yd_{33} \qquad [15]$$

where coefficients without a superscript are the true values. Likewise, if we assume that all three coefficients are, to some degree, non-linear and obey the Rayleigh Law, we can write:

$$d_{33} = d_{33}^0 + \alpha\sigma_3 \qquad [16]$$

$$d_{31} = d_{31}^0 + \beta\sigma_1 \qquad [17]$$

$$d_{32} = d_{32}^0 + \gamma\sigma_2 \qquad [18]$$

As shown above, β and γ are seemingly close to zero, at least at low stresses. For the longitudinal coefficient, substitution of equations [16] to [18] into equation [14] yields:

$$d_{33}^{eff} = \left(d_{33}^0 + Ad_{31}^0 + Bd_{32}^0\right) + \left(\alpha + A^2\beta + B^2\gamma\right)\sigma_3 = d_0' + \alpha'\sigma_3 \qquad [19]$$

Since β, γ, A^2 and B^2 are all very small, we expect the coefficient of non-linearity α' to change little with varying aspect ratio. This was indeed observed experimentally. Figure 23 shows measurements of the longitudinal piezoelectric coefficient in various $[001]_C$-poled samples of PZN-4.5PT with different geometries. The dimensions of each sample are marked as "*(a x b) x c* mm^3" in the figure where *a* and *b* are the dimensions of the electroded surfaces and *c* is the height of each sample along the poling direction. The weakest response was observed in the plate type sample (*AR* = 0.1). The response seemed to converge at aspect ratios *AR* > 1. Importantly, there is no evidence for a trend in the non-linearity with varying aspect ratio. In the longitudinal mode, lateral stresses lead to a decrease in the magnitude of d_{33}^{eff} but no affect on its non-linearity; this is due to the inherent linearity of the transverse piezoelectric coefficients, d_{31} and d_{32}.

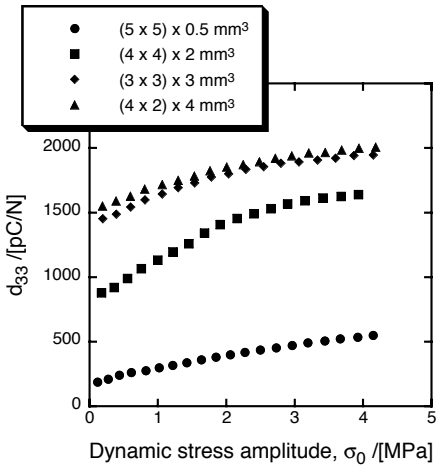

Fig. 23. Longitudinal response in $[001]_C$-poled samples of PZN-4.5PT of various aspect ratios. The intercept values (d_0) from these measurements are those plotted in figure 8.

Finally, since d_{33} is inherently non-linear it may well result in non-linearity in the measured transverse coefficient d_{31}^{eff} (see eq. [15]). Importantly, this is minimal in the special sample geometry chosen here.

IV. DISCUSSION

Two main questions remain unanswered from the above results. Firstly, why is the longitudinal response in $[001]_C$-poled, "4R" PZN-4.5PT hysteretic when the engineered-domain structure predicts an anhysteretic response analogous to that seen in converse measurements? Although PZN-4.5PT, PMN-31PT and PZN-8PT will not all be the same phase, and will therefore have different domain structures, their behaviors are qualitatively the same. And secondly, why is the longitudinal direct piezoelectric effect hysteretic for PMN-31PT and PZN-4.5PT whereas the transverse response is not? Some insight might be gained as follows:

In the longitudinal case, the unit cell deformation driven by pressure in each domain will cause rotation of the spontaneous polarization *away* from the $[001]_C$ poling direction. This is true of both "4R" and "4O" domain-engineered structures, as shown in figure 25(a). Conversely, in the transverse effect [fig. 25(b)], the polarization rotation will be driven *towards* the $[001]_C$ poling direction. Here, therefore, the rotation will be in the same sense as that for application of an electric field along the poling direction [fig. 25(c)]. It is notable that for the two latter situations, (b) and (c), the response is anhysteretic whereas in the longitudinal effect (a), the response is clearly hysteretic.

Interestingly, this analysis suggests that polarization rotations towards and away from the poling direction are not equivalent, at least in terms of hysteresis and non-linearity. Rotation *towards* the poling direction is apparently reversible and yields anhysteretic behavior whereas rotation *away from* the $[001]_C$ poling direction is seemingly irreversible and yields a hysteretic response. It is also interesting to speculate upon what would

happen if a tensile, longitudinal stress were applied parallel to the poling direction instead of a compression; this simple analysis would predict anhysteretic behavior.

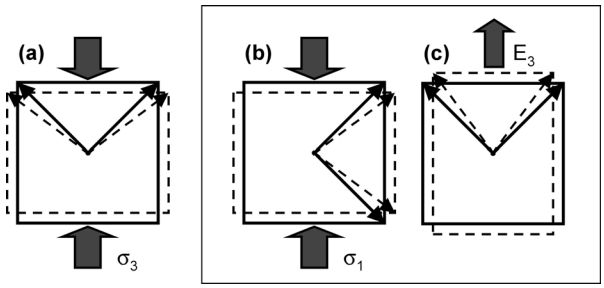

Fig. 25. Schematic representation of the spontaneous polarization vectors in a domain engineered "4O" or "4R" structure for longitudinal d_{33} (a) and transverse d_{31} (b) measurements in the press. Also shown are the polar vectors during converse (strain-field) measurements for application of an electric field along the poling direction.

As discussed in section I, one does not expect to see large-scale ferroelastic switching in a $[001]_C$-poled, "4R", rhombohedral crystal of PZN-4.5PT on application of a compressive stress although it could be expected in "4O" PZN-8PT. However, Rayleigh law behavior and comparison to the behavior of polycrystalline ceramics does indeed point to the motion of interfaces and, most-likely, domain walls. Perhaps for the "4R" crystal, only localized domain-wall displacements related to the polarization rotation mechanism are enough to account for the hysteretic behavior. This possibility will be explored further in the next chapter.

It may also be that other mobile interfaces are responsible for the quasi-Rayleigh behavior. The actual domain structure present in these crystals after poling will certainly be more complicated: composition gradients, two phase coexistences, trapped metastable phases, residual strains, varying domain sizes and degrees of ferroelectric ordering upon increasing $PbTiO_3$ content will all lead to a complex mesoscale structure, as discussed in chapters four and five. The fact that the "4O" and "4R" domain-engineered structures necessarily contain charged domain walls (chapter five) could also be relevant.

Other factors that could arouse hysteretic behavior in an otherwise ideal "4R" crystal include any miss-cut in the supplied crystals with respect to the cubic directions and, equally, any inhomogeneity in the loading conditions. However, all samples investigated were cut to better than ±1° and the anhysteretic transverse measurements suggest that neither problem is manifest here.

V. SUMMARY AND CONCLUSIONS

Significant hysteresis and non-linearity have been observed in the dynamic charge-stress response of $[001]_C$-poled, cuboid samples of PMN-31PT, PZN-4.5PT and PZN-8PT over wide ranges of static and dynamic

stresses. Application of a quasi-Rayleigh type law to the data has shown that these two effects are inherently coupled. The hysteretic component of d_{33} is a strong function of frequency, bias stress and dynamic stress amplitude. At higher dynamic stresses, lower frequencies and lower static stresses d_{33} is larger and the response becomes more hysteretic. High uniaxial prestresses can also depole the samples, thereby reducing the intrinsic (non-hysteretic) component of d_{33}; this effect is recoverable with time. Finally, the transverse d_{31} response of the crystals is found to be essentially anhysteretic, in marked contrast to the longitudinal response.

Comparison of this work to that of Viehland *et al.*[18] suggests that the hysteresis observed in the longitudinal mode is due to large-scale ferroelastic domain switching. However, although ferroelastic switching might be expected in a "4O" domain-engineered structure, it is not expected for the "4R" structure.

Importantly, the difference between the anhysteretic transverse and hysteretic longitudinal behaviors could be related to the relative direction of polarization rotation in each domain upon application of a compressive stress, the sense of which is opposite in each case. If this is true, the hysteresis is not due to large-scale domain switching but rather to an irreversibility of the polarization rotation. Importantly, it appears that polarization rotations towards and away from the poling direction are not equivalent.

Finally, the fact that the transverse piezoelectric response is characteristically anhysteretic, below a certain threshold stress, will have immediate relevance for sensor applications. In sonar applications, for example in Tonpilz transducers, hysteresis leads to loss in precision and "lossy" actuators are to be avoided. Domain-engineered single crystals used in the transverse mode, which demonstrate a large and anhysteretic piezoelectric response ($|d_{31}| > 1000$ pC/N), therefore look very promising for sensor applications. Since the publication[51] of these results in 2004, interest has indeed been shown in the transverse piezoelectric coefficient of domain-engineered PMN-xPT for use in Tonpilz-array type sensors[52].

In the next chapter, the longitudinal response in "4R", $[001]_C$-poled crystals will be compared to that in $[111]_C$-oriented samples. Secondly, the effect of temperature on the direct piezoelectric response will be discussed. Finally, evidence for *stress induced phase transitions* in both longitudinal and transverse modes will be given. Based on this, an explanation for the differing transverse and longitudinal effects will be postulated.

REFERENCES

1 D. Damjanovic, Rep. Prog. Phys. **61,** 1267-1324 (1998).

2 S.-E. E. Park and W. Hackenberger, Current Opinion in Solid State and Materials Science **6,** 11-18 (2002).

3 S.-F. Liu, S.-E. Park, T. R. Shrout, and L. E. Cross, J. Appl. Phys. **85,** 2810-2814 (1999).

4 B. Jaffe, W. R. Cook, and H. Jaffe, *Piezoelectric Ceramics* (Academic Press, 1971).

[5] S.-E. E. Park and T. R. Shrout, J. Appl. Phys. **82,** 1804-1811 (1997).
[6] J. F. Nye, *Physical properties of crystals*, 2nd ed. (Clarendon Press, Oxford, 1985).
[7] C.-S. Tu, I.-C. Shih, V. H. Schmidt, and R. Chien, Appl. Phys. Lett. **83,** 1833-1835 (2003).
[8] D. Viehland, L. Ewart, and J. Powers, J. Appl. Phys. **90,** 2479-2483 (2001).
[9] J. Erhart and L. Burianova, Journal of the European Ceramic Society **21,** 1413-1415 (2001).
[10] D. Stansfield, *Underwater electroacoustic transducers* (Bath University Press, Bath, 1990).
[11] K. Aizu, Phys. Rev. B **2,** 754-772 (1970).
[12] J. Fousek and V. Janovec, J. Appl. Phys. **40,** 135-142 (1969).
[13] D. Damjanovic and M. Demartin, J. Phys.: Condens. Matter **9,** 4943-4953 (1997).
[14] J. Erhart, Phase Transitions **77,** 989-1074 (2004).
[15] M. N. Shetty, V. C. S. Prasad, and E. C. Subbarao, Phys. Rev. B **10,** 4801-4802 (1974).
[16] V. C. S. Prasad and E. C. Subbarao, Appl. Phys. Lett. **22,** 424-425 (1973).
[17] O. Nakao, K. Tomomatsu, S. Ajimura, A. Kurosaka, and H. Tominaga, Jpn. J. Appl. Phys. Part 1 **31,** 3117-3119 (1992).
[18] K. Nakamura, N. Chiba, and S. Ito, in *Conversion of 45° rotated X-cut $KNbO_3$ plates to Y-cut plates by compression*, Montréal, Canada, 2004.
[19] E. Burcsu, G. Ravichandran, and K. Bhattacharya, Proc. SPIE, Smart Structures and Materials 2001: Active Materials: Behavior and Mechanics, C. S. Lynch, Ed. **4333** (2001).
[20] H. Cao and A. G. Evans, J. Am. Ceram. Soc **76,** 890-896 (1993).
[21] A. B. Schäufele and K. H. Härdtl, J. Am. Ceram. Soc **79,** 2637-2640 (1996).
[22] A. Schnell, Ferroelectrics **28,** 351-353 (1980).
[23] C. S. Lynch, Acta Mater. **44,** 4137-4148 (1996).
[24] Q. M. Zhang and J. Zhao, IEEE Transactions on Ultrasonics, Ferroelectrics and Frequency Control **46,** 1518-1526 (1999).
[25] D. Zhou and M. Kamlah, J. Appl. Phys. **96,** 6634-6641 (2004).
[26] W. Chen and C. S. Lynch, Acta Mater. **46,** 5303-5311 (1998).
[27] D. Viehland and J. Powers, Appl. Phys. Lett. **78,** 3112-3114 (2001).
[28] D. Viehland and J. Powers, J. Appl. Phys. **89,** 1820-1825 (2001).
[29] D. Viehland, J.-F. Li, E. McLaughlin, J. Powers, R. Janus, and H. Robinson, J. Appl. Phys. **95,** 1969-1972 (2004).
[30] D. Viehland, J. Powers, L. Ewart, and J. F. Li, J. Appl. Phys. **88,** 4907-4909 (2000).
[31] A. Barzegar, D. Damjanovic, and N. Setter, IEEE Transactions on Ultrasonics, Ferroelectrics and Frequency Control **51,** 262-270 (2003).
[32] A. Barzegar, D. Damjanovic, and N. Setter, Proc. IEEE Ultrasonics Symposium **2,** 1185-1188 (2002).
[33] A. Barzegar, D. Damjanovic, and N. Setter, (unpublished).
[34] W. Cao, in *Piezoelectric Single Crystals and Their Application*, edited by S. Trolier-McKinstry, L. E. Cross, and Y. Yamashita (2004), p. 236-256.

[35] J. Yin, B. Jiang, and W. Cao, IEEE Transactions on Ultrasonics, Ferroelectrics and Frequency Control **47,** 285-291 (2000).

[36] As will be shown in chapter ten, PMN-xPT and PZN-xT are generally more compliant than simpler perovskite ferroelectrics.

[37] www.ferroperm-piezo.com

[38] FEM work was done by Abdolghaffar Barzegar of the Laboratory of Ceramics.

[39] H. Cao, B. Fang, H. Luo, Y. Sun, and J. Guo, Ceramics International **29,** 145-150 (2003).

[40] R. Zhang, B. Jiang, and W. Cao, J. Appl. Phys. **90,** 3471-3475 (2001).

[41] J. Yin and W. Cao, J. Appl. Phys. **92,** 444-448 (2002).

[42] R. Zhang, B. Jiang, W. Jiang, and W. Cao, Materials Letters **57,** 1305-1308 (2003).

[43] R. Zhang, B. Jiang, W. Cao, and A. Amin, Journal of Materials Science Letters **21,** 1877-1879 (2002).

[44] S. A. Turik, L. A. Reznitchenko, A. N. Rybjanets, S. I. Dudkina, A. V. Turik, and A. A. Yesis, J. Appl. Phys. **97,** 064102 (2005).

[45] D. Damjanovic, J. Appl. Phys. **82,** 1788-1797 (1997).

[46] D. Damjanovic, M. Demartin, H. S. Shulman, M. Testorf, and N. Setter, Sensors and Actuators A **53,** 353-360 (1996).

[47] G. Robert, D. Damjanovic, and N. Setter, J. Appl. Phys. **89,** 5067-5074 (2001).

[48] G. Robert, D. Damjanovic, and N. Setter, J. Appl. Phys. **90,** 2459-2464 (2001).

[49] G. Robert, D. Damjanovic, and N. Setter, Appl. Phys. Lett. **77,** 4413-4415 (2000).

[50] B. Noheda, Z. Zhong, D. E. Cox, G. Shirane, S.-E. Park, and P. Rehrig, Phys. Rev. B **65,** 224101 (2002).

[51] M. Davis, D. Damjanovic, and N. Setter, J. Appl. Phys. **95,** 5679-5684 (2004).

[52] K. A. Snook, P. W. Rehrig, X. Jiang, R. J. Meyer, and D. Markley, Proc. IEEE Ultrasonics Symposium**,** 1065-1068 (2005).

Chapter nine

Stress-induced phase transitions

Further work on the dynamic, longitudinal response of $[001]_C$-poled PMN-xPT and PZN-xPT is presented. Notably, the effect of temperature is discussed. It is shown that both the *reversible* (including the intrinsic) contribution and *irreversible* (extrinsic) contribution increase in "4R" PZN-4.5PT and "4O" PZN-8PT as the phase transition to a tetragonal phase is approached. The latter is likely due to an increased interface mobility close to T_{FE-FE}. Most importantly, the reversible contribution is always much larger than the irreversible part in the domain-engineered structures, the latter accounting for around 20% of the response in "4O" PZN-8PT, at room temperature, and 5% in "4R" PZN-4.5PT.

Secondly, stress-induced phase transitions are evidenced in $[001]_C$-poled PZN-4.5PT and PMN-31PT by application of larger compressive stresses (< 100 MPa) both along and perpendicularly to the poling direction (longitudinal and transverse modes, respectively). The hysteretic behavior observed is quite different to that seen in non domain-engineered, $[111]_C$-poled PZN-4.5PT at large stresses due to *global* ferroelectric switching. In the latter (transverse) mode no depolarization of the sample occurs upon unloading, behavior which will be useful for implementation of these crystals in sensing applications. In the longitudinal mode, net depolarization commonly occurs. It is suggested that the difference in behavior, related to the results of the previous chapter, is due to differing directions of polarization rotation with respect to the poling direction. Importantly, "4R" crystals *remain* domain-engineered through the phase transition in the transverse mode. An explanation for the differing responses is postulated based on ferroelastic domain wall motion, driven by the stress-induced phase transition.

I. TEMPERATURE DEPENDENCE

In the previous chapter, the direct piezoelectric response of $[001]_C$-poled PMN-xPT and PZN-xPT to dynamic stresses applied both along and perpendicular to the poling direction was investigated. Whereas the transverse d_{31} response was anhysteretic and linear, the longitudinal d_{33} response was hysteretic and non-linear, and adherent to the Rayleigh law. For any sensor application it also is useful to know the *thermal stability* of a given piezoelectric material, i.e., the variation of its piezoelectric properties with temperature. The effect of temperature on the direct response will be discussed in this section.

Experimental

$[001]_C$-poled samples of ("4R") PZN-4.5PT and ("4O") PZN-8PT were used for this study, prepared as described in the last chapter. Direct measurements were made of the longitudinal response at temperatures between 25°C and 200°C, upon heating, using a small furnace (described in chapter two). The static stresses and dynamic stress amplitudes used for each measurement, as well as the sample dimensions, are marked in the figure captions. All samples were (HTFC) poled by cooling from 200°C under 200 V/mm; they were repoled before each new heating run.

Quantitative descriptions of non-linearity

From the previous chapter, Raleigh-law non-linearity can be written:

$$d_{33} = d_0 + \alpha\sigma_0 \qquad [1]$$

where α is the coefficient of non-linearity and d_0 is the static, or *reversible*, piezoelectric coefficient at zero stress ($\sigma_0 = 0$). Likewise, the logarithmic dependence of piezoelectric coefficient on frequency (chapter eight, fig. 11) might be written:

$$d_{33} = d_{33}^{(f=1\ \mathrm{Hz})} - \gamma \log(f/[\mathrm{Hz}]) \qquad [2]$$

It is defined by two parameters γ, again a measure of non-linearity, and $d_{33}^{(f=1\ \mathrm{Hz})}$, the coefficient measured at 1 Hz.

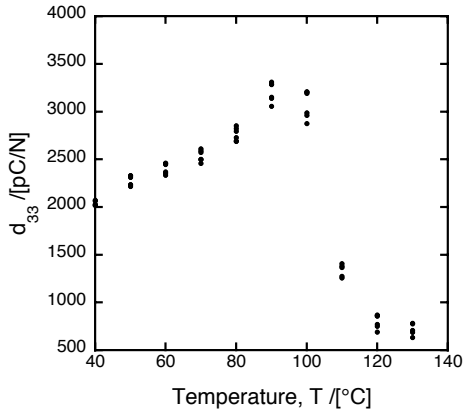

Fig. 1. d_{33} as a function of temperature for $[001]_C$-poled PZN-8PT measured in a Berlincourt-type press, upon heating, at four frequencies: 1, 7, 10 and 50 Hz. Higher response is observed at lower frequency. [($P + \sigma_{ST}$) = 2 MPa; σ_0 = 0.5 MPa]. The sample had dimensions 3 x 3 x 3 mm^3.

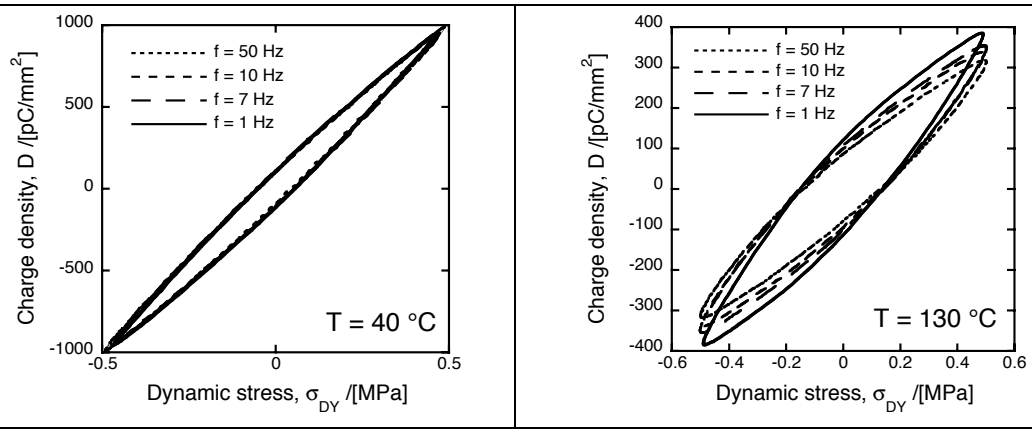

Fig. 2. Charge-stress loops at various frequencies for two temperatures: (left) at 40°C in the "O" phase; (right) at 130°C in the tetragonal phase. Data from $[001]_C$-poled PZN-8PT.

Results

The variation in $d_{33}(f)$ as a function of temperature is shown in figure 1 for a sample of $[001]_C$-poled, domain-engineered "4O" PZN-8PT. As shown previously, "O" PZN-8PT transforms to a tetragonal phase at a temperature (T_{FE-FE}) close to 100°C [see chapter six, figure 11(right)]. Hysteresis loops in both the "O" and T phases, at 40°C and 130°C respectively, are shown in figure 2. As discussed in chapter six, assuming it remains poled, the sample will be quasi-monodomain "1T" above T_{FE-FE}.

Notably, there is a clear increase in d_{33} as the temperature is increased towards T_{FE-FE} in the "O" phase (figure 1). Similar behavior has been shown elsewhere, for example in $[001]_C$-poled PMN-30PT[1,2] and PZN-9PT[3], based on resonance measurements; it was also shown in the strain-field measurements of chapter seven (fig. 14) for $[001]_C$-poled PZN-6.5PT. Moreover, it is qualitatively similar to the behavior observed in $[001]_C$-oriented

barium titanate upon heating through the orthorhombic-tetragonal phase transition[4]; its origins will be discussed in the next chapter.

$d_{33}(f)$ is characteristically large (> 2000 pC/N) in the "4O", domain-engineered state. It is much lower above T_{FE-FE} in the quasi[5]-monodomain "1T" state, where the direct response is measured along the $[001]_C$ polar-axis of the tetragonal phase. This might be expected from *piezoelectric anisotropy*, as will be discussed in the next chapter; it is related to the dielectric anisotropy evidenced in chapter six where the relative permittivity was characteristically low in "1R", "1O" and "1T" samples.

Noticeably, figure 1 suggests that the frequency dispersion increased near the "O"/T transition. By fitting equation [2] to the $d_{33}(f)$ data at each temperature from figure 1, as shown in fig. 3(left), we can plot the variation of non-linearity γ as a function of temperature. This is shown in the right of figure 3. Notably the frequency dispersion quantified by the parameter γ does indeed increase toward the FE-FE phase transition in both "O" and tetragonal phases.

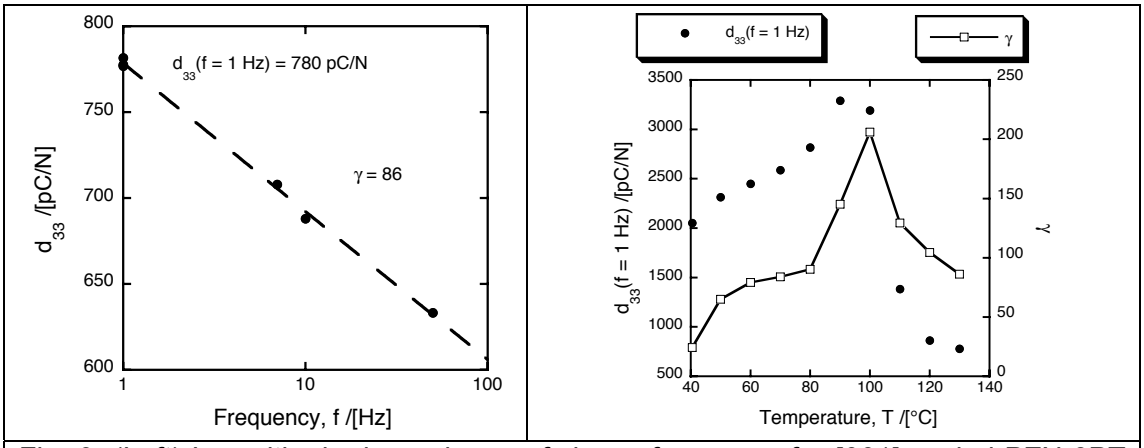

Fig. 3. (Left) Logarithmic dependence of d_{33} on frequency for $[001]_C$-poled PZN-8PT at 130°C. (Right) Variation of the low frequency (1 Hz) piezoelectric coefficient and the coefficient γ with temperature upon heating.

Very similar behavior was observed in "4R", $[001]_C$-poled PZN-4.5PT, as shown in figure 4. From chapter six, figure 11, pseudo-rhombohedral PZN-4.5PT also transforms to a tetragonal phase at a temperature (T_{FE-FE}) close to 100°C. Accordingly, $d_{33}(f)$ increased in the low temperature "R" phase as the "R"/T phase transition was approached [fig. 4(left)]. Again, the frequency dispersion, quantified by γ, was maximum very close to T_{FE-FE}. Notably, there was no qualitative difference between the behaviors of "4O" PZN-8PT and "4R" PZN-4.5PT, both of which are domain-engineered at room temperature and undergo a temperature-induced phase transition to a tetragonal phase.

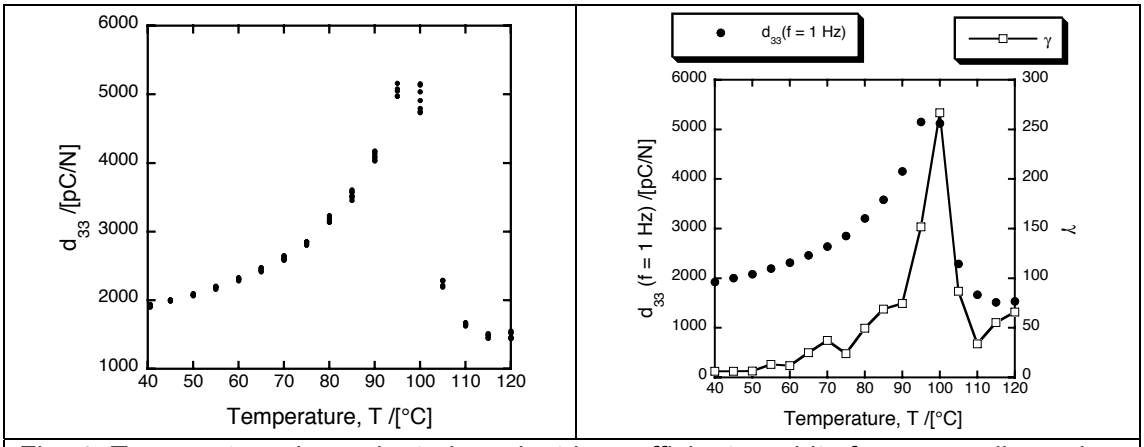

Fig. 4. Temperature dependent piezoelectric coefficient, and its frequency dispersion, in $[001]_C$-poled PZN-4.5PT [3 x 3 x 3 mm^3]. Measurements were made at 1, 7, 10 and 50 Hz. [($P + \sigma_{ST}$) = 2 MPa; σ_0 = 0.5 MPa].

Origin of the frequency dispersion

As noted in chapter eight, quasi-logarithmic frequency dependence of $d_{33}(f)$, as observed in various ferroelectric ceramics, is characteristic of irreversible domain wall motion[6,7]. As shown above, frequency dispersion in the longitudinal, direct response of $[001]_C$-poled PZN-4.5PT and PZN-8PT increases to a maximum at the transition temperature T_{FE-FE}. If the frequency dispersion is indeed due to the motion or "vibration[6]" of pinned domain walls then it seems that the extent of this motion is maximal near first order phase transitions[8].

Notably, the dielectric loss tangent ($D = \tan\delta$) also peaks at both T_{FE-FE} and T_C in $[001]_C$-poled, "4R" and "4O" PMN-xPT and PZN-xPT (see chapter six, fig. 12). Importantly, the peak in dielectric loss *D* (and the minimum in mechanical quality factor *Q*) that occurs just below the Curie temperature in ferroelectrics and ferroelastics is commonly attributed to domain walls[9]. Upon increasing temperature towards T_C there is a decrease in order parameter, or polarization in the case of ferroelectrics (see chapter seven, fig. 1). For tetragonal barium titanate, this corresponds to a decrease in tetragonality[10]. Accordingly, the domain wall energy is reduced near T_C, which leads to an increase in domain wall mobility[9]. This is manifest in a peak in loss tangent at the Curie temperature followed by a sharp decrease in the paraelectric phase; above T_C, all extrinsic contribution from domain walls vanishes as they do.

The situation at transitions *between* ferroelectric phases at T_{FE-FE} is less clear. However, in both barium titanate and potassium niobate, the orthorhombic distortion (see appendix I) does decrease with increasing temperature before the FE-FE transition to a tetragonal phase[10]. Notably, the coercive field E_C also falls[10]. Similar behavior is observed close to the morphotropic phase boundary in PZT which, as discussed in chapter seven, constitutes a chemically-induced, first-order phase transition. In the tetragonal phase, there is a very marked decrease in tetragonality with

decreasing PT towards the MPB[10]; this is accompanied by a strong decrease in coercive field[11].

We might postulate, therefore, that the increase in frequency dispersion $d_{33}(f)$ at T_{FE-FE} evidenced above and the related increase in dielectric loss evidenced in chapter six have the same origin: they are both related to an increased domain wall mobility close to the first-order phase transition between ferroelectric phases.

Separation of extrinsic and intrinsic contributions

As noted in the last chapter, according to the Rayleigh law, the charge-stress hysteresis loop width at the origin ($\sigma_{DY} = 0$) is given by $\Delta D = \alpha\sigma_0^2$. This can be taken from experimental charge-stress loops, for a given frequency, and used to calculate the theoretical (or Rayleigh) *extrinsic* contribution to the piezoelectric response: that is, $\alpha\sigma_0$ in equation [1]. Assuming that the reversible or static part of equation [1], d_0, is comprised only of the *intrinsic* contribution, the extrinsic part can be quite simply calculated from the measured piezoelectric coefficient d_{33} by subtracting $\alpha\sigma_0$. This was done for the data taken from $[001]_C$-poled PZN-8PT and PZN-4.5PT; the results are shown in figures 5 and 6.

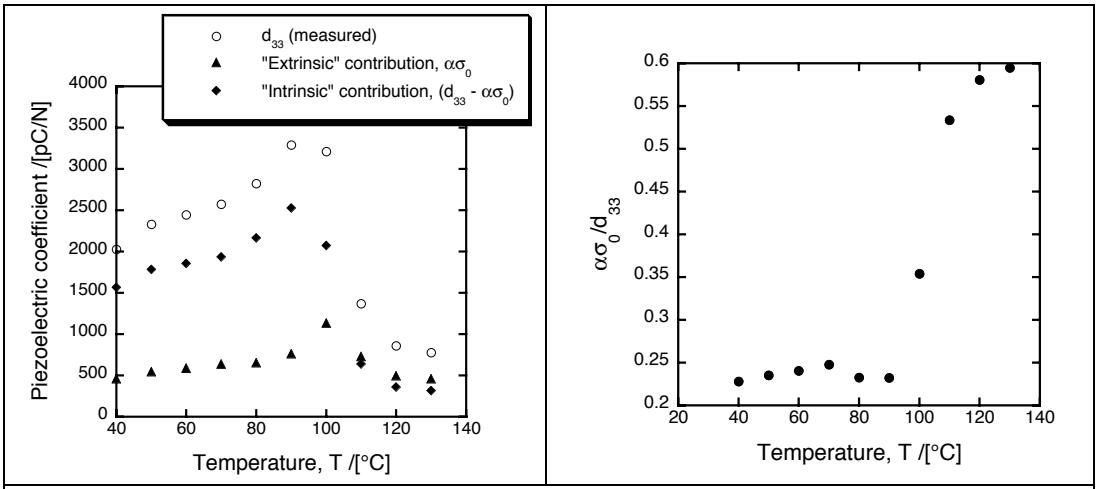

Fig. 5. (Left) Intrinsic and extrinsic contributions to d_{33} assuming Rayleigh behavior in the direct piezoelectric response of $[001]_C$-poled PZN-8PT (f = 1 Hz). (Right) Proportion of the extrinsic contribution to the total measured response.

Figure 5 shows the "intrinsic" (reversible) and "extrinsic" (irreversible) contributions to d_{33} (at 1 Hz) as a function of temperature for $[001]_C$-poled, "4O" PZN-8PT, assuming Rayleigh-law behavior. Notably, both the intrinsic and extrinsic contributions are shown to peak near T_{FE-FE} [fig. 5(left)]. Interestingly, the extrinsic contribution ($\alpha\sigma_0$) peaks 10°C after both the intrinsic contribution (d_0) and the total measured response (d_{33}).

Importantly, in the low temperature, domain-engineered, "O" phase, *the intrinsic contribution is always much larger than the extrinsic contribution*.

However, this is not true in the “1T” tetragonal state where it is smaller than the extrinsic contribution. The relative importance of the extrinsic contribution is more clearly shown in the right of figure 5, where it is plotted as a proportion of the total response ($\alpha\sigma_0 / d_{33}$). In the “4O” domain engineered state, the extrinsic contribution is never more than 25% of the total. In contrast, it reaches around 60% of the total response in the quasi-monodomain “1T” state.

The behavior of “4R”, $[001]_C$-poled PZN-4.5PT was similar, as shown in figure 6, except that here the intrinsic contribution was always larger than the extrinsic contribution, even in the tetragonal phase. However, the relative size of the extrinsic component was again larger in the “1T” tetragonal phase being > 15% compared to 5% at 40°C in the “4R” domain engineered state. The second peak in the extrinsic response upon heating near 120°C is perhaps due to the proximity of the Curie or depoling temperature ($T_d \approx 140$ °C in PZN-4.5PT) and the increased mobility of domain walls discussed above.

Importantly, in both domain-engineered “4R” PZN-4.5PT and “4O” PZN-8PT the reversible contribution is always much larger than the (purely extrinsic) irreversible contribution. Pinned interface motion, for example, accounts for less than 75% of the response in $[001]_C$-poled PZN-8PT and less than 5% of the response of $[001]_C$-poled PZN-4.5PT, at room temperature, for the range of stresses applied. The fact that the irreversible contribution is larger in higher PT-content PZN-8PT is likely related to its proximity to the MPB; as noted above, domain wall mobility seems to increase as FE-FE phase transitions are approached. However, a more systematic study would be needed to confirm this trend.

Finally, there remains the possibility that there is another extrinsic contribution to the piezoelectric response of domain-engineered PMN-xPT and PZN-xPT contained *within* d_0. As will be discussed in chapter ten, this could result from the *presence*, rather than motion, of domain walls.

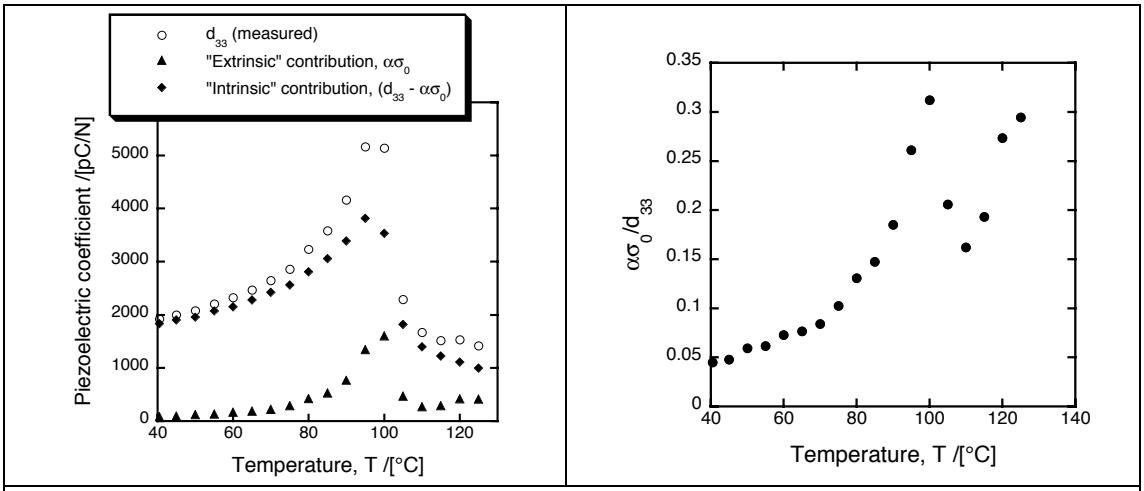

Fig. 6. (Left) Intrinsic and extrinsic contributions to d_{33} assuming Rayleigh behavior in the direct piezoelectric response of $[001]_C$-poled PZN-4.5PT (f = 1 Hz). (Right) Proportion of the extrinsic contribution to the total measured response.

Importance of domain engineering

The fact that the relative extrinsic contribution to the direct piezoelectric response is greatest above T_{FE-FE} in $[001]_C$-poled PZN-4.5PT and PZN-8PT might be expected from consideration of their domain structures. As discussed in chapter six, $[001]_C$-poled, tetragonal PMN-xPT and PZN-xPT will be quasi-monodomain ("1T"). Therefore, (90°) ferroelastic switching *is* expected upon application of a sufficiently-large compressive stress along the $[001]_C$ direction; this can be seen in figure 7(b). As discussed in the previous chapter, however, no ferroelastic domain wall motion is expected in the ideal "4R" structure of PZN-4.5PT under compressive stress [fig. 7(a)].

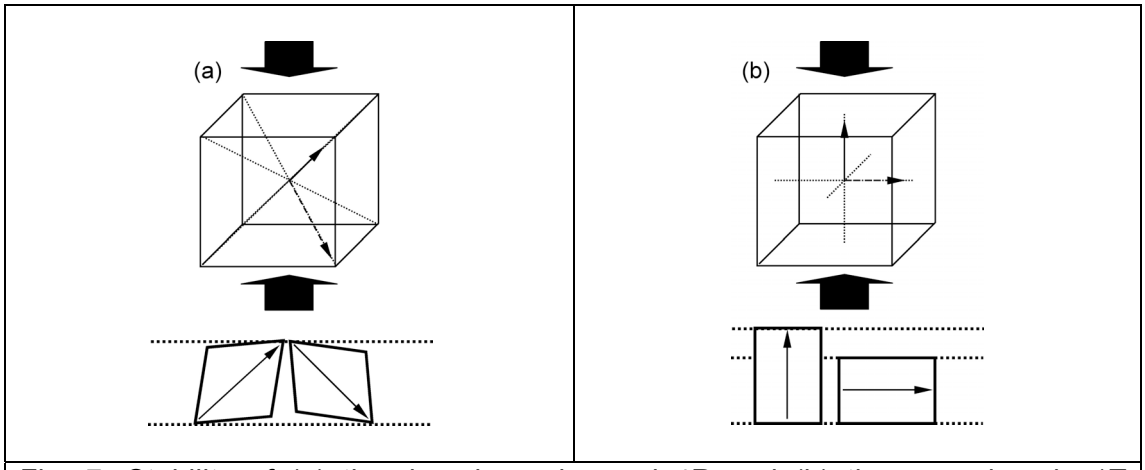

Fig. 7. Stability of (a) the domain-engineered 4R and (b) the monodomain 1T structures to a compressive stress ($\sigma > \sigma_C$) applied along the $[001]_C$ poling direction. In (b), formation of a perpendicular "*a*" domain (90° domain switching) will lead to a net decrease in strain energy. No ferroelastic switching is expected in the 4R structure.

Temperature dependent Rayleigh behavior

Next, measurements of d_{33} as a function of dynamic stress amplitude σ_0 were made at various temperatures to determine if the Rayleigh law also held in the tetragonal phase. This was indeed the case, as shown in figure 8. Rayleigh-type behavior was observed at *all* temperatures below T_d in $[001]_C$-poled PZN-4.5PT and PZN-8PT, in both the low temperature, domain-engineered "4R" and "4O" phases and the high temperature, quasi-monodomain "1T" phase.

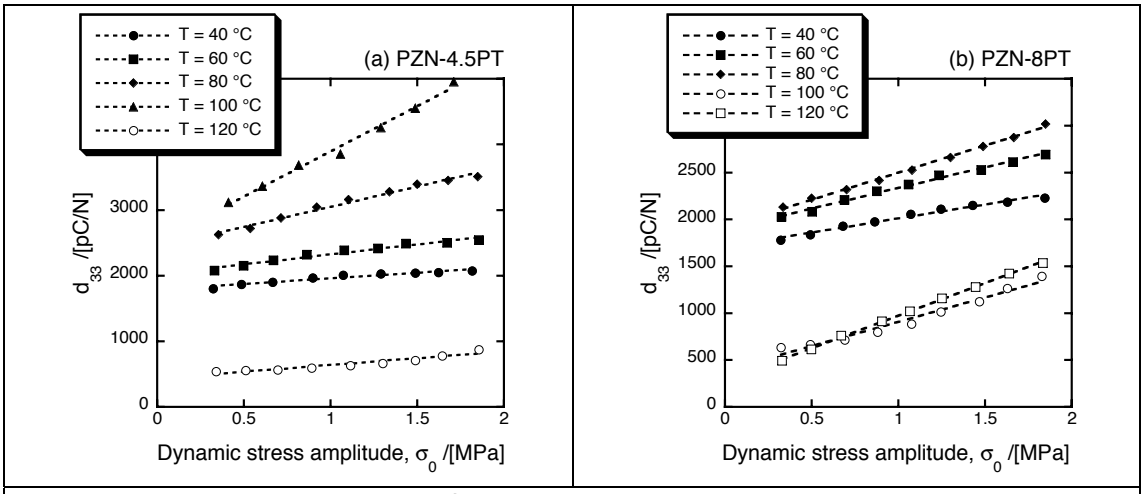

Fig. 8. Rayleigh law behavior of $[001]_C$-poled PZN-4.5PT (a) and PZN-8PT (b) at various temperatures upon heating. [f = 1 Hz, (P + σ_{ST}) = 4 MPa].

For PZN-4.5PT, the coefficient of non-linearity α (equation [1]) increased from 170 to 1380 pC/N/MPa between 40°C and 100°C in the "4R" state [fig. 8(a)]; in the tetragonal phase, at 120°C, the coefficient was 210 pC/N/MPa. For PZN-8PT [fig. 8(b)], α increased from 300 to 580 pC/N/MPa with temperature in the "4O" state; in the tetragonal phase α was 520 and 690 pC/N/MPa at 100°C and 120°C, respectively.

As noted in the previous chapter, Rayleigh law behavior is characteristic of *pinned interface motion*; such interfaces are generally identified as ferroelastic domain walls in ferroelectric materials[7]. Importantly, the coefficient α quantifies the hysteresis and non-linearity wherever the Rayleigh-law applies, and thus the extent of domain wall motion. Therefore, the increase in α upon heating towards T_{FE-FE} fits well with the increase in frequency dispersion (γ) discussed above.

Summary

In summary, the longitudinal, direct piezoelectric response $d_{33}(\sigma_0)$ of $[001]_C$-poled PZN-4.5PT and PZN-8PT is distinctly non-linear over a wide temperature range, in both low-temperature, domain-engineered "4R" and "4O" states and in the high temperature, "1T" tetragonal phase. At all temperatures below T_d, the non-linearity obeys a Rayleigh-type law suggesting an extrinsic contribution from the irreversible motion of *interfaces*. Moreover, quasi-logarithmic frequency dispersion $d_{33}(f)$ is also observed in the "4O", "4R" and "1T" states, giving further evidence for *pinned interface motion*.

In the quasi-monodomain, "1T" tetragonal phase, ferroelastic switching might be expected when a compressive stress is applied along the $[001]_C$ poling direction [fig. 7(right)]. In contrast, it is not expected in the "4R" domain-engineered state [fig. 7(left)], although it might be in the "4O" structure (see chapter eight, figure 4). Importantly, the behaviors of $[001]_C$-poled, "4O" PZN-8PT and $[001]_C$-poled, "4R" PZN-4.5PT are very similar, both at room

temperature and upon heating. Notably, in domain-engineered PZN-8PT and PZN-4.5PT, any irreversible, extrinsic contribution to d_{33} accounts for as little as 5% of the measured response. In the quasi-monodomain, "1T" tetragonal phase, however, the extrinsic contribution is much higher, lying between 15% and 60%.

II. ANISOTROPY OF THE DIRECT PIEZOELECTRIC EFFECT

By orienting and poling along different directions we can investigate the direct piezoelectric response of another quasi-monodomain state. The direct piezoelectric responses of $[111]_C$-poled, "1R" and $[001]_C$-poled, "4R" PZN-6.5PT at room temperature will be compared in this section.

Experimental

$[001]_C$- and $[111]_C$-oriented samples of PZN-6.5PT with nominal dimensions 5 x 5 x 3 mm^3 were donated by Professor Lim at Microfine Technologies. Again, the largest (5 x 5 mm^2) faces were electroded with gold and the samples were (HTFC) poled at 200 V/mm. According to the results of chapter six, a "4R" domain-engineered structure will be present at room temperature in $[001]_C$-poled PZN-6.5PT; in contrast, $[111]_C$-poled PZN-6.5PT is quasi-monodomain "1R".

The dielectric constant and loss tangent of the $[001]_C$-poled sample were 5480 and 0.010, respectively, at room temperature. For the $[111]_C$-poled sample they were 630 and 0.0005; as noted in chapter six, a low dielectric constant is characteristic of a quasi-monodomain state.

Results and discussion

Measurements of the direct (charge-stress) response of the two samples d_{33} were made at room temperature, at various dynamic stress amplitudes σ_0. The results, taken at moderate stresses (< 4 MPa) and with identical loading conditions, are shown in figures 9 and 10.

Notably, the charge-stress response of domain-engineered, "4R" PZN-6.5PT [fig. 9(left)] was noticeably more hysteretic than that of the $[111]_C$-oriented sample [fig. 9(right)]. This was also manifest in the non-linearity $d_{33}(\sigma_0)$, as shown in figure 10.

As for PZN-4.5PT, PZN-8PT and PMN-31PT (chapter eight), $[001]_C$-poled, "4R" PZN-6.5PT showed Rayleigh-law non-linearity [fig. 10(left)] with d_{33} a strong function of dynamic stress amplitude [$d_{33} = (1660 + 1090\sigma_0)$ pC/N]. In contrast, the direct response of $[111]_C$-poled PZN-6.5PT was much less dependent on stress amplitude with $d_{33} = (70 + 6\sigma_0)$ pC/N calculated from a line of best fit. In the $[001]_C$-poled sample, this corresponds to a 60%

increase in d_{33} over the stress range measured [fig. 10(right)]; for the $[111]_C$-poled sample, the coefficient increased by less than 10%.

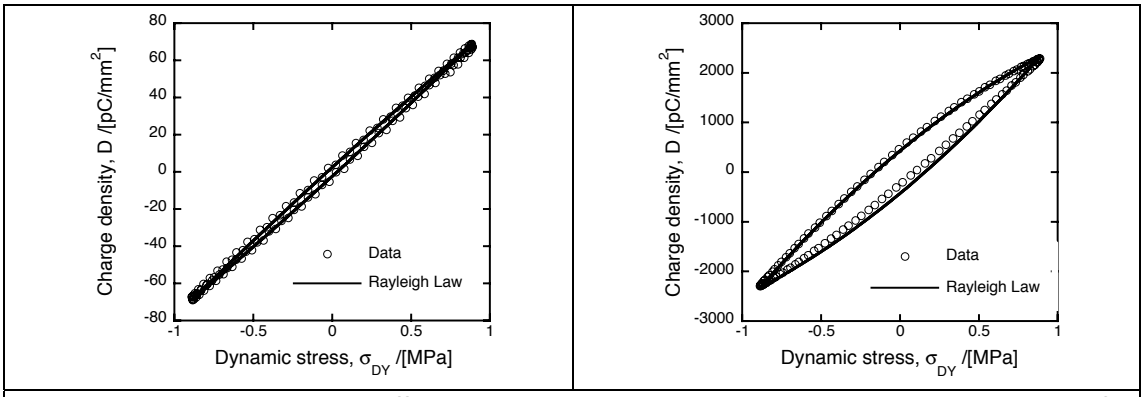

Fig. 9. Direct piezoelectric effect in PZN-6.5PT cut and poled along the $[111]_C$ (left) and $[001]_C$ directions (right). [($P + \sigma_{ST}$) = 3 MPa; f = 1 Hz].

After unloading, the dielectric constant of the $[001]_C$-poled sample had decreased to 4200; the loss tangent was 0.013. In contrast, the relative permittivity of the $[111]_C$ sample had increased to 700, suggesting depoling. The loss tangent was 0.001, slightly higher than before.

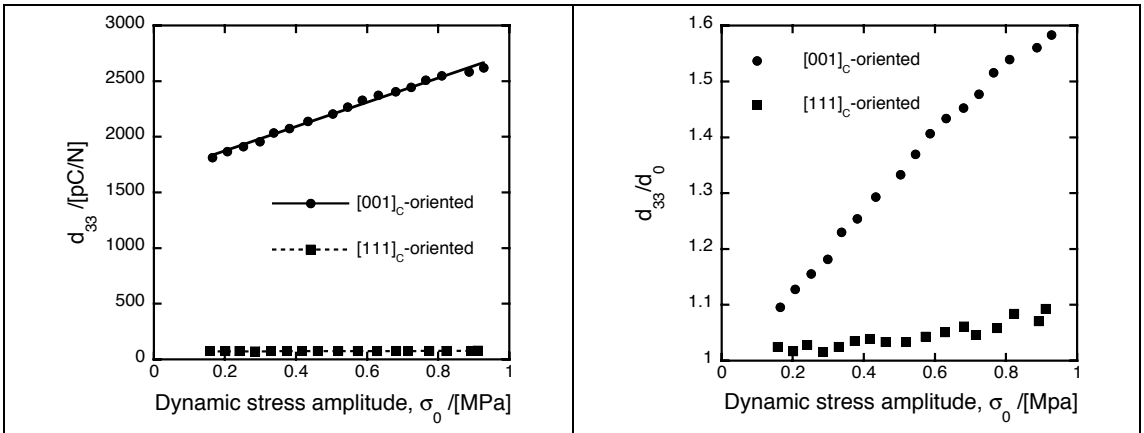

Fig. 10. Direct piezoelectric coefficient as a function of dynamic stress amplitude in PZN-6.5PT cut and poled along the $[111]_C$ and $[001]_C$ directions. [($P + \sigma_{ST}$) = 3 MPa; f = 1 Hz]. Normalized coefficients are shown on the right.

These results are unexpected. As will be shown in the next section, ferroelastic domain wall motion can be expected in $[111]_C$-poled PZN-6.5PT when compressive stress is applied along the poling direction. As stated previously, it is not expected in $[001]_C$-poled, "4R" crystals. However, adherence to the Rayleigh law suggests an irreversible contribution to the response of both samples from pinned interface motion. Further work is necessary to understand why the relative non-linearity is smaller in the $[111]_C$-poled sample. However, it could result from a directional dependence (*anisotropy*) in local coercive stress. Moreover, in $[111]_C$-oriented samples, with one side oriented along a $<1\bar{1}0>_C$-type direction and the other along a $<11\bar{2}>_C$-type direction, the aspect ratio effect (see chapter eight, section II)

due to contributions from the transverse effect is likely to be more complicated.

III. STATIC LOADING CURVES

All the above measurements presented above, and in chapter eight, were made under relatively low stresses (< 20 MPa), *dynamically*, at frequencies of 1 Hz or above. However, we might also investigate the *quasi-static* response at larger compressive stresses; these results could then by compared to the hysteretic charge-stress behavior observed in ferroelectric ceramics where gross ferroelastic switching is expected (chapter eight, section I). This was done by applying uniaxial stresses as large as -200 MPa (quasi-statically)[12], in the Berlincourt-type press, using the stepper motor alone (see chapter two).

Global vs. local switching

First, a note should be made about "global" and "local" domain switching. *Global* ferroelastic switching is usually characterized by *gross* hysteresis as observed, for example, in the strain-field response of "1R" PMN-28PT to unipolar fields ($E > E_C$) applied along the $[111]_C$ direction [see chapter seven, figure 3(left)]. As discussed in the previous chapter, it is also evident in the hysteretic stress-strain behavior of poled ceramic ferroelectrics under compressive stresses greater than the (global) coercive stress ($\sigma > \sigma_C$).

On the other hand, a smaller amount of hysteresis can result from *local* domain switching. Indeed, the Rayleigh law is only valid for *local* interface motion, at stresses below the global coercive field ($\sigma < \sigma_C$), in "sub-switching" conditions. This might be expected if we assume that, in reality, there is a *statistical distribution of coercive fields* σ_C within the sample. Moreover, *local stresses* might become higher than the global (applied) value in some parts of the crystal especially close to defects acting as stress-concentrators. In fact, this is one of the basic assumptions of the Preisach model[13] discussed briefly in chapter eight, which has been used to describe the hysteretic and non-linear behavior of many real ferroelectric materials[14,15].

As shown previously, Rayleigh-law hysteresis and non-linearity is observed in dynamic measurements at low stresses. As will be shown in this section and the next, the behavior under larger, quasi-static stresses, is quite different.

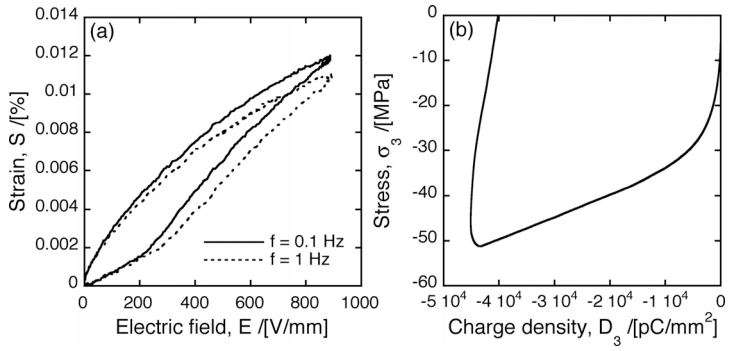

Fig. 11. (a) Unipolar strain-field loop for a (poled) sample of $[111]_C$-oriented PZN-4.5PT measured the Fotonic sensor. (b) Subsequent direct piezoelectric (charge-stress) response of the same sample upon application of a uniaxial compressive stress along the $[111]_C$ direction.

Static loading curves

The large-stress, quasi-static, direct response of a HTFC-poled, $[111]_C$-oriented (4 x 4 x 2 mm^3) sample of PZN-4.5PT is shown in figure 11(b). As for PZN-6.5PT, $[111]_C$-poled PZN-4.5PT is quasi-monodomain "1R" at room temperature. Therefore, as shown in figure 12, (109.5° or 70.5°) ferroelastic switching is expected at large compressive stresses. Importantly, the maximum stress applied in figure 11(b) was around 50 MPa, much greater than that applied dynamically in previous measurements (chapter eight) and close to the coercive stress of hard and soft PZT ceramics[16,17].

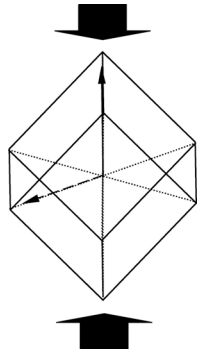

Fig. 12. Ferroelastic (109.5°) domain switching under compressive stress in a $[111]_C$-oriented, rhombohedral crystal.

The converse (strain-field) response of the same PZN-4.5PT sample is shown in figure 11(a). The converse response was measured first, using the optical probe method described in chapter two. It is characteristically weak, with a zero-field gradient of $d_{33} \approx 80$ pm/V, and hysteretic above a critical field E_C ($\approx$ 200 V/mm). Very similar behavior was shown for $[111]_C$-poled PMN-28PT in figure 3 of chapter seven. As discussed there, the hysteresis can be explained by (global) ferroelastic domain wall motion in the absence of

domain engineering. Notably, the coercive field E_C is also frequency dependent.

Notably, the static, charge-stress response of $[111]_C$-poled PZN-4.5PT was also strongly hysteretic, as shown in figure 11(b). At low stresses ($\sigma < \sigma_C$), the curve is linear with a steep gradient ($1/d_{33}$) indicating a small piezoelectric coefficient. Subsequently, at a critical stress ($\sigma_C \approx 10-30$ MPa), there is a sharp change in gradient. The gradient of the high stress portion of the curve is much shallower corresponding to a larger piezoelectric coefficient d_{33} (around 1500 pC/N); this suggests a large extrinsic contribution. Upon unloading, the crystal was significantly depoled with a net depolarization of ΔD_3 = -0.04 C/m^2.

The form of the loop is very similar to that observed in the charge-stress response of PZT ceramics[16-18] and non-domain engineered, single crystal barium titanate, oriented along the polar $[001]_C$ direction[19]. Therefore, we can explain with some confidence the hysteresis and depolarization observed in pseudo-rhombohedral, $[111]_C$-oriented PZN-4.5PT by *global*, ferroelastic (70.5° or 109.5°) switching driven by the application of a uniaxial, compressive stress (fig. 12).

To reiterate, the anhysteretic, low-stress, dynamic response of $[111]_C$-poled PZN-6.5PT, shown in the left of figure 9, is the sub-switching response; that is, the stress applied (4 MPa) was less than the *global* coercive stress (σ_C). The Rayleigh-law hysteresis and non-linearity observed at sub-coercive fields (figure 10) is due to *local* ferroelastic switching.

Summary

All the above results, and those of chapter eight, show that the direct piezoelectric response of PMN-xPT and PZN-xPT single crystals, when finite compressive stresses are applied *along the poling direction*, is generally hysteretic and non-linear. This is true of both domain-engineered ("4O" and "4R") and quasi-monodomain ("1R" and "1T") samples. Observance of the Rayleigh law and quasi-logarithmic frequency dispersion in all cases suggests that the hysteretic behavior is due to an extrinsic contribution from the motion of *mobile interfaces*; most likely, these are ferroelastic domain walls.

In *non domain-engineered*, "1R" and "1T" crystals, ferroelastic switching is expected under compressive stress. Rayleigh law non-linearity is observed below the global, coercive stress σ_C, below which gross ferroelastic switching does not occur. The bulk coercive stress is around 10 - 30 MPa in $[111]_C$-poled PZN-4.5PT [fig. 12(b)].

Finally, if local ferroelastic switching is indeed responsible for the Rayleigh-law behavior of $[001]_C$-poled, "1T" PZN-4.5PT and PZN-8PT above T_{FE-FE} (section I), its relative contribution to the piezoelectric response is seemingly much larger than that in $[111]_C$-poled, "1R" PZN-6.5PT (section II). This could be a consequence of the higher temperature, a higher domain wall mobility, or the different crystal structure.

IV. STRESS INDUCED PHASE TRANSITIONS

As discussed in chapter seven, *stress-induced phase transitions* might be expected in ferroelectric PMN-xPT and PZN-xPT under sufficiently-strong stresses. We can estimate, quite simply, the stress required to bring about such a transition. Taking a simple energetic approach, as used elsewhere to compare coercive fields and stresses[20], we can write:

$$E_T \Delta P_S = \sigma_T \Delta S_S \qquad [3]$$

where E_T and σ_T are the threshold electric field and stress, respectively, for a given phase transition (chapter seven), ΔP_S is the difference between the spontaneous polarizations of the two phases (at E_T or σ_T), and ΔS_S is the difference in spontaneous strain.

For example, for the "O" - T phase transition induced in PZN-8PT by application of an electric field along $[001]_C$ (see chapter seven, fig. 7), the "jump" in strain at $E_T \approx 1200$ V/mm corresponds to $\Delta S_S \approx 0.4\%$. The corresponding jump in polarization, reported elsewhere for the same transition in PZN-8PT (again at around 1200 V/mm)[21], gives $\Delta P_S \approx 0.04$ C/m^2. Thus, we calculate σ_T to be around 12 MPa. Notably, this corresponds to a *tensile* stress, which would be difficult to apply in practice. Importantly, however, it is relatively slight[22].

Stress-induced phase transitions in ferroelectric materials

Some work has been done to study stress-induced phase transitions in ferroelectric crystals and ceramics, although the majority has concentrated on the effect of *hydrostatic* compressive stress, or pressure, σ_H. Within the framework of sixth-order Landau-Ginzburg-Devonshire theory[23], and by including the relevant stress-dependent term to the free energy expansion ΔG, Amin et al. have predicted that the tetragonal phase of PZT will be favored over the rhombohedral phase under hydrostatic pressure[24]: that is, the morphotropic phase boundary will shift to lower PT contents (at σ_H < 700 MPa).

Such "pressure tuning[25]" of the MPB has been investigated experimentally in tetragonal PZT, *in situ*, using X-ray and neutron diffraction. Interestingly, at a pressure of 1.5 GPa, the structure was found to be monoclinic M_A (space group *Cm*). At even higher pressures (3 GPa) an *antiferroelectric* phase of space group *Cc* was evidenced. In this phase, tilting of the oxygen octahedra in the perovskite structure (appendix I) accommodates the shrinkage of the unit cell. Such a phase has also been observed, at very low temperatures[26], in PZT with MPB compositions[27,28]. The same authors later observed a triclinic phase (space group *F1*) in the same composition at even higher hydrostatic pressures (> 4 GPa)[29]. Finally,

a study of unpoled PZN-9.5PT has shown that the dielectric peak at T_m is shifted to lower temperatures by hydrostatic pressures, which favor the pseudocubic, short-range ordered, relaxor phase[30].

Seemingly, however, little work has been done on phase transitions induced by *uniaxial stress*. Recent first principles calculations have predicted a phase transition in rhombohedral PZT, with polarization vector $\boldsymbol{P_S}$ along $[111]_C$, when compressive stress is applied along the $[001]_C$ direction[31]. According to these calculations, the component of polarization along the $[001]_C$ direction is reduced by the applied stress whereas the other two components of polarization remain nearly constant. That is, the transition involves polarization rotation from $[111]_C$, within the M_B monoclinic plane, towards the orthorhombic limiting direction $[110]_C$; this R - M_B - T rotation can be visualized easily using figure 2 of chapter seven. In contrast, in tetragonal PZT, application of a compressive stress along the $[001]_C$ polar direction was shown to reduce the component of polarization along that direction[31]. No polarization rotation occurs, only the length of the polar vector is reduced.

Experimental

$[001]_C$-oriented, 4 x 4 x 2 mm^3 cuboid samples of PZN-4.5PT and PMN-31PT were chosen for the following measurements since they have aspect ratios suitable for transverse (d_{31}) measurements. For measurements in the transverse mode, gold electrodes were sputtered onto the two largest $(001)_C$ faces. For the longitudinal measurements, the crystals were cut into two 2 x 2 x 4 mm^3 columnar samples and gold electrodes were sputtered onto the two smallest 2 x 2 mm^2 faces. The samples were HTFC-poled under 200 V/mm. Static charge-stress loops were then measured by loading and unloading between 0 and 200 MPa. Five or more loops were taken on each as-poled sample. The stable response after two or three loops will be shown below, unless otherwise stated.

Transverse loading

The large-stress response of $[001]_C$-oriented, "4R" PZN-4.5PT, for both longitudinal and transverse loading, was quite different to the behavior observed in $[111]_C$-poled PZN-4.5PT (figure 11). Figure 13(a) shows the transverse ($D_3 - \sigma_1$) response of $[001]_C$-poled PZN-4.5PT; figure 13(b) shows the longitudinal ($D_3 - \sigma_3$) response. In the transverse mode (a), the charge-stress response was linear at low stresses with a reciprocal gradient ($d_{31} = dD_3/d\sigma_1$) of -1290 pC/N. Above a threshold stress σ_T of around 15 MPa, there are two kinks in the curve and an obvious hysteresis before a second, nearly linear, section at high stress (> 30 MPa). The gradient at the maximum compressive stress (d_{31}) was -170 pC/N. The loop is completely closed, indicating its complete reversibility, with *zero depolarization* (ΔD_3 = 0). Most notably, the form of figure 13(a) is very similar to certain

strain-field loops presented in chapter seven where they were evidence for *electric-field induced phase transitions*.

Similar behavior was observed for PMN-31PT, as shown in figure 14(a). Here, however, the threshold stress was lower (< 5 MPa) such that the initial linear region was much smaller. A tangent to the loop at zero stress gave the transverse piezoelectric coefficient d_{31} to be -1520 pC/N. At high stresses, the reciprocal gradient tended to d_{31} = -100 pC/N. Again, the loop was completely closed, with zero depolarization (ΔD_3 = 0).

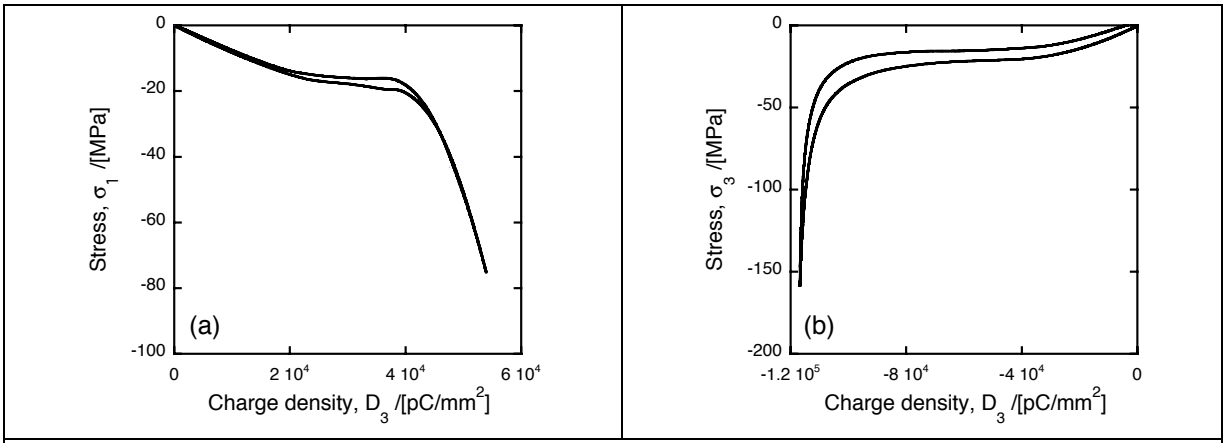

Fig. 13. Quasi-static, direct piezoelectric (charge-stress) loops for samples of $[001]_C$-oriented PZN-4.5PT. In the transverse mode (a) a uniaxial compressive stress σ_1 is applied along $<100>_C$ perpendicular to the poling direction and the charge density along the $[001]_C$ poling direction D_3 is measured; the reciprocal gradient is a measure of d_{31}. In the longitudinal mode (b), a uniaxial compressive stress σ_3 is applied along the $[001]_C$ poling direction, and the charge density D_3 is measured; the reciprocal gradient is a measure of d_{33}.

Longitudinal loading

The longitudinal response of PZN-4.5PT [fig. 13(b)] was also linear at low stresses with a reciprocal gradient at zero stress of around d_{33} = 1550 pC/N. As the stress was increased, the reciprocal gradient of the curve increased sharply at a threshold stress σ_T of around 20 MPa. At high stresses the response saturated and the reciprocal gradient tended to a very low value d_{33} < 30 pC/N. Upon unloading, the curve was hysteretic at all stresses and the loop did not close. The depolarization, reproducible for subsequent cycles, was around ΔD_3 = -0.005 C/m^2.

The behavior was again similar in PMN-31PT, as shown in figure 14(b). As for the transverse mode, the threshold stress was lower than for the sample of PZN-4.5PT being around 5 MPa. Again, the high-stress reciprocal gradient tended to zero; significant depolarization (ΔD_3 = -0.007 C/m^2), similar to that in PZN-4.5PT, was observed upon unloading.

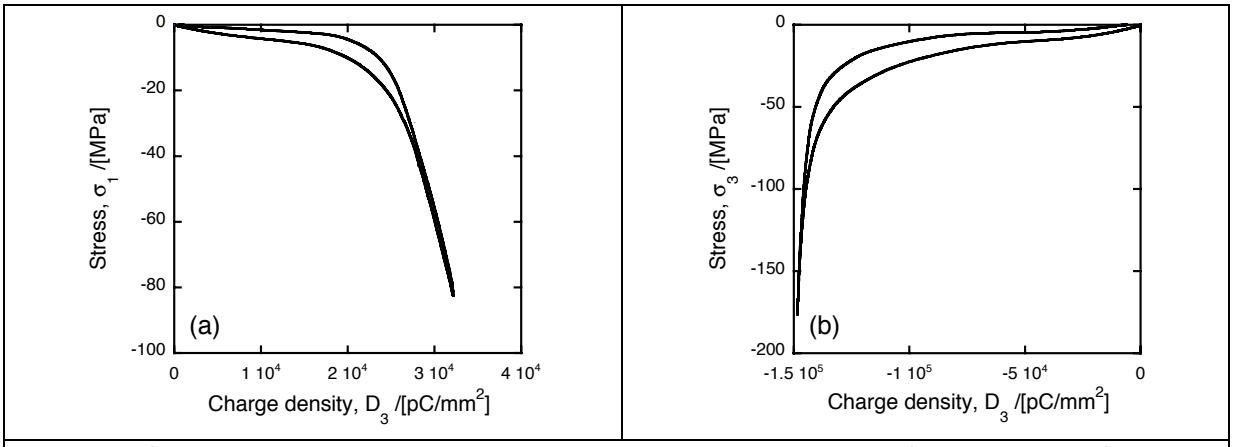

Fig. 14. Quasi-static, direct piezoelectric (charge-stress) loops for samples of $[001]_C$-oriented PMN-31PT: transverse mode (a) and longitudinal mode (b).

Comparison to other work

The longitudinal, charge-stress response of $[001]_C$-poled PZN-4.5PT [fig. 13(b)] and $[001]_C$-poled PMN-31PT [fig. 14(b)] is similar to that observed elsewhere for $[001]_C$-poled PMN-30PT and PMN-33PT[32], and PMN-32PT[33]. In nearly-identical charge-stress measurements, Wan *et al.* (PMN-32PT) and Feng *et al.* (PMN-30PT, PMN-33PT) also observed an initial, linear region at stresses below σ_T. This threshold stress was found to be composition dependent[32], increasing for decreasing PT content, but always of the order of 10 MPa. Above the threshold stress, large hysteresis was observed which saturated at high stresses (> 60 MPa)[33]. Very steep reciprocal gradients at high compressive stress again indicated small values of d_{33}. Moreover, the loops were never closed: remanent *depolarizations* ΔD_3 of the order -0.1 C/m^2 were observed for all compositions, as well as remanent strain.

Interestingly, the remnant depolarizations observed here for PZN-4.5PT (ΔD_3 = -0.005 C/m^2) and PMN-31PT (ΔD_3 = -0.005 C/m^2) were around an order of magnitude smaller than those observed by Feng, Wan and coworkers. The origin for this is unclear. However, as noted above, the charge-stress loops shown in figures 13 and 14 were taken after two or more load-unload cycles when the response had stabilized. Typically, the hysteresis and depolarization observed during the first load-unload cycle was larger than that in subsequent cycles. This is shown in figure 15 for a $[001]_C$-poled sample of PMN-31PT; after the first cycle the depolarization was -0.03 C/m^2 whereas it settled to around -0.007 C/m^2 in subsequent loops.

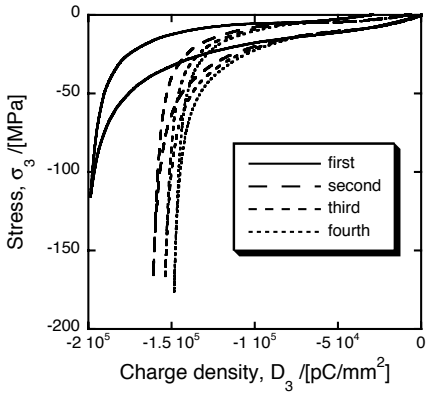

Fig. 15. Charge-stress loops from the first four load-unload cycles for $[001]_C$-oriented PMN-31PT. The first cycle is more hysteretic than the first before settling down in later cycles.

Stress-induced phase transition

Although no explanation for the behavior was offered by Feng *et al.*, Wan *et al.* suggested an underlying *stress-induced phase transition* (SIPT)[33] at the threshold stress, σ_T. However, this was not confirmed *in situ* by diffraction or optical microscopy.

Perhaps a more obvious explanation for the hysteresis would be global ferroelastic switching. The behavior observed is indeed qualitatively similar to the charge-stress response of soft PZT polycrystalline ceramics[18] (see chapter eight), where ferroelastic switching can be expected.

However, as discussed above, the "4R" domain-engineered structure formed in $[001]_C$-poled PZN-4.5PT (and perhaps PMN-31PT) should preclude any domain wall contribution to the direct piezoelectric response under application of a uniaxial stress σ_3. Secondly, there are significant differences between the behavior of domain engineered, $[001]_C$-poled PZN-4.5PT [fig. 13(b)] and $[001]_C$-poled PMN-31PT [fig. 14(b)], where no ferroelastic contribution is expected, and $[111]_C$-oriented PZN-4.5PT [fig. 12(b)], where non-180° domain switching will certainly occur. Thirdly, after a single load-unload cycle, the room temperature dielectric constant of $[111]_C$-poled PZN-4.5PT was found to *increase* significantly (by 40%) from 710, in the as-poled condition, to 1010 indicating a significant reduction in the number of "c" domains (*depoling*); an increase in dielectric constant was also observed in $[111]_C$-oriented PZN-6.5PT after dynamic loading. In contrast, the dielectric constant of $[001]_C$-poled, "4R" PZN-4.5PT changed little (by 5%), from 4970 after poling to 4730 after repeated loading and unloading. Interestingly, the slight increase suggests the domain-engineered sample was better *poled* by large compressive stresses; this will be discussed later.

Importantly, such a stress-induced phase transition would explain the hysteretic strain-field response of $[001]_C$-poled PMN-30PT under large compressive prestress[34] [see chapter eight, figure 2]. Notably, such hysteresis is always removed at high fields. If a SIPT is indeed responsible for the behavior, the bias electric field applied along the $[001]_C$ poling direction will act *oppositely* to the compressive stress.

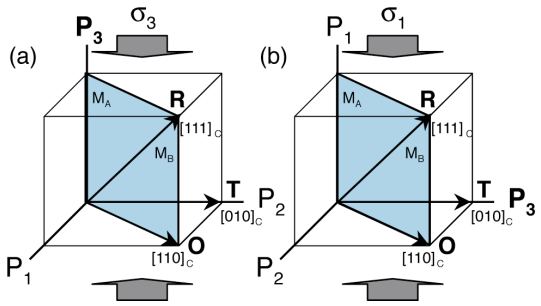

Fig. 16. Schematic illustration of a single rhombohedral domain variant with polarization ***P*** along $[111]_C$ under compressive stress along a pseudocubic $<001>_C$ direction. In this model, application of the stress will lead to a R - M_B - O rotation. In the longitudinal mode (a), the polar vector will rotate *away from* the P_3 poling direction. In the transverse mode (b) the rotation is *toward* the P_3 poling direction.

Polarization rotation path

Thus, there is some evidence to suggest that the hysteretic charge-stress response observed in $[001]_C$-poled, domain-engineered PZN-4.5PT and PMN-31PT when stress is applied along the poling direction is not due to bulk ferroelastic switching. If the behavior is indeed related to a stress-induced phase transition, it is interesting to speculate on the polarization rotation path taken and the resultant ferroelectric phase.

In their paper, Wan *et al.* suggested a stress induced phase transition from a rhombohedral phase to either an orthorhombic or tetragonal phase, via intermediate monoclinic phases[33]. In the simplest case, for a "4R" sample, the rotation will be R - M_B - O, the same as that predicted by first principles calculations for rhombohedral PZT[31].

The path is shown schematically in figure 16(a), for one of the four domain variants in the domain engineered structure. We assume in this schematic that the polar vector in each of the four domain variants of the "4R" structure can rotate freely, independent of the other three; we do not consider the presence of a domain structure. At zero stress, assuming no monoclinic distortion, the polar vector is defined by $P_1 = P_2 = P_3$. Upon application of a compressive stress σ_3 along the $[001]_C$ poling direction, the polar vector $\boldsymbol{P_S} = (P_1, P_2, P_3)$ will rotate away from $[001]_C$ in the M_B $(1\bar{1}0)_C$ monoclinic plane. Due to the symmetry of the loading conditions in this simple, single-variant model, the condition $P_1 = P_2$ should hold; this is one argument for the simplest R - M_B - O rotation and is confirmed by first principles calculations for PZT[31].

Within the framework of this model, the reciprocal gradient measured at zero stress (1550 pC/N for PZN-4.5PT) will correspond to d_{33} of the pseudo-rhombohedral phase for *polarization rotation in the M_B plane*. In the other limit, under large compressive stress, the reciprocal gradient will correspond to d_{22} of the final orthorhombic phase, i.e. zero (see appendix I). The reciprocal gradient does indeed tend to zero at high stresses for both PZN-4.5PT and PMN-31PT, as shown in figures 13(b) and 14(b). Notably,

however, the same would be true if a tetragonal phase were induced ($d_{22} = 0$); we cannot confirm the polarization rotation path in this way.

Importantly, in comparison with the results of chapter seven, the hysteretic, "S"-shaped charge-stress response suggests that the polarization rotation involves a first-order "jump" of the polar vector *within* the M_B monoclinic plane (or between monoclinic planes if a tetragonal phase is induced). That is, the transition will occur by nucleation and growth of the new phase at the threshold stress σ_T.

Phase transition in the transverse mode

The transverse, charge-stress response of PZN-4.5PT [fig. 13(a)] and PMN-31PT [fig. 13(b)] can also be explained by a stress induced phase transition.

For the simple, single-variant model [shown in figure 14(b)] the loading conditions in both longitudinal and transverse modes are completely identical and the R - M_B - O rotation is again expected. Notably, the only difference between the two cases is in the labeling. Importantly, this means the rotation is *toward* the x_3 poling direction in the transverse mode [fig. 14(b)] whereas it is clearly *away from* the poling direction in the longitudinal mode [fig. 14(a)]: this will have important consequences and will be discussed in section V.

Again the form of the charge-stress loop suggests a first-order like phase transition. In the transverse mode, however, the reciprocal gradients are different. At zero stress, for PZN-4.5PT at least, the reciprocal gradient corresponds to d_{31} of the "4R" domain-engineered structure. For $[001]_C$-poled PZN-4.5PT this was -1290 pC/N, slightly higher than the values reported elsewhere from strain-field (-850 pm/V)[35] and resonance measurements (-970 pm/V)[36]. For PZN-4.5PT, in the high stress limit, the reciprocal gradient did not tend to zero but tended instead to a finite value of -170 pC/N. This will correspond to d_{32} ($\neq d_{31}$) of the induced orthorhombic phase or, possibly, d_{31} ($= d_{32}$) of an induced tetragonal phase. Notably, the negative sign of the high field gradient is consistent with the d_{32} of other orthorhombic perovskites, which is commonly negative[37].

Finally, in contrast to the longitudinal measurements, *no remanent depolarization was measured after transverse loading*. This is especially clear for $[001]_C$-poled PZN-4.5PT: compare (a) and (b) in figure 13. Similar charge-stress loops have been reported by McLaughlin *et al.* for $[101]_C$-poled PMN-32PT under compressive stress *perpendicular* to the poling direction[38]. The absence of depolarization in the transverse mode will also be discussed in section V.

***In situ* X-ray diffraction study**

To confirm the stress-induced phase transition, and the polarization rotation path taken, evidence from *in situ* high resolution diffraction or optical

microscopy is needed. As part of this thesis, attempts were made to observe the stress-induced phase transitions in PZN-4.5PT and PMN-31PT by *in situ* X-ray diffraction. Samples were prepared as discussed above; all work was done at the Ecole Centrale de Paris[39].

$\theta / 2\theta$ scans were made around various prominent Bragg peaks using a high-accuracy, two-axis diffractometer in Bragg-Brentano geometry. Diffraction angles could be measured to an accuracy ($\Delta 2\theta$) of 0.002° using a photoelectronic sensor. A specially-built load-cell was fitted to the diffractometer in which loads could be applied between two parallel metal plates by manually turning a brass screw. Uniaxial, compressive stresses as large as 60 MPa could be applied for the sample geometries used.

Unfortunately, it proved very difficult to fit the resultant Bragg peaks to rhombohedral, orthorhombic, tetragonal or monoclinic symmetries; as of February 2006, the data was still not yet fully analyzed. Thus, the polarization rotation path in each case could not be confirmed. However, the work still provided good evidence that the hysteretic charge-stress loops shown in figures 13 and 14 are indeed due to *intrinsic* lattice deformation, that is, rather than extrinsic domain switching.

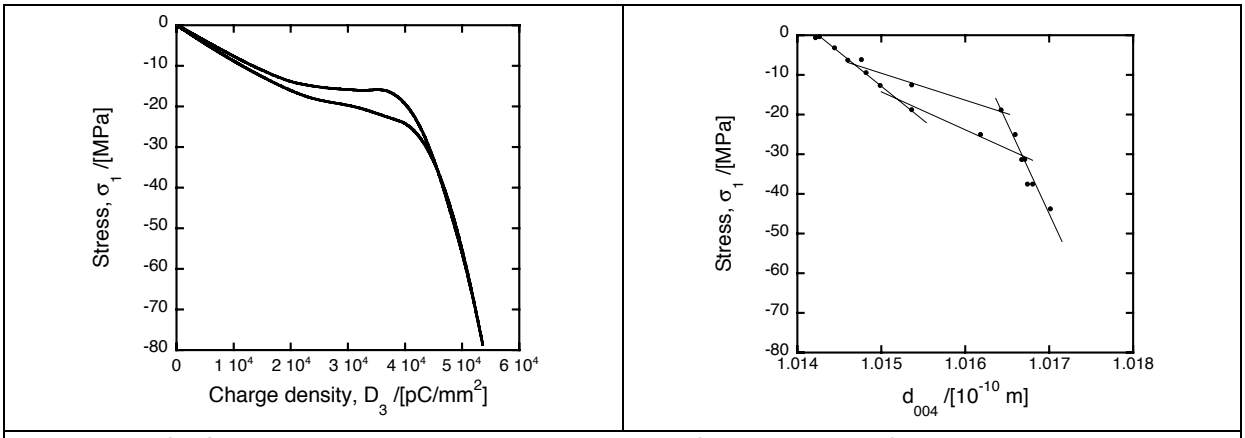

Fig. 17 (Left) Static, transverse charge-stress loop for a sample of $[001]_C$-poled PZN-4.5PT. (Right) $(004)_C$ plane spacing as a function of transverse compressive stress measured in a separate charge stress loop. The lines are shown as a guide for the eye.

The $(004)_C$ plane-spacing d_{004} parallel to the $[001]_C$ poling direction is shown as function of transverse compressive stress σ_1 in the right of figure 17. Alongside is shown the macroscopic charge-stress loop measured from the same sample [fig. 17(left)]. The $(004)_C$ planes are shown schematically in figure 18 with respect to the polarization vectors of the "4R" domain-engineered structure. The charge-stress loop was measured, without repoling, after the *in situ* measurement.

Notably, there is clear hysteresis in the evolution of the d_{004} plane spacing [fig. 17(right)]. Importantly, the hysteresis opens at very similar stress ($\sigma_T \sim 20$ MPa) in both the macroscopic charge-stress loop and in the lattice strain.

More work is needed to confirm the polarization rotation path. However, there is significant evidence in figure 17 alone that a stress-induced phase transition does indeed underlie the behavior observed in figures 13 and

14 for $[001]_C$-poled PZN-4.5PT and PMN-31PT, respectively, when compressive stresses are applied either along or perpendicular to the poling direction. The reason why this leads to differing longitudinal and transverse, direct piezoelectric responses will be discussed in the next section.

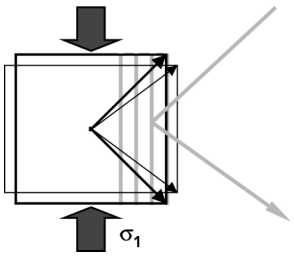

Fig. 18. Schematic for the *in situ* diffraction study shown in figure 17(b): Bragg reflections from the $(004)_C$ planes.

V. COMPARISON OF LONGITUDINAL AND TRANSVERSE RESPONSES

The most important difference between the charge-stress responses of $[001]_C$-poled, domain-engineered PZN-4.5PT and PMN-xPT is that, in the transverse mode, the loops are completely *closed*; no depolarization is observed after unloading indicating complete reversibility of the R - M_B - O path. In contrast, in the longitudinal measurements observed here, and elsewhere[32,33], the loops are not closed and net depolarization *is* observed after unloading.

Importantly, these results fit well with the low-stress (< 10 MPa), dynamic measurements presented in sections I and II, and in chapter eight. For example, the *dynamic*, transverse response of $[001]_C$-poled PZN-4.5PT is anhysteretic and quasi-linear (see chapter eight, figure 21); likewise, so is the *static*, transverse response before a stress-induced phase transition at σ_T [fig. 13(a)]. Therefore, the non-linearity in d_{31} evidenced at higher stresses (> 8 MPa) in PZN-4.5PT (chapter eight, figure 22) can now be explained by the same stress induced phase transition.

Moreover, for $[001]_C$-poled PZN-4.5PT and PMN-31PT, the *dynamic*, longitudinal response is hysteretic and non-linear (see chapter nine, figures 9 and 16). Accordingly, the *static*, longitudinal response at low stresses is also hysteretic [figures 13(b) and 14(b)].

Finally, compressive stresses applied *along* the $[001]_C$ poling direction (in longitudinal measurements) tend to depole the samples; in contrast, stresses applied *perpendicular* to the $[001]_C$ poling direction (transverse measurements) tend to pole the samples. This is observed in both static measurements (section III) and dynamic measurements (chapter eight). The depolarization of $[001]_C$-poled PMN-31PT and PZN-4.5PT manifest in static, longitudinal measurements (section III) seems directly related to the hysteretic behavior observed in dynamic measurements (chapter eight).

Importantly, depoling by ferroelastic switching is not expected in a “4R” domain-engineered crystal under application of a compressive stress along the $[001]_C$ poling direction. Nor is poling by ferroelastic switching expected in

a “4R” crystal upon application of a compressive stress perpendicular to poling direction. A more complex mechanism is required, which will be discussed below.

Mechanism for depolarization

The remanent polarization and strain in $[001]_C$-poled PMN-32PT[33] after loading to high compressive stress (60 MPa) was explained by Wan et al. by the presence of residual tetragonal (though not orthorhombic) domains. In the previous chapter, however, it was postulated that the hysteretic, dynamic d_{33} response is due to a polarization rotation mechanism where the rotation is *away* from the $[001]_C$ poling direction; this is manifest in a net depolarization after loading above σ_T. In contrast, rotation *towards* the poling direction leads to a linear and anhysteretic direct response; no net depolarization, and even a net poling effect, is observed after static loading. Both proposals can be reconciled, as follows.

We start by reexamining the simple R - M_B - O polarization rotation model (figure 16) for transverse and longitudinal loading of a “4R” domain-engineered crystal. As noted above, the two loading conditions are equivalent except for the labeling of the axes. In the longitudinal case [fig. 16(a)] we apply a stress along the poling direction x_3 (such that symmetry fixes $P_1 = P_2$) and measure the P_3 component of polarization. In the transverse case [fig. 16(b)], we apply stress along the transverse x_1 direction (fixing $P_2 = P_3$) again measuring the polarization P_3 along the poling direction. The difference between the two situations is that in the transverse mode the polarization rotation is *toward* the poling direction whereas in the longitudinal mode it is *away*. This has an important consequence: *in the transverse mode, the final orthorhombic structure is domain-engineered with respect to the $[001]_C$ poling direction whereas in the longitudinal case it is not.* This is shown explicitly in figure 19.

Any residual orthorhombic (or tetragonal) domains after unloading in longitudinal measurements would be manifest as a net depolarization and a net remnant compressive strain. The decrease in permittivity would then be due to a lower net transverse permittivity ε_{22} of the orthorhombic (tetragonal) domains compared to the rhombohedral phase[40]. In contrast, residual orthorhombic (or tetragonal) domains in the transverse mode would not lead to net depolarization and might even lead to a net poling effect.

Furthermore, if the reverse path O - M_B - R proceeded in the *opposite* direction upon unloading in the longitudinal mode, leading to (“down”) domains with polar vectors oriented away from the poling direction, a net depolarization would result. This can not occur in the domain-engineered transverse case.

Finally, for “4O” domain-engineered crystals, such as $[001]_C$-poled PZN-8PT, similar arguments predict a stress-induced phase transition to a tetragonal phase via (O - M_C - T) polarization rotation in the M_C monoclinic plane (see figure 2, chapter seven). In the transverse mode the resultant structure would be quasi-monodomain “1T”, and still $[001]_C$-poled, whereas in

the longitudinal mode the resultant structure would consist of four in-plane "*a*" domains and would no longer be domain-engineered. Although it remains to be verified experimentally, the difference in behaviors in the transverse and longitudinal modes is expected to be the same for both "4R" and "4O" domain-engineered crystals.

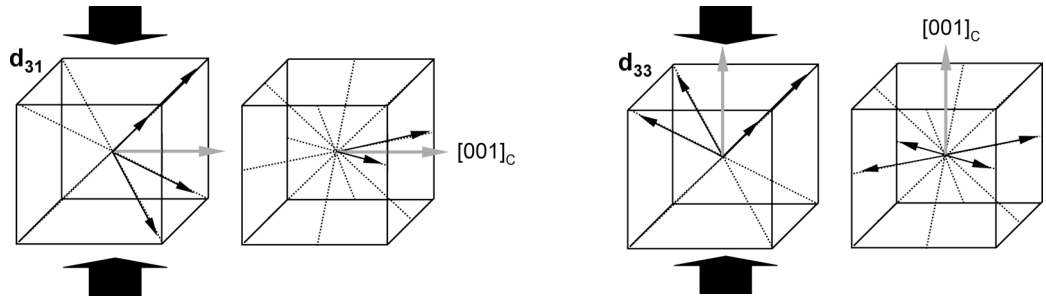

Fig. 19. Schematic showing the <111>$_C$ polarization vectors of the domain variants in a "4R", domain-engineered crystal during stress-induced phase transitions to an orthorhombic phase. In the transverse (d_{31}) mode (left), the resultant structure is domain engineered with respect to the $[001]_C$ poling direction. In the longitudinal (d_{33}) mode (right), the resultant structure is not domain engineered.

Synthesis of ferroelastic switching and phase transition models

The differing small-stress, dynamic responses still remain to be explained. Hysteresis in the static loops (section III), above a critical stress σ_T in the transverse mode but at all stresses in the longitudinal mode, is manifest as Rayleigh-type hysteresis and non-linearity in the dynamic response (chapter eight). Observance of the Rayleigh law is characteristic of irreversible *interface* motion. The Rayleigh law non-linearity and hysteresis in $[111]_C$-poled PZN-6.5PT (section II), $[001]_C$-oriented, "1T" tetragonal PZN-4.5PT and PZN-8PT above T_{FE-FE} (section III), and in a range of ferroelectric ceramics[6,7,41] is commonly explained by ferroelastic switching such that these interfaces can be identified as non-180° *domain walls*. *Global* ferroelastic switching is manifest as gross hysteresis and non-linearity in PZT ceramics[16,17,42], $[001]_C$-oriented barium titanate[43] and $[111]_C$-poled PZN-4.5PT [fig. 11(b)] at compressive stresses above the bulk coercive value ($\sigma > \sigma_C$). In contrast, Rayleigh-type hysteresis (chapter eight) is observed in dynamic measurements at sub-switching stresses ($\sigma < \sigma_C$) and is likely due to *local*, irreversible domain wall "jumps" between pinning centers[7] (defects) due to the locally-reduced coercive stresses and local stress-concentrators. It is better, therefore, to talk of a statistical distribution of coercive stresses: this forms the basis of the Preisach model[13,15] (chapter eight).

Rayleigh-law hysteresis and non-linearity is also observed in "4R" and "4O" domain-engineered PZN-4.5PT, PMN-31PT and PZN-8PT. However, at least in the "4R" domain-engineered structure [fig. 7(a)], ferroelastic domain wall motion is *not* expected when a compressive stress is applied along the $[001]_C$ poling direction; notably, the dynamic, longitudinal responses of both

"4R" and "4O" domain-engineered structures are qualitatively identical (chapter eight and section I).

Thus, another model is proposed based on a stress-induced phase transition to an orthorhombic phase, in the case of "4R" crystals, or to a tetragonal phase, in the case of "4O" crystals. Importantly, in the longitudinal mode, the phase transition leads to net depolarization after loading to high stresses ($\sigma > \sigma_T$). This can be explained by the presence of a residual induced phases. However, for "4O" and "4R" crystals it can also be partially explained by *ferroelastic switching, occurring because the induced phase is no longer domain-engineered with respect to the [001]$_C$ poling direction*. If this were true, the Rayleigh-type hysteresis and non-linearity observed in the dynamic, longitudinal response at low stresses ($\sigma < \sigma_T$) might also be explained by ferroelastic domain-wall motion as a result of a stress-induced phase transition. As for the coercive stress, this would require a statistical distribution of stresses and threshold fields σ_T and, therefore, the possibility of *local* phase transitions at sub-threshold stresses ($\sigma < \sigma_T$). In fact, this might be expected, especially in relaxor-ferroelectric PMN-xPT and PZN-xPT, which show complex mesoscale structures (chapter four) and which are strongly affected by the presence of random fields[44,45]. As discussed briefly in chapter seven, random fields and the resultant statistical distribution in E_T can explain the "diffuseness" of electric-field induced phase transitions in low PT-content PMN-xPT and PZN-xPT[45].

In the transverse mode, however, the stress-induced phase transition leads to a domain-engineered state (at least for "4R" crystals) and will *not* drive ferroelastic switching, locally or otherwise. No hysteresis or non-linearity is observed in the static *or* dynamic, transverse response of PZN-4.5PT or PMN-31PT, at small stresses ($\sigma < \sigma_T$).

Thus, according to this model, domain wall motion and stress-induced phase transitions will be inherently coupled in all but monodomain crystals, except in the transverse mode where the crystal remains domain engineered at high stresses. This gives rise to the interesting possibility that the gross hysteretic behavior in polycrystalline ferroelectric ceramics such as PZT[16,17,42] under compressive stresses is not *purely* due to ferroelastic switching; that is, there is a finite contribution from stress-induced phase transitions, locally or otherwise, in certain grains. Again, this might be expected to occur at reasonably small stresses in PZT, especially with morphotropic phase boundary compositions, where the rhombohedral and tetragonal phases become very close in energy.

Finally, it should be noted that this model remains to be confirmed. Importantly, structural evidence for domain-wall motion under small, longitudinal stresses in domain-engineered "4R" and "4O" crystals is required; likewise, so is evidence for the lack of such motion under transverse stresses. The possibility that other interfaces in the crystal, such as two-phase boundaries, lead to Rayleigh-type behavior needs exploring; however, the motion of first-order phase boundaries, as evidenced by PLM in chapter seven, would not explain the differing longitudinal and transverse behaviors. Lastly, the presence of residual bias fields, as discussed in chapter six, could also have an effect.

Relevance to sensing applications

Whatever the mechanism, as discussed in chapter eight, the difference between the transverse and longitudinal behaviors will have distinct consequences for the use of PMN-xPT and PZN-xPT single crystals in sensing applications. Where linear, anhysteretic (as apposed to "lossy") behavior is required and a small sacrifice in responsiveness can be made (d_{31} is around half the magnitude of d_{33} in $[001]_C$-poled crystals)[36,46,47], the transverse mode should be used. Although both modes become non-linear above a critical stress (around 20 MPa in PZN-4.5PT), due to a stress induced phase transition, this does not lead to depoling in the transverse mode. This is a helpful result.

VI. SUMMARY AND CONCLUSIONS

Firstly, the dynamic, direct piezoelectric response of $[001]_C$-poled PZN-4.5PT and PZN-8PT has been investigated as a function of temperature. Qualitative differences have been evidenced between the behavior in the low temperature, domain-engineered "4R" and "4O" structures, where polarization rotation is expected, and the high temperature, quasi-monodomain "1T" state, where it is not. Importantly, over the entire range of stresses and temperatures considered here, the *reversible* (or "intrinsic") contribution to the piezoelectric response of "4R" and "4O" domain engineered crystals is always greater than the *irreversible* (extrinsic) contribution; the maximum irreversible contribution observed was around 30% in $[001]_C$-poled, "4R" PZN-4.5PT close to T_{FE-FE}. Notably, both reversible and irreversible contributions increase towards the phase transition temperature; the latter is likely a result of increased interface mobility.

Secondly, stress-induced phase transitions have been evidenced by static charge-stress measurement in $[001]_C$-poled PZN-4.5PT and PMN-31PT under application of a compressive stress both along, and perpendicularly to, the poling direction. For "4R" PZN-4.5PT, an "R" - "O" phase transition via polarization rotation in the M_B monoclinic plane (R - M_B - O) is postulated, although it remains to be confirmed by an *in situ* structural study. A first-order like, hysteretic jump is evident within the M_B plane; in comparison with the results of chapter seven, this suggests the induced phase nucleates and grows within the old.

Where the compressive stress is applied along the $[001]_C$ poling direction (longitudinal mode) the induced phase is *no longer domain-engineered* and net depolarization is evident upon unloading. This will be due, at least partly, to local ferroelastic switching, even at low stresses; *local* ferroelastic domain wall motion is manifest in the low-stress, dynamic response as Rayleigh-law hysteresis and non-linearity. In contrast, when a stress is applied perpendicular to the $[001]_C$ poling direction (transverse mode), the resultant structure is domain-engineered with respect to $[001]_C$; no depolarization is observed upon unloading and ferroelastic domain wall

motion, local or otherwise, is not observed in the dynamic response at low stresses.

Finally, the fact that the reversible contribution to d_{33} (i.e., d_0) in $[001]_C$-poled, domain-engineered PMN-xPT and PZN-xPT increases dramatically close to the ferroelectric-ferroelectric (FE-FE) phase transition to a tetragonal phase at T_{FE-FE} is important. As will be shown in the next chapter the *intrinsic* part of d_0 can be expected to increase in proximity to ferroelectric-ferroelectric phase transitions. Furthermore, the possibility of extrinsic contributions to d_0, from the *presence* rather than motion of domain walls, will also be discussed.

Most importantly, ferroelectric-ferroelectric phase transitions are a common feature of PZN-xPT and PMN-xPT around the morphotropic phase boundary, even for small changes in temperature (chapter six), electric field (chapter seven) and stress; this follows from their near degeneracy, especially close to the morphotropic phase boundary. The relevance of phase transitions to the enhanced piezoelectric properties of PZN-xPT and PMN-xPT in *non-polar* directions will be discussed in the next chapter.

REFERENCES

1 D. Viehland and J. F. Li, J. Appl. Phys. **92,** 3985-3989 (2002).

2 A. Amin, in *Electromechanical properties of high coupling single crystals under large electric drive and uniaxial compression*, Montréal, Canada, 2004.

3 J. Kuwata, K. Uchino, and S. Nomura, Jpn. J. Appl. Phys. **21,** 1298-1302 (1982).

4 A. J. Bell, J. Appl. Phys. **89,** 3907-3914 (2001).

5 The hysteresis is gives good validity to the term "quasi-monodomain"; hysteresis would not be expected in a truly monodomain sample.

6 D. Damjanovic, M. Demartin, H. S. Shulman, M. Testorf, and N. Setter, Sensors and Actuators A **53,** 353-360 (1996).

7 D. Damjanovic, J. Appl. Phys. **82,** 1788-1797 (1997).

8 The behavior at the Curie transition is not shown here although evidence was found to suggest that the frequency dispersion increases close to the ferroelectric-paraelectric phase transition as well.

9 X. B. Chen, C. H. Li, Y. Ding, Z. F. Zhang, H. M. Shen, J. S. Zhu, and Y. N. Wang, Phys. Stat. Sol. (a) **179,** 455-461 (2000).

10 B. Jaffe, W. R. Cook, and H. Jaffe, *Piezoelectric Ceramics* (Academic Press, 1971).

11 T. Yamamoto, Jpn. J. Appl. Phys. Part 1 **35,** 5104-5108 (1996).

12 Load/unload cycles usually took a few minutes, depending on the maximum stress and the sample dimensions.

13 G. Robert, D. Damjanovic, and N. Setter, J. Appl. Phys. **90,** 2459-2464 (2001).

14 G. Robert, D. Damjanovic, and N. Setter, Appl. Phys. Lett. **77,** 4413-4415 (2000).

15 G. Robert, D. Damjanovic, and N. Setter, J. Appl. Phys. **89,** 5067-5074 (2001).

[16] A. B. Schäufele and K. H. Härdtl, J. Am. Ceram. Soc **79,** 2637-2640 (1996).
[17] A. Schnell, Ferroelectrics **28,** 351-353 (1980).
[18] C. S. Lynch, Acta Mater. **44,** 4137-4148 (1996).
[19] M. N. Shetty, V. C. S. Prasad, and E. C. Subbarao, Phys. Rev. B **10,** 4801-4802 (1974).
[20] O. Steiner, A. K. Tagantsev, E. L. Colla, and N. Setter, Journal of the European Ceramic Society **19,** 1243-1246 (1999).
[21] M. K. Durbin, J. C. Hicks, S.-E. Park, and T. R. Shrout, J. Appl. Phys. **87,** 8159-8164 (2000).
[22] It is also comparable to the stresses an actuator or sensor might feel in practice.
[23] M. J. Haun, E. Furman, S. J. Jang, and L. E. Cross, Ferroelectrics **99,** 13-25 (1989).
[24] A. Amin, R. E. Newnham, and L. E. Cross, Phys. Rev. B **34,** 1595-1598 (1986).
[25] J. Rouquette, J. Haines, V. Bornand, M. Pintard, P. Papet, C. Bousquet, L. Konczewicz, F. A. Gorelli, and S. Hull, Phys. Rev. B **70,** 014108 (2004).
[26] Hydrostatic pressure and temperature might, here, be considered analagous thermodynamic parameters.
[27] B. Noheda, L. Wu, and Y. Zhu, Phys. Rev. B **66,** 060103(R) (2002).
[28] D. I. Woodward, J. Knudsen, and I. M. Reaney, Phys. Rev. B **72,** 104110 (2005).
[29] J. Rouquette, J. Haines, V. Bornand, M. Pintard, P. Papet, W. G. Marshall, and S. Hull, Phys. Rev. B **71,** 024112 (2005).
[30] G. A. Samara, E. L. Venturini, and V. H. Schmidt, Appl. Phys. Lett. **76,** 1327-1329 (2000).
[31] N. J. Ramer, S. P. Lewis, E. J. Mele, and A. M. Rappe, AIP Conference Proceedings **436,** 156-164 (1998).
[32] Z. Feng, D. Lin, H. Luo, S. Li, and D. Fang, J. Appl. Phys. **97,** 024103 (2005).
[33] Q. Wan, C. Chen, and Y. P. Shen, J. Appl. Phys. **98,** 024103 (2005).
[34] D. Viehland and J. Powers, J. Appl. Phys. **89,** 1820-1825 (2001).
[35] S.-F. Liu, S.-E. Park, T. R. Shrout, and L. E. Cross, J. Appl. Phys. **85,** 2810-2814 (1999).
[36] J. Yin, B. Jiang, and W. Cao, IEEE Transactions on Ultrasonics, Ferroelectrics and Frequency Control **47,** 285-291 (2000).
[37] M. Zgonik, R. Schlesser, I. Biaggio, E. Voit, J. Tscherry, and P. Gunter, J. Appl. Phys. **74,** 1287-1297 (1993).
[38] E. A. McLaughlin, T. Liu, and C. S. Lynch, Acta Mater. **52,** 3849-3857 (2004).
[39] The work was done by Mr Pierre-Eymeric Janolin and Dr. Brahim Dkhil of the Laboratory of Structures, Properties and Modeling of Solids (SPMS).
[40] It cannot be explained by ferroelastic switching since a decrease in permittivity by domain wall motion alone usually means better poling.
[41] D. Damjanovic and M. Demartin, J. Phys.: Condens. Matter **9,** 4943-4953 (1997).
[42] H. Cao and A. G. Evans, J. Am. Ceram. Soc **76,** 890-896 (1993).

[43] V. C. S. Prasad and E. C. Subbarao, Appl. Phys. Lett. **22,** 424-425 (1973).
[44] D. Viehland, J. Powers, L. E. Cross, and J. F. Li, Appl. Phys. Lett. **78,** 3508-3510 (2001).
[45] A. J. Bell, Appl. Phys. Lett. **76,** 109-111 (2000).
[46] R. Zhang, B. Jiang, and W. Cao, J. Appl. Phys. **90,** 3471-3475 (2001).
[47] R. Zhang, B. Jiang, W. Jiang, and W. Cao, Materials Letters **57,** 1305-1308 (2003).

Chapter ten

Single crystal anisotropy and domain engineering

In this chapter, single domain properties are used to calculate longitudinal piezoelectric (d_{33}*) and dielectric (ε_{33}*) coefficients along the <001>$_C$, <101>$_C$ and <111>$_C$, poling directions of the domain-engineered structures formed in various rhombohedral, orthorhombic and tetragonal ferroelectric crystals. The values are then compared to experimental data to estimate any *extrinsic* contribution to the polydomain response in real domain-engineered crystals. It is shown that *intrinsic crystal anisotropy* accounts for at least 50% of the "giant" piezoelectric response ($d_{33}^* > 2000$ pm/V) of [001]$_C$-poled "4R" PMN-33PT and "4O" PZN-9PT. In both cases, the largest contribution to the intrinsic piezoelectric response is from the monodomain piezoelectric shear coefficient d_{15}: that is, from *polarization rotation*. In contrast, the contribution from the monodomain d_{33} coefficient, corresponding to *elongation* of the polar vector (the collinear effect), is relatively slight.

It is noted that in all ferroelectrics, a large *piezoelectric anisotropy* (d_{15}/d_{33}) is related to a high *dielectric anisotropy* ($\varepsilon_{11}/\varepsilon_{33}$) and is a consequence of proximity to ferroelectric-ferroelectric phase transitions. This includes temperature-induced phase transitions, such as those in the simpler perovskites $BaTiO_3$ and $KNbO_3$; it also includes the electric-field and composition induced phase transitions that occur in PMN-xPT and PZN-xPT, close to the MPB, where phases become nearly degenerate. Accordingly, room temperature $BaTiO_3$, $KNbO_3$, PMN-33PT and PZN-9PT can be classified as "*rotators*"; in such materials, enhanced piezoelectric coefficients are expected in non-polar directions and, therefore, can be domain engineered. In contrast, lead titanate is an "*extender*" due to an absence of ferroelectric-ferroelectric phase transitions at all temperatures: in such materials, the collinear effect dominates and reduced piezoelectric coefficients are expected in non-polar directions.

Importantly, the "giant" piezoelectric coefficients observed in [001]$_C$-poled, "4R" and "4O", PMN-xPT and PZN-xPT are *uncommonly* large. This results from the fact that *all* monodomain compliances, piezoelectric coefficients and permittivities are around an order of magnitude larger in PMN-xPT and PZN-xPT compared to their simpler perovskite relatives.

Finally, possible *extrinsic* contributions to the "giant" piezoelectric properties of domain-engineered PMN-xPT and PZN-xPT are discussed. These are likely related to the *presence*, rather than motion, of domain walls.

I. INTRODUCTION

So, what is the origin of the "giant" piezoelectric response of $[001]_C$-poled PMN-xPT and PZN-xPT? Is it purely *intrinsic*, due to the *polarization rotation mechanism in the presence of monoclinic phases*? As noted in chapter seven, it is not clear whether truly zero-field monoclinic phases exist in PMN-xPT and PZN-xPT; indeed, the polarization rotation mechanism might equally be described in terms of field-distorted rhombohedral or orthorhombic phases. The possibility remains that the "ease" of polarization rotation lies, more simply, in the *intrinsic crystal anisotropy* of the zero-field rhombohedral and orthorhombic, rather than monoclinic, phases.

Intrinsic crystal anisotropy

As originally suggested by Kuwata et al. in 1982[1], the origin of the "giant" piezoelectric coefficients of $[001]_C$-poled, domain-engineered, "4R" and "4O" PMN-xPT and PZN-xPT might be to some extent explained by a strong *crystalline anisotropy*: i.e., an intrinsically large variation of the piezoelectric coefficient in space. For example, the longitudinal piezoelectric coefficient of $[001]_C$-poled PZN-4.5PT (d_{33}*), measured using the resonance technique, is 2000 pC/N[2]; the superscript "*" means measurement in a non-polar direction. Similarly, strain-field measurements yield a value of 2100 pm/V[3]. In contrast, the value measured along the rhombohedral polar axis is much smaller. From chapter nine, the sub-coercive, converse (strain-field) response for $[111]_C$-poled (quasi-monodomain) PZN-4.5PT d_{33} is around 80 pm/V. The value reported based on resonance measurements by Liu et al. was 92 pm/V[3].

Therefore, the difference between the piezoelectric response of $[111]_C$-oriented "1R" PZN-4.5PT, and $[001]_C$-oriented, "4R" PZN-4.5PT is huge, greater than a factor of 16. Similar ratios are found for higher PT-content, pseudo-rhombohedral PZN-xPT[1], and in pseudo-rhombohedral PMN-xPT[4,5] as well. Likewise, for pseudo-orthorhombic PZN-9PT, d_{33} measured in a $[101]_C$-poled, "1O" crystal is 250 pm/V[6]; in $[001]_C$-poled, "4O" crystals d_{33}* is 2500 pm/V or more[6], such that the ratio between the two is at least 10. If there is no extrinsic contribution to the response in the polydomain, "4R" and "4O" states, these ratios do indeed imply an inherently-large monodomain anisotropy.

Extrinsic contributions

However, it is also not clear whether or not there is any significant *extrinsic* contribution to the enhanced piezoelectric properties of domain-engineered PMN-xPT and PZN-xPT. As explained in the previous two chapters, such contributions could come from the *motion* of microstructural features such as domains walls, two phase boundaries and so on. However, the domain walls in the "4R" and "4O" domain-engineered structures are expected to be stable to fields applied along the $[001]_C$ poling direction[3]; no domain wall motion is expected and resultant stress-strain curves are

characteristically anhysteretic[3,7,8]. Likewise, there is no evidence of ferroelastic domain wall motion when a uniaxial stress is applied perpendicular to the poling direction of "4R" crystals.

On the other hand, if there were no domain wall motion, might there be an effect simply from the *presence* of a microstructure including, for example, charged domain walls?

General approach

Some insight can be gained in the following way. First, we need to experimentally measure all the independent piezoelectric coefficients d_{ij} of the *monodomain* crystal (5 for *mm2* orthorhombic crystals, 4 for *3m* rhombohedral crystals) with respect to its standard orthogonal basis set. Then, assuming zero extrinsic contribution and "domain average engineering", we can calculate the properties of the off-axis oriented, domain engineered crystal via a simple coordinate transform of the piezoelectric tensor for each domain variant. Finally, we can compare the calculated value of piezoelectric coefficient d_{ij}* to that measured experimentally in a polydomain crystal. The difference between the two values will be a measure of the extrinsic contribution to the response. As will be shown in this chapter, much can be learned about the nature of PMN-xPT and PZN-xPT with such an approach.

II. ORIENTATIONAL DEPENDENCE OF TENSOR PROPERTIES

Calculations of piezoelectric coefficients d_{ijk}*, and likewise mechanical compliances s_{ijkl}* and dielectric permittivities ε_{ij}* and other electromechanical properties, as a function of orientation involve transformations of the coordinate system[9]. They generally start with a complete set of electromechanical coefficients (ε_{ij}, d_{ijk} and s_{ijkl}) for the single domain state, defined with reference to an orthogonal set of axes $\{x_1, x_2, x_3\}$: this will be referred to as the *standard orthogonal basis set*. In perovskites, it is useful to define these axes with respect to those of the cubic parent phase, i.e., the basis set formed by the $<001>_C$ psuedocubic directions.

Standard orthogonal basis sets

In the following, we will use the orthogonal sets of axes for the rhombohedral (R, *3m*), orthorhombic (O, *mm2*) and tetragonal (T, *4mm*) crystal classes as given in Nye[9], that is, as defined relative to one or more symmetry elements of the point group. Defined in this way the tensors ε_{ij}, d_{ijk} and s_{ijkl} for each crystal class have a certain 'standard' form: these are shown explicitly in appendix I for R, O, T and monoclinic phases. We use a

standard right-handed set. The x_3 direction is always the crystal's polar axis, or the direction of spontaneous polarization $\boldsymbol{P_S}$.

For a *4mm* crystal x_1 : $[100]_C$, x_2 : $[010]_C$, x_3 : $[001]_C$ define the obvious set of axes (':' here means 'parallel to'). However, for the rhombohedral and orthorhombic classes there is still some arbitrariness in our choice of axes which can switch or invert the sign of certain coefficients even if the form of the tensor is unchanged[10]. For the rhombohedral *3m* class, we choose x_1 : $[1\bar{1}0]_C$, x_2 : $[11\bar{2}]_C$, x_3 : $[111]_C$ and exercise some caution in using the single domain data from the literature[10]; this will be discussed later. For the orthorhombic *mm2* class, we choose x_1 : $[10\bar{1}]_C$, x_2 : $[010]_C$, x_3 : $[101]_C$. All three sets of axes are shown with respect to the pseudocubic unit cell in appendix I.

Coordinate transforms from the standard basis set

The monodomain, electromechanical properties of various ferroelectric perovskites and, notably, a few relaxor-ferroelectric compositions are available in the literature. They are commonly measured using low-field, resonance or ultrasound techniques, as will be discussed in section III. Using these monodomain values we can calculate the piezoelectric coefficients d_{ijk}^*, compliances s_{ijkl}^* and dielectric permittivities ε_{ij}^* that we would measure in some arbitrary direction via a coordinate transform. Again, "*" refers to measurement away from the polar axis.

Essentially, if we imagine cutting the monodomain crystal in some arbitrary way and measuring its piezoelectric properties, we would actually be choosing a 'new' *measurement coordinate system* with axes $\{x_1', x_2', x_3'\}$. As will become apparent, *x_3'* is thus the poling direction in a domain engineered crystal. To calculate the coefficient in another direction we transform the tensor from the 'old' crystallographic coordinate system $\{x_i\}$, with which we defined ε_{ij}, d_{ijk} and s_{ijkl}, to this new set. This involves use of a *transformation matrix* a_{ij} as shown in equations [1] to [3].

$$\varepsilon_{ij}^* = a_{im}a_{jn}\varepsilon_{mn} \qquad [1]$$

$$d_{ijk}^* = a_{im}a_{jn}a_{ko}d_{mno} \qquad [2]$$

$$s_{ijkl}^* = a_{im}a_{jn}a_{ko}a_{lp}s_{mnop} \qquad [3]$$

The transformation matrix a_{ij} is defined as the cosines of the angles α_{ij} between the 'old' axis x_j and the 'new' axis x_i' ($a_{ij} = \cos\alpha_{ij}$). Equivalently, a_{ij} can be written in terms of the *Euler angles* (ϕ, θ, ψ) which describe sequential, anticlockwise rotations of the coordinate system about the x_3 axis

(by ϕ), the then-rotated x_1 axis (by θ) and the final x_3' axis (by ψ). This is known as the 'ZXZ' convention[11] and is shown in figure 1. In terms of the three Euler angles, the elements of a_{ij} are then:

$$
\begin{aligned}
a_{11} &= \cos(\psi)\cos(\phi) - \cos(\theta)\sin(\phi)\sin(\psi);\\
a_{12} &= \cos(\psi)\sin(\phi) + \cos(\theta)\cos(\phi)\sin(\psi);\\
a_{13} &= \sin(\psi)\sin(\theta);\\
a_{21} &= -\sin(\psi)\cos(\phi) - \cos(\theta)\sin(\phi)\cos(\psi);\\
a_{22} &= -\sin(\psi)\sin(\phi) + \cos(\theta)\cos(\phi)\cos(\psi);\\
a_{23} &= \cos(\psi)\sin(\theta);\\
a_{31} &= \sin(\theta)\sin(\phi);\\
a_{32} &= -\sin(\theta)\cos(\phi);\\
a_{33} &= \cos(\theta)
\end{aligned}
\qquad [4]
$$

Other definitions of the Euler angles are also possible, which give different forms of a_{ij}.

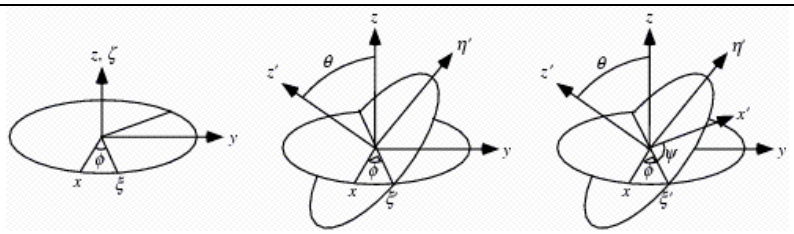

Fig. 1. Definition of the Euler angles describing a coordinate transform from 'old' axes {x, y, z} to 'new' axes {x', y', z'}; this is the 'ZXZ' convention.

III. SINGLE DOMAIN PROPERTIES

Evaluation of all the electromechanical properties of a given monodomain, piezoelectric material is non-trivial. As shown in appendix I, there are 6 independent compliances, 3 independent piezoelectric coefficients and 2 independent dielectric permittivities for a *4mm* crystal. For *3m* rhombohedral and *mm2* orthorhombic crystals there are more. A complete set of measurements generally requires a set of crystals cut in various orientations and is thus susceptible to property fluctuation from compositional variation[12,13], especially for relaxor-ferroelectric PMN-xPT and PZN-xPT. Variations due to incomplete poling are also possible.

Measurements of permittivity

The relative permittivities ε_{11}, ε_{22} and ε_{33} can be quite simply measured by electroding different parallel faces of a pre-poled cube with sides

oriented along the standard orthogonal axes. An impedance analyzer can be used, as discussed in chapter two.

Piezoelectric properties

Some piezoelectric coefficients can also be measured in a straightforward way. As shown in chapter eight, *direct* measurements can be made of the longitudinal coefficient d_{333} (d_{33} in matrix notation[9]) and the transverse coefficients d_{311} and d_{322} (d_{31} and d_{32}). However, in a Berlincourt-type press, the effect of sample aspect ratio can be quite severe and the response will often by a strong function of driving field and frequency due to extrinsic effects. Likewise, measurements of d_{33} made using more simple Berlincourt-type "piezo-meters" can be strongly dependent on the metal contacts used[14]. Moreover, depolarization of the monodomain crystal might be expected when compressive stress is applied along the poling direction.

Otherwise, converse (strain-field) measurements can be made. The piezoelectric coefficient should generally be taken from the zero-field gradient, since piezoelectric coefficients tend to decrease under large biases. As shown in chapter seven, measurements of the longitudinal coefficient d_{33} are quite straight-forward. Likewise, by measuring the strain perpendicular to the applied field, transverse piezoelectric coefficients can be also be determined[3].

Interferometric strain-field measurements are also possible, although they are generally less straight-forward. However, interferometry is much more sensitive than the optical and inductance methods explained in chapter two; thus truly low-field measurements can be taken, which will be less sensitive to extrinsic effects. Longitudinal[15], transverse and even shear coefficients[16] d_{15} ($2d_{113}$)[9] and d_{24} ($2d_{223}$) can be measured.

Resonance measurements

The most common method used to determine the electromechanical properties of a given crystal is the *resonance technique*, based on measurements of impedance (admittance) as a function of frequency. The method is well described elsewhere[17-20], but briefly involves measuring frequencies of *resonance* and *antiresonance* for various vibration "*modes*" (defined by the geometry of the sample used and its boundary conditions) and relating these to the relevant *coupling coefficient* (appendix II). Four important modes are the longitudinal, transverse, planar and thickness coupling mode, defined in appendix II, which correspond to coupling coefficients k_{33}, k_{31}, k_P and k_T, respectively.

Since coupling coefficients are functions of different dielectric, mechanical and piezoelectric properties (appendix II), various electromechanical coefficients can be derived from them. The method is laid out in an IEEE standard[21]. All independent materials coefficients (ε_{ij}, d_{ijk} and

s_{ijkl}) of any *3m*[22,23], *mm2*[6] or *4mm*[24-26] crystal can be determined using the resonance method, provided sufficient, differently-oriented samples are available[13]. The method is most straight-forward for poled ceramic ferroelectrics (Curie group ∞m)[27], which have the same number of material constants as crystals with point group *6mm* (10) and for *4mm* tetragonal crystals which have one more (11). For the other two symmetries, *3m* and *mm2*, more sample orientations are generally required for complete characterization, which will generally lead to more error from property fluctuation, especially in PMN-xPT and PZN-xPT[13].

Ultrasound method

Stiffnesses (compliances) and piezoelectric coefficients can also be determined by measuring the speed of sound through the crystal, in various directions: this is known as the *ultrasonic pulse-echo technique*[28,29]. The speed of an elastic wave propagating through a solid is a function of one or more elastic constants[29]. Thus, measurements of wave velocity for a given propagation mode give direct measurements of elastic stiffnesses. Moreover, since the piezoelectric effect tends to "stiffen[19]" the effective elastic constant of piezoelectric crystals, the method can also be used to derive piezoelectric coefficients as well.

The advantage of the method is that less samples are generally needed to determine all electromechanical properties, which is especially good where property fluctuation might be a problem. In one study, a single sample of complex geometry was used to measure *all* the elastic, piezoelectric and dielectric properties of *3m* lithium tantalate[28]. However, since many velocity measurements are of "impure" modes where the velocity depends on more than one elastic constant, many coefficients must be *derived* from measured values instead of being measured directly; this can lead to significant error[4]. Therefore, "hybrid" methods combining both ultrasonic and resonance methods are sometimes used[4,12,13].

Finally, Brillouin scattering has also been used to measure the piezoelectric and elastic coefficients of various perovskite crystals[30,31].

In conclusion, the best method will often depend on the material being characterized and its symmetry. All measurements of such properties are generally prone to some kind of error, and are sometimes refined in later publications[32-34].

Monodomain values

The monodomain, room-temperature, dielectric, mechanical and piezoelectric coefficients of various ferroelectric crystals with point groups *3m*, *mm2* and *4mm* are shown in tables I, II and III. Values for unclamped permittivity $\varepsilon_{ij}^{\sigma}$, piezoelectric coefficient d_{ij} and compliance at constant field s_{ijkl}^{E} are given relative to the standard orthogonal axes defined above. Non-independent quantities are shown in parentheses.

Properties of *4mm* $BaTiO_3$, $PbTiO_3$, $K_{2.9}Li_{1.6}Nb_{5.1}O_{15}$ (KLN), PMN-38PT and PZN-42PT were lifted from [Zgonik et al. (1994)][33], [Haun et al. (1987)][35], [Adachi et al. (1978)][26], [Cao et al. (2002)[36]] and [Cao et al. (2004)[12]]. The properties of PMN-42PT and PMN-38PT were determined using a hybrid ultrasound-resonance technique; the properties of KLN were determined using the resonance technique. The properties quoted by Zgonik for $BaTiO_3$ are mainly a refinement of previous measurements. Good $PbTiO_3$ crystals cannot easily be grown, and are difficult to characterize due to their high conductivity. Therefore, the monodomain values used for $PbTiO_3$ were those calculated by Haun et al[35] using phenomenological theory, although it would change little here to use others measured experimentally[34]. Compliances are not quoted by Haun and so were taken from Li et al. (1993)[34].

A full set of properties for *mm2* $KNbO_3$ is given in Zgonik et al. (1993)[32]; again the coefficients constitute a refinement of previously published values. The compliances s^E_{ijkl} are not quoted, however, and thus had to be calculated from the stiffnesses c^E_{ijkl}. The properties quoted for PZN-9PT were taken from Dammak et al. (2003)[6] and are based on resonance measurements. The data set is complete, except for four of the compliances. Here, the data was measured from three differently-oriented, $[101]_C$-poled pseudo-orthorhombic (M_C) crystals assuming orthorhombic symmetry since the monoclinic distortion is small[6]; the samples were assumed to be monodomain at zero field. The piezoelectric coefficients were attributed the same signs as for $KNbO_3$.

Table I
Un-clamped relative permittivities for various ferroelectrics with various point groups. Dependent quantities are shown in parentheses.

/[-]	$\varepsilon_{11}^{\sigma}$	$\varepsilon_{22}^{\sigma}$	$\varepsilon_{33}^{\sigma}$	$\varepsilon_{11}^{\sigma}/\varepsilon_{33}^{\sigma}$
Tetragonal *(4mm)*				
$BaTiO_3$[33]	4400	(4400)	130	34
$PbTiO_3$[35]	125.4	(125.4)	67.6	2
$K_{2.9}Li_{1.6}Nb_{5.1}O_{15}$ (KLN)[26]	306	(306)	115	3
PMN-38PT[36]	4301	(4301)	734	6
PMN-42PT[12]	8627	(8627)	660	13
Orthorhombic *(mm2)*				
$KNbO_3$[32]	150	985	44	3
PZN-9PT ($[101]_c$-poled, "O")[6]	**9000**	**21000**	**800**	**11**
Rhombohedral *(3m)*				
$LiTaO_3$[22]	51	(51)	45	1
$LiNbO_3$[22]	84	(84)	30	3
$KrBO_3$[37]	6.6	(6.6)	6.1	1
PMN-33PT ($[111]_c$-poled, "R", biased)[4,10]	**3950**	**(3950)**	**640**	**6**

Table II
Piezoelectric coefficients for various ferroelectrics with various point groups. Dependent quantities are shown in parentheses.

/[pC/N]	d_{31}	d_{32}	d_{33}	d_{22}	d_{24}	d_{15}	d_{15}/d_{33}
Tetragonal *(4mm)*							
$BaTiO_3$[33]	-33.4	(-33.4)	90	0	(564)	564	6.0
$PbTiO_3$[35]	-23.1	(-23.1)	79.1	0	(56.1)	56.1	0.7
$K_{2.9}Li_{1.6}Nb_{5.1}O_{15}$ (KLN)[26]	-14	(-14)	57	0	(68)	68	1.2
PMN-38PT[36]	-123	(-123)	300	0	(380)	380	1.3
PMN-42PT[12]	-91	(-91)	260	0	(131)	131	0.5
Orthorhombic *(mm2)*							
$KNbO_3$[32]	9.8	-19.5	29.3	0	156	206	7.0
PZN-9PT ($[101]_c$-poled, "O")[6]	**120**	**-270**	**250**	**0**	**950**	**3200**	**12.8**
Rhombohedral *(3m)*							
$LiTaO_3$[22]	-2	(-2)	8	+7	(26)	26	3.3
$LiNbO_3$[22]	-1	(-1)	6	+21	(68)	68	11.3
$KrBO_3$[37]							
PMN-33PT ($[111]_c$-poled, "R", biased)[4,10]	**-90**	**(-90)**	**190**	**-1340**	**(4100)**	**4100**	**21.6**

Table III
Elastic compliances (at constant field) for various ferroelectric crystals with various point groups. Dependent quantities are shown in parentheses.

/[10^{-12} m^2N^{-1}]	s_{11}^E	s_{22}^E	s_{33}^E	s_{12}^E	s_{13}^E	s_{23}^E	s_{14}^E	s_{44}^E	s_{55}^E	s_{66}^E
Tetragonal *(4mm)*										
$BaTiO_3$[33]	7.4	(7.4)	13.1	-1.4	-4.4	(-4.4)	0	16.4	(16.4)	7.6
$PbTiO_3$[34]	7.1	(7.1)	21.3	-0.4	-6.3	(-6.3)	0	15.4	(15.4)	9.6
$K_{2.9}Li_{1.6}Nb_{5.1}O_{15}$ (KLN)[26]	5.6	(5.6)	11.8	-1.2	-2.4	(-2.4)	0	14.7	(14.7)	14.3
PMN-38PT[36]	11.7	(11.7)	21.5	-2.7	-8.2	(-8.2)	0	18.0	(18.0)	14.4
PMN-42PT[12]	9.4	(9.4)	19.2	-1.7	-6.1	(-6.1)	0	35.1	(35.1)	12.5
Orthorhombic *(mm2)*										
$KNbO_3$[32]	5.4	5.1	7	-1.5	-1.2	-2.2	0	13.5	40	10.5
PZN-9PT ($[101]_C$-poled, "O")[6]	**11**	**25**	**18**				**0**	**13**	**187**	
Rhombohedral *(3m)*										
$LiTaO_3$[22]	4.9	(4.9)	4.4	-0.6	-1.3	(-1.3)	0.6	10.8	(10.8)	(10.9)
$LiNbO_3$[22]	5.8	(5.8)	5.0	-1.0	-1.5	(-1.5)	-1.0	17.0	(17.0)	(13.6)
$KrBO_3$[37]										
PMN-33PT ($[111]_C$-poled, "R", biased)[4,10]	**62.2**	**(62.2)**	**13.3**	**-53.9**	**-5.6**	**(-5.6)**	**166.2**	**511**	**(511)**	**(232.0)**

The properties of *3m* $LiTaO_3$ and $LiNbO_3$ were taken from Warner et al. (1968)[22] where they were derived from resonance measurements. Coefficients for *3m* $KBrO_3$ are taken from Haussühl et al. (1977)[37] and were measured using both ultrasonic and resonance techniques.

Finally, the coefficients for "PMN-33PT" are those reported by Zhang et al. (2003)[4], as derived from ultrasound and resonance measurements. Notably, the composition (33 mol. % PT) seems a little high for the "R" phase shown in the phase diagram of chapter six (fig. 13) and those reported elsewhere[38,39]. However, it is very possible that the true composition of their samples was lower than that assumed.

As discussed in previous chapters, due to the generally fine domain structure of low PT-content, PMN-xPT and PZN-xPT and their low domain wall energy[40], the monodomain state is often unstable[4,16]. This was found to be the case for $[111]_C$-poled PMN-33PT by Zhang and coworkers such that measurements had to be made under a bias field. Properties were all measured under bias fields > 200 V/mm[4], above the coercive field for the sample. Unfortunately, measurement under bias has been shown to significantly effect values of permittivity, compliance and piezoelectric coefficient[4,6,16]. Firstly, even where no domain wall motion occurs, the piezoelectric response tends to decrease at higher bias fields. This is evident in small decreases in gradient at high fields in the anhysteretic strain-field measurements shown in chapter seven. Secondly, extrinsic contributions from domain wall motion also decrease with increasing bias field. As shown in strain-field measurements for $[111]_C$-oriented, pseudo-rhombohedral PMN-28PT (chapter seven, fig. 3) the hysteresis becomes closed at high fields (>2000 V/mm) where a nearly monodomain state forms. Finally, however, since resonance measurements are typically made at very small fields (around 1 V/mm), little intrinsic contribution might be expected according to the Rayleigh law (chapter eight).

In summary, there is some doubt as to the accuracy of the monodomain values of PMN-33PT given in tables I to III. However, it is most likely the values quoted are an under- rather than an over-estimation.

Attribution of signs to coefficients

Lastly, a note should be made about the signs given to the piezoelectric coefficients for the *3m* crystals. For the tetragonal crystals there is no confusion and for "orthorhombic" PZN-8PT the signs are assumed to be the same as those for $KNbO_3$. However, the d_{22} coefficient of *3m* rhombohedral crystals lends an additional complication.

As noted above, the tensor properties are defined with respect to a standard orthogonal basis set, itself defined with respect to certain symmetry elements of the material's point group[9]. As shown in appendix I, in *3m* materials, x_1 is defined to lie perpendicular to one of the mirror planes; x_2 therefore must lie within that mirror plane.

The complication arises from the fact that the d_{22} coefficient must have a 'polarity' in the same way as d_{33}. Of course, d_{33} is defined as positive when

x_3 is oriented parallel to the polar vector $\boldsymbol{P_S}$. Thus, unless the 'polarity' of x_2 is explicitly measured via the sign of d_{22} it can be chosen arbitrarily to lie in either direction. This is shown in figure 2. Both possible choices for x_1 and x_2 are valid within the definition laid out by Nye[9] since they are both equivalent in relation to the symmetry elements of the point group. Both choices are right-handed sets. However, for one choice of x_2, d_{22} will be positive (and thus d_{16} and d_{21} positive). For the other choice, its sign will be reversed.

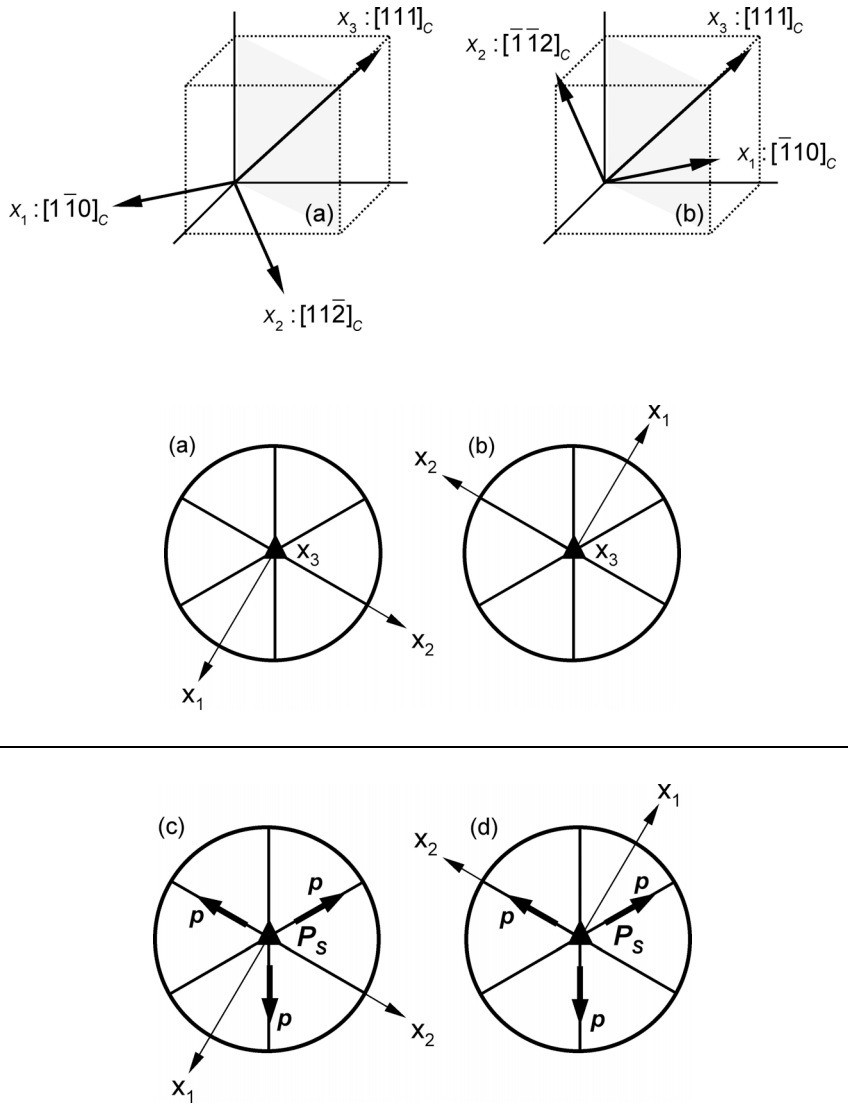

Fig. 2. (Top) Two possible choices for the "standard orthogonal basis set" for a rhombohedral *3m* material. Both are equivalent with respect to the point group symmetry of the material since the x_1 axis is always perpendicular to the same mirror plane; both are right handed sets. However, changing from (a) to (b) will reverse the sign of the d_{22} coefficient. (Bottom) The correctly defined x_2 axis must be along one of the three secondary polar axes of the *3m* crystal. In (c) d_{22} will be negative. Defined relative to the correct orthogonal basis set, d_{22} will be positive (d).

In fact, convention does dictate the sign of the quoted values. The old IRE convention[17] is to select the signs of the piezoelectric coefficients e_{22} and e_{15} such that d_{22} is positive. That is[22]:

$$d_{22} = e_{22}(s_{11}^E - s_{12}^E) - e_{15}s_{14}^E > 0 \qquad [5]$$

d_{22} is quoted as a positive quantity for $LiNbO_3$ and $LiTaO_3$[22]. However, it is quoted as a negative quantity for PMN-33PT by Zhang et al. (2004)[10] for the "standard coordinates" $x_1 : [1\bar{1}0]_C$, $x_2 : [11\bar{2}]_C$ and $x_3 : [111]_C$.

Which of these is correct in terms of notation is anyway irrelevant. Since both choices are equivalent with respect to the point group symmetry, they will look identical in diffraction experiments. Even if they are correctly assigned following measurement on the reference sample, they will always need to be *measured* on a new sample. This is because, in a crystal cut and oriented using Laue diffraction, there is no way of knowing in which direction the positive x_2 axis lies; the orientation of x_2 can only be correctly assigned by *measurement* of d_{22}.

Necessarily, the two choices for x_2 in (a) and (b) of figure 2 are not equivalent with respect the symmetry elements of the *space group* (*R3m*) and, therefore, the atomic arrangement. Hidden within the three mirror planes of the *3m* point group lie *secondary* polar axes[41]. They are *polar* in that the ends of these axes are not made equivalent by the symmetry elements of the point (or space) group[9]. However, they are not *unique* and the vector sum of the three axes is zero[9]. Therefore, the secondary axes are not *pyroelectric* in the same way as the *primary* polar axis x_3 since upon changing the temperature the averaged change in charge is zero; this is except, of course, for any component parallel to the unique polar axis x_3[42]. The secondary polar axes $\boldsymbol{p}$ are shown in figures 2(c) and 2(d) with respect to the point group symmetry elements. In the IRE convention, with d_{22} positive (and therefore d_{21} and d_{16} negative), x_2 of the orthogonal basis set must lie parallel to one of the three secondary polar axes [fig. 2(d)].

This will have immediate consequences for any calculation of the anisotropy of the piezoelectric coefficient; we will return to this point later.

IV. DOMAIN AVERAGE ENGINEERING

The six possible domain engineered structures formed in ferroelectric perovskites by poling along one of the $<111>_C$, $<101>_C$ or $<001>_C$ crystallographic directions is listed in table IV. They are also shown graphically in chapter six (fig. 5).

Table IV
Engineered and mono-domain states in perovskite single crystals ('C' denotes reference to the pseudocubic unit cell).

Crystal class	Polar direction (x_3)	Poling direction (x_3')	Polar directions (x_3) for the resultant set of equivalent domain variants	Domain-engineered structure
Rhombohedral *3m*	$<111>_C$	$[111]_C$ $[101]_C$ $[001]_C$	$[111]_C$ $[1\bar{1}1]_C$, $[111]_C$ $[111]_C$, $[\bar{1}11]_C$, $[1\bar{1}1]_C$, $[\bar{1}\bar{1}1]_C$	1R 2R 4R
Orthorhombic *mm2*	$<101>_C$	$[111]_C$ $[101]_C$ $[001]_C$	$[101]_C$, $[011]_C$, $[110]_C$ $[101]_C$ $[101]_C$, $[011]_C$, $[\bar{1}01]_C$, $[0\bar{1}1]_C$	3O 1O 4O
Tetragonal *4mm*	$<001>_C$	$[111]_C$ $[101]_C$ $[001]_C$	$[001]_C$, $[010]_C$, $[100]_C$ $[001[_C$, $[100]_C$ $[001]_C$	3T 2T 1T

As discussed in chapter six, ignoring the boundary conditions formed at permissible domain walls (the case of "*domain average engineering*" defined by Fousek and coworkers[43]) and any *extrinsic* contribution, we can calculate the expected properties of a domain engineered crystal by taking a volume average of the calculated response for each individual domain variant. This approach was shown to work well the (rank-two) pyroelectric vector and polarization of domain-engineered "R" and "O" PMN-xPT and PZN-xPT.

Using the same approach, for the dielectric permittivities, piezoelectric coefficients and compliances we can write:

$$\left\langle \varepsilon_{ij}{}^{*} \right\rangle = \sum_{t=1}^{N} f^{t} (\varepsilon_{ij}{}^{*})^{t} = \sum_{t=1}^{N} f^{t} (a_{im} a_{jn} \varepsilon_{mn})^{t} \qquad [6]$$

$$\left\langle d_{ijk}{}^{*} \right\rangle = \sum_{t=1}^{N} f^{t} (d_{ijk}{}^{*})^{t} = \sum_{t=1}^{N} f^{t} (a_{im} a_{jn} a_{ko} d_{mno})^{t} \qquad [7]$$

$$\left\langle s_{ijkl}{}^{*} \right\rangle = \sum_{t=1}^{N} f^{t} (s_{ijkl}{}^{*})^{t} = \sum_{t=1}^{N} f^{t} (a_{im} a_{jn} a_{ko} a_{lp} s_{mnop})^{t} \qquad [8]$$

In equation [6], $\left\langle \varepsilon_{ij}{}^{*} \right\rangle$ is the volume averaged dielectric response of N domain variants ($t = 1...N$). f^{t} is the volume fraction of the tth variant lending a contribution $(\varepsilon_{ij}{}^{*})^{t}$ to the total response. This value can be calculated using equation [1] for each variant in the structure and will in general be a function of *three* Euler angles (ϕ, θ, ψ). Similar is true of the other two volume averaged coefficients.

When making such calculations, we therefore make coordinate transforms for every domain variant in the structure. Importantly the 'new' measurement axes $\{x_i'\}$ must be the same for each domain variant in the structure and are defined by the orientation of the domain-engineered crystal. As noted above x_3' is necessarily the *poling direction* and, for the domain

engineered structures listed in table I, must be along a <111>$_C$, <101>$_C$ or <001>$_C$ direction. In contrast, the 'old' standard orthogonal axes $\{x_i\}$ from which we make our coordinate transform will be *different for every domain variant in the structure*. By definition, the x_3 polar axis of each domain variant will take a different spatial orientation in each domain variant and will thus be defined differently with respect to the pseudocubic reference system. Likewise, the other two axes x_1 and x_2 will also be different. Importantly, this means that the three Euler angles will be different for each domain variant in the crystal.

Importance of the third Euler angle

It turns out that, for all the domain engineered structures, the first two Euler angles, ϕ and θ, will be the *same* for every domain variant in the structure. Only the third Euler angle ψ will change. In fact, in this way, ψ can be seen to define each domain variant in the structure. For example, in a 4R domain engineered crystal, the four domain variants are related by rotations of $\Delta\psi = \pm 90°$ in the $(001)_C$ plane.

The transformed coefficients $\varepsilon_{ij}{}^*$, $d_{ij}{}^*$ and $s_{ij}{}^*$ are generally dependent on *all three* Euler angles for *3m* rhombohedral, *mm2* orthorhombic and *4mm* tetragonal symmetries. Only the longitudinal coefficients $\varepsilon_{33}{}^*$, $d_{33}{}^*$ $(= d_{333}{}^*)$ and $s_{33}{}^*$ $(= s_{3333}{}^*)$ are independent of ψ. Usefully, this means that the longitudinal coefficients of domain engineered structures can be calculated quite simply; each domain variant in the structure will contribute the same value to the response and thus their relative volume fractions can be ignored. That is, the parentheses $\langle\ \rangle$ in equations [6] to [8] can be dropped since the volume averaged response will be the same as the response for each individual variant in the structure.

In this way, $\varepsilon_{33}{}^*$, $d_{33}{}^*$, and $s_{33}{}^*$ were calculated for the six possible domain engineered structures using the values listed in tables I, II and III for assorted ferroelectric materials. The longitudinal coupling coefficient $k_{33}{}^*$ was also calculated using the definition given in appendix II:

$$k_{33}{}^* = \frac{d_{33}{}^*}{\sqrt{\varepsilon_0 \varepsilon_{33}{}^* s_{33}{}^*}} \qquad [9]$$

It is also independent of ψ.

V. LONGITUDINAL COEFFICIENTS

The dielectric, piezoelectric and compliance coefficients calculated for various domain engineered structures are collected together in tables V, VI and VII. The results will be discussed individually, by material, below.

(i) PMN-33PT

Taking the values shown in tables I to III for rhombohedral PMN-33PT and transforming to the $[001]_C$ direction, that relevant to the 4R domain engineered structure, we find a value of d_{33}* = 2310 pC/N (see table V). This is around 12 times larger than the value measured along the polar direction $[111]_C$, d_{33} = 190 pm/V (table II). Critically, it is around 80% of the experimental value measured using a resonance-ultrasound technique for $[001]_C$-poled "4R" PMN-33PT[5]: that is, d_{33}* = 2820 pm/V.

According to this calculation, therefore, the *intrinsic* single-crystal anisotropy of "rhombohedral PMN-33PT" accounts for as much 80% of the $[001]_C$-poled, multidomain value. Seemingly, the strong crystal anisotropy of individual, pseudo-rhombohedral, component domains can explain the largest part of the "giant" piezoelectric response of domain-engineered PMN-33PT.

This large anisotropy can be investigated further. Combining equations [2] and [4] for *3m* rhombohedral symmetry, the piezoelectric coefficient d_{33}* can be written as a function of orientation as follows:

$$d_{33}^* = \left(\cos\theta \sin^2\theta\right) d_{31} + \cos\phi \sin^3\theta \left[3\sin^2\phi - \cos^2\phi\right] d_{22} + \left(\cos\theta \sin^2\theta\right) d_{15} + \left(\cos^3\theta\right) d_{33} \qquad [10]$$

d_{33}* is thus a function of two Euler angles and four independent components of the piezoelectric tensor: that is the (longitudinal) d_{33}, (transverse) d_{31}, (shear) d_{15}, and d_{22} coefficients. For transformation to the $[001]_C$ direction (ϕ = 0° and $\theta = 54.74°$), equation [10] reduces to:

$$d_{33}^* = \frac{1}{3\sqrt{3}}\left[2d_{31} - 2\sqrt{2}d_{22} + 2d_{15} + d_{33}\right] \qquad [11]$$

d_{31} is small and negative (-190 pm/V) and its effect is to reduce d_{33}*; d_{33} is small (90 pm/V) and has only a small, positive effect on d_{33}*. d_{22} is large and negative (-1340 pm/V) such that it contributes around +730 pm/V to the total. Finally, d_{15} is large and positive (4100 pm/V) and contributes by far the largest amount to the total: i.e., +1580 pm/V.

Importance of the shear coefficient

Thus, according to this calculation, the piezoelectric shear coefficient d_{15} (= $d_{113} + d_{131}$) and its equivalent d_{24} (= $d_{223} + d_{232}$) are most important to the large piezoelectric response along the non-polar $[001]_C$ direction in "4R",

domain-engineered PMN-33PT. This has also been pointed out by others and, indeed, was suggested by Kuwata et al. in 1982[1].

Identifying its importance, researchers have made various attempts to measure the shear coefficient in other PMN-xPT and PZN-xPT compositions. For example, Zhang et al. have reported shear coefficients d_{15} of 2500 pm/V in $[111]_C$-poled PZN-4.5PT based on resonance measurements[16]. According to equation [14], the shear coefficient in this case will account for nearly 50% (+960 pm/V) of the polydomain value measured in samples of "4R" PZN-4.5PT ($d_{33}^* \approx 2000$ pm/V[2,3]). Liu et al. have reported an even larger shear coefficient for $[111]_C$-poled PZN-4.5PT, d_{15} = 5500 pm/V, based on strain-field, interferometric measurements under DC bias (80 V/mm AC field amplitude). However, in their results, frequency variation even under bias fields of 1600 V/mm suggested a non-monodomain sample and, therefore, some extrinsic contribution to the measured value. Extrapolation of their data to higher fields, and taking a conservative estimate of around 60% of their zero bias-field value, suggests a shear coefficient of around 3300 pm/V. This would account for a contribution to d_{33}^* of at least +1270 pm/V.

Three-dimensional crystal anisotropy

Using equation [10], we can visualize the anisotropic nature of monodomain PMN-33PT by plotting d_{33}^* as a function of orientation in three dimensions. This is shown in figure 3.

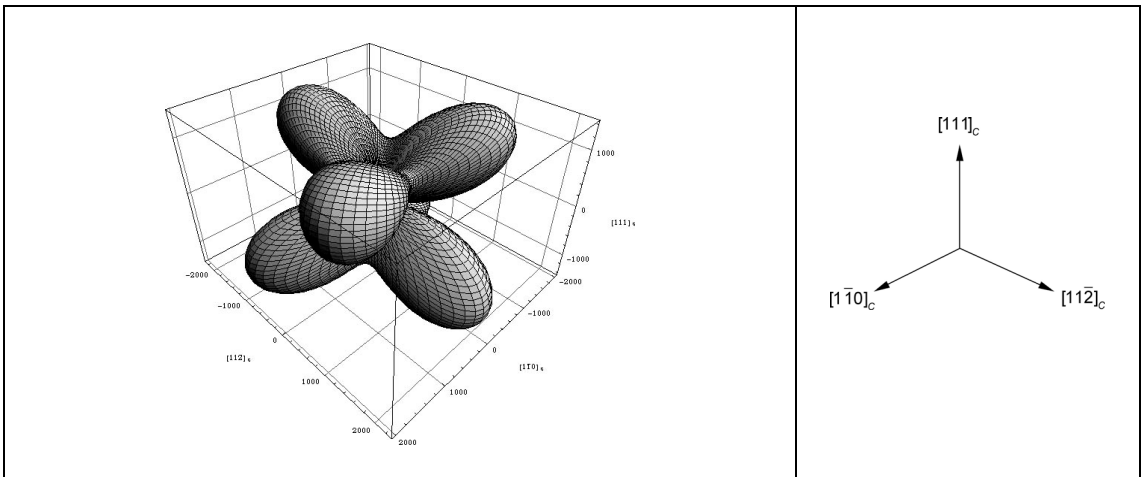

Fig. 3. Longitudinal piezoelectric coefficient d_{33}^* as a function of orientation with respect to the standard orthogonal axes of the monodomain rhombohedral crystal. The vertical axis is the polar axis $[111]_C$. The distance from the origin to the 3D surface in a certain direction gives a measure of d_{33}^* in that direction.

Immediately apparent is the small value of d_{33}^* along the polar $[111]_C$ direction and a strong enhancement in other orientations. The response is maximum along six equivalent directions; they lie, in fact, very close to the six pseudocubic directions $<001>_C$. Rotating by Euler angle θ (about x_1) in the

$(1\bar{1}0)_C$ plane, d_{33}* is maximum (2410 pm/V) at an angle of 62.9°. This is very close to the angle $\theta = 54.74°$, corresponding to the pseudocubic $[001]_C$ direction, where d_{33}* = 2310 pm/V (see table V). This is shown in figure 4.

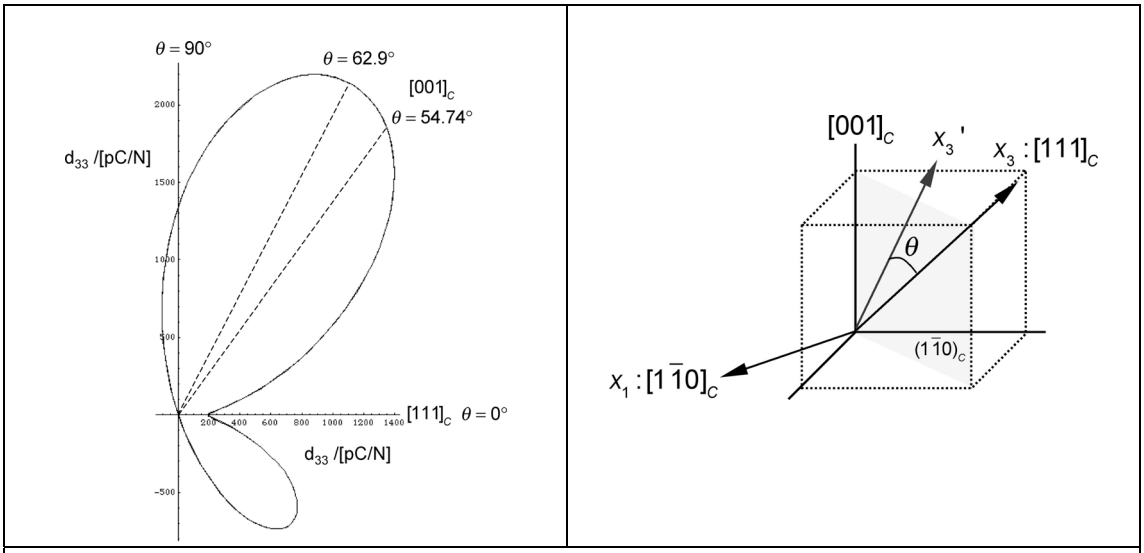

Fig. 4. Variation of d_{33}* as a function of the second Euler angle θ. It is maximum very close to the $[001]_C$ direction.

Origin of the piezoelectric anisotropy

The large anisotropy evident in figures 3 and 4 is, as already mentioned, due to a large extent to the shear coefficient d_{15}. In fact, we might quantify the piezoelectric anisotropy of a given crystal by the ratio of the shear coefficient to the longitudinal coefficient: d_{15}/d_{33}. Such ratios are shown in the right hand column of table II for each ferroelectric material. Comparing the assortment of rhombohedral *3m* crystals, the ratio d_{15}/d_{33} is highest in PMN-33PT (≈ 22). It is significant but smaller in $LiNbO_3$ (≈ 11), although much smaller in $LiTaO_3$ (≈ 3). As shown elsewhere[44], the longitudinal piezoelectric coefficient d_{33}* of $LiNbO_3$ has a similar three-dimensional form to that of PMN-33PT (fig. 3). In $LiTaO_3$, maxima also apparent close to the $<001>_C$ directions although they are relatively much smaller.

Within the framework of phenomenological Landau-Ginzburg-Devonshire (LGD) theory[45,46], the intrinsic, monodomain shear coefficient d_{15} is related to the transverse permittivity ε_{11} by the following expression[46]:

$$d_{15} = d_{24} = \varepsilon_0(\varepsilon_{11} - 1)Q_{44}P_3 \qquad [12]$$

where Q_{44} is the electrostrictive coefficient and P_3 is the magnitude of the spontaneous polarization. This expression also holds for both rhombohedral and tetragonal phases; for the orthorhombic phase[47], however, where $d_{15} \neq d_{24}$:

$$d_{15} = \varepsilon_0(\varepsilon_{11} - 1)Q_{44}P_3 \qquad [13]$$

$$d_{24} = 2\varepsilon_0(\varepsilon_{22} - 1)(Q_{11} - Q_{12})P_3 \qquad [14]$$

Thus, in all three phases, *a large piezoelectric shear coefficient can be seen to follow from a large permittivity* ε_{11} *(or* ε_{22}*) perpendicular to the polar direction*.

In contrast, the longitudinal piezoelectric coefficient is related to the permittivity along the polar direction, ε_{33}. For the tetragonal phase[46]:

$$d_{33} = 2\varepsilon_0(\varepsilon_{33} - 1)Q_{11}P_3 \qquad [15]$$

For rhombohedral, tetragonal and orthorhombic phases, a large longitudinal piezoelectric coefficient d_{33} follows from a large, longitudinal permittivity ε_{33}.

Collinear piezoelectric effect and polarization rotation

It is worth discussing here the meaning of both the longitudinal and shear coefficients. The *longitudinal piezoelectric coefficient* d_{33} (= d_{333}) describes the strain resulting from application of an electric field, or the displacement field resulting from a (tensile) stress, *along the polar axis* (x_3): i.e. $S_{33} = d_{333}E_3$ or $D_3 = d_{333}\sigma_{33}$. Thus, it defines the e*longation* of the polar vector $\boldsymbol{P_s}$ in response to an collinear electric field or tensile stress: that is, the *collinear piezoelectric effect*. Moreover, it might be expected to be related to the longitudinal permittivity ε_{33} (equation [15]) since lengthening of the polar vector will also correspond to the dielectric response $D_3 = \varepsilon_0\varepsilon_{33}E_3$. This is shown schematically in figure 5.

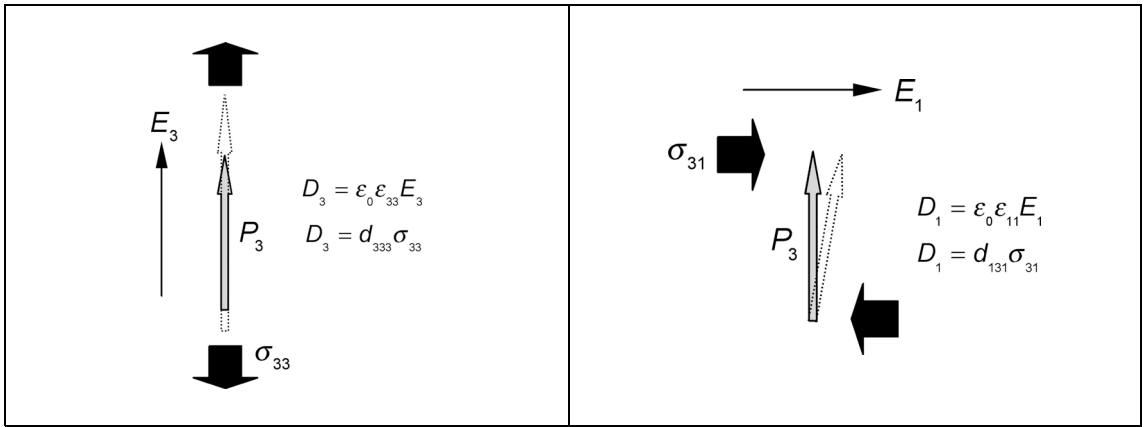

Fig. 5. (Left) Relationship between the collinear piezoelectric effect and permittivity ε_{33} viewed as an elongation of the polar vector P_3. (Right) Relationship between the piezoelectric shear coefficients and the transverse permittivity ε_{11} in terms of rotation of the polar vector.

On the other hand, the *piezoelectric shear coefficient* $d_{15} = 2d_{131}$ (or $d_{24} = 2d_{232}$) describes the shear strain resulting from an electric field applied *perpendicular to the polar axis*, or the transverse displacement field resulting from an applied shear stress: i.e. $S_{31} = d_{131}E_1$ ($S_{32} = d_{232}E_2$) or $D_1 = d_{131}\sigma_{31}$ ($D_2 = d_{232}\sigma_{32}$). Thus, it incorporates the degree of rotation of the polar vector in response to a transverse perturbation. Importantly, in the language used throughout this thesis to explain the large piezoelectric properties of $[001]_C$-poled PMN-xPT and PZN-xPT, a large shear coefficient is directly related to a large *polarization rotation* for a given perturbation. Moreover, it might be expected to be related to the transverse permittivity ε_{11} since rotation of the polar vector will also correspond to the transverse dielectric response $D_1 = \varepsilon_0\varepsilon_{11}E_1$ [fig. 5(right)].

Dielectric anisotropy of PMN-33PT

The transverse permittivity ε_{11} of PMN-33PT is indeed high. According to the data in table I, it is 3950, around 6 times higher than that along the polar direction (640). From equations [1] and [4], the longitudinal dielectric permittivity as a function of orientation for rhombohedral (and tetragonal and orthorhombic) crystals is given by:

$$\varepsilon_{33}^* = \left(\sin^2\theta\sin^2\phi\right)\varepsilon_{11} + \left(\cos^2\phi\sin^2\theta\right)\varepsilon_{22} + \cos^2\theta\varepsilon_{33} \qquad [16]$$

For all the ferroelectric materials in table I, the transverse permittivities ε_{11} and ε_{22} are larger than ε_{33}. Along the polar axis, $\varepsilon_{33}^* = \varepsilon_{33}$ and is characteristically small. At all other orientations, however, the dielectric response will pick up contributions from ε_{11} or ε_{22}, or both. The form of ε_{33}^* given by equation [16] is similar for all rhombohedral and tetragonal perovskite materials and is shown in figure 6. The minimum along the polar direction is evident.

The anisotropy in ε_{33}^* can, in fact, be quantified by the anisotropy factor $\xi = \varepsilon_{11}/\varepsilon_{33}$, which has been calculated for all materials in the right hand column of table I. For the *3m* rhombohedral materials it increases in the same order as d_{15}/d_{33} (table II). For $LiNbO_3$, $\zeta \approx 1$ and $d_{15}/d_{33} \approx 3$ whereas for PMN-33PT $\zeta \approx 6$ and $d_{15}/d_{33} \approx 22$.

Of course, comparing the relative ratios and the three-dimensional forms of ε_{33}^* (fig. 6) and d_{33}^* (fig. 3), it is obvious that the piezoelectric anisotropy cannot be explained by dielectric anisotropy alone. In the framework of LGD theory, a certain amount will come from the anisotropy of the electrostrictive coefficients. However, there is certainly a correlation between the dielectric anisotropy, the strong anisotropy in piezoelectric coefficient and, thus, the propensity large piezoelectric coefficients in non-

polar directions. In *3m* rhombohedral crystals, the largest d_{33}* coefficients tend to be found close to the <001>$_C$ psuedocubic directions.

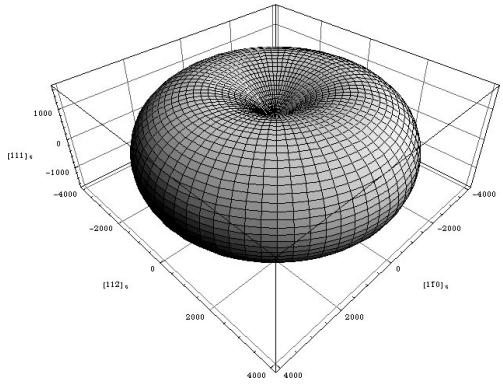

Fig. 6. Permittivity ε_{33}* as a function of orientation with respect to the standard orthogonal axes of a monodomain, rhombohedral crystal of PMN-33PT. The vertical axis is the polar axis [111]$_C$.

Domain engineering and the secondary polar axes

There is one problem with this calculation, and one which has been the subject of some discussion[10,48,49]. When we pole our *3m* crystal into a 4R domain engineered state by application of an electric field along the [001]$_C$ direction we necessarily bias four out of the eight possible <111>$_C$ polar directions (x_3). However, what is not clear is the effect on the secondary polar axes and the choice of x_2.

As shown in figure 4, to calculate d_{33}* = 2310 pm/V we started with $x_2:[11\bar{2}]_C$ and d_{22} negative (see table II) since this is the definition given by Zhang and Cao[10]. However, this means that in reality we chose the polarity of x_2 to lie along the $[\bar{1}\,\bar{1}2]_C$. As shown in figure 2 [by changing from (c) to (d), for example], we could equally choose the polarity of x_2 to lie antiparallel to this: i.e., along $[11\bar{2}]_C$. If we did this the calculation of d_{33}* would be exactly the same, except that the sign of d_{22} would be reversed. Substituting d_{22} = +1340 pm/V into equation [11] we calculate d_{33}* = 850pm/V, much smaller than the value (2310 pm/V) calculated previously.

Therefore, for this single domain variant defined by $x_3:[111]_C$ there are, in fact, two "orientation states". Their atomic arrangements are related by a rotation of 60° about the primary polar axis x_3 [consider (c) and (d) of figure 2]. The two orientation states are shown in figure 7 where, in both cases, x_2 lies along one of the three secondary polar axes such that d_{22} is positive. One orientation state [fig. 7(b)] will contribute a value of 2310 pm/V to d_{33}* measured along the [001]$_C$ poling direction; the other [fig. 7(a)] will contribute

only 850 pm/V. In fact, for four of the domain variants in the 4R domain engineered structure there will be two such orientation states.

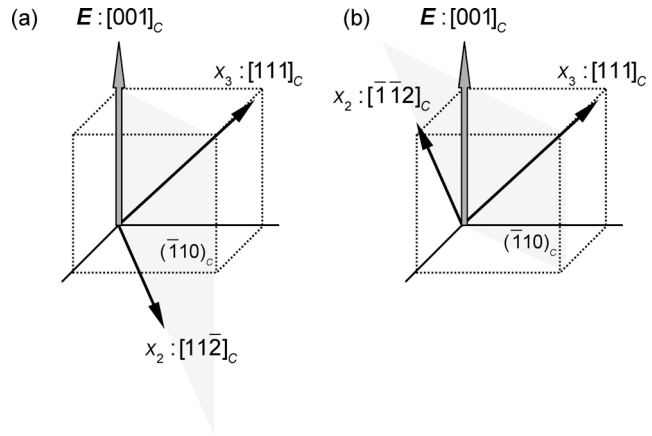

Fig. 7. Two possible orientation states for a single $[111]_C$ "domain variant" in the $[001]_C$-poled domain engineered structure defined by antiparallel directions for the secondary polar axis x_2 in the mirror plane. In orientation state (b), the positive d_{22} coefficient will contribute positively to the response d_{33}* measured along $[001]_C$: thus d_{33}* = 2310 pm/V. In orientation state (a), the d_{22} coefficient will contribute negatively to the piezoelectric response along $[001]_C$ and d_{33}* = 850 pm/V.

The question remains, which of these orientation states will be present in each of the domain variants of the 4R structure? Assuming we were correct earlier, it seems that the orientation state shown in figure 7(b) forms: that is, the one that gives the largest piezoelectric response (d_{33}*). Although this will need verifying, evidence suggests that in 4R domain engineered structures all domain variants contribute the same (large) value of d_{33}*.

Thus, the possibility arises that the poling field also biases the secondary polar axes x_2 of *3 m* rhombohedral crystals such that *one* is inclined *as close as possible to the poling direction*. Energetically, the poling field will interact with all four polar axes: the primary $\boldsymbol{P_S}$ along x_3 and the three secondary polar vectors $\boldsymbol{p}^{(i)}$ where $i = 1...3$. Assuming linearity, the interaction energy is:

$$\begin{aligned}\Delta G &= -\boldsymbol{E}.\boldsymbol{P_S} - \boldsymbol{E}.\boldsymbol{p}^{(1)} - \boldsymbol{E}.\boldsymbol{p}^{(2)} - \boldsymbol{E}.\boldsymbol{p}^{(3)} \\ &= -\boldsymbol{E}.\boldsymbol{P_S} - \boldsymbol{E}.(\boldsymbol{p}^{(1)} + \boldsymbol{p}^{(2)} + \boldsymbol{p}^{(3)}) \\ &= -\boldsymbol{E}.\boldsymbol{P_S}\end{aligned} \qquad [17]$$

since the vector sum of $\boldsymbol{p}^{(i)}$ is necessarily zero. However, if the linearity of this equation breaks down in a real crystal it is possible that one orientation state, where one secondary polar axis x_2 is as close as possible to the poling direction, will be favored over the other. This would solve all previous ambiguity[10,48] and would thus be worthy of future investigation.

However, further evidence that this does indeed occur can be seen upon consideration of the other domain engineered structure formed in *3m* crystals.

2R domain engineered structure

The other engineered domain structure possible in a rhombohedral crystal, 2R, is that formed upon poling along $[101]_C$. The first two Euler angles relevant to this transformation are $\phi = 60°$ and $\theta = 35.26°$, as listed in table IV. Substituting these angles into equation [10] we arrive at:

$$d_{33}^* = \frac{1}{3\sqrt{3}}\left[\sqrt{2}d_{31} + d_{22} + \sqrt{2}d_{15} + 2\sqrt{2}d_{33}\right] \qquad [18]$$

Depending on the orientation state that forms, and thus whether d_{22} is positive or negative, the piezoelectric response along $[101]_C$ will be either 940 pm/V or 1450 pm/V. This is shown schematically in figure 8.

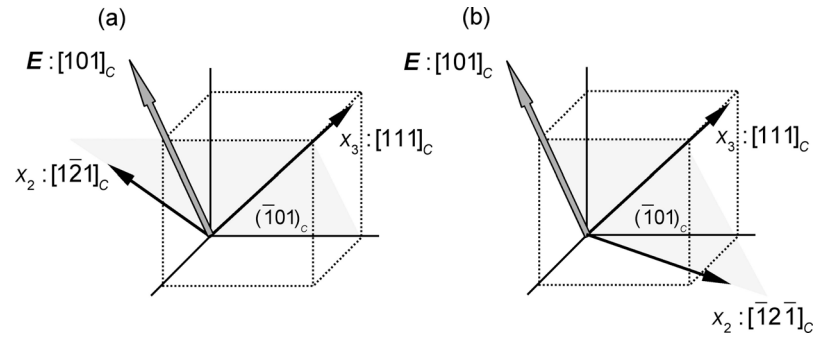

Fig. 8. Two possible orientation states for a single $[111]_C$ "domain variant" in the $[101]_C$-poled domain engineered structure. In orientation state (a), the positive d_{22} coefficient will contribute positively to the response d_{33}* measured along $[001]_C$: thus d_{33}* = 1450 pm/V. In orientation state (a), the d_{22} coefficient will contribute negatively to the piezoelectric response along $[101]_C$ and d_{33}* = 940 pm/V.

The latter value (1450 pm/V) is again high, being around 8 times larger than that along the polar axis (190 pm/V). To reiterate, it will result whenever the angle between the poling direction and one of the secondary polar axes (x_2) is minimized [fig. 8(a)].

In fact, large piezoelectric coefficients are reported in $[101]_C$-poled "2R" PMN-xPT and PZN-xPT crystals. Measurements by Viehland et al. give d_{33}* as around 1200 pm/V for $[001]_C$-poled ("4R") PMN-30PT and around 1000 pm/V for $[101]_C$-poled ("2R") crystals[50]. d_{33}* values are also found to be very similar in $[001]_C$- and $[101]_C$-poled PZN-4.5PT over a wide temperature range before transition to the tetragonal phase[51,52].

Quantitative similarities are also found between the compliances and permittivities in these two directions. This has led the authors to talk of

special “electromechanical and elastic isotropy[50]” in the $\{101\}_C$ plane and a near equivalence of responses in the $<001>_C$ and $<101>_C$ directions contained therein. This plane is one of the dodecahedral, monoclinic M_A “bridging” planes. In chapter seven, it was shown that polarization rotation within this plane is responsibly for large field-induced strains. Elastic isotropy in such a $\{101\}_C$ plane has been reported elsewhere for ferroelastic martensitic phase transitions[50] and may indeed be, as Viehland and coworkers suggest, directly related to the order-disorder nature of relaxor-ferroelectric PMN-xPT and PZN-xPT.

Importantly, for now, this “isotropy” is not evident based on a simple coordinate transformation of the monodomain properties of PMN-33PT. As shown in figure 4, the monodomain piezoelectric coefficient d_{33}* is strongly *anisotropic* in the $(1\bar{1}0)_C$ mirror plane due to the directional polarity of the x_2 axis contained within it. However, this will not be true in domain engineered crystals if the x_2 axis is switched by the poling field. That is, if x_2 always lies at a minimal angle away from the poling (and measurement) direction x_3' then the anisotropy shown in figure 4 will be much reduced. This is shown in figure 9.

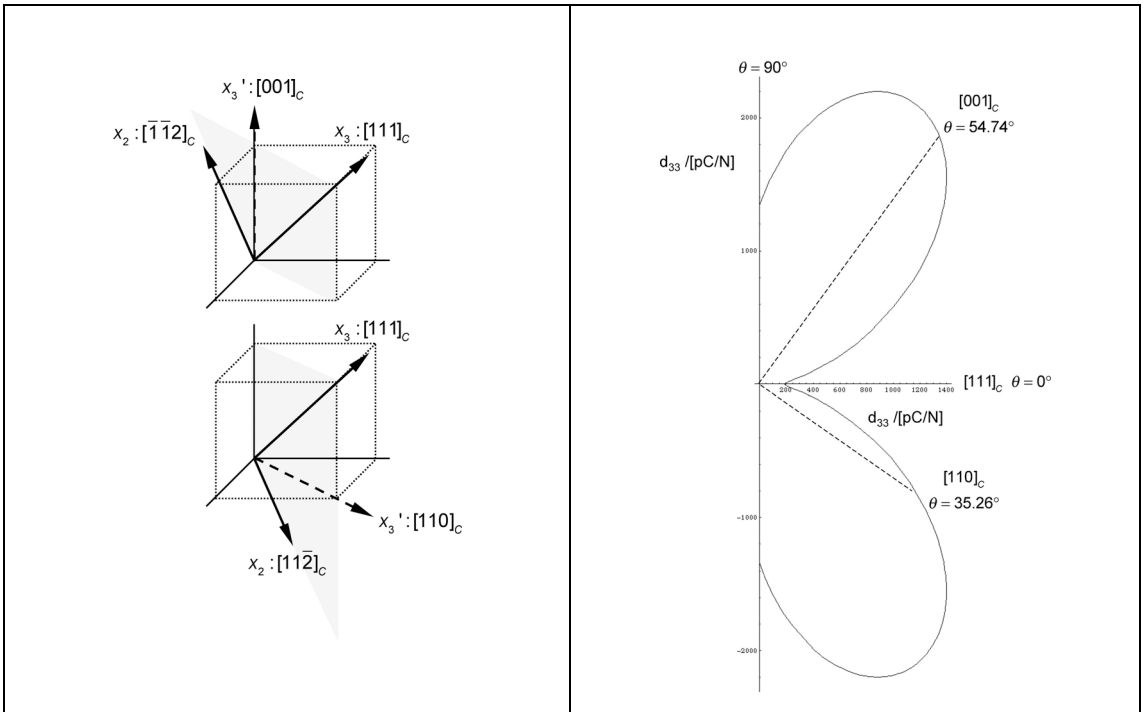

Fig. 9. Variation of d_{33}* as a function of the Euler angle θ assuming that the secondary polar axis x_2 is always inclined as close as possible to the x_3' measurement (poling) direction. If this is the case both 4R and 2R domain engineered structures will yield piezoelectric coefficients > 1000 pm/V along the $[001]_C$ and $[110]_C$ measurement directions, respectively.

Coupling coefficient

Using equation [9], the coupling coefficient k_{33}* calculated along the $[001]_C$ poling direction of 4R domain engineered PMN-33PT is 0.93. This is extremely close to the value of 0.94 measured experimentally, in polydomain crystals, by Zhang and coworkers[5]. Such high values of coupling coefficient (>0.9) in "4R" and "4O" domain engineered PZN-xPT[1,2,53,54] and PMN-xPT[5,55] make them extremely attractive for use in various sensor applications[56].

This calculation, already published by Zhang and coworkers[57], suggests that there is little extrinsic contribution to k_{33}* since it follows almost perfectly from intrinsic, monodomain properties. However, attention should be paid to the details of this calculation.

As shown in table VI, the permittivity ε_{33}* predicted by a simple coordinate transform for $[001]_C$-poled PMN-33PT is 2850. This is large, but less than half of the value (ε_{33}* = 8200) measured experimentally by Zhang[5]. In contrast to the piezoelectric response, therefore, calculations suggest there *is* a large extrinsic contribution to the polydomain permittivity in domain-engineered PMN-33PT (around 65%). Furthermore, the transformed compliance 245×10^{-12} m^2N^{-1} is around twice as high as the experimental one (120×10^{-12})[5]. From what seems like pure coincidence, combination of these two values in equation [9] leads to cancellation of these two discrepancies and a theoretical coupling factor that fits well with the experimental one.

The origin of this anomaly is not clear, although it could have two main origins. Firstly, the monodomain data listed in table I to III for PMN-33PT could be inaccurate. As discussed in section III, error in the data could result from property fluctuation due to compositional differences between samples used for measurement and the use of a bias field. Any small compositional difference between the "PMN-33PT crystals used to measure the monodomain properties and the $[001]_C$-poled, polydomain "PMN-33PT" would lead to some discrepancy.

Alternatively, the simple domain averaging model is not valid for the permittivity and higher rank tensor properties. This is in spite of the fact that it works well for rank-one tensor (vector) properties, the pyroelectric coefficient and polarization, as shown in chapter six. Importantly, the model might break down for higher rank properties due to a non-insignificant *extrinsic* contribution from the presence of a domain-engineered structure and/or the mechanical boundary conditions of strain compatibility domain walls would bring. This will be discussed further in section VI.

(ii) PZN-9PT

The general, three-dimensional dielectric and piezoelectric anisotropy of PZN-9PT has been calculated by Topolov[58] based on the data from Dammak and coworkers shown in tables I to III. Dammak et al. also reported transformed coefficients relevant to the $[001]_C$-poled, "4O" domain engineered structure[6]. Calculations for d_{33}* and ε_{33}* have been repeated here for the

4O and 3O domain engineered structures formed by poling along the $[001]_C$ and $[111]_C$ directions, respectively; the results are listed in tables V and VI.

For an *mm2* orthorhombic crystal, the piezoelectric coefficient transforms as:

$$\begin{aligned} d_{33}{}^* &= \left(\cos\theta\sin^2\theta\sin^2\phi\right)d_{15} + \left(\cos\theta\sin^2\theta\cos^2\phi\right)d_{24} \\ &+ \left(\cos\theta\sin^2\theta\sin^2\phi\right)d_{31} + \left(\cos\theta\sin^2\theta\cos^2\phi\right)d_{32} \\ &+ \left(\cos^3\theta\right)d_{33} \end{aligned} \qquad [19]$$

For orthorhombic crystals there are no secondary polar axes and calculations are much simpler. The variation of $d_{33}{}^*$ in space for PZN-9PT is shown in figure 10. Transforming to the $[001]_C$ direction relevant to a 4O domain engineered structure, the expression becomes:

$$d_{33}{}^* = \frac{1}{2\sqrt{2}}\left[d_{31} + d_{15} + d_{33}\right] \qquad [20]$$

This yields a piezoelectric coefficient of 1260 pm/V, five times the value measured along the $[101]_C$ polar axis (250 pm/V).

Notably, the largest contribution to the response (+1130 pm/V) is again from the d_{15} shear coefficient, itself related to a large transverse permittivity ε_{11} by equation [13]. As shown in table II, monodomain PZN-9PT also shows strong piezoelectric anisotropy with $d_{15}/d_{33} \approx 13$. This is related to an anisotropy factor $\zeta = \varepsilon_{11}/\varepsilon_{33}$ of around 11 (table I). Again a large piezoelectric shear coefficient d_{15}, suggesting a large contribution from polarization rotation in the plane perpendicular to x_2, results from a large permittivity perpendicular to the polar axis ε_{11}. Again it is manifest in a large piezoelectric coefficient close to four non-polar $<001>_C$ directions (fig. 10). Notably, a large piezoelectric response is not observed along the two $<001>_C$ directions corresponding to the orthorhombic *b*-axis (x_2); they are perpendicular to the plane of strong polarization rotation, along $\pm[010]_C$, as shown in figure 10.

Large extrinsic contribution

Importantly, the value calculated along the $[001]_C$ direction (1260 pm/V) is only around half the value (2500 pm/V)[6] measured experimentally by Dammak and coworkers in "4O" polydomain PZN-9PT. Assuming the monodomain data set used is free from error (and that it was indeed measured from monodomain crystals of the same composition) this calculation suggests a much larger extrinsic contribution, as much as 50%, to the piezoelectric response of domain engineered PZN-9PT. The possible origins for this extrinsic contribution will be discussed in section VI.

However, a significant part of the enhanced response away from the polar axis can again be seen to result from a large shear coefficient and a large transverse permittivity. We will now go on to investigate if such effects are possible in simpler ferroelectrics as well.

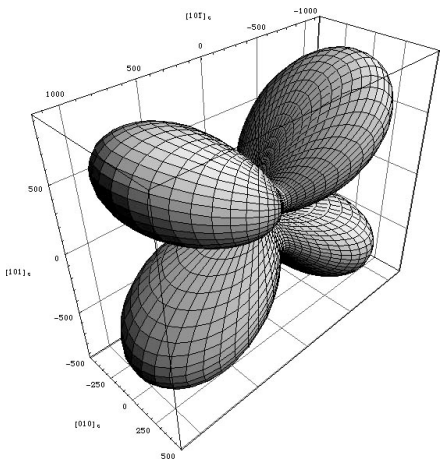

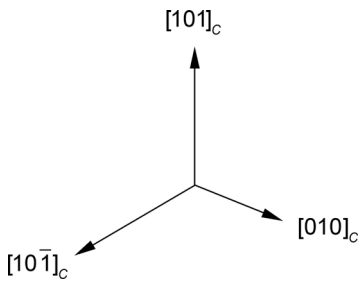

Fig. 10. Longitudinal piezoelectric coefficient d_{33}* as a function of orientation with respect to the standard orthogonal axes for monodomain PZN-9PT. The vertical axis is the polar axis $[101]_C$.

(c) $KNbO_3$

Using the piezoelectric coefficients for monodomain potassium niobate (table II) and transforming to $x_3' : [001]_C$ we calculate a value of d_{33}* = 86.7 pm/V: this is around three times the value along the $[101]_C$ polar axis (29.3 pm/V). Although not shown here, the three-dimensional d_{33}* surface for $KNbO_3$ has a very similar form to that of PZN-9PT albeit on a smaller scale. Again there is an important effect from the d_{15} shear coefficient. Indeed, potassium niobate shows significant dielectric and piezoelectric anisotropy; as shown in tables I and II, $\varepsilon_{11}/\varepsilon_{33} \approx 3$ and $d_{15}/d_{33} \approx 13$.

Thus, although there are qualitative similarities between the anisotropy of *mm2* PZN-9PT and *mm2* $KNbO_3$, there are significant quantitative differences. Importantly, a large part of the difference between the piezoelectric coefficients of "4O" PZN-9PT (1260 pm/V) and $KNbO_3$ (86.7 pm/V) can be explained by the fact that *all* monodomain permittivities and piezoelectric coefficients are around a factor of ten smaller for the simpler perovskite, $KNbO_3$ (tables I and II). Moreover, potassium niobate is also around two to five times stiffer in its elastic constants (table III). Most notably, the s_{55} coefficient is around five times larger in PZN-9PT (187×10^{-12} m^2N^{-1}) than it is in potassium niobate. This point will be returned to later in this section.

The piezoelectric (strain-field) response of $[001]_C$-poled, 4O $KNbO_3$ has been reported by Nakamura and coworkers[59]. After etching, the strain-field loop was anhysteretic and quasi-linear, similar to the behavior in domain

engineered PMN-xPT and PZN-xPT; the gradient was d_{33}* = 92 pm/V. Again, this is around three times the value measured along the polar axis. As do relaxor-ferroelectric PMN-33PT and PZN-9PT, simpler perovskite, potassium niobate also benefits from domain-engineering. Notably, as pointed out by others[59], the calculated value (86.7 pm/V) accounts for the largest part of the experimental value suggesting that any extrinsic contribution to the response is very small in $KNbO_3$.

Finally, the other possible domain-engineered structure for an orthorhombic crystal is 3O, that formed by poling along the $[111]_C$ direction. d_{33}* calculated in this case is 53.1 pC/N (table VI), nearly twice as much as the monodomain value.

(d) $BaTiO_3$

The simplest domain engineered structure for the *4mm* tetragonal class, 2T, is that formed by poling along the $[101]_C$ direction. In theory, two degenerate domain variants will be present, each with polar vectors equally inclined to the poling direction. The calculate value for d_{33}* is 219.4 pm/V, more than twice the corresponding monodomain value of (90 pm/V).

For a general *4mm* crystal, the longitudinal piezoelectric coefficient as a function of orientation is given by:

$$d_{33}^* = \left(\cos\theta \sin^2\theta\right) d_{31} + \left(\cos\theta \sin^2\theta\right) d_{15} + \cos^3\theta d_{33} \qquad [21]$$

Its three-dimensional surface is shown in figure 11.

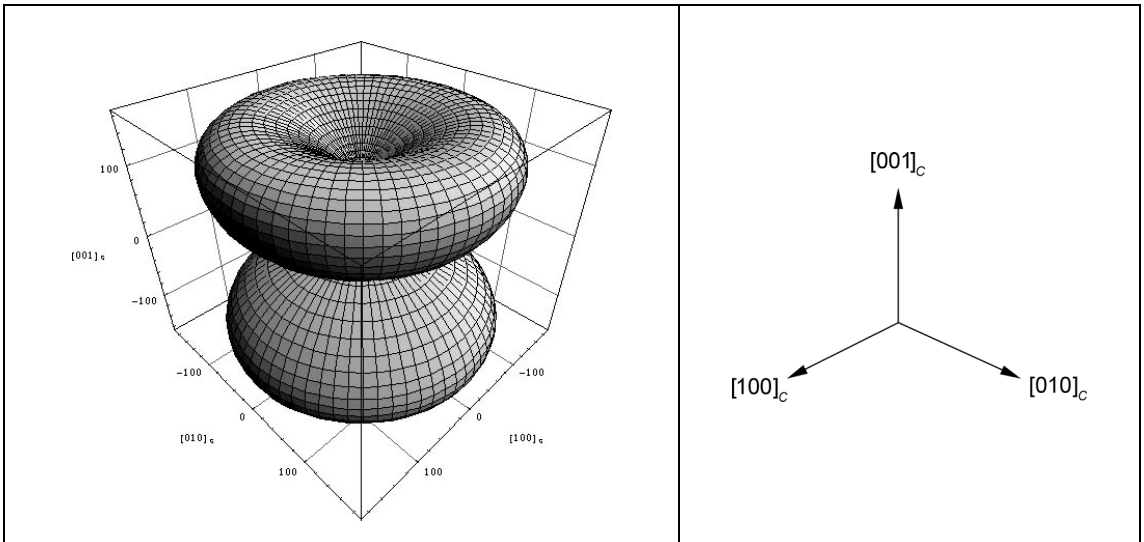

Fig. 11. Longitudinal piezoelectric coefficient d_{33}* as a function of orientation with respect to the standard orthogonal axes for monodomain barium titanate. The vertical axis is the polar axis $[001]_C$.

As for PMN-33PT, PZN-9PT and $KNbO_3$, the maximum piezoelectric response lies away from the $[001]_C$ polar axis. From consideration of the

monodomain piezoelectric coefficients in table II and equation [21], it is again apparent that strong anisotropy in d_{33}* results from a large d_{15} shear coefficient. For room temperature *4mm* barium titanate, the maximum response[60] lies close to an angle θ of 50°, very close to that of the <111>$_C$ directions (54.74°), the poling direction in 3T domain-engineered crystals.

Transforming to the coordinate system relevant to the 3T domain engineered structure ($\phi = -45°$; $\theta = -54.74°$) we can write:

$$d_{33}^* = \frac{1}{3\sqrt{3}}\left[2d_{31} + 2d_{15} + d_{33}\right] \qquad [22]$$

Thus, for barium titanate, we calculate a value of 221.5 pm/V for d_{33}*, around two and a half times the value along the [001]$_C$ polar direction (90 pm/V); to reiterate, the largest contribution to this value is from a large d_{15} shear coefficient (564 pm/V).

Again, $BaTiO_3$ shows strong piezoelectric anisotropy ($d_{15}/d_{33} \approx 6$) which is related to an extremely large dielectric anisotropy factor ($\zeta \approx 34$). As for relaxor-ferroelectric PMN-33PT and PZN-9PT, and simpler perovskite $KNbO_3$, barium titanate profits from domain engineering. Its monodomain piezoelectric coefficients are of a similar order of magnitude to *mm2* potassium niobate, albeit slightly larger in general (see table II).

Extrinsic contribution

The converse, strain-field response of [111]$_C$-poled, 3T $BaTiO_3$ has been experimentally measured by Wada and coworkers. The response is anhysteretic, characteristic of the stable domain-engineered structure, before an electric-field induced phase transition, most likely, to an orthorhombic phase[61]. The low-field gradient gives a d_{33}* value of 203 pm/V, comparing favorably to the calculated value (221.5 pm/V). This suggests that the piezoelectric response of 3T $BaTiO_3$ can be explained by *intrinsic* crystal anisotropy alone; there seems to be no extrinsic contribution to the response[61].

Next, we consider the materials in tables I to III that do not show elevated piezoelectric properties in non-polar directions; as will be apparent, these crystals will not profit from domain engineering.

(e) $PbTiO_3$, PMN-38PT, PMN-42PT and KLN

Using the values listed in table II and equation [21], the three-dimensional anisotropy of d_{33}* in lead titanate ($PbTiO_3$) has been plotted in figure 12. Clearly evident is behavior quite different to that seen in $BaTiO_3$ (fig. 11); here, the piezoelectric response is *strongest along the [001]$_C$ polar axis*. Thus, for example, the value of d_{33}* relevant to the 3T domain

engineered structure is only 27.9 pm/V, lower than that along the polar direction (79.1 pm/V).

The reason for this can be seen to lie, principally, in a small piezoelectric shear coefficient d_{15}. Comparing the monodomain piezoelectric coefficients of $BaTiO_3$ and $PbTiO_3$ (table II) it is clear that they are all similar in magnitude for the two materials *except* for the shear coefficient; d_{15} is around a factor of ten smaller in lead titanate. Clearly, lead titanate will not benefit from domain engineering.

The same is true of three more materials listed in tables I to III. *4mm* PMN-38PT, PMN-42PT and KLN are all expected to show highest piezoelectric response along the $[001]_C$ polar direction. This is because, importantly, all four materials show weak piezoelectric anisotropy with d_{15}/d_{33} ranging from between 1.3 and 0.5 (table II). Indeed, in all four materials the form of the d_{33} * surface is similar to that shown in figure 12.

Evidently, however, weak piezoelectric anisotropy cannot be entirely explained by a small dielectric anisotropy. In $PbTiO_3$ and KLN the anisotropy factor is small, being $\zeta = 2$ and 3, respectively (table 1). However, in PMN-38PT and PMN-42PT the dielectric anisotropy is relatively large (6 and 13, respectively), larger than that shown by "R" PMN-33PT.

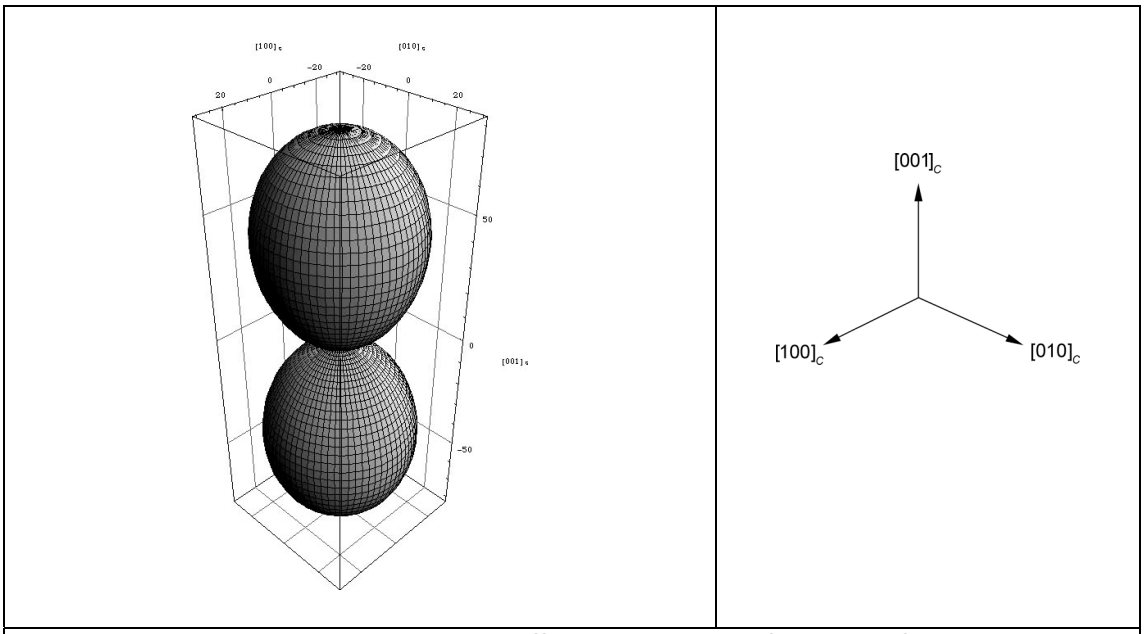

Fig. 12. Longitudinal piezoelectric coefficient d_{33}* as a function of orientation with respect to the standard orthogonal axes for monodomain lead titanate. The vertical axis is the polar axis $[001]_C$. Compare this to the piezoelectric response of barium titanate (figure 11).

"Rotators" and "extenders"

Based on their room temperature properties, we might put the materials listed in table II into two categories. In the first set of ferroelectrics, the piezoelectric anisotropy d_{15}/d_{33} is significant, ranging from around 3 in

$LiNbO_3$ to around 22 in PMN-33PT. These materials show their highest longitudinal piezoelectric response *along non-polar axes*; as a result, they benefit from domain engineering. This is the result of an important relative contribution from d_{15}, and thus *polarization rotation*, and is related to a large transverse permittivity ε_{11}. Let us refer to these materials, at room temperature, as "*rotators*".

In the second set of materials, all of which are *4mm* tetragonal, d_{15}/d_{33} is close to one or below; for lead titanate the ratio is around 0.7. These materials show their highest piezoelectric response *along the polar axis* and will not, therefore, profit from domain engineering. This is because the relative contribution from d_{15} is close to that from the d_{33} due to *elongation* of the polar vector; this follows, at least partially, from a weaker dielectric anisotropy. Let us refer to these materials, at room temperature, as "*extenders*".

Interestingly, it has been shown elsewhere that "extender" $PbTiO_3$ can be made a "rotator" by application of large, compressive bias stresses along the $[001]_C$ polar direction[62].

Importance of ferroelectric-ferroelectric phase transitions

Thus, at room temperature, the perovskite ferroelectric $BaTiO_3$ is a *rotator* whereas its relative, $PbTiO_3$, is an *extender*. The origin of their differing behaviors has recently been pointed out by Budimir and coworkers[47], and will be summarized below.

The monodomain piezoelectric coefficients of lead titanate and barium titanate, as a function of temperature, are shown in figure 13. The values were calculated by Budimir et al. within the framework of 6th order LGD theory for the two materials using equations [12], [15] and similar[47,63].

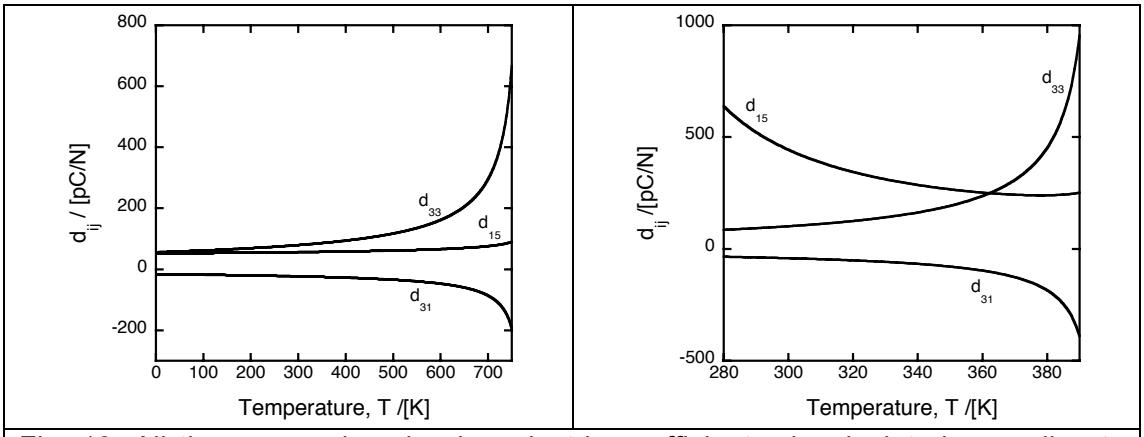

Fig. 13. All three monodomain piezoelectric coefficients d_{ij} calculated according to Landau-Ginzburg-Devonshire theory for the tetragonal phases of lead titanate (left) and barium titanate (right).

Importantly, lead titanate is tetragonal at all temperatures below the Curie point: it does not undergo any transition to another ferroelectric phase[34]. In contrast, tetragonal barium titanate does undergo a ferroelectric-

ferroelectric (FE-FE) phase transition to an *mm2* orthorhombic phase at around 0°C (and again to a *3m* rhombohedral phase at lower temperatures)[27].

The effect of this phase transition is quite clear in figure 13. In lead titanate, all monodomain piezoelectric coefficients decrease monotonically upon cooling below T_C [fig. 13(a)]. In barium titanate, d_{33} and d_{31} show similar behavior. In contrast, however, the shear coefficient in barium titanate begins to decrease but then actually increases (below around 100°C) as the FE-FE phase transition is approached [fig. 13(b)]. The proximity of the phase transition is manifest in an enhanced piezoelectric shear coefficient d_{15} and, therefore, an increased contribution to the piezoelectric response in non-polar directions from polarization rotation; again, this can be shown[47] to follow from an increase in transverse permittivity ε_{11}.

In fact, the same is true for the second FE-FE phase transition to the rhombohedral phase[47]. Likewise, in the rhombohedral phase d_{15} increases upon heating towards the FE-FE phase transition. Importantly, whereas lead titanate is an "extender" at all temperatures, barium titanate becomes a "rotator" at lower temperatures as the FE-FE phase transition is approached; this occurs as the tetragonal and orthorhombic phases become closer and closer in energy.

Large shear coefficients in PZN-xPT and PMN-xPT

Budimir and coworkers suggest that this effect will be general wherever a *first order* FE-FE phase transition (and therefore degeneracy between two ferroelectric phases) is approached[47]. Moreover, they suggest that this will include transitions brought about by changes in any thermodynamic parameter; that is, including changes in temperature, stress, electric field and, notably, composition.

Therefore, in any morphotropic phase boundary system, including PZT, PMN-xPT and PZN-xPT, elevated shear coefficients can be expected at all compositions close to the MPB. An increase in piezoelectric coefficient d_{33}* towards the MPB has indeed been observed in phenomenological calculations[64] based on 6th order LGD theory for PZT[46]; again this is a direct result of an elevated shear coefficient.

This hypothesis also seems to be corroborated by the limited monodomain data available (tables I to III) for PMN-xPT and PZN-xPT. In "R" PMN-33PT and "O" PZN-9PT, both lying close to the first order "R"/"O" transition (see chapter six), the piezoelectric shear coefficients are large, being 4100 and 3200 pm/V, respectively. As the PT content is increased in tetragonal PMN-xPT, moving from PMN-38PT to PMN-42PT, the shear coefficient drops from 380 to 131 pm/V (table II).

Synthesis

We might conclude that "R" and "O" PZN-xPT and PMN-xPT are *rotators* close to the morphotropic phase boundary. They show an elevated

piezoelectric response in non-polar directions, due to large d_{15} piezoelectric shear coefficients, which can be exploited in domain engineered crystals. This follows from the degeneracy of the phases near the MPB.

Importantly, a large d_{15} coefficient corresponds to a relative "ease" of polarization rotation in the M_A monoclinic plane of the "R" phase and the M_C monoclinic plane of the "O" phase. As evidenced by strain-field measurements in chapter seven, such rotations are indeed the origin of the large piezoelectric coefficients in $[001]_C$-oriented PMN-xPT and PZN-xPT.

Therefore, easy polarization rotation can be seen to result from proximity to first order FE-FE phase transitions and does not necessarily presuppose a monoclinic *phase* nor a "bridging plane". *Intrinsic* crystal anisotropy has been shown to account for at least 50% of the "giant" piezoelectric response of $[001]_C$-poled rhombohedral PMN-33PT and $[001]_C$-poled, orthorhombic PZN-8PT.

Importantly, the effect is not unique to relaxor-ferroelectric single crystals and is observed in other ("rotator") ferroelectrics, including room temperature $BaTiO_3$ and $KNbO_3$. However, the effect is *uncommonly* large in relaxor-ferroelectric PMN-xPT and PZN-xPT. This can be seen in monodomain permittivities, piezoelectric coefficients and compliances which are around an order of magnitude higher than those in the simpler ferroelectrics (tables I to III). Relaxor-ferroelectric PMN-xPT and PZN-xPT with low-PT or MPB compositions are simply much softer dielectrically, piezoelectrically and elastically than the simpler perovskites. One might speculate that this is a result of their background "relaxor" character.

VI. EXTRINSIC CONTRIBUTION

Thus, simple crystal anisotropy seems to account for the large piezoelectric response of domain engineered (4O) $KNbO_3$ and (3T) $BaTiO_3$[59,61]. However, in $[001]_C$-poled, relaxor-ferroelectric, "4R" PMN-33PT and "4O" PZN-9PT *intrinsic* crystal anisotropy can only account for between 50% to 80% of the measured piezoelectric response. There is evidence, therefore, of a second significant, *extrinsic* contribution to the enhanced piezoelectric properties of domain-engineered PMN-xPT and PZN-xPT.

However, as noted in previous chapters, there is no evidence for *domain wall motion* in strain-field measurements when an electric field is applied along the $[001]_C$ poling direction of "4O" and "4R" crystals (see chapter seven). Due to the inherent stability of the domain engineered structure, ferroelastic domain switching does not occur. Thus, a different extrinsic contribution must be responsible. Recent work on this subject by others, reviewed below, has sought to find this contribution simply in the *presence* of domain walls in the polydomain crystal.

In the above calculations (equations [6] to [8]), the electrical and mechanical boundary conditions formed at the boundaries between neighboring domains were ignored. This is the basic assumption of "domain average engineering", as defined in chapter five; importantly, it might only be valid in cases where the domain size is close to the dimensions of the sample.

This is not the case, especially in PMN-xPT and PZN-xPT at low PT contents[65], where the domain size becomes fine.

Wherever the domain wall density becomes significant than effects of electrical and mechanical compatibility at those domain walls must be considered. The domain structure itself should be taken into account. As discussed in chapter five, "4R" and "4O" domain structures tends to be composed of alternating, "cross-hatched" layers of different pairs of twins. In "4R" crystals each twin layer is composed of two domain variants separated by $\{010\}_C$ or $\{10\bar{1}\}_C$ domain walls. The domain width varies with PT content being around 1-5 μm in $[001]_C$-poled PMN-28PT and PMN-32PT[66]. In "4O" PZN-8PT each layer is composed of two domain variants each separated by $\{10\bar{1}\}_C$ domain walls; the domain width is around 20-40 μm. Each layer has a thickness of around 40 μm in "4R" PMN-32PT[66]. A similar domain structure is observed in 4O $KNbO_3$, where the layers have a similar thickness. According to Erhart and Cao, such "two-variant twinning" is the basis of all multidomain structures[67].

Liu and Li have used "laminate theory[68,69]" to calculate the effective piezoelectric properties of PMN-33PT (using the same data from table II) having this hierarchical domain structure[69]. Importantly, the boundary conditions of stress, field and displacement field continuity at domain walls were included in their model[68]. However, the calculated piezoelectric response $\langle d_{33}^* \rangle$, 2210 pm/V, was little different to the value calculated assuming simple crystal anisotropy (2310 pm/V). It is still accounts for around 80% of the experimental value (2820 pm/V)[5].

As discussed in chapter five, the domain walls within each twin layer are necessarily charged[70] (or "head-to-head"). Charged domain walls are generally unexpected in ferroelectrics unless they can be neutralized in some way by migration of charged defects. The presence of a charged layer of finite thickness between ferroelectric variants has been explicitly added to the simple two-twin, laminate model by Delaunay et al. (2005)[71]. Using the same data for "PMN-33PT", the authors calculate a slightly lower piezoelectric coefficient (2156 pm/V)[71]. However, the calculated permittivity (5007) is around twice that calculated from a simple averaging approach (2850), much closer to the experimental value of 8200[5].

However, the problem with such mean-field, laminate theory is that it has no dependence on length scale, i.e., the density of domain walls in the specimen. Recent work by Wada and coworkers has shown experimentally that an increased domain density does lead to increased piezoelectric properties in 3T barium titanate and 4O potassium niobate[72-76]. For example, in $[111]_C$-oriented $BaTiO_3$, the measured response of a monodomain crystal was found to be 224 pm/V[76], very close to the theoretical value calculated in table V (222 pm/V). In a multidomain crystal, however, the response was found to be dependent on the average domain size, controllable via the poling technique used. Decreasing the domain size from >30 μm to 14 μm led to an increase in $\langle d_{33}^* \rangle$ from 241 pm/V to 289 pm/V, albeit without change in permittivity. Such a 30% increase in piezoelectric response with increasing domain wall density suggests that there is a significant extrinsic response

from the *presence* of a domain structure, especially when this structure becomes fine. As shown in chapter five, fine domain structures are often found in domain engineered PMN-xPT and PZN-xPT, especially for low PT-contents.

Finally, the reason for this observed domain density dependence remains unclear. However, recent continuum modeling suggests that polarization vectors become more rotated from their zero-field direction in crystals with fine domain structures [Ahluwalia et al. (2005)[77]]. Moreover, first-order, electric-field induced phase transitions have been shown to nucleate at domain walls[77,78]. Local bias fields applied antiparallel to polarization can lead to large enhancements of the piezoelectric response in non-polar directions[79].

VII. SUMMARY AND CONCLUSIONS

Intrinsic crystal anisotropy accounts for at least 50% of the "giant", longitudinal piezoelectric response of $[001]_C$-poled "4R" PMN-33PT and "4O" PZN-9PT. In both cases, an elevated response in a non-polar direction follows from a large contribution from the shear coefficient d_{15}. This is related to the relative ease of polarization rotation over elongation of the polar vector and its origin lies, at least partly, in a large transverse permittivity ε_{11}. This can be expected in all ferroelectric materials close to first-order ferroelectric-ferroelectric phase transitions[47], whether in temperature, electric field, stress or composition; this includes the simpler perovskites $KNbO_3$ and $BaTiO_3$. Accordingly, large shear coefficients are expected close to any morphotropic phase boundary where two or more ferroelectric phases become degenerate. The effect is observed experimentally in PMN-xPT and PZN-xPT, and has been calculated in PZT[64].

Most importantly, a large shear coefficient relates well to an "easy" polarization rotation in the M_A and M_C monoclinic planes of the "R" and "O" phases, respectively. Importantly, this is true of all perovskite ferroelectrics and is not unique to PMN-xPT and PZN-xPT. Thus, monoclinic distortions will occur in the simpler perovskites, although they will be around ten times smaller in magnitude. This is because all the piezoelectric coefficients, permittivities and elastic compliances are an order of magnitude smaller in $KNbO_3$ and $BaTiO_3$ compared to PMN-xPT and PZN-xPT. Enhanced piezoelectric properties are always expected close to ferroelectric-ferroelectric phase transitions and can be harnessed by domain engineering. The effect is common to all perovskite ferroelectrics; however, it is *uncommonly* large in relaxor-ferroelectric PMN-xPT and PZN-xPT.

Finally, a further extrinsic contribution (<50%) arises in domain engineered crystals from the *presence* (as apposed to motion) of domain walls. The effect becomes larger as domain structures become finer, which is the case in PMN-xPT and PZN-xPT, especially at low PT-contents.

Table V

Longitudinal piezoelectric coefficients d_{33}* calculated for possible domain engineered structures at room temperature. The Euler angles relevant to the coordinate transform made are given. Also listed is the monodomain value of d_{33} corresponding to that along the polar axis of the crystal (x_3).

Material	Monodomain value along polar axis, d_{33} /[pC/N]	Poling direction (x_3')	Domain engineered structure	ϕ /[°]	θ /[°]	Value calculated along poling direction, d_{33}* /[pC/N]
PMN-33PT ("R")	190	$[101]_C$ $[001]_C$	2R 4R	60 0	35.26 54.74	940 2310
$KNbO_3$ (O)	29.3	$[111]_C$ $[001]_C$	3O 4O	0 90	-35.26 -45	53.8 87.1
PZN-9PT ("O")	250	$[111]_C$ $[001]_C$	3O 4O	0 90	-35.26 -45	320 1260
$BaTiO_3$ (T)	90	$[111]_C$ $[101]_C$	3T 2T	-45 90	-54.7 45	222 219
PMN-38PT (T)	300	$[111]_C$ $[101]_C$	3T 2T	-45 90	-54.7 45	169 208
$PbTiO_3$ (T)	79.1	$[111]_C$ $[101]_C$	3T 2T	-45 90	-54.7 45	27.9 39.6

Table VI

Longitudinal dielectric permittivities ε_{33}* calculated for possible domain engineered structures at room temperature. The Euler angles relevant to the coordinate transform made are given. Also listed is the monodomain value of ε_{33} corresponding to that along the polar axis of the crystal (x_3).

Material	Monodomain value along polar axis, ε_{33} /[-]	Poling direction (x_3')	Domain engineered structure	ϕ /[°]	θ /[°]	Value calculated along poling direction, ε_{33}* /[-]
PMN-33PT ("R")	640	$[101]_C$ $[001]_C$	2R 4R	60 0	35.26 54.74	1740 2850
$KNbO_3$ (O)	44	$[111]_C$ $[001]_C$	3O 4O	0 90	-35.26 -45	358 99
PZN-9PT ("O")	800	$[111]_C$ $[001]_C$	3O 4O	0 90	-35.26 -45	7530 4900
$BaTiO_3$ (T)	130	$[111]_C$ $[101]_C$	3T 2T	-45 90	-54.7 45	2980 2270
PMN-38PT (T)	734	$[111]_C$ $[101]_C$	3T 2T	-45 90	-54.7 45	3110 2520
$PbTiO_3$ (T)	67.6	$[111]_C$ $[101]_C$	3T 2T	-45 90	-54.7 45	106 96.5

Table VII
Longitudinal compliances s_{33}* calculated for possible domain engineered structures at room temperature. The Euler angles relevant to the coordinate transform made are given. Also listed is the monodomain value of s_{33} corresponding to that along the polar axis of the crystal (x_3).

Material	Monodomain value along polar axis, s_{33} /[10^{-12} m^2N^{-1}]	Poling direction (x_3')	Domain engineered structure	ϕ /[°]	θ /[°]	Value calculated along poling direction, s_{33}* /[10^{-12} m^2N^{-1}]
PMN-33PT ("R")	13.3	$[101]_C$ $[001]_C$	2R 4R	60 0	35.26 54.74	150 245
$KNbO_3$ (O)	7	$[111]_C$ $[001]_C$	3O 4O	0 90	-35.26 -45	5.7 12.5
PZN-9PT ("O")	18	$[111]_C$ $[001]_C$	3O 4O	0 90	-35.26 -45	
$BaTiO_3$ (T)	13.1	$[111]_C$ $[101]_C$	3T 2T	-45 90	-54.7 45	5.3 7.0
PMN-38PT (T)	21.5	$[111]_C$ $[101]_C$	3T 2T	-45 90	-54.7 45	6.4 8.7
$PbTiO_3$ (T)	21.3	$[111]_C$ $[101]_C$	3T 2T	-45 90	-54.7 45	5.5 7.8

REFERENCES

[1] J. Kuwata, K. Uchino, and S. Nomura, Jpn. J. Appl. Phys. **21,** 1298-1302 (1982).

[2] J. Yin, B. Jiang, and W. Cao, IEEE Transactions on Ultrasonics, Ferroelectrics and Frequency Control **47,** 285-291 (2000).

[3] S.-F. Liu, S.-E. Park, T. R. Shrout, and L. E. Cross, J. Appl. Phys. **85,** 2810-2814 (1999).

[4] R. Zhang, B. Jiang, and W. Cao, Appl. Phys. Lett. **82,** 787-789 (2003).

[5] R. Zhang, B. Jiang, and W. Cao, J. Appl. Phys. **90,** 3471-3475 (2001).

[6] H. Dammak, A.-E. Renault, P. Gaucher, M. P. Thi, and G. Calvarin, Jpn. J. Appl. Phys. Pt. 1 **10,** 6477-6482 (2003).

[7] S.-E. E. Park and T. R. Shrout, J. Appl. Phys. **82,** 1804-1811 (1997).

[8] J. Peng, H.-s. Luo, D. Lin, H.-q. Xu, T.-h. He, and W.-q. Jin, Appl. Phys. Lett. **85,** 6221-6223 (2004).

[9] J. F. Nye, *Physical properties of crystals*, 2nd ed. (Clarendon Press, Oxford, 1985).

[10] R. Zhang and W. Cao, Appl. Phys. Lett. **85,** 6380-6382 (2004).

[11] H. Goldstein, *Classical Mechanics* (Addison-Wesley, Reading, MA, 1978).

[12] H. Cao, V. H. Schmidt, R. Zhang, W. Cao, and H. Luo, J. Appl. Phys. **96,** 549-554 (2004).

[13] W. Jiang, R. Zhang, B. Jiang, and W. Cao, Ultrasonics **41,** 55-63 (2003).

[14] J. Erhart and L. Burianova, Journal of the European Ceramic Society **21,** 1413-1415 (2001).

[15] J. Nosek and J. Erhart, Microelectronic Engineering **66,** 733-737 (2003).

[16] S.-F. Liu, W. Ren, B. K. Mukherjee, S. J. Zhang, T. R. Shrout, P. W. Rehrig, and W. S. Hackenberger, Appl. Phys. Lett. **83,** 2886-2888 (2003).

[17] Proc. IRE **49,** 1161 (1961).

[18] D. Berlincourt, D. R. Curran, and H. Jaffe, *Physical Acoustics*, Vol. 1A (Academic Press, New York, 1964).

[19] H. F. Tiersten, J. Acoust. Soc. Am. **35,** 53-58 (1963).

[20] M. Onoe, H. F. Tiersten, and A. H. Mietzler, J. Acoust. Soc. Am. **35,** 36-42 (1963).

[21] American National Standards Institute (1987).

[22] A. W. Warner, M. Onoe, and G. A. Coquin, J. Acoust. Soc. Am. **42,** 1223-1231 (1966).

[23] T. Yamada, H. Iwasaki, and N. Niizeki, Jpn. J. Appl. Phys. **8,** 1127-1132 (1969).

[24] A. Schaefer, H. Schmitt, and A. Dörr, Ferroelectrics **69,** 253-266 (1986).

[25] M. Adachi, M. Nakatsuji, and T. Karaki, Ferroelectrics **262,** 257-262 (2001).

[26] M. Adachi and A. Kawabata, Jpn. J. Appl. Phys. **17,** 1969-1973 (1978).

[27] B. Jaffe, W. R. Cook, and H. Jaffe, *Piezoelectric Ceramics* (Academic Press, 1971).

[28] R. T. Smith, Appl. Phys. Lett. **11,** 146-148 (1967).

[29] I. Koga, M. Aruga, and Y. Yoshinaka, Phys. Rev. **109,** 1467-1473 (1958).
[30] A. G. Kalinichev, J. D. Bass, C. S. Zha, P. D. Han, and D. A. Payne, J. Appl. Phys. **74,** 6603-6608 (1993).
[31] M. Ahart, A. Asthagiri, P. Dera, H.-k. Mao, R. E. Cohen, and R. J. Hemley, Appl. Phys. Lett. **88,** 042908 (2006).
[32] M. Zgonik, R. Schlesser, I. Biaggio, E. Voit, J. Tscherry, and P. Gunter, J. Appl. Phys. **74,** 1287-1297 (1993).
[33] M. Zgonik, P. Bernasconi, M. Duelli, R. Schlesser, P. Günter, M. H. Garrett, D. Rytz, Y. Zhu, and X. Wu, Phys. Rev. B **50,** 5941-5949 (1994).
[34] Z. Li, M. Grimsditch, X. Xu, and S.-K. Chan, Ferroelectrics **141,** 313-325 (1993).
[35] M. J. Haun, E. Furman, S. J. Jang, H. A. McKinstry, and L. E. Cross, J. Appl. Phys. **62,** 3331-3338 (1987).
[36] H. Cao and H. Luo, Ferroelectrics **274,** 309-315 (2002).
[37] S. Haussühl, Acta. Cryst. A **33,** 320-322 (1977).
[38] B. Noheda, D. E. Cox, G. Shirane, J. Gao, and Z.-G. Ye, Phys. Rev. B **66,** 054104 (2002).
[39] D. Zekria, V. A. Shuvaeva, and A. M. Glazer, J. Phys.: Condens. Matter **17,** 1593-1600 (2005).
[40] D. Viehland, J. Appl. Phys. **88,** 4794 (2000).
[41] A very similar arrangement of non-unique polar axes is found in 32 quartz.
[42] R. E. Newnham, *Properties of materials* (Oxford University Press, Oxford, 2005).
[43] J. Fousek, D. B. Litvin, and L. E. Cross, J. Phys.: Condens. Matter **13,** L33-L38 (2001).
[44] W. Yue and J. Yi-jian, Optical Materials **23,** 403-408 (2003).
[45] M. E. Lines and A. M. Glass, *Principles and applications of ferroelectrics and related materials* (Clarendon Press, Oxford, 1977).
[46] M. J. Haun, E. Furman, S. J. Jang, and L. E. Cross, Ferroelectrics **99,** 13-25 (1989).
[47] M. Budimir, D. Damjanovic, and N. Setter, J. Appl. Phys. **94,** 6753-6761 (2003).
[48] D. Damjanovic, M. Budimir, M. Davis, and N. Setter, Appl. Phys. Lett. **83,** 2490 (2003).
[49] D. Damjanovic, M. Budimir, M. Davis, and N. Setter, Appl. Phys. Lett. **83,** 527-529 (2003).
[50] D. Viehland and J. F. Li, J. Appl. Phys. **92,** 3985-3989 (2002).
[51] A. Amin and D. Viehland, J. Appl. Phys. **96,** 5140-5142 (2004).
[52] D. Viehland, A. Amin, and J. F. Li, Appl. Phys. Lett. **79,** 1006-1008 (2001).
[53] R. Zhang, B. Jiang, W. Cao, and A. Amin, Journal of Materials Science Letters **21,** 1877-1879 (2002).
[54] R. Zhang, B. Jiang, W. Jiang, and W. Cao, Materials Letters **57,** 1305-1308 (2003).
[55] W. Cao, in *Piezoelectric Single Crystals and Their Application*, edited by S. Trolier-McKinstry, L. E. Cross, and Y. Yamashita (2004), p. 236-256.

[56] S.-E. E. Park and W. Hackenberger, Current Opinion in Solid State and Materials Science **6,** 11-18 (2002).
[57] R. Zhang, B. Jiang, and W. Cao, Appl. Phys. Lett. **82,** 3737-3739 (2003).
[58] V. Y. Topolov, Sensors and Actuators A**,** In print (2005).
[59] K. Nakamura, T. Tokiwa, and Y. Kawamura, J. Appl. Phys. **91,** 9272-9276 (2002).
[60] D. Damjanovic, F. Brem, and N. Setter, Appl. Phys. Lett. **80,** 652-654 (2002).
[61] S. Wada, S. Suzuki, T. Noma, T. Suzuki, M. Osada, M. Kakihana, S.-E. Park, L. E. Cross, and T. R. Shrout, Jpn. J. Appl. Phys. Pt. 1 **38,** 5505-5511 (1999).
[62] M. Budimir, D. Damjanovic, and N. Setter, Phys. Rev. B **72,** 064107 (2005).
[63] M. Davis, D. Damjanovic, and N. Setter, Appl. Phys. Lett. **87,** 102904 (2005).
[64] X.-h. Du, J. Zheng, U. Belegundu, and K. Uchino, Appl. Phys. Lett. **72,** 2421-2423 (1998).
[65] F. Bai, J. Li, and D. Viehland, Appl. Phys. Lett. **85,** 2313-2315 (2004).
[66] J. Han and W. Cao, Appl. Phys. Lett. **83,** 2040-2042 (2003).
[67] J. Erhart and W. Cao, J. Appl. Phys. **86,** 1073-1081 (1999).
[68] D. Liu and J. Li, Appl. Phys. Lett. **83,** 1193-1195 (2003).
[69] D. Liu and J. Li, Appl. Phys. Lett. **84,** 3930-3932 (2004).
[70] J. Erhart, Phase Transitions **77,** 989-1074 (2004).
[71] T. Delaunay, E. L. Clézio, M. Lematre, and G. Feuillard, Proc. IEEE Ultrasonics Symposium**,** 1069-1071 (2005).
[72] S. Wada, K. Muraoka, H. Kakemoto, T. Tsurumi, and H. Kumagai, Jpn. J. Appl. Phys. Part 1 **43,** 6692-6700 (2004).
[73] S. Wada, K. Yako, H. Kakemoto, J. Erhart, and T. Tsurumi, Key Engineering Materials **269,** 19-22 (2004).
[74] S. Wada, H. Kakemoto, and T. Tsurumi, Materials Transactions **45,** 178-187 (2004).
[75] S. Wada, K. Yako, H. Kakemoto, T. Tsurumi, and T. Kiguchi, J. Appl. Phys. **98,** 014109 (2005).
[76] K. Yako, H. Kakemoto, T. Tsurumi, and S. Wada, Materials Science and Engineering B **120,** 181-185 (2005).
[77] R. Ahluwalia, T. Lookman, A. Saxena, and W. Cao, Phys. Rev. B **72,** 014112 (2005).
[78] R. Ahluwalia, T. Lookman, A. Saxena, and W. Cao, Appl. Phys. Lett. **84,** 3450-3452 (2004).
[79] M. Budimir, D. Damjanovic, and N. Setter, Appl. Phys. Lett. **85,** 2890-2892 (2004).

Chapter eleven

Anisotropy and domain engineering of the transverse piezoelectric coefficient

In an extension to the work of the previous chapter, the effect of crystal anisotropy on the transverse piezoelectric coefficient in domain engineered and ceramic ferroelectric perovskites is discussed; the results of two publications, reprinted in their entirety in appendices IV and V, are summarized. It is shown generally how the transverse piezoelectric coefficient can also be tailored by domain engineering. Importantly, whereas large, negative transverse piezoelectric coefficients can be achieved by domain engineering in rotator ferroelectrics, where polarization rotation is the dominant response, there is a propensity for small or even *positive* coefficients in extender ferroelectrics.

I. INTRODUCTION

In the previous chapter, the importance of piezoelectric anisotropy and a large shear coefficient d_{15} to the longitudinal piezoelectric coefficient d_{33}* measured in *non-polar* directions was discussed. Two types of ferroelectrics were defined. In "rotators" such as barium titanate, potassium niobate and PMN-33PT close to room temperature, the piezoelectric anisotropy is significant ($d_{15}/d_{33} \gg 1$); as a result, polarization rotation is the dominant mechanism of piezoelectric response to fields applied away from the polar axis and enhanced d_{33}* coefficients are expected in non-polar directions. Such materials benefit from domain-engineering. In contrast, the piezoelectric anisotropy of "extenders" such as lead titanate and tetragonal barium titanate at high temperatures is weak ($d_{15}/d_{33} \approx 1$) and the collinear piezoelectric effect is dominant; such materials do not benefit from domain-engineering.

As part of this thesis, calculations were also made of the *transverse* piezoelectric coefficient d_{31}* in various domain-engineered, ferroelectric perovskites. Large (negative) d_{31}* values can be exploited in certain niche applications[1], for example in a variety of flextensional transducers[1], including unimorphs, bimorphs, and cymbal actuators[2]. In some cases, however, a small (or ideally zero) transverse coefficient is preferred, for example in array transducers where a large transverse response leads to undesired "cross-talk" between elements. Additionally, a *positive* d_{31}* is desired in hydrophones to maximize the hydrostatic piezoelectric coefficient[3] ($d_h = d_{33} + d_{31} + d_{32}$). Thus, the possibility of "tailoring" the transverse piezoelectric coefficient by domain-engineering is worthy of investigation.

The results will not be presented in detail here, but will be summarized for the sake of brevity. However, the work has been published elsewhere[4,5] and the articles are reprinted in their entirety in appendices IV and V.

II. DOMAIN ENGINEERING OF THE TRANSVERSE PIEZOELECTRIC COEFFICIENT

In the first publication[4] (see appendix IV) the transverse piezoelectric coefficient d_{31}* was calculated for the six domain-engineered structures occurring in *4mm* barium titanate (BT), *mm2* potassium niobate (KN), *3m* "PMN-33PT" and, finally, *4mm* lead titanate. The data listed in table II of chapter ten was again used, along with the methodology detailed in the same chapter.

Importantly, it is shown that whereas the longitudinal piezoelectric coefficient d_{33}* is not dependent on the third Euler angle ψ (see chapter ten), d_{31}* generally is. This has two important consequences.

Differing contributions from component domain variants

Firstly, it means that different domain variants in a domain-engineered crystal can contribute different values of d_{31}^* to the total response $\langle d_{31}^* \rangle$ of the polydomain structure. This is generally the case, except in the special 2R domain engineered structure formed by poling rhombohedral crystals along a $\langle 101 \rangle_C$ direction where both domain variants (related by a rotation $\Delta\psi = 180°$) contribute the same value.

For example, in the 3T structure formed by poling tetragonal crystals along a $\langle 111 \rangle_C$ direction, two domain variants will contribute the same d_{31}^* whereas the third will contribute a different value. Likewise, in the 4R[6] and 4O domain engineered structures, for certain choices of x_1', two variants will give the same response (again those separated by $\Delta\psi = 180°$), whereas the other two will contribute different values.

As a result, the transverse piezoelectric response $\langle d_{31}^* \rangle$ of the polydomain, domain-engineered crystal will be difficult to predict. Even if domain average engineering holds (see chapter five), it is very difficult to predict which domain variants will appear in which quantity. Recent work by Wada and coworkers suggests that in the 3T structure formed in $BaTiO_3$, only two of the three domain variants form[7,8]. Interestingly, it seems these are the two that give identical d_{31}^* contributions[4]. As discussed in chapter 5, in real ferroelectrics, permissible walls must form between the domains. The interesting possibility therefore arises that, during poling of a domain-engineering crystal, the different strains induced piezoelectrically in the component domain variants by the electrical poling field must also be mutually accommodated. This might explain why domain variants with the same d_{31}^* contribution form in 3T barium titanate. It might also have some importance to the "two-variant twinning[9]" prominent in many perovskite ferroelectrics (see chapter five). Finally, it might have some relevance to the choice of "orientation state" (or direction of the *secondary polar axes* x_1) taken by each domain variant in domain-engineered rhombohedral *3m* crystals, as discussed in the previous chapter. It seems that in 4R domain-engineered crystals, all four variants take the orientation state which contributes the same (high) value of d_{33}^*. This would be worthy of future investigation.

Importance of the second measurement direction

Secondly, the fact that d_{31}^* is a function of ψ means that, whereas d_{33}^* only depends on the choice of the poling (or principal measurement) direction x_3' (see chapter ten), d_{31}^* is also dependent on the choice of the *second measurement direction* x_1'. That is, when we cut a transverse "resonator", care is needed when choosing the "length" direction x_1'.

Advantageously, however, this also means there is greater scope for tailoring the transverse piezoelectric coefficient in domain-engineered crystals.

Generally, we can choose any direction for x_1' in the "*poling plane*" perpendicular to the poling direction x_3'; however, it makes most sense to choose directions of type $\langle 001 \rangle_C$, $\langle 10\bar{1} \rangle_C$ and $\langle 11\bar{2} \rangle_C$. In $\langle 001 \rangle_C$-poled (4O and 4R) crystals, there are $4 \times 2 = 8$ such directions. In $\langle 101 \rangle_C$-poled (2R or 2T) domain-engineered crystals, there are $6 \times 2 = 12$. In $\langle 111 \rangle_C$-poled crystals, there are also $6 \times 2 = 12$ sensible ways of choosing x_1'.

For example, in $[001]_C$-poled, 4R PMN-33PT, a large piezoelectric coefficient ($d_{31}^* \approx -1150$ pm/V) is predicted for a certain choice of x_1'; usefully this is the same for all domain variants. More interestingly, in $[101]_C$-poled, 2R PMN-33PT, even larger transverse coefficients ($d_{31}^* \approx -1630$ pm/V) are predicted for a certain choice of x_1' (along $\pm[010]_C$); again the contribution is the same from each variant. Even higher values (-2520 pm/V) have been reported elsewhere by resonance measurements for the same domain engineered structure and choice of x_1' in $[101]_C$-poled PMN-30PT[1]. Combined with the fact that the transverse direct piezoelectric effect is characteristically anhysteretic (see chapter eight), this is a useful result for sensor applications. The use of $[101]_C$-poled, 2R PMN-xPT in Tonpilz-type transducers has recently been investigated elsewhere[10].

Furthermore, in the same 2R structure a *positive* d_{31}^* is predicted when x_1' is chosen to lie perpendicular to $\pm[010]_C$. Interestingly, this mirrors the positive d_{31} coefficient found in monodomain potassium niobate (see chapter ten, table II); notably, both the 2R domain engineered structure (for equal volume fractions) and $KNbO_3$ have the same *mm2* symmetry[11,12]. Such a positive transverse coefficient may be exploitable in 2-2 type composites[3,13] or one-dimensional array transducers[14-16]; this remains work in progress[17].

Domain engineering of barium titanate and lead titanate

Finally, the (theoretical) 3T domain-engineered structures formed in room temperature $BaTiO_3$ and $PbTiO_3$ were compared. Importantly, whereas d_{31}^* is always predicted to be negative in $BaTiO_3$, *positive* and zero transverse piezoelectric coefficients *are* predicted for $PbTiO_3$. It is shown conceptually that, in domain-engineered crystals, enhanced, negative values of d_{31}^* are observed in materials with large piezoelectric anisotropy ($d_{15}/d_{33} \gg 1$); that is, in materials where polarization rotation is more important than the collinear effect. As discussed in the previous chapter, barium titanate is a "rotator" at room temperature whereas lead titanate is an "extender". The propensity for *zero* or *positive* transverse piezoelectric coefficients in domain-engineered crystals results from a weak piezoelectric anisotropy (d_{15}/d_{33}).

On the other hand, the positive d_{31}* in $[101]_C$-poled PMN-33PT, clearly an extender (as discussed in chapter ten), is related to the positive d_{22} coefficient.

III. POSITIVE OR ZERO TRANSVERSE PIEZOELECTRIC COEFFICIENTS

In the second publication[5] (see appendix V), the tendency for positive or zero d_{31}* coefficients in lead titanate and barium titanate was explored further, specifically with varying temperature. As shown in the previous chapter, tetragonal lead titanate is an *extender* at all temperatures due to the absence of a ferroelectric-ferroelectric phase transition to a lower symmetry phase and, accordingly, a weak dielectric anisotropy ($\varepsilon_{11}/\varepsilon_{33}$). In contrast, barium titanate is a *rotator* close to the ferroelectric-ferroelectric phase transition to an orthorhombic phase that occurs at around 0°C[18].

Importantly, however, the piezoelectric anisotropy of barium titanate is reduced at higher temperatures close to T_C (see chapter ten, figure 13). As a result, polarization rotation becomes less important relative to the collinear effect; there is also a tendency for small or positive transverse coefficients at high temperature in $BaTiO_3$.

During the 1980s, such small or positive transverse piezoelectric coefficients were discovered in modified lead titanate ceramics[19-21]. It was shown[22] that a weak transverse effect in polycrystalline ceramics was a consequence of averaging the piezoelectric response of individual grains and domains, and the intrinsically weak dielectric anisotropy. The work summarized here extends this result to include domain-engineered single crystals.

In summary, where polarization extension is the dominant effect due to a weak dielectric anisotropy, there is a propensity for small or *positive* transverse d_{31}* coefficients in single crystal perovskites oriented in non-polar directions: the effect is not unique to polycrystalline ceramics *nor* lead titanate.

REFERENCES

1 J. Peng, H.-s. Luo, D. Lin, H.-q. Xu, T.-h. He, and W.-q. Jin, Appl. Phys. Lett. **85,** 6221-6223 (2004).

2 K.-H. Lam, H. L.-W. Chan, H.-S. Luo, Q.-R. Yin, and C.-L. Choy, Ferroelectrics **263,** 235-240 (2001).

3 L. E. Cross, Jpn. J. Appl. Phys. Pt. 1 **34,** 2525-2532 (1995).

4 M. Davis, D. Damjanovic, D. Hayem, and N. Setter, J. Appl. Phys. **98,** 014102 (2005).

5 M. Davis, D. Damjanovic, and N. Setter, Appl. Phys. Lett. **87,** 102904 (2005).

6 In this chapter, the notation "4R" will not be used since all work was based on calculations assuming true rhombohedral symmetry for PMN-33PT.

[7] S. Wada, H. Kakemoto, and T. Tsurumi, Materials Transactions **45,** 178-187 (2004).
[8] S. Wada, K. Yako, H. Kakemoto, T. Tsurumi, D. Damjanovic, A. J. Bell, and L. E. Cross, (To be published) (2005).
[9] J. Erhart and W. Cao, J. Appl. Phys. **86,** 1073-1081 (1999).
[10] K. A. Snook, P. W. Rehrig, X. Jiang, R. J. Meyer, and D. Markley, Proc. IEEE Ultrasonics Symposium**,** 1065-1068 (2005).
[11] M. Zgonik, R. Schlesser, I. Biaggio, E. Voit, J. Tscherry, and P. Gunter, J. Appl. Phys. **74,** 1287-1297 (1993).
[12] D. M. Hatch, H. T. Stokes, and W. Cao, J. Appl. Phys. **94,** 5220-5227 (2003).
[13] T. A. Ritter, T. R. Shrout, R. Tutwiler, and K. K. Shung, IEEE Transactions on Ultrasonics, Ferroelectrics and Frequency Control **49,** 217-230 (2002).
[14] S. Saitoh, T. Kobayashi, K. Harada, S. Shimanuki, and Y. Yamashita, Jpn. J. Appl. Phys. Pt. 1 **37,** 3053-3057 (1998).
[15] H. Koyama, K. Kakamura, and T. Takano, in *High coupling $KNbO_3$ width-extensional vibrators with a polar multidomain structure*, Montréal, Canada, 2004.
[16] Y. Hosono, T. Kobayashi, K. Harada, K. Itsumi, M. Izumi, and Y. Yamashita, Proc. IEEE Ultrasonics Symposium**,** 1225-1228 (2002).
[17] M. Davis, D. Damjanovic, and N. Setter, Proc. IEEE International Ultrasonics Symposium (2005).
[18] B. Jaffe, W. R. Cook, and H. Jaffe, *Piezoelectric Ceramics* (Academic Press, 1971).
[19] Y. Yamashita, K. Yokoyama, H. Honda, and T. Takahashi, Jpn. J. Appl. Phys. **20,** 183 (1981).
[20] H. Takeuchi, S. Jyomura, E. Yamamoto, and Y. Ito, J. Acoust. Soc. Am. **72,** 1114 (1982).
[21] D. Damjanovic, T. R. Gururaja, and L. E. Cross, Am. Ceram. Soc. Bull. **66,** 699-703 (1987).
[22] A. V. Turik, E. G. Fesenko, V. G. Gavrilyatchenko, and G. I. Khasabova, Sov. Phys. Crystallogr. **19,** 677-678 (1975).

Chapter twelve

Conclusions and further work

The thesis is summarized and concluded. Possible future work is discussed.

I. SUMMARY

PMN-xPT and PZN-xPT remain very complex materials to study. Firstly, they melt incongruously and hence single crystals are usually synthesized by flux (or solution) growth. However, this results in compositional heterogeneity in as-grown crystals due to unavoidable lead titanate (PT) segregation[1] in the molten phase. This has been evidenced by both electron dispersive spectroscopy (EDS) and dielectric measurement (chapter three). As a result the target composition of a crystal, as determined by the relative amounts of reagents used, can not be assumed in as-grown crystals. Compositional differences and hence property fluctuation, between samples of a given target composition, are the main problems facing the technological application of PMN-xPT and PZN-xPT single crystals.

Moreover, whereas $PbTiO_3$ is an example of a "classical" ferroelectric whose dielectric, piezoelectric and ferroelectric properties are well understood[2], the physics of relaxor-ferroelectric PMN-xPT and PZN-xPT are less clear (chapter four). Importantly, the transition from the high-temperature, cubic, paraelectric phase in $PbTiO_3$ occurs at a well defined temperature T_C and is clearly the result of a displacive, structural phase transition to a long-range ordered, ferroelectric, *4mm* tetragonal phase[2,3]. In low PT-content PMN-xPT and PZN-xPT, however, the transition from the high-temperature cubic phase is characteristically "diffuse[4]", like that of martensites[4], occurring over a wide range of temperatures (chapter four). There is evidence[5] that the transition begins with the nucleation and growth of locally-ordered polar "nanoregions" of nominally rhombohedral symmetry, within the cubic matrix, at temperatures high above the permittivity maximum T_m.

In certain compositions, a truly long-range ordered, *3m* rhombohedral ferroelectric phase can only be induced by application of an electric field (in accordance with the martensitic analogy[4]), or by further doping with lead titanate. The complex "*relaxor to ferroelectric*" phase transition that occurs upon increasing PT content and decreasing temperature is evident in the temperature and frequency dependence of permittivity and dielectric loss (chapter six); the "diffuseness", quantified empirically, decreases at higher PT contents.

The relaxor-to-ferroelectric transition can also be visualized in a single temperature vs. composition (*T*-*x*) phase diagram by plotting the *depoling* temperature T_d, above which all long-range ordered polarity is lost upon heating, and T_m as a function of composition. This has been done by collecting and rationalizing large amounts of data from the literature (chapter four). Such a diagram shows much about the relaxor nature of PMN-xPT and PZN-xPT and can be used, in lieu of more time-consuming experimental methods, to determine the composition of as-grown crystals (chapter four). Refined phase diagrams are reprinted in figure 1.

It has been pointed out that the compositions at which T_m and T_d converge (figure 1) are very similar to those at which the morphotropic phase boundary appears in both PMN-xPT and PZN-xPT between rhombohedral and tetragonal phases (around 45 mol.% and 9 mol.%, respectively). Notably,

this is true in other "$x = 1/3$[6]" relaxor-ferroelectrics as well, including (1-x)$Pb(W_{1/3}F_{2/3})O_3$-x$PbTiO_3$ [PFW-xPT][7] and (1-x)$Pb(Ni_{1/3}Nb_{2/3})O_3$-x$PbTiO_3$ [PNN-xPT][8]. In such materials, the formation of finite volumes of material with *ordering* of the heterovalent cations on the B-site, at low PT-contents[6], is related to increased *structural disorder* (chapter four). The possibility arises that the presence of a rhombohedral, rather than a tetragonal, phase is correlated with this increase in structural disorder; this would be worthy of future investigation.

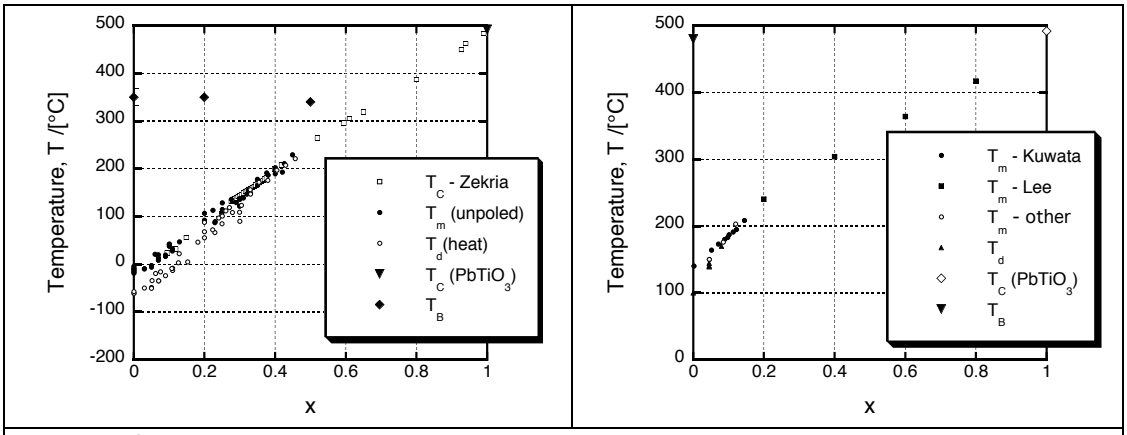

Fig. 1. Collected data demonstrating the short- to long-range ordered phase transition that occurs in PMN-xPT (left) and PZN-xPT (right). The plotted temperatures are defined in chapter four.

Notably, the phase diagrams shown in figure 1 are of little technological use since they do not show the phase fields of the low temperature, ferroelectric (and thus *piezoelectric*) phases and, hence, the position of the morphotropic phase boundary. Unfortunately, the phase transitions between ferroelectric phases that occur in PMN-xPT and PZN-xPT upon cooling are superimposed upon, and *presuppose*, the relaxor-to-ferroelectric transition in a very complex way (chapter six). It would be difficult to draw up a phase diagram for *unpoled* PMN-xPT and PZN-xPT that included low-temperature, ferroelectric phases.

However, it is noted that when low PT-content PMN-xPT and PZN-xPT are poled, they do become long-range ordered and polar such we can treat them as "classically" ferroelectric phases. We *can* draw up a phase diagram for *poled* PMN-xPT and PZN-xPT that shows the position of the MPB and its phases.

In considering the poled phases of PMN-xPT and PZN-xPT as true *ferroelectrics*, we leave their "relaxor" nature as a background effect; however, it remains a very important one. For example, fine, diffuse, "*tweed-like*" microstructures are observed in PMN-28PT and PMN-33PT (but not PZN-8PT) in the as-polished state (chapters three and five). This is related to residual strains in the sample surface, and is indicative of a *low domain wall energy* in low PT-content samples.

Importantly, for these compositions, such fine microstructures can be removed by annealing at high temperatures, which relaxes the residual stresses (chapter three). A proper annealing step should be a matter of course when investigating the microstructure of PMN-xPT and PZN-xPT,

whether by polarized light microscopy (PLM)[9,10], transmission electron microscopy (TEM)[11] or scanning force microscopy (SFM)[12-14], especially for low PT-content crystals. The "tweed-like" microstructures are also removed by poling (chapter five), in keeping with the martensite analogy[4].

The microstructure of PMN-33PT and PZN-8PT in the as-annealed (unpoled) state, as observed by polarized light microscopy, is noticeably complex, partly due to compositional heterogeneity, and possibly due to two-phase coexistence in proximity to the MPB. Furthermore, a monoclinic phase has been evidenced in unpoled PMN-33PT by PLM as a finite tilt of the polar vector away from the direction expected for rhombohedral or orthorhombic symmetry (chapter five).

Such complex microstructures are also removed by poling (chapter five). Nominally 4O, $[001]_C$-poled PZN-8PT and nominally 4R, $[001]_C$-poled PMN-28PT are composed of "interwoven" domains, as observed elsewhere in PMN-32PT[15], characteristic of "two-variant twinning[16]". The domain walls observed are those predicted by Sapriel theory[17,18], although domain sizes are typically smaller than those seen in simpler perovskites (1.5 μm in PMN-28PT, 20-40 μm in PZN-8PT), especially in low PT-content samples. This is again related to their background "relaxor" nature of PMN-xPT and PZN-xPT.

Finally, the fact that the domain structures observed in poled crystals are conceptually similar to those observed in the simpler perovskites gives some validity to a phase diagram that shows truly ferroelectric phases for *poled* PMN-xPT and PZN-xPT. However, construction of such a phase diagram is not straightforward.

Firstly, different monoclinic phases result in PMN-xPT and PZN-xPT from poling (field cooling) in different orientations[19-21]. However, the monoclinic distortion, quantified by the rotation of the polar vector from its position in the higher-symmetry rhombohedral and orthorhombic phases, is typically less than 10°, at room temperature, under zero field (chapter six). Moreover, the pyroelectric coefficient and spontaneous polarization of PMN-28PT and PZN-8PT, measured in different orientations, can be predicted (to within 15%) by the crystal anisotropy of *truly* rhombohedral and orthorhombic phases, respectively. Thus, it is proposed that the M_A and M_B phases, where the polar vector is rotated by a *small* angle away from $<111>_C$ can be considered "pseudo-rhombohedral" (or "R"); likewise, the M_C and M_B phases, wherever they are related by a small distortion to a truly orthorhombic phase, can be considered "pseudo-orthorhombic" (or "O").

Thus a phase diagram for *poled* PMN-xPT and PZN-xPT, encompassing the M_A, M_C and orthorhombic (O) phases recently found at the MPB (chapter one), can be drawn up instead in terms of "R", "O" and tetragonal (T) phases. Notably, the "R" - "O" - T transition sequence observed upon increasing PT composition (and upon heating in $[101]_C$- and $[111]_C$-poled samples) is similar to the R - O - T sequence observed upon heating in the simpler perovskite ferroelectrics, barium titanate (BT) and potassium niobate (KN).

Secondly, however, the thermal stabilities of the "R", "O" and T phases are altered by poling in *different directions*. Transition temperatures are different in $[001]_C$-, $[101]_C$- and $[111]_C$-poled crystals (chapter six). Notably, the effect of poling is similar to the effect of applied electric fields[22-24] such that we should consider the presence of *residual bias fields* (a "memory[25]" effect)

in as-poled crystals, possibly due to the rearrangement of defect dipoles. Therefore, we need to specify the poling direction in phase diagrams for PMN-xPT and PZN-xPT. Since "giant" piezoelectric properties are observed in $[001]_C$-poled crystals, it makes sense to choose this orientation.

For $[001]_C$-poled PMN-xPT and PZN-xPT, the tetragonal phase field can be determined by dielectric measurements (chapter six). However, the "R"/"O" phase boundary is *nearly vertical* for $[001]_C$-poled crystals such that it is *not* observed upon heating. Instead, the present phase ("R" or "O") needs to be determined, for each composition, at room temperature.

This cannot be done by PLM in $[001]_C$-poled crystals (chapter five). However, in lieu of high resolution diffraction experiments, the "R" and "O" phases can be distinguished, indirectly, by measurements of permittivity, spontaneous polarization and pyroelectric coefficient in $[001]_C$-, $[101]_C$- and $[111]_C$-poled crystals of a given composition (chapter six). Phase diagrams based on such bulk, electrical measurements alone have been drawn up agreeing well with phase diagrams based on high-resolution diffraction[26,27]; they are reprinted in figure 2.

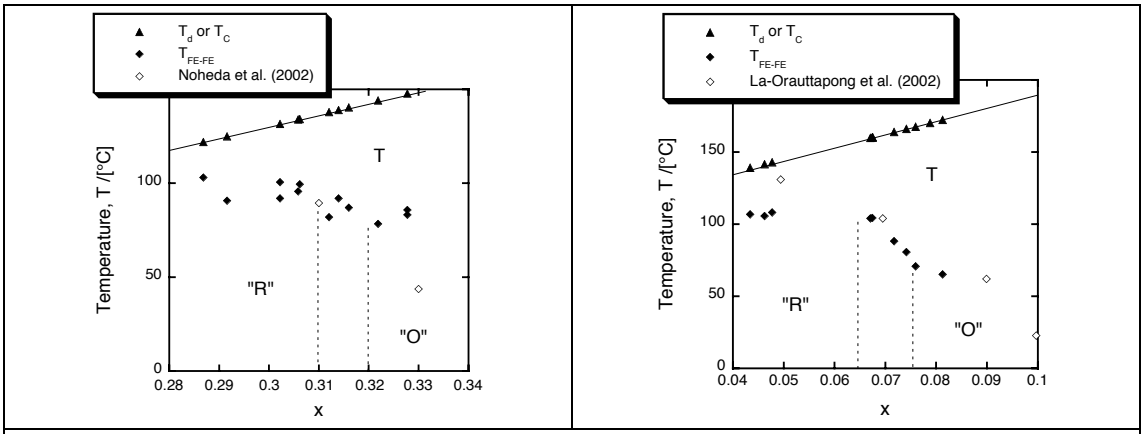

Fig. 2. Phase diagram for $[001]_C$-poled PMN-xPT (left) and PZN-xPT (right) based on bulk electrical measurements. More work is needed to precise the position of the "R"/"O" phase boundary.

As a result of such systematic, bulk characterization, large pyroelectric coefficients (greater than 1000 $\mu C m^{-2} K^{-1}$) have been evidenced in $[111]_C$-poled, pseudo-rhombohedral PMN-28PT (chapter six). These might prove exploitable in thermal imaging and heat sensing devices[28-30].

Moreover, it has been shown that a *metastable*, nominally-rhombohedral phase can be induced in an otherwise pseudo-orthorhombic sample of PZN-8PT by poling along the $[111]_C$ direction at sub-zero temperatures (chapter six). Notably, the same phase transition can be induced at room temperature by application of an electric field alone (chapter seven). This *electric-field induced phase transition* (EFIPT) has been evidenced (macroscopically) in unipolar strain-field loops and (microscopically) by *in situ* PLM. The "O" - R transition occurs via *polarization rotation* in the M_B monoclinic plane. A hysteretic "jump" in strain (chapter seven) and polarization (chapter six) is evidence of a *first order* phase transition; the corresponding "jump" of the polar vector *within* the M_B plane occurs, physically, by the *nucleation and growth* of the high-field rhombohedral phase.

EFIPTs have also been evidenced, by unipolar strain-field measurements, in $[001]_C$-oriented PMN-xPT (x = 25, 30.5, 31 mol.%) and PZN-xPT (x = 5, 6.5, 8.5 mol.%) over a range of temperatures (0 - 100°C). For lower PT contents (PMN-25PT), the polarization rotation path is "R" - T where the polar vector rotates continuously in the M_A plane before a first-order jump to the high-field T phase. At higher PT contents (PZN-5PT, PZN-6.5PT, PMN-30.5PT, PMN-31PT) the more complex path "R" - "O" - T is evident as two hysteretic "jumps" in strain, firstly, between M_A and M_C planes and, secondly, *within* the M_C plane to the T phase. Finally, at higher PT contents (PZN-8.5PT), the "O" phase is stable at room temperature and zero field; instead, only the "O" - T phase transition is evident, occurring by continuous rotation in the M_C plane followed by a first order transition to the induced tetragonal phase (chapter seven).

Using the strain-field data, electric-field vs. temperature (*E*-*T*) phase diagrams have been drawn up showing various trends in the stability of the "R", "O" and T phases for various compositions. The varying phase stabilities with increasing field along $[001]_C$ can be predicted based on simple energetic arguments (chapter seven). Such phase diagrams, along with those plotted in figure 2, highlight the complex *inter-competition* between pseudo-rhombohedral, pseudo-orthorhombic and tetragonal phases close to the morphotropic phase boundary in PZN-xPT and PMN-xPT; this must follow from their near degeneracy.

Importantly, the large piezoelectric response ($d_{33}^* > 2000$ pm/V) of domain-engineered, "4R" and "4O" PMN-xPT and PZN-xPT, along the *non-polar* $[001]_C$ direction, results primarily from *rotation* of the polar vector (*polarization rotation*) in the M_A and M_C monoclinic planes (chapter seven). In contrast, the piezoelectric response of $[001]_C$-poled, "1T" tetragonal PMN-xPT and PZN-xPT, in both converse and direct measurements, is much lower (chapters seven and nine); here, polarization rotation is not driven by an applied field and the response is due to *elongation* of the polar vector (the *collinear piezoelectric effect*).

It has been pointed out that "easy" polarization rotation in the M_A and M_C monoclinic planes of the "R" and "O" phases, respectively, is related to a large, monodomain shear coefficient d_{15} (chapter ten); in contrast, a strong collinear effect is related to a large monodomain longitudinal coefficient d_{33}. Calculations based on simple crystal anisotropy show that an enhanced piezoelectric response can always be expected along *non-polar* directions in materials with strong *piezoelectric anisotropy* ($d_{15}/d_{33} \gg 1$). This is generally related to a large *dielectric anisotropy* ($\varepsilon_{11}/\varepsilon_{33}$), that is, dielectric softness perpendicular to the polar direction (chapter ten).

Two types of crystals can be distinguished. In "*rotators*", piezoelectric anisotropy is strong, polarization rotation is more important than the collinear effect and an enhanced piezoelectric response can be expected in non-polar directions. Such materials do benefit from domain-engineering: enhanced longitudinal coefficients d_{33}^* (chapter ten) and even "application-tailored" transverse piezoelectric coefficients d_{31}^* (chapter eleven) can be domain-engineered. *4mm* $BaTiO_3$ and *mm2* $KNbO_3$ are both rotators at room

temperature, as are "R" PMN-33PT and "O" PZN-9PT. In contrast, *4mm* lead titanate is an "*extender*" at all temperatures (chapter ten); likewise, so is barium titanate close to the Curie temperature. In such materials, piezoelectric anisotropy is weak ($d_{15}/d_{33} \approx 1$), polarization rotation has less importance relative to the collinear effect and the largest piezoelectric response d_{33}* is expected *along* the polar axis. Such materials do *not* benefit from domain engineering (chapters ten and eleven). They also show a propensity for small or *positive* transverse piezoelectric coefficients d_{31}* in non-polar directions (chapter eleven).

Budimir et al. have pointed out that large dielectric anisotropy, and thus large piezoelectric anisotropy, is related to the proximity of *ferroelectric-ferroelectric (FE-FE) phase transitions* whether in temperature (chapter six), electric-field (chapter seven), composition (chapter six) or stress (chapter nine)[31]. This occurs when two or more ferroelectric phases approach *degeneracy*. For example, $BaTiO_3$ is a rotator at room temperature due to the proximity of a transition to an orthorhombic phase at around 0°C[2]. In contrast, $PbTiO_3$ is an extender (in the absence of external fields[32]) at *all* temperatures due to the absence of FE-FE phase transitions.

Therefore, enhanced piezoelectric properties might be expected in $[001]_C$-poled, domain-engineered PMN-xPT and PZN-xPT with morphotropic phase boundary compositions due, solely, to their inherent crystal anisotropy. Importantly, although the effect is not unique to PMN-xPT and PZN-xPT, "giant" piezoelectric coefficients (> 2000 pm/V) perhaps are. This is due to the fact that all of monodomain compliances (s_{ijkl}), piezoelectric coefficients (d_{ijk}) and permittivities (ε_{ij}) of PMN-33PT[33] and PZN-9PT[34] are around 10 times larger than they are in the simpler perovskite rotators $BaTiO_3$ and $KNbO_3$ (chapter ten). This inherent "softness" is likely related to their background relaxor character. Although enhanced piezoelectric properties can be commonly expected along non-polar directions in "rotator" ferroelectrics, they are *uncommonly* large in PMN-xPT and PZN-xPT.

Moreover, it has been noted that polarization rotation does not *require* the presence of *zero-field* monoclinic phases and could equally be described by the field-induced, *piezoelectric*[35] distortion of the higher-symmetry *3m* rhombohedral and *mm2* orthorhombic phases; these phases appear in the simpler perovskites $BaTiO_3$, $KNbO_3$ and $PbTiO_3$[2] and are predicted by 6th order Landau-Ginzburg-Devonshire theory[36]. It is suggested that monoclinic phases might be observed under zero electric field due to the presence of *residual stresses* in unpoled crystals, perhaps due to heterophase coexistence[37-39], or *residual bias fields* in poled crystals (chapter seven). Further work is needed to quantify such residual fields. Notably, however, any monoclinic distortions resulting from residual fields are likely to be relatively large, again, due to the intrinsic elastic, dielectric and piezoelectric "softness" of PMN-xPT and PZN-xPT (chapter ten).

Thus, there remain two seemingly conflicting paradigms. In the first, outlined in chapter one, it is the monoclinic phases that are responsible for the "giant" piezoelectric response of PMN-xPT and PZN-xPT when fields are applied in non-polar directions; monoclinic phases present the "structural bridges[40]" necessary for polarization rotation to occur. In the second

paradigm, developed from that of Kisi and coworkers[35], the monoclinic phases are due to the *piezoelectric distortion* of higher-symmetry rhombohedral and orthorhombic phases; in truly zero-field conditions, they will not be observed. That is, the first paradigm is turned around: in other words, *the large piezoelectric response is responsible for the observation of monoclinic phases*. In this model, the large piezoelectric response follows from a large piezoelectric anisotropy in vicinity of the morphotropic phase boundary *and* an intrinsic "softness", especially at low PT contents, due to a background "relaxor" character.

This will remain the subject of some debate. However, it perhaps suffices to say that the observation of monoclinic phases and a large piezoelectric response along non-polar directions are intrinsically linked. Where one is found, the other is likely to follow. Which one is sought first will probably be determined by which tools are at hand to a given researcher. In any case, PMN-xPT and PZN-xPT can be rationalized to a large extent in terms of pseudo-rhombohedral, pseudo-orthorhombic and tetragonal phases.

Finally, although *intrinsic* crystal anisotropy can account for 80% of the "giant" piezoelectric response of $[001]_C$-poled, "4R" PMN-33PT and 50% of the response of "4O" PZN-9PT (chapter nine), this still leaves room for a significant *extrinsic* contribution. As evident from anhysteretic strain-field loops (chapter seven), domain wall motion does not occur when electric fields are applied *along* the $[001]_C$ poling direction of "4R" and "4O" crystals. However, this does not preclude a contribution from the *presence* of a domain wall structure. As shown in chapter five, domain structures are characteristically fine in PMN-xPT and PZN-xPT especially at low PT contents. Indeed, recent experimental[41-46] and theoretical[47,48] work suggests that finer domain structures do lead to enhanced piezoelectric properties in domain-engineered crystals. This could be related to the presence of *charged* domain walls, which occur necessarily in domain-engineered crystals.

As an aside, this might explain the fact that "giant" piezoelectric coefficients are observed even in low PT-content crystals such as PZN-4.5PT, far away from the MPB, where lower piezoelectric anisotropy is expected. A recent Brillouin scattering study, albeit in stark contrast to measurements elsewhere[49,50], suggests a weak piezoelectric anisotropy in monodomain PZN-4.5PT ($d_{15}/d_{33} = 328/202 \approx 1.6$)[49]. The large piezoelectric response in $[001]_C$-poled PZN-4.5PT ($d_{33}^* > 2000$ pm/V), shown for example in the direct measurements of chapter eight, might thus arise from an even larger extrinsic contribution (> 90%). Accordingly, domain sizes are shown to decrease with decreasing PT content as a result of a lower domain wall energy (chapter five).

On the other hand, although no domain wall *motion* is observed upon application of an electric field along the poling direction, it is observed upon application of a compressive stress. Rayleigh-law hysteresis and non-linearity in the direct, dynamic, charge-stress response of $[001]_C$-poled PZN-4.5PT, PZN-8PT and PMN-31PT clearly suggests an irreversible (extrinsic) contribution from the pinned motion of *interfaces* (chapter eight).

Notably, the irreversible, extrinsic contribution to the direct response is always less than the reversible contribution in "4R" and "4O" crystals, although both increase upon heating as the phase transition to the tetragonal

phase is approached (chapter nine). The increase in Rayleigh-law non-linearity $d_{33}(\sigma_0)$ and quasi-logarithmic frequency dependence $d_{33}(f)$ both indicate an increase in interface mobility near the phase transition (T_{FE-FE}).

Similar behavior is observed in ferroelectric ceramics[51-53] where the interfaces can be identified as *ferroelastic domain walls*. However, ferroelastic switching is not expected in "4R" domain engineered crystals. Thus, it is postulated that the hysteresis is related to a *stress-induced phase transition*, even at small stresses, which locally breaks the domain-engineered structure and drives ferroelastic domain wall motion. The phase transition is evident in both macroscopic charge-stress loops and *in situ* X-ray diffraction measurements in $[001]_C$-poled PZN-4.5PT and PMN-31PT under application of large, quasi-static compressive stresses (< 100 MPa). Although not confirmed, an orthorhombic phase is likely induced in "4R" crystals by polarization rotation in the M_B monoclinic plane (chapter nine).

The same stress-induced phase transition can also be driven by application of a compressive stress *perpendicular to* the poling direction (in the *transverse* d_{31} mode). In contrast to the *longitudinal* d_{33} mode, however, where the compressive stress is applied *along* the poling direction, no depolarization is observed upon unloading (chapter nine). Accordingly, the dynamic, transverse response of $[001]_C$-poled PMN-31PT and PZN-4.5PT is anhysteretic and linear at low stresses (chapter eight). It is postulated that the difference between the longitudinal and transverse behaviors arises from *differing directions of polarization rotation*. It is noted that in the transverse mode, rotation is *towards* the $[001]_C$ poling direction; in the longitudinal mode it is *away*. Because of this, "4R" crystals remain domain-engineered through the phase transition in the transverse mode and ferroelastic domain wall motion is not driven as a result. However, this has not been confirmed; for example, the possibility remains that two-phase boundaries could be partly responsible, especially in MPB compositions.

Whatever the mechanism, this result is extremely useful for sensing applications where "lossy", hysteretic materials, which lead to energy dissipation and a lack of precision, are generally avoided. Although the transverse piezoelectric coefficient of "4R" crystals measured in the direct effect ($d_{31} \sim -1000$ pC/N) is small compared to that in the longitudinal response ($d_{33} \sim 2000$ pC/N), it is characteristically linear and anhysteretic. In fact, the result will have far reaching consequences for the use of domain-engineered PMN-xPT and PZN-xPT, and possibly other ferroelectrics as well, in both sensing and actuation applications. Importantly, it suggests that the stability of the domain engineered structure is only retained when the applied perturbation (compressive stress in the direct piezoelectric effect, electric field in the converse effect) leads to polarization rotation *toward* the poling direction. This is true when an electric field is applied along the poling direction, or when a compressive stress is applied perpendicular to it.

Finally, even larger transverse piezoelectric coefficients are predicted for other domain-engineered structures (chapter eleven). For example, large coefficients ($d_{31}^* \approx -1600$ pm/V) are predicted for the "2R" structure of $[101]_C$-poled PMN-33PT. Combining this with an inherently anhysteretic response,

the use of the transverse mode in "2R", domain engineered PMN-xPT might thus be attractive for a range of sensing applications[54].

To conclude, the above is just one of the possible advantages that the renewed interest in piezoelectric single crystals has brought, mainly thanks to relaxor-ferroelectric PMN-xPT and PZN-xPT. First of all, domain-engineering can be used, with the important condition given above, to yield an anhysteretic and quasi-linear, piezoelectric response. By exploiting single crystal anisotropy alone, the longitudinal and transverse piezoelectric coefficients can also be both enhanced and application-tailored by domain engineering. Moreover, a fine domain structure might also lead to even larger piezoelectric responses[45]. Secondly, it has been shown that domain engineering has the most *intrinsic* benefit in ferroelectrics with strong piezoelectric anisotropy, or "rotators". Recent work has shown how such materials might be predicted[31]. Finally, the inherent "softness" of relaxor-ferroelectric crystals has been shown to be of extreme importance to their "giant" piezoelectric properties. Importantly, by careful choice of material, composition, poling direction and geometry all of these factors can be combined to *engineer* and *tailor* enhanced piezoelectric properties for a wide range of applications.

In many ways, the possibilities are endless.

II. CONCLUSIONS

The bulk dielectric, pyroelectric, ferroelectric and piezoelectric properties of single crystal PMN-xPT and PZN-xPT with morphotropic phase boundary (MPB) compositions have been investigated.

The "*relaxor to ferroelectric*" phase transition that occurs in PMN-xPT and PZN-xPT has been quantified by measurements of permittivity and demonstrated in temperature vs. composition (*T*-*x*) phase diagrams. Measurements of the permittivity maximum T_m and the depoling temperature T_d have been collected from the literature, rationalized and plotted as a function of composition. These refined diagrams can be used, in lieu of more time-consuming methods, to back-determine the composition of as-grown crystals. A link between the position of the morphotropic phase boundary and the relaxor-to-ferroelectric phase transition has been postulated.

The concept of "*pseudo-rhombohedral*" ("R") and "*pseudo-orthorhombic*" ("O") phases has been introduced to encompass the rhombohedral, orthorhombic, and monoclinic (M_A, M_B and M_C) ferroelectric phases occurring in *poled* crystals; it has been shown that all bulk measurements can be rationalized in this way. Poling in different orientations has been shown to affect the thermal stabilities of the "R", "O" and tetragonal (T) phases; it is postulated that this is a result of *residual bias fields*.

Phase diagrams have been constructed for $[001]_C$-poled crystals based on bulk electrical measurements; these agree well with those derived elsewhere from diffraction experiments. Large pyroelectric coefficients ($>1000\ \mu Cm^{-2}K^{-1}$) have been evidenced in $[111]_C$-poled PMN-28PT; these might be exploitable in heat sensing and thermal imaging applications.

It has been shown that a *metastable* pseudo-rhombohedral phase can be induced in otherwise pseudo-orthorhombic PZN-8PT by poling along the $[111]_C$ direction at sub-zero temperatures. The related *electric field induced* ("O" - "R") *phase transition* has been evidenced in strain-field measurements and, *in situ*, by polarized light microscopy at room temperature. Hysteresis, and discontinuities in polarization and strain, have been shown to result from the nucleation and growth of the induced phase; in PZN-8PT, the *first-order* phase transition corresponds to a discontinuous "jump" of the polar vector within the M_B plane.

Further electric-field induced phase transitions have been evidenced by unipolar strain-field measurements in $[001]_C$-poled PZN-xPT and PMN-xPT, with various MPB compositions, at temperatures between 25°C and 100°C. In PZN-6.5PT, PMN-30PT and PMN-30.5PT, the polarization rotation path "R" - "O" - T is evident in *two* first-order "jumps" in strains, one between the M_A and M_C monoclinic planes, and one within the M_C plane to the tetragonal phase. Electric field-temperature (*E-T*) phase diagrams have been constructed from the experimental data. By comparing both *T-x* and *E-T* phase diagrams, the trends for the complex electrical and thermal stabilities of the "R", "O" and T phases close to the MPB have been clarified.

The (direct) piezoelectric response of $[001]_C$-poled PZN-4.5PT, PZN-6.5PT, PZN-8PT and PMN-31PT has been investigated under compressive stresses both *along* and *perpendicular to* the poling direction (*longitudinal* d_{33} and *transverse* d_{31} modes, respectively). Dynamic measurements have been made in a Berlincourt-type press, over a range of stresses (< 20 MPa) and temperatures (25 to 200°C). In the longitudinal mode, Rayleigh-law hysteresis and non-linearity indicates a significant *extrinsic* contribution from the irreversible (pinned) motion of *interfaces*, and likely ferroelastic domain walls; however, domain switching is not generally expected in domain engineered, pseudo-rhombohedral crystals. It has been postulated that domain wall motion is driven by a local *stress-induced phase transition*; this transition has been clearly evidenced in quasi-static, charge-stress loops and *in situ* X-ray diffraction at larger stresses (< 100 MPa).

The reversible contribution to the response is always found to be larger than the irreversible (extrinsic) contribution in the "R" and "O" phases, the latter accounting for around 20% of d_{33} in PZN-8PT, at room temperature, and 5% in PZN-4.5PT. Both contributions have been shown to increase upon heating towards the tetragonal phase; the increase in extrinsic contribution is likely due to increased domain wall mobility as the ferroelectric-ferroelectric phase transition temperature is approached.

In contrast, the transverse response of PMN-31PT and PZN-4.5PT has been shown to be anhysteretic ("non-lossy") and linear at low stresses (< 10 MPa). This might be exploitable in sensing applications. It has been proposed that the difference between the behaviors is related to differing *directions* of polarization rotation. In the transverse mode, rotation is towards the $[001]_C$ poling direction and the domain engineered structure is retained during the stress-induced phase transition.

Lastly, published monodomain properties have been used to calculate the piezoelectric (d_{33}* and d_{31}*) coefficients of domain-engineered *3m* PMN-33PT and *mm2* PZN-9PT; it has been shown how both positive and negative

transverse coefficients can be application "tailored" by domain-engineering. According to such calculations, *intrinsic crystal anisotropy* accounts for at least 50% of the "giant" piezoelectric response of polydomain, $[001]_C$-poled, PMN-33PT and PZN-9PT. Both compositions show inherently strong piezoelectric anisotropy ($d_{15}/d_{33} \gg 1$) in accordance with an "easy" *polarization rotation*. This is related to a high *dielectric anisotropy* ($\varepsilon_{11}/\varepsilon_{33}$) and the degeneracy of the "R", "O" and T phases near the MPB. It has been noted that similar effects are observed in other ferroelectric perovskites, although the effect is *uncommonly* large in PMN-xPT and PZN-xPT: *all* monodomain compliances, piezoelectric coefficients and permittivities are around an order of magnitude larger in PMN-xPT and PZN-xPT compared to their simpler perovskite relatives. This is likely a result of their background "relaxor" nature.

Finally, it has been suggested that the presence of zero-field monoclinic phases in PMN-xPT and PZN-xPT is related to their inherently large piezoelectric response in the presence of residual stresses and bias fields; this is a reversal of the commonly accepted paradigm.

III. FUTURE WORK

A great deal remains to be understood about relaxor-ferroelectrics in general and many new physical models, not mentioned in chapter four, have been postulated to described them[55-60]. Much work has also been done elsewhere to characterize the mesoscale structure of PMN-xPT and PZN-xPT and, especially, the nature of polar nanoregions and their gradual condensation upon cooling below T_B. Descriptions of the sub-micron scale structure have been based on high resolution (X-ray and neutron), diffraction and scattering studies[60-70], scanning force microscopy work[12,13,71-77] and, in a few cases, transmission electric microscopy[11,78]. Although this work will not be reviewed here, it suffices to say that much of it remains to be mutually reconciled, very much in keeping with the parable of the four blind men and the elephant.

Based on the results of this thesis, various future work is proposed. Firstly, the possibility of a relationship between the position of the morphotropic phase boundary (figure 2) and the point of convergence of T_d and T_m (figure 1) should be explored in both PMN-xPT and PZN-xPT and other "$x = 1/3$[6]" relaxor-ferroelectrics. Such a relationship between structural disorder and the presence of a rhombohedral phase might not be unexpected in the light of the behavior of the simpler perovskites. For example, in $BaTiO_3$ and $KNbO_3$, which are both rhombohedral in their ground state at 0 K[2,79,80], the phase transition from the paraelectric phase at T_C is shown to have some *order/disorder* character[3,81-86]; it is not purely displacive in nature as expected from soft mode[87] theory. In fact, the presence of root mean square polarization below a Burns temperature, far above T_C, has been evidenced in both $KNbO_3$ and $BaTiO_3$[3,88]. In contrast, the phase transition in $PbTiO_3$ is purely *displacive*, with no order/disorder character[3,86]; it shows no evidence

for a Burns temperature. Notably, perhaps due to its hybridized Pb-O bonds[89], it remains *4mm* tetragonal to very low temperatures[90,91]. Moreover, the link between order/disorder and the appearance of monoclinic phases in PZT at the morphotropic phase boundary has already been postulated[92-94]. Further investigation into the relationship between symmetry and disorder in perovskite ferroelectrics would be of great theoretical importance.

Secondly, the stress-induced phase transition postulated in chapter nine should be confirmed by diffraction experiments. Moreover, further work should be done to confirm the link between the phase transition and the resultant hysteresis and non-linearity in the longitudinal mode. The experiments should be repeated with simpler domain-engineered perovskites, for example $[001]_C$-poled (4O) potassium niobate. Any irreversible, extrinsic contribution from the complex mesoscale structure of PMN-xPT and PZN-xPT, and the presence of heterophase interfaces, will not be expected in $KNbO_3$.

Moreover, the presence of residual bias fields in poled PMN-xPT and PZN-xPT should be verified. If they do exist they should be quantified and the resultant monoclinic distortion estimated. The origin of such residual fields should also be determined. Shen et al. postulate that they arise from the alignment of defect dipoles, especially during field cooling[25]; the effect of various poling protocols should be investigated.

More work is needed to find an origin for the enhanced piezoelectric properties of domain-engineered $BaTiO_3$ and $KNbO_3$ with fine domain structures. The experiments of Wada and coworkers[42] should also be repeated on domain-engineered PMN-xPT and PZN-xPT; this would help clarify the size of any extrinsic contribution to the "giant" piezoelectric properties of PMN-xPT and PZN-xPT and its variation with composition.

The effect of the electric field on the *secondary polar axes* during the poling of *3m* ferroelectric crystals should be investigated further. The fact that, upon domain engineering, the resulting orientation states (variants) tend to be those that show the same piezoelectric response to the poling field is of interest (chapters ten and eleven). Perhaps Sapriel theory, based on zero-field spontaneous strain[17,18], should be modified for domain-engineered crystals to include mutual compatibility of the strain induced, piezoelectrically, *during* the poling process.

The presence of a d_{22} coefficient alone in *3m* ferroelectrics, and its effect on piezoelectric anisotropy, should be given further consideration. In many ways it is analogous to d_{33} having corresponding shear (d_{16}) and transverse coefficients (d_{21}). It is d_{22} that is responsible for the large positive transverse coefficient d_{31}* in $[101]_C$-poled, 2R PMN-33PT. As stated in chapter twelve, positive transverse coefficients might be exploited in 1D array and 2-2 composite transducers; this should be confirmed experimentally.

Indeed, there remains much to be explored about the basic crystal anisotropy of perovskite crystals. Recent developments in lead free piezoelectrics[95,96] have centered around the discovery of anomalously-large thickness mode coupling factors $k_T \approx 0.69$ in a special cut of potassium niobate[97]. The origin of this should be determined by looking for similar

behavior in other orthorhombic crystals and perhaps in the low temperature, *mm2* phase of barium titanate.

One recent model for the large piezoelectric response of PMN-xPT and PZN-xPT has been ignored in this thesis until now: that is, is the "*adaptive phase*" model proposed by Viehland and coworkers[98,99]. Noting the similarity between relaxor-ferroelectrics and martensites (chapter four), the authors propose a model based on the *fine-scale twinning* of tetragonal (or rhombohedral) domains. In their model, the lattice parameters of the observed monoclinic phases, derived from X-ray diffraction measurements with a finite beam size, are actually the volume-averaged parameters of the finely-twinned tetragonal (or rhombohedral) phase. Upon application of an electric field, the progressive switching of more and more domains leads to a rotation of the *volume-averaged polarization*, rather than the intrinsic polar vector, and thus the observation of increased monoclinic distortion in diffraction experiments. Such a model is indeed in agreement with the experimental evolution of the lattice parameters as a function of electric field and temperature, which satisfy the required "invariance conditions[99]".

However, such fine-scale twinning has yet to be observed experimentally; the model will certainly need reconciling with the vast amounts of evidence from TEM, SFM, and X-ray and neutron scattering. Moreover, since polarization rotation is inherently coupled to local ferroelastic domain wall motion in the adaptive phase model, albeit on a very fine scale, it will be irreversible wherever domain walls are *pinned*; that is, Rayleigh-law hysteresis might be expected as a result. However, no hysteresis is observed in the strain-field response of $[001]_C$-poled "4R" and "4O" PMN-xPT and PZN-PT. Moreover, the reversible contribution to the direct d_{33} response of "4R" and "4O" crystals is much greater than any extrinsic, irreversible part (chapter nine). More work is needed to confirm the adaptive phase model and to better understand the link between ferroelastic martensites and relaxor-ferroelectrics in general.

Finally, ferroelectric single crystals with even better properties than PMN-xPT and PZN-xPT might be sought. The search for "next generation" materials is perhaps the main reason for trying to rationalize the current generation. When we fully understand PZN-xPT and PMN-xPT then the search for even better materials will be greatly facilitated.

And there is little doubt that better materials will be found since, in the words of Robert Browning[100]:

"What youth deemed crystal, age finds out was dew."

REFERENCES

1 Z.-G. Ye, in *Piezoelectric Single Crystals and Their Application*, edited by S. Trolier-McKinstry, L. E. Cross, and Y. Yamashita (2004), p. 297-322.

2 B. Jaffe, W. R. Cook, and H. Jaffe, *Piezoelectric Ceramics* (Academic Press, 1971).

3 G. Burns, F. H. Dacol, J. P. Remeika, and W. Taylor, Phys. Rev. B **26,** 2707-2709 (1982).

[4] G. Schmidt, Ferroelectrics **78,** 199-206 (1988).
[5] G. Burns and F. H. Dacol, Solid State Communications **48,** 853-856 (1983).
[6] A. D. Hilton, C. A. Randall, D. J. Barber, and T. R. Shrout, Ferroelectrics **93,** 379-386 (1989).
[7] L. Feng and Z.-G. Ye, Journal of Solid State Chemistry **163,** 484-490 (2002).
[8] C. Lei, K. Chen, X. Zhang, and J. Wang, Solid State Communications **123,** 445-450 (2002).
[9] D. Zekria, V. A. Shuvaeva, and A. M. Glazer, J. Phys.: Condens. Matter **17,** 1593-1600 (2005).
[10] V. A. Shuvaeva, A. M. Glazer, and D. Zekria, J. Phys.: Condens. Matter **17,** 5709-5723 (2005).
[11] D. Viehland, M.-C. Kim, Z. Xu, and J.-F. Li, Appl. Phys. Lett. **67,** 2471-2473 (1995).
[12] F. Bai, J. Li, and D. Viehland, Appl. Phys. Lett. **85,** 2313-2315 (2004).
[13] I. K. Bdikin, V. V. Shvartsman, and A. L. Kholkin, Appl. Phys. Lett. **83,** 4232-4234 (2003).
[14] V. V. Shvartsman and A. L. Kholkin, Phys. Rev. B **69,** 014102 (2004).
[15] J. Han and W. Cao, Appl. Phys. Lett. **83,** 2040-2042 (2003).
[16] J. Erhart and W. Cao, J. Appl. Phys. **86,** 1073-1081 (1999).
[17] J. Sapriel, Phys. Rev. B **12,** 5128-5140 (1975).
[18] J. Erhart, Phase Transitions **77,** 989-1074 (2004).
[19] H. Cao, J. Li, D. Viehland, G. Xu, and G. Shirane, Appl. Phys. Lett. **88,** 072915 (2006).
[20] F. Bai, N. Wang, J. Li, D. Viehland, P. M. Gehring, G. Xu, and G. Shirane, J. Appl. Phys. **96,** 1620-1627 (2004).
[21] H. Cao, F. Bai, N. Wang, J. Li, D. Viehland, G. Xu, and G. Shirane, Phys. Rev. B **72,** 064104 (2005).
[22] A.-E. Renault, H. Dammak, G. Calvarin, P. Gaucher, and M. P. Thi, J. Appl. Phys. **97,** 044105 (2005).
[23] M. Shen, D. Yao, and W. Cao, Materials Letters **59,** 3276-3279 (2005).
[24] J. Han and W. Cao, Phys. Rev. B **68,** 134102 (2003).
[25] M. Shen and W. Cao, Appl. Phys. Lett. **86,** 192909 (2005).
[26] D. La-Orauttapong, B. Noheda, Z.-G. Ye, P. M. Gehring, J. Toulouse, D. E. Cox, and G. Shirane, Phys. Rev. B **65,** 144101 (2002).
[27] B. Noheda, D. E. Cox, G. Shirane, J. Gao, and Z.-G. Ye, Phys. Rev. B **66,** 054104 (2002).
[28] X. Wan, K.-H. Chew, H. L. W. Chan, C. L. Choy, X. Zhao, and H. Luo, J. Appl. Phys. **97,** 064105 (2005).
[29] Y. Tang, X. Wan, X. Zhao, X. Pan, D. Lin, H. Luo, J. Sun, X. Meng, and J. Zhu, J. Appl. Phys. **98,** 084104 (2005).
[30] Y. Tang, X. Zhao, X. Feng, W. Jin, and H. Luo, Appl. Phys. Lett. **86,** 082901 (2005).
[31] M. Budimir, D. Damjanovic, and N. Setter, J. Appl. Phys. **94,** 6753-6761 (2003).
[32] M. Budimir, D. Damjanovic, and N. Setter, Phys. Rev. B **72,** 064107 (2005).
[33] R. Zhang, B. Jiang, and W. Cao, Appl. Phys. Lett. **82,** 787-789 (2003).

[34] H. Dammak, A.-E. Renault, P. Gaucher, M. P. Thi, and G. Calvarin, Jpn. J. Appl. Phys. Pt. 1 **10,** 6477-6482 (2003).
[35] E. H. Kisi, R. O. Piltz, J. S. Forrester, and C. J. Howard, J. Phys.: Condens. Matter **15,** 3631-3640 (2003).
[36] M. E. Lines and A. M. Glass, *Principles and applications of ferroelectrics and related materials* (Clarendon Press, Oxford, 1977).
[37] M. K. Durbin, J. C. Hicks, S.-E. Park, and T. R. Shrout, J. Appl. Phys. **87,** 8159-8164 (2000).
[38] K. K. Rajan and L. C. Lim, Appl. Phys. Lett. **83,** 5277-5279 (2003).
[39] V. Y. Topolov, Phys. Rev. B **65,** 094207 (2002).
[40] B. Noheda, Current Opinion in Solid State and Materials Science **6,** 27-34 (2002).
[41] S. Wada, K. Yako, H. Kakemoto, J. Erhart, and T. Tsurumi, Key Engineering Materials **269,** 19-22 (2004).
[42] S. Wada, H. Kakemoto, and T. Tsurumi, Materials Transactions **45,** 178-187 (2004).
[43] S. Wada, K. Muraoka, H. Kakemoto, T. Tsurumi, and H. Kumagai, Jpn. J. Appl. Phys. Part 1 **43,** 6692-6700 (2004).
[44] S. Wada, K. Yako, H. Kakemoto, T. Tsurumi, D. Damjanovic, A. J. Bell, and L. E. Cross, (To be published) (2005).
[45] S. Wada, K. Yako, H. Kakemoto, T. Tsurumi, and T. Kiguchi, J. Appl. Phys. **98,** 014109 (2005).
[46] K. Yako, H. Kakemoto, T. Tsurumi, and S. Wada, Materials Science and Engineering B **120,** 181-185 (2005).
[47] R. Ahluwalia, T. Lookman, A. Saxena, and W. Cao, Appl. Phys. Lett. **84,** 3450-3452 (2004).
[48] R. Ahluwalia, T. Lookman, A. Saxena, and W. Cao, Phys. Rev. B **72,** 014112 (2005).
[49] M. Ahart, A. Asthagiri, P. Dera, H.-k. Mao, R. E. Cohen, and R. J. Hemley, Appl. Phys. Lett. **88,** 042908 (2006).
[50] T. Liu and C. S. Lynch, Acta Mater. **51,** 407-416 (2003).
[51] D. Damjanovic and M. Demartin, J. Phys.: Condens. Matter **9,** 4943-4953 (1997).
[52] D. Damjanovic, J. Am. Ceram. Soc **88,** 2663-2676 (2005).
[53] D. Damjanovic, J. Appl. Phys. **82,** 1788-1797 (1997).
[54] K. A. Snook, P. W. Rehrig, X. Jiang, R. J. Meyer, and D. Markley, Proc. IEEE Ultrasonics Symposium**,** 1065-1068 (2005).
[55] A. A. Bokov and Z.-G. Ye, J. Mat. Sci. **41,** 31-52 (2006).
[56] R. Blinc, V. V. Laguta, B. Zalar, and J. Banys, J. Mat. Sci. **41,** 27-30 (2006).
[57] W. Kleemann, J. Mat. Sci. **41,** 129-136 (2006).
[58] V. Bobnar, Z. Kutnjak, R. Pirc, R. Blinc, and A. Levstik, Phys. Rev. Lett. **84,** 5892-5895 (2000).
[59] K. Hirota, Z.-G. Ye, S.-. Wakimoto, P. M. Gehring, and G. Shirane, Phys. Rev. B **65,** 104105 (2002).
[60] Z.-G. Ye, Y. Bing, J. Gao, A. A. Bokov, P. Stephens, B. Noheda, and G. Shirane, Phys. Rev. B **67,** 104104 (2003).
[61] B. Dkhil, J. M. Kiat, G. Calvarin, G. Baldinozzi, S. B. Vakhrushev, and E. Suard, Phys. Rev. B **65,** 024104 (2001).

[62] D. La-Orauttapong, J. Toulouse, J. L. Robertson, and Z.-G. Ye, Phys. Rev. B **64,** 212101 (2001).
[63] D. La-Orauttapong, J. Toulouse, Z.-G. Ye, W. Chen, R. Erwin, and J. L. Robertson, Phys. Rev. B **67,** 134110 (2003).
[64] P. M. Gehring, W. Chen, Z.-G. Ye, and G. Shirane, J. Phys.: Condens. Matter **16,** 7113-7121 (2004).
[65] P. M. Gehring, K. Ohwada, and G. Shirane, Phys. Rev. B **70,** 014110 (2004).
[66] P. M. Gehring, S.-E. Park, and G. Shirane, Phys. Rev. B **63,** 224109 (2001).
[67] A. Naberezhnov, S. Vakhrushev, B. Dorner, D. Strauch, and H. Moudden, Eur. Phys. J. B **11,** 13-20 (1999).
[68] N. d. Mathan, E. Husson, G. Calvarin, J. R. Gavarri, A. W. Hewat, and A. Morell, J. Phys.: Condens. Matter **3,** 8159-8171 (1991).
[69] A. Lebon, H. Dammak, G. Calvarin, and I. O. Ahmedou, J. Phys.: Condens. Matter **14,** 7035-7043 (2002).
[70] A. Lebon, H. Dammak, and G. Calvarin, J. Phys.: Condens. Matter **15,** 3069-3078 (2003).
[71] M. Abplanalp, D. Barosova, P. Bridenbaugh, J. Erhart, J. Fousek, P. Gunter, J. Nosek, and M. Sulc, J. Appl. Phys. **91,** 3797-3805 (2002).
[72] H. R. Zeng, Q. R. Yin, G. R. Li, H. S. Luo, and Z. K. Xu, Journal of Crystal Growth **254,** 432-436 (2003).
[73] H. R. Zeng, H. F. Yu, R. Q. Chu, G. R. Li, H. S. Luo, and Q. R. Yin, Journal of Crystal Growth **267,** 194-198 (2004).
[74] M. Iwata, T. Araki, M. Maeda, I. Suzuki, H. Ohwa, N. Yasuda, H. Orihara, and Y. Ishibashi, Jpn. J. Appl. Phys. Pt. 1 **11B,** 7003-7006 (2002).
[75] H. Okino, J. Sakamoto, and T. Yamamoto, Jpn. J. Appl. Phys. **43,** 6808-6811 (2004).
[76] H. Okino, J. Sakamoto, and T. Yamamoto, Jpn. J. Appl. Phys. **44** (2005).
[77] S. Madeswaran, S. V. Rajasekaran, R. Jayavel, S. Ganesamoorthy, and G. Behr, Materials Science and Engineering B **120,** 32-36 (2005).
[78] Z. Xu, M.-C. Kim, J.-F. Li, and D. Viehland, Philosophical Magazine A **74,** 395-406 (1996).
[79] M. Zgonik, P. Bernasconi, M. Duelli, R. Schlesser, P. Günter, M. H. Garrett, D. Rytz, Y. Zhu, and X. Wu, Phys. Rev. B **50,** 5941-5949 (1994).
[80] M. Zgonik, R. Schlesser, I. Biaggio, E. Voit, J. Tscherry, and P. Gunter, J. Appl. Phys. **74,** 1287-1297 (1993).
[81] R. Comès, M. Lambert, and A. Guinier, Solid State Communications **6,** 715-719 (1968).
[82] R. Comés, M. Lambert, and A. Guinier, Acta. Cryst. A **26,** 244-254 (1969).
[83] P. J. Edwardson, Phys. Rev. Lett. **63,** 55-58 (1989).
[84] S. Wada, T. Suzuki, M. Osada, M. Kakihana, and T. Noma, Jpn. J. Appl. Phys. Part 1 **37,** 5385-5393 (1998).
[85] W. Zhong, D. Vanderbilt, and K. M. Rabe, Phys. Rev. Lett. **73,** 1861-1864 (1994).

[86] B. D. Chapman, E. A. Stern, S.-W. Han, J. O. Cross, G. T. Seidler, V. Gavrilyatchenko, R. V. Vedrinskii, and V. L. Kraizman, Phys. Rev. B **71,** 020102(R) (2005).
[87] C. Kittel, *Introduction to solid state physics*, 7th ed. (Wiley, New York, 1996).
[88] G. Burns and F. H. Dacol, Solid State Communications **42,** 9-12 (1982).
[89] R. E. Cohen and H. Krakauer, Ferroelectrics **136,** 65-83 (1992).
[90] Z. Li, M. Grimsditch, X. Xu, and S.-K. Chan, Ferroelectrics **141,** 313-325 (1993).
[91] M. J. Haun, E. Furman, S. J. Jang, and L. E. Cross, IEEE Transactions on Ultrasonics, Ferroelectrics and Frequency Control **36,** 393-401 (1989).
[92] I. Grinberg, V. R. Cooper, and A. M. Rappe, Nature **419,** 909-911 (2002).
[93] J. Frantti, S. Eriksson, S. Hull, V. Lantto, H. Rundlöf, and M. Kakihana, J. Phys.: Condens. Matter **15,** 6031-6041 (2003).
[94] A. M. Glazer, P. A. Thomas, K. Z. Baba-Kishi, G. K. H. Pang, and C. W. Tai, Phys. Rev. B **70,** 184123 (2004).
[95] Y. Saito, H. Takao, T. Tani, T. Nonoyama, K. Takatori, T. Homma, T. Nagaya, and M. Nakamura, Nature **432,** 84-87 (2004).
[96] M. D. Maeder, D. Damjanovic, and N. Setter, Journal of Electroceramics **13,** 385-392 (2004).
[97] K. Nakamura and Y. Kawamura, IEEE Transactions on Ultrasonics, Ferroelectrics and Frequency Control **47,** 750-755 (2000).
[98] Y. M. Jin, Y. U. Wang, and A. G. Khachaturyan, J. Appl. Phys. **94,** 3629-3640 (2003).
[99] D. Viehland, J. Appl. Phys. **88,** 4794 (2000).
[100] Robert Browning (1812-1889), *Jocoseria* (1883).

Appendix I

Crystallographic and symmetry aspects of the ferroelectric phases of perovskite ferroelectrics

Crystallographic descriptions of the ferroelectric phases found in mixed-oxide perovskites are reviewed. Both the crystallographic axes and the standard orthogonal basis set used to define the tensor properties of each phase are listed with reference to the symmetry elements of the relevant point group. The form of the dielectric, compliance (stiffness) and piezoelectric tensors are also given for each phase. Finally, the group-subgroup relationships between the point groups of the various phases are listed.

Crystalline reference axes

In describing a crystalline lattice the simplest description uses the *crystalline axes* {x, y, z}, i.e., those oriented along the edges of the *unit cell* and defined by six lattice parameters: edge lengths (*a*, *b*, *c*) and angles (α, β, γ)[1]. The crystal axes of the cubic system {x : $[001]_C$, y : $[010]_C$, z : $[001]_C$} are orthogonal by definition. However, excepting the tetragonal phase, the crystalline axes of the ferroelectric phases appearing in perovskite crystals are not generally orthogonal. In some cases, to define the tensor properties of a crystal we thus need to define an orthogonal basis set {x_1, x_2, x_3}. To do this, one or more of the axes are defined with respect to various symmetry elements of the point group[1]. For example, x_3 is always parallel to the polar axis, except in the monoclinic *m* phase where the polar axis is free to lie within the mirror plane. The tensor properties are then defined with respect to these reference axes.

Ideal cubic perovskite structure

The *ideal cubic perovskite* structure for crystals with the general formula ABO_3 is shown in figure 1. A common example of a mixed oxide taking this structure is barium titanate above its Curie point (around 130°C)[2]. The A-site cation (Ba^{2+}) defines the primitive cubic lattice, the B-site cation (Ti^{4+}) sits at the center of the cube and the oxygen anions (O^{2-}) sit at the face centers.

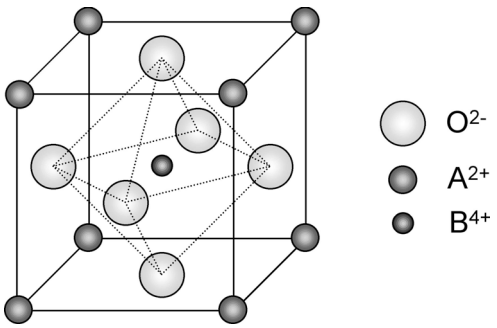

Fig. 1. The ideal perovskite structure ABO_3.

Upon passing through the paraelectric-ferroelectric phase transition at the Curie point various atomic shifts occur and, in simple terms, this can be thought of as the displacement of the B-site cation in the $<001>_C$, $<101>_C$ and $<111>_C$ (pseudocubic) directions to form tetragonal (T), orthorhombic (O) and rhombohedral (R) phases, respectively[2]. The B-site shift for monoclinic phases will be somewhere between two of these limiting directions[3]. The crystallographic definitions of the unit cells for each of the phases occurring in ferroelectric perovskites are listed in table I.

Crystalline directions and planes within the lower-symmetry phases are often defined with respect to the edges of the distorted perovskite unit cell: this is the "*pseudocubic*" description.

Table I
Crystallographic description of the various phases appearing in the mixed-oxide perovskite ferroelectrics. The symbol ":" here means "parallel to".

Phase	Unit cell parameters {x, y, z}	Common choice for orthogonal basis set $\{x_1, x_2, x_3\}$	Point group
Cubic (C)	$a_C = b_C = c_C$ $\alpha_C = \beta_C = \gamma_C = 90°$	$x_1 : [100]_C$ $x_2 : [010]_C$ $x_3 : [001]_C$	*m3m*
Tetragonal (T)	$a_T = b_T \neq c_T$ $\alpha_T = \beta_T = \gamma_T = 90°$	$x_1 : [100]_C$ $x_2 : [010]_C$ $x_3 : [001]_C$	*4mm*
Orthorhombic (O)	$a_O \neq b_O \neq c_O$ $\alpha_O = \beta_O = \gamma_O = 90°$	$x_1 : [10\bar{1}]_C$ $x_2 : [010]_C$ $x_3 : [101]_C$	*mm2*
Rhombohedral (R)	$a_R = b_R = c_R$ $\alpha_R = \beta_R = \gamma_R \neq 90°$	$x_1 : [1\bar{1}0]_C$ $x_2 : [11\bar{2}]_C$ $x_3 : [111]_C$	*3m*
Monoclinic[4] (M_A)	$a_M \neq b_M \neq c_M$ $\alpha_M = \gamma_M = 90 \neq \beta_M$	$x_2 : [1\bar{1}0]_C$	*m*
Monoclinic[4] (M_C)	$a_M \neq b_M \neq c_M$ $\alpha_M = \gamma_M = 90 \neq \beta_M$	$x_2 : [010]_C$	*m*

Cubic phase

The cubic *m3m* phase is the *prototype*[5] of all the ferroelectric phases in the mixed-oxide perovskites; that is, it contains all the symmetry elements of the lower symmetry R, O and T phases. It is centrosymmetric and therefore neither piezoelectric or polar[1]. For this point group, the compliance coefficients s_{ij}, piezoelectric coefficients d_{ij} and dielectric constants ε_{ij} have the following forms[1] (in condensed Voigt or "matrix" notation[1]):

$$s_{ij} = \begin{bmatrix} s_{11} & s_{12} & s_{12} & 0 & 0 & 0 \\ & s_{11} & s_{12} & 0 & 0 & 0 \\ & & s_{11} & 0 & 0 & 0 \\ & & & s_{44} & 0 & 0 \\ & & & & s_{44} & 0 \\ & & & & & s_{44} \end{bmatrix}$$

$$d_{ij} = \begin{bmatrix} 0 & 0 & 0 & 0 & 0 & 0 \\ 0 & 0 & 0 & 0 & 0 & 0 \\ 0 & 0 & 0 & 0 & 0 & 0 \end{bmatrix}$$

$$\varepsilon_{ij} = \begin{bmatrix} \varepsilon_{11} & 0 & 0 \\ & \varepsilon_{11} & 0 \\ & & \varepsilon_{11} \end{bmatrix}$$

There are 3 independent compliance coefficients, and 1 independent dielectric constant. The cubic phase is not piezoelectric and is dielectrically isotropic.

Tetragonal phase

The tetragonal *4mm* phase results from a relative shift of the B-site cation along a <001>$_C$ direction, elongating one of the edges of the cubic unit cell and thus leading to "tetragonality" $c / a > 1$. All three-fold rotation axes are destroyed in this symmetry-breaking[6] transition. The orthogonal basis set of the cubic lattice can still be used with the x_3 direction chosen to lie along the polar four-fold axis; defined relative to this, the tensor properties have the following forms[1]:

$$s_{ij} = \begin{bmatrix} s_{11} & s_{12} & s_{13} & 0 & 0 & 0 \\ & s_{11} & s_{13} & 0 & 0 & 0 \\ & & s_{33} & 0 & 0 & 0 \\ & & & s_{44} & 0 & 0 \\ & & & & s_{44} & 0 \\ & & & & & s_{66} \end{bmatrix}$$

$$d_{ij} = \begin{bmatrix} 0 & 0 & 0 & 0 & d_{15} & 0 \\ 0 & 0 & 0 & d_{15} & 0 & 0 \\ d_{31} & d_{31} & d_{33} & 0 & 0 & 0 \end{bmatrix}$$

$$\varepsilon_{ij} = \begin{bmatrix} \varepsilon_{11} & 0 & 0 \\ & \varepsilon_{11} & 0 \\ & & \varepsilon_{33} \end{bmatrix}$$

There are 6 independent compliance coefficients, 3 independent piezoelectric coefficients and 2 independent dielectric constants.

Orthorhombic phase

The orthorhombic phase results from a B-site cationic shift in a <101>$_C$, or face-diagonal, direction. The unit cell as described with respect to the edges of the pseudocubic cell is no longer orthogonal. However, it is still

possible to define a non-primitive, orthogonal unit cell from the distorted lattice by rotating 45° about the y-axis. This is shown in figure 2.

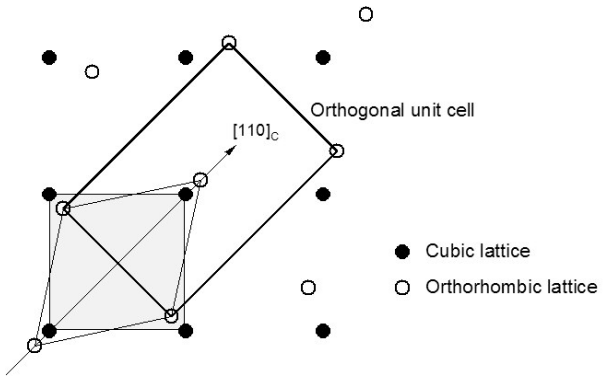

Fig. 2. Schematic representation of how an orthogonal unit cell can be defined in the orthorhombic phase formed by an elongation of the cubic cell along a face diagonal direction.

The x_2 axis of this unit cell is always chosen perpendicular to the body diagonal along which the shift occurred such that the lattice parameter b_O of the resultant orthogonal unit cell is the shortest of the three. Since the orthogonal cell is rotated 45° degrees relative to the pseudocubic one, the other two lattice parameters are often similar and related to the pseudocubic lattice parameter by $a_0 \approx c_O \approx a_C\sqrt{2}$. The orthogonal unit cell is shown with respect to the pseudocubic cell in figure 3; also shown are the unit cell axes with respect to a stereographic projection of the symmetry elements of the point group. The x_3 (and z) axis is parallel to the two-fold symmetry (i.e. polar) axis. The other two are perpendicular to mirror planes.

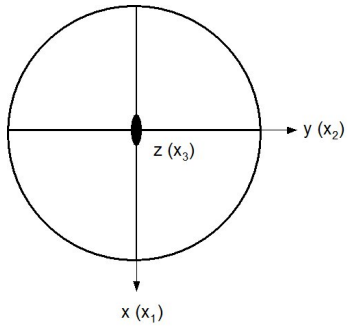

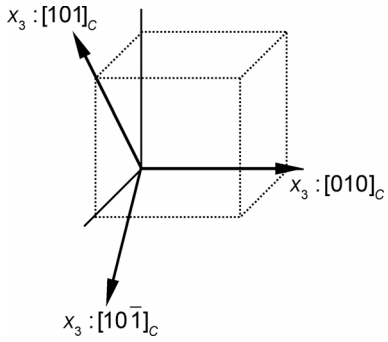

Fig. 3. Symmetry elements of the point group of the *mm2* orthorhombic phase and their relation to the crystallographic axes (left). The axes of the orthogonal basis set shown with respect to the pseudocubic unit cell (right).

With respect to the orthogonal axes, the tensor properties are[1]:

$$s_{ij} = \begin{bmatrix} s_{11} & s_{12} & s_{13} & 0 & 0 & 0 \\ & s_{22} & s_{23} & 0 & 0 & 0 \\ & & s_{33} & 0 & 0 & 0 \\ & & & s_{44} & 0 & 0 \\ & & & & s_{55} & 0 \\ & & & & & s_{66} \end{bmatrix}$$

$$d_{ij} = \begin{bmatrix} 0 & 0 & 0 & 0 & d_{15} & 0 \\ 0 & 0 & 0 & d_{24} & 0 & 0 \\ d_{31} & d_{32} & d_{33} & 0 & 0 & 0 \end{bmatrix}$$

$$\varepsilon_{ij} = \begin{bmatrix} \varepsilon_{11} & 0 & 0 \\ & \varepsilon_{22} & 0 \\ & & \varepsilon_{33} \end{bmatrix}$$

There are 9 independent compliances, 5 independent piezoelectric coefficients and 3 independent dielectric constants. Note that, with this definition, the d_{31} coefficient of orthorhombic perovskite ferroelectrics like potassium niobate[7] turns out to be *positive*.

Rhombohedral phase

A B-site cationic shift along a <111>$_C$ body diagonal results in a trigonal phase. One three-fold axis from the cubic phase remains, along with three mirror planes. The rhombohedral primitive unit cell is defined in table I. The rhombohedral angle is defined by a small distortion from perpendicularity: $\alpha_R = 90° - \delta$ where the value of δ is usually small (e.g. 89.97° for barium titanate[2]). However, a trigonal unit cell can also be chosen to define the crystal lattice {x, y, z}, with $a_R = b_R \neq c_R$ and $\alpha_R = \beta_R = 90°$, $\gamma_R = 120°$. The relationship between the latter crystalline axes and the commonly chosen orthogonal basis set is shown in figure 4. More is said about the relationship between the standard coordinate system and the symmetry elements of the *3m* point group in chapter ten.

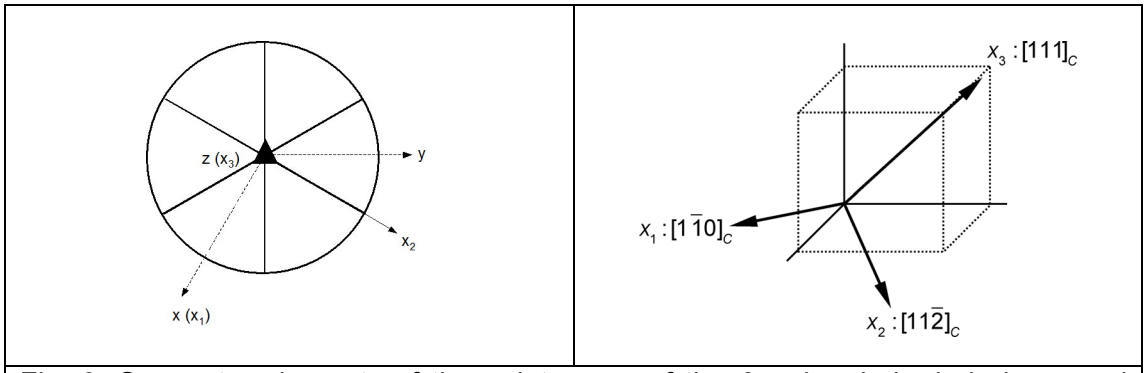

Fig. 3. Symmetry elements of the point group of the *3m* rhombohedral phase and their relation to the crystallographic axes (left). The conventional orthogonal axes with respect to the pseudocubic unit cell (right).

With respect to the orthogonal basis set:

$$s_{ij} = \begin{bmatrix} s_{11} & s_{12} & s_{13} & s_{14} & 0 & 0 \\ & s_{11} & s_{13} & -s_{14} & 0 & 0 \\ & & s_{33} & 0 & 0 & 0 \\ & & & s_{44} & 0 & 0 \\ & & & & s_{44} & -2s_{14} \\ & & & & & 2(s_{11}-s_{12}) \end{bmatrix}$$

$$d_{ij} = \begin{bmatrix} 0 & 0 & 0 & 0 & d_{15} & -2d_{22} \\ -d_{22} & d_{22} & 0 & d_{15} & 0 & 0 \\ d_{31} & d_{31} & d_{33} & 0 & 0 & 0 \end{bmatrix}$$

$$\varepsilon_{ij} = \begin{bmatrix} \varepsilon_{11} & 0 & 0 \\ & \varepsilon_{11} & 0 \\ & & \varepsilon_{33} \end{bmatrix}$$

There are 6 independent compliance coefficients, 4 independent piezoelectric coefficients, and 2 independent dielectric constants.

Monoclinic phases

In the simplified model, when the B-site cation shift is in a direction between two of the limiting <001>$_C$, <101>$_C$ and <111>$_C$ directions a phase with monoclinic symmetry results[3], where the only unbroken symmetry element is a solitary mirror plane. Importantly, the polar axis of the ferroelectric monoclinic phase must lie within this mirror plane. In the M_A monoclinic phase[4] the mirror plane is a $\{1\bar{1}0\}_C$ plane of the parent phase; in the M_C phase, the mirror plane is a $\{010\}_C$ cube face[4]. The two phases have identical point groups (*m*), although differing space groups. The non-

orthogonal conventional unit cell[1] {x, y, z} is described by the lattice parameters given in table I. The y-axis of the unit cell and the x_2-axis of the orthogonal basis set are always chosen to be *perpendicular to the remaining mirror plane*. There are no other restrictions on the axes.

The tensor properties with respect to the orthogonal basis set are:

$$s_{ij} = \begin{bmatrix} s_{11} & s_{12} & s_{13} & 0 & s_{15} & 0 \\ & s_{22} & s_{23} & 0 & s_{25} & 0 \\ & & s_{33} & 0 & s_{35} & 0 \\ & & & s_{44} & 0 & s_{46} \\ & & & & s_{55} & 0 \\ & & & & & s_{66} \end{bmatrix}$$

$$d_{ij} = \begin{bmatrix} d_{11} & d_{12} & d_{13} & 0 & d_{15} & 0 \\ 0 & 0 & 0 & d_{24} & 0 & d_{26} \\ d_{31} & d_{32} & d_{33} & 0 & d_{35} & 0 \end{bmatrix}$$

$$\varepsilon_{ij} = \begin{bmatrix} \varepsilon_{11} & 0 & \varepsilon_{13} \\ & \varepsilon_{22} & 0 \\ & & \varepsilon_{33} \end{bmatrix}$$

There are 13 compliances, 10 piezoelectric coefficients and 4 dielectric coefficients[1].

A third monoclinic phase, M_B, has also been defined[4]. It is, in fact, identical in space group symmetry to the M_A phase.

Group-subgroup relationships

The pairs of phases in which the symmetry elements of one space group is a subgroup of the elements of the other have been derived[8-10]. They are shown in figure 4. According to Landau theory[11], second order phase transitions are only permitted between these pairs.

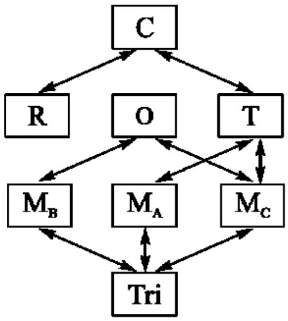

Fig. 4. Pairs of rhombohedral (R), orthorhombic (O), tetragonal (T) and monoclinic phases of the mixed-oxide perovskites sharing a group-subgroup relationship. All monoclinic phases share a group-subgroup relationship with a triclinic phase (Tri). [Diagram taken from Sergienko et al. (2002)[8]].

REFERENCES

1 J. F. Nye, *Physical properties of crystals*, 2nd ed. (Clarendon Press, Oxford, 1985).

2 B. Jaffe, W. R. Cook, and H. Jaffe, *Piezoelectric Ceramics* (Academic Press, 1971).

3 B. Noheda, Current Opinion in Solid State and Materials Science **6,** 27-34 (2002).

4 D. Vanderbilt and M. H. Cohen, Phys. Rev. B **63,** 094108 (2001).

5 K. Aizu, Phys. Rev. B **2,** 754-772 (1970).

6 E. K. H. Salje, Acta Cryst. A **47,** 453-469 (1991).

7 M. Zgonik, R. Schlesser, I. Biaggio, E. Voit, J. Tscherry, and P. Gunter, J. Appl. Phys. **74,** 1287-1297 (1993).

8 I. A. Sergienko, Y. M. Gufan, and S. Urazhdin, Phys. Rev. B **65,** 144104 (2002).

9 E. H. Kisi, R. O. Piltz, J. S. Forrester, and C. J. Howard, J. Phys.: Condens. Matter **15,** 3631-3640 (2003).

10 J. S. Forrester, R. O. Piltz, E. H. Kisi, and G. J. McIntyre, J. Phys.: Condens. Matter **13,** L825-L833 (2001).

11 M. E. Lines and A. M. Glass, *Principles and applications of ferroelectrics and related materials* (Clarendon Press, Oxford, 1977).

Appendix II

Thermodynamic aspects of the thermal, electrical and mechanical properties of crystals at equilibrium

The thermodynamics of crystalline materials are briefly reviewed and definitions are given of their most important thermal, electrical and mechanical properties. The complex interrelationships of the properties are described in order to define the difference between adiabatic and isothermal, short-circuit and open-circuit, and clamped and free experimental measurements. As a consequence, the concept of thermodynamic coupling is explained and the static electromechanical coupling factor is formulated for various geometries. Furthermore, the constitutive relations are given for a variety of choices of thermodynamic variables. *The equivalence of the converse and direct piezoelectric coefficients, assuming linearity at small fields, is shown.*

I. THERMODYNAMICS

Whenever we describe the physical properties of a crystal (as tensors of a given rank[1]), we do so with respect to an equilibrium state. That is, we measure the properties with the crystal in equilibrium with its surroundings such that the state of the crystal and its environment does not change with time. Such properties are then defined by reference to changes which are thermodynamically *reversible*[1].

In general , the thermodynamic properties of a crystal, such as piezoelectric and stiffness, can be seen to relate the fundamental "*forces*" (e.g. temperature T, stress σ_{ij} and electric field E_i) to the direct "*responses*" to these forces (e.g. entropy Σ, strain S_{ij} and displacement field D_i). Note that we ignore in this discussion other variables such as magnetic flux. These three forces connect to the three responses by "*effects*", of which there are nine, if all forces connect to all responses[1].

Principal and coupled effects

The *principal effects* relate *conjugate variables*, as follows:

(i) *The effect of heat capacity*. In a reversible change, per unit volume, an increase in temperature of dT produces a change in entropy given by:

$$d\Sigma = \frac{C}{T} dT \qquad [1]$$

where C is the heat capacity.

(ii) *The dielectric effect*. A small change in electric field dE_i leads to a change in electric displacement given by:

$$dD_i = \varepsilon_0 \varepsilon_{ij} dE_j \qquad [2]$$

where ε_{ij} is the relative permittivity tensor.

(iii) *The elastic effect*. A small change in stress $d\sigma_{kl}$ produces a strain given by:

$$dS_{ij} = s_{ijkl} d\sigma_{kl} \qquad [3]$$

where s_{ijkl} is the fourth rank compliance tensor.

Six "*coupled effects*" are also possible. Strain is coupled to changes in temperature by *thermal expansion*. Furthermore, the displacement field is coupled to temperature by the *pyroelectric effect*. Changes in entropy are coupled to changes in stress by the *piezocaloric effect*. Moreover, changes in stress produce changes in displacement field, for certain point group

symmetries, via the *direct piezoelectric effect*. Likewise, changes in electric field produce strains by the *converse piezoelectric effect*. Finally, changes in entropy can be produced by changes in electric field: this is known as the *electrocaloric effect*.

The converse piezoelectric effect is written $S_{jk} = d_{ijk}E_i$. The direct effect can either be written as $dD_i = d_{ijk}d\sigma_{jk}$ or $dP_i = d_{ijk}d\sigma_{jk}$; both formulas are equivalent if the electric field in the crystal is zero or held constant. Likewise, the pyroelectric effect can be written as $dP_i = p_i dT$ or $dD_i = p_i dT$ and can be regarded as either a change in electric displacement or polarization caused by a temperature change. Thermal expansion is defined by the relation:

$$dS_{ij} = \alpha_{ij} dT \qquad [4]$$

where α_{ij} is the second rank thermal expansion tensor.

Coupling of thermal, electrical and mechanical properties

Due to the complex interconnectivity of the three forces and responses, all the crystal properties (effects) are interrelated and it is necessary to state precisely under which conditions they are measured. For example, we should state whether the change is *isothermal* ($dT = 0$), where the material remains in thermal equilibrium with its surroundings, or *adiabatic* ($d\Sigma = 0$) where no heat flow can occur to or from the crystal. The elastic compliances measured under the two conditions will, in general, be different (to the order of around 1%[1]).

Another important result of their interconnectivity is that apart from the nine *primary* effects already listed, *secondary* effects are possible via more complex pathways between the forces and responses. For example, the primary pyroelectric effect takes the direct path $dT \Rightarrow dD_i$. However, the *secondary pyroelectric effect* also occurs as thermal expansion of the crystal can lead to piezoelectrically induced polarization along the path $dT \Rightarrow dS_{ij} \Rightarrow dD_i$. Whether a contribution to the measured change in displacement field from the secondary effect is observed depends on whether the latter path is available, i.e., whether the crystal is allowed to deform freely.

The difference between the isothermal and adiabatic compliances, and primary and secondary pyroelectric coefficients, can be derived analytically using the following thermodynamic approach.

Firstly, we define the thermodynamic "forces" listed above as *independent* variables (T, σ_{ij}, E_i) and the "responses" as *dependent* variables (Σ, S_{ij}, D). This is because in most cases we work in isothermal conditions and "apply" electric fields and stresses. We note, however, that we could define the "forces" by taking one from every one pair of conjugate variables connected by the principal effects, that is: (T or Σ), (σ_{ij} or ε_{ij}) and (E_i or D_i). This is discussed in more detail below. Assuming unit volume we can

immediately write down differentials describing the nine primary effects, or material properties:

$$dS_{ij} = \left(\frac{\partial S_{ij}}{\partial \sigma_{kl}}\right)_{E,T} d\sigma_{kl} + \left(\frac{\partial S_{ij}}{\partial E_k}\right)_{\sigma,T} dE_k + \left(\frac{\partial S_{ij}}{\partial T}\right)_{\sigma,E} dT \qquad [5]$$

$$dD_i = \left(\frac{\partial D_i}{\partial \sigma_{jk}}\right)_{E,T} d\sigma_{jk} + \left(\frac{\partial D_i}{\partial E_j}\right)_{\sigma,T} dE_j + \left(\frac{\partial D_i}{\partial T}\right)_{\sigma,E} dT \qquad [6]$$

$$d\Sigma = \left(\frac{\partial \Sigma}{\partial \sigma_{ij}}\right)_{E,T} d\sigma_{ij} + \left(\frac{\partial \Sigma}{\partial E_i}\right)_{\sigma,T} dE_i + \left(\frac{\partial \Sigma}{\partial T}\right)_{\sigma,E} dT \qquad [7]$$

The subscripts E, T and σ indicate partial differentiation with these variables held constant.

Reading from left to right, equation [5] shows the combined elastic, converse piezoelectric and thermal expansion effects. Equation [6] shows the combined direct piezoelectric, dielectric, and pyroelectric effects. Equation [7] shows the piezocaloric, electrocaloric effect and heat capacity effects. A reversible change in the internal energy of the crystal can then be written, by the combination of first and second laws of thermodynamics, as follows:

$$dU = \sigma_{ij} dS_{ij} + E_i dD_i + T d\Sigma \qquad [8]$$

We then make the appropriate Legendre transformation to the more convenient *Gibbs free energy* (G) description of the thermodynamic state of the system, defined by:

$$G = U - T\Sigma - S_{ij}\sigma_{ij} - E_i D_i \qquad [9]$$

Differentiating this and combining with [8] leads to:

$$dG = -S_{ij} d\sigma_{ij} - D_i dE_i - \Sigma dT \qquad [10]$$

Since all the quantities on the right of equation [10] are functions of the independent variables (T, σ_{ij}, E_i), which define the state of the system, we can expand the dG as follows:

$$dG = \left(\frac{\partial G}{\partial \sigma_{ij}}\right)_{E,T} d\sigma_{ij} + \left(\frac{\partial G}{\partial E_i}\right)_{\sigma,T} dE_i + \left(\frac{\partial G}{\partial T}\right)_{\sigma,E} dT \qquad [11]$$

Hence, comparing equations [10] and [11] we find the following expressions:

$$S_{ij} = -\left(\frac{\partial G}{\partial \sigma_{ij}}\right)_{E,T}, \; D_i = -\left(\frac{\partial G}{\partial E_i}\right)_{\sigma,T}, \; \Sigma = -\left(\frac{\partial G}{\partial T}\right)_{\sigma,E} \qquad [12]$$

Finally, by further differentiation of the three expressions given in [12] with respect to the independent variables (T, σ_{ij}, E_i) we can derive various expressions for the coefficients describing the "effects": the piezoelectric coefficient, pyroelectric coefficients, and so on. For example, differentiating the first of the expressions with respect to field and the second with respect to stress we arrive at:

$$-\left(\frac{\partial^2 G}{\partial \sigma_{jk} \partial E_i}\right)_T = \left(\frac{\partial S_{jk}}{\partial E_i}\right)_T \equiv d_{ijk}^T \equiv \left(\frac{\partial D_i}{\partial \sigma_{jk}}\right)_T = -\left(\frac{\partial^2 G}{\partial E_i \partial \sigma_{jk}}\right)_T \qquad [13]$$

Thus we arrive at expressions for the piezoelectric coefficient d_{ijk}^T (where the superscript "T" means that the temperature is held constant, i.e. "isothermal conditions) and due to the equivalence of the two second partial derivatives we also prove that *the coefficients of the converse and direct piezoelectric effects are equivalent*.

Similarly we can show that the coefficients of thermal expansion and the piezocaloric effect (α_{ij}^E) are identical, as are the pyroelectric coefficients and those for the electrocaloric effect (p_i^σ)[1]. Integrating equations [5-7], and substituting the results of equation [13], and the other two equations like it, and the definitions of the various effects such as in [1-4], we obtain:

$$S_{ij} = s_{ijkl}^{E,T} \sigma_{kl} + d_{kij}^T E_k + \alpha_{ij}^E \Delta T \qquad [14]$$

$$D_i = d_{ijk}^T \sigma_{jk} + \varepsilon_0 \varepsilon_{ij}^{\sigma,T} E_j + p_i^\sigma \Delta T \qquad [15]$$

$$\Delta\Sigma = \alpha_{ij}^E \sigma_{ij} + p_i^\sigma E_i + \left(\frac{C^{E,\sigma}}{T}\right)\Delta T \qquad [16]$$

These are known as the *constitutive equations*. Notably, however, whereas the differential equations are exact, these constitutive equations only hold for linear effects; they will not generally hold in strong fields, or in highly non-linear materials such as ferroelectrics[2].

Other sets of variables

As noted above the choice of independent variables is arbitrary and other systems of equations result from other choices of "forces" and "responses". Assuming isothermal conditions, and ignoring the subscripts for convenience, the constitutive equations [14-16] can be written:

$$S = s^E\sigma + dE \quad [17]$$

$$D = d\sigma + \varepsilon_0\varepsilon^\sigma E \quad [18]$$

Taking other independent variables, still assuming constant temperature, we can arrive at the six remaining constitutive equations. Firstly, taking strain and electric field as independent variables we arrive at:

$$\sigma = c^E S - eE \quad [19]$$

$$D = eS + \varepsilon_0\varepsilon^S E \quad [20]$$

where c^E is the stiffness at constant electric field, ε^S is the relative permittivity at constant strain and e is another piezoelectric coefficient relating electric field to stress and electric displacement to strain. Taking displacement field and strain as independent variables (D, S), we have:

$$\sigma = c^D S - hD \quad [21]$$

$$E = -hS + \frac{\beta^S}{\varepsilon_0} D \quad [22]$$

where h is yet another piezoelectric coefficient, and β^S is the dielectric stiffness at constant strain. Finally, taking displacement field and stress as the independent variables (D, σ), we arrive at:

$$S = s^D\sigma + gD \quad [23]$$

$$E = -g\sigma + \frac{\beta^\sigma}{\varepsilon_0} D \quad [24]$$

where g is a fourth piezoelectric coefficient, which describes "piezostriction[3]", the linear relationship between strain and polarization.

In total there are four possible ways of formulating the piezoelectric coefficient. d is known as the charge or strain coefficient, e is the stress or charge coefficient, h is the stress or voltage coefficient, and g is the strain or voltage coefficient[2]. Which one is measured will depend on the boundary conditions of the experiment, that is, the choice of independent and dependent variables, and some piezoelectric coefficients may be more convenient to measure than other.

For example, if the sample is *open-circuited* the charge due to the application of a stress will accumulate on the crystal surfaces and give rise to an electric field. Hence g would be the appropriate piezoelectric coefficient ($E = -g\sigma$) and the voltage should be measured (at constant or zero displacement field, $dD = 0$). In *short-circuited* conditions the charge will flow freely into the external electronic circuit. Charge should be measured (at zero

or constant field, $dE = 0$) and the d coefficient is the appropriate one ($D = d\sigma$). The mechanical boundary conditions should also be specified, i.e., whether the sample is "clamped" ($dS = 0$) or "unclamped" ($d\sigma = 0$) and free to deform.

Various relationships between the coefficients can be derived[1,2] and are shown below:

$$d = s^E e = \varepsilon_0 \varepsilon^\sigma g \qquad \text{(m/V or C/N)} \qquad [25]$$

$$e = c^E d = \varepsilon_0 \varepsilon^S h \qquad \text{(C/m}^2\text{ or Vm/N)} \qquad [26]$$

$$g = s^D h = \frac{\beta^\sigma}{\varepsilon_0} d \qquad \text{(m}^2\text{/C or N/Vm)} \qquad [27]$$

$$h = c^D g + \frac{\beta^S}{\varepsilon_0} e \qquad \text{(N/C or V/m)} \qquad [28]$$

Sometimes, the use of other piezoelectric coefficients can have direct technological application. For example, although a complex driving circuit would be required, an actuator based on a ferroelectric ceramic might be "charge-driven". Under normal field-drive conditions, the deformation of a ferroelectric material at high fields is often hysteretic due to inherent extrinsic contributions such as domain wall motion to the piezoelectric coefficient d. Hysteresis necessarily means the displacement is a multi-valued function for a given driving field and, thus, is contrary to precision. However, much of this non-linearity is also manifest in the dielectric response of a material, that is, in the permittivity ε^σ. Therefore, the charge-driven deformation of the sample given by $\Delta S = g \Delta D$ is often much less hysteretic since the two hysteretic effects compensate in the g coefficient: from equation [25], $g = d/(\varepsilon_0 \varepsilon^\sigma)$.

Coupling coefficients

As well as the mechanical (clamped/free) and electrical (short/open-circuited) boundary conditions determining the choice of piezoelectric coefficient, due to the coupling between electric and elastic fields, they will also affect the values of stiffness (compliance) and dielectric permittivity. For example, consider the measurement of relative permittivity in a clamped sample (S = 0). The displacement field is given by $D = \varepsilon_0 \varepsilon^S E$. However, the stress produced by this clamping effect $\sigma = -eE$ will lead to a further contribution to the displacement field via the direct piezoelectric effect $D = d\sigma = -deE$. Therefore, the displacement that would be measured in clamped conditions is the same as that which would be measured under free conditions ($D = \varepsilon_0 \varepsilon^\sigma E$) plus the contribution from the coupled effect:

$$D = \varepsilon_0 \varepsilon^\sigma E - deE = \varepsilon_0 \varepsilon^S E \qquad [29]$$

Hence:

$$\varepsilon_0 \varepsilon^{\sigma} - de = \varepsilon_0 \varepsilon^{S} \qquad [30]$$

So:

$$\varepsilon^{S} = \varepsilon^{\sigma}\left(1 - \frac{de}{\varepsilon_0 \varepsilon^{\sigma}}\right) \qquad [31]$$

And, finally, using equation [25] to substitute for the *e* coefficient:

$$\varepsilon^{S} = \varepsilon^{\sigma}\left(1 - \frac{d^2}{\varepsilon_0 \varepsilon^{\sigma} s^{E}}\right) = \varepsilon^{\sigma}(1 - k^2) \qquad [32]$$

where *k* is known as the *electromechanical coupling coefficient*:

$$k^2 = \frac{d^2}{\varepsilon_0 \varepsilon^{\sigma} s^{E}} \qquad [33]$$

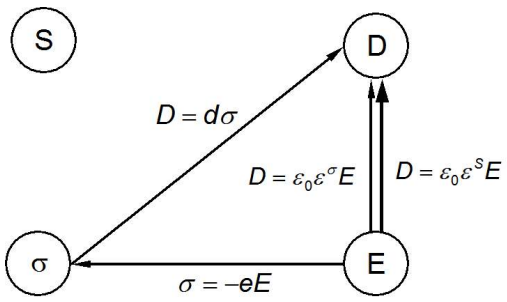

Fig. 1. Method for calculating the difference between clamped and unclamped permittivities.

This approach can be helpfully viewed using the diagram shown in figure 1. The four thermodynamic variables are shown as four circles. The bold arrow shows the clamped dielectric effect. It can be thought of as the sum of the two other paths shown in the diagram: $E \Rightarrow \sigma \Rightarrow D$ (a secondary effect via a change in stress) and $E \Rightarrow D$ (the primary effect at zero stress). No path through the strain variable is taken since we are considering the clamped case (*S = 0*). Summing the secondary effect and the unclamped primary effect we get $D = -edE + \varepsilon_0 \varepsilon^{\sigma} E$ which is then equated to the clamped effect $D = \varepsilon_0 \varepsilon^{S} E$ as in equation [29]. The difference between the two values of permittivity follows easily.

The same coupling coefficient can be shown to relate the compliance measured under constant or zero field (short-circuited conditions) and that under constant or zero displacement field (open-circuited)[1,2]:

$$s^D = s^E\left(1-\frac{d^2}{\varepsilon_0\varepsilon^\sigma s^E}\right) = s^E(1-k^2) \qquad [34]$$

Static coupling coefficients

The coupling coefficient *k* defined above gives a measure of the "*coupling*" between the electrical and mechanical response of a material due to the piezoelectric effect. The coupling factor may be defined as "the ratio of the mutual elastic and dielectric energy density to the geometric mean of the elastic and dielectric self-energy densities[4]". Neglecting thermal terms in equation [8] and integrating we can write the internal energy of a linear system as:

$$U = \frac{1}{2}S_{ij}\sigma_{ij} + \frac{1}{2}D_m E_m \qquad [35]$$

Using the constitutive equations for the independent variables E_m and σ_{ij} (equations [14-15]) for isothermal conditions, we can write:

$$\begin{aligned} U &= \frac{1}{2}\sigma_{ij}(s^E_{ijkl}\sigma_{kl} + d_{mij}E_m) + \frac{1}{2}E_i(d_{ijk}\sigma_{jk} + \varepsilon_0\varepsilon^\sigma_{ij}E_j) \\ &= \frac{1}{2}\sigma_{ij}s^E_{ijkl}\sigma_{kl} + \frac{1}{2}\sigma_{ij}d_{mij}E_m + \frac{1}{2}E_i d_{ijk}\sigma_{jk} + \frac{1}{2}E_i\varepsilon_0\varepsilon^\sigma_{ij}E_j \\ &= \frac{1}{2}\sigma_{ij}s^E_{ijkl}\sigma_{kl} + \sigma_{ij}d_{mij}E_m + \frac{1}{2}E_i\varepsilon_0\varepsilon^\sigma_{ij}E_j \\ &= U_{mechanical} + 2U_{mutual} + U_{electrical} \end{aligned} \qquad [36]$$

Thus, from the above definition of the coupling factor,

$$k = \frac{U_{mutual}}{\sqrt{U_{electrical}U_{mechanical}}} \qquad [37]$$

we can easily derive:

$$k = \frac{\sigma_{ij}d_{mij}E_m}{\sqrt{\sigma_{ij}s^E_{ijkl}\sigma_{kl}E_m\varepsilon_0\varepsilon^\sigma_{mn}E_n}} \qquad [38]$$

It is easy to see that upon dropping the indices we would immediately arrive back at the coupling factor defined in equations [32-34]. Equation [38] is the general form of the coupling coefficient for the constitutive equations as defined; other forms are possible for different choices of independent variables. Upon taking strain S_{ij} and electrical displacement D_i as independent variables, and the constitutive equations given in [21] and [22] with appropriate indices, we arrive at:

$$k = \frac{S_{ij} h_{mij} D_m}{\sqrt{S_{ij} s^D_{ijkl} S_{kl} D_m \frac{\beta^S_{mn}}{\varepsilon_0} D_n}} \qquad [39]$$

In three dimensions for a general anisotropic crystal the indices of the tensor properties must be retained and the coupling factor will then depend upon both the geometry and the boundary conditions of the crystal (i.e. S_{ij} and D_i in equation [39]). Various coupling factors can defined for *various geometries and boundary conditions* which simplify enormously the expression for *k*. In every case, the constitutive equations should be chosen depending on the boundary conditions, especially the mechanical boundary conditions of zero stress (unclamped) or zero strain (clamped).

For example, the coupling coefficient k_{31} is defined for a bar of piezoelectric material electroded perpendicularly to the x_3 direction, where a stress is applied along the x_1 direction ($\sigma_{11} \neq 0$). The bar is unclamped so that all other stresses are zero and we measure only the electric field in the x_3 direction (E_3). Equation [39] then reduces to:

$$k_{31} = \frac{d_{311}}{\sqrt{\varepsilon_0 \varepsilon^\sigma_{33} s^E_{1111}}} \qquad [40]$$

Equations [38] and [39] are generally only valid for static systems and are known as *static coupling coefficients*. We note that in dynamic systems the coupling factor will be dependent on the overall distribution of stress in the system and will be in general less the static one since not all elastic energy is elastically coupled[4]. However, at certain frequencies where *resonance* occurs, the *dynamic* and *static* coupling factors sometimes become identical[4].

Other common coupling geometries are listed in table I. Coupling coefficients are general difficult to calculate and are dependent on the point group symmetry of the piezoelectric crystal. However, the static coupling coefficients for various modes can often be calculated quite simply. For example, k_{33} can be calculated using the E_m and σ_{ij} system with the boundary conditions $\sigma_{11} = \sigma_{22} = 0$ as:

$$k_{33} = \frac{d_{333}}{\sqrt{\varepsilon_0 \varepsilon^\sigma_{33} s^E_{3333}}} \qquad [41]$$

This is independent of crystal symmetry. The thickness coupling coefficient k_T can be calculated using the S_{ij} and D_i system, and the boundary conditions $S_{11} = S_{22} = 0$, as:

$$k_T = \frac{h_{333}}{\sqrt{\frac{\beta_{33}^S}{\varepsilon_0} c_{3333}^D}} \quad [42]$$

Using equation [28] we can simplify this to:

$$k_T = e_{333} \sqrt{\frac{\beta_{33}^S}{\varepsilon_0 c_{3333}^D}} \quad [43]$$

Importantly, both coupling factors share common features. They are in fact related to each other as limiting aspect ratios of the same resonator: an infinitely long bar and an infinitely thin plate[5].

Table I
Boundary conditions for standard coupling coefficient geometries taken from Berlincourt et al. (1964)[4].

Coupling factor	Description	Mechanical boundary conditions	Typical resonant element
k_{31}	Transverse mode	$\sigma_1 \neq 0; \sigma_2 = \sigma_3 = 0$ $S_1 \neq 0; S_2 \neq 0; S_3 \neq 0$	Flat bar vibrating along its length, perpendicularly to the applied field
k_{33}	Longitudinal mode	$\sigma_1 = \sigma_2 = 0; \sigma_3 \neq 0$ $S_1 = S_2 \neq 0; S_3 \neq 0$	Long bar vibrating along its length, parallel to the applied field
k_P	Radial (planar) mode	$\sigma_1 = \sigma_2 \neq 0; \sigma_3 = 0$ $S_1 = S_2 \neq 0; S_3 \neq 0$	Flat disc vibrating in the radial direction
k_T	Thickness mode	$\sigma_1 = \sigma_2 \neq 0; \sigma_3 \neq 0$ $S_1, S_2 = 0; S_3 \neq 0$	Flat plate vibrating in the thickness direction

REFERENCES

1 J. F. Nye, *Physical properties of crystals*, 2nd ed. (Clarendon Press, Oxford, 1985).
2 D. Damjanovic, Rep. Prog. Phys. **61,** 1267-1324 (1998).
3 V. Sundar and R. E. Newnham, Ferroelectrics **135,** 431-446 (1992).
4 D. Berlincourt, D. R. Curran, and H. Jaffe, *Physical Acoustics*, Vol. 1A (Academic Press, New York, 1964).
5 M. Kim, J. Kim, and W. Cao, Appl. Phys. Lett. **87,** 132901 (2005).

Appendix III

Principles of polarized light microscopy

The fundamental principles of polarized light microscopy are explained; its use in the visualization of ferroelectric domains is briefly discussed.

I. FUNDAMENTAL OF POLARIZED LIGHT MICROSCOPY

Polarized light microscopy (PLM) works on the principal of *optical anisotropy*. Optically isotropic materials, such as liquids and cubic crystals demonstrate the same optical properties in all directions; they have one refractive index n ($=\sqrt{\varepsilon}$) and no not restrict the vibration directions that light passing through them can take. In *optically anisotropic* media (90% of all solid materials), however, the refractive index is dependent on the orientation of the crystallographic axes with respect to the direction of propagating light[1].

We start with the definition of a dielectrically anisotropic material[2] having a tensor dependency of displacement field ***D*** on applied electric field ***E***. That is:

$$D_i = \varepsilon_0 \varepsilon_{ij} E_j \qquad [1]$$

where ε_0 is the permittivity of free space and ε_{ij} is the tensor of relative permittivities[3]. The relative permittivities can usually be represented by a 3D surface, an ellipsoid, defined by:

$$\varepsilon_{ij} x_i x_j = const. \qquad [2]$$

The general ellipsoid will have three principal axes, i.e. special directions along which ***D*** and ***E*** are *parallel*. They are known as the *principal dielectric axes* and are defined by the eigenvectors of the permittivity tensor. The corresponding eigenvalues correspond to the permittivity along each of these axes, that is, the *principal dielectric constants*; these are the three independent components of the diagonalized matrix:

$$\varepsilon_i = \begin{bmatrix} \varepsilon_1 & 0 & 0 \\ & \varepsilon_2 & 0 \\ & & \varepsilon_3 \end{bmatrix} \qquad [3]$$

In terms of these indices, equation [2] can be rewritten

$$\varepsilon_1 x_1^2 + \varepsilon_2 x_2^2 + \varepsilon_3 x_3^2 = const. \qquad [4]$$

which is known as "Fresnel's ellipsoid[1]".

Optical properties of a medium are dependent on the refractive index *n* which defines the ratio of the speed of light in a vacuum to the speed of light in the medium $n = c/v$ ($n > 1$). In a non-magnetic media the refractive index is directly related to the dielectric constant by the Maxwell relation[1]:

$$n_i = \sqrt{\varepsilon_i} \qquad [5]$$

where n_i are the *principle indices of refraction*. Hence we can write:

$$n_1^2 x_1^2 + n_2^2 x_2^2 + n_3^2 x_3^2 = const. \qquad [6]$$

The lengths of the principal axes of this surface are the reciprocals of three principal indices of refraction. However, we can also formulate a representative surface where the lengths of the principal axes are equal to the refractive indices and not their reciprocals. This is called the *optical ellipsoid*:

$$\frac{x_1^2}{n_1^2} + \frac{x_2^2}{n_2^2} + \frac{x_3^2}{n_3^2} = const. \qquad [7]$$

It is shown in figure 1.

Importance of crystal symmetry

Information about the symmetry of this ellipsoid, and thus the symmetry of the dielectric tensor, can be gained directly by polarized light microscopy. For a general solid (e.g. a triclinic crystal) there are three different principal dielectric constants ε_i and hence three principal refractive indices. However, where two dielectric constants are equal due to symmetry constraints[3], for instance in tetragonal *4mm* crystals, the optical ellipsoid becomes an *ellipsoid of revolution*. Where all three are equal, the ellipsoid becomes a sphere: the medium is *optically isotropic*.

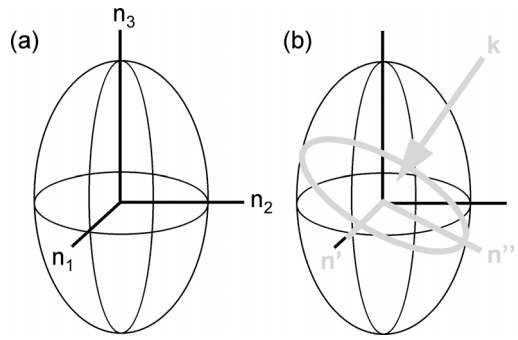

Fig. 1. (a) *Optical ellipsoid* for a general optically anisotropic medium showing its principal refractive indices $\{n_i\}$. (b) An incident plane wave $\boldsymbol{k}$ is resolved onto the two perpendicular principal axes of the *optical ellipse* formed by the intersection of the plane perpendicular to $\boldsymbol{k}$ and the optical ellipsoid. These principal axes have refractive indices *n'* and *n''*.

Interaction of light with the optical ellipsoid

By solving the Maxwell equations for a plane wave in an optically anisotropic medium it can be shown that a plane-polarized wave $[\boldsymbol{E_0} \exp i(\boldsymbol{k} \cdot \boldsymbol{r} - \omega t)]$, with propagation direction $\boldsymbol{k}$ and component electrical

field $\boldsymbol{E_0}$, will split into two components. These have differing wave velocities and *perpendicular* polarizations $E_0^{(1)}$ and $E_0^{(2)}$. It turns out that: *the plane wave is resolved along the principal axes of the ellipse formed by the intersection of the plane perpendicular to the propagation direction and the optical ellipsoid*[1]. The formation of the relevant ellipse, known as the "*optical ellipse*", from the intersection of the incident light with the optical ellipsoid is shown in figure 1(b).

Moreover, the velocities of these two waves are given by the principal axes of that ellipse n' and n''. That is, the crystal structure of an anisotropic medium permits two waves with different linear polarizations and different velocities to propagate in any given direction since they feel two different refractive indices[4]. This is the reason, for example, behind the double refraction in hexagonal calcite crystals[1].

The corresponding "*birefringence*" is defined as the difference between the extreme values of refractive index: that is, $\Delta n = |n' - n''|$. For certain special directions in the crystal, e.g. along a high symmetry axis, the optical ellipse will be a circle ($\Delta n = 0$); such directions, along which crystals appear *optically isotropic*, are known as *optic axes*.

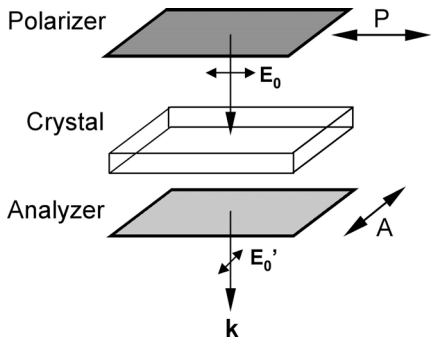

Fig. 2. Setup for polarized light microscopy (PLM) showing a thin, transparent specimen between "crossed" polarizers (A and P).

II. STUDY OF FERROELECTRIC DOMAINS

A general ferroelectric or ferroelastic will contain domain variants with differently-oriented permittivity tensors. They will therefore show different birefringences to a beam of light propagating in a given direction; the main exception is for 180° domains which are dielectrically equivalent.

To image non-180° domain walls we must first plane-polarize the light, for example, with a sheet of Polaroid film (the "*polarizer*"). The general setup is shown in figure 2. The plane polarized light is then allowed to pass through a thin plate of the material. Here, as explained, it will split into two perpendicularly polarized rays which traverse the crystal with differing velocities. To analyze the two rays that emerge the other side it is useful to recombine them. This is done with a second sheet of Polaroid perpendicular to the first, known as the "*analyzer*", which resolves both rays onto the same polarized direction direction; this is shown in figure 3.

Notably, there will be a phase difference between the recombined rays at the analyzer since the two rays will pass through the materials at different speeds. The phase difference picked up by the two rays will depend on the thickness of the crystal plate *t*. The product of the thickness and the birefringence is called the *retardation R*: it is the difference in *optical path*[1] between the two rays:

$$R = \Delta n \cdot t \qquad [8]$$

When *R* is equal to an integer number of wavelengths there will be positive interference between the two recombined rays. When *R* is equal to an integer number of half-wavelengths, the two rays will recombine destructively. Hence, when polychromatic (white) light is used, certain wavelengths will be removed depending on the crystal thickness and birefringence; the pattern of colors observed is given in the *Michel-Levy chart*.

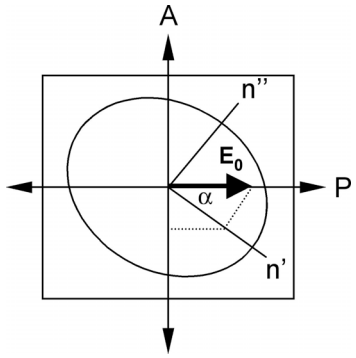

Fig. 3. Schematic representation of the resolution of the electric field vector $\boldsymbol{E_0}$ of the incident ray first onto the principal axes of the optical ellipse, and then onto the analyzer (A).

Positions of extinction

For the investigation of ferroelectrics, "*positions of extinction*" are sought to ascertain the high-symmetry, or polar, axis of a domain (i.e. the direction of spontaneous polarization $\boldsymbol{P_S}$). The principal axes of the optical ellipse will be related to this polar axis by the geometry of the specimen. In certain conditions, where the principal axes of the optical ellipse coincide with the axes of the polarizer (P) and analyzer (A) no light can be transmitted through the crystal. This is called *extinction*. Otherwise, if the beam direction is parallel to an optic axis (high symmetry axis) the crystal is isotropic along this direction and no light will pass through the crossed polarizers; again we have extinction. Both types of extinction are shown in figure 4.

Thus, the general method involves rotating the crystal about the beam axis between the two polarizers; a rotating stage is often used. By looking for positions of extinction, the symmetry and the domain structure of ferroelectric crystals can be investigated. More detailed explanations of the method can be found elsewhere[5-9].

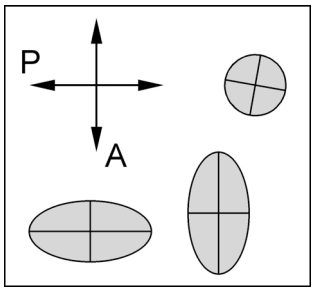

Fig. 4. Various positions of extinction for the optical ellipse, for example, of individual ferroelectric domains.

REFERENCES

1 A. Sommerfeld, *Optics* (Academic Press, New York, 1964).

2 C. Kittel, *Introduction to solid state physics*, 7th ed. (Wiley, New York, 1996).

3 J. F. Nye, *Physical properties of crystals*, 2nd ed. (Clarendon Press, Oxford, 1985).

4 If the ray is polarized parallel to a high-symmetry axis it is often known as the "extraordinary ray". A ray polarized perpendicularly to a high-symmetry axis is known as the "ordinary ray".

5 A. A. Bokov and Z.-G. Ye, J. Appl. Phys. **95,** 6347-6359 (2004).

6 D. Zekria, V. A. Shuvaeva, and A. M. Glazer, J. Phys.: Condens. Matter **17,** 1593-1600 (2005).

7 C.-S. Tu, I.-C. Shih, V. H. Schmidt, and R. Chien, Appl. Phys. Lett. **83,** 1833-1835 (2003).

8 C.-S. Tu, H. Schmidt, I.-C. Shih, and R. Chien, Phys. Rev. B **67,** 020102(R) (2003).

9 R. R. Chien, V. H. Schmidt, C.-S. Tu, L.-W. Hung, and H. Luo, Phys. Rev. B **69,** 172101 (2004).

Appendix IV

Domain engineering of the transverse piezoelectric coefficient in perovskite ferroelectrics[1]

The transverse piezoelectric coefficient d_{31}* has been calculated for the six domain engineered structures occurring in perovskite single crystals, using data for rhombohedral PMN-33PT [$0.67Pb(Mg_{1/3}Nb_{2/3})O_3$-$0.33PbTiO_3$], orthorhombic potassium niobate ($KNbO_3$), tetragonal barium titanate ($BaTiO_3$) and tetragonal lead titanate ($PbTiO_3$). Unlike the longitudinal coefficient (d_{33}*), d_{31}* is found to be strongly dependent on the transverse (x_1') direction of the as-cut crystal. In general, different domains in a domain engineered structure will contribute different values of d_{31}* to that measured. Predicting the global d_{31}* is therefore difficult since it will depend on the proportion of each domain variant in the structure. Important qualitative differences between tetragonal $BaTiO_3$ and $PbTiO_3$ are discussed. Whereas polarization rotation is important in $BaTiO_3$, $PbTiO_3$ shows a stronger collinear piezoelectric effect due the absence of a low temperature ferroelectric-ferroelectric phase transition. This leads to low values of d_{33}* and even positive values of d_{31}* in the $[111]_C$-poled (C: pseudocubic) domain engineered structure. The methodology described can be usefully applied to all perovskites.

[1] As published in Journal of Applied Physics [M. Davis, D. Damjanovic, D. Hayem, and N. Setter, J. Appl. Phys., **98**, 014105 (2005)]

I. INTRODUCTION

Relaxor-ferroelectric single crystals (1-*x*)$Pb(Mg_{1/3}Nb_{2/3})O_3$-*x*$PbTiO_3$ (PMN-*x*PT) and (1-*x*)$Pb(Zn_{1/3}Nb_{2/3})O_3$-*x*$PbTiO_3$ (PZN-*x*PT) continue to draw a lot of attention. Following the rediscovery of their very high piezoelectric coefficients for rhombohedral or orthorhombic compositions oriented along the non-polar $[001]_C$ (C: pseudocubic) direction[1], much work has concentrated on the concept of domain engineering[2] not only in these materials[3-7] but in simpler perovskite crystals as well[8-10].

A good definition of 'domain engineering' is that given by Bell[2]: 'A domain engineered crystal is one which has been poled by the application of a sufficiently high field along one of the possible polar axes of the crystal other than the zero-field polar axis, creating a set of domains in which the polarizations are oriented such that their angles to the poling direction are minimized'. In a perovskite material there are therefore three possible sets of poling directions $<111>_C$, $<101>_C$ and $<001>_C$ (if monoclinic phases are ignored). These directions correspond, respectively, to the polar axes of rhombohedral (R, point group *3m*), orthorhombic (O, *mm2*) and tetragonal (T, *4mm*) crystal phases. According to the definition, this results in six possible domain engineered structures, formed by cutting and poling a perovskite crystal along certain directions; these are listed in table I. Also given are the three possible monodomain structures '1R', '1O' and '1T' formed by poling a perovskite crystal along its polar axis.

Table I
Engineered and mono- domain states in perovskite single crystals ('C' denotes reference to the pseudocubic unit cell).

Crystal class	Polar direction (x_3)	Poling direction (x_3')	Polar directions (x_3) for the resultant set of equivalent domain variants	Domain-engineered structure
Rhombohedral *3m*	$<111>_C$	$[111]_C$ $[101]_C$ $[001]_C$	$[111]_C$ $[1\text{-}11]_C$, $[111]_C$ $[111]_C$, $[11\text{-}1]_C$, $[1\text{-}11]_C$, $[1\text{-}1\text{-}1]_C$	1R 2R 4R
Orthorhombic *mm2*	$<101>_C$	$[111]_C$ $[101]_C$ $[001]_C$	$[101]_C$, $[011]_C$, $[110]_C$ $[101]_C$ $[101]_C$, $[011]_C$, $[\text{-}101]_C$, $[0\text{-}11]_C$	3O 1O 4O
Tetragonal *4mm*	$<001>_C$	$[111]_C$ $[101]_C$ $[001]_C$	$[001]_C$, $[010]_C$, $[100]_C$ $[001[_C$, $[100]_C$ $[001]_C$	3T 2T 1T

Room temperature, longitudinal piezoelectric coefficients of up to 2820 pC/N have been measured for $<001>_C$-poled 4R domain engineered PMN-33PT ($0.67Pb(Mg_{1/3}Nb_{2/3})O_3$-$0.33PbTiO_3$)[5]. This is nearly 15 times larger than the value (d_{33} = 190 pC/N) measured for single domain, rhombohedral PMN-33PT along its polar $<111>_C$ axis[11,12]. The obvious benefits of domain engineering have since been demonstrated for simpler, more classical perovskites as well. A longitudinal piezoelectric coefficient of 203 pC/N was reported by Wada et al for 3T $<111>_C$-poled tetragonal barium titanate ($BaTiO_3$)[8]. This is more than twice the single domain value (d_{33} = 90 pC/N) measured along the $<001>_C$ polar axis[13].

Many authors have tried to ascertain the origins of the elevated piezoelectric coefficients in domain engineered crystals. Since domain walls in a domain engineered structure won't be expected to move under application of an electric field along the poling direction[1], most work has concentrated on intrinsic, lattice effects. One important intrinsic characteristic of perovskite materials is the strong anisotropy of their piezoelectric tensor d_{ijk} in the vicinity of a ferroelectric phase transition, whether induced by electric field, stress, or changes in temperature and composition[14]. Near a phase transition, the direction of maximum measured longitudinal coefficient d_{33}* is expected to lie at some angle away from the polar axis ('*' is used here to denote coefficients with respect to a non-crystallographic coordinate system - see Section II). Using monodomain values for rhombohedral PMN-33PT, d_{33}* has been calculated along the $[001]_C$ direction as 2309 pC/N[12,15-17]. Upon comparison with the experimental value for the 4R, $[001]_C$-poled, domain engineered state of 2820 pC/N it seems that any extrinsic contribution to the response is limited to less than 20%[16].

As an aside, it has recently been shown that the transverse piezoelectric coefficient (d_{31}*) in $[111]_C$-poled 3T $BaTiO_3$ and $[001]_C$-poled 4O potassium niobate ($KNbO_3$) does actually increase with an increase of domain wall density; this suggests that the presence of domain walls in the domain engineered structure can also play a significant role in the piezoelectric response, especially when the domain structure becomes fine[9,18]. However, these domain-wall related effects will not be discussed here. Since intrinsic effects will be dominant in most cases, calculations of piezoelectric coefficients along non-polar directions based on single-domain data are still useful in predicting the properties of domain-engineered crystals. They can be useful in selecting domain engineered structures worthy of further investigation and, indeed, in helping to quantify the extrinsic contribution to the piezoelectric response when the crystal has been grown and characterized.

Various calculations have already been made of the longitudinal and transverse piezoelectric coefficients (d_{33}* and d_{31}*)[3,7,15,16,19] although only for a limited number of domain engineered structures. High d_{31}* values can be exploited in certain niche applications[20], for example in 'flextensional' transducers working as 'bimorphs', and have recently been reported for $[101]_C$-poled PMN-30PT[20]. In this work, d_{31}* has been calculated for all six domain engineered structures, using single domain data for PMN-33PT (R), $KNbO_3$ (O), $BaTiO_3$ (T). The 3T structure formed by $BaTiO_3$ is then compared to that formed by lead titanate ($PbTiO_3$). It is demonstrated that in certain structures, for a fixed poling direction (named x_3'), the d_{31}* coefficient measured is strongly dependent on which direction is chosen as the transverse direction (x_1'). Care is therefore needed when designing domain engineered crystals for use in the transverse mode. Secondly, it is shown that, unlike with the longitudinal coefficient, different variants in the domain engineered crystal can sometimes contribute different values of d_{31}* to that measured. In these cases, the d_{31}* of the final crystal can change significantly depending on which domains are present and in what quantity. Finally, it is shown that an important qualitative difference exists between tetragonal crystals which exhibit phase transitions into a lower symmetry

ferroelectric phase ($BaTiO_3$) and those which remain tetragonal at all temperatures ($PbTiO_3$).

II. METHODOLOGY

Calculations of piezoelectric coefficients (d_{ijk}) as a function of orientation are done via coordinate transforms[21]. In all cases, they must start with a complete set of coefficients for the single domain state defined with reference to an orthogonal set of axes $\{x_1, x_2, x_3\}$. In perovskites it is useful to define these axes with respect to those of the cubic parent phase - i.e. the basis set formed by the $<001>_C$ psuedocubic directions. In this paper we use the orthogonal sets of axes for the rhombohedral (R, *3m*), orthorhombic (O, *mm2*) and tetragonal (T, *4mm*) crystal classes as given in Nye[21] (i.e. as defined relative to one or more symmetry elements of the point group). Defined in this way the piezoelectric tensors d_{ijk} for each crystal class have a certain 'standard' form. We also use a standard right-handed set. The x_3 direction is always the crystal's polar axis, or the direction of spontaneous polarization $\mathbf{P}_S$. For a *4mm* crystal $x_1 : [100]_C$, $x_2 : [010]_C$, $x_3 : [001]_C$ define the obvious set of axes (':' here means 'parallel to'). However, for the rhombohedral and orthorhombic classes there is still some arbitrariness in our choice of axes which can switch or invert the sign of certain coefficients even if the form of the tensor is unchanged[12]. For the rhombohedral *3m* class, we choose $x_1 : [1\text{-}10]_C$, $x_2 : [11\text{-}2]_C$, $x_3 : [111]_C$ and exercise caution in using the single domain data from the literature[12]. For the orthorhombic *mm2* class, we choose $x_1 : [10\text{-}1]_C$, $x_2 : [010]_C$, $x_3 : [101]_C$. All three sets of axes are shown with respect to the basis set of the pseudocubic unit cell in figure 1.

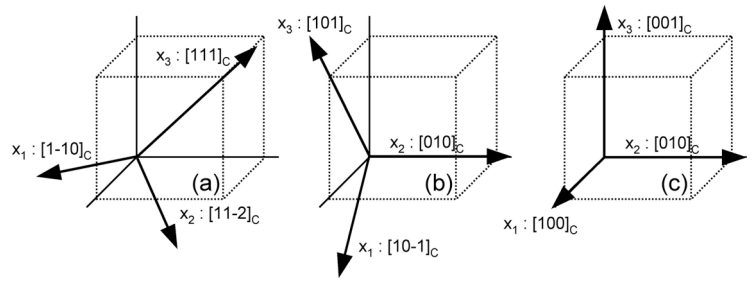

Fig. 1. The sets of axes $\{x_i\}$ used, corresponding to the data given in table II, for (a) *3m* rhombohedral, (b) *mm2* orthorhombic and (c) *4mm* tetragonal monodomains.

The materials chosen for study were PMN-33PT, potassium niobate ($KNbO_3$) and barium titanate ($BaTiO_3$) which are rhombohedral *3m*, orthorhombic *mm2* and tetragonal *4mm* at room temperature, respectively[11,13,22]. Complete sets of material properties as measured by Zhang et al[11] and Zgonik et al[13,22] are available for all of these materials, at room temperature, corresponding to the axes chosen. Lead titanate ($PbTiO_3$), also *4mm* tetragonal[23], was investigated for comparison with $BaTiO_3$. Good $PbTiO_3$ crystals cannot easily be grown, and are difficult to characterize due to their high conductivity. Therefore, the monodomain values used for $PbTiO_3$ were those calculated by Haun et al[24] using phenomenological theory,

although it would change little here to use those measured experimentally[23]. All the values of piezoelectric coefficient used (d_{ijk} or d_{ij} in condensed notation), corresponding to the sets of axes given above, are listed in table II.

Table II
Monodomain piezoelectric coefficients used in this study, based on the coordinate systems shown in figure 1. The room temperature data is from Cao et al[11] (PMN-33PT), Zgonik et al[13,22] ($BaTiO_3$ and $KNbO_3$) and Haun et al[24] ($PbTiO_3$). Values in brackets are not independent.

Material	d_{15} /[pC/N]	d_{22} /[pC/N]	d_{24} /[pC/N]	d_{31} /[pC/N]	d_{32} /[pC/N]	d_{33} /[pC/N]
PMN-33PT	4100	-1340	(4100)	-90	(-90)	190
$BaTiO_3$	564		(564)	-33.4	(-33.4)	90
$PbTiO_3$	56.1		(56.1)	-23.1	(-23.1)	79.1
$KNbO_3$	206		156	9.8	-19.5	29.3

As stated above, using these monodomain values we can calculate the piezoelectric coefficient d_{ijk}* that we would measure in some other system of axes via a coordinate transform. Essentially, when we cut a crystal and measure its piezoelectric properties, we choose a 'new' measurement coordinate system with axes {x_1', x_2', x_3'}. In a domain engineered crystal x_3' is thus the poling direction. To calculate the piezoelectric coefficient we make a coordinate transformation from the crystallographic coordinate system {x_1, x_2, x_3}, with which we defined d_{ijk}, to this new set. This is done using the transformation matrix a_{ij} as written in equation 1.

$$d_{ijk}^* = a_{im}a_{jn}a_{ko}d_{mno} \qquad [1]$$

a_{ij} is defined as the cosines of the angles α_{ij} between the 'old' axis x_j and the 'new' axis x_i' ($a_{ij} = \cos \alpha_{ij}$). Equivalently, a_{ij} can be written in terms of the Euler angles (ϕ,θ,ψ) which describe sequential, anticlockwise rotations of the coordinate system about the x_3 axis (by ϕ), the then-rotated x_1 axis (θ) and the final x_3' axis (ψ). This is known as the 'ZXZ' convention[25]. In terms of the three Euler angles, the elements of a_{ij} are then:

$$\begin{aligned}
a_{11} &= \cos(\psi)\cos(\phi) - \cos(\theta)\sin(\phi)\sin(\psi);\\
a_{12} &= \cos(\psi)\sin(\phi) + \cos(\theta)\cos(\phi)\sin(\psi);\\
a_{13} &= \sin(\psi)\sin(\theta);\\
a_{21} &= -\sin(\psi)\cos(\phi) - \cos(\theta)\sin(\phi)\cos(\psi);\\
a_{22} &= -\sin(\psi)\sin(\phi) + \cos(\theta)\cos(\phi)\cos(\psi);\\
a_{23} &= \cos(\psi)\sin(\theta);\\
a_{31} &= \sin(\theta)\sin(\phi);\\
a_{32} &= -\sin(\theta)\cos(\phi);\\
a_{33} &= \cos(\theta) \qquad [2]
\end{aligned}$$

Other definitions of the Euler angles are also possible, which will give different forms of a_{ij}.

When we cut a domain engineered crystal for measurement we must first choose our poling axis x_3' (<111>$_C$, <101>$_C$ or <001>$_C$), by setting the first

two Euler angles ϕ and θ. We then have certain freedoms in how we cut the crystal to define the other two perpendicular measurement directions x_1' and x_2' in the "poling plane" (the plane of the crystal perpendicular to the poling direction). In choosing x_1' (and therefore x_2') we are setting the third Euler angle ψ, as shown in figure 2(a); the three poling planes are shown in figure 2(b). Any choice of x_1' is possible but we shall only consider the most obvious directions: those of type $<112>_C$, $<110>_C$ and $<100>_C$. For example, if we choose $[001]_C$ as the poling direction, we can set x_1' along either the edges of the pseudocubic unit cell ($\pm[100]_C$ and $\pm[010]_C$) or its face diagonals ($\pm[1\text{-}10]_C$ and $\pm[110]_C$). There are therefore 4 x 2 = 8 ways to define x_1' in the $(001)_C$ plane. For both $[111]_C$ and $[101]_C$ poling directions there are 6 x 2 = 12 possible ways of defining x_1' in the $(111)_C$ and $(101)_C$ planes, respectively. All of these definitions of x_1' are listed in table III and shown schematically in figure 3, for the three poling directions. The direction x_2' is not given but is, in all cases, the direction forming an orthogonal, right-handed set with the other two.

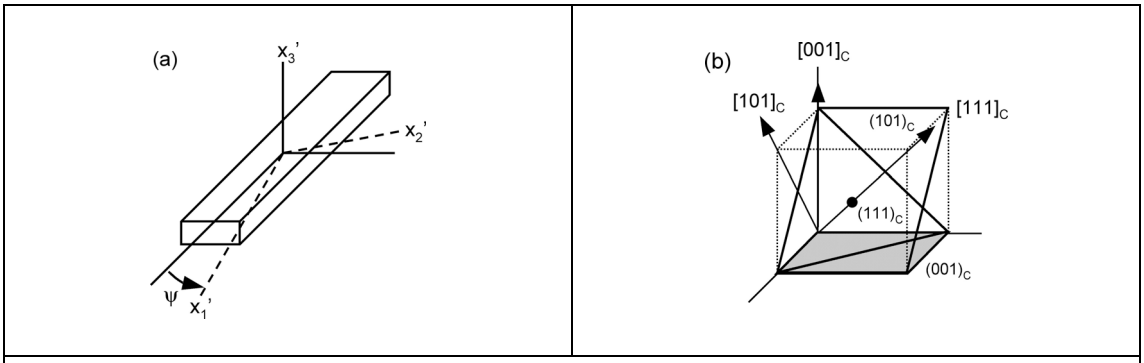

Fig. 2. (a) Definition of the third Euler angle ψ with respect to the measurement axes x_1', x_2' and x_3' shown for a d_{31} resonator. (b) The three "poling planes" $(111)_C$, $(101)_C$ and $(001)_C$ perpendicular to the three poling directions $[111]_C$, $[101]_C$ and $[001]_C$, respectively.

Table III
Low-index choices of measurement direction x_1' for the three poling directions relevant to domain engineering in perovskites.

Poling direction (x_3')	Possible choices of measurement direction (x_1')
$[111]_C$	$\pm[10\text{-}1]_C$, $\pm[11\text{-}2]_C$, $\pm[01\text{-}1]_C$, $\pm[\text{-}12\text{-}1]_C$, $\pm[\text{-}110]_C$, $\pm[\text{-}211]_C$
$[101]_C$	$\pm[10\text{-}1]_C$, $\pm[11\text{-}1]_C$, $\pm[12\text{-}1]_C$, $\pm[010]_C$, $\pm[\text{-}121]_C$, $\pm[\text{-}111]_C$
$[001]_C$	$\pm[100]_C$, $\pm[110]_C$, $\pm[010]_C$, $\pm[\text{-}110]_C$

Using this methodology, d_{33}* and d_{31}* were calculated for all of the domain engineered structures listed in table I, based on the monodomain data for PMN-33PT (R), $KNbO_3$ (O), $BaTiO_3$ (T) in table II, for all of the x_1' directions listed in table III. Calculations were also made for the 3T structure formed by poling $PbTiO_3$ along the $[111]_C$ direction.

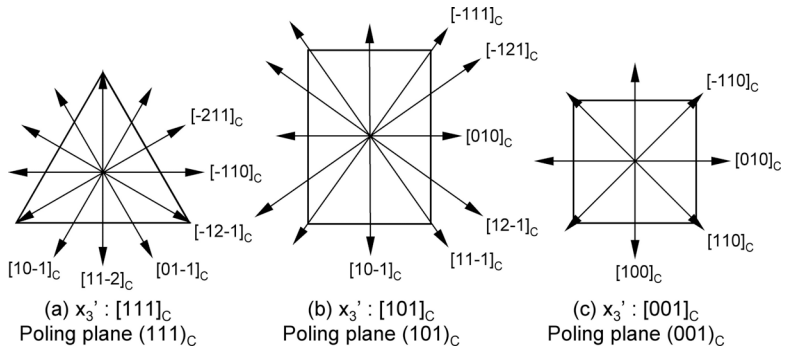

Fig. 3. Possible choices of the measurement direction x_1' for perovskite crystals cut and poled along x_3' : $[111]_C$ (a), $[101]_C$ (b) and $[001]_C$ (c). x_3' is perpendicular to the plane of the paper. The directions are shown in the $(111)_C$, $(101)_C$ and $(001)_C$ poling planes, respectively.

III. RESULTS AND DISCUSSION

It turns out that, for *3m*, *mm2* and *4mm* crystal classes, the longitudinal piezoelectric coefficient d_{33}* is never dependent on the third Euler angle ψ (i.e. that defining x_1') although d_{31}* always is. x_1' is thus an important direction when we orient our bar-shaped d_{31} resonator in the plane of the crystal (figure 2(a)). However, it doesn't matter which axes we choose as x_1' and x_2' for our elongated d_{33} resonator; only the axial direction x_3' (defined by Euler angles ϕ and θ) matters.

The angle ψ is particularly important because it can be interpreted in two ways. Firstly, and as stated above, it defines the measurement direction x_1' (after x_3' has been chosen) when calculating the response of a single, fixed variant in the domain engineered structure. Secondly, it will also define the variant in the domain engineered structure whose contribution we are considering when the measurement directions x_1' and x_3' are both fixed. This is shown graphically in figure 4 taking two variants in the 4R structure as an example.

Each variant in a domain engineered structure will have a different polar axis (x_3) as one of a set of its own, individual crystallographic axes $\{x_i\}$. Critically, for a domain engineered structure and fixed measurement axes $\{x_i'\}$ the first two Euler angles ϕ and θ will be the same for every variant whereas ψ won't. For a domain-engineered structure *n*R (or *n*O or *n*T), the variants in the structure will be rotated relative to each other by an angle $\Delta\psi = 360°/n$ about the poling axis. For a $[001]_C$-poled rhombohedral crystal (4R) the four variants are related to each other by rotations of $\Delta\psi = 90°$.

It follows that the contribution to d_{33}* from each variant in a domain engineered structure, which can depend only on θ and ϕ, will be the same; it only matters that the polar axis (x_3) in each variant is equally inclined to the poling direction. In contrast, since d_{31}* is a function of ψ, different variants in the domain engineered structure might therefore give different contributions to the transverse piezoelectric coefficient. This possibility is explored below for the six possible domain engineered structures. Results for d_{33}* and d_{31}* are

summarized in tables IV and V, respectively. Also given in the tables are the first two Euler angles used in the calculation as relevant to the poling direction and the choice of basis defined in figure 1. For all seven cases investigated the function $d_{31}^*(\psi)$ was found to be of the form $X \cos^2\psi + Y \sin^2\psi$ where X and Y are the upper and lower bounds of the function. In most, but not all, cases X and Y are negative.

Table IV
Longitudinal piezoelectric coefficients d_{33}^* calculated for possible domain engineered structures of $BaTiO_3$, $KNbO_3$, $PbTiO_3$ and PMN-33PT at room temperature. The Euler angles (ϕ and θ) relevant to the coordinate transform made are given. Also listed is the monodomain value of d_{33} corresponding to that along the polar axis of the crystal (x_3).

Material	Monodomain value along polar axis, d_{33} /[pC/N]	Poling direction (x_3')	Domain engineered structure	ϕ /[°]	θ /[°]	Value calculated along poling direction, d_{33}^* /[pC/N]
PMN-33PT	190	$[101]_C$ $[001]_C$	2R 4R	60 0	35.26 54.74	937 2309
$KNbO_3$	29.3	$[111]_C$ $[001]_C$	3O 4O	0 90	-35.26 -45	53.1 86.7
$BaTiO_3$	90	$[111]_C$ $[101]_C$	3T 2T	-45 90	-54.7 45	221.5 219.4
$PbTiO_3$	79.1	$[111]_C$	3T	-45	-54.7	27.9

Table V
Transverse piezoelectric coefficients d_{31}^* calculated for possible domain engineered structures of $BaTiO_3$, $KNbO_3$, $PbTiO_3$ and PMN-33PT, at room temperature, as a function of the third Euler angle ψ. Also given is the x_1' measurement direction corresponding to $\psi = 0°$.

Material	Poling direction (x_3')	Domain engineered structure	$d_{31}^*(\psi)$ /[pC/N]	x_1' direction for $\psi = 0$
PMN-33PT	$[101]_C$ $[001]_C$	2R 4R	$+700.2 \cos^2\psi -1628.9 \sin^2\psi$ $-1146.1 \cos^2\psi -1157.6 \sin^2\psi$	$[10\text{-}1]_C$ $[1\text{-}10]_C$
$KNbO_3$	$[111]_C$ $[001]_C$	3O 4O	$+8.0 \cos^2\psi -45.1 \sin^2\psi$ $-13.8 \cos^2\psi -59.0 \sin^2\psi$	$[10\text{-}1]_C$ $[010]_C$
$BaTiO_3$	$[111]_C$ $[101]_C$	3T 2T	$-19.3 \cos^2\psi -188.9 \sin^2\psi$ $-23.6 \cos^2\psi -179.4 \sin^2\psi$	$[1\text{-}10]_C$ $[010]_C$
$PbTiO_3$	$[111]_C$	3T	$-13.3 \cos^2\psi +4.4 \sin^2\psi$	$[1\text{-}10]_C$

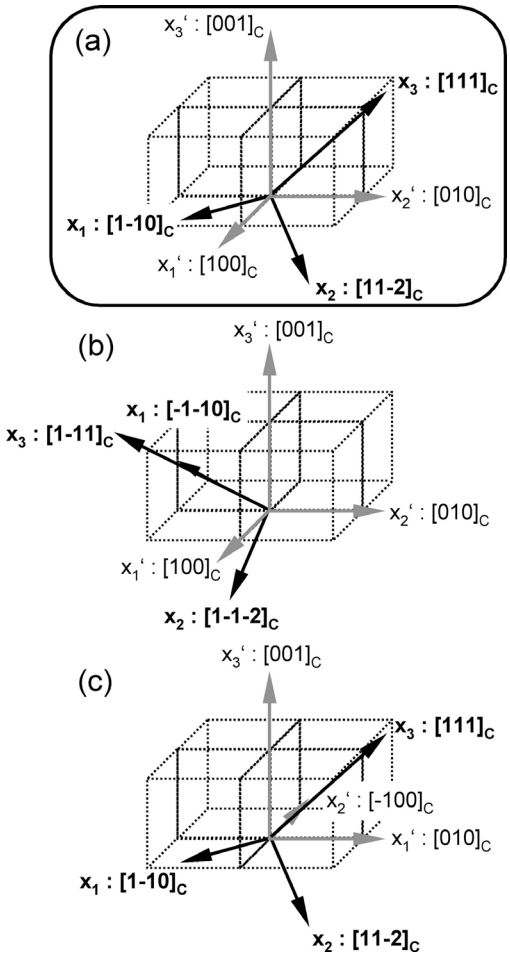

Fig. 4. Meaning of the angle ψ as a rotation about the poling axis x_3'. The inset figure (a) defines the coordinate transform from $\{x_i\}$ to $\{x_i'\}$ relevant to a 4R domain engineered structure for Euler angles ϕ=0° and θ=54.74° (for ψ = 45° as shown we have x_1' : $[100]_C$). A further rotation of $\Delta\psi$ = 90° corresponds to rotating the measurement direction x_1' from $[100]_C$ to $[010]_C$ (c). This is equivalent to starting with another variant (that with polar direction x_3 : $[1\text{-}11]_C$) and transforming to the coordinate system with x_1' : $[100]_C$ (b). Rotating $\{x_i'\}$ *anticlockwise* by $\Delta\psi$ is equivalent to rotating $\{x_i\}$ by $\Delta\psi$ *clockwise*.

A. PMN-33PT

Taking the values shown in table II for rhombohedral PMN-33PT and transforming to the $[001]_C$ direction (taking ϕ=0°, θ=54.74), we find a value of d_{33}* = 2309 pC/N (see table IV), independent of the angle ψ and, therefore, the choice of x_1'. To reiterate, all four variants in the 4R structure will give the same contribution to the measured d_{33}* value. As stated in section I this value, and thus the crystal anisotropy of PMN-33PT at room temperature, will account for as much as 80% of the multidomain value (2820 pC/N).

For PMN-33PT in the 4R structure, d_{31}* *is* found to be, albeit only slightly, dependent on our choice of x_1'. d_{31}* varies as a function of ψ between X = -1146.1 pC/N and Y = -1157.6 pC/N, as shown in figure 5(a).

The function $d_{31}^*(\phi=0°, \theta=54.74°, \psi)$ is given explicitly in table V. The fact that d_{31}^* is not affected by a rotation of $\Delta\psi = 180°$ is intuitive since stress and strain have no sense of 'polarity'. The position $\psi = 0°$ corresponds here to x_1' : $[1\text{-}10]_C$ where d_{31}^* is least negative. The most negative d_{31}^* value of -1157.6 is found at $\psi = \pm 90°$ corresponding to x_1' : $\pm[110]_C$.

Figure 6(a) shows d_{31}^* graphically for the various choices of x_1' in the $(001)_C$ poling plane. The values given here are only valid for the variant in the domain engineered structure with polar axis $\mathbf{P}_S$ (or x_3) : $[111]_C$, as shown projected onto $(001)_C$ as a thick arrow. The diagram can be used to calculate the contribution from the other three domain variants in the structure, when the x_1' direction is fixed. For example with x_1' : $[1\text{-}10]_C$, the contribution from the variant shown (x_3 : $[111]_C$) is -1146.1 pC/N. Calculating the d_{31}^* contribution from the variant in the structure with x_3 : $[1\text{-}11]_C$ involves rotating the projected $[111]_C$ polar vector by 90° clockwise. Therefore, equivalently to this from consideration of figure 4, we can simply rotate the x_1' direction in figure 6(a) by the same amount anticlockwise and read the value directly from the diagram. The contribution from this domain variant is thus -1157.6 pC/N.

We can similarly see all the permutations: if we choose x_1' as one of the face diagonals of the pseudocubic cell $\langle 110 \rangle_C$, two variants will yield a value of d_{31}^* = -1146.1 pC/N and the other two will contribute d_{31}^* = -1157.6 pC/N. However, if we choose x_1' to be along one of the edges of the pseudocubic unit cell, $\langle 100 \rangle_C$, each variant will contribute the same value of d_{31}^* = -1151.8 pC/N. Two of the four domain variants in this case correspond to (a) and (b) of figure 4. The value here of -1151.8 pC/N accounts for more than 80% of the experimental value (d_{31}^* = -1330 pC/N) reported by Zhang et al[5]. Most interestingly, in the former case with x_1' along a face diagonal $\langle 110 \rangle_C$, the contributions from the different variants in the domain engineered crystal are *different*. The value of d_{31}^* measured, therefore, will be strongly dependent on the relative presences of each domain, something which will be discussed later.

Lastly, it should be noted that the direction of largest (most negative) d_{31}^* is found where the projection of the variant's polar direction in the $(001)_C$ plane is *parallel* to the measurement axis x_1'. The most positive response is found where these two directions are perpendicular.

The other engineered domain structure for a rhombohedral crystal, 2R, is that formed upon poling along $[101]_C$. The first two Euler angles relevant to this transformation are $\phi=60°$ and $\theta=35.26°$, as listed in table IV. The value of d_{33}^* estimated for this domain engineered structure is 937 pC/N, still nearly 5 times larger than the monodomain value.

The transverse piezoelectric response for $[101]_C$-poled PMN-33PT is more interesting. The function $d_{31}^*(\phi=60°, \theta=35.26°, \psi)$ is shown in figure 5(b) where $\psi = 0$ corresponds to x_1' : $[10\text{-}1]_C$. The values are plotted, for all 12 choices of x_1' in the plane of $(101)_C$, in figure 6(b). In this structure, both variants are rotated by $\Delta\psi = 180°$ relative to each other so, for any given choice of x_1', both must contribute exactly the same value of d_{31}^*. d_{31}^* varies here between X = +700.2 pC/N (for x_1' : $\pm[10\text{-}1]_C$) and Y = -1628.9 pC/N (for x_1' : $\pm[010]_C$).

As for the 4R structure, the most negative value of d_{31}^* (-1628.9 pC/N) is found where x_1' is parallel to the projection of the polar axis into the $(101)_C$

plane. This value is more than 19 times larger than the monodomain value of -90 pC/N for PMN-33PT (table II). And as for the 4R structure, the large enhancement is related directly to the very large value of d_{15} (= 4100 pC/N) in PMN-33PT. With the same domain engineered configuration (2R) an even higher value of d_{31}* (-2517 pC/N) was recently reported for rhombohedral PMN-30PT[20]. With the 2R structure in PMN-*x*PT, therefore, we can engineer very high d_{31}* values, by careful choice of x_1', without worrying about the relative presences of each domain. This might be exploitable in certain applications.

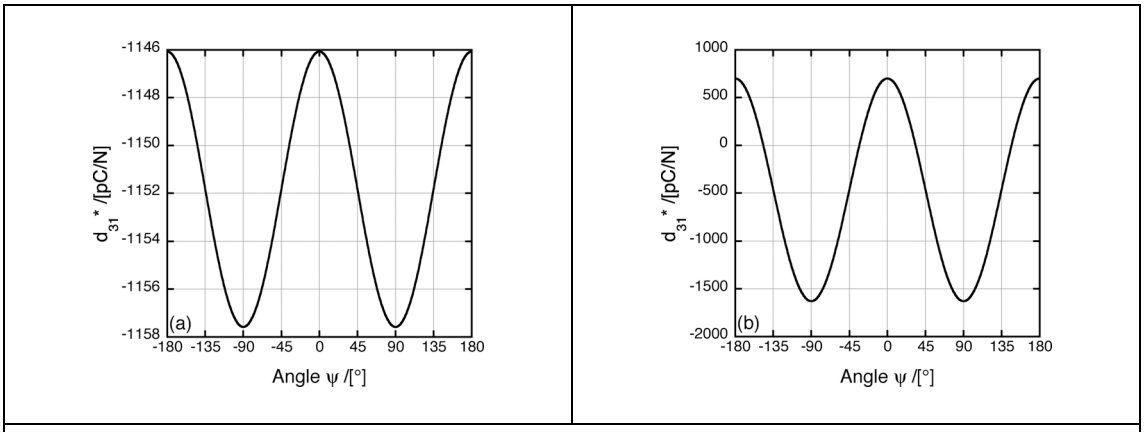

Fig. 5. (a) d_{31}*(ϕ=0°, θ=54.74°) calculated as a function of ψ in the $(001)_C$ poling plane of 4R domain engineered PMN-33PT. ψ = 0° and ψ = 45° correspond to x_1' : $[1\text{-}10]_C$ and x_1' : $[100]_C$, respectively. (b) d_{31}*(ϕ=60°, θ=35.26°) calculated as a function of ψ in the $(101)_C$ poling plane of 2R domain engineered PMN-33PT. ψ = 0° and ψ = 90° correspond to x_1' : $[10\text{-}1]_C$ and x_1' : $[010]_C$, respectively.

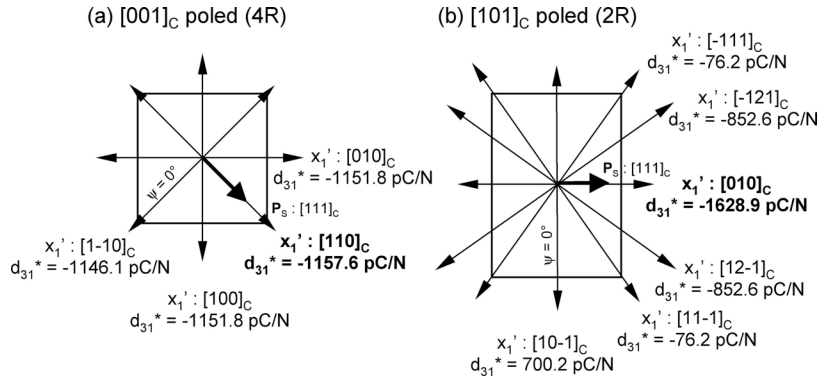

Fig. 6. (a) The $(001)_C$ poling plane of a 4R sample of PMN-33PT (with x_3' : $[001]_C$). Values of d_{31}* calculated for various choices of measurement direction x_1' are shown for a domain with spontaneous polarization $\mathbf{P}_S$ (or x_3) : $[111]_C$ ($\mathbf{P}_S$ is also shown projected onto the plane as a thick arrow). The most negative value is shown in bold and lies at x_1' : $\pm[110]_C$. (b) The $(101)_C$ poling plane of a 2R sample of PMN-33PT (with x_3' : $[101]_C$). Values of d_{31}* calculated for various choices of measurement direction x_1' are shown for a domain with spontaneous polarization $\mathbf{P}_S$ (or x_3) : $[111]_C$ ($\mathbf{P}_S$ is also shown projected onto the plane as a thick arrow). The most negative value is shown in bold and lies at x_1' : $\pm[010]_C$.

B. POTASSIUM NIOBATE ($KNbO_3$)

Using the values for monodomain potassium niobate and transforming to x_3' : $[001]_C$ (ϕ=90°, θ=-45°) we calculate a value of d_{33}* = 86.7 pC/N, independent of ψ. This accounts for the largest part of the equivalent, experimental value (92 pC/N) measured for the 4O structure by Nakamura et al[10]. The transverse piezoelectric coefficient d_{31}*(ϕ=90°, θ=-45°, ψ) is a strong function of ψ, varying between X = -13.8 pC/N and Y = -59.0 pC/N (table V). ψ = 0° corresponds to x_1' : $[010]_C$. The values are shown graphically in figure 7(a) where d_{31}* is given for various x_1' for a domain with $\mathbf{P}_S$: $[101]_C$. Also marked is the projection of this polar axis onto the $(001)_C$ plane, the direction parallel to which x_1' yields the most negative value of d_{31}* (x_1' : ±$[100]_C$).

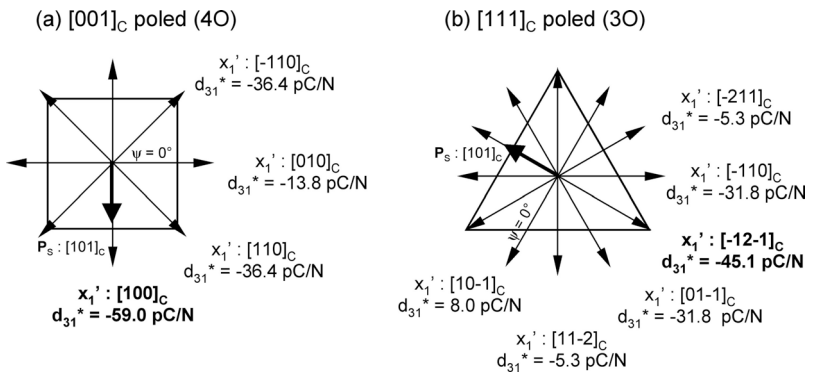

Fig. 7. (a) The $(001)_C$ poling plane of a 4O sample of $KNbO_3$ (with x_3' : $[001]_C$). Values of d_{31}* calculated for various choices of measurement direction x_1' are shown for a domain with spontaneous polarization $\mathbf{P}_S$ (or x_3) : $[101]_C$ ($\mathbf{P}_S$ is also shown projected onto the plane as a thick arrow). The most negative value is shown in bold and lies at x_1' : ±$[100]_C$. (b) The $(111)_C$ poling plane of a 3O sample of $KNbO_3$ (with x_3' : $[111]_C$). Values of d_{31}* calculated for various choices of measurement direction x_1' are shown for a domain with spontaneous polarization $\mathbf{P}_S$ (or x_3) : $[101]_C$ ($\mathbf{P}_S$ is also shown projected onto the plane as a thick arrow). The most negative value is shown in bold and lies at x_1' : ±$[-12-1]_C$.

In the 4O structure all domain variants are related by rotations of $\Delta\psi$ = 45°. If we choose x_1' along a direction $<110>_C$, all four variants will contribute the same value of d_{31}* to the overall: we can expect to measure a value of -36.4 pC/N. However, as for the 4R structure, if we choose an edge of the pseudocubic unit cell as x_1' (i.e. $<100>_C$) two variants will contribute a value of d_{31}* = -13.8 pC/N and the other two will contribute the more negative value of -59.0 pC/N. The transverse piezoelectric coefficient measured will be some function of these two values depending on the relative proportion of domains, of each variant, in the poled crystal.

The other possible domain-engineered structure for an orthorhombic crystal is 3O, that formed upon poling along the $[111]_C$ direction. d_{33}* calculated in this case (for ϕ=0°, θ=-35.26°) is 53.1 pC/N, nearly twice as much as the monodomain value of 29.3 pC/N (table IV). d_{31}* varies between X = +8.0 pC/ and Y = -45.1 pC/N (table V) where ψ = 0° corresponds to x_1' :

$[10\text{-}1]_C$. As for the 2R structure the upper and lower bounds of d_{31}* are of different sign.

The results are shown figuratively in figure 7(b) in the plane $(111)_C$, perpendicular to the poling direction. The most negative value is found for x_1' : $\pm$ $[\text{-}12\text{-}1]_C$ parallel to the projection of $\mathbf{P}_S$. In the 3O structure we will have 3 variants rotated relative to each other by $\Delta\psi = 120°$. Therefore, depending on our choice of x_1', there will be a set of three different contributions to d_{31}* from the three variants. For x_1' along one of the directions $\langle 11\text{-}2\rangle_C$ in the $(111)_C$ plane, two domains will contribute a value of -5.3 pC/N and the third will contribute a larger value of -45.1 pC/N. Again, the value we would measure is difficult to predict as it will depend on the concentration of each variant in the sample. With x_1' along one of the directions $\langle 10\text{-}1\rangle_C$ in the $(111)_C$ plane one domain type will contribute +8.0 pC/N and the other two will contribute -31.8 pC/N. Here, surprisingly, different domains will contribute transverse piezoelectric coefficients of different sign to the measured value. It is interesting to speculate on the possibility of having a zero net d_{31}* at some partition of concentrations of the two domain variants.

C. BARIUM TITANATE ($BaTiO_3$)

The simplest domain engineered structure for the 4mm tetragonal class, 2T, is that formed by poling along the $[101]_C$ direction. The two resultant variants have polar axes (x_3) equally inclined to the poling direction. Starting with the monodomain defined in figure 1(c) and the values given in table II (with ϕ=90° and θ=45°), we calculate a value of d_{33}* = 219.4; this is more than twice the corresponding monodomain value of d_{33} = 90 pC/N (see table IV).

In this case d_{31}*(ϕ=90°, θ=45°, ψ) varies greatly between X = -23.6 pC/N (for x_1' : $\pm[010]_C$) and Y = -179.4 pC/N (for x_1' : $\pm[10\text{-}1]_C$); ψ = 0° here corresponds to x_1' : $[010]_C$. The results are plotted in the $(101)_C$ plane for all choices of x_1' in figure 8(a). The most negative d_{31}* value is found for x_1' : $\pm[10\text{-}1]_C$, i.e. again parallel to the projection of the polar axis $[001]_C$ in the $(101)_C$ plane.

Since in the 2T structure, as in the 2R structure, the two variants are related to each other by a rotation of $\Delta\psi$ = 180°, they will both yield the same value of d_{31}*. Therefore, we can engineer the crystal to have a predictable d_{31}* value of either -23.6 pC/N, -75.5 pC/N, -127.5 pC/N or -179.4 pC/N.

The structure 3T is more interesting, and has already been the subject of investigation[8,18]. d_{33}* (at ϕ=-45°, θ=-54.74°) for the $[111]_C$ direction was calculated as 221.5 pC/N, comparing favorably with the experimental value of 203 pC/N[8]. It is slightly higher that the value found for the 2T structure. d_{31}* as a function of ψ (for ϕ=-45° and θ=-54.74°) varies between X = -19.3 pC/N (at x_1' : $\pm[1\text{-}10]_C$) and Y = -188.9 pC/N (at x_1' : $\pm[11\text{-}2]_C$); ψ = 0° corresponds to x_1' : $[1\text{-}10]_C$. The results are shown graphically in figure 8(b). For a variant with $\mathbf{P}_S$ (x_3) : $[001]_C$, the most negative d_{31}* is found by cutting the crystal with x_1' : $\pm[11\text{-}2]_C$.

Since in the 3T structure all three variants are rotated by $\Delta\psi = 120°$ relative to each other, the set of three d_{31}* contributions from the three domain types will be separated by 120° in figure 8(b). Thus, if we choose x_1' parallel to one of the directions $<11\text{-}2>_C$ in the $(111)_C$ plane, two variants will contribute d_{31}* = -61.7 pC/N and the other one will contribute -188.9 pC/N. However, if we choose x_1' parallel to one of the directions $<10\text{-}1>_C$ two variants will contribute d_{31}* = -146.5 pC/N and the third will contribute -19.3 pC/N. Again, the actual d_{31}* measured will depend on which domains are present and in what quantity.

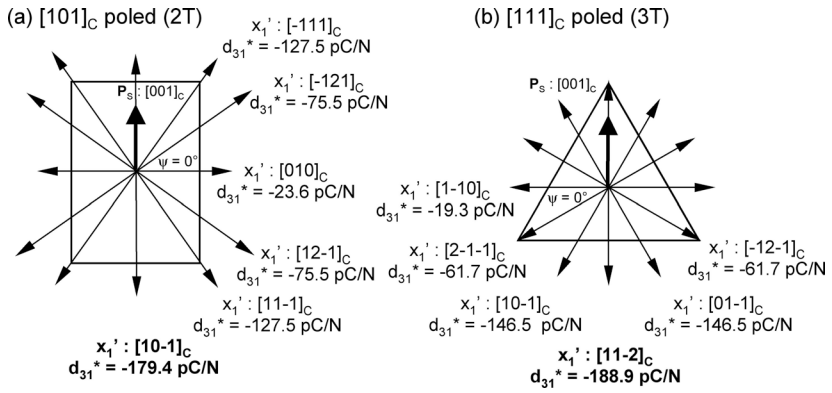

Fig. 8. (a) The $(101)_C$ poling plane of a 2T sample of $BaTiO_3$ (with x_3' : $[101]_C$). Values of d_{31}* calculated for various choices of measurement direction x_1' are shown for a domain with spontaneous polarization $\mathbf{P}_S$ (or x_3) : $[001]_C$ ($\mathbf{P}_S$ is also shown projected onto the plane as a thick arrow). The most negative value is shown in bold and lies at x_1' : $\pm[10\text{-}1]_C$. (b) The $(111)_C$ poling plane of a 3T sample of $BaTiO_3$ (with x_3' : $[111]_C$). Values of d_{31}* calculated for various choices of measurement direction x_1' are shown for a domain with spontaneous polarization $\mathbf{P}_S$ (or x_3) : $[001]_C$ ($\mathbf{P}_S$ is also shown projected onto the plane as a thick arrow). The most negative value is shown in bold and lies at x_1' : $\pm[11\text{-}2]_C$.

The fact that different variants in a domain-engineered structure can contribute different values of d_{31}* to that measured is perhaps not expected, especially since no similar effect is possible for d_{33}*. In fact, excepting the $[101]_C$-poled structures, 2R and 2T, the effect is general. Only in the $[001]_C$-poled 4O and 4R structures can the potential problem be avoided by careful choice of x_1'. Therefore, $[111]_C$-poled structures like those of *4mm* barium titanate (3T) and *mm2* potassium niobate (3O) are best avoided when domain engineering crystals are for use in the transverse mode, unless the presence of the undesired variants can be minimized.

When we do have a structure with differing d_{31}* contributions from each domain variant, it is not trivial to predict the measured value. For calculations of d_{33}* in domain engineered structures, most researchers have settled on taking a volume average, often assuming that all domain families in the structure will be present in equal measure. Yet, the real domain structure in domain engineered crystals, or the relative proportions of each domain, is actually difficult to predict. For example, in 4R PMN-*x*PT and PZN-*x*PT a prevalence of just two of the four domain types is possible leading to a macroscopically orthorhombic, not tetragonal, crystal[6]. Although in this case

the measured value of d_{33}* should be the same, d_{31}* might not (depending on the choice of x_1'). It is even possible that in structures like 3T barium titanate, where the d_{31}* contribution from one variant can be much larger than from the other two, this imbalance might mean one type of domain is formed preferentially upon poling if strain compatibility is important. This is a non-trivial problem, which is worthy of future analysis.

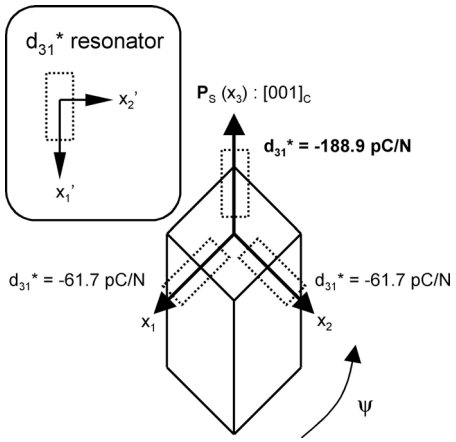

Fig. 9. Schematic illustrating the relationship between the tetragonal monodomain and the possible values of d_{31}*, in the 3T engineered structure, for different choices of measurement direction x_3'. The polar axis $\mathbf{P}_S$ of the domain is shown projected in the $(111)_C$ poling plane. The most negative value of d_{31}* is found when x_1' is parallel to this projection.

The physical reason behind the differing d_{31}* contributions from different variants can be explained as follows: Looking at a projection of a tetragonal domain in the $(111)_C$ plane (figure 9), we see that there are always two equivalent directions for the transverse direction x_1' in our d_{31}* sample, relative to the polar direction (x_3), and one which is unique. For simplicity, this is shown on the diagram for x_1' along $<11\text{-}2>_C$ directions only. It follows, therefore, that for a fixed x_1' direction in a 3T poled crystal, we may get one unique and two equal contributions to d_{31}*. The question remains, why do we get the most negative d_{31}* contribution when x_1' is parallel to the projection of the domain's polar axis in the $(001)_C$ poling plane? When we apply an electric field along the poling direction x_3', the polar axis x_3 will rotate towards it (and away from the plane of figure 9), causing the projection of the domain to shrink along its length. The largest contraction, and therefore the most negative d_{31}*, will be seen where x_1' is parallel to that direction. This 'polarization rotation' effect[26] is strongest in materials where the piezoelectric shear coefficient d_{15} is large[14].

D. LEAD TITANATE ($PbTiO_3$)

Finally, calculations were made for the 3T structure formed by poling lead titanate along the $[111]_C$ direction. d_{33}* (at ϕ=-45°, θ=-54.74°) was calculated as 27.9 pC/N (table IV), lower this time than the monodomain value

of 79.1 pC/N. Lead titanate is tetragonal over all temperatures below the Curie temperature: there are no ferroelectric-ferroelectric phase transitions[23]. Because of the absence of a proximal phase transition, the shear coefficient d_{15} is small (compare $PbTiO_3$ and $BaTiO_3$ in table II) and the anisotropy of the piezoelectric tensor d_{ijk} is much weaker[14]. In fact, the maximum value of d_{33}* for $PbTiO_3$ is that measured along its polar axis (i.e. that due to the collinear piezoelectric effect).

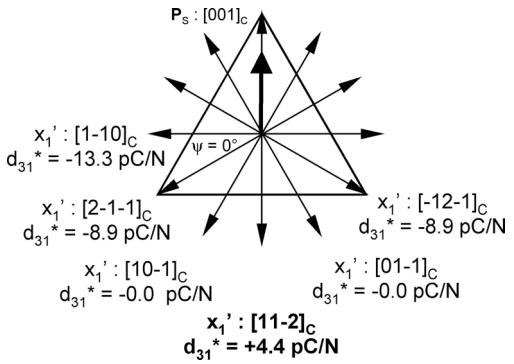

Fig. 10. The $(111)_C$ poling plane of a 3T sample of $PbTiO_3$ (with x_3' : $[111]_C$). Values of d_{31}* calculated for various choices of measurement direction x_1' are shown for a domain with spontaneous polarization $\mathbf{P}_S$ (or x_3) : $[001]_C$ ($\mathbf{P}_S$ is also shown projected onto the plane as a thick arrow). The most *positive* value is shown in bold and lies at x_1' : $\pm[11\text{-}2]_C$.

The most interesting effect occurs for the transverse coefficient. d_{31}*(ϕ=-45°, θ=-54.74°, ψ) is given in table V and varies between X = -13.3 pC/N (at x_1' : $\pm[1\text{-}10]_C$) and Y = +4.4 pC/N (at x_1' : $\pm[11\text{-}2]_C$); ψ = 0° corresponds to x_1' : $[1\text{-}10]_C$. In this case the general form of the equation is switched relative to 3T $BaTiO_3$. The values are plotted figuratively in the $(111)_C$ poling plane in figure 10. It is noticeable that for certain choices of x_1' (along $\pm[10\text{-}1]_C$ or $\pm[01\text{-}1]_C$) d_{31}* is close to zero. Most importantly, in contrast to all of the other domain engineered structures investigated, the direction that coincides with the projection of the polar axis is that of most *positive* d_{31}*, not most negative. This can again be understood with reference to figure 9. For $PbTiO_3$, in contrast to the other three, the collinear piezoelectric effect is more important than 'polarization rotation'[26]. That is, as explained above, d_{33}* is highest along the polar axis due to a weak contribution from d_{15}. Therefore, upon application of an electric field along $[111]_C$, the projected tetragonal domain will expand along its projected length more than it will contract due to polarization rotation. d_{31}* is thus positive for $PbTiO_3$ when x_1' is parallel to its projected polar axis. Lead titanate will form domain engineered structures with properties unlike the other three materials at room temperature.

IV. CONCLUSIONS

Calculations have been made of the longitudinal and transverse piezoelectric coefficients, d_{33}* and d_{31}*, in the six possible domain engineered

structures for rhombohedral PMN-33PT, orthorhombic $KNbO_3$ and tetragonal $BaTiO_3$ at room temperature. The tetragonal (3T) domain engineered structure formed in $BaTiO_3$ by poling along $[111]_C$ has been compared to that of $PbTiO_3$. The main conclusions of this paper are as follows:

Firstly, for all domain engineered structures, d_{31}* is strongly dependent on the choice of the measurement direction x_1' in the plane of the crystal perpendicular to the poling direction x_3', whereas d_{33}* is not. Care is therefore required when cutting a domain engineered crystal for use in the transverse mode.

In general, different variants in a domain engineered structure will contribute *different* values of d_{31}* to that measured. This is never the case for d_{33}* certainly, at least, for the *3m*, *mm2* and *4mm* crystal classes. It follows, that the actual value of d_{31}* measured will be a non-trivial function of the relative proportions of each domain variant. The value of d_{31}* is thus difficult to predict unless the domain structure of the material can be controlled. This problem is avoided completely in $<101>_C$-poled domain engineered structures (2R and 2T) and can be avoided in the $<001>_C$-poled 4R and 4O structures by careful choice of x_1'. In fact, recent work suggests that in some cases (e.g. 3T[27]), it may be possible to avoid undesired variants entirely via careful control of the poling conditions.

A very high value of d_{31}* (-1630 pC/N) is predicted for the 2R domain structure formed by PMN-33PT, via a careful choice of x_1'. Similarly high values have recently been measured experimentally for 2R PMN-30PT[20].

Finally, key differences have been highlighted between the tetragonal phases in $BaTiO_3$ and $PbTiO_3$. Room temperature barium titanate exhibits its largest longitudinal piezoelectric coefficient d_{33}* away from its polar axis as do PMN-33PT and $KNbO_3$. In these materials, polarization rotation is significant upon application of an off- polar axis field, behavior related to their large shear coefficients (d_{15}). In contrast, monodomain $PbTiO_3$ has a low d_{15} and exhibits its maximum d_{33}* along the polar axis. That is, it demonstrates a collinear piezoelectric effect much stronger than the effect of rotation of its polarization, a fact related to the lack of ferroelectric phase transitions in $PbTiO_3$. This property of lead titanate leads to low d_{33}* coefficients in the 3T domain engineered structure and, more surprisingly, positive d_{31}* values that don't occur in the equivalent $BaTiO_3$ structure.

The methodology used can be followed to make similar calculations for domain engineered structures based on other materials; this might be helpful in designing future crystals for use in the transverse piezoelectric mode.

ACKNOWLEDGEMENTS

The authors acknowledge financial support from the Swiss National Science Foundation.

REFERENCES

1 S.-E. E. Park and T. R. Shrout, J. Appl. Phys. **82,** 1804-1811 (1997).
2 A. J. Bell, J. Appl. Phys. **89,** 3907-3914 (2001).

[3] T. Liu and C. S. Lynch, Acta Mater. **51,** 407-416 (2003).
[4] D. Liu and J. Li, Appl. Phys. Lett. **84,** 3930-3932 (2004).
[5] R. Zhang, B. Jiang, and W. Cao, J. Appl. Phys. **90,** 3471-3475 (2001).
[6] J. Yin and W. Cao, J. Appl. Phys. **92,** 444-448 (2002).
[7] H. Dammak, A.-E. Renault, P. Gaucher, M. P. Thi, and G. Calvarin, Jpn. J. Appl. Phys. Pt. 1 **10,** 6477-6482 (2003).
[8] S. Wada, S. Suzuki, T. Noma, T. Suzuki, M. Osada, M. Kakihana, S.-E. Park, L. E. Cross, and T. R. Shrout, Jpn. J. Appl. Phys. Pt. 1 **38,** 5505-5511 (1999).
[9] S. Wada, K. Muraoka, H. Kakemoto, T. Tsurumi, and H. Kumagai, Jpn. J. Appl. Phys. Part 1 **43,** 6692-6700 (2004).
[10] K. Nakamura, T. Tokiwa, and Y. Kawamura, J. Appl. Phys. **91,** 9272-9276 (2002).
[11] R. Zhang, B. Jiang, and W. Cao, Appl. Phys. Lett. **82,** 787-789 (2003).
[12] R. Zhang and W. Cao, Appl. Phys. Lett. **85,** 6380-6382 (2004).
[13] M. Zgonik, P. Bernasconi, M. Duelli, R. Schlesser, P. Günter, M. H. Garrett, D. Rytz, Y. Zhu, and X. Wu, Phys. Rev. B **50,** 5941-5949 (1994).
[14] M. Budimir, D. Damjanovic, and N. Setter, J. Appl. Phys. **94,** 6753-6761 (2003).
[15] R. Zhang, B. Jiang, and W. Cao, Appl. Phys. Lett. **82,** 3737-3739 (2003).
[16] D. Damjanovic, M. Budimir, M. Davis, and N. Setter, Appl. Phys. Lett. **83,** 527-529 (2003).
[17] D. Damjanovic, M. Budimir, M. Davis, and N. Setter, Appl. Phys. Lett. **83,** 2490 (2003).
[18] S. Wada, H. Kakemoto, and T. Tsurumi, Materials Transactions **45,** 178-187 (2004).
[19] V. Y. Topolov, J. Phys.: Condens. Matter **16,** 2115-2128 (2004).
[20] J. Peng, H.-s. Luo, D. Lin, H.-q. Xu, T.-h. He, and W.-q. Jin, Appl. Phys. Lett. **85,** 6221-6223 (2004).
[21] J. F. Nye, *Physical properties of crystals*, 2nd ed. (Clarendon Press, Oxford, 1985).
[22] M. Zgonik, R. Schlesser, I. Biaggio, E. Voit, J. Tscherry, and P. Gunter, J. Appl. Phys. **74,** 1287-1297 (1993).
[23] Z. Li, M. Grimsditch, X. Xu, and S.-K. Chan, Ferroelectrics **141,** 313-325 (1993).
[24] M. J. Haun, E. Furman, S. J. Jang, H. A. McKinstry, and L. E. Cross, J. Appl. Phys. **62,** 3331-3338 (1987).
[25] H. Goldstein, *Classical Mechanics* (Addison-Wesley, Reading, MA, 1978).
[26] H. Fu and R. E. Cohen, Nature **403,** 281-283 (2000).
[27] S. Wada, K. Yako, H. Kakemoto, T. Tsurumi, D. Damjanovic, A. J. Bell, and L. E. Cross, (To be published) (2005).

Appendix V

Correlation between dielectric anisotropy and positive or zero transverse piezoelectric coefficients in perovskite ferroelectric single crystals[1]

The transverse piezoelectric coefficient (d_{31}*) has been calculated for tetragonal barium titanate (BT) and lead titanate (PT) cut along non-polar axes, over a range of temperatures, using phenomenological Landau-Ginzburg-Devonshire theory. It is shown that negative values of d_{31}* are favored when the transverse dielectric susceptibility η_{11} and shear coefficient d_{15} are large, such that polarization rotation is more significant than the collinear piezoelectric effect. This occurs in tetragonal BT close to its ferroelectric-ferroelectric phase transition to an orthorhombic phase. In PT, however, where no phase transition occurs, d_{15} is small and polarization "extension" due to d_{33} dominates: small or positive values of d_{31}* become prominent. This extends a previous result found for polycrystalline modified PT ceramics.

[1] As published in Applied Physics Letters [M. Davis, D. Damjanovic, and N. Setter, Appl. Phys. Lett., **87**, 102904 (2005)]

The recent resurgence of relaxor-ferroelectric single crystals[1,2] (especially (1-*x*)$Pb(Mg_{1/3}Nb_{2/3})O_3$-*x*$PbTiO_3$ [PMN-*x* PT] and (1-x)$Pb(Zn_{1/3}Nb_{2/3})O_3$-*x*$PbTiO_3$ [PZN-*x*PT]) and the concept of "domain engineering[3]" have led to renewed interest in *crystal anisotropy*, that is, the variation of a crystal's properties with its orientation in space[4]. Rhombohedral PMN-xPT and PZN-xPT crystals oriented and poled along a pseudocubic $<001>_C$ direction show longitudinal piezoelectric coefficients d_{33}* around fifteen times larger than that measured along the $<111>_C$ polar axis (the asterisk refers to a measurement away from the polar axis)[5,6].

Large enhancements can similarly be made to the transverse piezoelectric coefficient d_{31} by domain engineering. Monodomain, rhombohedral PMN-33PT exhibits a value of d_{31} = -90 pC/N yet, when oriented and poled along the $[001]_C$ direction[5], the resultant multidomain PMN-33PT exhibits values of d_{31}* as high as -1330 pC/N[6], depending on the choice of length (or vibration) direction (x_1')[7]. Large (negative) values of d_{31}* are exploitable in a variety of flextensional transducers[8], including unimorphs, bimorphs, cymbal actuators[9] and magneto-electric composites[10].

In some cases, however, a small (or ideally zero) transverse coefficient is preferred, for example in array transducers where a large transverse response leads to undesired "cross-talk" between elements. Additionally, a *positive* d_{31} is desired in hydrophones to maximize the hydrostatic piezoelectric coefficient ($d_h = d_{33} + 2d_{31}$). During the 1980s, such small or positive d_{31} coefficients were discovered in modified lead titanate ceramics[11-13]. It was shown[14] that a weak transverse effect in polycrystalline ceramics is a consequence of averaging the piezoelectric response of individual grains and domains. Specifically, for a polycrystalline material to exhibit a low or positive d_{31} it must be weakly anisotropic in its dielectric permittivity, i.e. with a small anisotropy factor $\zeta = \eta_{11}/\eta_{33}$ (η_{11} and η_{33} denote the monodomain dielectric susceptibility perpendicular and parallel to the polar axis).

In this letter we show, within the phenomenological Landau-Ginzburg-Devonshire (LGD) theory[15], that *positive* or zero values of d_{31}* are also possible in monodomain single crystals of tetragonal lead titanate (PT) *and* barium titanate (BT) cut along nonpolar axes. Moreover, positive or zero d_{31}* coefficients in single crystals have the same origin as in ceramics, i.e. in a weak dielectric anisotropy; in BT this is found at high temperatures far away from ferroelectric-ferroelectric phase transitions.

For the present calculations we use the LGD coefficients from references 16 and 3, determined with respect to the prototypic cubic axes (x_i). According to LGD theory[17] the three piezoelectric coefficients of the tetragonal phase with respect to x_i are given by

$$\begin{aligned} d_{33} &= 2\varepsilon_0\eta_{33}Q_{11}P_3 \\ d_{31} &= d_{32} = 2\varepsilon_0\eta_{33}Q_{12}P_3 \\ d_{15} &= d_{24} = \varepsilon_0\eta_{11}Q_{44}P_3 \end{aligned} \qquad [1]$$

where η_{ij} are the dielectric susceptibilities, P_3 is the spontaneous polarization in the tetragonal phase and Q_{ij} are the electrostrictive coefficients in the cubic phase.

To calculate the piezoelectric coefficient in an orientation d_{ij}* away from the polar axis, we make a coordinate transformation to a new system (x_i'). The transformation can be defined in terms of three Euler angles (ϕ,θ,ψ)[18], which refer to anticlockwise rotations about the x_3, the transformed x_1 and the x_3' axes, respectively.

At first we consider a single domain variant in the "3T" domain engineered structure, that formed by poling a tetragonal crystal along $[111]_C$. After poling, three domain variants remain with polarization vectors $[100]_C$, $[010]_C$ and $[001]_C$ equally inclined to the poling direction. We consider the latter domain variant such that the first two Euler angles for this transformation are ϕ = -45° and θ = -54.74°. The third angle ψ is very important to the transverse piezoelectric coefficient d_{31}* as it defines the "length" or "vibration" direction (x_1'). It has been shown elsewhere that d_{31}* is strongly dependent on the choice of x_1' and that different variants in a domain engineered structure can contribute very different values of d_{31}* to the one measured[7].

For a tetragonal crystal the transformed transverse coefficient is given by

$$\begin{aligned} d_{31}^* &= \cos\theta \sin^2\theta \sin^2\psi d_{33} \\ &+ \cos\theta(\cos^2\psi + \cos^2\theta \sin^2\psi) d_{31} \\ &- \cos\theta \sin^2\psi \sin^2\theta d_{15} \end{aligned} \qquad [2]$$

For the 3T domain engineered structure, the relevant Euler angle is θ = -54.77° and the expression becomes:

$$\begin{aligned} d_{31}^* &= \left(2/3\sqrt{3}\right) \sin^2\psi d_{33} \\ &+ \left(1/\sqrt{3}\right)\left(\cos^2\psi + \frac{1}{3}\sin^2\psi\right) d_{31} \\ &- \left(2/3\sqrt{3}\right) \sin^2\psi d_{15} \end{aligned} \qquad [3]$$

d_{31}* is plotted in figure 1 as a function of ψ, for both PT and BT, at a variety of temperatures across the tetragonal phase. (The use of the d_{31}*(ψ) curve in predicting the contribution of the chosen domain variant for a given choice of x_1' is described in detail elsewhere[7]). Regarding figure 1, we see immediate differences between the behaviors of the two materials. For PT, the form of the curve is the same at all temperatures and it is evident that positive values of d_{31}* are favored by higher temperatures. Clearly, positive d_{31}* values are possible in "3T" lead titanate at temperatures above around 100 K. In BT the behavior is different. Positive d_{31}* values are only possible close to the Curie temperature where the form of the curve is the same as for PT. However, as the temperature is decreased negative values of d_{31}* become more prevalent until, at around 370 K, no positive values are seen. At a critical temperature 349 K the form of the curve shifts by 90° such that it now finds its maximum at ψ = 0°. Near the tetragonal-orthorhombic phase transition at 278 K[19] negative values of d_{31}* are favored.

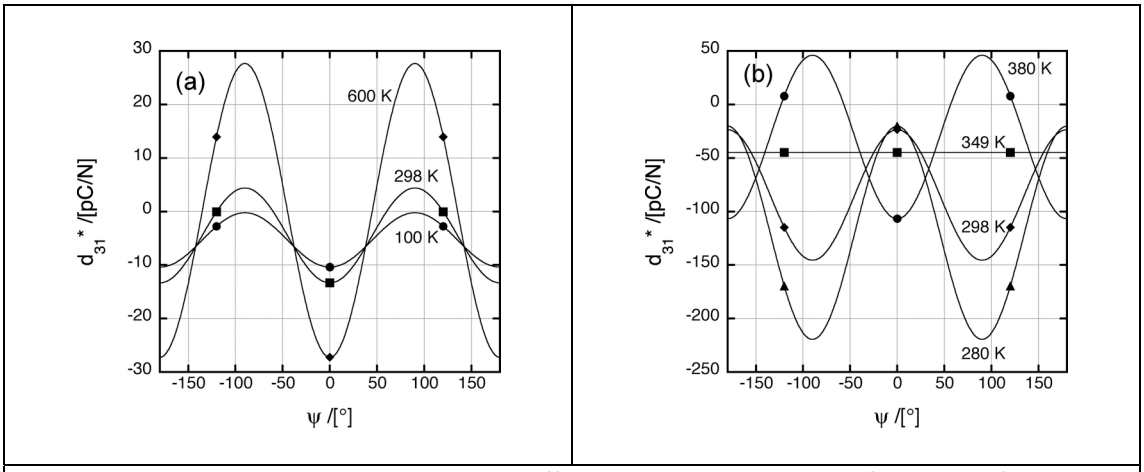

Fig. 1. The transverse piezoelectric coefficient d_{31}* plotted as a function of the third Euler angle ψ for a range of temperatures across the tetragonal phase in (a) lead titanate and (b) barium titanate. The first Euler angle is θ = -54.77° as relevant to the "3T" domain engineered structure formed by poling along a $<111>_C$ direction.

To explain this behavior we consider how the piezoelectric coefficients from equation [1] vary as a function of temperature due to changes in η_{11} and η_{33}. This is shown in figure 2 where d_{33}, d_{31} and d_{15} are plotted for the tetragonal phases of PT and BT. As pointed out by Budimir *et al.*, the presence of a neighboring orthorhombic phase in tetragonal barium titanate is significant[19]. In lead titanate, all three coefficients decay slowly as the temperature is decreased. In barium titanate, however, d_{15} actually increases (with η_{11}) at low temperature, anticipating the phase change. Furthermore, a large shear coefficient d_{15} is directly related to an easy polarization *rotation*[20] when an electric field is applied away from the polar axis. In contrast, a large d_{33} (or η_{33}) is related to an easy *extension* of the polar vector when a field is applied along the axis (the "collinear effect"). Where d_{33} is large in PT, and in BT close to the Curie temperature, the collinear effect dominates the transverse piezoelectric response d_{31}*; when d_{15} becomes significant in BT, polarization rotation dominates.

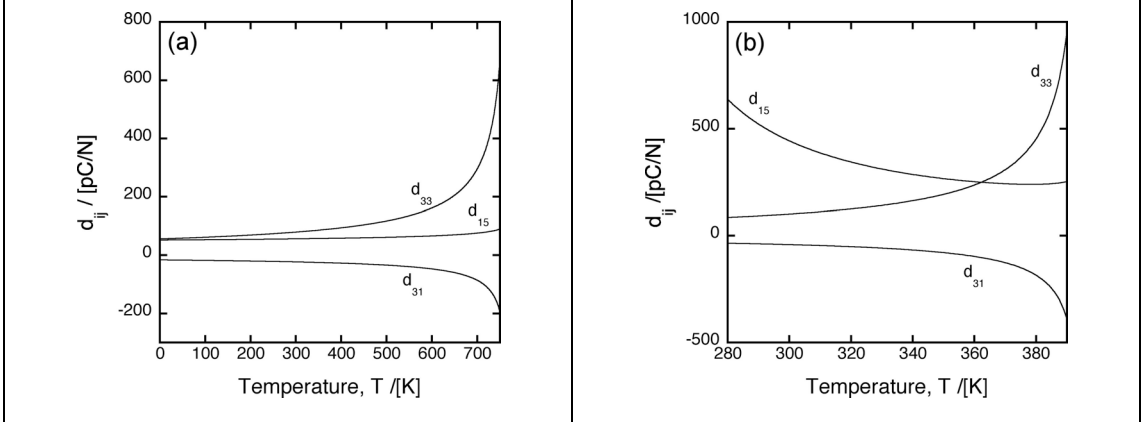

Fig. 2. All three piezoelectric coefficients d_{ij} calculated according to Landau-Ginzburg-Devonshire theory for the tetragonal phases of lead titanate (a) and barium titanate (b).

The varying contributions of d_{33} and d_{15} on d_{31}* can be visualized as follows. Fig. 3(b) shows our single tetragonal monodomain with polar axis x_3 : $[001]_C$ *projected* in the $(111)_C$ "poling plane[7]". Two imaginary d_{31}* bar "resonators" cut from the monodomain crystal *in* the $(111)_C$ plane are also shown with x_1' directions perpendicular and parallel to the projected polar axis, at $\psi = 0°$ and $\psi = \pm 90°$, respectively. For clarity, the $(111)_C$ poling plane of figure 3(b) is shown relative to the tetragonal monodomain in figure 3(a).

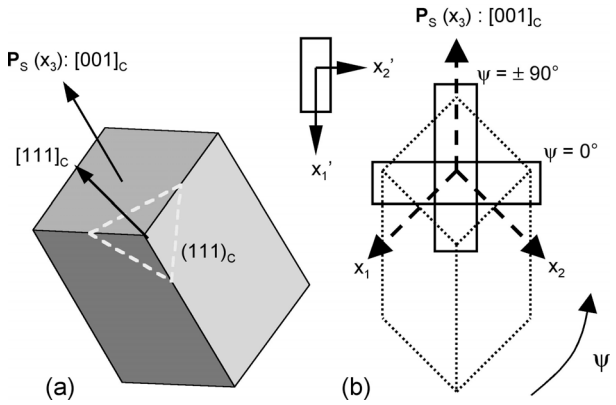

Fig. 3. (a) Schematic illustration of a tetragonal monodomain with its polar axis along $[001]_C$ and its relation to the $(111)_C$ "poling plane" perpendicular to the direction of applied electric field $[111]_C$. (b) Two transverse piezoelectric "bar resonators" cut at right angles to each other *in* the $(111)_C$ poling plane (dark lines); the $[111]_C$ direction is out of plane. The tetragonal monodomain (dotted lines) is also shown *projected* into the poling plane as are its crystal axes x_i (dashed arrows). The "length" direction of the resonator x_1' and the projection of the polar axis x_3 define the angle ψ.

We consider application of an electric field out of the plane of figure 3(b), along $[111]_C$. For the first, perpendicular resonator, rotation or extension of the polar vector will not itself affect the resonator's length. Therefore, application of a field along $[111]_C$ will lead to a contraction of the resonator due to the related effect of the crystal's intrinsic d_{31} alone; equation 3 reduces to $d_{31}^* = d_{31}/\sqrt{3}$ so that $d_{31}^*(\psi = 0°)$ is always negative.

In contrast, for any other ψ, the resonator will pick up conflicting effects from all three coefficients (eq. [3]). The conflict is most pronounced when the resonator is cut parallel to the projected axis ($\psi = \pm 90°$). In BT at lower temperatures, d_{15} is large and the polarization rotation effect dominates. With regard to figure 3(b), application of an electric field along $[111]_C$ will rotate the tetragonal monodomain, and its polar vector $\mathbf{P}_S$, "upwards" out of the plane of the diagram more than it will extend it. The net effect is a shrinkage of the resonator along its length, within the $(111)_C$ plane, so that d_{31}^* is negative at $\psi = \pm 90°$. In contrast, in BT and PT at higher temperatures, d_{33} dominates. The monodomain in figure 3(b) expands along its length more than it rotates and there is a net extension of the resonator: d_{31}^* is thus positive. There is therefore a crossover in behavior for barium titanate at 349 K, very close to the point at which the ratio d_{15}/d_{33} changes sign (360 K, see figure 2(b)). This ratio is correlated with the anisotropy factor ζ (eq. [1]). Positive values of d_{31}^*

are therefore favored by small anisotropy factors, not just only in polycrystalline modified lead titanate, but in 3T domain engineered crystals as well.

The analysis is valid for all values of θ and thus for all monodomain crystals cut along non-polar axes and in multigrain ceramics as well. When $\theta = 0°$, and the monodomain is perpendicular to the plane of figure 3, equation [2] reduces to $d_{31}^* = (\cos^2\psi + \sin^2\psi)\, d_{31}$. However, at *all other* angles of θ there will be competing effects from polarization rotation and the collinear effect. In a tetragonal polycrystalline ceramic there will be a distribution of domains with corresponding Euler angles in the range $0 \le \theta \le 90°$ and $-180° \le \psi \le 180°$. Therefore, small or positive d_{31}^* values will be favored not only in tetragonal lead titanate but, at temperatures away from the orthorhombic phase, in barium titanate ceramics as well. (The trend towards a small transverse coefficient is indeed observed in ceramic BT upon heating[21]).

To conclude, transverse piezoelectric coefficients of tetragonal crystals poled along non-polar directions have been calculated for barium and lead titanate at a range of temperatures, using phenomenological theory. In tetragonal BT, except at high temperatures, d_{15} is large due to the proximity of an orthorhombic phase and a large dielectric anisotropy. Polarization rotation thus dominates its transverse piezoelectric response when an electric field is applied in a non-polar direction, making it negative. In PT, however, where there is no phase transition, d_{33} is the dominant coefficient and polarization extension will dominate the transverse piezoelectric response. Moreover, where polarization extension is the dominant effect due to a weak dielectric anisotropy, there is a propensity for small or *positive* transverse d_{31}^* coefficients in single crystal perovskites oriented in any non-polar direction - the effect is not unique to polycrystalline ceramics nor lead titanate.

The authors acknowledge support from the Swiss National Science Foundation.

REFERENCES

1 S.-E. E. Park and W. Hackenberger, Current Opinion in Solid State and Materials Science **6,** 11-18 (2002).

2 B. Noheda, Current Opinion in Solid State and Materials Science **6,** 27-34 (2002).

3 A. J. Bell, J. Appl. Phys. **89,** 3907-3914 (2001).

4 J. F. Nye, *Physical properties of crystals*, 2nd ed. (Clarendon Press, Oxford, 1985).

5 R. Zhang, B. Jiang, and W. Cao, Appl. Phys. Lett. **82,** 787-789 (2003).

6 R. Zhang, B. Jiang, and W. Cao, J. Appl. Phys. **90,** 3471-3475 (2001).

7 M. Davis, D. Damjanovic, D. Hayem, and N. Setter, J. App. Phys. (2005) (in review).

8 J. Peng, H.-S. Luo, D. Lin, H.-Q. Xu, T.-H. He, and W.-Q. Jin, Appl. Phys. Lett. **85,** 6221-6223 (2004).

9 K.-H. Lam, H. L.-W. Chan, H.-S. Luo, Q.-R. Yin, and C.-L. Choy, Ferroelectrics **263,** 235-240 (2001).

[10] S. Dong, J. F. Li, D. Viehland, J. Cheng, and L. E. Cross, Appl. Phys. Lett. **85,** 3534-3536 (2004).
[11] Y. Yamashita, K. Yokoyama, H. Honda, and T. Takahashi, Jpn. J. Appl. Phys. **20,** 183 (1981).
[12] H. Takeuchi, S. Jyomura, E. Yamamoto, and Y. Ito, J. Acoust. Soc. Am. **72,** 1114 (1982).
[13] D. Damjanovic, T. R. Gururaja, and L. E. Cross, Am. Ceram. Soc. Bull. **66,** 699-703 (1987).
[14] A. V. Turik, E. G. Fesenko, V. G. Gavrilyatchenko, and G. I. Khasabova, Sov. Phys. Crystallogr. **19,** 677-678 (1975).
[15] T. Mitsui, I. Tatsuzaki, and E. Nakamura, *An Introduction to the Physics of Ferroelectrics* (Gordon and Breach, London, 1976).
[16] M. J. Haun, E. Furman, S. J. Jang, H. A. McKinstry, and L. E. Cross, J. Appl. Phys. **62,** 3331-3338 (1987).
[17] D. Damjanovic, F. Brem, and N. Setter, Appl. Phys. Lett. **80,** 652-654 (2002).
[18] H. Goldstein, *Classical Mechanics* (Addison-Wesley, Reading, MA, 1978).
[19] M. Budimir, D. Damjanovic, and N. Setter, J. Appl. Phys. **94,** 6753-6761 (2003).
[20] H. Fu and R. E. Cohen, Nature **403,** 281-283 (2000).
[21] T. A. Perls, T. J. Diesel, and W. I. Dobrov, J. Appl. Phys. **29,** 1297-1302 (1958).

Curriculum Vitae

Matthew Davis
Laboratory of Ceramics, Institute of Materials,
Ecole Polytechnique Fédérale de Lausanne (EPFL),
Lausanne, CH-1015 Switzerland
Tel.: +41 (0)21 693 4956
Fax.: +41 (0)21 693 5810
matthew.davis@epfl.ch

I. PERSONAL DETAILS

Date of birth	21st September 1979
Nationality	British

II. EDUCATION

1998 - 2002	*MSci* and *BA* in Natural Sciences, University of Cambridge, Magdalene College (1st Class Honors, Materials Science and Metallurgy)
1994 - 1998	4 *A-levels* (grade A), 2 *S-levels* (grade I), 9 *GCSEs* (8 at grade A*, 1 at A), Arnold Hill Comprehensive School, Nottingham, UK

III. ACADEMIC AWARDS

Cambridge Corus Scholarships (3rd and 4th years)
Magdalene College Mynors Bright Prize (2001)
Magdalene College Natural Sciences Prize (1999, 2000, 2001)
Department ICI Prize (2002)
Magdalene College Scholarship (1999-2002)

IV. ACADEMIC EXPERIENCE

Nov. 2002 -	Ph.D. student at Laboratory of Ceramics, EPFL, Switzerland
2001 - 2002	Master's thesis: "Application of the FFC-Cambridge process to the production of titanium and zirconium coatings on steel", Materials Chemistry Group, Department of Materials Science and Metallurgy, University of Cambridge
Summer 2001	Ten week internship: Materials failure investigation in high pressure/high temperature vessels used for energy generation, *PowerGen* Technology Center, Nottingham, UK
Summer 2000	Two month student research placement: "Damage mechanisms in aluminum - alumina metal matrix composites", Mechanical Metallurgy Laboratory, EPFL, Switzerland

V. PERSONAL INTERESTS

- Rugby: junior for Arnold Hill School, Nottingham RFC, Nottinghamshire; senior for Magdalene College RFC and Lausanne Université Club. Captain of Magdalene College RFC (2001-2002)
- Travel: Europe (France, Italy, Germany, Switzerland, Croatia), USA (NYC), Canada (Quebec), Africa (Kenya, Tanzania, Morocco, Tunisia), SE Asia (Thailand, Malaysia, Singapore), New Zealand
- Playing the guitar; music in general, especially folk music from the British Isles
- Reading (especially non-fiction), film

VI. LANGUAGES

English (mother tongue)
French (fluent spoken)
German (intermediate knowledge)

List of publications

I. PEER REVIEWED ARTICLES

1. D. Damjanovic, M. Budimir, M. Davis, and N. Setter, "Monodomain versus polydomain piezoelectric response of 0.67Pb($Mg_{1/3}Nb_{2/3}$)O_3-0.33$PbTiO_3$ single crystals along nonpolar directions," *Appl. Phys. Lett.*, vol. 83, pp. 527-529, 2003.

2. M. Davis, D. Damjanovic, and N. Setter, "Direct piezoelectric effect in relaxor-ferroelectric single crystals," *J. Appl. Phys.*, vol. 95, pp. 5679-5684, 2004.

3. M. Davis, D. Damjanovic, and N. Setter, "Pyroelectric properties of (1-x)Pb($Mg_{1/3}Nb_{2/3}$)O_3-x$PbTiO_3$ and (1-x)Pb($Zn_{1/3}Nb_{2/3}$)O_3-x$PbTiO_3$ single crystals measured using a dynamic method," *J. Appl. Phys.*, vol. 96, pp. 2811-2815, 2004.

4. M. Davis, D. Damjanovic, and N. Setter, "Electric-field-induced orthorhombic to rhombohedral phase transition in $[111]_C$-oriented 0.92Pb($Zn_{1/3}Nb_{2/3}$)O_3-0.08$PbTiO_3$," *J. Appl. Phys.*, vol. 97, pp. 064101, 2005.

5. M. Davis, D. Damjanovic, D. Hayem, and N. Setter, "Domain engineering of the transverse piezoelectric coefficient in perovskite ferroelectrics," *J. Appl. Phys.*, vol. 98, pp. 014102, 2005.

6. M. Davis, D. Damjanovic, and N. Setter, "Correlation between dielectric anisotropy and positive or zero transverse piezoelectric coefficients in perovskite ferroelectric single crystals," *Appl. Phys. Lett.*, vol. 87, pp. 102904, 2005.

7. E. Hollenstein, M. Davis, D. Damjanovic, and N. Setter, "Piezoelectric properties of Li- and Ta-modified ($K_{0.5}Na_{0.5}$)NbO_3 ceramics," *Appl. Phys. Lett.*, vol. 87, pp. 182905, 2005.

8. D. Damjanovic, M. Budimir, M. Davis, and N. Setter, "Piezoelectric anisotropy: Enhanced piezoelectric response along nonpolar directions in perovskite crystals," *J. Mat. Sci.*, vol. 41, pp. 65-76, 2006.

9. M. Davis, D. Damjanovic, and N. Setter, "Electric-field-, temperature-, and stress-induced phase transitions in relaxor-ferroelectric single crystals," *Phys. Rev. B*, vol. 73, pp. 014115, 2006.

II. CONFERENCE PROCEEDINGS

1. M. Davis, D. Damjanovic, and N. Setter, "Pyroelectric properties and orthorhombic to rhombohedral electric field induced phase transition in relaxor-ferroelectric single crystals," *Proc. 14th IEEE International Symposium on Applications of Ferroelectrics*, Montreal, Canada, 2004.

2. M. Davis, D. Damjanovic, and N. Setter, "The direct piezoelectric effect in $[001]_C$-poled relaxor-ferroelectric single crystals: contrasting longitudinal and transverse modes," *Proc. 14th IEEE International Symposium on Applications of Ferroelectrics*, Montreal, Canada, 2004.

3. M. Davis, D. Damjanovic, and N. Setter, "Optimization of the transverse piezoelectric coefficient by domain engineering," *Proc. IEEE International Ultrasonics Symposium*, Rotterdam, The Netherlands, 2005.